Burial and exhumation history of the Mackenzie Mountains and Plain, NWT, through integration of low-temperature thermochronometers

Jeremy Powell

Thesis submitted to the
Faculty of Graduate and Postdoctoral Studies
in partial fulfillment of the requirements
for a doctoral degree in Earth Sciences

Department of Earth and Environmental Sciences
Faculty of Science
University of Ottawa

Abstract

The integration of low-temperature thermochronometers, including apatite and zircon (U-Th)/He (AHe, ZHe) and apatite fission-track (AFT) methods, allows for a quantification of the thermal history experienced by rocks as they heat and cool through upper crustal temperature regimes (<200°C). Whereas these methods are practical in geologic terranes that have undergone rapid cooling, application to strata with protracted cooling histories is complicated by the enhanced role of grain-specific parameters (volume, chemistry, radiation damage) on the kinetics of helium diffusion and fission track annealing. The effects of these variables are most prevalent in sedimentary samples, where natural variance in detrital accessory mineral populations results in a broad range of diffusion kinetics and great dispersion in corresponding cooling dates.

This thesis integrates contemporary thermochronometer diffusion and annealing kinetics to investigate the burial and exhumation history of two natural laboratories. In the Mackenzie Mountains and Plain of the Northwest Territories, long-term radiation damage accumulation in zircon from Neoproterozoic siliciclastic units produces ZHe dates that track Albian to Paleocene burial and exhumation in front of the foreland-propagating fold-thrust belt. For the Phanerozoic stratigraphic section, AFT annealing kinetics are calculated from Devonian and Cretaceous samples, and are incorporated into multi-kinetic AFT modeling. These kinetics also constrain AHe date-radiation damage trends, and when combined allow for an estimation on the magnitude of eroded sediment across regional pre-Albian and post-Paleocene unconformities. Finally, conodont (U-Th)/He data from Anticosti Island, Québec in the Gulf of the St. Lawrence, are compared with ZHe, AHe and AFT data to test their utility as a thermochronometer for carbonate basin analysis. These data evince a Mesozoic thermal history previously unattributed to the region. Ultimately, this thesis provides a novel assessment on the ways in which

thermochronometer date dispersion can be quantified to assess the thermal evolution of sedimentary basins from burial through to inversion.

Résumé

L'intégration de thermochronomètres à basse température tels les méthodes (U-Th)/He avec apatite et zircon (AHe, ZHe) et les traces de fission dans l'apatite (TFA) permet la quantification de l'histoire thermique des roches lorsque leur température a augmenté ou diminué dans la croûte supérieure (<200°C). Tandis que ces méthodes sont utiles dans les terranes ayant subi un refroidissement rapide, leurs applications pour les strates ayant subi un refroidissement prolongé est compliqué par l'effet rehaussé des paramètres spécifiques aux grains (volume, composition chimique, détérioration causée par radiation) sur la diffusion d'hélium et le recuit des traces de fission. L'effet de ces variables est important dans les échantillons sédimentaires, où la variance naturelle en minéraux accessoires détritiques résulte en une grande variation en termes de cinétique de diffusion, et par conséquent une grande dispersion en âges de refroidissement.

Cette thèse applique des modèles de diffusion et recuit de thermochronomètres pour résoudre l'histoire d'enfouissement et d'exhumation de deux laboratoires naturels. Dans les monts Mackenzie et la Plaine des Territoires du Nord-Ouest, l'accumulation à long-terme de la détérioration par radiation des zircons d'unités siliciclastiques néoprotérozoïques produit des âges ZHe qui révèlent une histoire d'enfouissement et exhumation de l'Albien au Paléocène de la propagation vers l'avant-pays de la chaîne plissée. Pour la section stratigraphique phanérozoïque, la cinétique de recuit des TFA est calculée pour les échantillons du Dévonien et Crétacé, et sont incorporés dans des modèles de TFA multi-cinétiques. La cinétique de recuit calculée pour

chaque échantillon donne aussi des contraintes pour la relation entre l'âge et la détérioration par radioactivité. Ensemble, ces modèles réussissent à estimer la magnitude de sédiments érodés des non-conformités pré-albiennes et post-paléocènes. Finalement, des résultats (U-Th)/He de l'île d'Anticosti, Québec, dans le golfe du St. Laurent, sont comparés avec les résultats ZHe, AHe et AFT afin de tester l'utilité de ces thermochronomètres pour l'analyse de bassins carbonatés. Ces résultats démontrent une histoire thermique du Mésozoïque qui n'était pas attribuée à cette région auparavant. En fin de compte, cette thèse démontre une nouvelle évaluation des façons dont la dispersion d'âge des thermochronomètres peut être quantifiée afin d'évaluer l'évolution thermique des bassins sédimentaires de l'enfouissement jusqu'à l'inversion tectonique.

Acknowledgments

This thesis marks 5 years of scientific, professional and personal growth in my life. I am so very fortunate that I've had the opportunity to meet and learn from many incredible people, and am grateful for their contributed time, knowledge and unwavering support and enthusiasm.

Foremost, I thank my supervisor, David Schneider, who has been instrumental in the success of this project. Dave has been an overwhelmingly positive force, and has been equal parts patient, knowledgeable, curious and excited throughout the duration of my studies. He's been nothing but supportive of me trying new techniques and actively pushed me to collaborate with other researchers at home and abroad. Thank you for helping me find the confidence needed to grow as a scientist and human.

I thank Dale Issler for his mentorship. Dale has been incredibly accessible, and has spent hours instructing me on the science behind apatite fission-track analysis and numerical thermal history modeling. Additionally, he has very generously provided me access to his proprietary software for modeling of apatite fission track and organic thermal maturity data.

I am very grateful to Danny Stockli and his team at the Jackson School of Geoscience UTChron labs who were instrumental in data acquisition. Danny welcomed me into his workgroup on many occasions and has been a great source of expertise and advice. I'd also like to thank Roman Kislitsyn, who guided me through my (U-Th)/He analysis from mineral picking through to ICP-MS analysis.

I extend a thank you to the many collaborators who were part of our TAFFEE consortium. These include our partners at the Geological Survey of Canada, who graciously welcomed us to their field expedition in 2011 and provided us with analytical and scientific support in the years since. Particularly, I'd like to extend a major thank you to Karen Fallas and Robert MacNaughton. Karen has been a continual source of expertise on the regional geology of the Mackenzie Corridor and Rob was extremely accommodating with project logistics.

I am grateful to the TAFFEE consortium industry partners ConocoPhillips Canada and Chevron Canada who provided me with continual scientific support and access to many of their resources. A special thank you to Justin MacDonald and Trevor Gray for their enthusiasm and support for my research.

I'd also like to acknowledge the support of other TAFFEE colleagues, including Isabelle Coutand and Bertha Louis at Dalhousie University for their help with mineral separation, Katelyn Breker who a subset of my zircon (U-Th)/He data as part of her B.Sc thesis, and Bernard Guest and his team at University of Calagary's CPAT laboratory for ongoing discussions and access to their mineral picking laboratory.

Thank you to the various agencies that have funded this research. These include the Natural Sciences and Engineering Research Council of Canada (NSERC) who for have granted NSERC awards to the TAFFEE consortium (Collaborative Research and Development), Dr. Schneider (Discovery), and myself (PGSD). I've also been lucky to receive funding from other agencies,

including the Ontario Graduate Scholarship, Government of Canada RAP program, and the Geological Society of America.

I thank Glenn Poirier of the Canadian Museum of Nature for his instruction and assistance on the SEM and electron microprobe.

Thanks are extended to Ray Donelick and his team at Apatite to Zircon Inc. who conducted our AFTA. A special thank you to Paul O'Sullivan who performed the fission track counting and who kindly answered my many questions.

I am grateful to Richard Ketcham at the Jackson School of Geoscience, UTAustin who wrote many of the computer programs I used for this project (HeFTy, Blob3D) and kindly provided me with copies of his updated software prior to their public release.

I thank Matthew Heizler from New Mexico Tech, and Nancy Joyce and Dawn Kellett from the Geological Survey of Canada for assistance with $^{40}Ar/^{39}Ar$ data collection.

My conodont project benefited greatly from the contributions of many colleagues. I thank Andre Desrochers for his help with sampling and continued guidance on Anticosti Island geology. I greatly appreciate Alyssa Bancroft's efforts separating conodonts, and Stephen Leslie for sending me examples of Ordovician conodonts. I am very grateful to Fred Gaidies for his help in acquiring x-ray micro-computed tomography images. I'd also like to thank Becky Flowers, Jim Metcalfe and Rachel Landman at UCBoulder with whom I collaborated on a separate conodont (U-Th)/He project.

Chapters 2 and 3 benefitted greatly from the thorough reviews of William Guenthner, Cecile Gautheron, Richard Ketcham, Sam Johnstone and one anonymous reviewer.

A very special thank you to all of my friends from the OCGC – Travis M., Erin A., Shamus D., Colter K., Chris B., Jamie C., Seamus M., Tom C., John. J., Mike P., Lindsay C., Mary D., David D., Matt H., Diane S., Justin E., Anne W., Jacob N., Rebecca H., and Derek. M. Between coffees, beers, ISWANs and AESRCs you've all helped make these years the best of my life.

I am so thankful to have such a wonderful family who are endlessly encouraging and supportive of my studies and who have patiently nodded their heads and pretended to know what it is I study all of this time. I am very excited to have more time to spend with you all.

Finally, my most heartfelt thank you to my wonderful girlfriend, Stacey Wetmore, who has been so incredibly supportive (and tremendously patient…) over these last *many* years. I can't imagine having gone through this without you.

Table of Contents

Chapter 1. Introduction 1
References 8
Figures 12

Chapter 2. Zircon (U-Th)/He thermochronology of Neoproterozoic strata from the Mackenzie Mountains, Canada: implications for the Phanerozoic exhumation and deformation history of the northern Canadian Cordillera 14
Abstract 15
1. Introduction 16
2. Geological Setting 18
2.1. Stratigraphy 18
2.2. Structure 21
3. Previous Work 23
4. Methods and Results 25
4.1. Sampling strategy 25
4.2. Muscovite $^{40}Ar/^{39}Ar$ geochronology 27
4.3. Muscovite $^{40}Ar/^{39}Ar$ results 28
4.4. Zircon (U-Th)/He thermochronology 29
4.5. Zircon (U-Th)/He results 32
5. Numerical Modeling 34
5.1. HeFTy modeling results and interpretations 38
6. Discussion 43
6.1. Neoproterozoic sources of the Mackenzie Mountains 43
6.2. Utility of reset and partially reset zircon (U-Th)/He dates 45
6.3. Phanerozoic evolution of the Mackenzie Mountains 48
6.4. Regional geodynamic implications 53
7. Conclusions 55
Acknowledgments 57
References 57
Tables 67
Figures 70
Appendix 81

Chapter 3. Application of multi-kinetic apatite fission track and (U-Th)/He thermochronology to source rock thermal history: A case study from the Mackenzie Plain, NWT, Canada 111
Abstract 112
1. Introduction 113
2. Geological Setting 114
2.1. Cretaceous stratigraphy of the Mackenzie Plain 114
2.2. Source rock potential of the Slater River Formation 115
3. Methods and Results 116
3.1. Apatite geochemistry 116
3.2. Apatite fission track thermochronology 117

3.3. Apatite (U-Th)/He thermochronology 121
4. Thermal History Modeling 122
4.1. AFT inverse thermal history modeling 122
4.2. AHe and AFT inverse thermal history modeling 124
5. Discussion 127
5.1. Multiple populations as indicated by r_{mr0} 127
5.2. Comparison of kinetic parameters D_{par} and r_{mr0} 128
5.3. Implications of kinetic parameter r_{mr0} for the AHe system 130
5.4. Elemental measurements for r_{mr0} 131
5.5. Slater River Formation burial history and petroleum potential 133
6. Conclusions 134
Acknowledgments 136
References 136
Figures 141
Appendix 152

Chapter 4. Thermal history of the Mackenzie Plain, NWT, Canada: insights from low-temperature thermochronology of the Devonian Imperial Formation 171
Abstract 172
1. Introduction 173
2. Geological Setting 174
2.1. Stratigraphy 174
2.2. Structural geology 176
2.3. Thermal history and petroleum potential 177
3. Methods and Results 178
3.1. Apatite and zircon (U-Th)/He 178
3.2. Apatite fission-track thermochronology 180
4. Thermal History Modeling 183
4.1. ZHe thermal history modeling 183
4.2. AFT thermal history modeling 185
4.3. AHe thermal history modeling 188
5. Discussion 192
5.1. Low temperature thermochronology of sedimentary basins 192
5.2. Application of thermal models to Mackenzie Plain burial history 194
5.3. Implications for Mackenzie Plain unroofing history and petroleum systems 199
6. Conclusions 202
Acknowledgments 203
References 204
Tables 211
Figures 213
Appendix 224

Chapter 5. Low-temperature thermochronology of Anticosti Island: a case study on the application of conodont (U-Th)/He thermochronology to carbonate basin analysis 262
Abstract 263

1. Introduction....264
2. Regional Geology....265
3. Conodont Bioapatite....268
4. Methods and Results....270
4.1. Sampling and separation....270
4.2. AFT thermochronology....271
4.3. AHe and ZHe thermochronology....273
4.4. CAHe thermochronology....275
5. Thermal History Modeling....277
5.1. AFT, AHe, ZHe modeling....278
5.2. CAHe forward modeling....280
6. Discussion....282
6.1. CAHe dispersion....282
6.2. Precambrian cooling history of Anticosti Island....286
6.3. Anticosti Basin thermal history....286
6.4. Implications for petroleum systems....289
6.5. Thermochronology in carbonate basins....289
7. Conclusions....290
Acknowledgments....292
References....292
Tables....299
Figures....303
Appendix....314

Chapter 6. Conclusions....337
6.1. Unroofing and uplift history of the northern Canadian Cordillera foreland fold-thrust belt....338
6.2. Burial history of the hydrocarbon-bearing Mackenzie Plain....340
6.3. Implications for low-temperature thermochronology....343
6.3. Future work....346
References....347
Figures....351

CHAPTER 1

Introduction

This thesis builds on almost 50 years of regional geologic exploration into the tectonic, structural and stratigraphic evolution of the northern Canadian Cordillera: whereas older studies, such as the Geological Survey of Canada's Operation Norman [*Cook and Aitken*, 1971], focused on reconnaissance mapping at the 1:250,000 or 1:500,000 scale, more recent mapping operations have incorporated these historic data with modern outcrop studies to produce 1:100,000 maps that update paleogeographic and tectonic interpretations [*Fallas et al.*, 2015]. Likewise, many reconnaissance-scale lithostratigraphic interpretations [*Aitken et al.*, 1973] have been substantially revised by detailed outcrop-scale studies of sedimentary depositional facies and structure [e.g. *Long and Turner*, 2012]. In that spirit, the thermochronology data presented in this study probes the Mackenzie Mountains and Plain at an even finer scale, using radioactive accessory minerals to elucidate protracted histories of sedimentary burial and basin inversion from the rock record (Fig. 1).

This study also comes at an interesting crossroad in the field of thermochronology. Prior to initial data collection in 2012, apatite and zircon (U-Th)/He thermochronology (AHe, ZHe) was mostly interpreted on the basis of the closure temperature concept [*Dodson*, 1973], in which the measured date represented the time that the mineral cooled through a specified isotherm (ZHe = 180 °C; AHe = 60 °C). At the time, it was standard to analyze few (n: 4) grains per sample and average the results into a single cooling date. As a result, thermochronology studies had limited utility in terranes that did not meet assumptions of the closure temperature model (rapid, monotonic cooling) [*Reiners and Brandon*, 2006]. Additionally, diffusion models that accounted for the effect of radiation damage accumulation and annealing in the apatite (U-Th)/He system [*Flowers et al.*, 2009; *Gautheron et al.*, 2009] had only just been published and

were not commonly invoked in the literature. A similar diffusion model for the zircon (U-Th)/He system would not be published for another four years [*Guenthner et al.*, 2013]. The chapters that compose this thesis are some of the first studies to analyze a high "n" (grains) per sample and use contemporary diffusion and annealing kinetics to explain the observed intrasample thermochronometer date dispersion. As a result, it provides a novel assessment on the present-day utility, and problems, associated with the application of thermochronology to sedimentary basin analysis.

The Mackenzie Mountains of the Northwest Territories denote the northern extent of the Canadian Cordilleran Foreland Belt, and formed as a result of Late Cretaceous to early Tertiary compression. Its structural style is dominated by broad anticlines that are cored by Neoproterooic strata, with Paleozoic strata preserved in the narrow synclines [*Gordey et al.*, 2011]. In the low-relief Mackenzie Plain to the north, Neoproterozoic and Paleozoic strata are buried under a shallow Cretaceous to Paleocene foreland basin [*Hadlari et al.*, 2014]. Overall, the Mackenzie Mountains and Plain mark a structural transition from highly deformed strata of the Cordilleran Omineca belt in the hinterland to the relatively undeformed northern Interior Plains to the north [*Gabrielse*, 1991; *Hyndman et al.*, 2005]. Several episodes of deformation have affected the region since the Neoproterozoic, with episodic burial and unroofing resulting in regional Cryogenian, sub-Cambrian, mid-Silurian, sub-Albian, sub-Cenomanian and post-Paleocene unconformities in the Neoproterozoic-Paleocene sedimentary succession [*Jefferson and Parrish*, 1989; *Maclean and Cook*, 1999].

The two main objectives of this thesis involve using quantitative thermochronology to evaluate 1) the unroofing and uplift history of the Mackenzie Mountains fold-thrust belt, and 2) the burial history of the hydrocarbon-bearing Mackenzie Plain. Tangentially, the thesis strives to

investigate novel ways in which thermochronology can be applied to both siliciclastic and carbonate strata. The four chapters presented herein are independent works that are connected thematically by the objectives outlined above.

Constraining the spatiotemporal evolution of the Mackenzie Mountains fold-thrust belt has long been a challenge due to the scarcity of dateable syn-tectonic strata and absence of a magmatic record. In general, the timing of deformation is loosely constrained by an outlier of folded Lower Cretaceous strata in southwest of the fold-thrust belt [*Blusson*, 1971] and deformed Paleocene strata in the Mackenzie Plain [*Aitken et al.*, 1982]. Consequently, the kinematic connection between the timing of Cordilleran tectonic events in the hinterland, including accretion of the Yukon-Tanana terrane and exhumation of the Selwyn Basin, and the final Late Cretaceous-Cenozoic evolution of the Mackenzie Mountains remains enigmatic.

Chapter 2 presents the results of a ZHe study that investigates the timing of exhumation across the fold-thrust belt. For Chapter 2, 15 samples were collected from Neoproterozoic strata that occupy the cores of anticlines. Of these 15 samples, 13 were analyzed for ZHe and 5 contained sufficient mica for detrital muscovite $^{40}Ar/^{39}Ar$ dating. The results presented in the chapter contribute significantly to the regional understanding of the Mackenzie Mountains. Notably, $^{40}Ar/^{39}Ar$ dates refine Neoproterozoic depositional ages, whereas ZHe dates detail the cooling history of individual structures along the fold-thrust belt. Chapter 2 is among the first studies to apply the zircon radiation damage and annealing model (ZRDAAM) [*Guenthner et al.*, 2013] to a suite of natural zircon, and as a result the dataset tests the rigours of the ZRDAAM against detrital zircon populations that have been accumulating radiation damage from the Neoproterozoic through to the Recent. This chapter was published in the journal *Tectonics* [*Powell et al.*, 2016], and includes a subset of $^{40}Ar/^{39}Ar$ data previously reported in a Current

Research report prepared for the Geological Survey of Canada [*Powell and Schneider*, 2013]. In addition to the supervision and guidance provide by David Schneider, the main co-author contributions include: assistance on regional geology and kinematic relationships from Karen Fallas, and laboratory assistance and advice on numerical modeling by Daniel Stockli.

Given that over 200 million barrels of oil have been recovered from the prolific Norman Wells oil field [*Hadlari*, 2015] it is plausible that other petroleum systems exist throughout the Phanerozoic stratigraphy that occupy the Mackenzie Plain [*Hannigan et al.*, 2011]. Probable source rocks for these systems include a number of aerially extensive organic-rich shales, such as units within the Devonian Horn River Group and the Late Cretaceous Slater River Formation [*Feinstein et al.*, 1988]. In modern times, discoveries of natural gas in two wells from the eastern edge of the Mackenzie Mountains [*Hannigan et al.*, 2011] has fuelled a new wave of interest in the Mackenzie Plain generating $2.3B in work commitments over the course of three land sales from 2011 – 2013 [*INAC*, 2013]. However, a major uncertainty for regional hydrocarbon prospectivity concerns the timing of hydrocarbon generation. An understanding of when Devonian source rocks reached maximum paleotemperatures is confounded by regional sub-Albian and post-Paleocene unconformities, as unknown amounts of material may have been deposited and eroded during these times [*Issler et al.*, 2005]. Whereas studies of organic thermal maturity and shale compaction have suggested maximum burial in the Paleocene [*Feinstein et al.*, 1991, 1996], apatite fission track (AFT) modeling results from the only other thermochronology study for the region [*Issler et al.*, 2005] advocated for a pre-Albian thermal maximum. Chapters 3 and 4 integrate low-temperature thermochronometers from Devonian and Cretaceous samples to investigate the relative magnitude of these thermal events.

In Chapter 3, apatite grains from a bentonite unit at the base of the Slater River Formation are analyzed for AFT and AHe thermochronology. Both LA-ICP-MS and EPMA are used to collect apatite chemistry from individual grains, and these data are in turn used to calculate the annealing parameter r_{mr0}. Derived r_{mr0} values are used to distinguish separate kinetic AFT populations and are incorporated into multi-kinetic thermal history modeling. The results have significant ramifications for modeling of partially annealed AFT samples, as well as AHe data that have undergone slow heating and cooling at relatively low temperatures. Additionally, Chapter 3 provides a framework to understand the more comprehensive study detailed in Chapter 4. This work is in press at *Basin Research* [*Powell et al.*, 2017]. Co-author contributions include guidance and supervision from David Schneider, and assistance with stoichiometric calculations of apatite chemistry and guidance on AFT modeling software from Dale Issler.

Chapter 4 combines many elements introduced in Chapters 2 and 3 (inherited radiation damage; multi-kinetic fission track modeling) to investigate the burial history of Devonian Imperial Formation samples from the Mackenzie Mountain front, the Imperial Anticline and the Norman Range. The Imperial Formation is an excellent natural laboratory for low-temperature thermochronology, as it has experienced a multi-phase burial and cooling history to temperatures that span the apatite fission track partial annealing zone. The temperature sensitivity of techniques used in this study are such that the models in Chapter 4 detail both the Devonian to Albian and Cretaceous to present burial and unroofing histories. Thermal histories derived from outcrop samples are ground truthed with organic thermal maturity profiles from proximal hydrocarbon exploration wells. The results of Chapter 4 are important as it: 1) suggests that Devonian source rocks in the Mackenzie Plain reached peak thermal maturity during the Paleozoic to early Mesozoic; 2) tests the rigour of the new basin%Ro vitrinite reflectance model

[*Nielsen et al.*, 2015] in comparison with the earlier EASY%Ro model [*Sweeney and Burnham*, 1990]; 3) extracts t-T information from the relationship between AHe date dispersion and the observed variation in AFT annealing kinetics. This work has been submitted for review to *Chemical Geology*. In addition to David Schneider's supervision, co-author contributions are as follows: Dale Issler provided the AFT data, chemistry and thermal history modeling for the Husky7 sample. He also provided guidance in kinetic population identification, thermal history modeling with the software AFTINV [*Issler*, 1996] and assisted with interpretation of the 10FNARL008 sample; Karen Fallas provided critical review on the implications of these data on regional geologic interpretation; Daniel Stockli aided in data collection and provided advice on numerical modeling of apatite (U-Th)/He data. This chapter references detrital muscovite $^{40}Ar/^{39}Ar$ dates from the Imperial Formation that were published in a separate Geological Survey of Canada Current Research document [*Powell and Schneider*, 2013].

One of the complications of a thermochronology study in the carbonate-dominated northern Canadian Cordillera is the dearth of strata with sufficient accessory minerals for analysis (igneous intrusions, metamorphic and siliciclastic rocks). As a result, sampling in Chapters 2 to 4 was restricted to the few Neoproterozoic to Paleozoic siliciclastic horizons present across the Mackenzie Mountains. No apatite was recovered from any of the Neoproterozoic strata, potentially due to the long distance source-to-sink pathways of the detritus [*Rainbird et al.*, 1997], and apatite grains from the Devonian Imperial Formation samples were often too small to analyze [*Farley*, 2002]. As a result of these sampling issues, a tertiary project was designed to assess the applicability of conodont apatite (U-Th)/He thermochronology [*Peppe and Reiners*, 2007; *Landman et al.*, 2016] to resolving the cooling history of carbonate strata (Chapter 5).

Chapter 5 reports an empirical test of helium diffusion in the conodont (U-Th)/He thermochronometer that was conducted to determine the applicability of the method to carbonates from the Mackenzie Mountains and Plain. This study investigates the effect of increasing present-day and paleo-temperatures on observed conodont (U-Th)/He dates of subsurface samples collected from two wells in Anticosti Island, Québec (Fig. 2). Ordovician to Silurian carbonate rocks that outcrop on Anticosti Island are the eastern continuation of the St. Lawrence platform and record the depositional transition between passive and active margin carbonates during the opening and closing of the Iapetus Ocean [*Desrochers et al.*, 2012]. Conodont (U-Th)/He dates are compared with AFT, AHe and ZHe data from the Grenvillian basement, and AHe data from an Ordovician sandstone. The results of Chapter 5 are significant as it: 1) highlights the complexities of helium diffusion through porous bioapatite; and 2) elucidates a Mesozoic thermal history not previously attributed to the St. Lawrence Platform in the Gulf of the St. Lawrence. Indeed, the results presented in this work invoke far-field influences of the Mesozoic opening of the Atlantic Ocean, and are sure to change how future studies model the evolution of the Anticosti Basin. Chapter 5 has been submitted for review to *Marine and Petroleum Geology*. In addition to the guidance and support of David Schneider, co-author contributions are as follows: André Desrochers provided assistance with project sampling and guidance on regional geologic history; Rebecca Flowers and James Metcalf provided analytical assistance and critical review on the conodont (U-Th)/He system; Fred Gaidies assisted with X-ray micro-computed tomography data collection and reduction.

References

Aitken, J. D., R. W. Macqueen, and J. L. Usher (1973), Reconaissance studies of Proterozoic and Cambrian stratigraphy, lower Mackenzie River area (Operation Norman), District of Mackenzie, *Geol. Surv. Canada Pap. 73-9*, 178 p.

Aitken, J. D., Cook. D. G., and C. J. Yorath (1982), Upper Ramparts River (106 G) and Sans

Sault Rapids (106 H) map areas, district of Mackenzie, *Geol. Surv. Canada, Mem.*, *388*, 48 p.

Blusson, S. (1971), Sekwi Mountain map-area, Yukon Territory and district of Mackenzie, *Geol. Surv. Canada, Pap. 71-22*, 17 p.

Chi, G., D. Lavoie, R. Bertrand, and M.-K. Lee (2010), Downward hydrocarbon migration predicted from numerical modeling of fluid overpressure in the Paleozoic Anticosti Basin, eastern Canada, *Geofluids*, *10*(3), 334–350, doi:10.1111/j.1468-8123.2010.00280.x.

Cook, D. G., and J. D. Aitken (1971), Operation Norman, District of Mackenzie (86D, E, L, M; 87B, C; 96; 97A, B, C, D, F; 106A, B, G, H, I, J, O, P; 107A, D, E)., *Geol. Surv. Canada, Pap. 71-1A*, 197–201, doi:10.4095/119853.

Desrochers, A., P. Brennan-Alpert, D. Lavoie, and G. Chi (2012), Regional stratigraphic, depositional and diagenetic patterns of the interior of St. Lawrence Platform: the Lower Ordovician Romain Formation, Western Anticosti Basin, Quebec, in *The great American carbonate bank: The geology of economic resources of the Cambrian - Ordovician Sauk meagasequence of Laurentia: AAPG Memoir 98*, vol. 98, edited by J. R. Derby, R. D. Fritz, S. A. Longacre, W. A. Morgan, and C. A. Sternbach, pp. 525–543.

Dodson, M. H. (1973), Closure temperature in cooling geochronological and petrological systems, *Contrib. to Mineral. Petrol.*, *40*(3), 259–274.

Fallas, K. M., R. B. MacNaughton, and M. J. Sommers (2015), Maximizing the value of historical bedrock field observations: An example from northwest Canada, *GeoResJ*, *6*, 30–43, doi:10.1016/j.grj.2015.01.004.

Farley, K. A. (2002), (U-Th)/He Dating: Techniques, Calibrations, and Applications, *Rev. Mineral. Geochemistry*, *47*(1), 819–844, doi:10.2138/rmg.2002.47.18.

Feinstein, S., P. W. Brooks, M. G. Fowler, L. R. Snowdon, and G. K. Williams (1988), Families of oils and source rocks in the central Mackenzie corridor: a geochemical oil-oil and oil-source rock correlation, *Can. Soc. Pet. Geol. Mem.*, *15*, 543–552.

Feinstein, S., G. K. Williams, L. R. Snowdon, F. Goodarzi, and T. Gentzis (1991), Thermal maturation of organic matter in the Middle Devonian to Tertiary section, Fort Norman area (central Mackenzie Plain), *Can. J. Earth Sci.*, *28*(7), 1009–1018, doi:10.1139/e91-092.

Feinstein, S., D. R. Issler, L. R. Snowdon, and G. K. Williams (1996), Characterization of major unconformities by paleothermometric and paleobarometric methods: application to the Mackenzie Plain, Northwest Territories, Canada, *Bull. Can. Pet. Geol.*, *44*(1), 55–71.

Flowers, R. M., R. A. Ketcham, D. L. Shuster, and K. A. Farley (2009), Apatite (U-Th)/He thermochronometry using a radiation damage accumulation and annealing model, *Geochim. Cosmochim. Acta*, *73*(8), 2347–2365, doi:10.1016/j.gca.2009.01.015.

Gabrielse, H. (1991), Structural Styles, in *Geology of the Cordilleran Orogen in Canada*, edited by H. Gabrielse and C. J. Yorath, pp. 571 – 675, Geological Survey of Canada, Geology of Canada, no. 4.

Gautheron, C., L. Tassan-Got, J. Barbarand, and M. Pagel (2009), Effect of alpha-damage annealing on apatite (U-Th)/He thermochronology, *Chem. Geol.*, *266*(3-4), 166–179, doi:10.1016/j.chemgeo.2009.06.001.

Gordey, S. P., J. D. Macdonald, E. C. Turner, and D. G. F. Long (2011), Chapter 5. Structural Geology of the Central Mackenzie Mountains, in *Geology of the Central Mackenzie Mountains of the Northern Canadian Cordillera, Sekwi Mountain (105P), Mount Eduni (106A), and the northwestern Wrigley Lake (95M) Map Areas, Northwest Territories*, edited by E. Martel, E. C. Turner, and B. J. Fischer, pp. 215 – 250, NWT Geoscience Office.

Guenthner, W. R., P. W. Reiners, R. A. Ketcham, L. Nasdala, and G. Giester (2013), Helium diffusion in natural zircon: Radiation damage, anisotropy, and the interpretation of zircon (U-Th)/He thermochronology, *Am. J. Sci.*, *313*(3), 145–198, doi:10.2475/03.2013.01.

Hadlari, T. (2015), Oil migration driven by exhumation of the Canol Formation oil shale: A new conceptual model for the Norman Wells oil field, northwestern Canada, *Mar. Pet. Geol.*, *65*, 172–177, doi:10.1016/j.marpetgeo.2015.03.027.

Hadlari, T., B. C. MacLean, J. M. Galloway, A. R. Sweet, J. M. White, D. Thomson, J. Gabites, and C. J. Schröder-Adams (2014), The flexural margin, the foredeep, and the orogenic margin of a northern Cordilleran foreland basin: Cretaceous tectonostratigraphy and detrital zircon provenance, northwestern Canada, *Mar. Pet. Geol.*, *57*, 173–186, doi:10.1016/j.marpetgeo.2014.05.019.

Hannigan, P. K., D. W. Morrow, and B. C. MacLean (2011), Petroleum resource potential of the northern mainland of Canada (Mackenzie Corridor), *Geol. Surv. Canada, Open File 6757*, 271 p., doi:289095.

Hyndman, R. D., P. Flück, S. Mazzotti, T. J. Lewis, J. Ristau, and L. Leonard (2005), Current tectonics of the northern Canadian Cordillera, *Can. J. Earth Sci.*, *42*(6), 1117–1136, doi:10.1139/e05-023.

INAC (2013), Central Mackenzie Valley, *Indig. North. Aff. Canada North, North. Pet. Resour.* Available from: https://www.aadnc-aandc.gc.ca/eng/1100100036430/1100100036431

Issler, D. R. (1996), An inverse model for extracting thermal histories from apatite fission track data: instructions and software for the Windows 95 environment, *Geol. Surv. Canada, Open File 2325*, 85 p.

Issler, D. R. D., A. Grist, and L. Stasiuk (2005), Post-Early Devonian thermal constraints on hydrocarbon source rock maturation in the Keele Tectonic Zone, Tulita area, NWT, Canada, from multi-kinetic apatite fission track thermochronology, vitrinite reflectance and shale compaction, *Bull. Can. Pet. Geol.*, *53*(4), 405–431, doi:10.2113/53.4.405.

Jefferson, C. W., and R. R. Parrish (1989), Late Proterozoic Stratigraphy, U-Pb Zircon Ages, and Rift Tectonics, Mackenzie Mountains, Northwestern Canada, *Can. J. Earth Sci.*, *26*, 1784 – 1801.

Landman, R. L., R. M. Flowers, N. A. Rosenau, and J. Powell (2016), Conodont (U-Th)/He thermochronology: A case study from the Illinois Basin, *Earth Planet. Sci. Lett.*, *456*, 55–65, doi:10.1016/j.epsl.2016.10.003.

Long, D. G. F., and E. C. Turner (2012), Formal definition of the Neoproterozoic Mackenzie Mountains Supergroup (Northwest Territories), and formal stratigraphic nomenclature for terrigenous clastic units of the Katherine Group, *Geol. Surv. Canada Open File*, *7113*, 40 p.

Maclean, B. C., and D. G. Cook (1999), Salt tectonism in the Fort Norman area, Northwest Territories, Canada, *Bull. Can. Pet. Geol.*, *47*(2), 104–135.

Nielsen, S. B., O. R. Clausen, and E. Mcgregor (2015), Basin%Ro: A vitrinite reflectance model derived from basin and laboratory data, *Basin Res.*, 1–22, doi:10.1111/bre.12160.

Peppe, D. J., and P. W. Reiners (2007), Conodont (U–Th)/He thermochronology: Initial results, potential, and problems, *Earth Planet. Sci. Lett.*, *258*(3-4), 569–580, doi:10.1016/j.epsl.2007.04.022.

Powell, J., and D. A. Schneider (2013), Preliminary results of 40Ar/39Ar geochronology from the eastern Mackenzie Mountains and Mackenzie Plain, Northwest Territories, *Geol. Surv. Canada Curr. Res.*, *2013-18*, 16 p.

Powell, J., D. Schneider, D. Stockli, and K. Fallas (2016), Zircon (U-Th)/He thermochronology

of Neoproterozoic strata from the Mackenzie Mountains, Canada: Implications for the Phanerozoic exhumation and deformation history of the northern Canadian Cordillera, *Tectonics*, *35*(3), 663–689, doi:10.1002/2015TC003989.

Powell, J., D. A. Schneider, and D. R. Issler (2017), Application of multi-kinetic apatite fission track and (U-Th)/He thermochronology to source rock thermal history: a case study from the Mackenzie Plain, NWT, Canada, *Basin Res.*, doi:10.1111/bre.12233.

Rainbird, R., V. McNicoll, Thériault, R. J., L. M. Heaman, J. G. Abbot, D. G. F. Long, and D. J. Thorkelson (1997), Pan-continental river system draining Grenville Orogen recorded by U-Pb and Sm-Nd geochronology of Neoproterozoic quartzarenites and mudrocks, northwestern, *J. Geol.*, *105*(1), 1–17.

Reiners, P. W., and M. T. Brandon (2006), Using Thermochronology To Understand Orogenic Erosion, *Annu. Rev. Earth Planet. Sci.*, *34*(1), 419–466, doi:10.1146/annurev.earth.34.031405.125202.

Sweeney, J. J., and A. K. Burnham (1990), Evaluation of a simple model of vitrinite reflectance based on chemical kinetics, *Am. Assoc. Pet. Geol. Bull.*, *74*(10), 1559–1570.

Wheeler, J. O., P. F. Hoffman, K. D. Card, A. Davidson, B. V. Sanford, A. V. Okulitch, and W. R. Roest (1996), Geological map of Canada, *Geol. Surv. Canada, "A" Ser. Map*, *1860A*, doi:10.4095/208175.

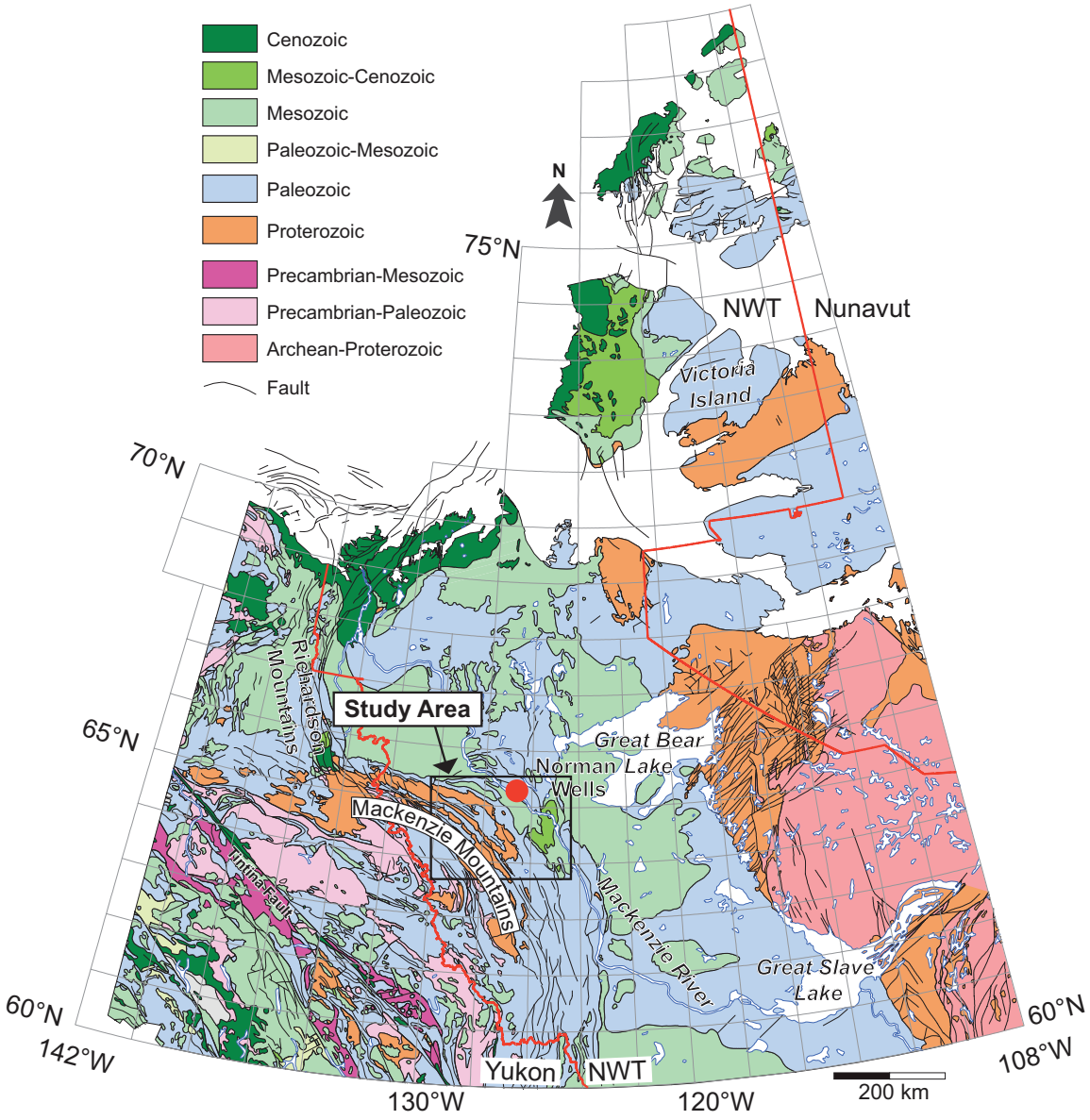

Fig. 1. Geologic map of northern Canada [*Wheeler et al.*, 1996]. The black square denotes the thesis study area whereas the red circle shows the location of the town of Norman Wells.

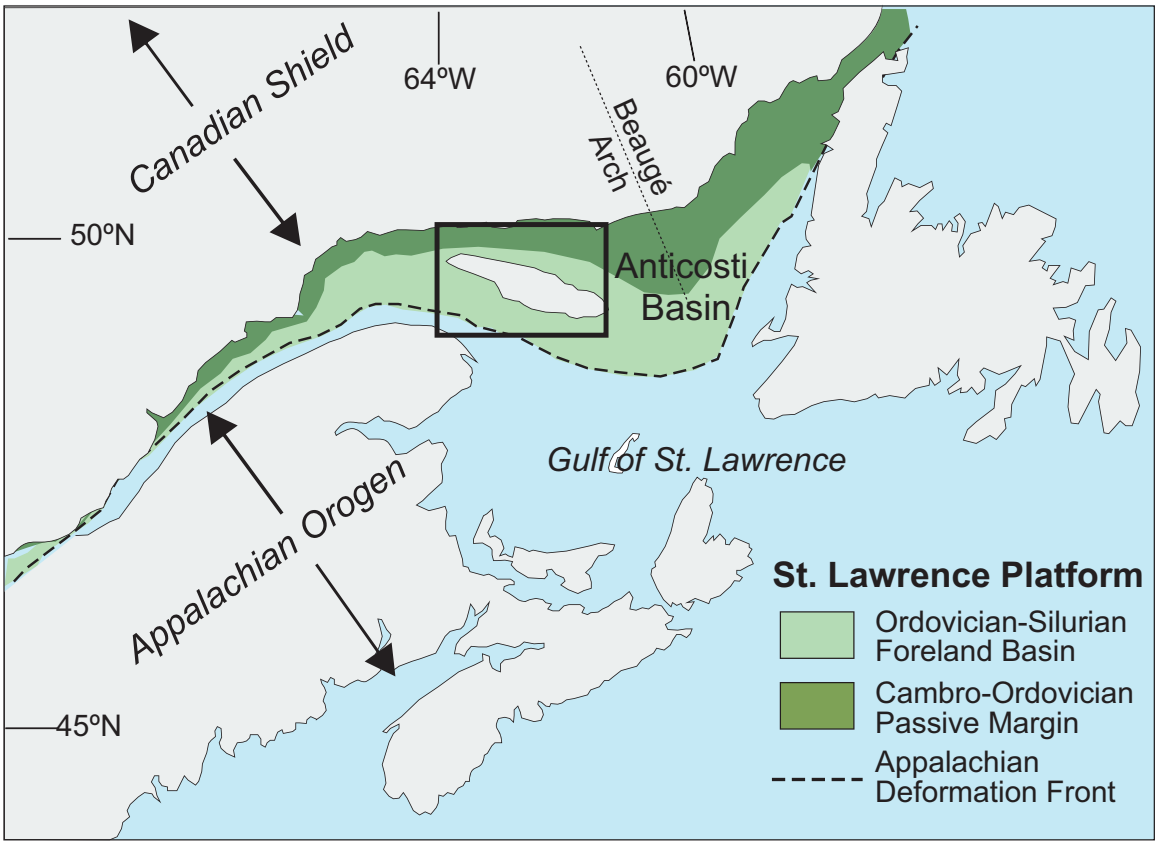

Fig. 2. Location of the Anticosti Island study area (black box) relative to the Gulf of the St. Lawrence. Map highlights major tectono-stratigraphic features, including the Canadian Shield, St. Lawrence Platform, and Appalachian Orogen [*Chi et al.*, 2010].

CHAPTER 2

Zircon (U-Th)/He thermochronology of Neoproterozoic strata from the Mackenzie Mountains, Canada: implications for the Phanerozoic exhumation and deformation history of the northern Canadian Cordillera

Jeremy Powell [1], David Schneider[1], Daniel Stockli[2], Karen Fallas[3]
1. Department of Earth & Environmental Sciences, University of Ottawa, Ottawa, Canada
2. Jackson School of Geosciences, University of Texas at Austin, Austin, USA
3. Geological Survey of Canada, Calgary, Canada

2016, *Tectonics*, 35 (3), 663-689

Abstract

Sedimentary strata of the Neoproterozoic Mackenzie Mountains Supergroup (MMSG) and Windermere Supergroup (WSG) occupy the cores of anticlines in the Mackenzie Mountains of the Canadian Cordilleran Foreland Belt. Stratigraphic and structural evidence suggest these rocks have undergone several episodes of burial and unroofing relatively intact. We report single grain detrital muscovite $^{40}Ar/^{39}Ar$ and zircon (U-Th)/He (ZHe) data from a suite of samples across the fold-thrust belt and the Neoproterozoic stratigraphic record. The strata have not reached high enough temperatures to reset the muscovite $^{40}Ar/^{39}Ar$ system, and instead our detrital muscovite data refine Tonian-Cryogenian depositional ages. Single crystal ZHe dates range from 432 ± 35 to 46 ± 4 Ma, indicating that MMSG and WSG strata have not been heated sufficiently to fully reset the ZHe system. These factors make the Neoproterozoic strata an attractive natural laboratory to test the utility of the zircon radiation damage and annealing model (ZRDAAM) on the quantification of thermal histories from detrital zircon populations that have accumulated radiation damage over long geologic timescales. Thermal modeling reveals that (1) a substantial sedimentary package was deposited following the Devonian and removed during Permo-Triassic cooling, and (2) the Cordilleran deformation front propagated through the study area from the Albian to the Paleocene, with a moderate increase in cooling rates between 75-67 Ma in the southwest, and 60-55 Ma at the deformation front. Ultimately, relationships between radiation

damage and helium diffusion kinetics in zircon explain substantial ZHe date dispersion and elucidate the time-temperature history of the northern Canadian Cordillera.

1. Introduction

Inliers of Neoproterozoic sedimentary strata punctuate the Phanerozoic cover throughout northern Canada. Whereas Neoproterozoic stratigraphy is presently exposed in the cores of structures and erosional windows including the Ogilvie, Wernecke and Mackenzie Mountains, they were deposited in a regionally extensive epicratonic basin of the supercontinent Rodinia and record its eventual rifting during the latest Cryogenian [*Rainbird et al.*, 1996; *Macdonald et al.*, 2012]. An investigation into the low-temperature thermal history of this strata using zircon (U-Th)/He (ZHe) thermochronology has the potential to resolve the timing and magnitude of burial and unroofing events that have influenced northern Canada since the Neoproterozoic. Thermochronology studies often avoid sedimentary strata due to problems associated with variance in detrital populations [*Guenthner et al.*, 2014, 2015], however the absence of crystalline basement in the Mackenzie Mountains restricts our sampling to the Neoproterozoic stratigraphy. The Neoproterozoic strata in the Mackenzie Mountains are unmetamorphosed and provide an excellent opportunity to test the zircon radiation damage and annealing model (ZRDAAM) [*Guenthner et al.*, 2013] on zircons derived from a variety of Proterozoic sources that have likely only experienced moderate reheating since deposition.

The Mackenzie Mountains are the northern extent of the Cordilleran Foreland Belt, forming as a consequence of Late Cretaceous to early Tertiary compression (Fig. 1). The fold-thrust belt marks a westward transition from undeformed strata of the northern Interior Plains to the highly deformed Selwyn Mountains of the Cordilleran Omineca Belt [*Gabrielse*, 1991;

Hyndman et al., 2005]. Several episodes of deformation have influenced the region since the Neoproterozoic, and the episodic burial and unroofing has resulted in regional Cryogenian, sub-Cambrian, mid-Silurian, sub-Albian, sub-Cenomanian and post-Paleocene unconformities in the Neoproterozoic-Tertiary sedimentary succession throughout the Mackenzie Mountains and the adjacent Mackenzie Plain (Fig. 2) [*Jefferson and Parrish*, 1989; *Norris*, 1997; *MacLean and Cook*, 1999]. Regionally, Neoproterozoic strata are exposed in the cores of the broad anticlines whereas Paleozoic strata are preserved in the narrow synclines (Fig. 1). Resolving the timing and magnitude of tectonism in the Mackenzie Mountains is complicated due to the paucity of cross-cutting relationships and lack of syn-tectonic strata throughout much of the region. In particular, the timing of Cordilleran deformation in the fold-thrust belt is only loosely constrained to be post-Albian to Paleocene, on the basis of folded Early Cretaceous strata in the hanging wall of the Plateau Fault and folded Paleocene strata in the Mackenzie Plain [*Gordey et al.*, 2010]. Consequently, the poor temporal constraints on the deformation history of the Mackenzie Mountains hinder our ability to develop detailed kinematic models for the evolution of the Cordilleran orogen in northern Canada.

In an effort to better understand the evolution of the Mackenzie Mountains, we conducted a strategic zircon (U-Th)/He thermochronology investigation of Neoproterozoic strata exposed in the central and northern Mackenzie Mountains (Fig. 1). Additionally, we carried out a detrital muscovite $^{40}Ar/^{39}Ar$ geochronology investigation on these same Neoproterozoic rocks to refine stratigraphic ages and to provide insight into the evolution of the sediment source region. Since deposition, the Neoproterozoic strata have experienced a protracted heating and cooling history through relatively low temperatures in the upper crust [*Asselin*, 2009]. As a result, single crystal ZHe dates in our dataset exhibit significant intra-sample dispersion. We utilized relationships

between radiation damage accumulation and helium diffusion in zircon [*Guenthner et al.*, 2013] to quantify the broad distribution of ZHe dates in our dataset. Interestingly, despite complexities associated with inherited ^{4}He and radiation damage [*Guenthner et al.*, 2015], we find that careful thermal modelling of these partially reset ZHe dates has the potential to reveal a wealth of information on the thermal history of a region throughout geologic time. Our results help resolve the regional geologic history that is missing across a major Devonian-Albian unconformity and the spatiotemporal evolution of the northern Cordilleran Foreland Belt from the Cretaceous to the Paleocene.

2. Geological Setting

2.1. Stratigraphy

The stratigraphic record (Fig. 2) of the Mackenzie Mountains and Plain spans approximately a billion years of geologic time, and can be separated into major tectonostratigraphic sequences on the basis of regional unconformities that punctuate the Neoproterozoic, Paleozoic and Cretaceous stratigraphy [*Norris*, 1997]. The Neoproterozoic Mackenzie Mountains Supergroup (MMSG) and Windermere Supergroup (WSG) strata preserved in our study area are a component of a broader Proterozoic stratigraphic assemblage that is exposed as erosional inliers across much of northwestern Canada [*Young et al.*, 1979]. The MMSG is composed of shallow water siliciclastic and carbonate units, and is inferred to have been deposited in an extensive intracratonic basin due to lithostratigraphic similarities with far-removed Neoproterozoic strata [*Narbonne and Aitken*, 1995; *Rainbird et al.*, 1996]. Stratigraphic thickness of the MMSG is variable across the region, increasing from 4 to 6 kilometers towards the southwest. For this study, the MMSG stratigraphy is subdivided into four units (Fig. 2) in

ascending order: Tabasco Formation, Tsezotene Formation, Katherine Group and Little Dal Group. The dolostone, shale, and sandstone units of the Tabasco Formation are exposed in only a few outcrops in the Mackenzie Mountains (Fig. 1). Elsewhere, these strata lie unconformably on deformed Mesoproterozoic rocks. Strata from the Tsezotene Formation and Katherine Group record an overall coarsening-upwards cycle from a mudstone-dominated shelf to fluvial deposits of the Katherine Group. The Little Dal Group is the youngest unit in the MMSG and is comprised of dominantly carbonate and evaporite rocks [*Narbonne and Aitken*, 1995; *Rainbird et al.*, 1996; *Turner and Long*, 2008]. A suite of diabase dikes and sills were intruded through the Mackenzie Mountains Supergroup strata during the Cryogenian at c. 779 Ma [*Harlan et al.,* 2003], and are geochemically similar to basaltic lava flows that overlie the Little Dal Formation [*Jefferson and Parrish*, 1989]. Coates Lake Group strata range in thickness from 0-1500 m across the Mackenzie Mountains and are bounded by unconformities with the MMSG below and WSG above. These strata transition from basal sandstones and conglomerate of the Thundercloud Formation, through the red mudstone and evaporites of the Redstone River Formation, to the carbonates of the Coppercap Formation [*Gordey and Roots*, 2011]. Rapitan Group strata, including the Mount Berg, Sayunei and Shezal Formations, are composed of conglomerates, turbidites and glacial diamictite and overlie the Coates Lake and Little Dal groups across the Central Mackenzie Mountains [*Narbonne and Aitken*, 1995]. These strata are the basal member to the WSG and are succeeded by three fine-grained siliciclastic to carbonate 'grand cycles' of the Hay Creek Group [*Turner et al.,* 2011]. The Keele Formation marks the end of the first Hay Creek Group grand cycle and consists of the carbonaceous limestone and ooilite dominated Keele Platform. Locally, shallow marine sandstones of the Keele Clastic Wedge developed adjacent to the Keele Platform during sea level lowstand [*James et al.,* 2001]

Regionally, the Windermere Supergroup is confined to the area west the Plateau Fault with thicknesses ranging from less than 2000 m to greater than 4000 m [*Gordey and Roots*, 2011].

Cambrian strata unconformably overlie the MMSG in the northeastern Mackenzie Mountains and conformably to unconformably overlie WSG strata in the hanging wall of the Plateau Fault. The Mackenzie Arch divides Early and Middle Cambrian deposition into the Mackenzie Trough depocentre to the northeast and the continental margin to the southwest, with equivalent strata missing on the top of the arch in northeast Mackenzie Mountains. Seismic interpretation of the Mackenzie Trough suggests that the system evolved from uniform subsidence and deposition recorded by the Mount Clark Formation to an extensional phase where Mount Cap Formation strata were deposited in a broad graben system [*MacLean*, 2011]. Early and Middle Cambrian strata range in thickness from 0-400 m on the northeast flank of the Mackenzie Arch [*Aitken et al.,* 1973] and 1000 to more than 2500 m southwest of the Plateau Fault [*Gordey and Roots*, 2011]. The post-extensional phase of Cambrian deposition is marked by a Late Cambrian transgression that established a regional carbonate platform above the Cambrian evaporitic basin. Observed thicknesses of the Late Cambrian to Middle Devonian carbonate platform indicate that less than 2000 m overly the MMSG across the Mackenzie Arch in northeast Mackenzie Mountains [*Aitken and Cook*, 1974]. Southwest of the Plateau Fault, Late Cambrian to Middle Devonian carbonate strata are 3000-4000 m thick [*Gordey and Roots*, 2011]. Another major transgressive pulse is marked by the abrupt change from the platform carbonate of the Middle Devonian Hume Formation to shale of the Horn River Group [*Gal et al.,* 2009]. This transgression was followed by south-westward progradation of more than 700 m of shale, siltstone, and sandstone deposits of the Imperial Formation [*Hadlari et al.*, 2009].

In the Mackenzie Plain, a major regional unconformity exists between the Upper Devonian Imperial Formation and Albian strata. Mesozoic stratigraphic section elsewhere in northern Canada and thermal maturity studies from wells in the Mackenzie Plain indicate that deposition must have continued following the Devonian and been eroded prior to the Albian [*Williams*, 1990; *Feinstein et al.*, 1996; *Issler et al.*, 2005]. Deposition in the Mackenzie Plain resumed by the Albian, where 750-1700 m of sediment derived from the craton to the east were deposited in a westerly deepening basin [*Yorath and Cook*, 1981; *Thomson et al.*, 2011]. With the exception of a fault-bounded outlier of more than 1300 m of post-Barremian to Campanian non-marine strata southwest of the Plateau Fault [*Blusson*, 1971; *Turner et al.*, 2011], there is no Cretaceous stratigraphic record in the Mackenzie Mountains. A hiatus in deposition at the end of the Albian marks the end of east-derived sedimentation in the Mackenzie Plain and Mackenzie Mountains. Renewed deposition in the Cenomanian, continuing through the Paleocene, is sourced from the emerging Mackenzie Mountains to the west [*Yorath and Cook*, 1981; *Thomson et al.*, 2011]. In the Mackenzie Plain these strata attain a thickness of 1800 m [*Yorath and Cook*, 1981].

2.2. Structure

Samples collected for this study come from the east-central and northern Mackenzie Mountains. In the southwest of the study area the Plateau Fault, a significant thrust fault that carries MMSG and WSG strata in its hanging wall, is the dominant feature (Fig. 1). This thrust fault possesses a strike length of ~270 km, and has a 20-30 km horizontal displacement [*MacNaughton et al.*, 2008; *Macdonald*, 2009] that results in a broad, 30 km wide plateau of relatively undeformed, flat-lying hanging wall stratigraphy [*Gabrielse*, 1991]. To the northeast the deformation is dominated by a series of long wavelength folds. The anticlines are cored by

strata of the MMSG with Paleozoic strata occupying the intervening synclines. The major folds in this study area are the Macdougal, Stony, Canyon, Rouge Mountain, Foran, Tawu, Bolstead, and Tigonankweine anticlines (Fig. 1). These folds are modified by a few moderate- to low-angle thrust faults with displacements of a few kilometres or less. The Canyon Fault, a thrust that is continuous across much of the frontal anticlines, is a possible exception, as its length and significant stratigraphic separation suggest that it is a major regional structural feature [*Fallas and MacNaughton*, 2014a]. Within the MMSG strata exposed in the cores of the anticlines, high-angle extensional faulting has offset Proterozoic strata by a few hundred metres [Fallas and MacNaughton, 2014c]. Locally these extensional faults were reactivated during Cretaceous to Tertiary compression. The Conundrum Fault in the eastern edge of the Tigonankweine anticline is an example of such a phenomenon. With increasing reverse displacement along strike to the north, this structure inverts from a normal fault in the south to a reverse fault in the north [*Fallas and MacNaughton*, 2014c].

Gabrielse [1991] suggests that structural detachment levels within the Mackenzie Mountains are relatively deep and underlie the MMSG strata, based on the presence of MMSG strata in the cores of long-wavelength anticlines. The symmetry and similar structural style and relief of these anticlines led *Gordey et al.* [2010] to speculate that the fold-thrust belt represents a detachment fold-train, with each structure detached at the same structural level. In this model, the MMSG and the overlying Paleozoic stratigraphy forms a mechanically competent unit that deforms via flexural slip above a basal, mechanically incompetent unit [*Mitra*, 2003]. Depth to detachment calculations based on the geometry of the Tawu and Shattered Range anticlines suggest that the main detachment surface lies at a depth of 7 to 12 km and is likely rooted in older Meso- or Paleoproterozoic strata not exposed in our field area [*Gordey et al.*, 2010].

Shallower detachment levels within the MMSG are also active both southwest and northeast of the Plateau Fault to accommodate thrust faulting. The Plateau Fault for example, is detached in the gypsum unit (Ten Stone Formation) of the Little Dal Group where exposed at surface [*Gabrielse*, 1991; *Gordey et al.*, 2010].

Unlike the Rocky Mountains south of 60°N, the Mackenzie Mountains remain seismically active [*Hyndman et al.*, 2005]. Ongoing subduction-collision of the Yakutat terrane under Alaska continues to exhume the Chugach-St. Elias Range [*Enkelmann et al.*, 2010] and also translates strain 600-800 km away across the Northern Cordillera. Seismicity in the Mackenzie Mountains is mostly concentrated on gently dipping thrust faults in the fold-thrust belt, which may accommodate as much as 4 mm/year of shortening [*Hyndman et al.*, 2005; *Leonard et al.*, 2008].

3. Previous Work

Whereas the stratigraphy and structure of the Mackenzie Mountains and the adjacent Mackenzie Plain are well studied, constraints on the burial and exhumation history of the region, including thermal maturity and thermochronology data, are limited and often contradictory. Thermal maturity studies on the Upper Cambrian to Upper Devonian strata of the Selwyn basin to the southwest of the Plateau Fault suggests that Paleozoic carbonates were buried to temperatures in excess of 200°C, resulting in potential source rocks that are overmature (%Ro equivalent: >3.0), having passed through the dry-gas generation window. Maximum burial temperatures decrease to the northeast, with thermal maturity parameters (%Ro equivalent: 1.2-2.0) from Paleozoic strata in the footwall of the Plateau Fault indicating that source rocks reached a temperature regime between approximately 150-200°C, conducive to dry-gas

generation and preservation [*MacNaughton et al.*, 2008]. Conodont alteration index (CAI) values from Paleozoic conodonts elsewhere in the central Mackenzie Mountains [*Nowlan*, 1995, 2010a] mostly range from CAI 4-5, and are in accord with a system where Paleozoic strata were heated to temperatures >190°C and matured to at least the dry-gas generation stage [*Epstein et al.*, 1977; *Rejebian et al.*, 1987]. CAI values from Paleozoic samples along the Mackenzie Mountains deformation front range from 2-4 [*McCracken*, 2007; *Nowlan*, 2010b] and provide similar paleotemperatures to the acritarch reflectance values from the Neoproterozoic Katherine Group and Cambrian Mount Cap Formation from the same region. These data suggest a temperature regime between 140-190°C for the Paleozoic to Neoproterozoic strata in the northern Mackenzie Mountains [*Asselin*, 2009]. CAI values from Cambro-Ordovician strata decrease to the northeast, with values as low as CAI 1.5-2 near Norman Wells corresponding to maximum temperatures between 50°C and 140°C [*Epstein et* al., 1977; McCracken, 2011a, 2011b].

Though these data give a broad overview of the maximum thermal maturity across the region, they do not specify the timing of when strata reached those temperatures. Quantifying when strata reached their thermal maximum is complicated by the regional sub-Albian unconformity (Fig. 2), where an unknown amount of material may have been deposited and eroded between the Late Devonian and Early Cretaceous. This is of particular importance in the present day sedimentary basin, where hydrocarbon generation from oil-prone Devonian source rocks [*Feinstein et al.*, 1988, 1991] may have occurred prior to formation of Late Cretaceous-Eocene trapping structures [*Issler et al.*, 2005]. Several studies have tried to estimate the magnitude of eroded section throughout the region [*Link and Bustin*, 1989; *Feinstein et al.*, 1996; *Issler et al.*, 2005] and have reached different conclusions. *Feinstein et al*. [1996] analyzed organic thermal maturity and shale compaction profiles from the Mackenzie Plain and concluded

that maximum burial occurred during the Cenozoic, in response to a Cretaceous-Tertiary section with a pre-eroded thickness of 3 km, compared to the 0.5 to 2 km of material removed below the sub-Albian unconformity. *Issler et al.* [2005] integrated borehole organic thermal maturity and a shale compaction profile with apatite fission track analysis of the Devonian Imperial Formation to suggest that maximum burial occurred between the Carboniferous-Triassic, where the Imperial Formation was buried to a depth of 2.7 to 3.6 km, compared to the 3 km burial depth in the Paleocene. Thermal histories derived from apatite (U-Th)/He analysis from the Archean Slave craton to the east suggest that Paleozoic burial reached depths as great as 3.3 km [*Ault et al.*, 2009, 2013] compared to the 1.4 km of Cretaceous material thought to have extended across the shield [*Stasiuk et al.*, 2006].

Numerical modeling of thermochronology data allows for an investigation into the timing of burial and exhumation across the sub-Albian unconformity. The time-temperature history modeled by *Ault et al.* [2009, 2003] indicates that Phanerozoic burial over the Slave craton reached maximum temperatures in the Carboniferous to Middle Triassic, with unroofing progressing westward from c. 340 Ma in the eastern Slave to c. 225 Ma on its western margin. The fission track modeled thermal history from the Mackenzie Plain [*Issler et al.*, 2005] yields a slightly different result, proposing that Paleozoic burial in the Mackenzie Plain continued into the Mesozoic followed by Early Triassic to Middle Jurassic exhumation. Clearly, more data is required to resolve regional trends and implications for the pre-Cretaceous evolution of northern Canada.

4. Methods and Results

4.1. Sampling strategy

Sampling for this study was conducted along a ~150 km transect perpendicular to regional strike of the Mackenzie Mountains. Samples span the northeast portion of the fold-thrust belt, from the hanging wall of the Plateau Fault in the southwest through the Mackenzie Mountain front in the northeast (Figs. 1, 4). As a result of the carbonate-dominated Phanerozoic stratigraphy, sampling was restricted to clastic Neoproterozoic strata that outcrop in the cores of anticlines. This method ensured that similar stratigraphic positions were sampled across the study area. Samples were collected from the Tsezotene Formation, Katherine Group and Little Dal Group of the MMSG, and the Keele Formation of the WSG. We elected against sampling for a vertical transect, in part because of problems resulting from limited outcrops of clastic strata and steep topography. Moreover, the wavelengths of many of the structures were sufficiently long to rule out the viability of an age-elevation thermochronology study [*Ehlers*, 2005].

In the southwest of our study area, two Keele Formation samples (JP015; JP018) were collected from the Redstone Plateau in the hanging wall of the Plateau Fault. Continuing to the northeast, a sample was collected from Katherine Group strata exposed in an anticline in the footwall of the Plateau Fault (JP017) and from Tsezotene Formation strata that core the Tigonankweine anticline in the same structural panel to the northwest (JP022). A single sample (JP026) from Katherine Group strata was gathered from the Bolstead anticline. In the Tawu anticline, samples were collected from both the Katherine Group and Tsezotene Formation (JP025; JP024). Samples from the outermost anticlines of the fold-thrust belt were collected on either side of the Canyon Fault, a laterally continuous regional thrust fault that dissects the mountain front from the Stony anticline in the northwest through to its southern terminus west of the Rouge Mountain anticline. Two samples were collected from Katherine Group strata of the Foran anticline to the west of the Canyon Fault (JP012; 12NA103). East of the Canyon Fault,

samples were collected from the Katherine Group strata in the Rouge Mountain anticline (JP008; JP009), Katherine Group and Tsezotene Formation from the Stony and Canyon anticlines (12FNA047; 11FNA010; JP001), and from the Dodo Creek Formation in the Macdougal anticline (JP007).

4.2. Muscovite $^{40}Ar/^{39}Ar$ geochronology

Detrital mineral geochronology is a common technique used in sedimentary basin analysis due to the techniques' ability to reveal information on sediment source regions, maximum age of the sedimentary strata and to infer relationships between orogenic systems and basin dynamics [*Fedo et al.*, 2003]. U-Pb dating of zircon is among the most popular of these techniques due to the robust chemical and physical properties of zircon and its abundance in the sedimentary record. However the closure temperature of zircon is sufficiently high that the U-Pb age reflects crystallization ages of the mineral and its source, and may not be indicative of tectonic events in the sediment source region [*Hodges*, 2005]. In particular, zircon's propensity to survive multiple orogenic cycles means that several zircon U-Pb age populations are not necessarily diagnostic of several source terranes [*Haines et al.*, 2004]. In comparison, detrital muscovite $^{40}Ar/^{39}Ar$ geochronology tends to reflect the timing of source terrane cooling through a 350-400°C isotherm. Additionally, muscovite is more susceptible to physical and chemical weathering and is unlikely to survive more than one cycle of uplift, erosion and deposition [*Gutiérrez-Alonso et al.*, 2005]. Thus, the detrital muscovite age spectra of sedimentary successions records a fairly simple portrait of the tectonic evolution of the hinterland compared to the corresponding zircon record, which may be reflective of the magmatic and metamorphic history of source regions throughout geologic time [*Haines et al.*, 2004].

Muscovites for $^{40}Ar/^{39}Ar$ dating were obtained via standard crushing and separation techniques. Individual grains were loaded into holes machined into aluminum disks and irradiated for 85 hours at the USGS TRIGA reactor (Denver, USA). Argon from individual grains was extracted with a 75W Photon-Machines CO_2 laser in an automated, all metal extraction line and isotopic analyses were conducted on an ARGUS VI mass spectrometer at New Mexico Tech (Socorro, USA). Complete analytical details are in the accompanying Appendix (Text A1).

4.3. Muscovite $^{40}Ar/^{39}Ar$ results

For this study, a suite of five detrital muscovite-bearing samples was selected for single-grain muscovite $^{40}Ar/^{39}Ar$ analysis. The samples span the Neoproterozoic stratigraphy and include the Tsezotene Formation, Katherine Group, and Dodo Creek Formation of Mackenzie Mountains Supergroup and the Keele Formation of the Windermere Supergroup. Density probability diagrams of single crystal total fusion ages for all stratigraphic levels are shown in Fig. 3 and a corresponding data table can be retrieved from the Appendix to this Chapter (Table A1).

Fifty single-grain analyses of muscovite from two Tsezotene Formation samples yielded dates between 2554 ± 2 Ma and 992 ±1 Ma. However, the vast majority of the dates were normally distributed with an 1100 to 1050 Ma mode. The twenty-six grains analyzed from the overlying Katherine Group range in age from 1160 ± 1 Ma to 963 ± 1 Ma, similar to the underlying Tsezotene Formation. However, the distribution of Katherine Group ages is different from the stratigraphy below as it has a bimodal character, with populations between 1000 to 950 Ma and 1150 to 1100 Ma. Overall, our ages from the Tsezotene Formation and Katherine Group are similar to published detrital zircon U-Pb geochronology for the Mackenzie Mountains

Supergroup [*Rainbird et al.*, 1997; *Lane and Gehrels*, 2014], which suggest significant contribution from a 1250 to 1000 Ma source.

For the sample from the Dodo Creek Formation at the base of the Little Dal Group, twenty-five analyses were normally distributed between 1126 ± 1 Ma to 818 ± 1 Ma, with a 950 to 900 Ma mode. These analyses are slightly younger than the population of 1250 to 1000 Ma detrital zircon U-Pb ages [*Leslie*, 2009; *Lane and Gehrels*, 2014]. Twenty-six single-grain analyses of muscovite from the Keele Formation yielded a broad range of dates from 2418 ± 4 Ma to 785 ± 2 Ma, with a 1950 to 1350 Ma component and a large population of 2400 to 2350 Ma dates. While many of these ages are coincident with the Paleo- and Mesoproterozoic provenance suggested for the Keele Formation [*Leslie*, 2009; *Lane and Gehrels*, 2014], the 1200 to 1000 Ma muscovite $^{40}Ar/^{39}Ar$ ages abundant in the underlying Mackenzie Mountains Supergroup and described in the detrital zircon U-Pb record are noticeably absent in our dataset.

4.4. Zircon (U-Th)/He thermochronology

Zircon (U-Th)/He thermochronology has seen increased use in geological studies due to the technique's ability to reveal information on the thermal evolution of strata in a variety of tectonic settings [*Stockli*, 2005; *Reiners and Brandon*, 2006; *Tian et al.*, 2012; *Guenthner et al.*, 2015]. With the ZHe system, radiogenic ^{4}He is produced through α-emission during the decay of ^{238}U, ^{235}U and ^{232}Th. Whereas some α-particles are emitted via decay of ^{147}Sm, the total contribution is negligible compared to the U and Th systems [*Harrison*, 2005]. Retention of ^{4}He is sensitive to the thermal conditions of the uppermost crust, with laboratory estimates suggesting an approximate closure temperature of 185ºC for grains with 40-100 μm widths that experience a cooling rate of 10ºC/m.y. [*Reiners et al.*, 2002, 2004]. To this extent, measured ZHe cooling dates should correspond to the time at which the sample cooled through a 185ºC crustal isotherm

[*Reiners and Brandon*, 2006]. However, investigations into the application of the ZHe thermochronometer in natural settings suggest that the system becomes increasingly retentive ^{4}He as it cools through a helium partial retention zone (PRZ) between 200-130ºC [*Wolfe and Stockli*, 2010]. Accordingly, the closure temperature concept may be applicable to zircons that have rapidly cooled through this PRZ, but prolonged residence in this temperature regime complicates such an interpretation. Instead, slower cooling allows for factors such as grain volume and radiation damage to influence diffusivity [*Reiners*, 2005; *Guenthner et al*., 2013]. Partial resetting, where the ZHe system is reheated to temperatures within - but not exceeding - the PRZ, further complicates the tracking of a sample through a closure isotherm. With partial resetting, some of the radiogenic helium from the previous cooling history is retained, and thus the cooling ages are a reflection of both the previous and most recent thermal histories. Whereas the effects of partial resetting are relatively easy to constrain in crystalline rocks, understanding how multiple thermal events and partial resetting is manifest in sedimentary rocks is significantly more difficult to quantify due to variation in pre-depositional histories and grain size in detrital zircon populations [*Guenthner et al.*, 2015].

The concentration of U and Th in natural zircon populations tends to vary from 100's to 1000's ppm. Self-irradiation caused by the high concentration of radiogenic elements has an adverse effect on the crystal structure of zircon. Damage to the crystal lattice occurs mainly through recoil of heavy daughter nuclei following α-particle emission, and less frequently by spontaneous fission of ^{238}U [*Ketcham et al.*, 2013]. The degree of damage in a zircon can be quantified by its α-dose, a parameter that assesses the number of alpha decay events per gram of zircon. Over geologic time, higher α-doses result in an amorphous crystal structure and the eventual metamictization of the zircon [*Nasdala et al.*, 2004a, 2004b]. While correlations

between ZHe date and radiation damage have long been recognized [*Nasdala et al.*, 2004a; *Reiners*, 2005], the relationship was poorly understood until recently. Work by *Guenthner et al.* [2013] suggests that increasing radiation damage produces damage zones in zircon that initially decrease helium diffusivity. However, once a threshold α-dose of ~2 x 10^{18} α/g is reached, these damage zones connect to form fast-diffusion pathways and helium diffusivity increases dramatically. The zircon radiation damage and annealing model (ZRDAAM) of *Guenthner et al.* [2013] calculates diffusion kinetics of individual zircons measured for (U-Th)/He analysis by integrating the effective uranium concentration (eU = U + 0.235 • Th) over the time since the zircon cooled below zircon fission track (ZFT) partial annealing temperatures (~310-223°C), allowing for quantification of thermal histories from ZHe datasets [*Guenthner et al.*, 2014, 2015]. Thus, positive correlations between ZHe date and eU are thought to represent the effects of increasing radiation damage on helium diffusion at low α-doses, whereas negative date-eU correlations are representative of zircon populations with moderate to high α-doses. To this extent, negative date-eU correlations should be pronounced in samples that have experienced a protracted thermal history at temperatures cooler than the ZFT partial annealing zone [*Guenthner et al*., 2013, 2014].

Following standard mineral separation procedures, individual zircons from thirteen detrital samples were handpicked for (U-Th)/He analysis. In an effort to maintain an unbiased population of zircons, grains of varying morphology and size were selected from each sample. Due to the potentially broad dispersion in cooling dates within a detrital population, eight to twelve single grains were analyzed per sample for a total of 133 single grain (U-Th)/He dates. Analyses were conducted at The Jackson School of Geosciences at the University of Texas at Austin using the analytical procedure outlined by *Wolfe and Stockli* [2010]. All ages were

corrected for the effects of α-ejection [*Farley et al.*, 1996] and are reported with an ~8% (2σ) analytical uncertainty (Table 1).

4.5. Zircon (U-Th)/He results

ZHe data are presented as date-eU graphs for each sample (Fig. 4). All (U-Th)/He dates are substantially younger than their Neoproterozoic depositional age, indicating that both the MMSG and WSG were buried sufficiently deep throughout the Phanerozoic to partially or fully reset the ZHe system. The dataset exhibits varying degrees of age dispersion in all samples indicating a potentially complex, protracted thermal history. Single ZHe dates range from 46 ± 4 Ma to 432 ± 35 Ma, with intra-sample ZHe date dispersion ranging in magnitude from 350 m.y. in sample JP012 to 75 m.y. in JP018 and JP024. The concentration of eU in individual zircons varies by 100's ppm throughout the dataset. All samples show some degree of negative correlation between date and eU, with the oldest dates occurring between 40-150 ppm eU. In general, this relationship becomes less dramatic with eU concentrations greater than 200 ppm, where the negative ZHe date-eU trend reaches a plateau and ZHe dates decrease very little with increasing eU (Fig. 4). All samples, with the exception of 11FNA010, have youngest single crystal ZHe dates between 46 ± 4 Ma to 88 ± 7 Ma. The pervasiveness of negative date-eU relationships throughout all samples suggests that the effect of radiation damage on helium diffusivity in zircon is a major factor in the complex distribution of dates in this study. Despite the tendency for ZHe ages to increase with elevation in mountain belts [*Spotila*, 2005; *Reiners and Brandon*, 2006], no such correlation was observed in our dataset. Instead, ZHe dates within a given sample are not simply a function of structural position and thermal history, but zircon-specific kinetic parameters. To facilitate a discussion on the relationship between ZHe date and

regional thermal history, these data are illustrated based on their structural position in the fold-thrust belt (Fig. 5).

Zircon (U-Th)/He dates in Group A are from samples from the Rouge Mountain, Canyon, Macdougal and Stony anticlines, and are presented together due to their position along the mountain front, east and north of the Canyon Fault (Fig. 5a). The thirty-five dates are broadly distributed between 432 ± 35 and 51 ± 4 Ma, and follow a negative date-eU trend with the oldest ZHe dates occurring between 67-118 ppm eU. In particular, the two most significant age populations are between 60-50 Ma, and 90-80 Ma. Approximately half of the ZHe dates are between 267 ± 21 to 155 ± 12 Ma, with a significant c. 160 Ma component. Interestingly, there is a paucity of ZHe dates between 155 Ma and 112 Ma in these four samples. The twenty-one ZHe dates in Group B are from the Foran anticline in the hanging wall of the Canyon Fault and are not as broadly dispersed as samples from the frontal anticlines yet still exhibit a negative trend in date-eU (Fig. 5b). Single grain ages mostly range from the 116 ± 9 to 67 ± 5 Ma, with age populations at c. 102 Ma and c. 73 Ma. Unlike the samples from the mountain front (Fig. 5a), the Foran anticline has no ZHe dates between 270 to 170 Ma. Instead, these samples have a small 171 ± 14 to 132 ± 11 Ma component (Fig. 5c) The Katherine Group and Tsezotene Formation ZHe dates from Tawu anticline samples in Group C (Fig. 5c) exhibit an even lower degree of dispersion than the previous two groups. The oldest values in Group C (213 ± 17 Ma; 122 ± 10 to 113 ± 9 Ma) occur between 40-132 ppm eU. The majority of the Group C data range from 71 ± 6 to 46 ± 4 Ma, and decrease in age with increasing eU concentration. (U-Th)/He dates in Group D are from the MMSG strata in the anticlines immediately to the east of the Plateau Fault. Although the Bolstead anticline is structurally intermediate between the Tawu anticline to the north and Tigonankweine anticline to the south, we opted to include these data in Group D (Fig.

5d). Group E is composed of the Keele Formation samples from the Redstone Plateau in the hanging wall of the Plateau Fault (Fig. 5e). Group D samples have widely distributed ZHe dates, with populations between 371 ± 30 to 317 ± 5 Ma, 249 ± 20 to 192 ± 15 Ma, 158 ± 13 to 84 ± 7 Ma, and 69 ± 5 to 56 ± 5 Ma. Comparatively, the Group E samples have dates that form a relatively continuous spectrum from 143 ± 11 to 65 ± 5 Ma. Both Group D and E exhibit negative date-eU correlations, with the oldest ages occurring between 57-105 and 69-116 ppm eU, respectively.

5. Numerical Modeling

Traditionally, modelling of thermal histories from low-temperature thermochronometers was mostly restricted to rocks that cooled rapidly from high temperatures due to the limited understanding of the effects of radiation damage accumulation and annealing on ^{4}He diffusivity in the apatite and zircon (U-Th)/He systems. However, advances by *Flowers et al*. [2009] on a radiation damage accumulation and annealing model (RDAAM) for the AHe system, and *Guenthner et al.* [2013] on the ZHe system (ZRDAAM) allow for quantification of thermal histories from rocks that have experienced protracted cooling histories and have thermochronometer datasets that would have previously been considered equivocal. However, application of ZRDAAM to our ZHe dataset is complicated by the variable provenance of the MMSG and WSG strata [*Lane and Gehrels*, 2014]. Owing to the detrital nature of these samples and potential for incomplete resetting of the ZHe system, individual ZHe dates may be influenced by radiation damage accumulation and inherited ^{4}He from Neoarchean through Neoproterozoic pre-depositional histories [*Guenthner et al.*, 2015]. Additionally, published estimates of the amount of material deposited and eroded between the Devonian and Albian

indicate that a substantial regional cooling event occurred prior to Cordilleran deformation [*Feinstein et al.*, 1996; *Issler et al.*, 2005; *Ault et al.*, 2009, 2013]. It is important to understand how these complexities may be manifest in our own dataset prior to thermal modelling. Fig. 6 simulates the ZHe date distributions expected in a Cambrian (500 Ma) sedimentary unit with provenance from 2000 Ma and 1000 Ma sources. For each of the five thermal histories, we show inheritance curves, which indicate the realm of expected ZHe date-eU relationships for zircons with equivalent spherical radii (ESR) of 35-80 μm, a common range of grain sizes for detrital zircon. Cumulatively, these curves form the 'inheritance envelope,' or the sum of all possible inheritance date-eU curves given the sample's provenance. The inheritance envelope concept is a useful way of addressing plausible post-depositional time-temperature hypotheses for ZHe datasets from rocks with variable pre-depositional histories [*Guenthner et al.*, 2015]. In thermal history A, the strata have experienced a single post-depositional thermal event, with heating due to burial terminating at a 300 Ma cooling event (C1). Here, cooling ages with zero-inherited ^{4}He and radiation damage have a narrow range of age with respect to grain size, and a slightly positive date-eU correlation with ZHe dates attaining a plateau at C1. Positive and negative correlations between date-eU exist in both the 2000 and 1000 Ma envelopes. In these simulations, the ZHe system becomes increasingly retentive of ^{4}He with increasing eU until a threshold eU concentration is reached, at which point added radiation damage increases diffusivity and results in younger ZHe dates. The longer damage accumulation time in the 2000 Ma population allows this threshold radiation damage level to be reached at lower eU values than in the 1000 Ma population.

In thermal histories B-E, the strata have experienced a second thermal event of varying magnitude, with reheating commencing at 200 Ma and progressing until 60 Ma (C2). In histories

B-D, all three date-eU curves display a complex distribution of ages that are younger than C1, but only partially to fully reset prior to C2. In these three scenarios, the threshold amount of radiation damage required to transition from decreasing to increasing ^{4}He diffusivity is a fixed eU concentration for each population, and in the 2000 Ma and 1000 Ma curves, dates attain a plateau at C2 with increasing radiation damage. However, the height and width of the inheritance curve is dependent on both the maximum temperature reached by the strata, and the time spent at this temperature range. In thermal history B, strata are only reheated to 160ºC. As a result, these zircons are highly retentive at low eU concentrations, where even the smallest grains are only partially reset before C2. In thermal histories C and D, strata are reheated to 180ºC. However, D spends twice as long as C at this isotherm. In both C and D, the height of the inheritance curves are substantially shorter than in B, indicating a higher degree of partial resetting, and their lower boundaries attain a plateau at C2 for lower concentrations of eU due to the increased temperature. The shorter duration that C spends at 180ºC compared to D results in older maximum ages and only partial resetting of the most retentive 35 μm grains during the second heating event. In thermal history E, the strata are heated to 200ºC, the higher temperature boundary of the ZHe PRZ. The (U-Th)/He system in zircon is completely reset for all eU concentrations and records cooling at C2.

Thus, when we account for a Neoarchean to Neoproterozoic pre-depositional history, even moderate changes in temperatures reached during reburial can have significant effects on the single crystal age distribution for an individual sample. In all of the thermal history simulations, inheritance date-eU curves reach a plateau asymptotically at an age that relates to regional cooling, and have oldest ages that correspond to the threshold amount of radiation damage required to transition from decreasing to increasing diffusivity in zircons from the 2000

Ma source. Additionally, these models highlight the extended range of temperatures to which ZHe systems that have accumulated radiation damage over long timescales are sensitive. The forward model in Fig. 6a predicts that the most retentive zircon are not fully reset at 200ºC, and the least retentive zircon may still be partially retentive at temperatures lower than 130ºC. Consequently, whereas the 200-130ºC ZHe PRZ [*Wolfe and Stockli*, 2010] is a pertinent temperature range for many ZHe systems, the ZRDAAM predicts that the ZHe system in damaged zircon may be sensitive to a broader range of temperatures [*Guenthner et al*., 2013].

Due to complexities associated with inherited radiation damage in poly-sourced detrital populations, and the comparably small sample size of most ZHe datasets, we caution against attributing individual cooling ages to geologic events without attempting to replicate the dispersion through numerical modeling. In many cases, a plateau in the ZHe date-eU curve may not be evident in a sample, and dates that appear to represent the timing of exhumation may be older or younger than the actual event. Likewise, averaging single grain dates to produce a weighted mean ZHe age for a single sample removes pertinent information on burial temperatures and cooling rates. Many ZHe dates that traditionally would be discarded because they are older than expected or reflective of partial resetting are actually quantifiable and help to constrain the time-temperature history of the strata [*Guenthner et al*., 2015].

In the following section, we present a series of thermal history models that help describe the distribution of dates in our own dataset. First, we use inverse and forward thermal history modeling as a means to assess plausible t-T histories for an individual sample (Fig. 7). Next, we use forward models to illustrate the relationship between regional t-T histories and structure dependent date-eU dispersion (Fig. 8).

5.1. HeFTy modeling results and interpretations

In order to assess the realm of plausible t-T histories for our dataset, inverse and forward thermal history modeling was performed using the software program *HeFTy* [*Ketcham*, 2005]. Whereas inverse modeling investigates many more thermal histories than a forward modeling approach, the pre-depositional thermal history experienced by individual zircons is a variable that is difficult to constrain *a priori* in our dataset. For that reason, we present our modeling results as a series of forward models (Figs. 7, 8), with the exception of sample 11FNA010, for which we include both forward and inverse models (Fig. 1). This approach best recognizes the complex ways in which pre- and post-depositional thermal history are manifest in our observed ZHe date-eU trends. The results from the remainder of our inverse models provide the same conclusions as our forward models, and are included in the Appendix to this Chapter (Figs. A4 – A13) alongside a detailed description of our geologic constraints and inverse modeling methodology (Text A2).

Katherine Group sample 11FNA010 (Fig. 7) from the Canyon anticline is unique in this dataset, as the absolute concentrations of eU are generally low and exhibit a smaller range of values compared with the remainder of our samples. Due to the low eU values, the zircons are more retentive to helium at higher temperatures (Fig. 6) and as a result the sample lacks the Late Cretaceous to Eocene ZHe dates common in the rest of the dataset. Instead, the ZHe data form three populations at c. 160, c. 225, and c. 400 Ma, and have an average ESR of 54 μm. An inverse thermal model derived from four grains suggests that burial continued following the Devonian and reached a thermal maximum of <200°C between the Permian and the Middle Triassic. Following the unroofing and erosion of this Devonian to Triassic stratigraphic record, the Katherine group was reheated to temperatures <160°C during the Late Cretaceous. In an

effort to understand the t-T conditions that best constrain these data, we extrapolated the best-fit t-T path from our inverse model, and used forward modeling to visualize the effects of changing the magnitude and timing of thermal maximums on date-eU relationships (Fig. 7a-d). Each forward model shows inheritance date-eU curves for 1000 Ma (non-inheritance) and 2200 Ma to outline the difference in expected date-eU trends for zircons with near-end member pre-depositional histories. Fig. 7a shows the expected inheritance curves generated from the best-fit path of our inverse model. In this scenario, the strata reach a maximum temperature of 185°C, which is sufficient to reset all but the most retentive zircons. The thermal maximum is followed by cooling between the Permian to Middle Triassic, which produces the c. 225 Ma cooling age common in the sample. Whereas the absence of Cretaceous and younger ages provides poor resolution on the timing of tectonic exhumation related to the formation of the Mackenzie Mountains, the c. 160 Ma dates allow for the model to constrain the maximum temperatures experienced by this sample in the Cretaceous to Tertiary. The higher eU values in the c. 160 Ma grains (104–128 ppm eU) result in a slightly less retentive kinetic population compared to the c. 225 Ma ages (28–74 ppm eU). Thermal modeling suggests that Cretaceous reheating to 160°C results in partial resetting of the Triassic thermal history in grains with lower retentivity, producing the c. 160 Ma dates in this sample.

Fig. 7b investigates the effect of a hotter thermal maximum (200°C) on the inheritance date-eU curves. In this scenario, the higher temperatures have resulted in a greater degree of partial resetting in the most retentive zircons, and the inheritance date-eU curves are no longer able to account for the c. 400 Ma population. In Fig. 7c, the Late Cretaceous thermal maximum has increased from 160°C to 185°C, resulting in partial resetting of the late Paleozoic to early Mesozoic cooling history to ages younger than our c. 225 Ma population. Whereas the good-fit

solutions from our inverse model suggest that the thermal maximum occurred between the Permian and Middle Triassic, the acceptable solutions in this model do not preclude burial continuing into the Jurassic. We investigate this possibility in Fig. 7d. In this simulation, Katherine Group strata reach a thermal maximum of 185°C prior to cooling in the Jurassic. According to this model, our c. 160 Ma ZHe dates are reflective of Jurassic cooling, as opposed to partial resetting of a Permian to Middle Triassic cooling history as predicted in the models shown in Figs. 7a–c. We are hesitant to support this interpretation, as t-T histories with a Jurassic cooling event have difficulty resolving the observed c. 225 Ma ZHe dates revealed in our data. Whereas it is possible that the absence of ZHe dates younger than the c. 160 Ma is a statistical problem, and that analyzing more zircons would reveal a higher eU population with younger ZHe dates, the overall t-T history would not change substantially as the maximum temperatures and heating and cooling rates are constrained by the kinetics of the three ZHe age populations.

Although thermal history modeling of ZHe data can provide a reasonable estimation of the range of plausible thermal histories experienced by a single sample, comparison of model results between samples is complicated: the relatively few (~10) zircon grains analyzed per sample compared with detrital variability means that samples with similar thermal histories can have very different thermal models if critical ZHe dates are missing. To increase the number of individual data points on the date-eU graphs and facilitate a discussion on regional thermal evolution, we follow the example of *Guenthner et al.* [2015] and combine data from samples at similar structural positions in the fold-thrust belt (Fig. 8). Given a large enough dataset, patterns between ZHe date, eU and grain size similar to those discussed in Fig. 6 can provide critical information on regional trends in thermal history. Fig. 8 shows ZHe date-eU graphs for each of the five structures discussed previously (Fig. 5), and forward models derived from candidate t-T

paths that are in accord with the thermal histories indicated from inverse thermal modeling of each sample. To provide a consistent pre-Cretaceous thermal history, Figs. 8a–e follow the same pre-Aptian t-T history as the best-fit path from the 11FNA010 inverse model (Fig. 7), experiencing partial resetting to 185°C in the Permian and cooling to below the ZHe PRZ through the late Paleozoic to early Mesozoic. Sensitivity analyses for each modeled history are available in the Appendix to this Chapter (Figs. A14 – A18), and test the effect of varying the timing and magnitude of thermal events on the position of the inheritance curves. While the maximum burial temperature and timing of cooling are likely the factors that most influence the position of the inheritance curves, we submit that the duration spent at temperatures within the ZHe PRZ is also critical. In fact, prolonged residence at lower temperatures in the ZHe PRZ can have as pronounced an effect on partial resetting of ZHe dates as a very short duration at much higher temperatures. Due to variations in stratigraphic level, geographic separation, and the effects of U and Th zonation, the forward models do not perfectly account for all of the data in each structure. They do, however, provide a decent approximation of the trends between date, eU and grain size for samples from similar structural positions in the fold-thrust belt, allowing for visualization and comparative analysis of an average t-T history for each structure.

Samples from the frontal anticlines (Fig. 8a) exhibit a broad dispersion in ZHe dates at low eU concentrations, with even the smallest grains varying by hundreds of millions of years over a small range of eU, and reach a plateau age of c. 55 Ma as eU increases above 200 ppm. This distribution can be explained by a thermal history where the strata are only reheated to the lower temperatures of the ZHe PRZ, with moderate cooling commencing at c. 60 Ma. In these samples, only the least retentive, more radiation damaged, grains are reset. The remainder retain their Triassic cooling history, or are partially reset to c. 160 Ma. An increase in temperature from

140°C to 190°C between 70 and 60 Ma is consistent with inverse thermal models for many of the samples from this region. Samples from the Foran anticline to the southwest (Fig. 8b) have a lower degree of age dispersion than the frontal anticlines due to reheating to higher temperatures (~175°C) in the Cretaceous. The higher temperatures and longer time spent in the ZHe PRZ allow for partial resetting of the Triassic cooling history to ZHe dates younger than 171 ± 14 Ma, and cooling at 75 Ma results in the c. 70 Ma plateau in cooling ages at eU concentrations greater than 150 ppm. The thermal history from the Tawu anticline (Fig. 8c) suggests a similar Albian through Campanian history as the Foran anticline, reaching maximum temperatures of ~175°C. However, the samples from the Tawu anticline reside in the ZHe PRZ for longer, cooling at c. 60 Ma, approximately the same time as exhumation in the frontal anticlines. The longer duration in the PRZ allows for a greater degree of partial resetting than the anticlines to the northeast. ZHe dates from the Tigonankweine and Bolstead anticlines (Fig. 8d) are significantly more dispersed than the Tawu and Foran anticlines, indicating reheating under lower temperature conditions in the Cretaceous. Compared with samples from the frontal anticlines (Fig. 8a), these data form a more continuous spectrum of cooling ages from 249 ± 20 Ma to 56 ± 5Ma. Forward models from these samples suggest a thermal history where the strata reached temperatures of ~165°C by the Cenomanian, and cooled gradually from the Santonian until c. 67 Ma, when cooling rates increased moderately. The thermal history required to satisfy the observed age distribution from Keele Formation samples in the Redstone Plateau (Fig. 8e) is starkly different than the structures to the east of the Plateau Fault. ZHe dates from the Keele Formation separate into Early Cretaceous, Cenomanian through Turonian and Maastrichtian populations. The proposed thermal history allows for temperatures as great as 200°C in the Aptian/Albian, fully resetting all but the most retentive grains. Slow cooling through the PRZ from the Cenomanian through the

Maastrichtian results in the 80-100 Ma cooling ages abundant in these two samples. Similar to the thermal history from the Tigonankeweine and Bolstead anticlines (Fig. 8d), an increase in cooling rate at c. 67 Ma coincides with the strata cooling to temperatures lower than the ZHe PRZ and produces the Maastrichtian cooling ages in the samples. ZHe date-eU relationships from all five structural domains exhibit a strong negative correlation as eU increases over a threshold concentration between 75-100 ppm. Our forward models suggest that radiation damage accumulation must have occurred from the Paleoproterozoic in order to yield the α-dose required to satisfy this observation.

6. Discussion

6.1. Neoproterozoic sources of the Mackenzie Mountains

Stratigraphic ages for units in the MMSG and WSG are in many cases constrained solely by the youngest ages from detrital zircon U-Pb studies. Because of the refractory nature of zircon, and its propensity to survive several depositional cycles, such an interpretation can overestimate that maximum depositional age of these units [*Haines et al.*, 2004]. Previously, the maximum stratigraphic ages for the Katherine Group and Tsezotene Formation were constrained to c. 1005 Ma from the youngest detrital zircon U-Pb age [*Leslie*, 2009]. U-Pb dating of basement derived granitic clasts (1175-1100 Ma) from diatremes that cross cut the MMSG and from baddeleyite from the Copper Creek basalt (1267 ± 2 Ma), which underlies the Shaler Supergroup, a correlative of the MMSG, help bracket the maximum age for the base of the MMSG [*Jefferson and Parrish,* 1989]. Ages from igneous bodies with geochemical similarities to the basalt flow that caps the Little Dal Formation, including Rb-Sr dates of sills that intrude the Tsezotene Formation (779 ± 2 Ma) and from U-Pb ages from a granitic intrusion in the Little

Dal Formation (778 +3/-2 Ma) provide a minimum age for the MMSG [*Armstrong et al.*, 1982; *Harlan et al.,* 2003].

Our muscovite $^{40}Ar/^{39}Ar$ data help to refine the stratigraphic age for the Mackenzie Mountains Supergroup and in doing so improve our understanding of the timing of Neoproterozoic basin formation prior to the breakup of Rodinia. Youngest muscovite ages from the Tsezotene Formation and Katherine Group are 992 ± 1 Ma and 963 ± 1 Ma, respectively. The 818 ± 1 Ma age from the Dodo Creek Formation, the basal unit of the Little Dal Group, is similar to an 811.0 ± 0.3 Ma [*Macdonald et al.*, 2010] tuff in carbonates from the reefal assemblage of the Upper Fifteenmile Group in the Ogilvie Mountains to the west (Fig. 1), supporting the lithostratigraphic correlation of these two units [*Macdonald et al.*, 2012]. The progressive decrease of modal ages from 1100-1050 Ma to 900-850 Ma in the Tsezotene to Dodo Creek Formations is consistent with models that suggest sediments in the MMSG were derived from Grenvillian sources, possibly thousands of kilometers to the southeast on the eastern margin of Laurentia [*Rainbird et al.*, 1997]. The Grenville orogeny involved several discrete collisional events from 1300 Ma to 900 Ma, and is well-exposed from the coast of Labrador to northern Mexico [*Whitmeyer and Karlstrom*, 2007]. The presence of muscovite ages younger than 900 Ma, and paucity of a 1300-1200 Ma population in our dataset is consistent with the lower temperature, and often younger, events recorded in muscovite data compared to the U-Pb system in zircon; the muscovite $^{40}Ar/^{39}Ar$ chronometer records the lower temperature aspect of the cooling path and should expectedly be younger than the metamorphic age of an orogen [*Montario and Garver*, 2009]. Detrital muscovite $^{40}Ar/^{39}Ar$ ages from the Keele Formation stand in stark contrast to published detrital zircon U-Pb studies [*Lane and Gehrels*, 2014], where an abundance of Grenvillian zircons suggested that sediments in the Keele clastic wedge were

recycled from the underlying Mackenzie Mountains Supergroup. Our data do not preclude this interpretation, as we would not expect Grenville-derived muscovite in the MMSG to survive orogenic recycling. We note that our two youngest detrital muscovite $^{40}Ar/^{39}Ar$ ages from the Keele Formation (785 ± 2 Ma, 978 ± 2 Ma) are nearly identical to muscovite cooling ages (788 ± 8 Ma, 980 ± 4 Ma) reported from metamorphic rocks of the Paleoproterozoic Wernecke Supergroup, exposed in the nearby Wernecke Mountains (Fig. 1) [*Thorkelson et al*., 2005]. This similarity potentially fingerprints one of the sediment sources for the Keele Formation and is in keeping with the hypothesis that Keele Formation sediments are derived from recycling of local Neoproterozoic sources [*Lane and Gehrels*, 2014].

6.2. Utility of reset and partially reset zircon (U-Th)/He dates

ZRDAAM [*Guenthner et al.*, 2013] is a powerful tool in assessing the thermal evolution of strata with protracted cooling histories through the uppermost crust. In particular, the model has its most utility in samples where self-irradiation of zircon has occurred over long geologic timescales without significant annealing of damaged zones. Partially- to fully-reset detrital datasets can contain a tremendous amount of t-T information, due to the wide range in grain size, eU, and potential for variable pre-depositional histories and inherited radiation damage in the zircon population. These variables result in a broad spectrum of closure temperatures within a single sample, and in tectonic settings where strata are never buried to sufficiently high temperatures, such as the Neoproterozoic stratigraphy of the Mackenzie Mountains, can potentially record more than the most recent thermal event. Additionally, modeling of these datasets has added value in strata where apatite is absent or too small for (U-Th)/He analysis, as highly damaged zircon can be sensitive to similar temperatures as the apatite (U-Th)/He system.

However, several factors complicate interpretation of these datasets. One particular complication centers around identifying the influences of pre-depositional history, including inherited ^{4}He and radiation damage, on ZHe ages and date-eU relationships. Determining how these variables affect the post-depositional thermal history can be very difficult without independent constraints on zircon crystallization age or α-dose [*Guenthner et al.*, 2015]. Secondly, sampling from different stratigraphic levels in the same succession can yield substantially different age populations should the strata have different grain sizes or provenance. For these reasons, we believe that detailed thermal modeling is required to understand the probable geologic history exhibited by the datasets. We do not recommend selecting only the youngest dates from samples or averaging (U-Th)/He date, as these methods do not acknowledge the complexity of the (U-Th)/He system and potentially exclude non-obvious, but equally probable, geologic scenarios [*Guenthner et al.*, 2014]. To this extent, using the vertical profile approach [*Ehlers*, 2005; *Reiners and Brandon*, 2006] where changes in (U-Th)/He date across a topographic profile is used to assess exhumation rates will provide an inaccurate result if the strata have not been buried to sufficient temperatures to completely reset any prior thermal history. As an alternative to the vertical profile sampling strategy, we analyzed more grains from individual samples and combined data from similar structural regions to assess regional trends in thermal history. We believe that this method does an appropriate job of acknowledging the errors and assumptions involved in the technique while providing meaningful information on thermal history.

Our thermal modeling requires radiation damage accumulation from the Paleoproterozoic in order to satisfy the relationships between ZHe date, eU and grain size observed throughout our dataset (Fig. 8). However, this observation is contrary to zircon U-Pb geochronology, which

suggest that the zircons are predominantly from a Grenvillian source [*Rainbird et al.*, 1992, 1996, 1997; *Lane and Gehrels*, 2014]. Whereas late Paleoproterozoic to early Mesoproterozoic zircons are present in the U-Pb record and may provide a suitable amount of radiation damage to explain our date-eU trends, the absence of a similar population in our muscovite $^{40}Ar/^{39}Ar$ dataset from the MMSG (Fig. 3) supports the theory that 1600-2000 Ma zircons are from a recycled source, likely derived from earlier crustal growth events on the southeast margin of Laurentia and reworked during the Grenville orogeny [*Rainbird et al.*, 2012]. We are inclined to believe that our Mesoproterozoic to Neoproterozoic muscovite ages represent not just the timing of unroofing in the source area, but likely provide an approximation as to when the majority of the zircons in our dataset cooled to sufficient temperatures to retain radiation damage. If this assumption is correct, then radiation damage accumulation has only occurred since the Mesoproterozoic to Neoproterozoic, a billion-year shorter duration than the Paleoproterozoic pre-depositional history required to explain the ZHe date-eU trends in our dataset.

One possible explanation for this divergence between data and model is that the threshold alpha dose of 2 x 10^{18} α/g, which the ZRDAAM model requires for diffusivity to decrease in zircon [*Guenthner et al.*, 2013], is simply too high. The ZRDAAM diffusion model is derived from the well-studied Sri Lankan dataset of *Nasdala et al.* [2004a; 2004b], which is perhaps not representative of all natural zircon populations. It is also possible that the early Mesoproterozoic to Paleoproterozoic zircon populations retain their radiation damage despite having been incorporated in and reworked by the Grenville orogeny. Thermal annealing of radiation damage in apatite is thought to behave kinetically similar to apatite fission track annealing [*Flowers et al.*, 2009]. Such an assumption for zircon is complicated, as several discrete mechanisms control alpha damage annealing [*Zhang et al.*, 2000; *Geisler et al.*, 2001], and zircon fission tracks

themselves appear to have annealing kinetics that are damage dependent [*Garver et al*., 2005; *Marsellos and Garver*, 2010]. Although zircon fission track kinetics do a sufficient job explaining alpha damage annealing, there is currently no kinetic model that accounts for the several recognized mechanisms that control alpha damage annealing in zircons at geologic timescales [*Guenthner et al.*, 2013]. To that extent, it is possible that our early Mesoproterozoic to Paleoproterozoic zircons retained some of their inherited radiation damage, even if they were subjected to conditions conducive to zircon fission track annealing.

A final potential source for the disparity between the expected pre-depositional history and those modeled in our dataset revolves around sampling bias. Zircon grains analyzed for (U-Th)/He analysis are chosen based on their crystal morphology and size. Ideal grains should have tetragonal prism widths greater than 60 μm due to uncertainties associated with the large alpha ejection corrections in small zircon [*Reiners et al.*, 2004]. If zircons were derived from the Grenville orogen [*Rainbird et al.*, 1997], they have possibly travelled up to 5000 km through river systems across the craton, and were likely abraded and rounded during transport. It is possible that the many Grenville detrital grains were too small or had non-ideal morphologies for (U-Th)/He analysis, and that the grains that met our criteria were from more local sources such as the Archean craton directly to the east. However, we believe this explanation to be the least likely of the three, as Archean zircons represent a very small portion of the overall detrital population.

6.3. Phanerozoic evolution of the Mackenzie Mountains

The presence of Paleozoic ZHe dates (c. 430-330 Ma; Figs. 4, 5) from Mackenzie Mountains Supergroup strata across the fold-thrust belt indicate that the Phanerozoic stratigraphic cover did not bury the Mackenzie Mountains Supergroup to sufficient depths and

high enough temperatures to completely reset the helium system in zircons. Thermal modeling of our Mackenzie Mountains Supergroup and Windermere Supergroup ZHe datasets (Fig. 8) indicates deeper burial across the Plateau Fault, where strata from the Keele Formation in the Redstone Plateau to the southwest of the fault have experienced substantially higher temperatures (>200°C) than strata from the Mackenzie Mountains Supergroup (~160-190°C) to the northeast. These model results are corroborative with a Paleozoic section that thickens substantially to the south [*Gordey and Roots,* 2011].

Owing to a preponderance of dates greater than c. 160 Ma, the modeled thermal history of Katherine Group sample 11FNA010 (Fig. 7) serves to illuminate the Paleozoic to early Mesozoic evolution of the Mackenzie Mountains. In our interpretation, burial of the Neoproterozoic strata continued following the deposition of the Imperial Formation in the Late Devonian, reaching a thermal maximum (<200°C) between the Permian and Early Triassic. Regional cooling likely began by the Middle Triassic, recording the Triassic cooling ages pervasive within our dataset (Figs. 4, 5). An investigation into the lower-temperature thermochronology of the Slave craton [*Ault et al.*, 2009, 2013] revealed progressive westward unroofing from 340 Ma in the eastern Slave craton to 225 Ma on its western margin. The 225 Ma cooling age and the minimum date of 240 Ma for peak Paleozoic temperatures from the western Slave craton are strikingly similar to our modeled thermal history in the Mackenzie Mountains, suggesting a regional, diachronous unroofing event across northwest Canada in the late Paleozoic to early Mesozoic. The 250-170 Ma thermal maximum derived from AFT models of the Devonian Imperial Formation by *Issler et al*. [2005] in the Keele Tectonic Zone of the Mackenzie Plain partially overlaps with the Permo-Triassic cooling history reported here for the Mackenzie Mountains and by *Ault et al.* [2013] for the western Slave craton.

The regional patterns in ZHe date, eU and grain size, and ramifications for t-T history discussed in Fig. 8 allow for us to interpret the spatiotemporal evolution of the Mackenzie Mountains throughout the Cretaceous (Fig. 9). Our model invokes a classic foreland propagating fold-thrust belt, propagating from the hinterland to the southwest of our study area in the Aptian/Albian, through to the current location of the Mackenzie Mountain deformation front by the latest Paleocene. We note that our ZHe dates record cooling in the hanging of a thrust fault, provided that erosion rates keep pace with thrusting [*Reiners and Brandon*, 2006]. Our model begins in the Early Cretaceous where Cordilleran deformation in the hinterland results in loading and flexure in the southwest of our study area, corresponding with subsidence in the present-day Redstone Plateau (Fig. 9a). The accommodation space is filled with an Aptian-Albian sedimentary package that thins to the northeast [*Hadlari et al.*, 2014]; heating due to this burial results in partial to full resetting of the ZHe system in Keele Formation samples from the Redstone Plateau. The MMSG strata in the northeast of our study area reside at cooler temperatures than the ZHe PRZ and experience heating to progressively higher temperatures in the southwest, reaching 160°C in the Tigonankweine anticline. Cenomanian cooling in the Redstone Plateau is the first evidence of uplift associated with the Cordilleran deformation front in our study area. Northeastward propagation of Cordilleran structures shifts the foredeep from the central to northern Mackenzie Mountains burying samples from the present day Foran and Tawu anticlines to higher temperatures in the ZHe PRZ (Fig. 9b). The creation of accommodation space extends to the Mackenzie Plain in the northeast, where deposition of the Slater River Formation records an upward shallowing sequence from an offshore marine to lower shoreface setting [*Thomson et al.*, 2011]. Our dataset cannot resolve whether Cenomanian cooling in the hinterland reflects the timing of initiation of the Plateau Fault or is a product of

regional exhumation. To this extent, we consider the Cenomanian as the maximum age of displacement along the Plateau Fault. The fold-thrust system continues to propagate through the Campanian, where initiation of movement on the Canyon Fault results in exhumation of the Foran anticline and shifts the foredeep to the northeast, (Fig. 9c) resulting in deposition of shoreface sandstones of the Little Bear Formation in the Mackenzie Plain [*Yorath and Cook*, 1981]. Our models suggest that a significant shortening in the Mackenzie Mountains occurs during the Maastrichtian, with cooling of the Redstone Plateau, Tigonankweine, Bolstead and Foran anticlines accelerating at c. 67 Ma (Fig. 9d, e). Late Maastrichtian acceleration in cooling rates is likely synchronous with the timing of formation of structures in the southwest of the study area, providing a minimum age for movement on the Plateau Fault and a maximum age for smaller structures such as reverse motion on the Conundrum Fault. The moderate exhumation also results in increased loading and the creation of significant accommodation space in the adjacent foreland basin, which is recorded in the Mackenzie Plain by the deposition of the up to one kilometer thick succession of Maastrichtian East Fork Formation marine shale. As exhumation of the fold-thrust belt continued into the Paleocene, alluvial fan deposits of the Summit Creek Formation prograded into the Mackenzie Plain [*Yorath and Cook*, 1981]. The final compressional pulse occurred between the latest Paleocene and earliest Eocene, resulting in the moderate exhumation of the frontal anticlines and Tawu anticline (Fig. 9f). This unroofing event also had a significant impact on the Mackenzie Plain eroding away a kilometer or more of Late Cretaceous-Paleocene strata [*Issler et al.*, 2005].

The difference in the thermal histories and youngest ZHe ages between the frontal anticlines (c. 54 Ma) and the proximal Foran anticline (74 Ma), supports recent remapping of the Canyon Fault as a major regional thrust fault with significant displacement [*Fallas and*

MacNaughton, 2014a]. We interpret that Maastrichtian cooling in the Foran anticline represents the timing of initiation of movement on the Canyon Fault. The similar Paleocene to Eocene ages in the Tawu and frontal anticlines suggest that exhumation due to folding in the outer fold-thrust belt postdates movement on the Canyon Fault and represents the final phase of deformation in the Mackenzie Mountains.

Our model requires an increase in Cretaceous temperatures to 165-200°C across the Mackenzie Mountains to account for our partially to fully reset ZHe dates. Although, increasing temperatures throughout the Cretaceous could be attributed to a change in geothermal gradient, the projected depth of the majority of these samples prior to the Albian (<3000 m) would require a dramatic increase in the regional temperature regime [*Aitken et al.*, 1971; *Yorath and Cook*, 1981; *Morrow*, 1991]. Instead, we invoke deposition of an Aptian-Campanian stratigraphic succession in front of the ancestral Mackenzie Mountains (across the present day northeast Mackenzie Mountains) to allow for this burial and reheating, despite little stratigraphic evidence for an extensive Cretaceous system in the region. The only preserved Cretaceous strata in the Mackenzie Mountains are found in a fault-bounded outlier in the hanging wall of the Plateau Fault [*Blusson*, 1971]. These strata have a minimum-thickness of 1300 m [*Turner et al.*, 2011], and the repetitive sandstone, conglomerate and coal successions are proposed to represent non-marine deposition from meandering streams [*Yorath*, 1991]. Analysis of pollen in the strata indicate the lower 700 m of the section has a post-Barremian to late Albian age, and a poorly-defined plant fossil assemblage in the upper 600 m suggests a youngest age of Coniacian to Campanian [*Turner et al.*, 2011]. Some authors have suggested that deposition of this Cretaceous succession occurred in an intermontane setting [*Dixon*, 2004], however we believe that our model results support the interpretation of these fluvial deposits filling an Aptian foredeep in

front of the emerging Mackenzie Mountains to the southwest, possibly developing into an intermontane basin as the Mackenzie Mountains evolved throughout the Late Cretaceous [*Gabrielse*, 1991; *Yorath*, 1991; *Gordey et al.*, 2010]. We are hesitant to predict exactly how far this Early Cretaceous system may have extended over the Mackenzie Mountains, as the source for the Albian strata 150 km to the northeast in the Mackenzie Plains is almost certainly from the craton to the east [*Yorath and Cook*, 1981; *Thomson et al.*, 2011]. The absence of time-correlative coarse clastic deposits to the Cretaceous marine shales and shoreface sands preserved in the Mackenzie Plain is explained by the physiographic evolution of the Mackenzie Mountains we propose (Fig. 9). In our model, proximal facies are deposited in the foredeep adjacent to the emerging highlands and are cannibalized by erosion and re-deposition during propagation of the fold-thrust system. The absence of an extensive Cretaceous section in the Mackenzie Mountains is not indicative of non-deposition, but instead well within the realm of the erosion patterns expected as strata are exhumed via thrust faults and broad detachment folds.

6.4. Regional geodynamic implications

Assessing the spatiotemporal evolution of the foreland belt in the Northern Cordillera has long been a challenge due to the dearth of dateable syn-tectonic strata and absence of a magmatic record. As a result, relatively little is known about the kinematic connection between the timing of Cordilleran events in the hinterland, including accretion of the Yukon-Tanana terrane (YTT) and exhumation of the Selwyn Basin, and the final Late Cretaceous-Tertiary evolution of the Mackenzie Mountains [*Gabrielse*, 1991; *Gordey et al.*, 2010]. Our dataset provides a missing link between the stable Laurentian (Slave) craton to the east with events occurring outboard of the margin to the west. *Ault et al.* [2013] hypothesized that the progressive westward unroofing of the Slave craton from the Carboniferous to the Triassic evinced by their dataset was a function

of long-wavelength dynamic topography caused by changes in mantle flow related to plate boundary processes to the north and west. The similarity between the unroofing history of the western Slave craton and the late Paleozoic to early Mesozoic thermal history presented in this study supports regional diachronous unroofing across northwest Canada. In particular, we note that the Middle Triassic unroofing event suggested by our thermal history models is contemporaneous with the 260-252 Ma Klondike orogeny described in the Klondike District of the western Yukon. The Klondike orogeny is perhaps the earliest evidence of arc-continent collisions related to accretion of the YTT [*Beranek and Mortensen*, 2011] and provides an example of the type of far-field plate boundary interactions that may have influenced interior processes throughout the Permian and Triassic.

Muscovite $^{40}Ar/^{39}Ar$ geochronology from crystalline basement indicates regional exhumation of the Yukon-Tanana terrane occurred in the early Jurassic in response to convergence between the Farallon and North American Plates [e.g. *Knight et al.*, 2013]. Continued convergence of these two plates resulted in northeast propagation of a deformation front as evinced by metamorphism in the Late Jurassic Lower Schist unit in the northwestern Selwyn basin [*Mair et al.*, 2006]. Widespread crustal extension following tectonic thickening during accretion of Yukon-Tanana terrane occurred in the hinterland by the Aptian/Albian, as revealed by the c. 115-100 Ma $^{40}Ar/^{39}Ar$ and (U-Th)/He cooling ages common in the footwall of normal faults [*Dusel-Bacon et al.*, 2002; *Mair et al.*, 2006; *Knight et al.*, 2013]. This crustal extension is thought to drive shearing in thrust sheets in the Selwyn Basin [*Mair et al.*, 2006]. These Aptian-Albian events in the hinterland are coincident with deposition of the oldest Cretaceous sediments in the Mackenzie Plain and resetting of the ZHe system in the Redstone Plateau [*Yorath and Cook*, 1981; *Thomson et al.*, 2011; this study]. We submit that subsidence

and deposition of Albian strata in the Mackenzie Mountains and Plain is best explained by crustal loading in the foredeep of the hinterland orogeny. $^{40}Ar/^{39}Ar$ analyses of metamorphic muscovite bracket the end of regional ductile deformation in the Selwyn Basin to 104-100 Ma [*Mair et al.*, 2006]. The temporal parallel between the waning stages of crustal extension in the YTT, cessation of ductile deformation in Selwyn basin thrust sheets and the initiation of cooling in the Redstone Plateau suggests that Cordilleran deformation had propagated as far northeast as the Central Mackenzie Mountains by the latest-Early Cretaceous.

7. Conclusions

Detrital muscovite $^{40}Ar/^{39}Ar$ analyses of the Tsezotene Formation, Katherine Group and Little Dal Group help refine our understanding of stratigraphic ages for MMSG. We report youngest ages of 992 ± 1 Ma for the Tsezotene Formation and 963 ± 1 Ma for the Katherine Group. Our youngest age from the Dodo Creek Formation constrains the timing of deposition of the Little Dal Group to c. 818-778 Ma. Additionally, our muscovite $^{40}Ar/^{39}Ar$ age spectra support the hypothesis that MMSG was mostly sourced from the Grenville orogen of Laurentia [*Rainbird et al.*, 1997, 2012].

Though interpretation of partially reset detrital ZHe datasets can be complicated due to the effects of inherited pre-depositional ^{4}He and radiation damage, detailed numerical modeling can offer a wealth of information on the thermal history of a sample through geological time [*Guenthner et al.*, 2015]. Zircon (U-Th)/He data from the central and northern Mackenzie Mountains provides a comprehensive assessment of the time-temperature evolution of the Mackenzie Platform throughout the Phanerozoic. Though the dataset contains significant dispersion in ZHe dates, patterns in date-eU and date-grain size are distinct for structures across the fold-thrust belt. Noticeably, a discrepancy exists between the youngest Paleocene cooling

ages in the frontal anticlines compared with youngest Campanian–Maastrichtian ages in the Foran anticline, indicating that the Canyon Fault that separates these features is a significant structure in the region. Thermal history modeling reveals a geologic history where burial continued throughout the Paleozoic and into Mesozoic following deposition of the Devonian Imperial Formation. The stratigraphic record of this depositional history was eroded in the early Mesozoic, recording the Middle Triassic cooling ages common in many samples in our dataset. Our modeled Middle Triassic cooling event overlaps with c. 240 Ma exhumation modeled on the western margin of the Slave craton [*Ault et al.*, 2009, 2013]. We propose that this early Mesozoic cooling occurred diachronously throughout the region, potentially in response to far-field stresses on the western margin of the continent. Burial in front of the emerging Mackenzie Mountains in the Cretaceous resulted in partial to full resetting of this earlier thermal history.

Our thermal models detail orogenic propagation across the study area starting at the Albian/Cenomanian boundary in the Redstone Plateau to the southwest and continuing through to the Paleocene in the deformation front. Abrupt changes in regional cooling rates occur at: 1) c. 100 Ma, possibly linked to initiation of displacement along the Plateau Fault; 2) c. 75-67 Ma, where cooling rates accelerate in the Redstone Plateau and Tigonankweine and Foran anticlines. Timing of movement on the Canyon Fault is likely synchronous with the onset of cooling in the Foran anticline; and 3) c. 60-55 Ma, when the frontal anticlines and Tawu anticline are moderately cooled below the ZHe PRZ. These data refine the timing of the deformation across the Mackenzie Mountains, and suggest that the formation of the northern Cordilleran Foreland Belt propagated northeastward in a series of pulses through the Late Cretaceous to Eocene.

Acknowledgments

Funding for this project was provided by an NSERC-CRD grant to DAS, with contributions from ConocoPhillips Canada and Chevron Canada. Additional financial and logistical support was generously made possible by the Geomapping for Energy and Minerals (GEM) program at Natural Resources Canada. We thank Robert MacNaughton for his insight and ongoing assistance, Matt Heizler at New Mexico Institute of Technology for assistance with the Ar-Ar data collection, and the University of Texas at Austin thermochronology laboratory for their analytical support. This paper benefitted from the reviews of William Guenthner and an anonymous reviewer, and the editorial handling of Nathan Niemi.

References

Aitken, J. D., and D. Cook (1974), Carcajou Canyon map-area, District of Mackenzie, Northwest Territories, *Geol. Surv. Canada, Paper 74-13,* 28 p.

Aitken, J. D., and D. Long (1978), Mackenzie tectonic arc - Reflection of early basin configuration?, *Geology*, *6*, 626–629.

Aitken, J. D., R. W. Macqueen, and J. L. Usher (1973), Reconnaissance studies of Proterozoic and Cambrian stratigraphy, lower Mackenzie River area (Operation Norman), District of Mackenzie, *Geol. Surv. Canada, Paper 73-9*, 178 p.

Armstrong, R. L., G. H. Eisbacher, and P. D. Evans (1982), Age and stratigraphic-tectonic significance of Proterozoic diabase sheets, Mackenzie Mountains, northwestern Canada, *Can. J. Earth Sci.*, *19*, 316–323.

Asselin, E. (2009), Palynological report on 15 samples from the Katherine Group and the Mount Cap Formation of the Peele sequence, NW Territories and Yukon (NTS 96C/08, D/07, 11,13,14,15, E/04 and 106H/01), *Geol. Surv. Canada Paleontol. Report 01-EA-2009*, 23 p.

Ault, A. K., R. M. Flowers, and S. A. Bowring (2009), Phanerozoic burial and unroofing history of the western Slave craton and Wopmay orogen from apatite (U–Th)/He thermochronometry, *Earth Planet. Sci. Lett.*, *284*, 1–11, doi:10.1016/j.epsl.2009.02.035.

Ault, A. K., R. M. Flowers, and S. A. Bowring (2013), Phanerozoic surface history of the Slave craton, *Tectonics*, *32*(5), 1066–1083, doi:10.1002/tect.20069.

Beranek, L. P., and J. K. Mortensen (2011), The timing and provenance record of the Late Permian Klondike orogeny in northwestern Canada and arc-continent collision along western North America, *Tectonics*, *30*(5), TC5017, doi:10.1029/2010TC002849.

Blusson, S. (1971), Sekwi Mountain map-area, Yukon Territory and district of Mackenzie, *Geol. Surv. Canada, Paper*, *71-22*, 17 p.

Cecile, M. P., and D. G. Cook (1981), Structural cross-cection northern Selwyn and Mackenzie Mountains, *Geol. Surv. Canada, Open File 807,* 1p.

Dixon, J. (2004), Lower Cretaceous (Albian) to Tertiary strata, Yukon Territory-Northwest Territories, *Geol. Surv. Canada, Open File 4633*, 26 p.

Dusel-Bacon, C., M. A. Lanphere, W. D. Sharp, P. W. Layer, and V. L Hansen (2002), Mesozoic thermal history and timing of structural events for the Yukon-Tanana Upland, east-central Alaska: $^{40}Ar/^{39}Ar$ data from metamorphic and plutonic rocks, *Can. J. Earth Sci.*, *39*, 1013–1051, doi:10.1139/E02-018.

Ehlers, T. A. (2005), Crustal thermal processes and the interpretation of thermochronometer data, *Rev. Mineral. Geochemistry*, *58*(1), 315–350, doi:10.2138/rmg.2005.58.12.

Enkelmann, E., P. K. Zeitler, J. I. Garver, T. L. Pavlis, and B. P. Hooks (2010), The thermochronological record of tectonic and surface process interaction at the Yakutat-North American collision zone in southeast Alaska, *Am. J. Sci.*, *310*(4), 231–260, doi:10.2475/04.2010.01.

Epstein, A. G., J. B. Epstein, and L. D. Harris (1977), Conodont color alteration—an index to organic metamorphism, *U.S. Geol. Surv., Paper 995,* 27 p.

Fallas, K. M., and R. B. MacNaughton (2014a), Geology, Carcajou Canyon (northwest), Northwest Territories, *Geol. Surv. Canada, Can. Geosci. Map 94, scale 1100,000*, doi:10.4095/292286.

Fallas, K. M., and R. B. MacNaughton (2014b), Geology, Carcajou Canyon (southeast), Northwest Territories, *Geol. Surv. Canada, Can. Geosci. Map 96, scale 1:100,000*, doi:10.4095/292288.

Fallas, K. M., and R. B. MacNaughton (2014c), Geology, Carcajou Canyon (southwest), Northwest Territories, *Geol. Surv. Canada, Can. Geosci. Map 97, scale 1:100,000*, doi:10.4095/292289.

Farley, K. A., R. Wolf, and L. Silver (1996), The effects of long alpha-stopping distances on (U-Th)/He ages, *Geochim. Cosmochim. Acta*, *60*(21), 4223–4229.

Fedo, C. M., K. N. Sircombe, and R. H. Rainbird (2003), Detrital zircon analysis of the sedimentary record, *Rev. Mineral. Geochemistry*, *53*, 277–303.

Feinstein, S., P. Brooks, M. Fowler, L. R. Snowdon, and G. K. Williams (1988), Families of oils and source rocks in the central Mackenzie corridor: a geochemical oil-oil and oil-source rock correlation, *Can. Soc. Pet. Geol. Mem.*, *15*, 543–552.

Feinstein, S., G. K. Williams, L. R. Snowdon, P. W. Brooks, M. G. Fowler, F. Goodarzi, and T. Gentzis (1991), Organic geochemical characterization and hydrocarbon generation potential of mid-Late Devonian Horn River bituminous shales, southern Northwest Territories, *Bull. Can. Pet. Geol.*, *39*(2), 192–202.

Feinstein, S., D. R. Issler, L. R. Snowdon, and G. K. Williams (1996), Characterization of major unconformities by paleothermometric and paleobarometric methods: application to the Mackenzie Plain, Northwest Territories, Canada, *Bull. Can. Pet. Geol.*, *44*(1), 55–71.

Flowers, R. M., R. A. Ketcham, D. L. Shuster, and K. A. Farley (2009), Apatite (U–Th)/He thermochronometry using a radiation damage accumulation and annealing model, *Geochim. Cosmochim. Acta*, *73*(8), 2347–2365, doi:10.1016/j.gca.2009.01.015.

Flück, P. (2003), Effective elastic thickness Te of the lithosphere in western Canada, *J. Geophys. Res.*, *108*(B9), 2430, doi:10.1029/2002JB002201.

Gabrielse, H. (1991), Structural styles, chapter 17, in *Geology of the Cordilleran Orogen in Canada*, edited by H. Gabrielse and C. J. Yorath, pp. 571 – 675, Geological Survey of Canada, Geology of Canada, no. 4.

Gabrielse, H., J. Roddick, and A. Blusson (1973), Geology, Wrigley Lake, District of Mackenzie, *Geol. Surv. Canada, Map 1315A, scale 1:250,000*.

Garver, J. I., P. W. Reiners, L. J. Walker, J. M. Ramage and S. E. Perry (2005), Implications for timing of Andean uplift from thermal resetting of radiation-damaged zircon in the Cordillera Huayhuash, Northern Peru, *J. Geol, 113*(2), 117–138.

Geisler, T., R. T. Pidgeon, W. van Bronswijk, and R. Pleysier (2001), Kinetics of thermal recovery and recrystallization of partially metamict zircon: a Raman spectroscopic study, *Eur. J. Mineral.*, *13*(6), 1163–1176, doi:10.1127/0935-1221/2001/0013-1163.

Gordey, S., H. Geldsetzer, D. Morrow, E. Bamber, C. Henderson, B. Richards, A. Mcgugan, D. Gibson, and T. Poulton (1991), Part A: Ancestral North America, in *Upper Devonian to Middle Jurassic assemblages, Chapter 8 of Geology of the Cordilleran Orogen in Canada*, edited by H. Gabrielse and C. Yorath, pp. 219–327, Geological Survey of Canada, Geology of Canada, no. 4.

Gordey, S. P. and C. F. Roots (2011), Chapter 2. Regional Setting, in *Geology of the Central Mackenzie Mountains of the Northern Canadian Cordillera, Sekwi Mountain (105P), Mount Eduni (106A), and the northwestern Wrigley Lake (95M) Map Areas, Northwest Territories*, edited by E. Martel, E. C. Turner, and B. J. Fischer, pp. 215 – 250, NWT Special Volume 1, NWT Geoscience Office.

Gordey, S. P., J. D. Macdonald, E. C. Turner, and D. G. Long (2010), Chapter 5. Structural Geology of the Central Mackenzie Mountains, in *Geology of the Central Mackenzie Mountains of the Northern Canadian Cordillera, Sekwi Mountain (105P), Mount Eduni (106A), and the northwestern Wrigley Lake (95M) Map Areas, Northwest Territories*, edited by E. Martel, E. C. Turner, and B. J. Fischer, pp. 215 – 250, NWT Special Volume 1, NWT Geoscience Office.

Guenthner, W. R., P. W. Reiners, R. A. Ketcham, L. Nasdala, and G. Giester (2013), Helium diffusion in natural zircon: Radiation damage, anisotropy, and the interpretation of zircon (U-Th)/He thermochronology, *Am. J. Sci.*, *313*(3), 145–198, doi:10.2475/03.2013.01.

Guenthner, W. R., P. W. Reiners, and Y. Tian (2014), Interpreting date–eU correlations in zircon (U-Th)/He datasets: A case study from the Longmen Shan, China, *Earth Planet. Sci. Lett.*, *403*, 328–339, doi:10.1016/j.epsl.2014.06.050.

Guenthner, W. R., P. W. Reiners, P. G. DeCelles, and J. Kendall (2015), Sevier belt exhumation in central Utah constrained from complex zircon (U-Th)/He data sets: Radiation damage and He inheritance effects on partially reset detrital zircons, *Geol. Soc. Am. Bull.*, *127*(3-4), 323–348, doi:10.1130/B31032.1.

Gutiérrez-Alonso, G., J. Fernández-Suárez, A. S. Collins, I. Abad, and F. Nieto (2005), Amazonian Mesoproterozoic basement in the core of the Ibero-Armorican Arc: $^{40}Ar/^{39}Ar$ detrital mica ages complement the zircon's tale, *Geology*, *33*(8), 637, doi:10.1130/G21485.1.

Hadlari, T., Y. Lemieux, S. Tylosky, W. Zantvoort, and O. Catuneanu (2009), Slope and submarine fan turbidite facies of the Upper Devonian Imperial Formation, northern Mackenzie Mountains, NWT, *Bull. Can. Pet. Geol.*, *57*(2), 192–208.

Hadlari, T., W. J. Davis, K. Dewing, L. M. Heaman, Y. Lemieux, L. Ootes, B. R. Pratt, and L. J. Pyle (2012), Two detrital zircon signatures for the Cambrian passive margin of northern Laurentia highlighted by new U-Pb results from northern Canada, *Geol. Soc. Am. Bull.*, *124*(7-8), 1155–1168, doi:10.1130/B30530.1.

Hadlari, T., B. C. MacLean, J. M. Galloway, A. R. Sweet, J. M. White, D. Thomson, J. Gabites, and C. J. Schröder-Adams (2014), The flexural margin, the foredeep, and the orogenic margin of a northern Cordilleran foreland basin: Cretaceous tectonostratigraphy and detrital zircon provenance, northwestern Canada, *Mar. Pet. Geol.*, *57*, 173–186, doi:10.1016/j.marpetgeo.2014.05.019.

Haines, P. W., S. P. Turner, S. P. Kelley, J. A. Wartho, and S. C. Sherlock (2004), $^{40}Ar/^{39}Ar$ dating of detrital muscovite in provenance investigations: a case study from the Adelaide Rift Complex, South Australia, *Earth Planet. Sci. Lett.*, *227*(3-4), 297–311, doi:10.1016/j.epsl.2004.08.020.

Harlan, S. S., L. Heaman, A. N. LeCheminant, and W. R. Premo (2003), Gunbarrel mafic magmatic event: A key 780 Ma marker for Rodinia plate reconstructions, *Geology, 31*(12), 1053-1056, doi: 10.1130/G19944.1

Harrison, T. M. (2005), Fundamentals of noble gas thermochronometry, *Rev. Mineral. Geochemistry*, *58*(1), 123–149, doi:10.2138/rmg.2005.58.5.

Hodges, K. V. (2005), 40Ar/39Ar thermochronology of detrital minerals, *Rev. Mineral. Geochemistry*, *58*(1), 239–257, doi:10.2138/rmg.2005.58.9.

Hyndman, R. D., P. Flück, S. Mazzotti, T. J. Lewis, J. Ristau, and L. Leonard (2005), Current tectonics of the northern Canadian Cordillera, *CANA*, *1136*, 1117–1136, doi:10.1139/E05-023.

Issler, D. R., A. Grist, and L. Stasiuk (2005), Post-Early Devonian thermal constraints on hydrocarbon source rock maturation in the Keele Tectonic Zone, Tulita area, NWT, Canada, from multi-kinetic apatite fission track thermochronology, vitrinite reflectance and shale compaction, *Bull. Can. Pet. Geol.*, *53*(4), 405–431, doi:10.2113/53.4.405.

James, N. P., G. M. Narbonne, and T. K. Kyser (2001), Late Neoproterozoic cap carbonates: Mackenzie Mountains, northwestern Canada: precipitation and global glacial meltdown, *Can. J. Earth Sci.*, *38*(8), 1229–1262, doi:10.1139/cjes-38-8-1229.

Jefferson, C. W., and R. R. Parrish (1989), Late Proterozoic stratigraphy, U-Pb zircon ages, and rift tectonics, Mackenzie Mountains, northwestern Canada, *Can. J. Earth Sci.*, *26*, 1784 – 1801.

Ketcham, R. A. (2005), Forward and inverse modeling of low-temperature thermochronometry data, *Rev. Mineral. Geochemistry*, *58*(1), 275–314, doi:10.2138/rmg.2005.58.11.

Ketcham, R. A., W. R. Guenthner, and P. W. Reiners (2013), Geometric analysis of radiation damage connectivity in zircon, and its implications for helium diffusion, *Am. Mineral.*, *98*(2003), 350–360.

Knight, E., D. Schneider, and J. Ryan (2013), Thermochronology of the Yukon-Tanana terrane, west-central Yukon: evidence for Jurassic extension and exhumation in the northern Canadian Cordillera, *J. Geol.*, *121*(4), 371–400, doi:10.1086/670721.

Lane, L. S., and G. E. Gehrels (2014), Detrital zircon lineages of late Neoproterozoic and Cambrian strata, NW Laurentia, *Geol. Soc. Am. Bull.*, *126*(3-4), 398–414, doi:10.1130/B30848.1.

Lemieux, Y., T. Hadlari, and A. Simonetti (2011), Detrital zircon geochronology and provenance of Devono-Mississippian strata in the northern Canadian Cordilleran miogeocline, *Can. J. Earth Sci.*, *48*(2), 515–541, doi:10.1139/E10-056.

Leonard, L. J., S. Mazzotti, and R. D. Hyndman (2008), Deformation rates estimated from earthquakes in the northern Cordillera of Canada and eastern Alaska, *J. Geophys. Res.*, *113*(B8), B08406, doi:10.1029/2007JB005456.

Leslie, C. (2009), Detrital zircon geochronology and rift-related magmatism: central Mackenzie Mountains, Northwest Territories, *M.Sc thesis, Dept. of Earth, Ocean, and Atmosph. Sci., University of British Columbia*, Vancouver, British Columbia, Canada.

Link, C. M., and R. M. Bustin (1989), Petroleum source potential and depositional setting of Phanerozoic strata in northern Yukon and northwestern district of Mackenzie, *Bull. Can. Pet. Geol.*, *37*(3), 293–315.

Long, D., and E. Turner (2012), Formal definition of the Neoproterozoic Mackenzie Mountains Supergroup (Northwest Territories), and formal stratigraphic nomenclature for terrigenous clastic units of the Katherine Group, *Geol. Surv. Canada, Open File 7113*, 40 p., doi:10.4095/292168.

Macdonald, F. A., G. Halverson, J. V. Strauss, E. Smith, G. Cox, E. Sperling, and C. Roots (2012), Early Neoproterozoic Basin Formation in Yukon, Canada: Implications for the make-up and break-up of Rodinia, *Geosci. Canada*, *39*, 77–99.

Macdonald, F. A., M. D. Schmitz, J. L. Crowley, C. F. Roots, D. S. Jones, A. C. Maloof, J. V Strauss, P. A. Cohen, D. T. Johnston, and D. P. Schrag (2010), Calibrating the Cryogenian, *Science, 327*(5970), 1241–1243.

Macdonald, J. (2009), The Ten Stone Ranges structural complex of the central Mackenzie Mountains fold-and-thrust belt: a structural analysis with implications on the Plateau Fault and regional detachment level, *MSc thesis, Earth and Environ. Sci.*, *University of Waterloo*, Waterloo, Ontario, Canada.

MacLean, B. (2011), Tectonic and stratigraphic evolution of the Cambrian basin of northern Northwest Territories, *Bull. Can. Pet. Geol.*, *59*(2), 172–194.

MacLean, B., and D. Cook (1999), Salt tectonism in the Fort Norman area, northwest territories, Canada, *Bull. Can. Pet. Geol.*, *47*(2), 104–135.

MacLean, B. C., K. M. Fallas, and T. Hadlari (2014), The multi-phase Keele Arch, central Mackenzie Corridor, Northwest Territories, *Bull. Can. Pet. Geol.*, *62*(2), 68–104, doi:10.2113/gscpgbull.62.2.68.

MacNaughton, R. B., K. M. Fallas, and W. Zantvoort (2008), Qualitative assessment of the Plateau Fault (Mackenzie Mountains, NWT) as a conceptual hydrocarbon play, *Geol. Surv. Canada, Open File 5831*, 29 p.

Mair, J. L., C. J. R. Hart, and J. R. Stephens (2006), Deformation history of the northwestern Selwyn Basin, Yukon, Canada: Implications for orogen evolution and mid-Cretaceous magmatism, *Geol. Soc. Am. Bull.*, *118*(3-4), 304–323, doi:10.1130/B25763.1.

Marsellos, A. E., and J. I. Garver, (2010), Radiation damage and uranium concentration in zircon as assessed by Raman spectroscopy and neutron irradiation, *Am. Mineral., 95*(8-9), 1192-1201, doi:10.2138/1m.2010.3264.

McCracken, A. D. (2007), Report on 14 conodont samples collected from Silurian and Devonian strata in the Mackenzie Mountains, Northwest Territories., *Geol. Surv. Canada, Paleontol. Report 1-ADM-2007*, 6 p.

McCracken, A. D. (2011a), Report on 18 conodont samples from the Cambrian-Ordovician Franklin Mountain Formation, the Silurian Mount Kindle Formation, the Devonian Hume, Imperial, Landry and Ramparts Formations, and the Cretaceous Slater River Formation, Norman Wells Area, NWT., *Geol. Surv. Canada, Paleontol. Report 3-ADM-2011*, 13 p.

McCracken, A. D. (2011b), Report on 20 conodont samples from the Cambrian-Ordovician Franklin Mountain Formation, The Ordovician-Silurian Mount Kindle Formation, the Devonian Bear Rock, Hume and Ramparts Formations, and Bluefish Member, Franklin and Mackenzie Mountains area, NWT., *Geol. Surv. Canada, Paleontol. Report 4-ADM-2011*, *4-ADM-2011*, 15 p.

Mitra, S. (2003), A unified kinematic model for the evolution of detachment folds, *J. Struct. Geol.*, *25*(10), 1659–1673, doi:10.1016/S0191-8141(02)00198-0.

Montario, M. J., and J. I. Garver (2009), The thermal evolution of the Grenville Terrane revealed through U-Pb and fission-track analysis of detrital zircon from Cambro-Ordovician quartz arenites of the Potsdam and Galway Formations, *J. Geol.*, *117*(6), 595–614, doi:10.1086/605778.

Morrow, D.W. (1991), The Silurian-Devonian sequence in the northern part of the Mackenzie Shelf, Northwest Territories, *Geol. Surv. Canada, Bulletin 413,* 121.

Narbonne, G. M., and J. D. Aitken (1995), Neoproterozoic of the Mackenzie Mountains, northwestern Canada, *Precambrian Res.*, *73*, 101–121.

Nasdala, L., P. W. Reiners, J. I. Garver, A. K. Kennedy, R. A. Stern, E. Balan, and R. Wirth (2004a), Incomplete retention of radiation damage in zircon from Sri Lanka, *Am. Mineral.*, *89*, 219–231.

Nasdala, L., M. Wenzel, G. Vavra, G. Irmer, T. Wenzel, and B. Kober (2004b), Metamictisation of natural zircon: accumulation versus thermal annealing of radioactivity-induced damage, *Contrib. to Mineral. Petrol.*, *141*(2), 125–144, doi:10.1007/s004100000235.

Norris, D. K. (1997), Geological setting, in *The Geology, Mineral and Hydrocarbon Potential of Northern Yukon Territory and Northwestern District of Mackenzie.*, edited by D. K. Norris, pp. 1–5, Geological Survey of Canada, Bulletin 422.

Nowlan, G. S. (1995), Report on thirteen samples from Ordovician - Silurian boundary strata in the Whittaker Formation at Avalanche Lake, section AV4B of Nowlan et al. (1988), Mackenzie Mountains, Northwest Territories., *Geol. Surv. Canada, Paleontol. Report 002-GSN-19*, 7 p.

Nowlan, G. S. (2010a), Report on eight samples from Upper Cambrian - Devonian strata collected by members of the Sekwi project in the Northwest Territories., *Geol. Surv. Canada, Paleontol. Report 002-GSN-20*, 8 p.

Nowlan, G. S. (2010b), Report on four samples of Ordovician and Silurian strata from Little Bear River, Mackenzie Plain, Northwest Territories., *Geol. Surv. Canada, Paleontol. Report 006-GSN-20*, 6 p.

Pyle, L. J., and Jones AL (2009), *Regional Geoscience Studies and Petroleum Potential, Peel Plateau and Plain, Northwest Territories and Yukon: Project Volume*, edited by L. J. Pyle and A. Jones, Northwest Territories Geoscience Office and Yukon Geological Survey, NWT Open File 2009-02 and YGS Open File 2009-25.

Rainbird, R., L. Hearnan, and G. Young (1992), Sampling Laurentia: Detrital zircon geochronology offers evidence for an extensive Neoproterozoic river system originating from the Grenville orogen, *Geology*, *20*, 351–354.

Rainbird, R., V. McNicoll, L. Theriault, J. Heaman, and D. Abbott (1997), Pan-continental river system draining Grenville Orogen recorded by U-Pb and Sm-Nd geochronology of Neoproterozoic quartzarenites and mudrocks, northwestern, *J. Geol.*, *105*(1), 1–17.

Rainbird, R., P. Cawood, and G. Gehrels (2012), The great Grenvillian sedimentation episode: record of supercontinent Rodinia's assembly, in *Tectonics of Sedimentary Basins: Recent Advances*, edited by C. Busby and A. Azor, pp. 583–601, Wiley-Blackwell, Oxford, UK.

Rainbird, R. H., C. W. Jefferson, and G. M. Young (1996), The early Neoproterozoic sedimentary Succession B of northwestern Laurentia: Correlations and paleogeographic significance, *Geol. Soc. Am. Bull.*, *108*(4), 454–470, doi:10.1130/0016-7606(1996)108<0454:TENSSB>2.3.CO;2.

Reiners, P. W, K. A. Farley, and H. Hickes (2002), He diffusion and (U–Th)/He thermochronometry of zircon: initial results from Fish Canyon Tuff and Gold Butte, *Tectonophysics*, *349*, 297–308.

Reiners, P. W. (2005), Zircon (U-Th)/He thermochronometry, *Rev. Mineral. Geochemistry*, *58*(1), 151–179, doi:10.2138/rmg.2005.58.6.

Reiners, P. W., and M. T. Brandon (2006), Using thermochronology to understand orogenic erosion, *Annu. Rev. Earth Planet. Sci.*, *34*(1), 419–466, doi:10.1146/annurev.earth.34.031405.125202.

Reiners, P. W., T. L. Spell, S. Nicolescu, and K. a. Zanetti (2004), Zircon (U-Th)/He thermochronometry: He diffusion and comparisons with $^{40}Ar/^{39}Ar$ dating, *Geochim. Cosmochim. Acta*, *68*(8), 1857–1887, doi:10.1016/j.gca.2003.10.021.

Rejebian, V., A. Harris, and J. Huebner (1987), Conodont color and textural alteration: An index to regional metamorphism, contact metamorphism, and hydrothermal alteration, *Geol. Soc. Am. Bull.*, *99*, 471–479.

Spotila, J. A. (2005), Applications of low-temperature thermochronometry to quantification of recent exhumation in mountain belts, *Rev. Mineral. Geochemistry*, *58*(1), 449–466, doi:10.2138/rmg.2005.58.17.

Stasiuk, L. D., A. R. Sweet, and D. R. Issler (2006), Reconstruction of burial history of eroded Mesozoic strata using kimberlite shale xenoliths, volcaniclastic and crater facies, Northwest Territories, Canada, *Int. J. Coal Geol.*, *65*(1-2), 129–145, doi:10.1016/j.coal.2005.04.011.

Stockli, D. F. (2005), Application of low-temperature thermochronometry to extensional tectonic settings, *Rev. Mineral. Geochemistry*, *58*(1), 411–448, doi:10.2138/rmg.2005.58.16.

Thomson, D., C. J. Schröder-Adams, T. Hadlari, G. Dix, and W. J. Davis (2011), Albian to Turonian stratigraphy and palaeoenvironmental history of the northern Western Interior Sea in the Peel Plateau Region, Northwest Territories, Canada, *Palaeogeogr. Palaeoclimatol. Palaeoecol.*, *302*(3-4), 270–300, doi:10.1016/j.palaeo.2011.01.017.

Thorkelson, D. J., J. G. Abbott, J. K. Mortensen, R. A. Creaser, M. E. Villeneuve, V. J. McNicoll, and P. W. Layer (2005), Early and Middle Proterozoic evolution of Yukon, Canada, *Can. J. Earth. Sci., 42*(6), 1045-1071, doi: 10.1139/e04-075.

Tian, Y., N. Qiu, B. P. Kohn, C. Zhu, S. Hu, A. J. W. Gleadow, and B. I. McInnes (2012), Detrital zircon (U–Th)/He thermochronometry of the Mesozoic Daba Shan Foreland Basin, central China: Evidence for timing of post-orogenic denudation, *Tectonophysics*, *570-571*, 65–77, doi:10.1016/j.tecto.2012.08.010.

Turner, E., C. Roots, R. B. MacNaughton, D. Long, B. Fischer, S. Gordey, E. Martel, and M. Pope (2011), Chapter 3. Stratigraphy, in *Geology of the Central Mackenzie Mountains of the Northern Canadian Cordillera, Sekwi Mountain (105P), Mount Eduni (106A), and the northwestern Wrigley Lake (95M) Map Areas, Northwest Territories*, edited by E. Martel, E. Turner, and B. Fischer, pp. 31–192, NWT Special Volume 1, NWT Geoscience Office.

Turner, E. C., and D. G. Long (2008), Basin architecture and syndepositional fault activity during deposition of the Neoproterozoic Mackenzie Mountains supergroup, Northwest Territories, Canada, *Can. J. Earth Sci.*, *45*(10), 1159–1184, doi:10.1139/E08-062.

Whitmeyer, S., and K. Karlstrom (2007), Tectonic model for the Proterozoic growth of North America, *Geosphere*, *3*(4), 220–259, doi:10.1130/GES00055.1.

Williams, G. (1990), Tectonics and structure, Mackenzie Corridor, Northwest Territories, *Geol. Surv. Canada, Open File 2248*, 25.

Wolfe, M. R., and D. F. Stockli (2010), Zircon (U–Th)/He thermochronometry in the KTB drill hole, Germany, and its implications for bulk He diffusion kinetics in zircon, *Earth Planet. Sci. Lett.*, *295*(1-2), 69–82, doi:10.1016/j.epsl.2010.03.025.

Yorath, C. J. (1991), Upper Jurassic to Paleogene assemblages, chapter 9, in *Geology of the Cordilleran Orogen in Canada*, edited by H. Gabrielse and C. Yorath, pp. 329–371, Geological Survey of Canada, Geology of Canada, no. 4.

Yorath, C. J., and D. Cook (1981), Cretaceous and Tertiary stratigraphy and paleogeography, Northern Interior Plains, District of Mackenzie, *Geol. Surv. Canada, Mem. 398*, 1–78.

Young, G., C. Jefferson, G. Delaney, and G. Yeo (1979), Middle and late Proterozoic evolution of the northern Canadian Cordillera and Shield, *Geology*, *7*, 125–128.

Zhang, M., E. K. H. Salje, G. C. Capitani, H. Leroux, A. M. Clark, J. Schl, and R. C. Ewing (2000), Annealing of α -decay damage in zircon: a Raman spectroscopic study, *J. Phys. Condens. Matter*, *12*, 3131–3148.

Table 1. Single grain (U-Th)/He analyses of zircon from the Mackenzie Mountains, NWT

Sample	Coordinates (x, y, z)	Stratigraphy	Corr. Age (Ma)	± (8%) (Ma)	U (ppm)	Th (ppm)	Th/U	eU (ppm)	He (nmol/g)	Mass (µg)
JP007-1	64.895 °N	Dodo Creek	51.3	4.1	250.5	102.7	0.41	274.2	53.5	2.5
JP007-2	127.250 °W	Fm. Little Dal	166.5	13.3	28.2	29.3	1.04	34.9	23.0	3.4
JP007-3	489 m	Gp.	83.6	6.7	34.7	21.8	0.63	39.7	12.8	2.4
JP007-5			166.9	13.3	81.5	73.3	0.90	98.4	68.2	5.4
JP007-6			267.0	21.4	51.8	36.8	0.71	60.3	61.2	2.3
JP007-7			72.6	5.8	81.4	36.8	0.45	89.8	24.4	1.9
JP007-8			52.3	4.2	225.5	129.8	0.58	255.4	48.9	2.1
JP007-9			83.0	6.6	136.5	102.1	0.75	160.0	52.4	3.5
JP007-10			54.8	4.4	219.0	140.5	0.64	251.4	51.0	2.1
12FNA047-1	64.959 °N	Katherine Gp.	54.3	4.3	281.1	243.4	0.87	337.2	72.6	3.4
12FNA047-2	127.973 °W		81.9	6.6	294.4	269.1	0.91	356.5	109.0	2.4
12FNA047-3	1602 m		84.3	6.7	68.3	50.5	0.74	79.9	28.7	7.9
12FNA047-5			184.3	14.7	208.9	213.9	1.02	258.5	190.7	3.7
12FNA047-6			351.7	28.1	63.8	53.4	0.84	76.1	106.6	3.1
12FNA047-7			111.4	8.9	93.8	73.3	0.78	110.7	46.6	2.4
12FNA047-8			195.1	15.6	72.9	60.6	0.83	86.9	66.7	3.0
12FNA047-9			263.7	21.1	52.0	87.4	1.68	72.1	70.0	1.8
12FNA047-10			159.5	12.8	146.0	61.7	0.42	160.2	103.1	3.6
JP008-2	64.444 °N	Katherine Gp.	183.6	14.7	192.4	72.6	0.38	209.2	162.3	7.1
JP008-3	127.002 °W		54.0	4.3	190.6	124.0	0.65	219.2	48.6	4.9
JP008-4	1134 m		159.8	12.8	93.5	79.2	0.85	111.7	70.3	3.3
JP008-5			57.7	4.6	670.1	304.8	0.45	740.3	159.9	2.2
JP008-6			160.4	12.8	106.2	52.4	0.49	118.3	76.4	3.8
JP008-7			219.8	17.6	95.8	56.9	0.59	108.9	101.0	6.5
JP008-9			95.8	7.7	121.5	101.1	0.83	144.8	52.8	2.9
JP008-10			89.8	7.2	111.5	81.8	0.73	130.3	45.7	3.8
11FNA010-1	64.701 °N	Katherine Gp.	363.9	29.1	104.0	58.3	0.56	117.5	183.8	6.6
11FNA010-2	127.414 °W		393.4	31.5	52.6	61.4	1.17	66.7	121.2	15.9
11FNA010-3	906 m		220.6	17.6	43.4	48.7	1.12	54.6	50.5	5.8
11FNA010-4			226.0	18.1	23.5	17.8	0.76	27.6	26.9	7.9
11FNA010-5			215.8	17.3	59.6	60.6	1.02	73.6	63.7	3.7
11FNA010-6			230.8	18.5	42.0	23.7	0.56	47.5	50.0	15.5
11FNA010-7			230.9	18.5	28.9	42.4	1.47	38.7	38.2	7.2
11FNA010-8			432.1	34.6	104.9	47.4	0.45	115.8	210.0	5.3
11FNA010-9			155.5	12.4	86.3	75.6	0.88	103.7	66.5	5.0
11FNA010-10			159.4	12.8	108.7	82.1	0.76	127.6	80.1	3.2
JP012-1	64.457 °N	Katherine Gp.	146.8	11.7	133.8	135.8	1.02	165.1	104.2	7.8
JP012-2	127.132 °W		72.8	5.8	125.4	116.8	0.93	152.2	48.4	11.1
JP012-3	1880 m		73.5	5.9	180.7	146.7	0.81	214.5	69.6	10.6
JP012-4			420.8	33.7	52.3	49.9	0.95	63.8	120.7	12.7
JP012-5			104.5	8.4	185.8	113.0	0.61	211.9	101.9	20.1
JP012-6			132.3	10.6	123.6	97.5	0.79	146.0	82.1	6.1
JP012-7			100.1	8.0	141.6	83.1	0.59	160.7	70.6	11.3
JP012-8			363.6	29.1	27.4	26.2	0.96	33.4	54.6	12.5
JP012-9			77.5	6.2	116.3	90.0	0.77	137.0	48.7	20.0
JP012-10			67.3	5.4	382.1	280.5	0.73	446.7	125.1	6.2
JP012-11			115.8	9.3	83.4	66.4	0.80	98.7	49.7	8.6
JP012-12			104.0	8.3	150.8	103.5	0.69	174.6	78.6	9.4

Sample	Coordinates (x, y, z)	Stratigraphy	Corr. Age (Ma)	± (8%) (Ma)	U (ppm)	Th (ppm)	Th/U	eU (ppm)	He (nmol/g)	Mass (µg)
12FNA103-2	64.238 °N	Katherine Gp.	70.0	5.6	137.3	161.1	1.17	174.4	46.5	3.1
12FNA103-3	126.809 °W		94.1	7.5	114.6	72.2	0.63	131.2	52.0	7.1
12FNA103-4	888 m		107.9	8.6	68.5	36.7	0.54	77.0	35.1	6.1
12FNA103-5			171.4	13.7	127.1	95.1	0.75	149.0	111.0	9.7
12FNA103-6			76.0	6.1	73.7	59.0	0.80	87.3	26.6	4.2
12FNA103-7			168.0	13.4	107.9	109.4	1.01	133.0	90.0	3.9
12FNA103-8			156.6	12.5	36.8	70.0	1.90	52.9	33.8	5.2
12FNA103-9			97.9	7.8	136.1	89.4	0.66	156.7	65.0	6.4
12FNA103-10			83.4	6.7	129.6	166.4	1.28	168.0	62.1	12.4
JP025-1	64.271 °N	Katherine Gp.	61.4	4.9	86.1	65.6	0.76	101.3	26.9	8.7
JP025-2	127.480 °W		113.2	9.1	93.5	49.7	0.53	105.0	50.0	6.0
JP025-3	927 m		65.8	5.3	115.5	103.3	0.89	139.3	37.7	4.9
JP025-4			62.1	5.0	209.3	128.3	0.61	238.9	66.4	13.8
JP025-7			51.0	4.1	365.7	112.1	0.31	391.5	82.3	5.0
JP025-8			212.7	17.0	34.6	22.3	0.64	39.8	36.0	6.8
JP025-9			71.6	5.7	101.0	89.9	0.89	121.7	38.4	10.7
JP025-10			45.8	3.7	1181.3	527.2	0.45	1303.1	250.5	6.6
JP024-1	64.205 °N	Tsezotene Fm.	65.6	5.3	75.3	62.0	0.82	89.6	25.4	8.8
JP024-2	127.319 °W		57.1	4.6	311.6	181.5	0.58	353.4	79.2	3.5
JP024-3	577 m		67.0	5.4	162.0	90.1	0.56	182.7	47.8	3.5
JP024-4			67.6	5.4	155.2	74.0	0.48	172.3	47.8	4.8
JP024-5			115.8	9.3	63.3	46.5	0.73	74.0	34.7	4.8
JP024-6			121.7	9.7	113.9	76.5	0.67	131.6	63.9	3.8
JP024-8			63.0	5.0	166.5	106.4	0.64	191.0	46.7	2.9
JP024-9			63.3	5.1	244.8	190.3	0.78	288.6	70.8	3.5
JP024-10			48.3	3.9	769.7	373.7	0.49	855.8	164.5	4.0
JP024-11			48.0	3.8	310.6	300.8	0.97	380.6	72.9	4.3
JP024-12			54.0	4.3	72.5	51.7	0.71	84.5	18.0	3.5
JP026-2	64.275 °N	Katherine Gp.	245.0	19.6	28.0	12.7	0.45	30.9	31.5	5.2
JP026-3	127.743 °W		323.1	25.9	99.3	25.6	0.26	105.2	138.8	4.8
JP026-4	788 m		248.5	19.9	62.6	15.0	0.24	66.1	66.5	4.0
JP026-5			192.2	15.4	62.6	20.2	0.32	67.2	53.6	5.0
JP026-6			98.4	7.9	95.4	35.3	0.37	103.6	41.5	4.3
JP026-9			84.0	6.7	192.6	46.4	0.24	203.3	73.6	7.4
JP026-10			55.7	4.5	453.1	144.9	0.32	486.5	112.9	6.9
JP026-11			69.1	5.5	68.6	21.4	0.31	73.5	21.9	8.2
JP026-12			63.6	5.1	173.1	71.8	0.41	189.6	50.0	5.9
JP022-1	64.157 °N	Tsezotene Fm.	158.5	12.7	101.6	43.5	0.43	111.7	73.1	5.0
JP022-2	128.010 °W		110.4	8.8	216.6	123.8	0.57	245.1	108.7	4.4
JP022-3	1177 m		148.5	11.9	53.1	24.2	0.46	58.7	38.3	10.0
JP022-4			330.2	26.4	46.7	21.8	0.47	51.7	75.9	8.7
JP022-5			143.4	11.5	115.1	84.7	0.74	134.7	82.0	7.9
JP022-6			64.1	5.1	297.9	143.8	0.48	331.0	83.8	3.5
JP022-7			108.3	8.7	278.8	46.2	0.17	289.5	125.5	4.1
JP022-8			101.2	8.1	65.6	90.6	1.38	86.7	37.0	6.6
JP022-9			212.5	17.0	64.2	31.6	0.49	71.5	65.1	6.8
JP022-10			121.4	9.7	50.5	32.5	0.64	58.1	30.9	10.8
JP022-11			124.1	9.9	175.2	101.0	0.58	198.4	107.8	9.4
JP022-12			157.9	12.6	99.3	48.3	0.49	110.5	76.9	9.2

Sample	Coordinates (x, y, z)	Stratigraphy	Corr. Age (Ma)	± (8%) (Ma)	U (ppm)	Th (ppm)	Th/U	eU (ppm)	He (nmol/g)	Mass (µg)
JP017-1	63.928 °N	Katherine Fm.	95.2	7.6	76.5	75.3	0.99	93.8	36.3	5.2
JP017-2	127.679 °N		116.9	9.4	60.4	43.1	0.71	70.4	35.7	9.1
JP017-3	1858 m		63.3	5.1	260.0	102.2	0.39	283.5	80.2	14.0
JP017-4			222.5	17.8	66.1	34.0	0.51	74.0	71.0	8.0
JP017-5			89.9	7.2	150.1	86.9	0.58	170.1	62.5	5.3
JP017-6			112.9	9.0	73.4	39.5	0.54	82.5	38.6	5.4
JP017-7			99.6	8.0	187.8	53.9	0.29	200.2	85.3	8.1
JP017-8			68.1	5.4	220.4	68.1	0.31	236.1	69.4	8.7
JP017-9			371.3	29.7	75.5	46.5	0.62	86.2	138.7	8.0
JP017-10			102.7	8.2	84.4	38.9	0.46	93.4	42.7	12.1
JP017-11			317.3	25.4	52.1	21.8	0.42	57.1	79.5	9.1
JP017-12			101.6	8.1	56.6	35.1	0.62	64.6	28.5	10.0
JP018-1	63.680 °N	Keele Fm.	86.0	6.9	188.1	110.6	0.59	213.5	68.0	2.1
JP018-2	127.391 °W		101.7	8.1	135.7	147.7	1.09	169.7	63.0	2.0
JP018-3	1980 m		65.7	5.3	338.7	238.0	0.70	393.5	99.7	2.9
JP018-4			107.2	8.6	102.1	66.3	0.65	117.4	43.3	1.3
JP018-5			85.8	6.9	200.8	115.0	0.57	227.3	63.4	1.0
JP018-6			86.9	7.0	118.0	98.8	0.84	140.7	45.7	2.2
JP018-7			66.8	5.3	478.6	456.3	0.95	583.7	134.2	1.4
JP018-8			88.0	7.0	259.2	264.5	1.02	320.1	100.4	1.6
JP018-9			139.0	11.1	94.6	86.4	0.91	114.5	64.0	4.2
JP018-10			96.2	7.7	112.5	141.6	1.26	145.2	52.3	2.2
JP018-11			80.0	6.4	380.5	992.7	2.61	609.2	177.5	1.9
JP018-12			65.2	5.2	154.7	80.2	0.52	173.2	39.0	1.2
JP015-1	63.639 °N	Keele Fm.	136.3	10.9	54.5	39.6	0.73	63.6	39.2	15.7
JP015-2	127.507 °W		142.8	11.4	43.3	67.7	1.56	58.9	38.6	22.9
JP015-3	1853 m		125.6	10.0	72.3	97.4	1.35	94.7	53.1	14.1
JP015-4			95.6	7.6	43.4	36.8	0.85	51.8	22.5	18.1
JP015-5			123.1	9.8	64.1	85.9	1.34	83.9	45.8	12.5
JP015-6			85.9	6.9	60.5	61.8	1.02	74.7	29.0	17.5
JP015-7			93.8	7.5	32.9	48.9	1.49	44.1	18.4	13.0
JP015-8			87.5	7.0	183.0	81.3	0.44	201.7	81.4	21.7
JP015-9			92.6	7.4	181.1	97.4	0.54	203.5	86.1	17.8
JP015-10			127.6	10.2	30.3	38.1	1.26	39.1	22.2	14.6
JP015-11			91.8	7.3	63.9	91.8	1.44	85.1	35.0	14.6
JP015-12			95.5	7.6	48.4	67.0	1.38	63.8	28.0	23.0

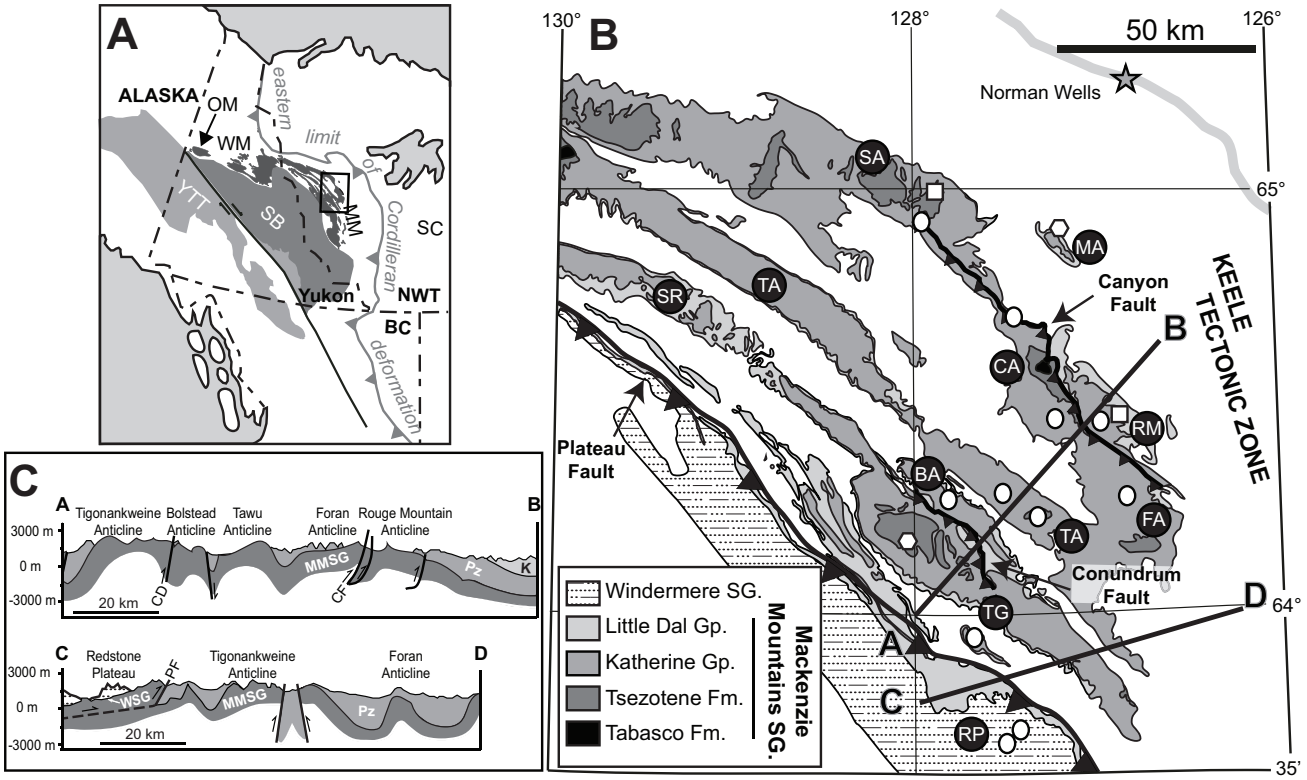

Fig. 1: (A) Simplified map of northwestern Canada and Alaska (modified after *Mair et al.* [2006], *Hadlari et al*. [2012]) showing the location of the Mackenzie Mountains (MM), Wernecke Mountains (WM) and Ogilvie Mountains (OM), Selwyn Basin (SB), composite Yukon-Tanana terrane (YTT) and Slave craton (SC). Study area is denoted by the black box and enlarged in (B). (B) Generalized geologic map highlighting the Neoproterozoic rocks of the Mackenzie Mountains (modified after *Armstrong et al.* [1982], *Turner and Long* [2008], *Fallas et al.* [2013], *Fallas and MacNaughton* [2014a, 2014b, 2014c]. SA = Stony anticline, CA = Canyon anticline, MA = Macdougal Anticline, RM = Rouge Mountain anticline, FA = Foran anticline, TA = Tawu anticline, BA = Bolstead anticline, TG = Tigonankweine anticline, SR = Shattered Range anticline, RP = Redstone Plateau. White circle = ZHe sample, white square = detrital muscovite $^{40}Ar/^{39}Ar$ sample, white hexagon = ZHe and detrital muscovite $^{40}Ar/^{39}Ar$ sample. The gray star indicates the location of the town of Norman Wells, NWT. (C) Structural cross-sections from the transects shown in (B) modified from *Gabrielse et al.* [1973] and *Aitken and Cook* [1974]. Cross-sections denote the location of Mackenzie Mountains Supergroup (MMSG), Windermere Supergroup (WSG), Paleozoic strata (Pz) and Cretaceous strata (K) across the study area. PF = Plateau Fault, CD = Conundrum Fault, and CF = Canyon Fault.

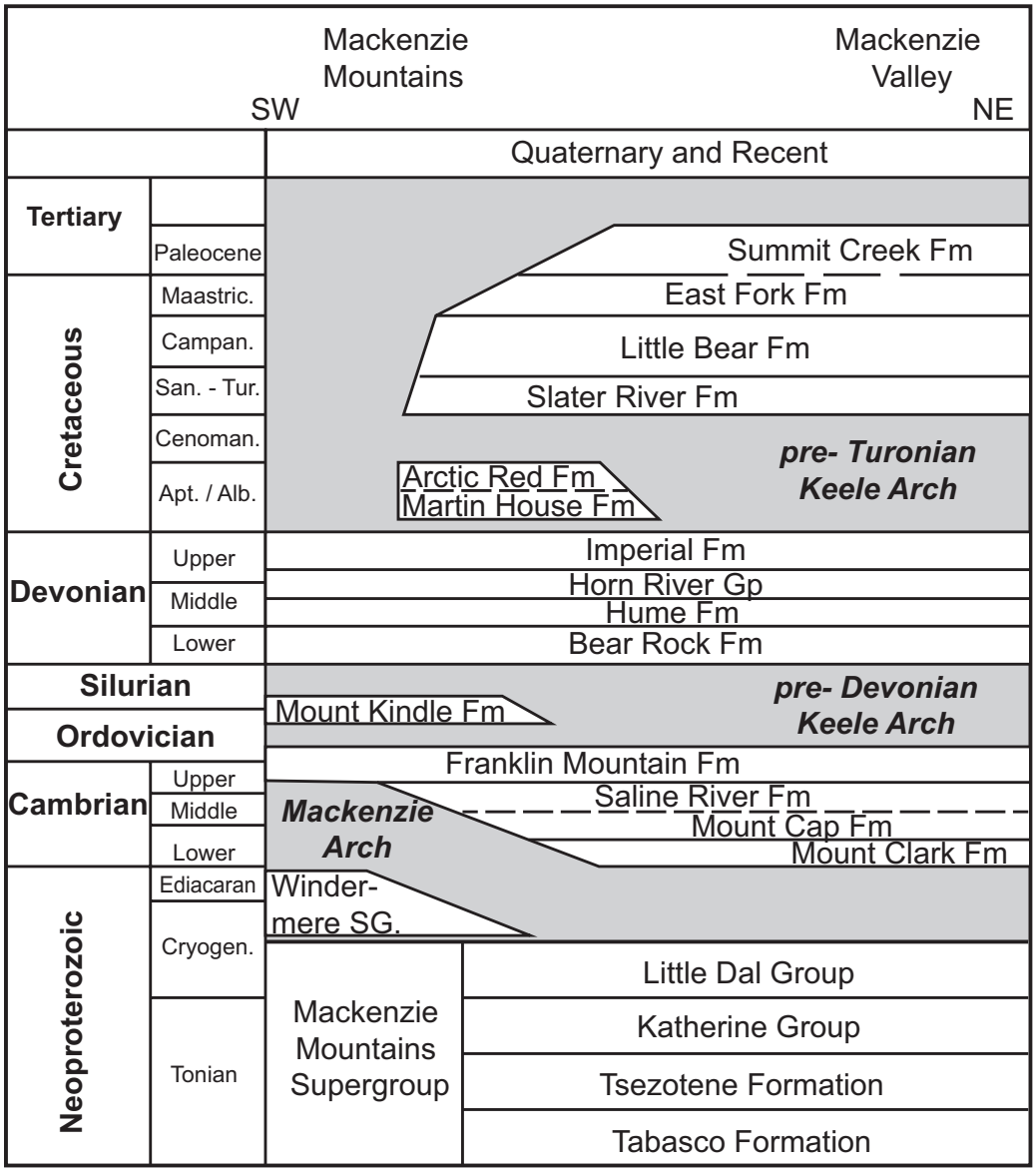

Fig. 2: Regional stratigraphic section for the Mackenzie Mountains and Mackenzie Valley. Stratigraphy is modified after *MacLean and Cook* [1999] and *Long and Turner* [2012]. Dashed lines indicate unconformable contacts. A more elaborate Neoproterozoic stratigraphic section is included in the Appendix (Fig. A1).

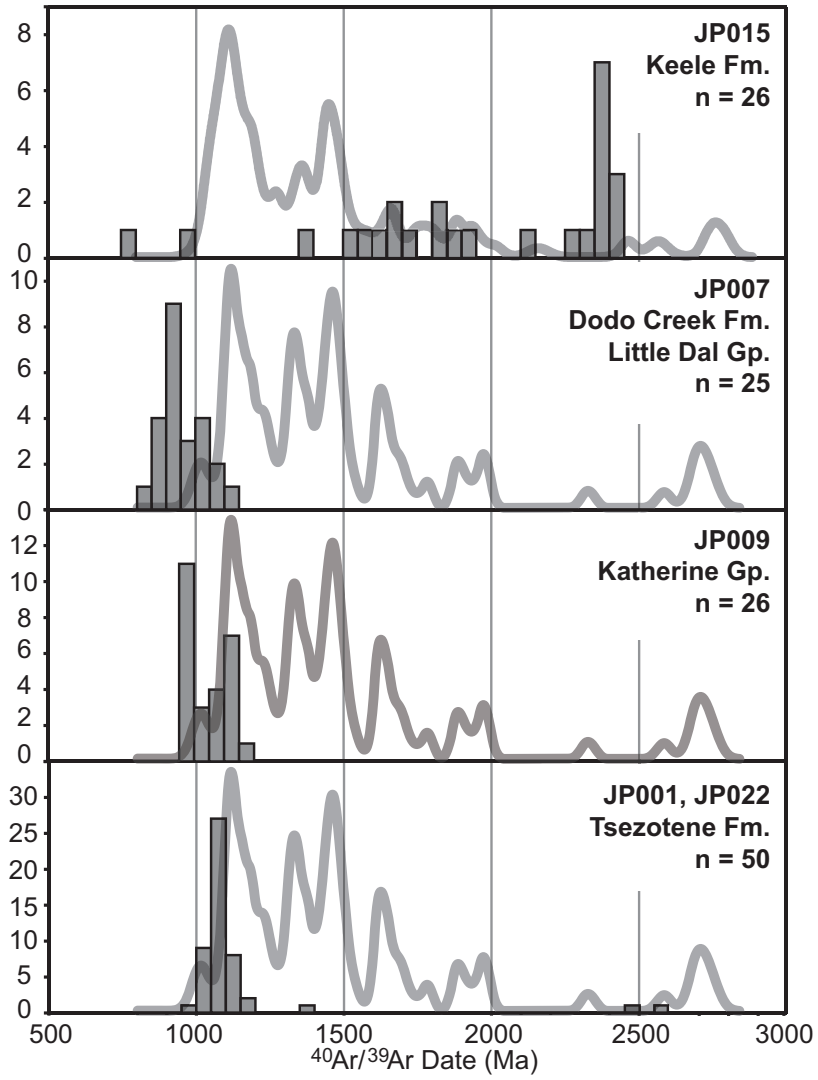

Fig. 3: Single grain muscovite $^{40}Ar/^{39}Ar$ age histograms from Tsezotene Formation, Katherine Group, Little Dal Group and Keele Formation samples. Vertical axis values indicate the number of single grain muscovite $^{40}Ar/^{39}Ar$ ages for a stratigraphic level with a 50 m.y. bin size. Density probability curves (gray curves) of published detrital zircon U-Pb age populations for the Mackenzie Mountains Supergroup and Keele Formation strata across the northern Cordillera (after *Lane and Gehrels* [2014]).

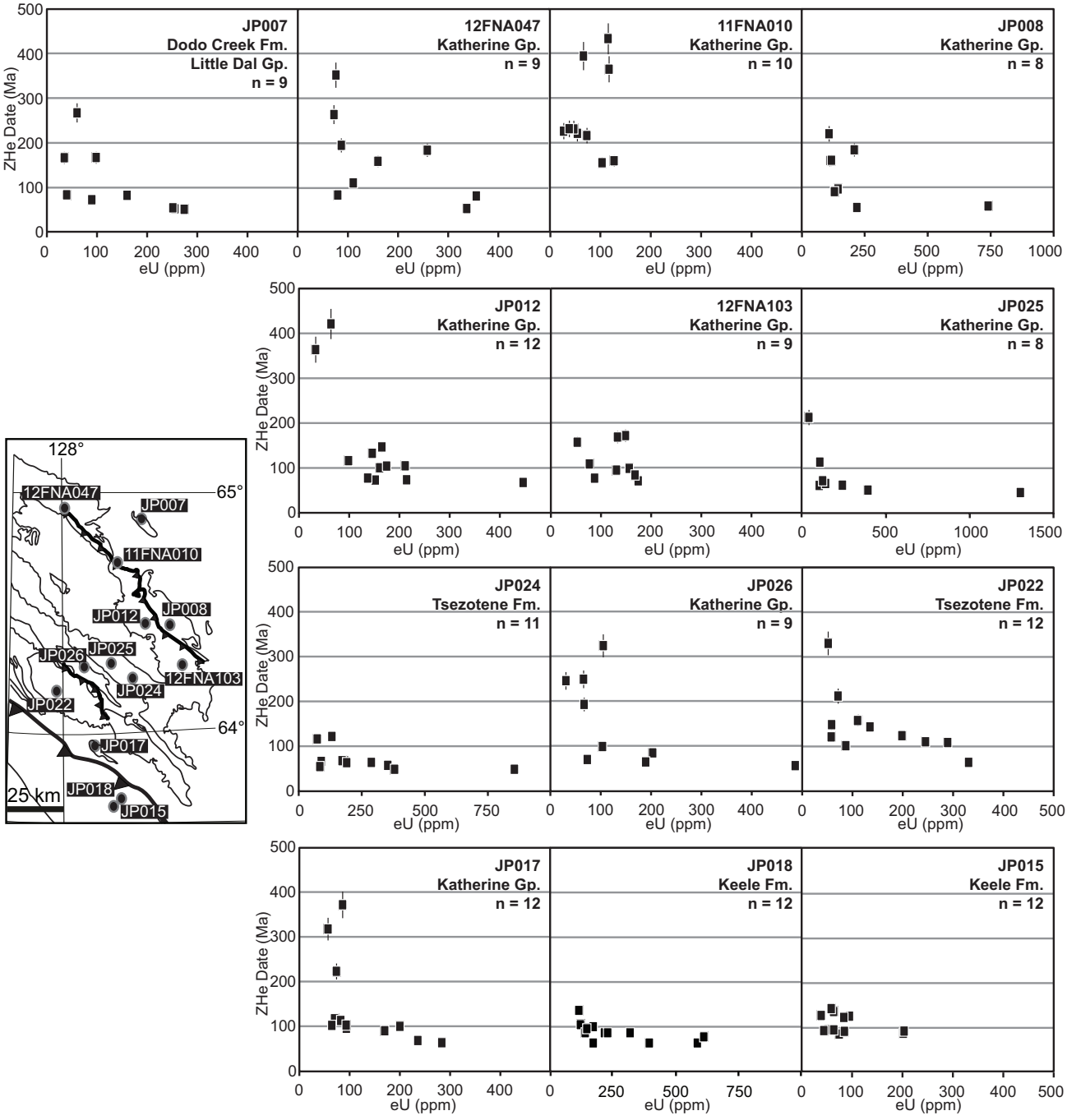

Fig. 4: ZHe date-eU graphs for samples from the Mackenzie Mountains examined in this study. Analytical errors displayed are 8% error. Corresponding ZHe date-ESR (equivalent spherical radius) graphs are also available in the Appendix (Fig. A3).

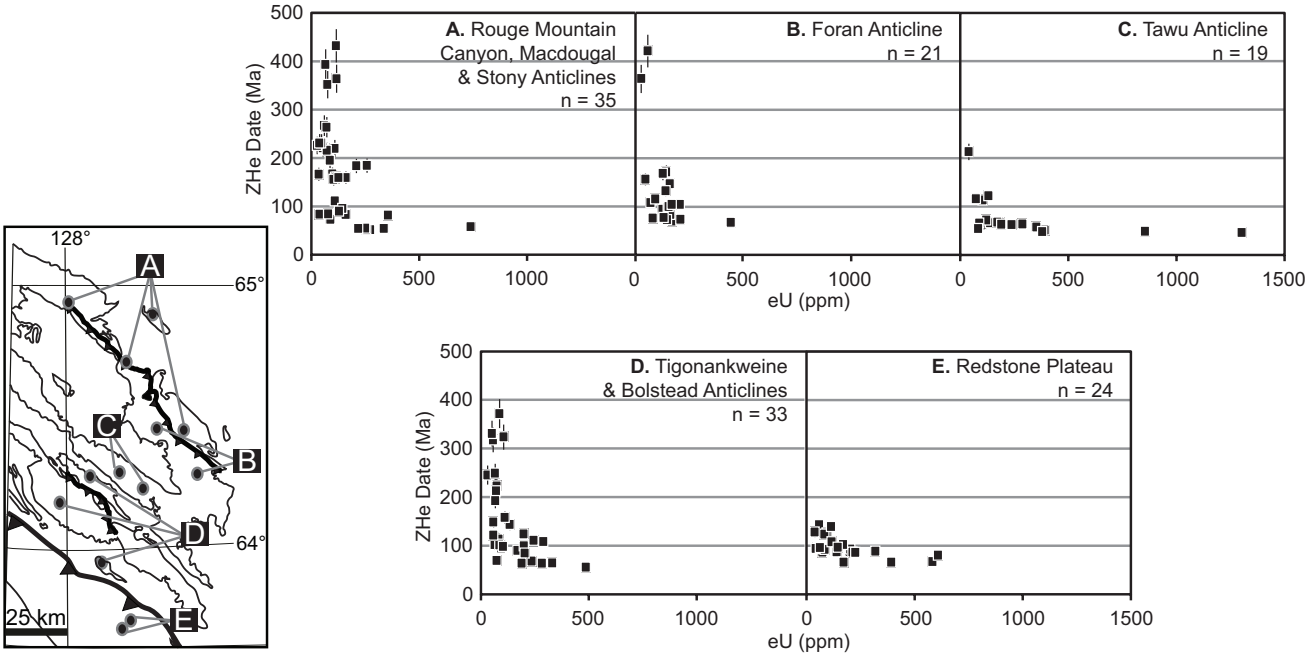

Fig. 5: ZHe date-eU graphs as a function of position in the fold-thrust belt, grouped into five structural panels (A-E) defined by main anticlines.

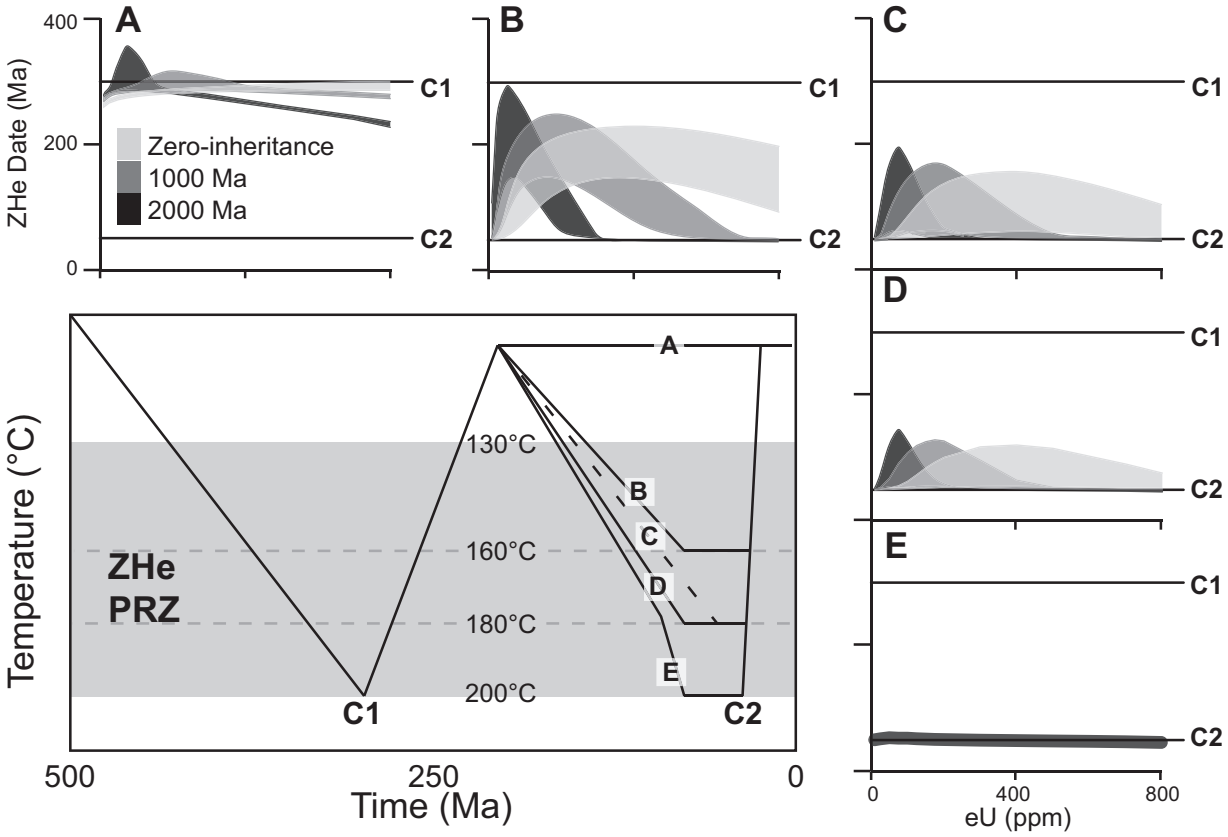

Fig. 6: Schematic temperature histories and corresponding ZHe inheritance date-eU curves for grains with 35-80 μm equivalent spherical radii. Three inheritance histories (zero-inheritance, 1000 Ma, 2000 Ma) for each path (A-E) are illustrated with shaded curves. Paths A-E were heated to the highest temperature of the ZHe partial retention zone (PRZ) until time C1, when they began to cool. Paths B-E experienced a second heating (burial) event of varying magnitude until cooling began at time C2.

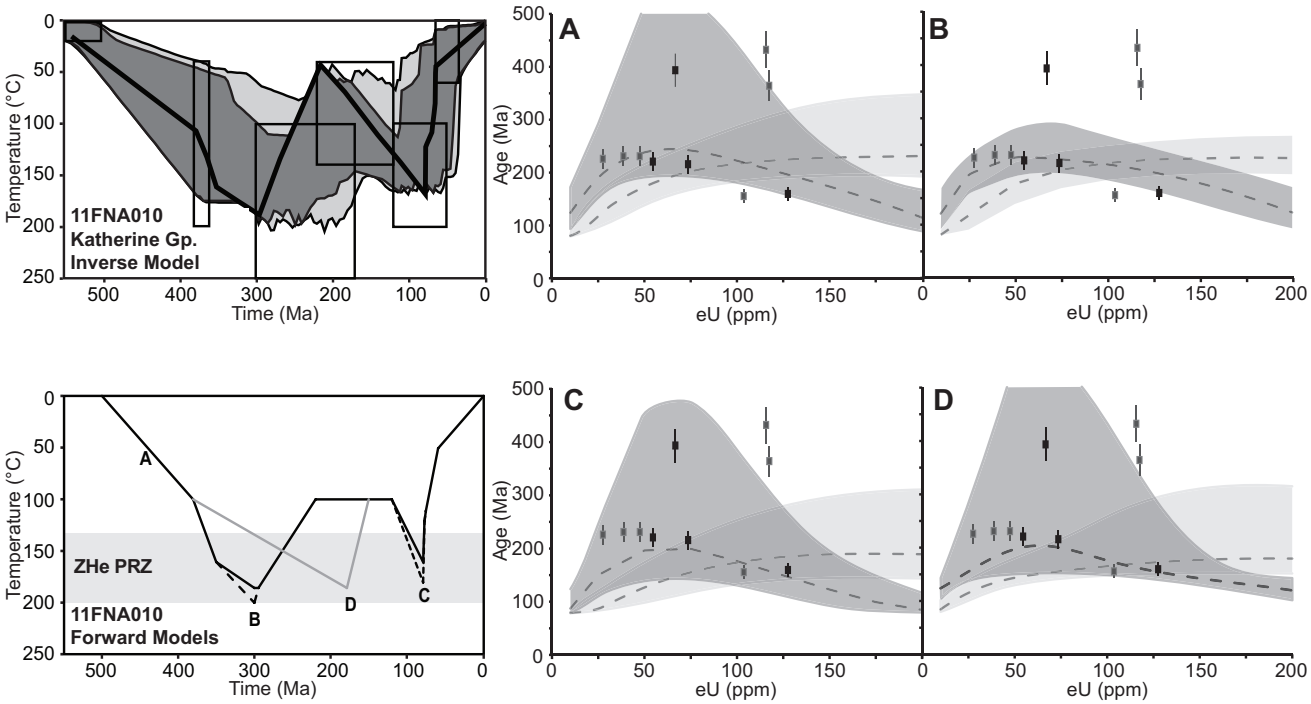

Fig. 7: Inverse and forward thermal history models for Katherine Group sample 11FNA010. For the inverse model, black boxes indicate t-T constraints and the solid black line shows the best-fit thermal history. 'Good fit' solutions are represented by the dark gray curve, whereas 'acceptable' solutions are represented by light gray curve. Forward models illustrate the expected ZHe inheritance date-eU curves for: (A) the inverse model derived best-fit thermal history. The thermal maximum (185ºC) occurs at c. 300 Ma and is followed by cooling throughout the late Paleozoic to early Mesozoic. Strata are reheated to 160ºC in the Late Cretaceous; (B) similar to A, but with a 200ºC thermal maximum; (C) similar to A, but with a 185ºC Late Cretaceous thermal maximum; (D) similar to A, but with a 180 Ma thermal maximum, Inheritance curves (dark gray = 2200 Ma, light gray = 1000 Ma) correspond to date-eU trends for zircons between 35-80 µm ESR and describe the effect of pre-depositional history on expected ZHe dates. The dashed line in each inheritance curve represents the projected date-eU trend for a zircon with a 50 µm ESR. ZHe dates in black indicate grains that were used for inverse thermal history modeling. The remainder of the inverse thermal history models for the dataset, as well as a detailed description of geologic constraints and inverse modeling methodology and interpretation, are available in the Appendix.

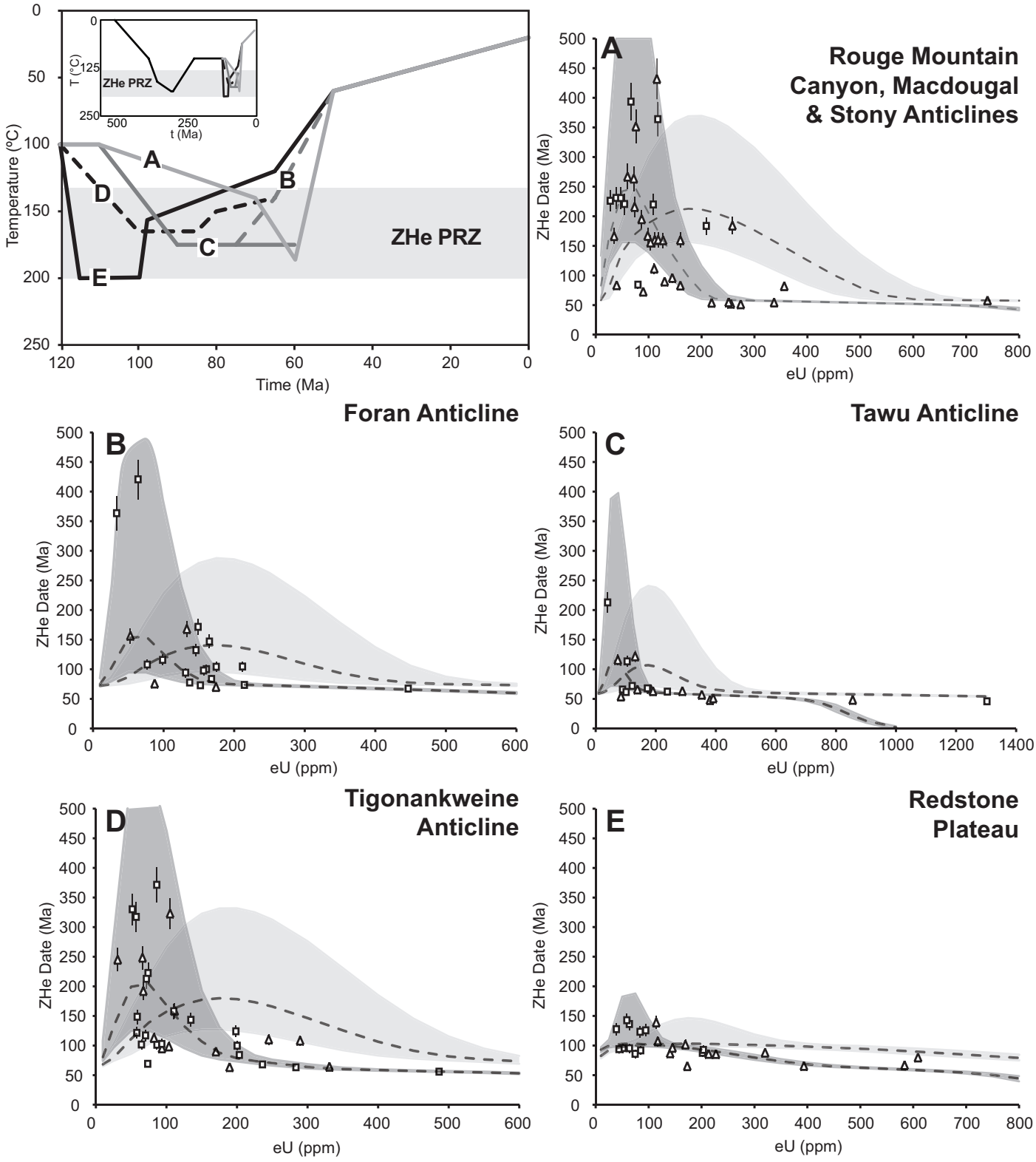
Temperature (ºC)
Time (Ma)
ZHe PRZ
A
B
C
D
E
T (ºC)
t (Ma)
Rouge Mountain
Canyon, Macdougal
& Stony Anticlines
ZHe Date (Ma)
eU (ppm)
Foran Anticline
Tawu Anticline
Tigonankweine
Anticline
Redstone
Plateau

Fig. 8 (previous page): Forward thermal models showing a generalized Cretaceous t-T history for each of the structures (A-E) outlined in Fig. 5. Candidate temperature time histories for each structure were selected on the basis of similarities between inverse models (Fig. 7; Figs. A4 – A13). All five t-T histories share the Paleozoic – early Mesozoic thermal history modeled from sample 11FNA010 (Fig. 7; inset graph). Inheritance curves (dark gray = 2200 Ma, light gray = 1000 Ma) correspond to date-eU trends for zircons between 35-80 μm ESR and describe the effect of pre-depositional history on expected ZHe dates. The dashed line in each inheritance curve represents the projected date-eU trend for a zircon with a 50 μm ESR. Triangles and squares indicate our single grain ZHe dates for grains with widths between 35-50, and 50-80 μm ESR, respectively. Diagrams that discuss the sensitivity of the candidate t-T histories in A-E to variations in timing and magnitude of thermal events are included in the Appendix to this Chapter (Figs. A14 – A18).

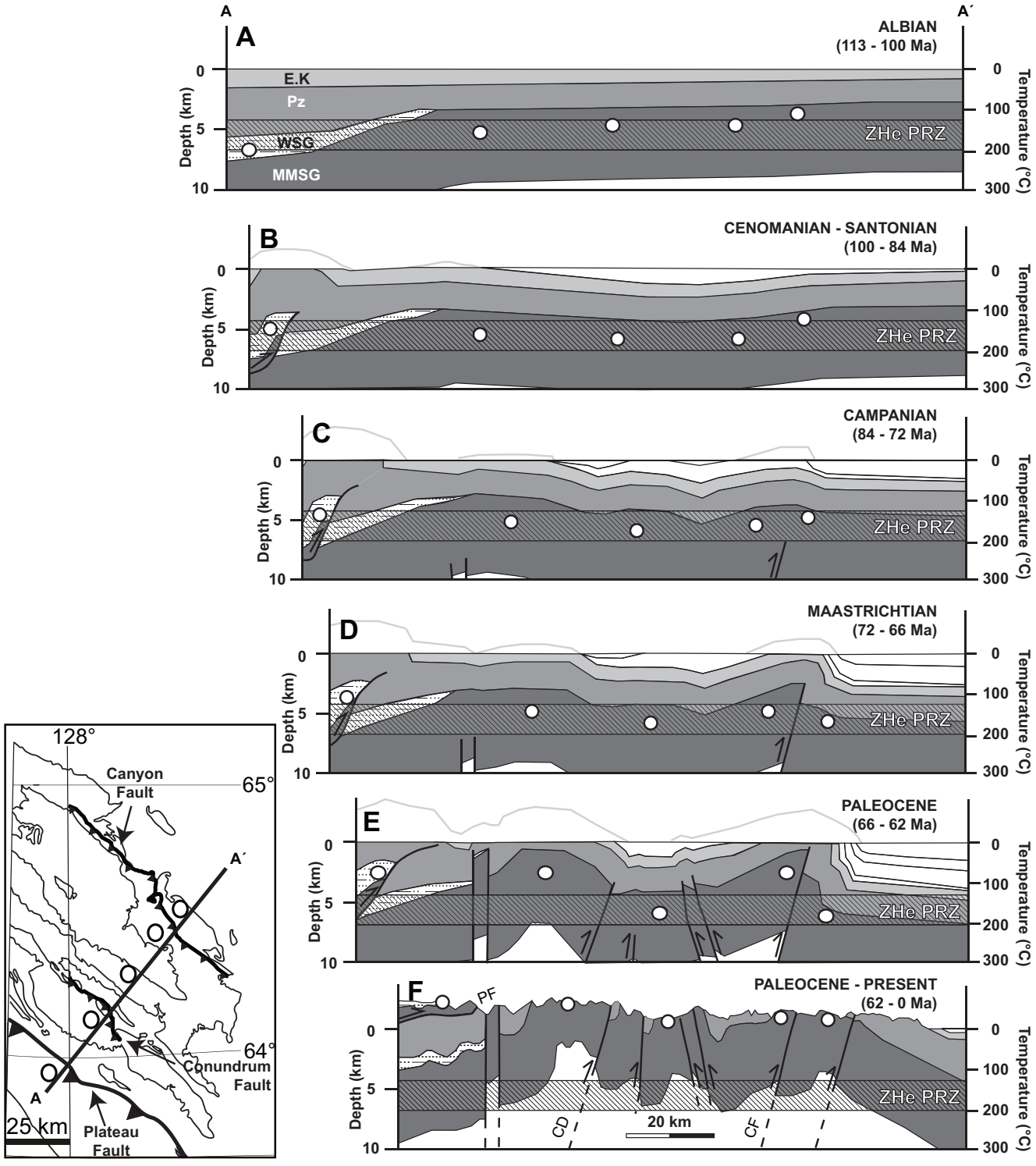
A
A´
A
ALBIAN
(113 - 100 Ma)
E.K
Pz
WSG
MMSG
ZHe PRZ
Depth (km)
Temperature (°C)
B
CENOMANIAN - SANTONIAN
(100 - 84 Ma)
C
CAMPANIAN
(84 - 72 Ma)
D
MAASTRICHTIAN
(72 - 66 Ma)
E
PALEOCENE
(66 - 62 Ma)
F
PALEOCENE - PRESENT
(62 - 0 Ma)
PF
CD
CF
20 km
128°
65°
64°
Canyon
Fault
Conundrum
Fault
Plateau
Fault
25 km

Fig. 9 (previous page): A series of diagrammatic SW-NE cross-sections for the Mackenzie Mountains illustrating the modeled thermal history for each of the sample groups (white circles) from Fig. 8 throughout the Late Cretaceous to Eocene. White circles on the inset map show the projected position of the sample groups (Figs. 5, 8) across the fold-thrust belt, whereas white circles in each cross-section indicates the modeled temperature of the sample group for that time period. Structural interpretations modified after *Cecile and Cook [1981]*. PF = Plateau Fault, CD = Conundrum Fault, and CF = Canyon Fault. Depths were calculated assuming a 30ºC/km geothermal gradient after *Hyndman et al* [2005]. 3x vertical exaggeration.

Appendix to

CHAPTER 2: Zircon (U-Th)/He thermochronology of Neoproterozoic strata from the Mackenzie Mountains, Canada: implications for the Phanerozoic exhumation and deformation history of the northern Canadian Cordillera

Jeremy Powell[1], David Schneider[1], Daniel Stockli[2], Karen Fallas[3]
1. Department of Earth Sciences, University of Ottawa, Ottawa, Canada
2. Jackson School of Geosciences, University of Texas at Austin, Austin, Texas
3. Geological Survey of Canada, Calgary, Canada

Contents of this file

- Text A1 to A2
- Figures A1 to A18
- Tables A1 to A2
- References

Introduction

This Appendix includes a description of the muscovite $^{40}Ar/^{39}Ar$ methodology used in this study, a description of our methodology for inverse modeling and a description of model results, a figure that highlights a more detailed Neoproterozoic stratigraphic section, and figures that show trends in ZHe date vs grain size and eU, and the grains used for inverse modeling. Additionally, we include the remainder of inverse thermal history models not shown in the main body of the article, and sensitivity tests for the forward models shown in Fig 8.

Instead of focusing on the relevance of inverse thermal history models for all zircon (U-Th)/He samples, we opted to show key models that summarize the variable thermal history across the fold-thrust belt in Chapter 2. We explore this variation, and how it is manifested in our dataset, in more detail through forward modeling of (inverse model-derived) candidate t-T histories for discrete structures in the fold-thrust belt. We believe that this combination of inverse and forward modeling does the best job of recognizing the complications and assumptions associated with interpreting our dataset, while providing meaningful geologic interpretations on the evolution of the Mackenzie Mountains.

Additionally, we include data tables that detail our single crystal muscovite $^{40}Ar/^{39}Ar$ ages (Table A1) and the estimated stratigraphic thicknesses for each sample in the fold thrust belt (Table A2).

Text A1. Description of muscovite $^{40}Ar/^{39}Ar$ methodology.

Sample preparation and irradiation:

Mineral separates for JP001, JP007, JP009, and JP022 were produced at the University of Ottawa and sent to the New Mexico Geochronology Research Laboratory for analysis. Separates were loaded into machined Al discs and irradiated for 85 hours, USGS TRIGA Reactor, Denver, CO. Neutron flux monitor Fish Canyon Tuff sanidine (FC-2). Assigned age = 28.02 Ma.

Instrumentation:

Thermo-Fisher Scientific ARGUS VI mass spectrometer on line with automated all-metal extraction system.

- Multi-collector configuration: ^{40}Ar-H1, ^{39}Ar-Ax, ^{38}Ar-L1, ^{37}Ar-L2, ^{36}Ar-L3.
- Amplification: H1, AX, L1, L2 all 1E12 ohm Faraday, L3 - CDD ion counter, deadtime 10 nS.

Laser fusion:

- Muscovite single crystals fused with 75W Photon-Machines CO_2 laser.
- Reactive gases removed by 4 min reaction with SAES D-50 getter operated at 90 volts.
- Gas also exposed to cold finger operated at -140°C and a W filament operated at ~2000°C.

Analytical parameters:

- Mass spectrometer sensitivity = 5E-17 mol/fA
  Total system blank and background: 30±0.4%, 0.13±108%, 0.05±150%, 0.08±83%, 0.01±2%, x10^{-17} moles for masses 40, 39, 38, 37, 36, respectively.
- J-factors determined to a precision of ~± 0.004% by CO_2 laser-fusion of 6 single crystals from each of 6 radial positions around the irradiation tray.
- Correction factors for interfering nuclear reactions were determined using K-glass and CaF_2 and are as follows: $(^{40}Ar/^{39}Ar)_K$ = 0.00807±0.000068; $(^{36}Ar/^{37}Ar)_{Ca}$ = 0.000273±0.0000002; and $(^{39}Ar/^{37}Ar)_{Ca}$ = 0.000698±0.0000078

Mineral separates for JP018 were produced at the University of Ottawa and sent to the Noble Gas Laboratory at the Geological Survey of Canada, and were analyzed following the methodology outline by *Kellett and Joyce* [2014].

Text A2. Inverse thermal history modeling methodology and constraints, and a description of results for Fig A4.

In order to assess the realm of plausible t-T histories for our dataset, and aid in forward modeling of the grouped samples discussed in Fig 5, inverse thermal history modeling was performed using the *HeFTy* program [*Ketcham*, 2005]. *HeFTy* generates t-T paths between user-specified t-T constraints using a Monte Carlo random search, and calculates a modeled age for the zircon grains considering zircon specific parameters, including composition and grain size. Should the model ages approximate the measured ages for all data, the generated paths are deemed as 'acceptable' or 'good,' dependent on a calculated goodness-of-fit value.

Due to the variable provenance of the zircon in MMSG and WSG strata, the pre-depositional history of individual grains cannot be constrained *a priori*. Consequently, we are strategic in choosing which grains to use from each sample, avoiding grains where the relationships between ZHe date, eU and grain size discussed above (Fig 6) suggest dissimilar pre-depositional histories. For each sample, we select grains that span the observed ZHe distribution. Where possible, grains from specific parts of the ZHe date-eU curve were targeted

for modeling, including the oldest grains that correspond with the threshold between positive and negative date-eU correlations, and from the plateau of the curve, where increasing eU has little effect on ZHe age. All grains were modeled with their corresponding 8% uncertainty (Table 1).

Following the selection of grains for modeling, a pre-depositional constraint was added to allow for inherited ^{4}He and accumulation of radiation damage. This pre-depositional constraint was adjusted until *HeFTy* was able to model the date-eU trend of the grains. Fig. A4 shows ZHe date-eU and date-ESR plots for four separate samples that are representative of the variable intra-sample date-eU dispersion in our dataset, and their corresponding inverse thermal models. For each inverse model, solution envelopes define the upper and lower temperature boundary of acceptable and good paths at any point in time. Models for the remainder of our samples are shown in Figs. A5 – A13. We acknowledge that prescribing a specific pre-depositional history is a significant assumption to these models. Given the very similar detrital zircon U-Pb ages for the strata [*Lane and Gehrels*, 2014] we elected to keep this pre-depositional constraint consistent between the MMSG samples and WSG samples. To that extent, the inverse models in Fig. A4 should be thought of as the realm of plausible t-T histories given a fixed pre-depositional history and are a useful for evaluating relative difference between samples. We expand upon these t-T histories and the effects of varying pre-depositional history using forward models in Fig 8.

The same eight time-temperature constraints were used for all samples. These constraints include: 1) a (0°C) pre-depositional constraint between 2000 and 2200 Ma for the MMSG and at 1400 Ma for the Keele Formation; 2) a (0°C) primary depositional constraint [*Armstrong et al.*, 1982; *Jefferson and Parrish*, 1989; *Narbonne and Aitken*, 1995]; 3) a (0-20°C) 542-505 Ma constraint corresponding to the unconformity between the basal Cambrian and underlying MMSG and WSG [*MacLean*, 2011; *Hadlari et al.*, 2012]; 4) a (40-200°C) Devonian constraint between 380-360 Ma to account for burial based on known stratigraphic thicknesses of pre-Carboniferous strata; 5) a (120-250°C) 300-170 Ma constraint accounting for postulated continued burial following deposition of the Imperial Formation [*Issler et al.*, 2005]; 6) a (40-140°C) Jurassic constraint between 175-120 Ma to allow for erosion to the present day Paleozoic stratigraphic thicknesses below the sub-Albian unconformity; 7) a (100-200°C) Cretaceous constraint between 120-50 Ma corresponding with burial in front of the emerging Cordillera; and 8) a (0-60°C) constraint between 65-35 Ma to account for exhumation of the Mackenzie Mountains. Constraint boxes were kept purposefully broad in temperature and time space to account for the range of plausible stratigraphic thicknesses across the fold-thrust belt and for an unknown Paleozoic geothermal gradient. Heating and cooling rates between constraint boxes were restricted to less than 10°C/m.y. to remove geologically implausible temperature time paths.

Inverse thermal modeling was performed on zircons from all 13 samples. We show thermal models from four select samples that are representative of the variable intra-sample and structure-dependent dispersion in our dataset (Fig. A4). These examples provide a summary of the variable time-temperature history across the fold-thrust belt, and are used to craft candidate thermal histories for forward modeling (Fig 8). Katherine Group sample 11FNA010 (Fig. 7; Fig. A4) from the Canyon anticline is unique in this dataset, as the absolute concentrations of eU are generally low and exhibit a smaller range of values compared with the remainder of our samples. Due to the low eU values, the zircons are more retentive to helium at higher temperatures (Fig. 6) and as a result the sample lacks the Late Cretaceous to Eocene cooling ages related to the formation of the Mackenzie Mountains. Instead, the ZHe data form three populations at c. 160, c. 225, and c. 400 Ma. An inverse thermal model derived from four grains suggests that burial

continued following the Devonian and reached a thermal maximum of <200°C between the Permian and the Early Triassic. These temperatures were sufficient to reset all but the most retentive of the zircons. Good fit solutions indicate that unroofing and erosion of the Carboniferous to Triassic stratigraphic record began by the Middle Triassic at the latest, recording the 225 Ma cooling age common in the sample.

While the absence of Cretaceous and younger ages provides poor resolution on the timing of tectonic exhumation related to the formation of the Mackenzie Mountains, the 160 Ma dates allow for the model to constrain the maximum temperatures experienced by this sample in the Cretaceous to Tertiary. The higher eU values in the c. 160 Ma grains (104–128 ppm eU) result in a slightly less retentive kinetic population compared to the 225 Ma ages (28–74 ppm eU). Thermal modeling suggests that Cretaceous reheating to 160°C results in partial resetting of the Triassic thermal history in grains with lower retentivity, producing the c. 160 Ma dates in this sample. Even though the acceptable solutions in this model do not preclude burial continuing into the Jurassic, we are hesitant to support this interpretation, as t-T histories with Jurassic cooling have difficulty resolving the c. 225 and c. 400 Ma ZHe dates due to the longer time spent within the ZHe PRZ. We believe that partial resetting of an early Mesozoic thermal history in the Cretaceous is a more elegant solution. Whereas it is possible that the absence of ZHe dates younger than the c. 160 Ma is a statistical problem, and that analyzing more zircons would reveal a higher eU population with younger ZHe dates, the overall t-T history would not change substantially as the maximum temperatures and heating and cooling rates are constrained by the kinetics of the three ZHe age populations.

Comparatively, Katherine Group sample JP012 from the Foran anticline has mostly 147–67 Ma dates. Thermal modeling of this sample provides a well constrained Cretaceous history, indicating reheating to ~180-190°C in the Late Cretaceous, with exhumation beginning between 75 and 80 Ma. Somewhat similarly, Tsezotene Formation sample JP024 from the Tawu anticline has even less dispersion than JP012, with ZHe dates between 48 and 122 Ma. The lack of Paleozoic to Early Cretaceous dates results in a poorly constrained thermal history prior to the Late Cretaceous. Instead, the model indicates that the strata were reheated to ~190°C in the Late Cretaceous, partially to fully resetting all of the pre-Cretaceous cooling history. Good fit paths suggest that exhumation began at c. 60 Ma. The thermal model from Keele Formation sample JP018 from the Redstone Plateau in the hanging wall of the Plateau fault is strikingly different from the other three models presented in Fig. A4. In this model, the strata were heated to temperatures well above the ZHe PRZ until 100-95 Ma when they began to cool at 2°C/m.y.

References

Aitken, J.D., R.W. Macqueen, and J.L. Usher (1973), Reconnaissance studies of Proterozoic and Cambrian stratigraphy, lower Mackenzie River area (Operation Norman), District of Mackenzie, *Geol. Surv. Canada, Paper 73-9*, 178 p.

Armstrong, R.L., G.H. Eisbacher, and P.D. Evans (1982), Age and stratigraphic-tectonic significance of Proterozoic diabase sheets, Mackenzie Mountains, northwestern Canada, *Can. J. Earth Sci.*, *19*, 316–323.

Hadlari, T., W.J. Davis, K. Dewing, L. M. Heaman, Y. Lemieux, L. Ootes, B.R. Pratt, and L.J. Pyle (2012), Two detrital zircon signatures for the Cambrian passive margin of northern

Laurentia highlighted by new U-Pb results from northern Canada, *Geol. Soc. Am. Bull.*, *124*(7-8), 1155–1168, doi:10.1130/B30530.1.

Issler, D.R., A. Grist, and L. Stasiuk (2005), Post-Early Devonian thermal constraints on hydrocarbon source rock maturation in the Keele Tectonic Zone, Tulita area, NWT, Canada, from multi-kinetic apatite fission track thermochronology, vitrinite reflectance and shale compaction, *Bull. Can. Pet. Geol.*, *53*(4), 405–431, doi:10.2113/53.4.405.

Jefferson, C.W., and R.R. Parrish (1989), Late Proterozoic stratigraphy, U-Pb zircon ages, and rift tectonics, Mackenzie Mountains, northwestern Canada, *Can. J. Earth Sci.*, *26 p*, 1784–1801.

Kellett, D., and N. Joyce (2014), Analytical details of single- and multicollection $^{40}Ar/^{39}Ar$ measurements for conventional step-heating and total-fusion age calculation using the Nu Noblesse at the Geological Survey of Canada, *Geol. Surv. Canada, Technical Note 8*, 27, doi: 10.4095/293465.

Ketcham, R.A. (2005), Forward and inverse modeling of low-temperature thermochronometry data, *Rev. Mineral. Geochemistry*, *58*(1), 275–314, doi:10.2138/rmg.2005.58.11.

Lane, L. S., and G.E. Gehrels (2014), Detrital zircon lineages of late Neoproterozoic and Cambrian strata, NW Laurentia, *Geol. Soc. Am. Bull.*, *126*(3-4), 398–414, doi:10.1130/B30848.1.

Long, D., and E. Turner (2012), Formal definition of the Neoproterozoic Mackenzie Mountains Supergroup (Northwest Territories), and formal stratigraphic nomenclature for terrigenous clastic units of the Katherine Group, *Geol. Surv. Canada, Open File 7113*, 40 p, doi:10.4095/292168.

MacLean, B. (2011), Tectonic and stratigraphic evolution of the Cambrian basin of northern Northwest Territories, *Bull. Can. Pet. Geol.*, *59*(2), 172–194.

Morrow, D.W. (1991), The Silurian-Devonian sequence in the northern part of the Mackenzie Shelf, Northwest Territories, *Geol. Surv. Canada, Bulletin 413,* 121 p.

Yorath, C. J., and D. Cook (1981), Cretaceous and Tertiary stratigraphy and paleogeography, Northern Interior Plains, District of Mackenzie, *Geol. Surv. Canada, Mem. 398*, 1–78.

Table A1. Single crystal total fusion $^{40}Ar/^{39}Ar$ analyses of muscovite from the Mackenzie Mountains, NWT. Detailed methodology available in supplementary Text A1

Samople	$^{40}Ar/^{39}Ar$	$^{37}Ar/^{39}Ar$	$^{36}Ar/^{39}Ar$ ($x10^{-3}$)	$^{39}Ar_K$ ($x10^{-15}$ mol)	Ca/K	$^{40}Ar^*$ (%)	Age (Ma)	±1s (Ma)
JP015: Keele Fm. (quartzite) UTM (NAD83): 63.638651, -127.506925; J: 0.021218								
JP015-26	25.73	0.00	1.95	0.88	0.0063	99.8	784.6	2.1
JP015-15	34.49	0.00	1.57	1.16	0.0058	98.3	977.5	2.4
JP015-19	55.07	0.00	2.14	1.72	0.0021	99.9	1395.4	3.0
JP015-21	62.72	0.00	2.90	0.99	0.0073	99.8	1524.3	3.2
JP015-23	67.17	0.00	1.59	0.88	0.0053	99.8	1596.4	3.3
JP015-12	67.49	0.00	5.55	1.92	0.0021	99.7	1600.4	3.2
JP015-17	71.85	0.00	3.75	0.91	0.0015	99.7	1667.9	3.4
JP015-14	73.78	0.00	0.83	0.69	0.0001	99.9	1698.8	3.5
JP015-16	76.65	0.00	2.10	0.69	0.0029	99.8	1739.7	3.6
JP015-20	81.88	0.00	0.05	0.61	0.0059	100.0	1816.6	3.8
JP015-02	83.25	0.00	1.38	0.11	0.0050	99.9	1834.0	3.6
JP015-18	84.92	0.00	1.30	0.68	0.0056	99.9	1857.6	3.7
JP015-25	89.67	0.00	1.42	1.00	0.0032	99.9	1921.1	3.7
JP015-09	105.58	0.00	4.41	1.43	0.0023	99.8	2119.0	3.8
JP015-13	117.39	0.00	2.38	1.13	0.0040	99.9	2253.7	3.9
JP015-05	124.30	0.00	4.05	1.21	0.0041	99.8	2326.6	4.0
JP015-10	127.17	0.00	3.87	1.70	0.0036	99.9	2357.9	4.0
JP015-22	127.68	0.00	1.62	0.33	0.0066	99.7	2360.7	4.5
JP015-03	129.86	0.00	6.04	2.17	0.0032	99.8	2385.0	3.9
JP015-04	129.95	0.00	6.47	1.90	0.0045	99.8	2385.4	3.9
JP015-07	130.16	0.00	1.13	0.91	0.0012	99.9	2389.2	4.1
JP015-06	130.15	0.00	0.22	4.47	0.0050	100.0	2389.9	4.1
JP015-01	130.95	0.00	3.80	1.78	0.0022	99.9	2397.0	4.0
JP015-24	131.64	0.00	2.65	0.96	0.0040	99.9	2403.3	4.1
JP015-08	132.14	0.00	6.96	1.90	0.0010	99.8	2408.0	4.0
JP015-11	133.15	0.00	6.14	1.61	0.0021	99.8	2417.6	4.0
Sample	$^{40}Ar/^{39}Ar$	$^{37}Ar/^{39}Ar$	$^{36}Ar/^{39}Ar$ ($x10^{-3}$)	$^{39}Ar_K$ ($x10^{-15}$ mol)	K/Ca	$^{40}Ar^*$ (%)	Age (Ma)	±1s (Ma)
JP001: Tsezotene Fm. (quartz wacke) UTM (NAD83): 65.019710, -127.809619; J: 0.018399								
JP001-11	40.81	-0.0307	0.947	0.892	-	99.3	1005.0	1.8
JP001-03	42.86	-0.0376	1.208	0.648	-	99.2	1042.1	2.3
JP001-08	43.17	-0.1475	1.052	1.035	-	99.3	1048.5	1.4
JP001-15	43.23	0.0199	0.775	0.960	25.7	99.5	1051.5	1.7
JP001-25	43.58	-0.0123	1.287	0.612	-	99.1	1055.1	2.6
JP001-23	43.81	0.0023	1.143	0.886	224.3	99.2	1060.1	1.8
JP001-17	44.12	-0.1325	0.934	0.885	-	99.3	1066.7	2.0
JP001-02	44.15	-0.0008	0.835	1.267	-	99.4	1068.1	1.2
JP001-18	44.69	-0.0815	2.422	0.367	-	98.4	1069.2	4.2
JP001-16	44.82	-0.0589	2.838	0.312	-	98.1	1069.4	5.2
JP001-21	44.47	0.0465	1.597	0.503	11.0	98.9	1069.9	3.2

Sample	$^{40}Ar/^{39}Ar$	$^{37}Ar/^{39}Ar$	$^{36}Ar/^{39}Ar$ ($x10^{-3}$)	$^{39}Ar_K$ ($x10^{-15}$ mol)	K/Ca	$^{40}Ar^*$ (%)	Age (Ma)	±1s (Ma)
JP001-05	44.25	-0.0123	0.789	1.793	-	99.5	1070.1	1.0
JP001-13	44.34	-0.0219	0.802	1.019	-	99.5	1071.6	1.8
JP001-04	44.50	0.0405	1.248	0.686	12.6	99.2	1072.2	2.6
JP001-24	44.66	-0.0254	1.457	0.535	-	99.0	1073.9	3.1
JP001-10	44.62	-0.0115	1.110	0.773	-	99.3	1075.1	1.9
JP001-22	44.65	0.0202	1.234	0.804	25.3	99.2	1075.1	2.0
JP001-14	44.62	0.0088	0.929	2.296	58.2	99.4	1076.2	0.8
JP001-06	44.78	-0.0095	0.637	3.179	-	99.6	1080.6	0.6
JP001-12	45.30	-0.0114	2.024	0.676	-	98.7	1082.7	2.3
JP001-20	45.15	-0.0180	0.980	0.793	-	99.4	1085.6	2.3
JP001-01	51.70	-0.0408	2.002	1.226	-	98.8	1195.7	1.6
JP001-07	61.31	-0.0014	1.121	0.867	-	99.5	1357.1	2.2
JP001-19	163.2	-0.0976	1.431	0.622	-	99.7	2498.9	4.7
JP001-09	169.8	0.0177	0.685	1.192	28.9	99.9	2554.2	2.3
JP007: Little Dal Gp. (quartz arenite) UTM (NAD83): 64.895236, -127.250024; J: 0.018409								
JP007-20	31.44	0.0256	0.960	1.637	19.9	99.1	817.8	0.9
JP007-01	33.97	0.0012	1.347	2.132	413.8	98.8	867.9	0.8
JP007-25	33.97	-0.0061	1.040	1.344	-	99.1	869.7	1.0
JP007-08	34.35	0.0465	1.479	2.784	11.0	98.7	875.1	1.0
JP007-06	34.74	0.0292	1.085	5.546	17.4	99.1	885.3	0.7
JP007-21	35.51	-0.0066	1.067	1.736	-	99.1	901.1	0.9
JP007-19	35.51	0.0425	0.935	1.188	12.0	99.2	901.8	1.2
JP007-09	35.58	0.0257	0.444	9.492	19.9	99.6	906.2	0.6
JP007-17	35.70	0.0025	0.545	3.844	202.5	99.5	907.9	0.4
JP007-07	36.88	0.0471	2.628	2.465	10.8	97.9	919.4	1.0
JP007-23	36.78	-0.0029	0.609	2.384	-	99.5	929.1	0.6
JP007-11	37.30	0.0043	1.675	2.683	118.3	98.7	933.1	0.5
JP007-22	37.50	0.0187	1.493	1.479	27.2	98.8	938.2	0.9
JP007-05	37.73	0.0151	0.977	3.776	33.8	99.2	945.7	0.5
JP007-16	38.84	0.0241	1.278	1.509	21.2	99.0	965.8	1.0
JP007-13	39.28	0.0031	0.633	5.497	166.5	99.5	977.8	0.4
JP007-24	39.83	0.0187	1.252	1.428	27.2	99.1	985.0	1.1
JP007-10	41.93	0.0002	2.183	0.987	2917.1	98.5	1019.7	1.6
JP007-04	42.27	0.0193	0.938	1.694	26.4	99.3	1033.1	1.0
JP007-03	43.04	0.0293	1.191	1.340	17.4	99.2	1046.0	1.2
JP007-12	42.97	0.0083	0.765	2.343	61.5	99.5	1047.1	0.7
JP007-14	44.05	0.0036	0.449	4.585	140.3	99.7	1068.7	0.4
JP007-15	44.64	0.0091	1.127	2.644	56.1	99.3	1075.9	0.6
JP007-02	47.34	0.0100	0.822	1.838	50.9	99.5	1126.2	1.0
JP009: Katherine Gp. (quartz arenite) UTM (NAD83): 64.474943, -126.882328; J: 0.018409								
JP009-15	38.68	0.0438	1.173	1.102	11.6	99.1	963.3	1.3
JP009-09	38.94	0.0469	1.859	0.715	10.9	98.6	964.3	2.3
JP009-14	38.71	-0.0024	0.876	2.357	-	99.3	965.4	0.7
JP009-12	38.86	-0.0015	1.165	2.534	-	99.1	966.7	0.6

Sample	$^{40}Ar/^{39}Ar$	$^{37}Ar/^{39}Ar$	$^{36}Ar/^{39}Ar$ ($x10^{-3}$)	$^{39}Ar_K$ ($x10^{-15}$ mol)	K/Ca	$^{40}Ar^*$ (%)	Age (Ma)	±1s (Ma)
JP009-21	39.08	0.0862	0.824	1.603	5.9	99.4	973.2	1.1
JP009-24	40.22	0.0581	3.391	0.895	8.8	97.5	980.5	1.8
JP009-02	39.53	-0.1035	0.898	1.359	-	99.3	981.0	1.1
JP009-10	40.25	0.0349	1.945	0.609	14.6	98.6	989.3	2.7
JP009-01	39.95	-0.0341	0.767	2.653	-	99.4	989.9	0.7
JP009-03	39.96	-0.0224	0.657	3.826	-	99.5	990.9	0.5
JP009-11	40.16	0.0143	1.195	0.989	35.6	99.1	991.6	1.5
JP009-05	41.31	0.0025	0.699	3.009	208.1	99.5	1016.3	0.5
JP009-17	42.81	0.0171	0.947	1.433	29.8	99.3	1043.2	1.3
JP009-13	43.18	-0.0174	1.215	1.572	-	99.2	1048.4	1.1
JP009-19	43.75	0.0171	1.423	1.066	29.8	99.0	1058.0	1.7
JP009-22	43.97	0.0097	1.336	1.334	52.9	99.1	1062.4	1.2
JP009-06	44.11	-0.0106	0.839	2.144	-	99.4	1067.6	0.8
JP009-04	44.46	-0.0042	1.190	1.710	-	99.2	1072.2	1.0
JP009-20	46.81	0.0374	1.074	1.050	13.6	99.3	1115.5	1.6
JP009-07	47.05	-0.0028	0.618	2.409	-	99.6	1122.1	0.7
JP009-26	47.87	-0.0236	1.208	0.957	-	99.3	1133.5	1.8
JP009-23	48.04	-0.0310	1.169	1.074	-	99.3	1136.8	1.6
JP009-16	48.02	-0.0111	0.967	1.205	-	99.4	1137.5	1.5
JP009-18	48.35	0.0121	1.887	1.508	42.3	98.8	1138.6	1.2
JP009-25	48.35	0.0294	0.772	1.304	17.3	99.5	1144.4	1.4
JP009-08	49.21	-0.0136	0.752	1.538	-	99.5	1159.5	1.3
JP022: Tsezotene Fm. (quartz arenite) UTM (NAD83): 64.157116, -128.099835; J: 0.018402								
JP022-17	18.22	0.0119	2.743	0.286	42.9	95.6	501.2	3.1
JP022-24	40.02	0.0110	0.644	1.504	46.2	99.5	991.9	1.0
JP022-11	41.34	0.0090	0.847	0.976	56.6	99.4	1015.8	1.6
JP022-26	42.14	0.0048	0.519	2.012	105.9	99.6	1032.7	0.8
JP022-23	42.60	0.0164	1.285	0.853	31.2	99.1	1037.0	1.8
JP022-22	43.13	-0.0179	1.186	1.071	-	99.2	1047.4	1.4
JP022-18	43.16	0.0153	1.097	0.743	33.4	99.3	1048.4	2.3
JP022-13	43.10	0.0184	0.635	1.473	27.7	99.6	1049.9	1.2
JP022-25	43.12	0.0333	0.606	1.362	15.3	99.6	1050.5	1.1
JP022-08	43.42	0.0474	0.726	1.142	10.8	99.5	1055.4	1.5
JP022-07	43.54	-0.0272	0.629	2.315	-	99.6	1058.1	0.8
JP022-12	43.67	0.0014	0.733	1.667	361.3	99.5	1060.0	1.0
JP022-16	44.01	-0.0051	0.451	2.240	-	99.7	1067.7	0.7
JP022-04	44.87	-0.0333	0.574	1.902	-	99.6	1082.7	0.9
JP022-03	44.85	0.0083	0.319	5.146	61.4	99.8	1083.8	0.3
JP022-05	45.35	0.0004	0.596	2.123	1243.5	99.6	1091.4	0.8
JP022-06	45.80	0.0723	0.654	1.845	7.1	99.6	1099.3	0.9
JP022-20	45.96	-0.0011	0.631	1.410	-	99.6	1102.2	1.1
JP022-21	46.41	0.0336	0.821	0.910	15.2	99.5	1109.4	1.9
JP022-02	46.62	0.0158	0.364	6.241	32.2	99.8	1115.5	0.3
JP022-10	46.80	0.0008	0.543	1.863	605.7	99.7	1117.8	0.9

Sample	$^{40}Ar/^{39}Ar$	$^{37}Ar/^{39}Ar$	$^{36}Ar/^{39}Ar$ ($x10^{-3}$)	$^{39}Ar_K$ ($x10^{-15}$ mol)	K/Ca	$^{40}Ar^*$ (%)	Age (Ma)	±1s (Ma)
JP022-09	47.14	-0.0885	0.902	1.107	-	99.4	1121.7	1.6
JP022-19	47.71	0.0298	0.991	1.086	17.1	99.4	1131.6	1.7
JP022-15	47.83	0.0154	1.091	1.130	33.0	99.3	1133.2	1.6
JP022-01	48.52	0.0099	0.360	7.089	51.4	99.8	1149.1	0.3
JP022-14	49.77	-0.0043	0.304	3.508	-	99.8	1171.3	0.6

Notes:

Isotopic ratios corrected for blank, radioactive decay, and detector calibrations not corrected for interfering reacti

Errors quoted for individual analyses include analytical error only, without interfering reaction or J uncertainties.

Error on J = ± 0.004%

Decay constants and isotopic abundances after Steiger and Jäger (1977).

Ages calculated relative to FC-2 Fish Canyon Tuff sanidine interlaboratory standard at 28.02 Ma.

Decay Constant (LambdaK (total)) = 5.543e-10/a

IC = Measured ($^{40}Ar/^{36}Ar$)/295.5

No ^{37}Ar detected above background.

Correction factors:

$(^{39}Ar/^{37}Ar)_{Ca}$ = 0.0006953 ± 1e-06

$(^{36}Ar/^{37}Ar)_{Ca}$ = 0.0002785 ± 2e-7

$(^{40}Ar/^{39}Ar)_K$ = 0.007951 ± 6.4e-05

Table A2. Estimated stratigraphic thickness for each ZHe sample. Thickness of stratigraphy is derived from measured stratigraphic thickness for Neoproterozoic, Paleozoic and Cretaceous sections proximal to sample localities (after *Aitken et al*., [1973], *Yorath and Cook* [1981], and *Morrow* [1991])

Sample Group	Sample Number	Stratigraphy	Upper Cretaceous and Paleocene Thickness (m)	Lower Cretaceous Thickness (m)	Upper Devonian Thickness (m)	Upper Silurian to Middle Devonian Thickness (m)	Upper Ordovician to Middle Silurian Thickness (m)	Upper Cambrian to Middle Ordovician Thickness (m)	Lower to Middle Cambrian Thickness (m)	Sample to Sub-Cambrian Unconformity Thickness (m)	Estimated Stratigraphic Thickness (m)
Group E	JP015	Keele Fm.	>500	800	>700	~900	300	~800	1500	1200	6700
	JP018	Keele Fm.	>500	800	>700	~900	300	~800	1500	1200	6700
	JP017	Katherine Gp.	~1000	~1200	>700	~700	300	500	150	800	5300
Group D	JP022	Tsezotene Fm.	~1000	~1200	>700	~700	300	500	150	2700	7200
Group C	JP026	Katherine Gp.	~1200	~1200	>700	~550	250	350	50	300	4600
	JP025	Katherine Gp.	~1200	~1200	>700	~550	250	350	50	1000	5300
	JP024	Tsezotene Fm.	~1200	~1200	>700	~550	250	350	50	1200	5500
Group B	12FNA103	Katherine Gp.	~1200	~1200	>700	~550	250	350	5	500	4800
	JP012	Katherine Gp.	~1200	~1200	>700	~550	250	350	50	1000	5300

Sample Group	Sample Number	Stratigraphy	Upper Cretaceous and Paleocene Thickness (m)	Lower Cretaceous Thickness (m)	Upper Devonian Thickness (m)	Upper Silurian to Middle Devonian Thickness (m)	Upper Ordovician to Middle Silurian Thickness (m)	Upper Cambrian to Middle Ordovician Thickness (m)	Lower to Middle Cambrian Thickness (m)	Sample to Sub-Cambrian Unconformity Thickness (m)	Estimated Stratigraphic Thickness (m)
Group A	12FNA047	Katherine Gp.	~1800	~1200	>700	~500	200	500	100	250	5200
	11FNA010	Katherine Gp.	~1800	~1200	>700	~500	200	500	100	100	5100
	JP008	Katherine Gp.	~1800	~1200	>700	~500	200	500	200	500	5600
	JP007	Dodo Creek Fm	~1800	~1200	>700	~500	200	500	200	100	5200

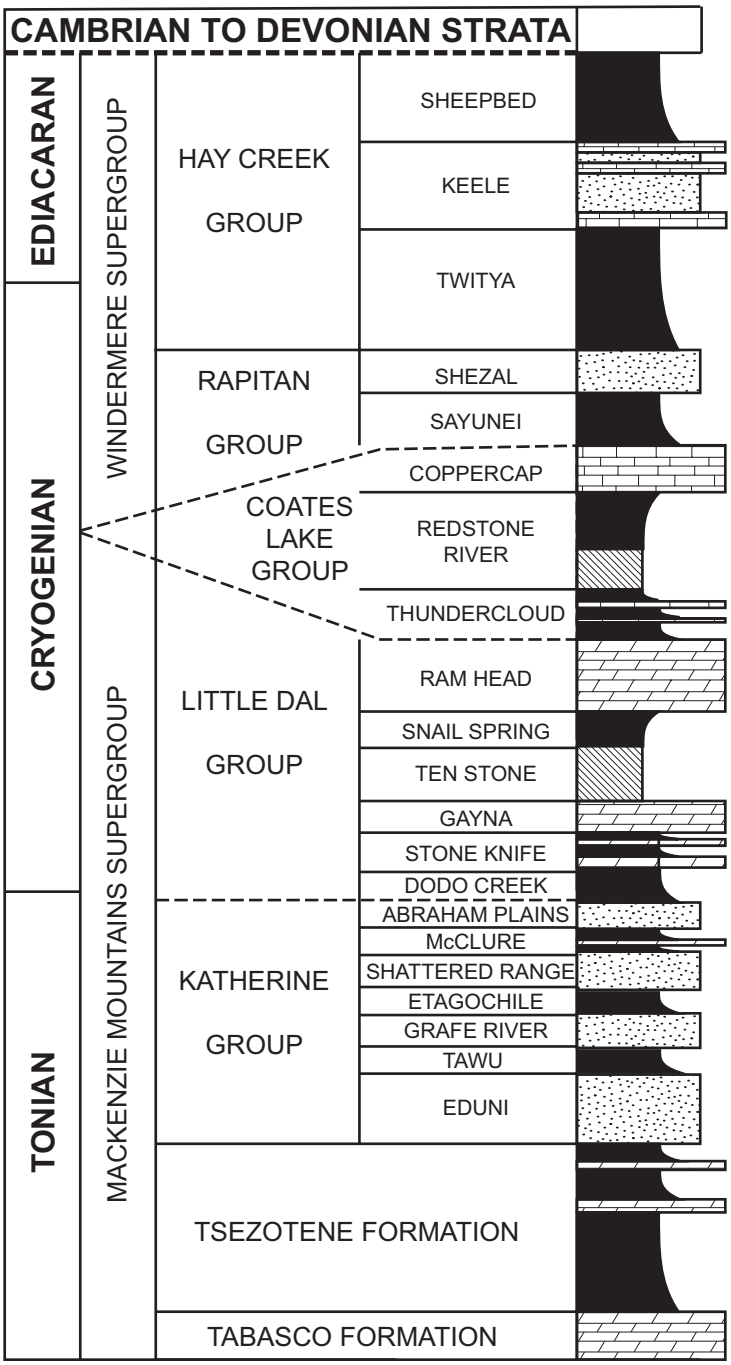

Fig. A1: Neoproterozoic stratigraphy of the Mackenzie Mountains Supergroup and Windermere Supergroup (modified after *Jefferson and Parrish* [1989], *Long and Turner* [2012]).

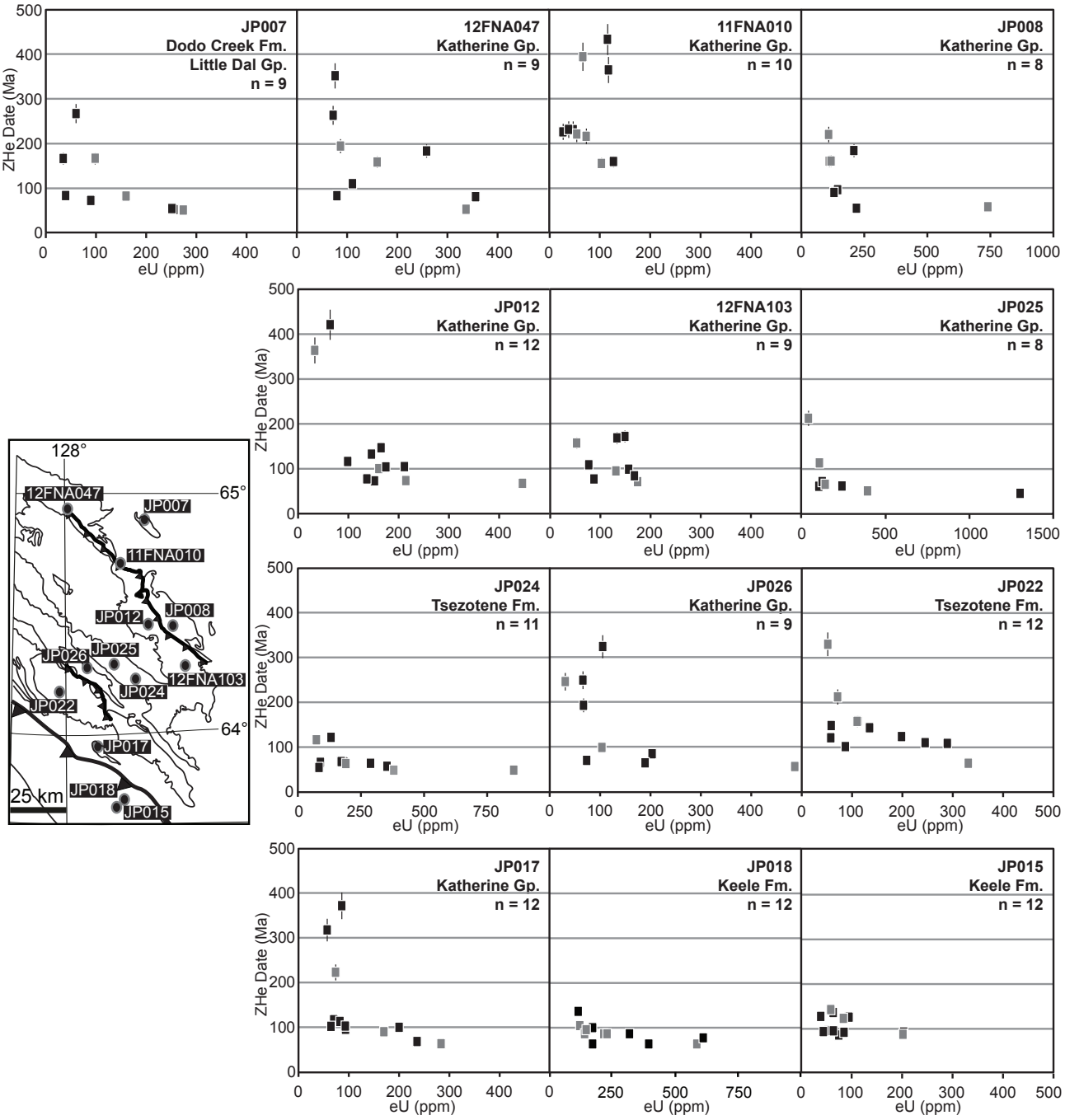

Fig. A2: Similar to Fig. 4 in Chapter 2, but now highlighting ZHe grains (gray) used in inverse thermal history modeling.

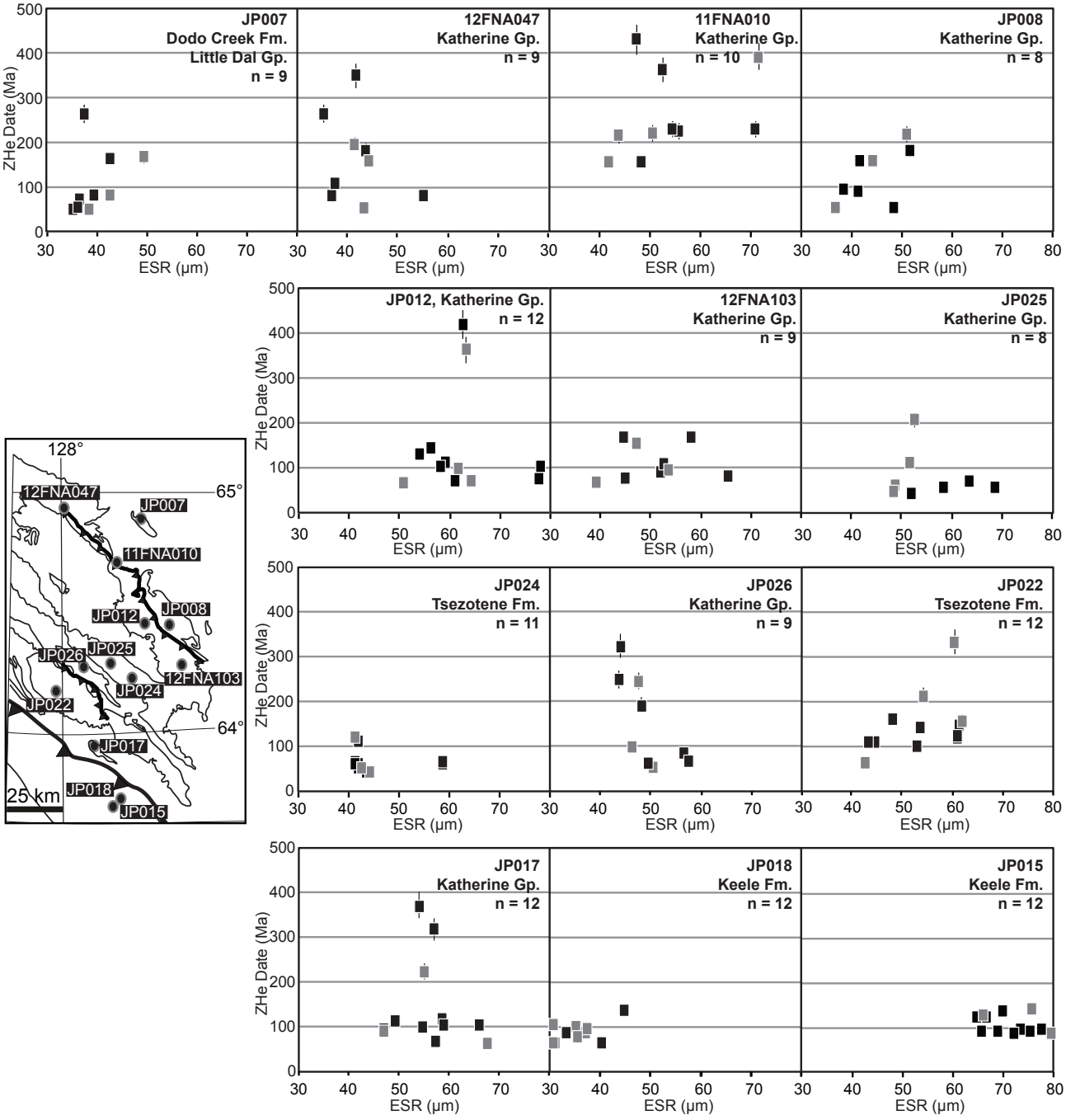

Fig. A3: Similar to Fig. 4 in Chapter 2, but now showing relationships between ZHe date and equivalent spherical radius (ESR). Whereas most samples exhibit negative correlations between ZHe date-eU (Fig. 4), there is little obvious relationship between ZHe date and grainsize in our dataset. Grains used in inverse thermal history models are highlighted in gray.

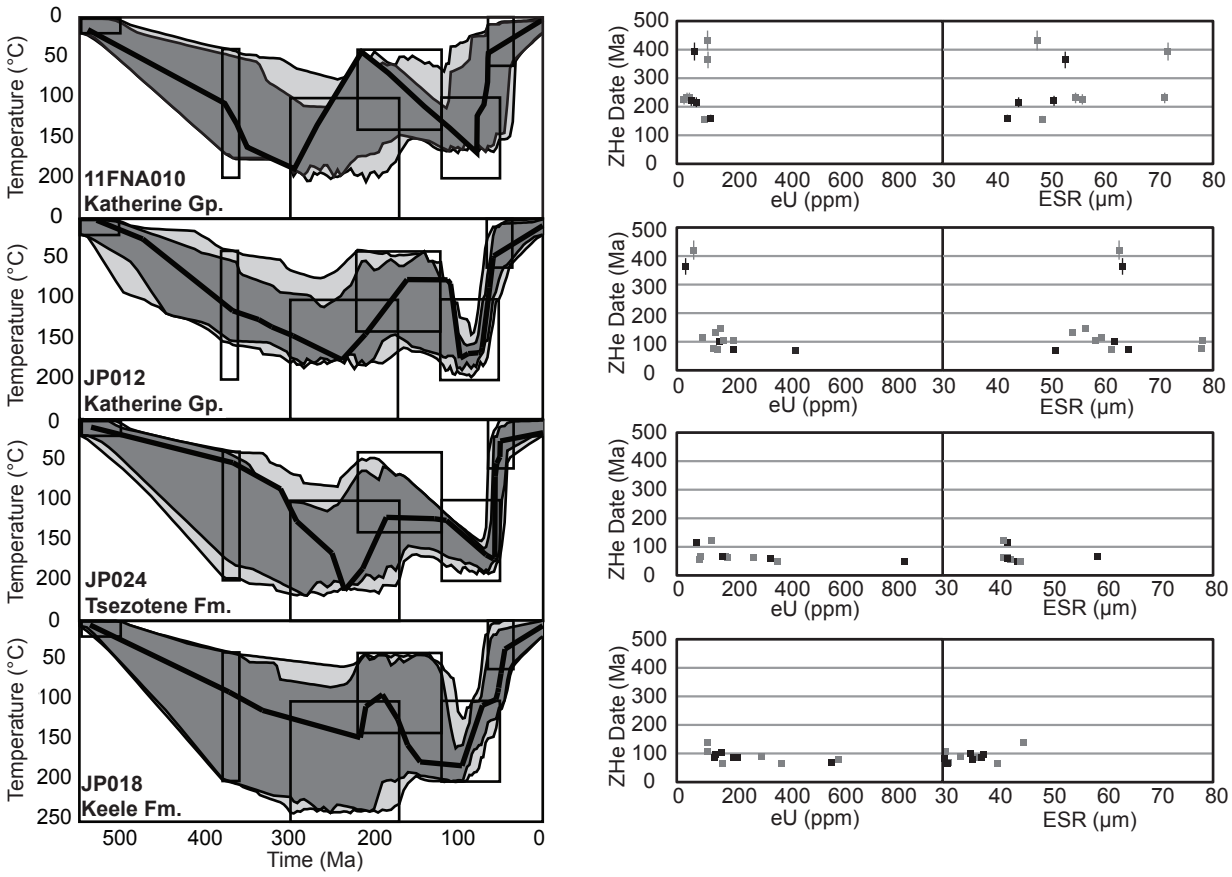

Fig. A4: Representative *HeFTy* inverse thermal history models from four select samples examined in this study. Black boxes indicate t-T constraints (see text A2 for explanation) and the solid black line shows the best-fit thermal history for each model. 'Good fit' solutions are represented by the dark gray curves, whereas 'acceptable' solutions are represented by light gray curves. Adjacent to each thermal history model are the corresponding date-eU and date-ESR graphs for the modeled samples. ZHe dates used in inverse thermal modeling are highlighted in black.

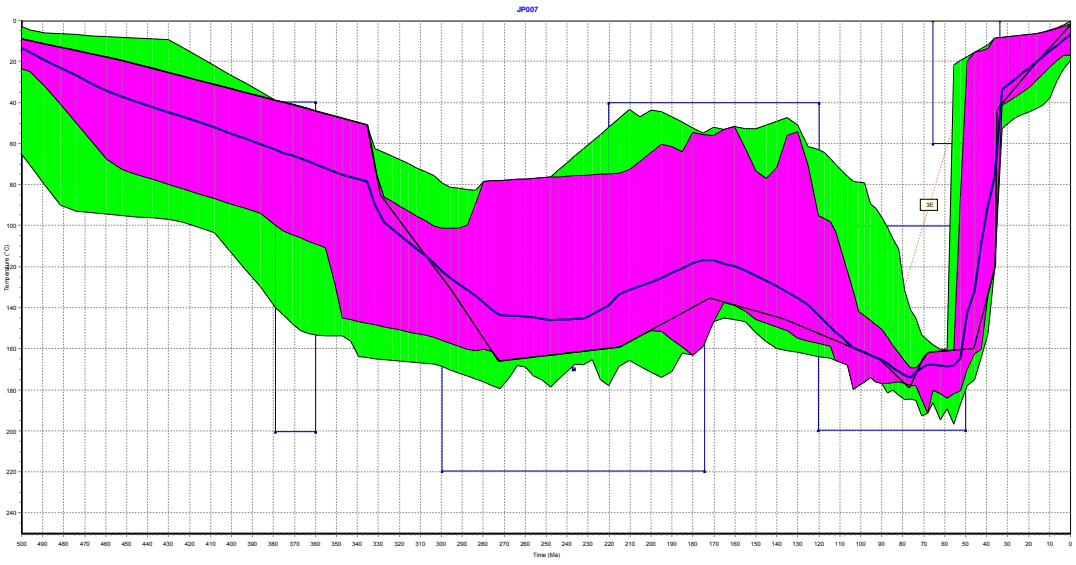

Fig. A5: Inverse thermal model for Little Dal Gp. sample JP007. 'Good fit' thermal histories are summarized by the purple envelope, whereas 'acceptable' solutions are highlighted in green. The solid black line indicates the best-fit temperature time path, whereas the blue line represents the weighted mean of all good and acceptable solutions.

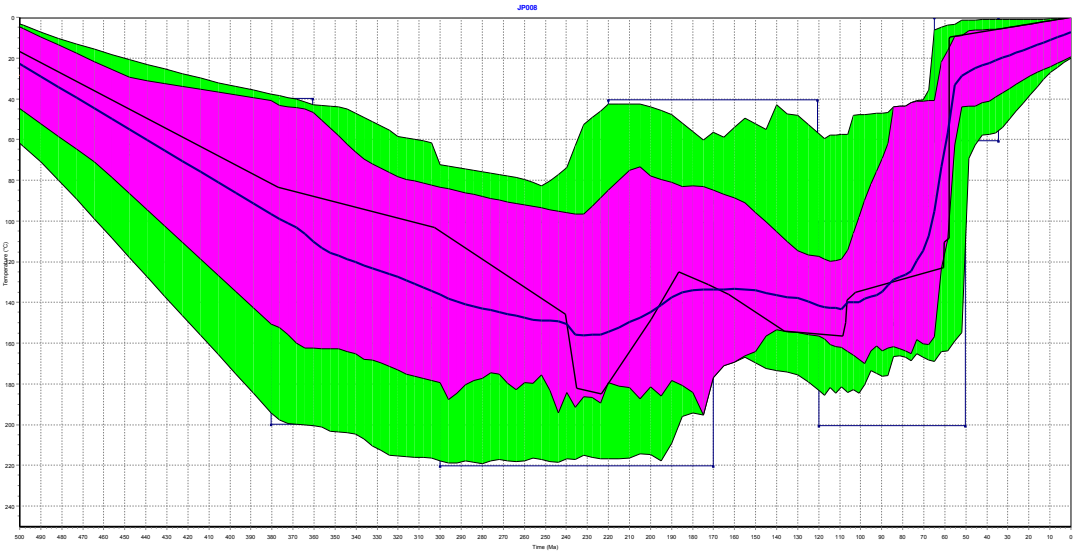

Fig. A6: Inverse thermal model for Katherine Gp. sample JP008. 'Good fit' thermal histories are summarized by the purple envelope, whereas 'acceptable' solutions are highlighted in green. The solid black line indicates the best-fit temperature time path, whereas the blue line represents the weighted mean of all good and acceptable solutions.

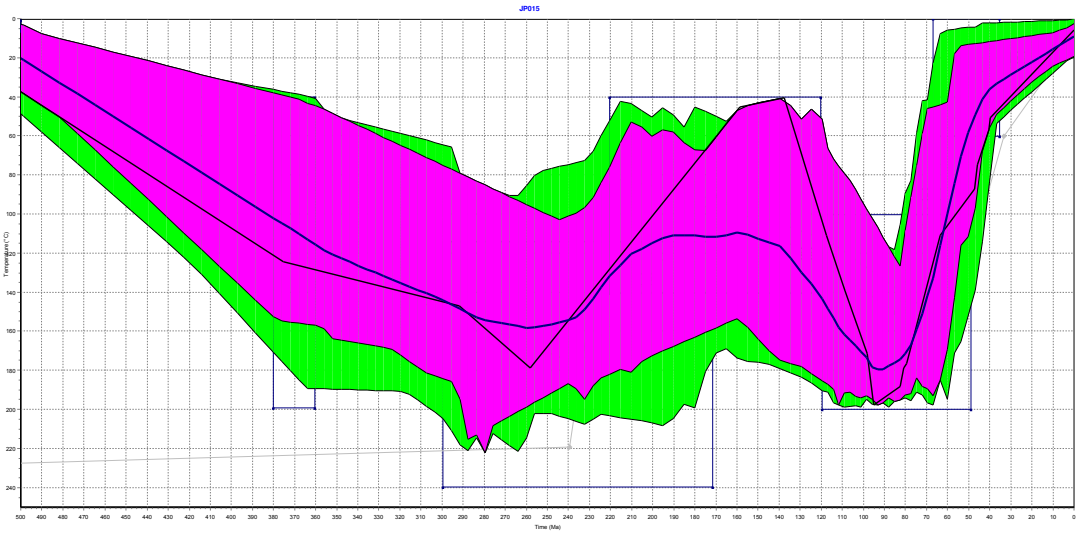

Fig. A7: Inverse thermal model for Keele Fm. sample JP015. 'Good fit' thermal histories are summarized by the purple envelope, whereas 'acceptable' solutions are highlighted in green. The solid black line indicates the best-fit temperature time path, whereas the blue line represents the weighted mean of all good and acceptable solutions.

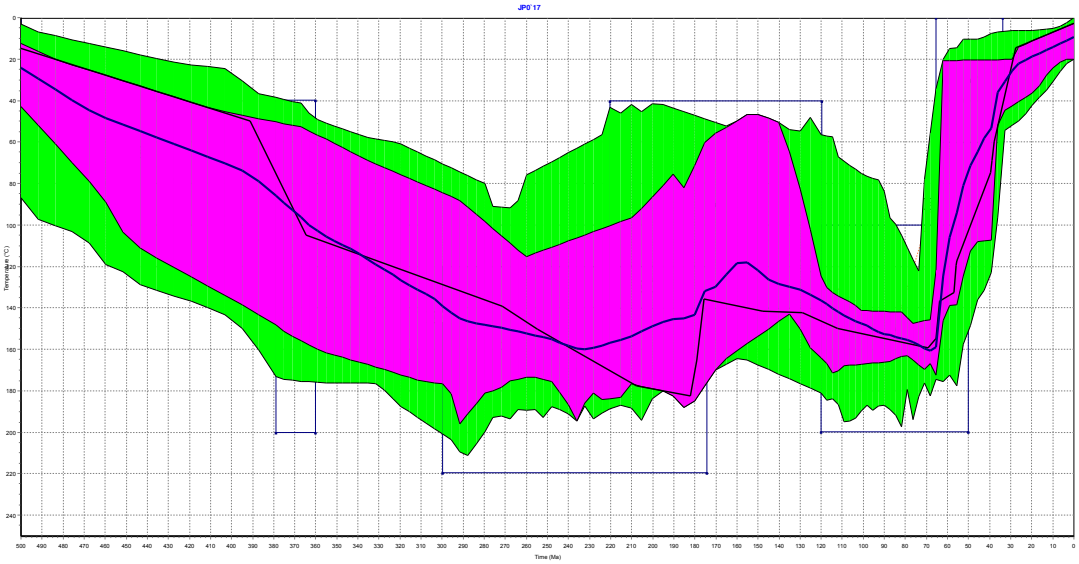

Fig. A8: Inverse thermal model for Katherine Gp. sample JP017. 'Good fit' thermal histories are summarized by the purple envelope, whereas 'acceptable' solutions are highlighted in green. The solid black line indicates the best-fit temperature time path, whereas the blue line represents the weighted mean of all good and acceptable solutions.

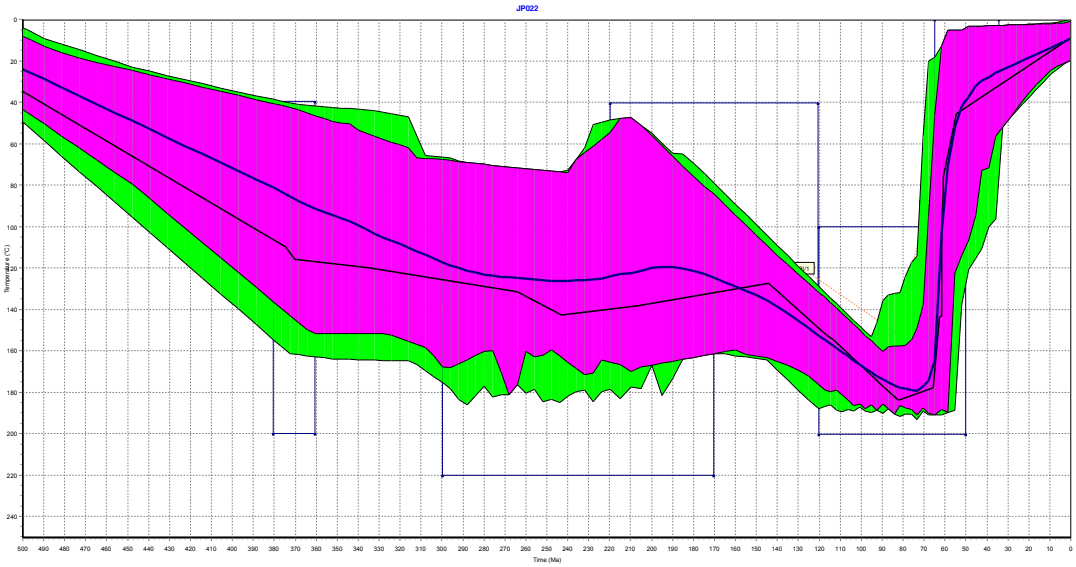

Fig. A9: Inverse thermal model for Tsezotene Fm. sample JP022. 'Good fit' thermal histories are summarized by the purple envelope, whereas 'acceptable' solutions are highlighted in green. The solid black line indicates the best-fit temperature time path, whereas the blue line represents the weighted mean of all good and acceptable solutions.

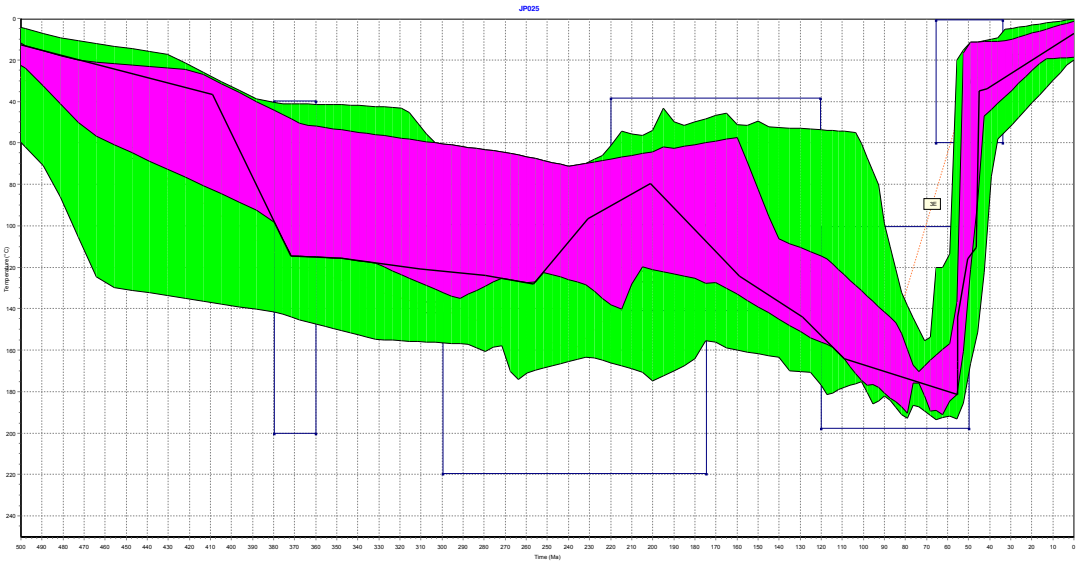

Fig. A10: Inverse thermal model for Katherine Gp.sample JP025. 'Good fit' thermal histories are summarized by the purple envelope, whereas 'acceptable' solutions are highlighted in green. The solid black line indicates the best-fit temperature time path, whereas the blue line represents the weighted mean of all good and acceptable solutions.

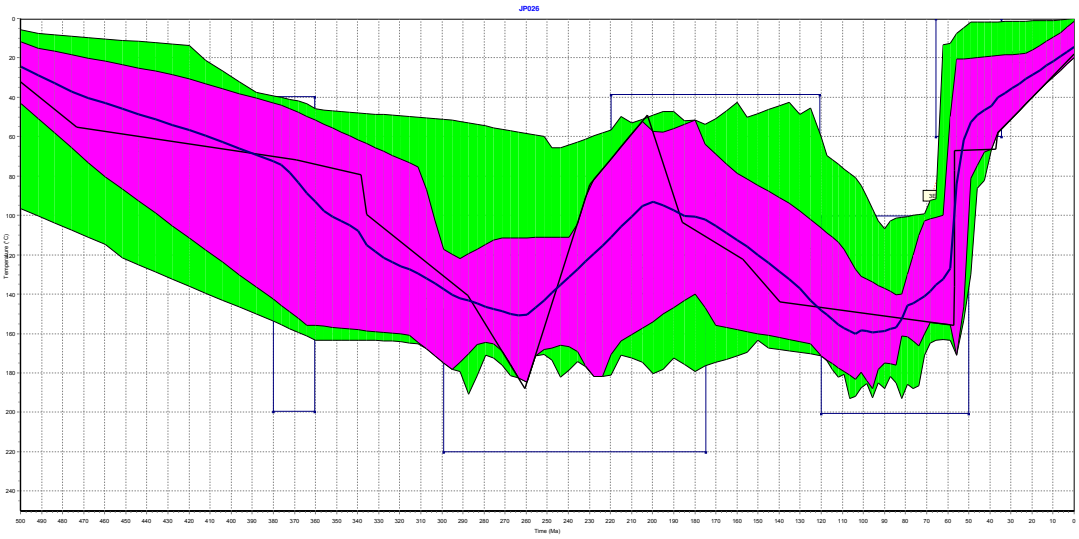

Fig. A11: Inverse thermal model for Katherine Gp. sample JP026. 'Good fit' thermal histories are summarized by the purple envelope, whereas 'acceptable' solutions are highlighted in green. The solid black line indicates the best-fit temperature time path, whereas the blue line represents the weighted mean of all good and acceptable solutions.

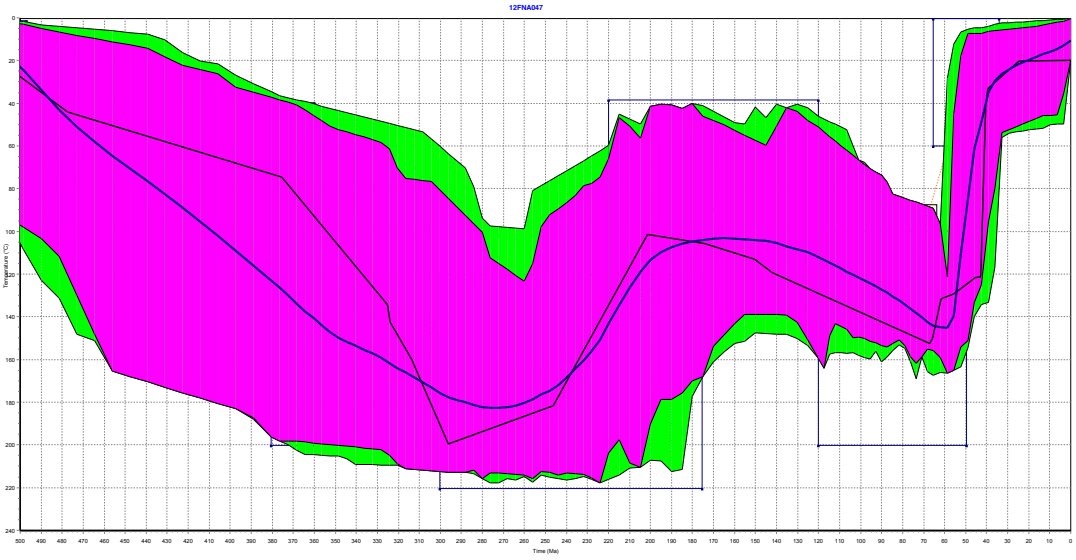

Fig. A12: Inverse thermal model for Katherine Gp. sample 12FNA047. 'Good fit' thermal histories are summarized by the purple envelope, whereas 'acceptable' solutions are highlighted in green. The solid black line indicates the best-fit temperature time path, whereas the blue line represents the weighted mean of all good and acceptable solutions.

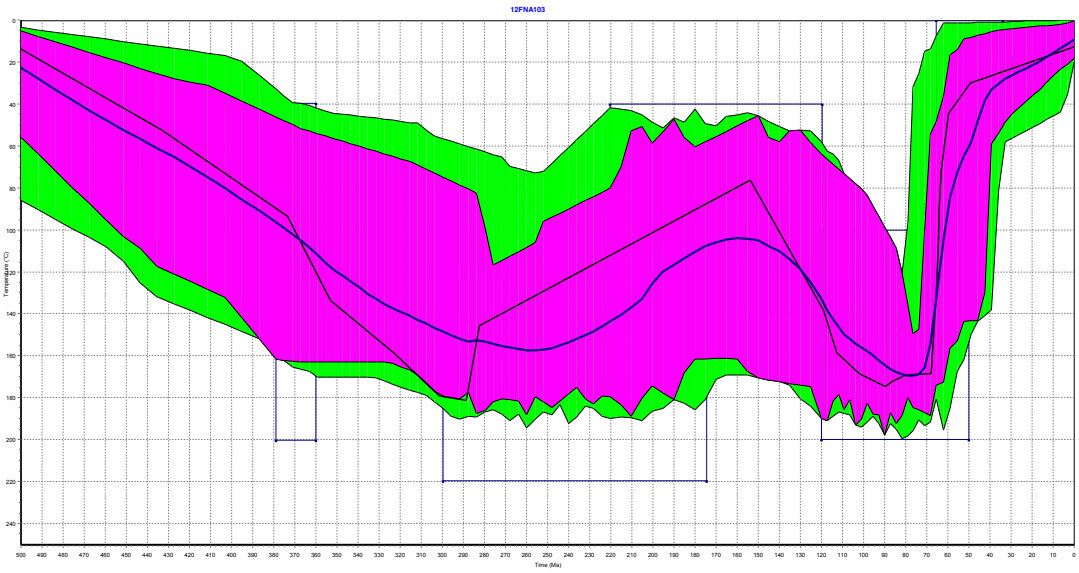

Fig. A13: Inverse thermal model for Katherine Gp. sample 12FNA103. 'Good fit' thermal histories are summarized by the purple envelope, whereas 'acceptable' solutions are highlighted in green. The solid black line indicates the best-fit temperature time path, whereas the blue line represents the weighted mean of all good and acceptable solutions.

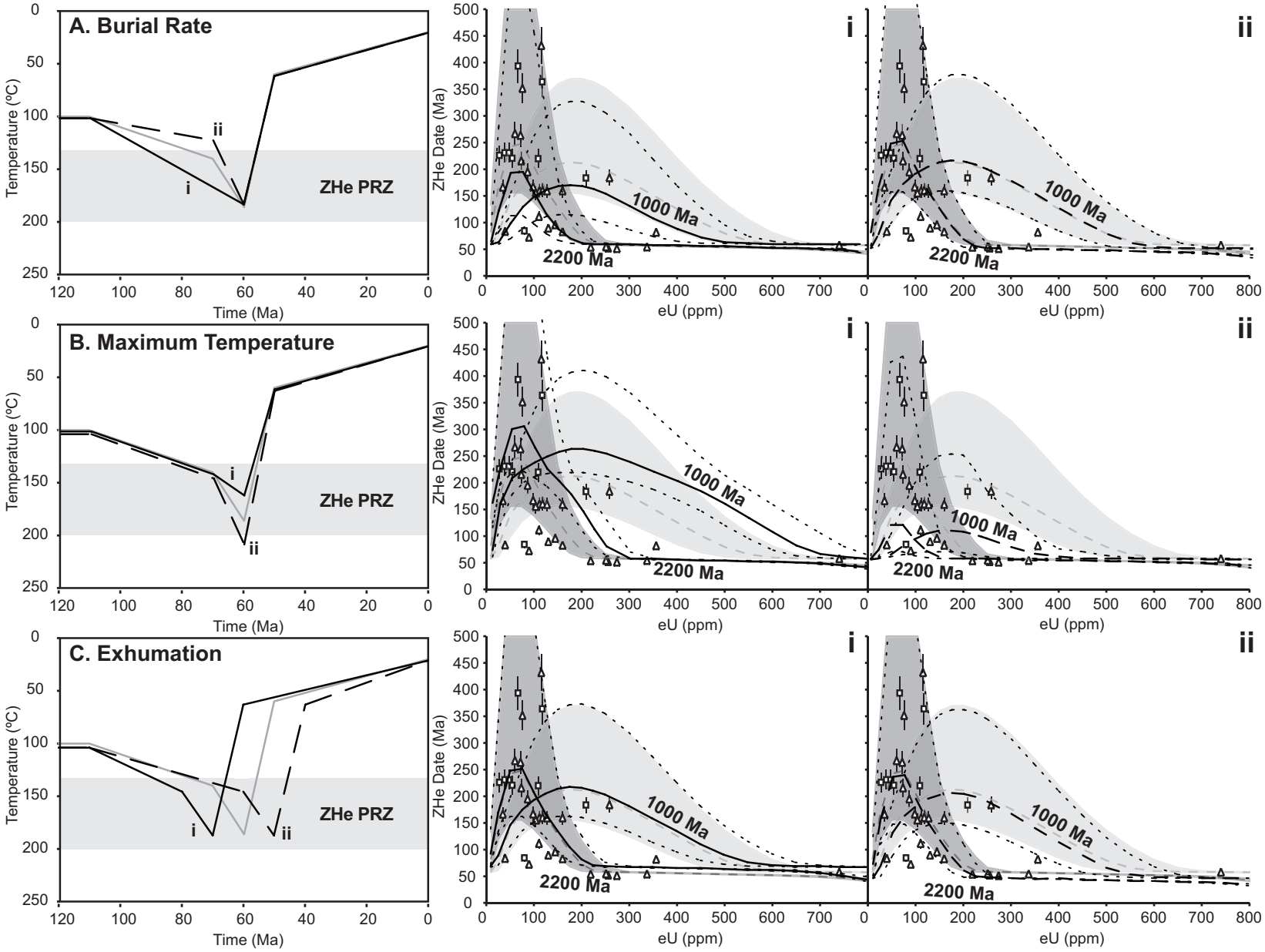
A. Burial Rate
B. Maximum Temperature
C. Exhumation
Temperature (ºC)
Time (Ma)
ZHe PRZ
i
ii
ZHe Date (Ma)
eU (ppm)
1000 Ma
2200 Ma

Fig. A14 (previous page). Time-temperature paths and corresponding date-eU plots showing the sensitivity of the forward model derived from "Group A" samples from Fig. 8a in the published paper to a varying thermal history. In A14a, b, and c, the solid gray t-T path is fixed and corresponds to the t-T history for Group A samples from Fig 8. The shaded envelopes in the date-eU plots display the inheritance curves derived from this t-T history at 2200 Ma (dark gray) and 1000 Ma (light gray) for 35-80 μm grain sizes (dashed gray curve = 50 μm date-eU trend). The dashed and solid black t-T curves (i, ii) exhibit the effect of changing A) burial rate, B) maximum burial temperatures (±20 °C), and C) the timing of exhumation (±10 Ma) on date-eU trends shown in Fig 8a. To the right, the corresponding date-eU inheritance curves (1000 Ma, 2200 Ma) for a 50 μm grain size are shown in the solid black (i) and dashed black (ii) lines. Dotted black lines for each inheritance curve correspond to 35 and 80 μm grain size date-eU trends.

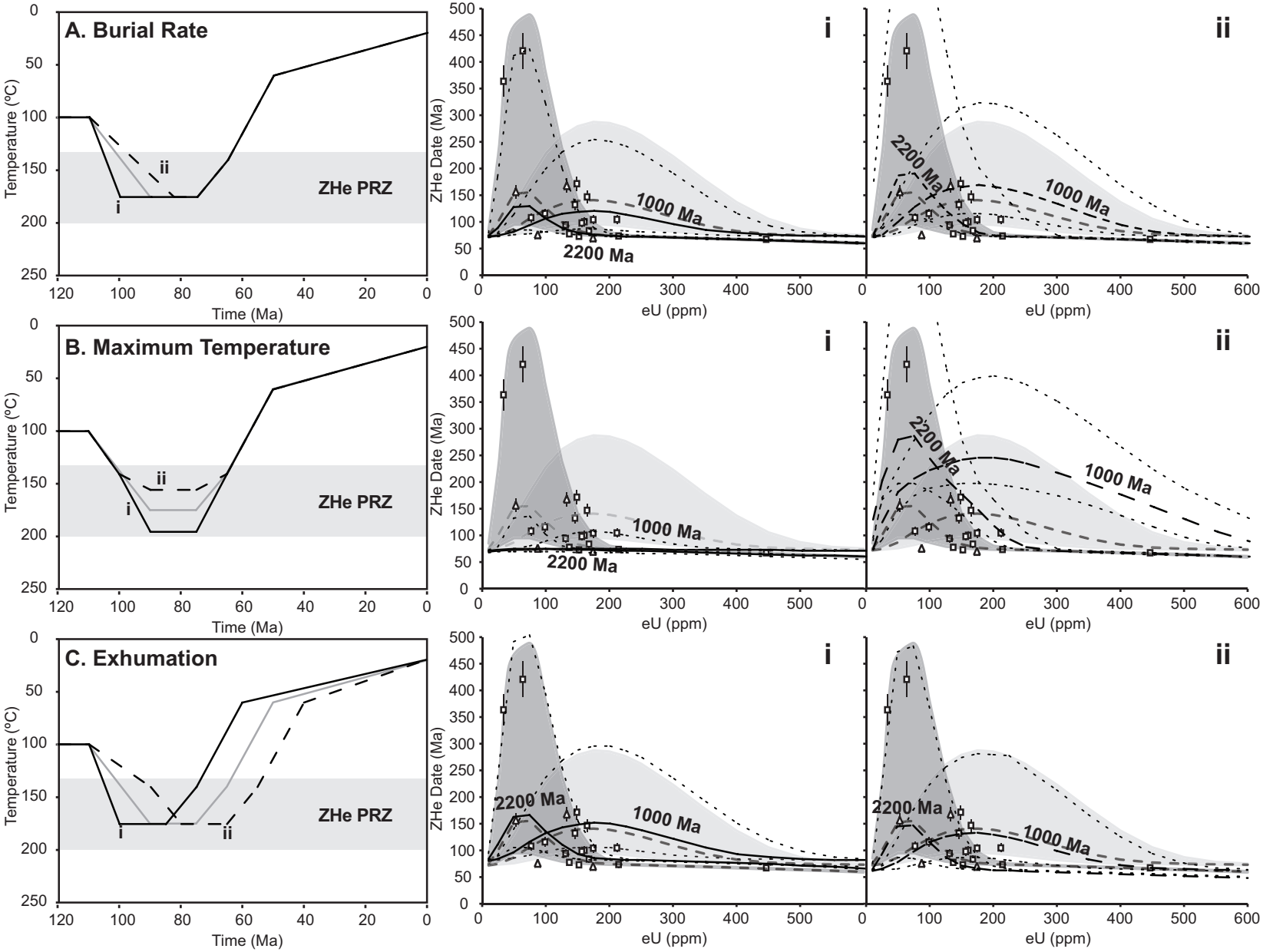
A. Burial Rate
B. Maximum Temperature
C. Exhumation
Temperature (ºC)
Time (Ma)
ZHe PRZ
i
ii
ZHe Date (Ma)
eU (ppm)
1000 Ma
2200 Ma

Fig. A15. Time-temperature paths and corresponding date-eU plots showing the sensitivity of the forward model derived from "Group B" samples from Fig. 8b in the published paper to a varying thermal history. In A15a, b, and c, the solid gray t-T path is fixed and corresponds to the t-T history for Group B samples from Fig 8. The shaded envelopes in the date-eU plots display the inheritance curves derived from this t-T history at 2200 Ma (dark gray) and 1000 Ma (light gray) for 35-80 μm grain sizes (dashed gray curve = 50 μm date-eU trend). The dashed and solid black t-T curves (i, ii) exhibit the effect of changing A) burial rate, B) maximum burial temperatures (±20 °C), and C) the timing of exhumation (±10 Ma) on date-eU trends shown in Fig 8b. To the right, the corresponding date-eU inheritance curves (1000 Ma, 2200 Ma) for a 50 μm grain size are shown in the solid black (i) and dashed black (ii) lines. Dotted black lines for each inheritance curve correspond to 35 and 80 μm grain size date-eU trends.

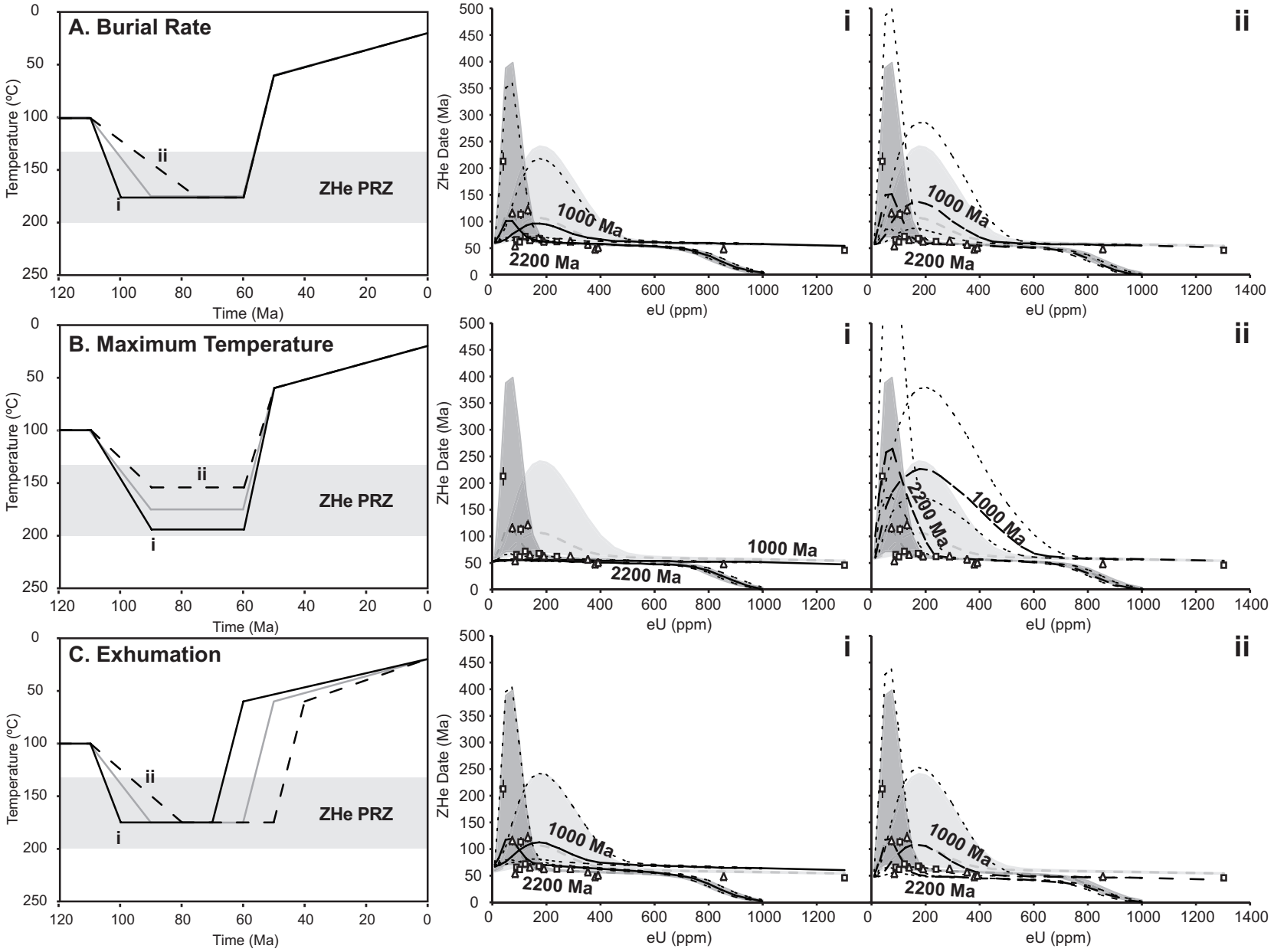
A. Burial Rate
B. Maximum Temperature
C. Exhumation
Temperature (ºC)
Time (Ma)
ZHe PRZ
i
ii
ZHe Date (Ma)
eU (ppm)
1000 Ma
2200 Ma

Fig. A16 (previous page). Time-temperature paths and corresponding date-eU plots showing the sensitivity of the forward model derived from "Group C" samples from Fig. 8c in the published paper to a varying thermal history. In A16a, b, and c, the solid gray t-T path is fixed and corresponds to the t-T history for Group C samples from Fig. 8. The shaded envelopes in the date-eU plots display the inheritance curves derived from this t-T history at 2200 Ma (dark gray) and 1000 Ma (light gray) for 35-80 μm grain sizes (dashed gray curve = 50 μm date-eU trend). The dashed and solid black t-T curves (i, ii) exhibit the effect of changing A) burial rate, B) maximum burial temperatures (±20 °C), and C) the timing of exhumation (±10 Ma) on date-eU trends shown in Fig 8c. To the right, the corresponding date-eU inheritance curves (1000 Ma, 2200 Ma) for a 50 μm grain size are shown in the solid black (i) and dashed black (ii) lines. Dotted black lines for each inheritance curve correspond to 35 and 80 μm grain size date-eU trends.

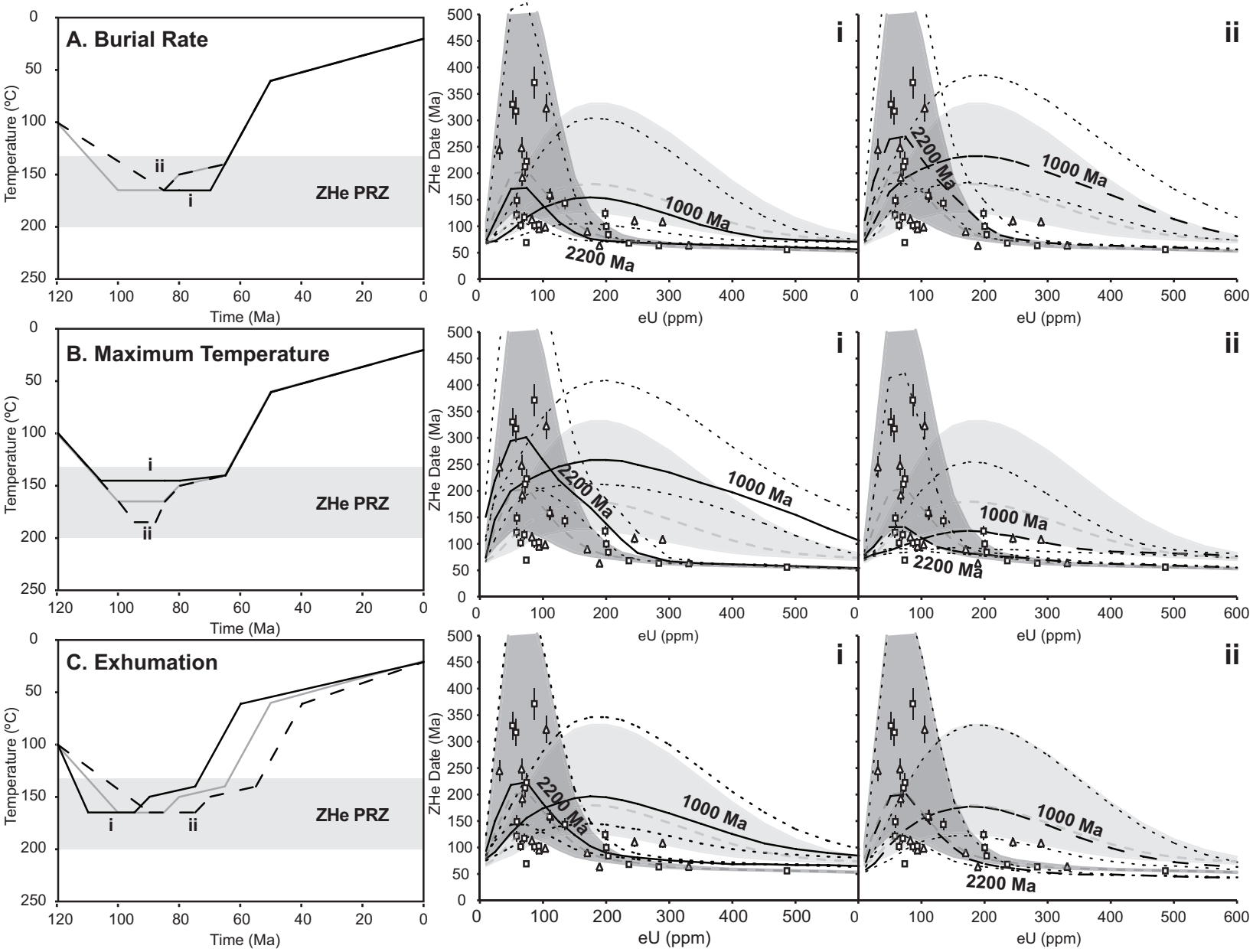
A. Burial Rate
B. Maximum Temperature
C. Exhumation
Temperature (ºC)
Time (Ma)
ZHe PRZ
i
ii
ZHe Date (Ma)
eU (ppm)
1000 Ma
2200 Ma

Fig. A17 (previous page). Time-temperature paths and corresponding date-eU plots showing the sensitivity of the forward model derived from "Group D" samples from Fig. 8d in the published paper to a varying thermal history. In A17a, b, and c, the solid gray t-T path is fixed and corresponds to the t-T history for Group D samples from Fig 8. The shaded envelopes in the date-eU plots display the inheritance curves derived from this t-T history at 2200 Ma (dark gray) and 1000 Ma (light gray) for 35-80 μm grain sizes (dashed gray curve = 50 μm date-eU trend). The dashed and solid black t-T curves (i, ii) exhibit the effect of changing A) burial rate, B) maximum burial temperatures (±20 °C), and C) the timing of exhumation (±10 Ma) on date-eU trends shown in Fig. 8d. To the right, the corresponding date-eU inheritance curves (1000 Ma, 2200 Ma) for a 50 μm grain size are shown in the solid black (i) and dashed black (ii) lines. Dotted black lines for each inheritance curve correspond to 35 and 80 μm grain size date-eU trends.

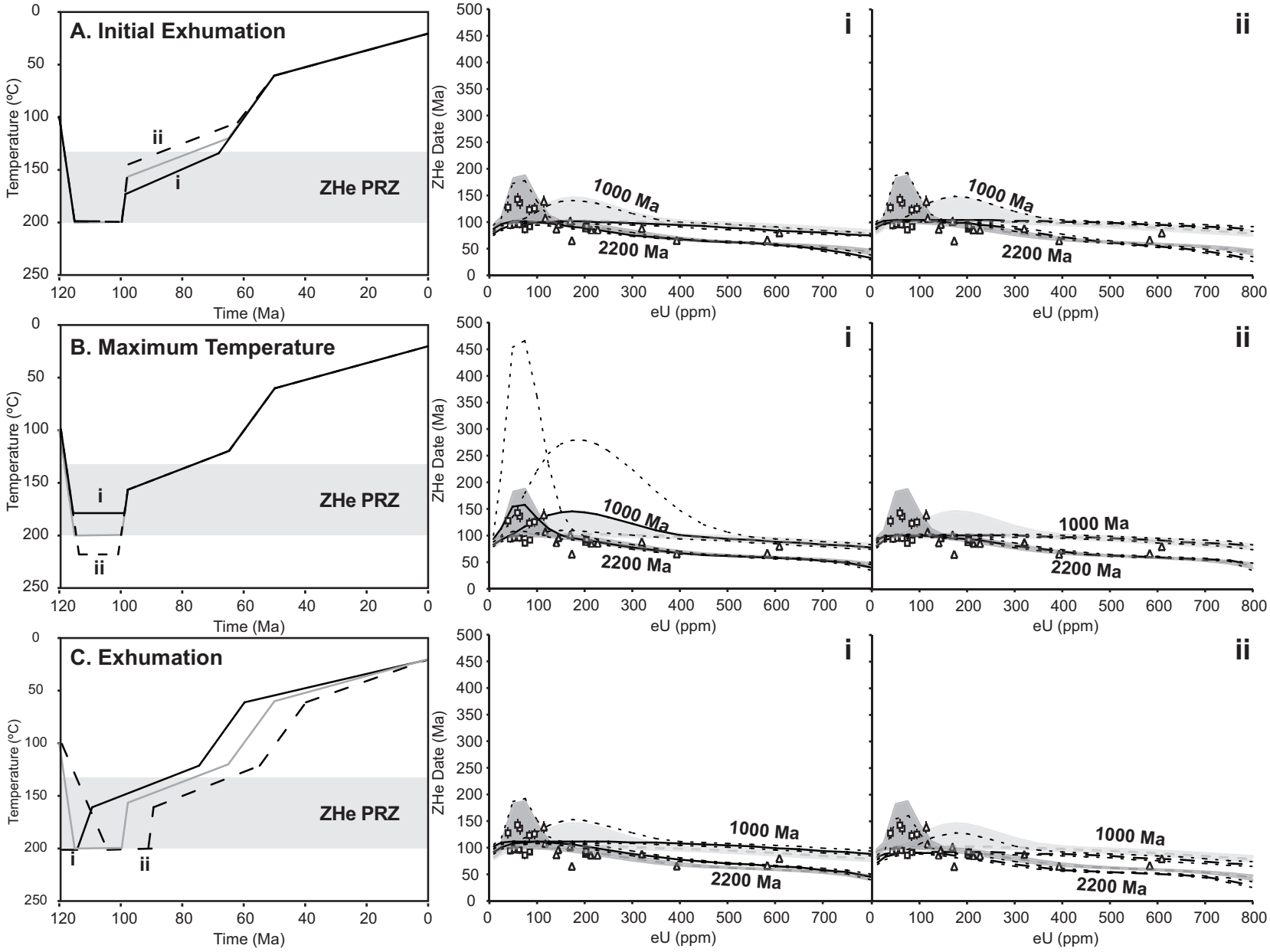
A. Initial Exhumation
B. Maximum Temperature
C. Exhumation
Temperature (ºC)
Time (Ma)
ZHe PRZ
i
ii
ZHe Date (Ma)
eU (ppm)
1000 Ma
2200 Ma

Fig. A18 (previous page). Time-temperature paths and corresponding date-eU plots showing the sensitivity of the forward model derived from "Group E" samples from Fig. 8e in the published paper to a varying thermal history. In A18a, b, and c, the solid gray t-T path is fixed and corresponds to the t-T history for Group E samples from Fig. 8. The shaded envelopes in the date-eU plots display the inheritance curves derived from this t-T history at 2200 Ma (dark gray) and 1000 Ma (light gray) for 35-80 μm grain sizes (dashed gray curve = 50 μm date-eU trend). The dashed and solid black t-T curves (i, ii) exhibit the effect of changing A) burial rate, B) maximum burial temperatures (±20 °C), and C) the timing of exhumation (±10 Ma) on date-eU trends shown in Fig. 8e. To the right, the corresponding date-eU inheritance curves (1000 Ma, 2200 Ma) for a 50 μm grain size are shown in the solid black (i) and dashed black (ii) lines. Dotted black lines for each inheritance curve correspond to 35 and 80 μm grain size date-eU trends.

CHAPTER 3

Application of multi-kinetic apatite fission track and (U-Th)/He thermochronology to source rock thermal history: A case study from the Mackenzie Plain, NWT, Canada

Jeremy Powell[1], David Schneider[1], Dale Issler[2]
1. Department of Earth & Environmental Sciences, University of Ottawa, Ottawa, Canada
2. Natural Resources Canada, Geological Survey of Canada, Calgary, Canada

In press, *Basin Research,* DOI: 10.1111/bre.12233

Abstract

Shale of the Upper Cretaceous Slater River Formation extends across the Mackenzie Plain of the Canadian Northwest Territories and has potential as a regional source rock due to the high organic content and presence of both oil- and gas-prone kerogen. An understanding of the thermal history experienced by the shale is required to predict any potential petroleum systems. Our study integrates multi-kinetic apatite fission track (AFT) and apatite (U-Th)/He (AHe) thermochronometers from a basal bentonite unit to understand the timing and magnitude of Late Cretaceous burial experienced by the Slater River Formation along the Imperial River. We use LA-ICP-MS and EPMA methods to assess the chemistry of apatite, and use these values to derive the AFT kinetic parameter r_{mr0}. Our AFT dates and track lengths, respectively, range from 201.5 ± 36.9 Ma to 47.1 ± 12.3 Ma, and 16.8 to 10.2 μm, and single crystal AHe dates are between 57.9 ± 3.5 and 42.0 ± 2.5 Ma with effective uranium concentrations from 17.3 ppm to 35.6 ppm. The fission track data show no relationship with the kinetic parameter D_{par} and fail the χ^2 test indicating that the data do not comprise a single statistically significant population. However, when plotted against their r_{mr0} value, the data are separated into two statistically significant kinetic populations with distinct track length distributions. Inverse thermal history modeling of both the multi-kinetic AFT and AHe datasets, reveal that the Slater River Formation reached maximum burial temperatures of ~65-90°C between the Turonian and Paleocene,

indicating that the source rock matured to the early stages of hydrocarbon generation, at best. Ultimately, our data highlight the importance of kinetic parameter choice for AFT and AHe thermochronology, as slight variations in apatite chemistry may have significant implications on fission track and radiation damage annealing in apatite with protracted thermal histories through the uppermost crust.

1. Introduction

Apatite fission track (AFT) and (U-Th)/He (AHe) thermochronology are popular techniques used to assess the low-temperature (<120°C) thermal history of geologic systems [*Ehlers and Farley*, 2003; *Donelick et al.*, 2005]. These methods are extremely useful in sedimentary basin analysis, as they are sensitive to temperatures that are conducive to oil and gas generation and can provide critical temporal constraints on these processes [*Armstrong*, 2005]. Technical advances for both techniques have highlighted the importance of apatite chemistry [*Carlson et al.*, 1999; *Barbarand et al.*, 2003a; *Ketcham et al.*, 2007; *Gautheron et al.*, 2013; *Djimbi et al.*, 2015] and radiation damage [*Shuster et al.*, 2006; *Flowers et al.*, 2009; *Gautheron et al.*, 2009] on the kinetics of thermally controlled fission track annealing and helium diffusion in apatite. The ability to isolate and interpret these variables in a dataset is crucial for accurate thermal history modeling, as they dramatically affect the temperatures to which the system is sensitive.

This paper discusses AFT and AHe data from a single bentonite horizon at the base of the Slater River Formation, a regional Cretaceous source rock (Fig. 1). These bentonite layers have previously been dated via U-Pb zircon geochronology at 97.6 ± 1.0 Ma (via ID-TIMS; Fallas et al. 2013; T. Hadlari pers. comm. 2016). We measure apatite chemistry using laser ablation inductively coupled plasma mass spectrometry (LA-ICP-MS) and electron probe microanalysis

(EPMA), using these data to generate the AFT kinetic parameter r_{mr0} [*Carlson et al.*, 1999; *Ketcham et al.*, 1999, 2007]. Even though apatite grains studied here were presumably derived from a single volcanic source, AFT dates do not form a single, statistically significant population. This provides the unique opportunity to test the rigour of various kinetic parameters (D_{par}, r_{mr0}) on a partially annealed AFT sample possessing slight variations in apatite chemistry. We compare results from both multi-kinetic AFT and combined AHe-AFT thermal history modeling to assess the plausible time-temperature history experienced by the Slater River Formation and the implications for hydrocarbon generation.

2. Geological Setting

2.1. Cretaceous stratigraphy of the Mackenzie Plain

Clastic foreland basin deposits blanket Northern Canada, forming in response to the Early Cretaceous to Paleocene propagation of the northern Canadian Cordillera [*Yorath and Cook*, 1981]. In the Mackenzie Plain and the adjacent Peel Plain (Fig. 1), Cretaceous to Paleocene strata are separated into two unconformity bound packages that detail subsidence and infill of a foreland basin in front of the emergent Mackenzie Mountains. The earliest Albian strata record an initial transgression related to Cretaceous sea level rise, and the subsequent infilling of accommodation space with a shallowing-upwards marine shale [*Thomson et al.*, 2011]. Regionally, an extensive unconformity related to Late Albian sea-level low stand separates Albian and Cenomanian stratigraphy [*Yorath and Cook*, 1981]. The Cenomanian Slater River Formation marks renewed subsidence in the basin, recording rapid fluctuations in sea level from marginal marine at the base to a shallowing-upwards offshore marine setting at the top of the section [*Thomson et al.*, 2011]. The Slater River Formation grades into sandstones of the Trevor

Formation in Peel Plain and the Little Bear Formation in the Mackenzie Plain [*Thomson et al.*, 2011]. In the southeastern Mackenzie Plain, strata of the East Fork and Summit Creek Formations document a Late Cretaceous to Paleocene transition from marine mudstones and sandstones to non-marine alluvial fan deposits [*Yorath and Cook*, 1981]. It is possible that similarly young strata were deposited in the study area and have since been eroded.

2.2. Source rock potential of the Slater River Formation

Several potential Cretaceous petroleum systems exist throughout the region due to the aerially extensive Cretaceous shale source rocks and clastic reservoir units (Hannigan et al., 2011). Rock-Eval pyrolysis data suggest that the shale of the Slater River Formation are a possible regional source rock, with total organic carbon (TOC) values as high as 9% across the Mackenzie Plain, and organic material that is both oil and gas-prone [*Feinstein et al.*, 1988; *Hannigan et al.*, 2011]. In the vicinity of our sample site (described below) the Slater River Formation has a TOC value of 3.4% [*Pyle and Gal*, 2014].

Limited knowledge on thermal maturity and burial history of the Slater River Formation leaves a major uncertainty for any Cretaceous petroleum system. The maximum regional burial depths and temperatures of the Slater River Formation are relatively unconstrained due to an unknown amount of eroded Cretaceous to Paleocene sediment and a laterally variable geothermal gradient [*Feinstein et al.*, 1996]. Although organic thermal maturity parameters such as percent vitrinite reflectance (%Ro) and Tmax values from Rock-Eval pyrolysis, exhibit little variation for Cretaceous strata across the region [*Feinstein et al.*, 1991], these data are difficult to interpret due to significant recycling of organic material from the underlying Paleozoic section [*Issler et al.*, 2005]. Additionally, the high sulphur content of the organic material in the Slater River Formation, and the corresponding low activation energy required to generate

hydrocarbons, may suppress Tmax values for the unit [*Issler et al.*, 2005]. Consequently, the Tmax value reported for our sampling site (413°C; Pyle and Gal 2014) may not be indicative of the true thermal maturity of the unit.

Oil and gas showings in several wells across the Mackenzie Plain were likely sourced from shales of the Slater River Formation [*Feinstein et al.*, 1988; *Hannigan et al.*, 2011], indicating that Cretaceous to Paleocene burial has at the very least locally generated hydrocarbons from the unit. Clearly, more work is required to understand the burial and thermal history of Slater River Formation across the region.

3. Methods and Results

3.1. Apatite geochemistry

We employ both LA-ICP-MS and EPMA methods to collect geochemistry for all 84 apatite grains analyzed for fission track analysis. Information on analytical methods, and results of the elemental analyses from LA-ICP-MS and EPMA approaches are available in the Appendix to this Chapter. Apatite chemistry in atoms per formula unit (apfu) was calculated following the stoichiometric relationships of Ketcham (2015) using weight% oxide values measured from LA-ICP-MS (Na, Mg, Mn, Fe, S) and EPMA (Ca, P, Cl, F).

Apatite rare earth elements (REE) were measured via LA-ICP-MS and exhibit consistent patterns (Fig. 2) amongst all analyzed grains, showing a depletion of heavy relative to light REE. We note a pronounced negative Eu anomaly with an average Eu/Eu* value of 0.40. These values are typical of felsic sources and are controlled by crystallization of feldspar in the melt [*Belousova et al.*, 2002]. Due to the consistent REE pattern among all grains, we are confident that our AFT data are not contaminated with sedimentary detrital apatite from the Slater River

Formation. Compositionally, Fe, Mn, Mg, S, and Na are present in trace amounts in our sample suite.

Whereas LA-ICP-MS is particularly apt at measuring trace elements in apatite [*Morton and Yaxley*, 2007; *Chew et al.*, 2016], the method has difficulty measuring Cl concentrations and an inability to measure F due the high first-ionization potential of halogens [*Tran et al.*, 2001; *Chew et al.*, 2014]. Determining Cl and F concentrations through EPMA is not without complications either, as measurements are sensitive to the orientation of the beam relative to the crystallographic c-axis, beam intensity and beam spot size [*Stock et al.*, 2015]. The Cl content is fairly low amongst the apatite in this dataset, with an average value of 0.11 apfu. Comparatively, the larger F (1.23 apfu) and OH (0.66 apfu) components place apatite from the bentonite on the F-OH apatite spectrum [*Ketcham*, 2015].

3.2. Apatite fission track thermochronology

Fission tracks are damage zones in the apatite crystal lattice that form due to spontaneous fission of ^{238}U [*Donelick et al.*, 2005]. Following fission track formation the apatite crystal lattice may undergo thermal annealing at elevated temperature, resulting in the progressive shortening of fission tracks and a decrease in overall fission track density [*Green*, 1988]. Factors such as crystallographic orientation (Donelick et al., 1999; Ketcham, 2005a) and chemical composition [*Carlson et al.*, 1999; *Ketcham et al.*, 1999, 2007; *Barbarand et al.*, 2003a] are also known to control fission track length and density. In particular, compositional variations between F, Cl and OH content have been shown to dramatically affect the annealing behaviour of fission tracks, with fluorapatite being the least resistant to thermal annealing [*Green et al.*, 1986; *Carlson et al.*, 1999; *Barbarand et al.*, 2003a]. Through the combination of apatite fission track dates, track length distributions and annealing kinetics, apatite fission track thermochronology can be used to

model the thermal history of rocks through a temperature window corresponding to ~50-150°C [*Armstrong*, 2005; *Donelick et al.*, 2005].

Several correlations have been drawn between measurable apatite-specific parameters and fission track annealing kinetics. Among the most commonly used kinetic parameters are D_{par} and Cl content [*Burtner et al.*, 1994; *Donelick et al.*, 2005].The kinetic parameter D_{par} measures the mean maximum diameter of the fission track etch pit as a proxy for fission track annealing kinetics [*Burtner et al.*, 1994]. Resistance to thermal annealing and D_{par} are positively correlated, with near-end-member fluorapatite ($D_{par} \leq 1.75$ μm) annealing at lower temperatures than higher D_{par} apatite grains [*Donelick et al.*, 2005]. Likewise, Cl content also exhibits a positive correlation with an apatite grain's resistance to thermal annealing [*Green et al.*, 1986]. However, neither D_{par} nor Cl content perfectly explain all observed annealing behaviour of apatite, as apatite grains with D_{par} values >1.75 μm are not always more resistant to annealing than lower D_{par} grains, and measurements of Cl may not capture the influence of other compositional components, such as high concentrations of Fe, Mn, OH and REE [*Carlson et al.*, 1999].

The kinetic parameter r_{mr0}, which characterizes the annealing behaviour of any apatite relative to the most-resistant apatite in an experimental dataset spanning multiple apatite compositions, is an alternative to defining annealing kinetics by D_{par} or Cl content [*Ketcham et al.*, 1999]. Since r_{mr0} can describe the relative differences between annealing rates of apatite phases with well-characterized chemistries and kinetic parameters, it is possible to derive a multi-kinetic model that relates the chemistry and kinetic parameters of any analyzed apatite grain to predicted annealing kinetics [*Carlson et al.*, 1999; *Ketcham et al.*, 2007]. Values for r_{mr0} can be derived from D_{par} measurements or Cl content, or can be calculated using a multiple composition equation that marries grain-specific chemistry with annealing kinetics. Multi-

compositional calculations used to calculate r_{mr0} include Equation 6 of *Carlson et al.* [1999], derived from a single annealing dataset, or Equation 11 of *Ketcham et al*. [2007], which combines annealing experiment data from two laboratories:

$$(6)\ r_{mr0} = [0.027 + 0.431|Cl - 1| + 0.107|OH - 1| - 1.01Mn - 2.67Fe - 0.144others]^{0.25}$$

$$(11)\ r_{mr0} = [-0.0495 - 0.0348F + 0.3528|Cl - 1| + 0.0701|OH - 1| - 0.8592Mn - 1.2252Fe - 0.1721others]^{0.1433}$$

In the equations, all compositional variables are in apfu, and "*others*" represents the sum of all other cation substituents. Smaller values of r_{mr0} correspond to increasing resistance to fission track annealing, whereas larger values represent apatite grains that are susceptible to thermal annealing at lower temperatures. Noticeable differences between the two models include the relative influence of OH and Mn on calculated r_{mr0}, which are de-emphasized in the *Ketcham et al*. [2007] equation.

Our fission track dates were calculated using the LA-ICP-MS method [*Hasebe et al.*, 2004; *Donelick et al.*, 2005; *Chew and Donelick*, 2012]. Following chemical etching, samples underwent ^{252}Cf irradiation to aid in fission track length measurement. We report 38 fission track dates and 195 fission track lengths (Fig. 3; Appendix Table A1, A2). Fission track ages range from 201.5 ± 36.9 Ma to 47.1 ± 12.3 Ma and lengths span 16.8 µm to 10.2 µm. We calculate r_{mr0} following the relationship of *Ketcham et al*. [2007] so as not to over-estimate retentive annealing kinetics in our F-OH apatite. For comparison, r_{mr0} values calculated after *Carlson et al*. [1999] are available in the Appendix (Table A3).

When plotted against D_{par} (Fig. 3a) or Cl content (Appendix Fig. A1), there is no

discernable relationship between fission track date or length and kinetic parameter. For fission track date grains, D_{par} varies from 1.8 μm to 2.6 μm, and the single population has a pooled age of 94.4 ± 3.4 Ma but fails the χ^2 test (Q: 0); thus the age is not representative of a single, statistically significant population [*Green*, 1981]. Likewise, D_{par} values for fission track lengths range from 1.9 μm to 2.8 μm and the mean track length is 14.0 ± 1.3 μm. Comparatively, when fission track date and length are plotted against r_{mr0} (Fig. 3b) a relationship becomes apparent between two kinetic populations: one retentive population with lower r_{mr0} values (<0.73), long track lengths and AFT dates older than the 97.6 Ma age of the bentonite [*Fallas et al.*, 2013], and a second population with higher r_{mr0} values (>0.73), younger dates and shorter track lengths. These kinetic populations both pass the χ^2 test and have pooled ages and mean track lengths of 154.3 ± 10.2 Ma and 14.6 ± 1.3 μm (kinetic population #1; Q: 90.2%), and 89.0 ± 3.7 Ma and 13.9 ± 1.3 μm (kinetic population #2; Q: 27.2%), respectively. We include a sensitivity test in the Appendix to this Chapter (Fig. A2) that illustrates how χ^2 test statistics, pooled ages and mean track length change dependent on the r_{mr0} value of the kinetic boundary. We also note the presence of three precise AFT dates with ages much younger than the balance of the dataset and r_{mr0} values that overlap the other two kinetic populations. We incorporate these three grains into a poorly defined third population (kinetic population #3; 53.5 ± 6.5 Ma).

Although we place the kinetic boundary at 0.73 r_{mr0}, we note that some compositional overlap exists among the age-grains. Some overlap between populations is expected, especially near the boundary between kinetic populations, due to the accuracy to which r_{mr0} values can be calculated from single point analyses and the application of r_{mr0} annealing models to natural apatite. Examples in our dataset include three fission track dates that are older than the age of the bentonite, but have r_{mr0} values >0.73 and four younger dates that are potential outliers (high Cl,

OH, or Fe). We ignore the calculated r_{mr0} values for these dates and incorporate them with similar age grains when calculating pooled ages and χ^2 statistics for each kinetic population (Fig. 3). We note that, excluding the young, high precision AFT dates of population #3, kinetic populations #1 and #2 can still pass the χ^2 test even with the observed compositional overlap between grains (Appendix Fig. A2). Although the pooled age of AFT kinetic population #1 is troubling as it is older than the bentonite age, we submit that these data are meaningful as they correspond with more retentive kinetics and longer track lengths. Plausible explanations as to the source of these dates are discussed later in the paper. Pooled ages for all three populations (Fig. 3b) are within error of the three populations (Fig. 4; 140 ± 10 Ma, 89 ± 10 Ma, 66 ± 11 Ma) identified from binomial peak fitting using the software RadialPlotter [*Vermeesch*, 2009].

3.3. Apatite (U-Th)/He thermochronology

In the apatite (U-Th)/He system, ^{4}He is produced via radioactive decay of ^{238}U, ^{235}U, ^{232}Th and ^{147}Sm, undergoing thermal diffusion at high temperatures and retained within the crystal structure at temperatures that are common in the uppermost crust [*Ehlers and Farley*, 2003]. Helium diffusion in apatite with protracted thermal histories is sensitive to the effects of cooling rate, grain size, radiation damage and grain chemistry [*Stockli et al.*, 2002; *Flowers et al.*, 2009; *Gautheron et al.*, 2013]. In particular, the amount of radiation damage, as assessed through the proxy "effective uranium concentration" (eU = [U] + 0.235 • [Th]), is positively correlated with increasingly retentive AHe systems [*Shuster et al.*, 2006; *Flowers et al.*, 2009; *Gautheron et al.*, 2009]. In effect, the AHe system may be sensitive to temperatures between 30-120°C depending on the amount of radiation damage to the crystal lattice [*Flowers et al.*, 2009; *Djimbi et al.*, 2015]. Recently, *Gautheron et al.* [2013] used the r_{mr0} parameter [*Carlson et al.*, 1999; *Ketcham et al.*, 1999] to investigate the connection between grain chemistry and radiation

damage annealing in the AHe system. Their results suggest that grain chemistry, and its effects on the annealing of radiation damage, may influence helium diffusion in apatite and the temperatures to which the system is sensitive [*Gautheron et al.*, 2013]. In addition to affecting the kinetics of radiation damage, multi-scale theoretical diffusion studies have shown that increasing Cl content in apatite results in increasing helium retentivity [*Djimbi et al.*, 2015].

Four inclusion free apatite grains were handpicked under a binocular microscope and analysed for (U-Th)/He dating and are reported with a 6% (2σ) analytical uncertainty (Appendix Table A4). More detailed information on (U-Th)/He methodology is available in the Appendix to this Chapter. To understand the factors controlling AHe date dispersion we plot AHe date as a function of eU concentration (Fig. 5a), and equivalent spherical radius (ESR), which is a proxy for grain volume (Fig. 5b). AHe dates range from 57.9 ± 3.5 Ma to 42.0 ± 2.5 Ma, with a mean AHe date of 48.4 ± 7.2 Ma. Although eU values vary from 17.3 ppm to 35.6 ppm, there is no obvious relationship between eU and AHe date (Fig. 5a). There is however a correlation between grain size (ESR) and AHe date, with progressively older AHe dates as ESR increases from 39.6 μm to 52.2 μm (Fig. 5b).

4. Thermal History Modeling

4.1. AFT inverse thermal history modeling

We performed inverse thermal history modeling to understand the time-temperature implications of our observed relationships between fission track date, track length and kinetic parameter r_{mr0} (Fig. 6). The model was calculated using an updated version of the software AFTINV [*Issler*, 1996], using a non-directed Monte Carlo method to search parameter space for 300 unique thermal histories that 1) provide a statistical fit at the 0.05 significance level between

modeled and observed track length distribution using the Kolmogorov-Smirnov (KS) statistic, and 2) have calculated AFT dates within two standard deviations of the measured data. Additionally, AFTINV incorporates multi-kinetic annealing equations [*Ketcham et al.*, 1999, 2007] allowing for concurrent modeling of up to four kinetic populations defined by either Cl content, D_{par}, or r_{mr0}.

We selected an r_{mr0} value of 0.65 to represent the average value for the spectrum of calculated r_{mr0} from the eight fission track dates and 24 lengths that comprise kinetic population #1. An average r_{mr0} value of 0.78 was calculated from the 27 fission track dates and 186 lengths of kinetic population #2 and used to characterize the population for inverse modeling. An initial track length was calculated for each population using the average D_{par} of the corresponding apatite (R. Donelick pers. comm. 2010). Although the pooled age of kinetic population #1 (154.3 ± 10.2 Ma) is older than the age of the bentonite, we choose to incorporate these data into the model as their resistance to thermal annealing and long track lengths provide important kinetic constraints for the kinetic population #2. To allow for fission track dates that are older than the volcanic depositional age, we model kinetic population #1 as an inherited population that experiences a random cooling history from 200°C at 250 Ma until deposition at 97.6 Ma. Kinetic population #2 is modeled as volcanic apatite, and as such experiences no thermal history prior to 97.6 Ma, but the same post-depositional thermal history as kinetic population #1. Our model randomizes heating and cooling rates over 2.5 m.y intervals and searches for a single heating and cooling event between 97.6 Ma and the present. We limit heating and cooling rates to 10°C/m.y. and 15°C/m.y., respectively, to rule out geologically implausible thermal histories, and account for plausible burial and exhumation rates of the foreland basin prior to and during the Cordilleran

orogeny. Models were run in conventional track length mode using the annealing kinetics of *Ketcham et al.* [2007].

Although the poorly defined kinetic population #3 has fission track dates that are similar to the proposed cooling history of the adjacent Mackenzie Mountains deformation front [*Powell et al.*, 2016] and may detail the lower temperature history of the sample, we elect to not incorporate these data due to the absence of any identifying trends in kinetic parameter or associated track lengths. Additionally, the younger dates (53.5 ± 6.5 Ma) are similar to the AHe data in this study (Fig. 5), and discussed in the following section.

Our AFT modeled time-temperature histories (Fig. 6a) indicate that maximum temperatures of the Slater River Formation never exceeded 96°C. Modeled %Ro values range from 0.37 to 0.54, with an average of 0.42 %Ro. The model results indicate that the only thermal histories where the Slater River Formation reached temperatures in excess of 80°C are scenarios in which maximum burial temperatures occur prior to c. 75 Ma. These scenarios are uncommon, as the maximum burial temperatures are mostly between 50 and 80°C (Fig. 6b). As suggested by the low r_{mr0} values, kinetic population #1 is very resistant to thermal annealing, and has had limited shortening of track lengths with the majority of tracks measuring between 14-16 μm (Fig. 6c). In comparison, the higher r_{mr0} value for kinetic population #2 makes this system more susceptible to thermal annealing at lower temperatures, resulting in the reduction of the modeled AFT date from 97.6 Ma (deposition) to 91.4 Ma (modeled from exponential mean temperature time path of all 300 solutions) and the shortening of observed track lengths.

4.2. AHe and AFT inverse thermal history modeling

Whereas the multi-kinetic fission track modeling provided strong control on the maximum burial temperature of the Slater River Formation, the model results reveal little on the

timing of when the strata reached those temperatures and when they cooled to the surface due to the low degree of post-depositional AFT annealing. To better elucidate the full thermal history, we integrate AFT dates and track lengths from kinetic population #2 with our AHe dataset and perform inverse thermal history modeling (Fig. 7) using HeFTy (Ketcham 2005b; version 1.9.1). Similar to AFTINV, HeFTy uses a Monte Carlo approach to generate time-temperature paths, and assess the agreement between model and empirical AHe and AFT data. Users select independent geological time-temperature constraints through which the generated candidate paths must be satisfied, and can specify the maximum heating and cooling rates between these constraints. HeFTy uses a combined merit function to evaluate how the model results compare with observed data, deeming paths as "acceptable" or "good" should they meet certain statistical precision limits.

Our modeling incorporates AFT kinetic population #2 discussed in the previous section with two AHe dates that span the range of eU concentrations observed in the dataset (Fig. 7). For each AHe grain we apply the apatite radiation damage accumulation and annealing model (RDAAM; Flowers et al., 2009) and select an r_{mr0} value of 0.75, reflective of the majority of the apatite analyzed in this study (Fig. 3b), to describe the damage annealing kinetics of the modeled apatite. Although we report our AHe data with a 6% error (Fig. 5) we note that this is likely an underestimation, and that high precision dates introduce significant challenges for inverse modeling of multiple apatite grains. In Fig. 7 we introduce modified AHe dates and errors for each apatite. These are based on variations in alpha ejection correction methods [*Farley et al.*, 1996; *Ketcham et al.*, 2011], broken grains and variable grain geometries [*Beucher et al.*, 2013; *Brown et al.*, 2013]. These modified ages were calculated using an alpha-ejection software

[*Gautheron et al.*, 2012] and factor in the effects of grain geometries (e.g., apatite with unequal widths and unique crystal habits) that were not accounted for during initial measurement.

Cretaceous to Paleocene time-temperature constraints for this study (Fig. 7) were selected based on the thickness of strata preserved locally and elsewhere in the Mackenzie Plain and Peel Plain (Fig. 1) and for a range of present day and paleo-geothermal gradients [*Feinstein et al.*, 1991, 1996; *Majorowicz and Morrow*, 1998]. These include: 1) a depositional constraint between 0 – 20 °C at c. 97.6 Ma; 2) two constraints between the Cenomanian and Turonian to account for deposition of the Slater River and Trevor/Little Bear Formations; 3) a broad constraint that allows for burial of Cretaceous to Paleocene strata that are not preserved locally but are present elsewhere in the basin [*Yorath and Cook*, 1981]; and 4) a constraint between 60 - 45 Ma that allows for the Cordilleran cooling history documented in the adjacent Mackenzie Mountains [*Powell et al.*, 2016]. Heating and cooling rates between constraint boxes were limited to < 10 °C/Ma. We present our model results in Fig. 7 as a combination of the path envelopes (for "good" and "acceptable" paths) and constraint points (inflection point of model time-temperature path in each constraint box) that encompass all successful thermal histories.

The maximum burial temperatures of 65 – 90°C, and high proportion of thermal histories with maximum temperatures between 65°C and 80°C, suggested by the good paths in Fig. 7 are in accord with the temperatures indicated through fission track modeling (Fig. 6). The inverse model suggests a protracted thermal history from the Cretaceous to present, indicating that Cordilleran unroofing of the adjacent Mackenzie Mountains had limited effect on cooling and unroofing of the basinal Cretaceous strata. Because our AHe inverse thermal history model results are only based on two apatite grains and assume a fixed composition of 0.75 r_{mr0}, we use forward modeling of three candidate time-temperature histories to illustrate how radiation

damage, grain size and compositional variance may be manifested in our AHe data (Fig. 8). These forward models indicate that thermal histories where the Slater River Formation undergoes initially rapid burial and prolonged residence at temperatures between 65 – 85°C throughout the Late Cretaceous (Fig. 8b, c) better explain the majority of the observed AHe date-eU data than a thermal history where strata undergoes slower burial to 65°C (Fig. 8a). Additionally these models illustrate that the older AHe date that does not fall within predicted date-eU trends can be explained if the apatite experiences a similar pre-depositional history as invoked for AFT kinetic population #1 (Fig. 6a).

5. Discussion

5.1. Multiple kinetic populations as indicated by r_{mr0}

Our AFT data would have limited interpretation capacity if only assessed on the basis of D_{par} or Cl content alone (Fig. 3a; Appendix Fig. A1) as the data fail the χ^2 test, indicating that they are not representative of a single population, but do not exhibit any relationships with these kinetic parameters that indicate multiple kinetic populations. However, multiple kinetic populations are revealed when apatite-specific chemistry is converted into the kinetic parameter r_{mr0} [*Carlson et al.*, 1999; *Ketcham et al.*, 2007]. We acknowledge that the AFT date for kinetic population #1 (154.3 ± 10.2) is older than bentonite deposition, and REE geochemistry does not indicate any detrital contamination. One possible explanation for the older AFT dates is that kinetic population #1 is xenocrystic and reflects earlier magmatic processes or bedrock material that was entrained in the eruption and re-deposited with the ash fall [e.g. *Eldrett et al.*, 2015]. This hypothesis is consistent with the abundant Late Triassic to Early Jurassic volcanic rocks of the adjacent Yukon Territory and their Jurassic cooling history [e.g. Knight et al., 2013].

Additionally, kinetic population #1 may be comprised of zoned crystals compared to the other apatite in the suite. Chemical zoning is common in apatite [*Ault and Flowers*, 2012] and may result in LA-ICP-MS uranium measurements that are not reflective of the true uranium concentration that contributes to measured fission tracks and the calculated AFT date [*Hasebe et al.*, 2004; *Donelick et al.*, 2005]. For example, in this study AFT dates corresponding to kinetic population #1 can be generated if the LA-ICP-MS spot is placed in a zone with ~50% lower uranium concentration than the region from which tracks are counted. This difference can be as small as ~1 ppm in low uranium apatite with few spontaneous tracks (Ns), or as large as ~7 ppm in grains with higher uranium content and Ns (Appendix Fig. A3; Table A5). However, it is standard operating procedure to place the LA-ICP-MS spot in the centre of the area from which Ns were measured, and not to date apatite with track density heterogeneities indicative of uranium zoning. Likewise, there is no visual indication as to whether the older AFT dates are xenocrystic or a function parent zoning, as the apatite in kinetic population # 1 are not morphologically different than apatite with younger AFT dates and do not exhibit heterogeneity in Ns density (Appendix Fig. A4). Regardless as to the source of these dates, the observation that they correspond to lower r_{mr0} values and longer track lengths is meaningful and provides important kinetic constraints for AFT population #2.

5.2. Comparison of kinetic parameters D_{par} and r_{mr0}

The discrepancy between the D_{par}-AFT and r_{mr0}-AFT relationships observed in this study is an important reminder that while D_{par} may provide an estimate of relative resistance to annealing, the etch pit dimension is a measurement of apatite solubility and is not a direct proxy for apatite chemistry (Donelick et al., 2005). Whereas low D_{par} grains anneal similarly to end-member fluorapatite, larger D_{par} values exhibit all manner of annealing behaviours [*Carlson et*

al., 1999]. As an example, D_{par}-AFT relationships in apatite with large OH components are spurious due to the differing effects of the OH component on apatite solubility and annealing resistance [*Ketcham et al.*, 1999].

We note that the D_{par} values for our AFT lengths are generally larger than our AFT date data (Fig. 3a). Although this could be a sampling issue, we believe that this observation is a systematic relationship in our dataset. A benefit of the LA-ICP-MS AFT method is that track lengths and AFT dates are measured on the same mount, providing the occasional replicate analysis for D_{par}. The discrepancy between D_{par} measurements is apparent when values measured during the age calculation are plotted against those for the same grain following ^{252}Cf irradiation and track length measurement (Fig. 9a). Whereas three of the duplicate measurements are near identical, the remainder of the analyses show that the D_{par} measurements from the corresponding length-grain are substantially larger than the original measurement. It is possible that this discrepancy is related to the error expected when measuring the extremely small etch pit diameters. Studies assessing inter-laboratory reproducibility of AFT data have shown that large variations between D_{par} measurements are common for the same sample [*Ketcham et al.*, 2009, 2015]. However, the same very experienced analyst performed the measurements in our study. We suspect that the change in measured D_{par} is related to the technique used to increase the amount of measurable fission tracks. In the LA-ICP-MS AFT method ^{252}Cf irradiation is commonly performed following the counting of spontaneous tracks used to calculate the AFT date and prior to track length measurement. The irradiation creates conduits that improve the penetration of the chemical etchant and greatly increase the amount of measurable tracks. However, discrepancies in the mean D_{par} values measured from spontaneous and ^{252}Cf tracks in the Fulford apatite [*Barbarand et al.*, 2003b] indicate that ^{252}Cf-irradiated fission tracks may be

slightly larger than partially-annealed and polished spontaneous fission tracks. Additionally, since the fission track mount is re-etched following ^{252}Cf irradiations, larger etch pits are expected if measurements were taken on doubly etched spontaneous tracks instead of fresh ^{252}Cf tracks.

To understand the implications of discrepancies in D_{par} on fission track annealing kinetics, we convert the measured D_{par} values to a calculated r_{mr0} (Fig. 9b) using both the relationships of *Ketcham et al.* [1999] and *Ketcham et al*. [2007]. Dependent on the conversion, the kinetic difference in measured D_{par} values for the same grain is relative to a difference as great as 0.04 – 0.07 r_{mr0}. Though this difference may seem small, it has dramatic effects on the overall annealing behaviour of the apatite, corresponding to a 6 – 18 °C difference in closure temperature (Appendix Table A6). This realization is especially troubling for multi-kinetic AFT samples, as track lengths that should belong to one kinetic population may be included in another if D_{par} is used as the kinetic parameter. Such an error in track length distributions may produce very different thermal history models and yield erroneous geological interpretations. Calculating an r_{mr0} value from apatite-specific chemistry [*Carlson et al.*, 1999; *Ketcham et al.*, 2007] is one potential solution to this problem, and may aid in the identification of statistically significant kinetic populations with meaningful track length distributions in multi-kinetic samples.

5.3. Implications of kinetic parameter r_{mr0} for the AHe system

Although not often discussed in the literature, apatite chemistry is an important consideration for the (U-Th)/He system [*Gautheron et al.*, 2013]. The RDAAM model used in our study stipulates that the radiation damage that interferes with helium diffusion in apatite anneals following the same kinetics as fission track annealing [*Flowers et al.*, 2009]. Depending on the thermal history of a sample, helium diffusion in damaged apatite with retentive AFT

annealing kinetics may behave very differently than helium diffusion from equivalently damaged end-member fluorapatite (Fig. 8). These effects will be compounded in apatite that have accumulated radiation damage over long timescales and have protracted heating and cooling histories. Although we see limited effects of this phenomenon in our own dataset, these relationships will be pronounced in detrital samples with widely variable grain chemistries and pre-depositional histories [*Gautheron et al.*, 2013]. A basic understanding of the range of apatite annealing kinetics within a sample is recommended prior to thermal history modeling, as the default r_{mr0} value in HeFTy when using the RDAAM model is 0.83, which corresponds to the annealing kinetics of fluorapatite. Although fluorapatite minerals are very common in most geologic systems [*Piccoli and Candela*, 2002], the default value will produce potentially meaningless thermal histories if used when modeling more retentive AHe systems, or if AHe data are modeled alongside a retentive AFT population.

5.4. Elemental measurements for r_{mr0}

Our dataset demonstrates how accurate measurements of halogen content are important for AFT thermochronology. Since we collected chemistry from both LA-ICP-MS and EPMA techniques, we are able to evaluate how r_{mr0} values calculated using F, Cl, P, and Ca chemistry from EPMA compare with values derived using LA-ICP-MS (Fig. 10a). The r_{mr0} values calculated using only the LA-ICP-MS chemistry range from 0.79 to 0.81. Comparatively, r_{mr0} values calculated using chemistry from both LA-ICP-MS and EPMA methods have a much larger variance, with values between 0.58 and 0.81 r_{mr0}.

Although Cl content has a strong control on annealing characteristics of apatite and the calculated r_{mr0}, the discrepancies between r_{mr0} measurements in our dataset are not a function of variable Cl measurements between the two techniques. In fact, the Cl content from LA-ICP-MS

and EPMA methods are within the same narrow range of 0.08-0.13 apfu (Fig. 10b). However, F content is considerably different between the two techniques, yielding 1.1-1.4 apfu from EPMA and 1.7-1.9 apfu from LA-ICP-MS (Fig. 10c). This dissimilarity calls attention to the most significant difference between r_{mr0} values derived from only LA-ICP-MS elemental analyses and those that factor in EPMA data. EPMA is able to directly measure both Cl and F weight% in apatite, whereas LA-ICP-MS can determine Cl weight% [*Chew et al.*, 2014], but F content (apfu) must be calculated using stoichiometric difference between the measured Cl content (apfu) and the unoccupied space in the halogen site. Such a method assumes that the apatite is anhydrous, with no substitution of OH ions [*Ketcham*, 2015]. This is a problematic assumption, as apatite with OH ions substituting into the halogen site will be more resistant to annealing than if the equivalent space was occupied by only F [*Carlson et al.*, 1999; *Barbarand et al.*, 2003a]. When both F and Cl are measured through EPMA, it is possible to calculate the OH content through stoichiometric difference [*Ketcham*, 2015]. Indeed, our apatite has a significant OH component (~0.66 apfu).

These observations again raise the question on the explanatory power of AFT kinetic parameters compared to the practicality of their measurement. Although r_{mr0} may explain the AFT-date dispersion in our F-OH apatite, an EPMA approach was required to discern the F content. For our dataset, an r_{mr0} value calculated using only LA-ICP-MS data has as limited utility as D_{par} or Cl content for discerning kinetic populations and modeling thermal history. Both D_{par} and LA-ICP-MS-derived r_{mr0} values are likely adequate to describe the annealing kinetics of F-Cl apatite for a wide range of thermal histories. However, EPMA methods are advisable for samples with protracted thermal histories that fail the χ^2 test or exhibit significant overlap in kinetic populations when AFT ages are plotted with respect to conventional kinetic parameters.

5.5. Slater River Formation burial history and petroleum potential

Millimetre- to centimetre-thick bentonite beds are common in both the Albian Arctic Red Formation [*Thomson et al.*, 2011] and Cenomanian Slater River Formation [*Yorath and Cook*, 1981; *Hannigan et al.*, 2011] across the Mackenzie and Peel Plains. The 97.6 Ma age of the Slater River Formation bentonite at the Imperial River section [*Fallas et al.*, 2013], and the negative Eu anomaly (Eu/Eu*: 0.4) measured from our mineral geochemistry are compatible with the c. 110-90 Ma magmatism abundant throughout the northern Canadian Cordillera [*Morris and Creaser*, 2008], linking the timing of subsidence in the foreland basin to orogenic development in the hinterland [*Hadlari et al.*, 2014].

When combined, our multi-kinetic AFT and integrative AFT-AHe inverse thermal history modeling suggest that the bentonite at the base of the Slater River Formation reached maximum burial temperatures of ~65-90 °C. Given that present day geothermal gradients for the Mackenzie Plain range from 30-40°C/km [*Majorowicz and Morrow*, 1998] and are similar to the speculated paleogeothermal gradients for the Cretaceous to Paleocene [*Feinstein et al.*, 1991, 1996], the modeled temperatures correspond to a maximum burial depth of ~1.6-3.0 km for the Slater River Formation along the Imperial River section. Moreover, our AHe models allow for burial to continue from the Turonian to the Paleocene. Equivalent age strata (East Fork and Summit Creek formations; Fig. 1) are only present in the southeast Mackenzie Plain [*Yorath and Cook*, 1981], suggesting that the Late Cretaceous proximal foreland basin deposits may have extended across the region during fold-thrust belt development [*Powell et al.*, 2016].

Issler et al. [2005] noted that in the nearby Brackett basin, Rock-Eval Tmax values are suppressed in the Slater River Formation due to low activation energy required to generate

hydrocarbons from the sulphur-rich shale [*Earnshaw and Grant*, 1992]. Similar suppression in Tmax values is observed in some Slater River Formation samples from the Peel Plain directly west of our study area [*Thomson et al.*, 2011]. For that reason, we believe that the Tmax of 413°C (%Ro_{equiv}: 0.27) measured at the Imperial River section [*Pyle and Gal*, 2014] is a poor indication of the thermal maturity of our sample. Instead, the range of %Ro (0.37-0.54; Fig. 6a) calculated through multi-kinetic AFT modeling is a more likely representation of the true maturity of the shale. These values are in accord with vitrinite reflectance measurements from Late Cretaceous samples elsewhere in the basin [*Feinstein et al.*, 1991]. Whereas these values are still lower than the 0.55-0.8 %Ro range commonly associated with oil and gas generation [*Nielsen et al.*, 2015], it is possible that our proposed temperature regime was sufficient to generate oil from the high sulphur kerogen in the shale. Such a phenomenon has been detailed for the Slater River Formation in the southeastern Mackenzie Plain where Tmax values are only between 418-425°C (%Ro_{equiv}: 0.36-0.49; Earnshaw and Grant, 1992). Since the Slater River Formation along the Imperial River is, at best, marginally mature with regard to hydrocarbon generation, we suspect that any petroleum system would behave similar to those described in the southeastern Mackenzie Plain, where hydrocarbons are generated locally and reservoirs are in contact with the source rock [*Feinstein et al.*, 1988].

6. Conclusions

Our study integrates apatite chemistry from LA-ICP-MS and EPMA methods to derive the AFT kinetic parameter r_{mr0} for a bentonite sample from the base of the Late Cretaceous Slater River Formation at an outcrop along the Imperial River, NWT, Canada. Two kinetic AFT date populations (154.3 ± 10.2 Ma; 89.0 ± 3.7 Ma) were identified in this partially annealed sample

on the basis of their different r_{mr0} values. A third poorly defined kinetic population (53.5 ± 6.5 Ma) was inferred but was not considered during thermal modeling. AHe dates (57.9 ± 3.5 Ma to 42.0 ± 2.5 Ma) overlap the third AFT kinetic population, and exhibit a range of eU concentrations from 17 ppm to 36 ppm.

Inverse thermal history modeling was performed on 1) our multi-kinetic AFT data, using relationships between annealing kinetics predicted from the parameter r_{mr0} and AFT-date and track length distributions, and 2) integrated AFT and AHe data, accounting for the effects of chemistry and radiation damage accumulation and annealing on helium diffusion in apatite. When combined, both thermal history models suggest that the sample underwent burial from the Cenomanian to the Maastrichtian–Paleocene, reaching maximum temperatures of 65-90°C, and experienced a protracted cooling history throughout the Cenozoic. These data suggest that the Slater River Formation is at best a marginally mature source rock, and reached temperatures that may coincide with the onset of oil generation.

These data emphasize the importance of kinetic parameter choice in AFT thermochronology, as both the D_{par} measurements and the r_{mr0} values calculated without F measurements are unable to explain the AFT date dispersion and track length distribution recognized in our dataset of F-OH apatite. Apatite chemistry will have an effect on the helium diffusion in the AHe system as well, as it dictates the temperatures at which radiation damage anneals in apatite. Studies that integrate AFT and AHe thermochronology should consider these implications or risk thermal history model results that are inconsistent with the present understanding of annealing and diffusion kinetics in apatite.

Acknowledgements

Funding for this project was provided by an NSERC-CRD grant to DAS, with contributions from ConocoPhillips Canada and Chevron Canada. Additional financial and logistical support was generously made possible by the Geomapping for Energy and Minerals (GEM) program at Natural Resources Canada. This manuscript benefited greatly from the reviews of Rich Ketcham, Cécile Gautheron, and Sam Johnstone. We thank Thomas Hadlari (GSC) for his insight on the regional Mesozoic volcanic history, Paul O'Sullivan and Apatite to Zircon Inc. for assistance with the apatite fission track data collection, Danny Stockli and the University of Texas at Austin thermochronology laboratory for their analytical support, and Glenn Poirier (Canadian Museum of Nature) for assistance with EPMA data collection.

References

Armstrong, P. A. (2005), Thermochronometers in Sedimentary Basins, *Rev. Mineral. Geochemistry*, *58*(1), 499–525, doi:10.2138/rmg.2005.58.19.

Ault, A. K., and R. M. Flowers (2012), Is apatite U-Th zonation information necessary for accurate interpretation of apatite (U-Th)/He thermochronometry data?, *Geochim. Cosmochim. Acta*, *79*, 60–78, doi:10.1016/j.gca.2011.11.037.

Barbarand, J., A. Carter, I. Wood, and T. Hurford (2003a), Compositional and structural control of fission-track annealing in apatite, *Chem. Geol.*, *198*(1-2), 107–137, doi:10.1016/S0009-2541(02)00424-2.

Barbarand, J., T. Hurford, and A. Carter (2003b), Variation in apatite fission-track length measurement: Implications for thermal history modelling, *Chem. Geol.*, *198*(1-2), 77–106, doi:10.1016/S0009-2541(02)00423-0.

Belousova, E. A., W. L. Griffin, S. Y. O'Reilly, and N. I. Fisher (2002), Apatite as an indicator mineral for mineral exploration: Trace-element compositions and their relationship to host rock type, *J. Geochemical Explor.*, *76*(1), 45–69, doi:10.1016/S0375-6742(02)00204-2.

Beucher, R., R. W. Brown, S. Roper, F. Stuart, and C. Persano (2013), Natural age dispersion arising from the analysis of broken crystals. Part II: Practical application to apatite (U-Th)/He thermochronometry, *Geochim. Cosmochim. Acta*, *120*, 395–416, doi:10.1016/j.gca.2013.05.041.

Brown, R. W., R. Beucher, S. Roper, C. Persano, F. Stuart, and P. Fitzgerald (2013), Natural age dispersion arising from the analysis of broken crystals. Part I: Theoretical basis and

implications for the apatite (U-Th)/He thermochronometer, *Geochim. Cosmochim. Acta*, *122*(120), 478–497, doi:10.1016/j.gca.2013.05.041.

Burtner, R. L., A. Nigrini, and R. a. Donelick (1994), Thermochronology of Lower Cretaceous source rocks in the Idaho-Wyoming thrust belt., *Am. Assoc. Pet. Geol. Bull.*, *78*(10), 1613–1636, doi:10.1306/A25FF233-171B-11D7-8645000102C1865D.

Carlson, W. D., R. A. Donelick, and R. A. Ketcham (1999), Variability of apatite fission-track annealing kinetics: I. Experimental results, *Am. Mineral.*, *84*(9), 1213–1223, doi:10.2138/am-1999-0901.

Chew, D. M., and R. A. Donelick (2012), Combined apatite fission track and U-Pb dating by LA–ICP–MS and its application in apatite provenance analysis, *Mineral. Assoc. Canada Short Course 42*, 219–247.

Chew, D. M., R. A. Donelick, M. B. Donelick, B. S. Kamber, and M. J. Stock (2014), Apatite Chlorine Concentration Measurements by LA-ICP-MS, *Geostand. Geoanalytical Res.*, *38*(1), 23–35, doi:10.1111/j.1751-908X.2013.00246.x.

Chew, D. M., M. G. Babechuk, N. Cogné, C. Mark, G. J. O'Sullivan, I. A. Henrichs, D. Doepke, and C. A. McKenna (2016), (LA,Q)-ICPMS trace-element analyses of Durango and McClure Mountain apatite and implications for making natural LA-ICPMS mineral standards, *Chem. Geol.*, *435*, 35–48, doi:10.1016/j.chemgeo.2016.03.028.

Djimbi, M. D., C. Gautheron, J. Roques, L. Tassan-Got, C. Gerin, and E. Simoni (2015), Impact of apatite chemical composition on (U-Th)/He thermochronometry: An atomistic point of view, *Geochim. Cosmochim. Acta*, *167*, 162–176, doi:10.1016/j.gca.2015.06.017.

Donelick, R. A., R. A. Ketcham, and W. D. Carlson (1999), Variability of apatite fission-track annealing kinetics: II. Crystallographic orientation effects, *Am. Mineral.*, *84*(9), 1224–1234.

Donelick, R. A., P. B. O'Sullivan, and R. A. Ketcham (2005), Apatite Fission-Track Analysis, *Rev. Mineral. Geochemistry*, *58*(1), 49–94, doi:10.2138/rmg.2005.58.3.

Earnshaw, H. C., and B. D. Grant (1992), The Porphyrin Maturity Parameter as an Indicator of Oil Maturity and the Onset of Oil Generation in the Cretaceous Slater River Formation, Fort Norman Area, Northwest Territories, *Geol. Surv. Canada, Open File 2542*, 20 p.

Ehlers, T. A., and K. A. Farley (2003), Apatite (U-Th)/He thermochronometry: Methods and applications to problems in tectonic and surface processes, *Earth Planet. Sci. Lett.*, *206*(1-2), 1–14, doi:10.1016/S0012-821X(02)01069-5.

Eldrett, J. S. et al. (2015), An astronomically calibrated stratigraphy of the Cenomanian, Turonian and earliest Coniacian from the Cretaceous Western Interior Seaway, USA: Implications for global chronostratigraphy, *Cretac. Res.*, *56*, 316–344, doi:10.1016/j.cretres.2015.04.010.

Fallas, K. M., R. B. MacNaughton, B. C. MacLean, and T. Hadlari (2013), Geology, Norman Wells (southwest), Northwest Territories, *Geol. Surv. Canada, Can. Geosci. Map*, *101*, doi:10.4095/292293.

Farley, K. A., R. A. Wolf, and L. T. Silver (1996), The effects of long alpha-stopping distances on (U-Th)/He ages, *Geochim. Cosmochim. Acta*, *60*(21), 4223–4229.

Feinstein, S., P. W. Brooks, M. G. Fowler, L. R. Snowdon, and G. K. Williams (1988), Families of oils and source rocks in the central Mackenzie corridor: a geochemical oil-oil and oil-source rock correlation, *Can. Soc. Pet. Geol. Mem.*, *15*, 543–552.

Feinstein, S., G. K. Williams, L. R. Snowdon, F. Goodarzi, and T. Gentzis (1991), Thermal maturation of organic matter in the Middle Devonian to Tertiary section, Fort Norman area (central Mackenzie Plain), *Can. J. Earth Sci.*, *28*(7), 1009–1018, doi:10.1139/e91-092.

Feinstein, S., D. R. Issler, L. R. Snowdon, and G. K. Williams (1996), Characterization of major unconformities by paleothermometric and paleobarometric methods: application to the Mackenzie Plain, Northwest Territories, Canada, *Bull. Can. Pet. Geol.*, *44*(1), 55–71.

Flowers, R. M., R. A. Ketcham, D. L. Shuster, and K. A. Farley (2009), Apatite (U-Th)/He thermochronometry using a radiation damage accumulation and annealing model, *Geochim. Cosmochim. Acta*, *73*(8), 2347–2365, doi:10.1016/j.gca.2009.01.015.

Gautheron, C., L. Tassan-Got, J. Barbarand, and M. Pagel (2009), Effect of alpha-damage annealing on apatite (U-Th)/He thermochronology, *Chem. Geol.*, *266*(3-4), 166–179, doi:10.1016/j.chemgeo.2009.06.001.

Gautheron, C., L. Tassan-Got, R. A. Ketcham, and K. J. Dobson (2012), Accounting for long alpha-particle stopping distances in (U-Th-Sm)/He geochronology: 3D modeling of diffusion, zoning, implantation, and abrasion, *Geochim. Cosmochim. Acta*, *96*, 44–56, doi:10.1016/j.gca.2012.08.016.

Gautheron, C., J. Barbarand, R. A. Ketcham, L. Tassan-Got, P. Van Der Beek, M. Pagel, R. Pinna-Jamme, F. Couffignal, and M. Fialin (2013), Chemical influence on α-recoil damage annealing in apatite: Implications for (U-Th)/He dating, *Chem. Geol.*, *351*(August 2013), 257–267, doi:10.1016/j.chemgeo.2013.05.027.

Green, P. F. (1981), A new look at statistics in fission-track dating, *Nucl. Tracks*, *5*(1-2), 77–86, doi:10.1016/0191-278X(81)90029-9.

Green, P. F. (1988), The relationship between track shortening and fission track age reduction in apatite: combined influences of inherent instability, annealing anisotropy, length bias and system calibration, *Earth Planet. Sci. Lett.*, *89*(3-4), 335–352, doi:10.1016/0012-821X(88)90121-5.

Green, P. F., I. R. Duddy, A. J. W. Gleadow, P. R. Tingate, and G. M. Laslett (1986), Thermal annealing of fission tracks in apatite 1. Variable temperature behaviour, *Chem. Geol. Isot. Geosci. Sect.*, *59*, 237–253, doi:10.1016/0168-9622(88)90019-X.

Hadlari, T., B. C. MacLean, J. M. Galloway, A. R. Sweet, J. M. White, D. Thomson, J. Gabites, and C. J. Schröder-Adams (2014), The flexural margin, the foredeep, and the orogenic margin of a northern Cordilleran foreland basin: Cretaceous tectonostratigraphy and detrital zircon provenance, northwestern Canada, *Mar. Pet. Geol.*, *57*, 173–186, doi:10.1016/j.marpetgeo.2014.05.019.

Hannigan, P. K., D. W. Morrow, and B. C. MacLean (2011), Petroleum resource potential of the northern mainland of Canada (Mackenzie Corridor), *Geol. Surv. Canada, Open File 6757*, 271, doi:289095.

Hasebe, N., J. Barbarand, K. Jarvis, A. Carter, and A. J. Hurford (2004), Apatite fission-track chronometry using laser ablation ICP-MS, *Chem. Geol.*, *207*(3-4), 135–145, doi:10.1016/j.chemgeo.2004.01.007.

Issler, D. R. (1996), An inverse model for extracting thermal histories from apatite fission track data: instructions and software for the Windows 95 environment, *Geol. Surv. Canada, Open File 2325*, 85 p.

Issler, D. R. D., A. Grist, and L. Stasiuk (2005), Post-Early Devonian thermal constraints on hydrocarbon source rock maturation in the Keele Tectonic Zone, Tulita area, NWT, Canada, from multi-kinetic apatite fission track thermochronology, vitrinite reflectance and shale compaction, *Bull. Can. Pet. Geol.*, *53*(4), 405–431, doi:10.2113/53.4.405.

Ketcham, R. A. (2005a), Forward and Inverse Modeling of Low-Temperature Thermochronometry Data, *Rev. Mineral. Geochemistry*, *58*(1), 275–314,

doi:10.2138/rmg.2005.58.11.
Ketcham, R. A. (2005b), The role of crystallographic angle in characterizing and modeling apatite fission-track length data, in *Radiation Measurements*, vol. 39, pp. 595–601.
Ketcham, R. A. (2015), Technical Note: Calculation of stoichiometry from EMP data for apatite and other phases with mixing on monovalent anion sites, *Am. Mineral.*, *100*(7), 1620–1623, doi:10.2138/am-2015-5171.
Ketcham, R. A., R. A. Donelick, and W. D. Carlson (1999), Variability of apatite fission-track anneling kinetics: III. Extrapolation to geological time scales, *Am. Mineral.*, *84*, 1235–1255.
Ketcham, R. A., A. Carter, R. A. Donelick, J. Barbarand, and A. J. Hurford (2007), Improved modeling of fission-track annealing in apatite, *Am. Mineral.*, *92*(5-6), 799–810, doi:10.2138/am.2007.2281.
Ketcham, R. A., R. A. Donelick, M. L. Balestrieri, and M. Zattin (2009), Reproducibility of apatite fission-track length data and thermal history reconstruction, *Earth Planet. Sci. Lett.*, *284*(3-4), 504–515, doi:10.1016/j.epsl.2009.05.015.
Ketcham, R. A., C. Gautheron, and L. Tassan-Got (2011), Accounting for long alpha-particle stopping distances in (U-Th-Sm)/He geochronology: Refinement of the baseline case, *Geochim. Cosmochim. Acta*, *75*(24), 7779–7791, doi:10.1016/j.gca.2011.10.011.
Ketcham, R. A., A. Carter, and A. J. Hurford (2015), Inter-laboratory comparison of fission track confined length and etch figure measurements in apatite, *Am. Mineral.*, *100*(7), 1452–1468, doi:10.2138/am-2015-5167.
Knight, E., D. A. Schneider, and J. Ryan (2013), Thermochronology of the Yukon-Tanana Terrane, West-Central Yukon: Evidence for Jurassic Extension and Exhumation in the Northern Canadian Cordillera, *J. Geol.*, *121*(4), 371–400, doi:10.1086/670721.
Majorowicz, J. A., and D. W. Morrow (1998), Subsurface temperature and heat flow - Yukon and Northwest Territories, *Geol. Surv. Canada, Open File 3626*, 6 p.
Morris, G. A., and R. A. Creaser (2008), Correlation of mid-Cretaceous granites with source terranes in the northern Canadian Cordillera, *Can. J. Earth Sci.*, *45*(3), 389–403, doi:10.1139/E08-002.
Morton, A., and G. Yaxley (2007), Detrital apatite geochemistry and its application in provenance studies, in *Sedimentary Provenance and Petrogenesis: Perspectives from Petrography and Geochemistry: Geological Society of America, Special Paper 420*, edited by J. Critelli and M. J. Johnsson, pp. 319–344.
Nielsen, S. B., O. R. Clausen, and E. Mcgregor (2015), Basin%Ro: A vitrinite reflectance model derived from basin and laboratory data, *Basin Res.*, 1–22, doi:10.1111/bre.12160.
Piccoli, P. M., and P. A. Candela (2002), Apatite in Igneous system, *Rev. Mineral. Geochemistry*, *48*(1), 255–292, doi:10.2138/rmg.2002.48.6.
Powell, J., D. Schneider, D. Stockli, and K. Fallas (2016), Zircon (U-Th)/He thermochronology of Neoproterozoic strata from the Mackenzie Mountains, Canada: Implications for the Phanerozoic exhumation and deformation history of the northern Canadian Cordillera, *Tectonics*, *35*(3), 663–689, doi:10.1002/2015TC003989.
Pyle, L. J., and L. P. Gal (2014), Analytical Results from Cretaceous and Devonian Studies in Mackenzie Plain, *Northwest Territ. Geosci. Off. NWT Open Rep. 2014-006*, 1–28.
Shuster, D. L., R. M. Flowers, and K. A. Farley (2006), The influence of natural radiation damage on helium diffusion kinetics in apatite, *Earth Planet. Sci. Lett.*, *249*(3-4), 148–161, doi:10.1016/j.epsl.2006.07.028.
Stock, M. J., M. C. S. Humphreys, V. C. Smith, R. D. Johnson, and D. M. Pyle (2015), New

constraints on electron-beam induced halogen migration in apatite, *Am. Mineral.*, *100*, 281–293, doi:10.2138/am-2015-4949.

Stockli, D. F., B. E. Surpless, T. A. Dumitru, and K. A. Farley (2002), Thermochronological constraints on the timing and magnitude of Miocene and Pliocene extension in the central Wassuk Range, western Nevada, *Tectonics*, *21*(4), 10–19, doi:10.1029/2001TC001295.

Thomson, D., C. J. Schröder-Adams, T. Hadlari, G. Dix, and W. J. Davis (2011), Albian to Turonian stratigraphy and palaeoenvironmental history of the northern Western Interior Sea in the Peel Plateau Region, Northwest Territories, Canada, *Palaeogeogr. Palaeoclimatol. Palaeoecol.*, *302*(3-4), 270–300, doi:10.1016/j.palaeo.2011.01.017.

Tran, M., Q. Sun, B. W. Smith, and J. D. Winefordner (2001), Determination of F, Cl, and Br in Solid Organic Compounds by Laser-Induced Plasma Spectroscopy, *Appl. Spectrosc.*, *55*(6), 739–744, doi:10.1366/0003702011952433.

Vermeesch, P. (2009), RadialPlotter: A Java application for fission track, luminescence and other radial plots, *Radiat. Meas.*, *44*(4), 409–410, doi:10.1016/j.radmeas.2009.05.003.

Yorath, C. J., and D. G. Cook (1981), Cretaceous and Tertiary Stratigraphy and Paleogeography, Northern Interior Plains, District of Mackenzie, *Geol. Surv. Canada, Mem.*, *398*, 1–76, doi:10.1017/CBO9781107415324.004.

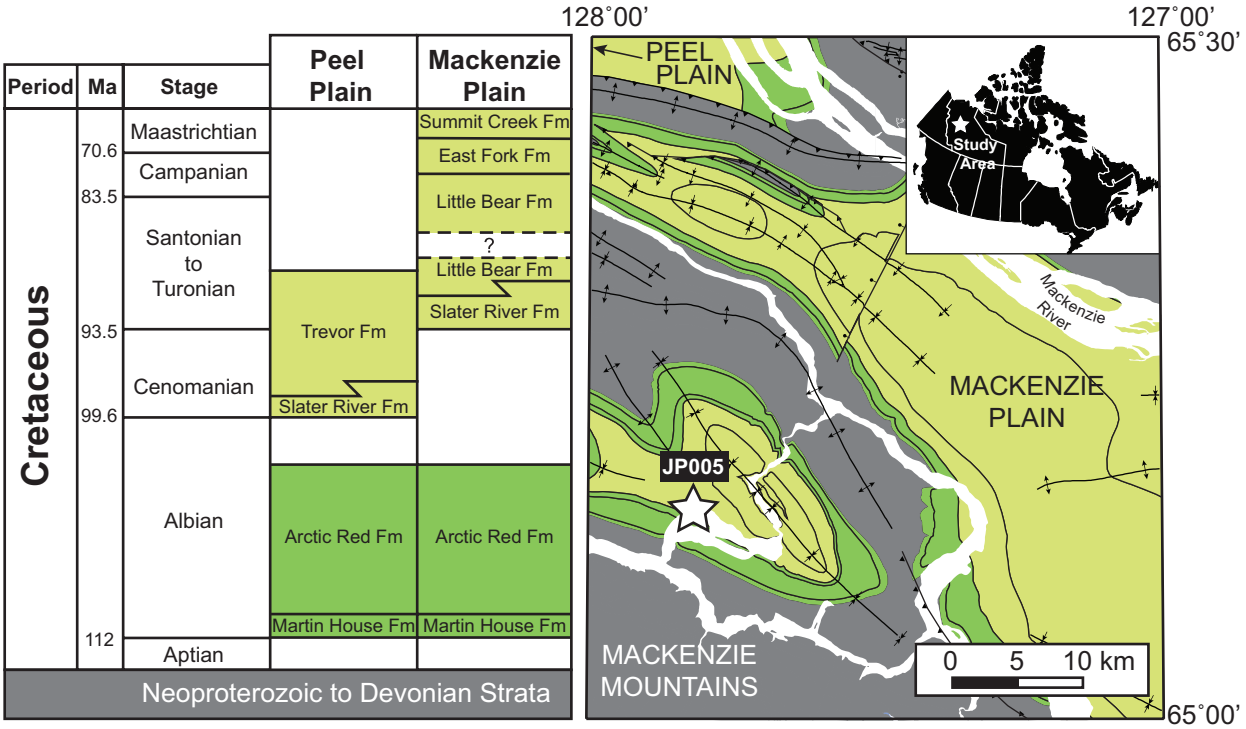

Fig. 1: Cretaceous stratigraphic section modified after *Thomson et al.* [2011] and Hadlari *et al*. [2014]. Adjacent map shows the regional Paleozoic to Cretaceous geology and structural elements (after *Fallas et al*., 2013) and the location of the Imperial River sample site (JP005; white star). Colours on the stratigraphic section correlate to the colours on the map; map symbols denote syncline and anticline structures.

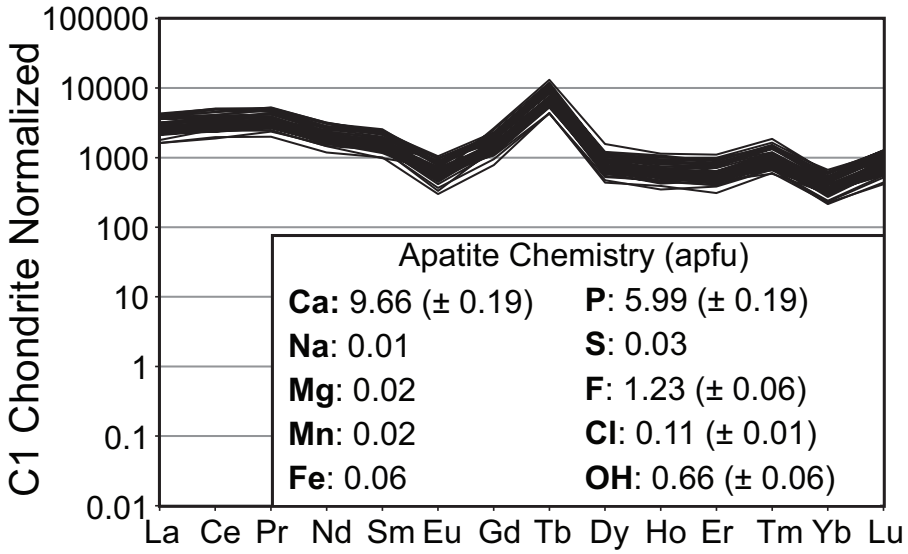

Fig. 2: C1 chondrite-normalized REE plot for apatite from the Slater River Formation bentonite sample. Apatite chemistry in atoms per formula unit (apfu) was calculated following the stoichiometric relationships of *Ketcham* [2015] using weight% oxide values measured from LA-ICP-MS (Na, Mg, Mn, Fe, S) and EPMA (Ca, P, Cl, F). OH was calculated based on the difference between measured and expected halogen content. All 84 grains (38 AFT age-grains; 46 AFT length-grains) analyzed for AFT analyses were measured for major, minor and REE geochemistry.

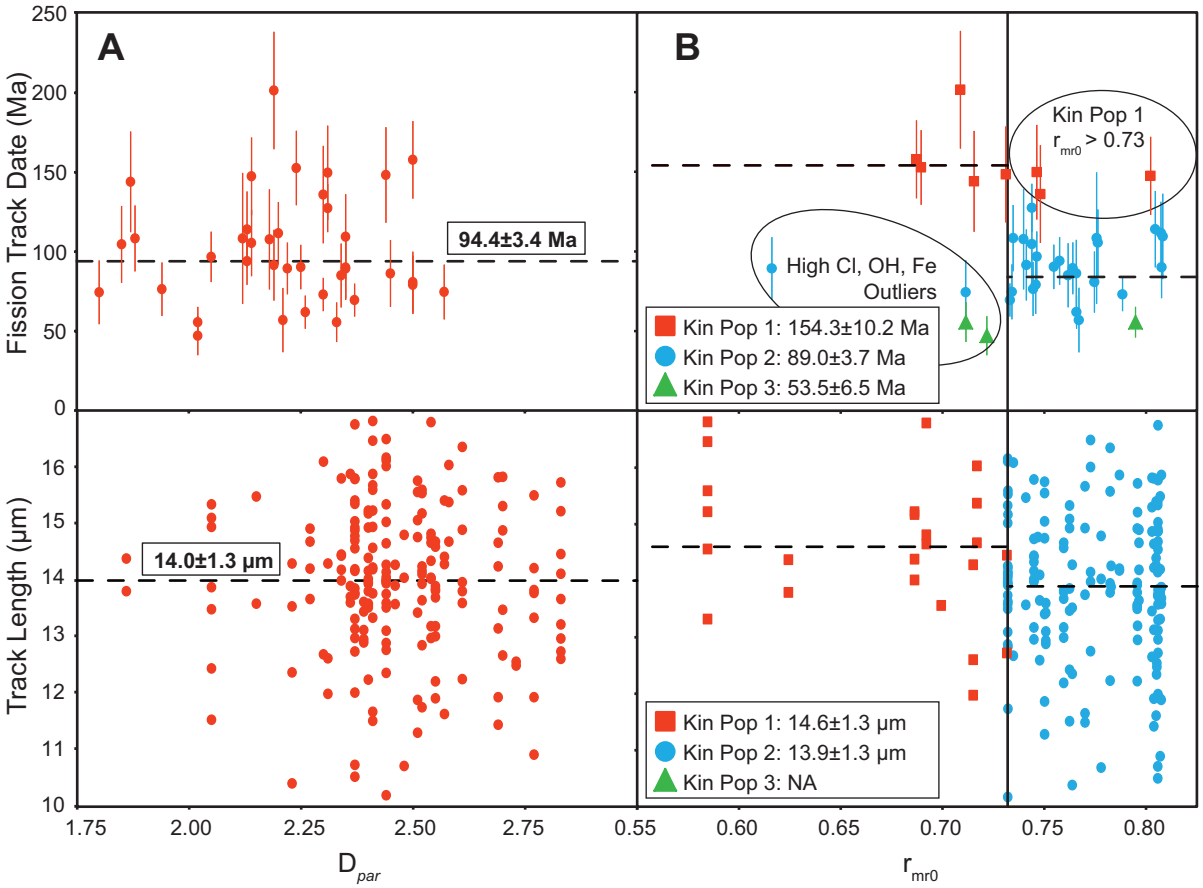

Fig. 3: Apatite fission track date and individual track length data plotted as a function of the kinetic parameter A) D_{par}, and B) r_{mr0}. Horizontal dashed lines indicate the pooled age (top) and mean track length (bottom) of a population. The solid black line in B illustrates the boundary between kinetic populations #1 and #2. No boundary is plotted between kinetic populations #2 and #3, as the latter is poorly defined in kinetic space. A corresponding plot of AFT date and track length versus Cl content, and an experiment that addresses the sensitivity of kinetic population pooled age and mean track length to the r_{mr0} value of the kinetic boundary are available in the Appendix (Figs. A1, A2).

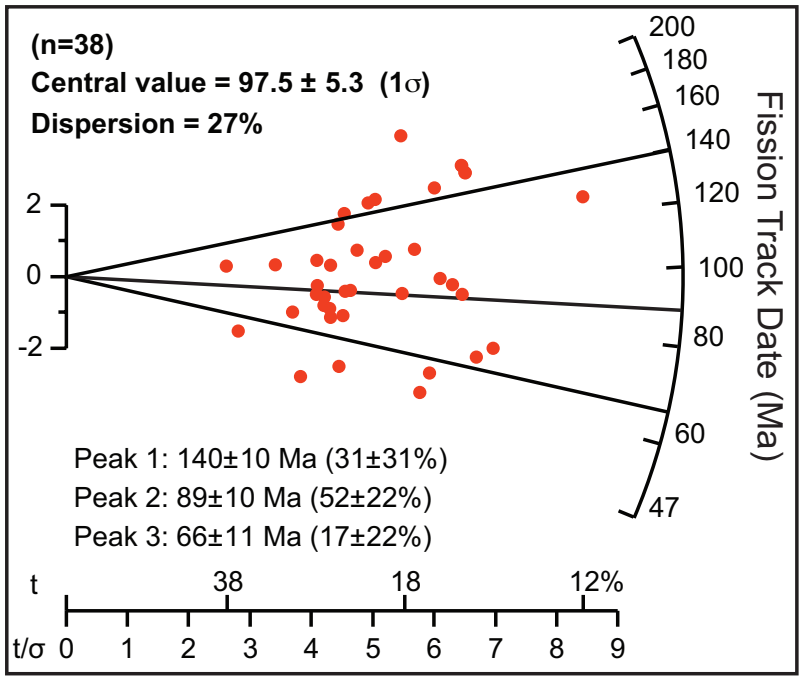

Fig. 4: Radial plot of the apatite fission track data using RadialPlotter [*Vermeesch*, 2009]. Fission track dates and their associated error are plotted as a function of the degree of rotation along, and distance from, the curved axis. Pooled ages from proposed kinetic populations (Fig. 3) are within error of the peak ages predicted from the radial plot.

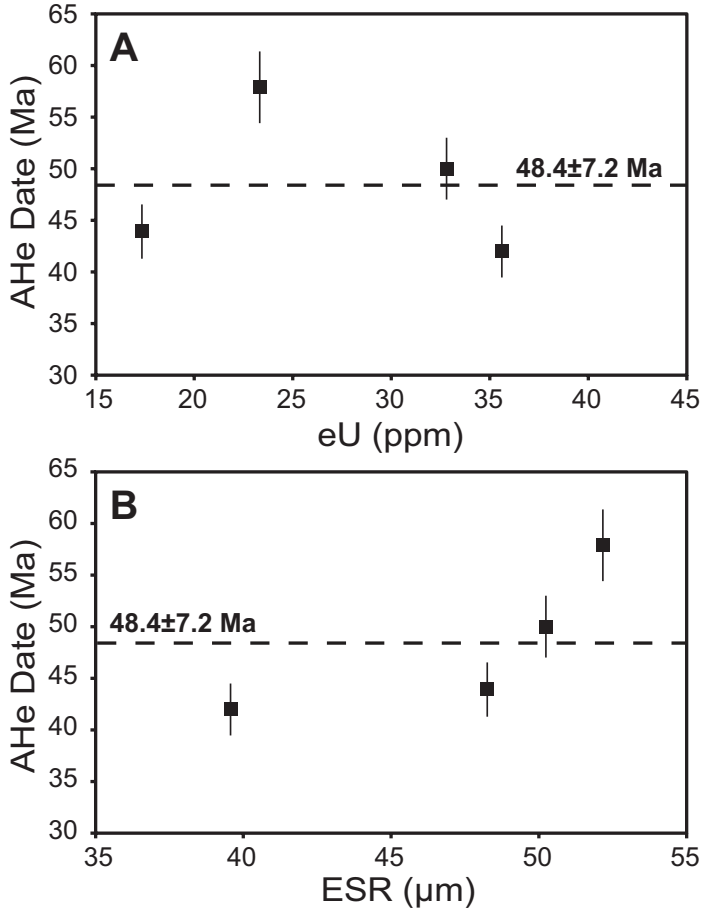

Fig. 5: Apatite (U-Th)/He dates as a function of A) effective uranium concentration (eU), and B) equivalent spherical radius (ESR). Dashed black line shows the average date calculated from all AHe data.

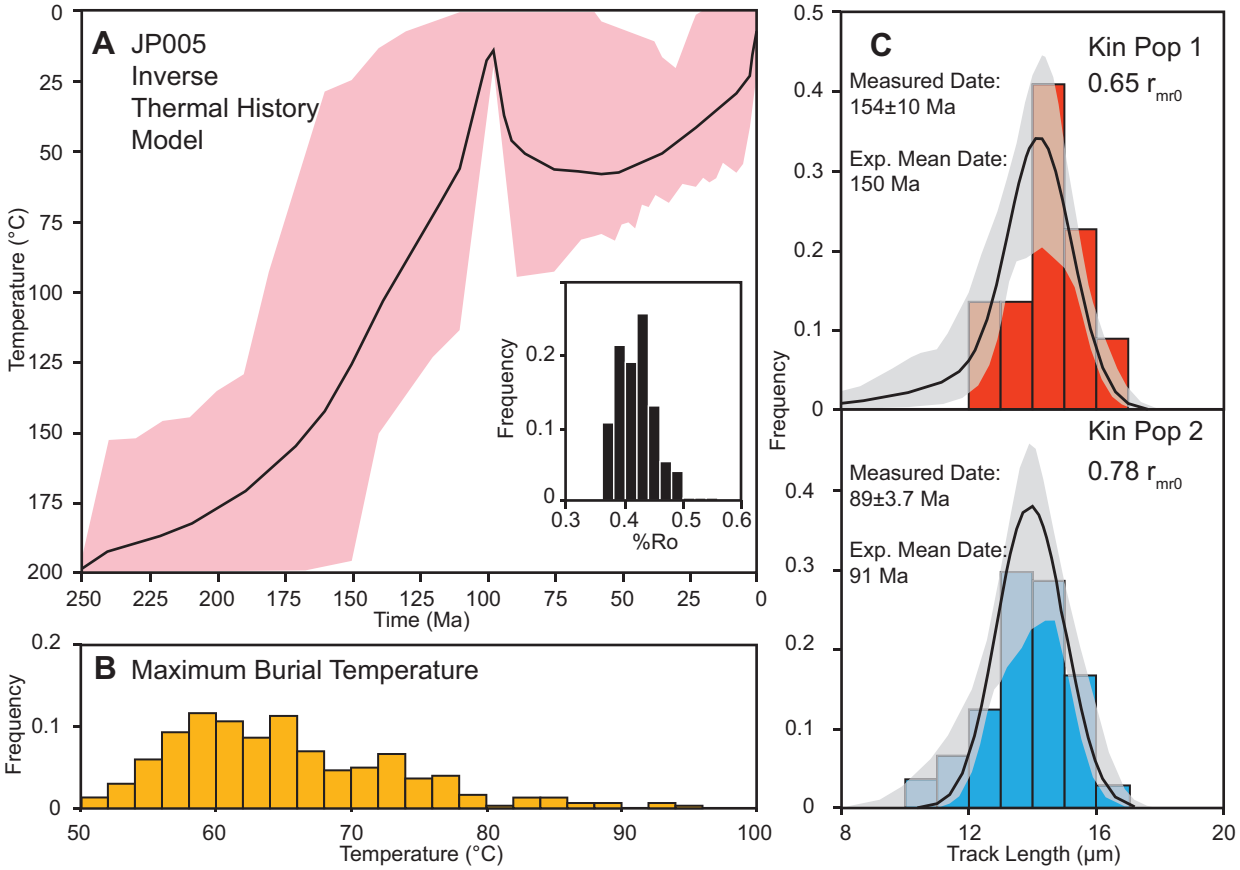

Fig. 6: A) Inverse thermal history model derived from AFT kinetic populations #1 and #2 using the software AFTINV [*Issler*, 1996]. The model allows for a random cooling history from 250 Ma to deposition (97.6 Ma) to account for the older dates in AFT kinetic population #1. The pink envelope indicates the solution boundary of 300 statistically significant Monte Carlo solutions. The black curve is the exponential mean of all 300 solutions and the inset histogram shows the corresponding calculated %Ro values. B) Histogram indicating the maximum burial temperatures predicted from the thermal history model. C) Histograms showing track length distribution for each kinetic population. Black curves represent the probability density functions for the exponential mean thermal history (shown in A). Grey shaded regions show the solution bounds for probability density functions calculated from all 300 Monte Carlo solutions. The inverse thermal history model was run in conventional track length mode to compare calculated length distributions with observed length distributions.

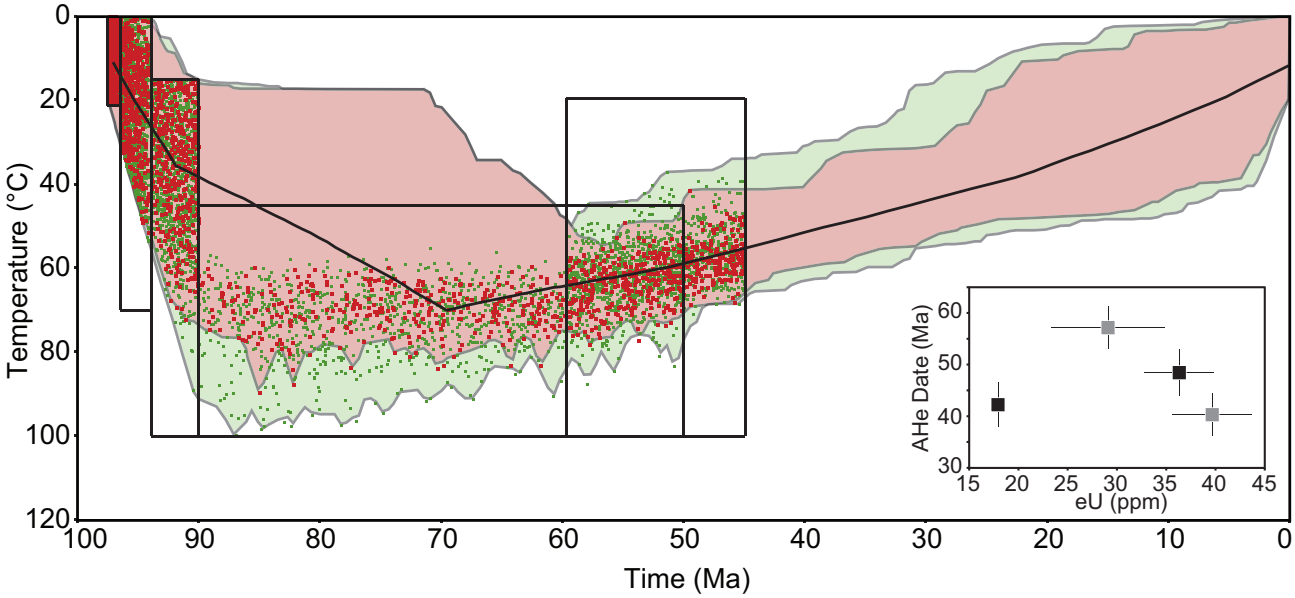

Fig. 7: Inverse thermal history model generated from AHe data and the AFT kinetic population #2 (Fig. 3b) created using HeFTy (Ketcham 2005b). Light green and pink envelopes indicate the realm of time-temperature solutions for acceptable and good paths, respectively. Green and red dots indicate inflection points of acceptable and good time-temperature paths, respectively. The solid black line indicates the weighted mean path of all time-temperature solutions. Black rectangles represent independent time-temperature constraints. Inset graph shows AHe dates, modified from Fig. 5a to account for variable geometries and broken grains. AHe grains in black were incorporated into the inverse model.

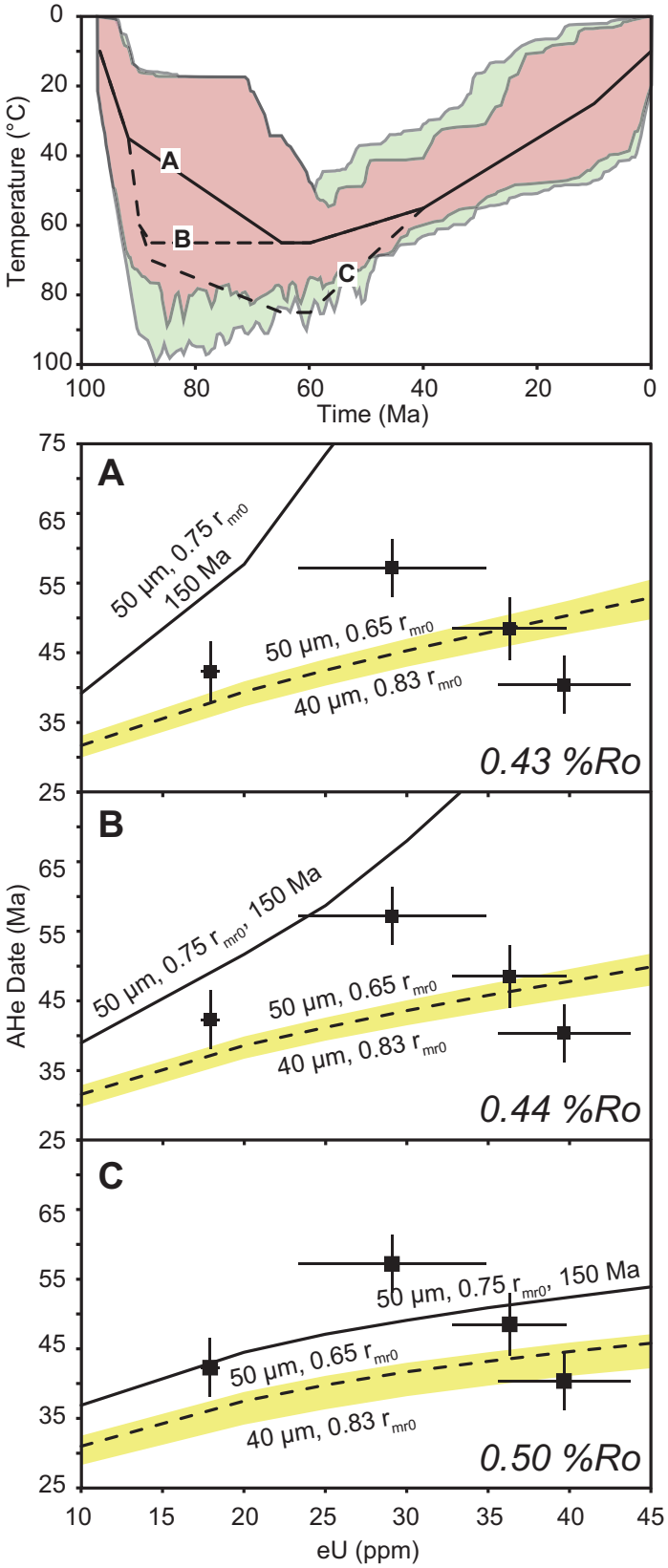
Temperature (°C)
Time (Ma)
A
B
C
AHe Date (Ma)
eU (ppm)
50 µm, 0.75 r mr0, 150 Ma
50 µm, 0.65 r mr0
40 µm, 0.83 r mr0
0.43 %Ro
0.44 %Ro
0.50 %Ro

Fig. 8 (previous page): Forward models are used to test the rigour of the thermal history solutions generated from inverse modeling in Fig. 6. Three time-temperature paths of variable heating and cooling rates and maximum temperature were used to generate AHe date-eU trends (A-C). Yellow envelopes in A - C account for all plausible date-eU relationships for apatite grains between 40-50 μm in size and 0.65-0.83 r_{mr0}. Bold dashed curve represents the expected AHe date-eU trend for a 45 μm apatite with an r_{mr0} value of 0.75. The solid line shows the expected AHe date-eU trend for a 50 μm apatite of 0.75 r_{mr0} that experiences radiation damage accumulation starting at 150 Ma. %Ro values were calculated for each forward model using the basin%Ro model [*Nielsen et al.*, 2015].

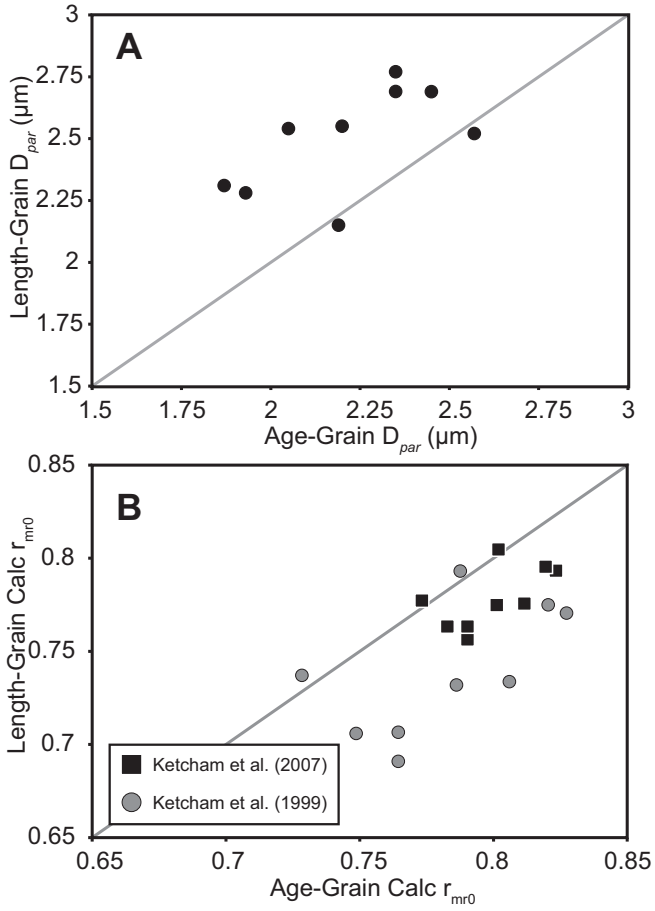

Fig. 9: A) Plot of D_{par} measurements from the same apatite grains comparing measurements of the etch pit diameter before (AFT age-grain) and after (AFT length-grain) ^{252}Cf irradiation. D_{par} values are the average of four separate measurements. B) Identical as A, except that D_{par} measurements have been converted to a calculated r_{mr0} value [*Ketcham et al.*, 1999, 2007] to convey the implications of the discrepancy in D_{par} measurements on fission track annealing kinetics. Gray lines illustrate the expected 1:1 for D_{par} and calculated r_{mr0}.

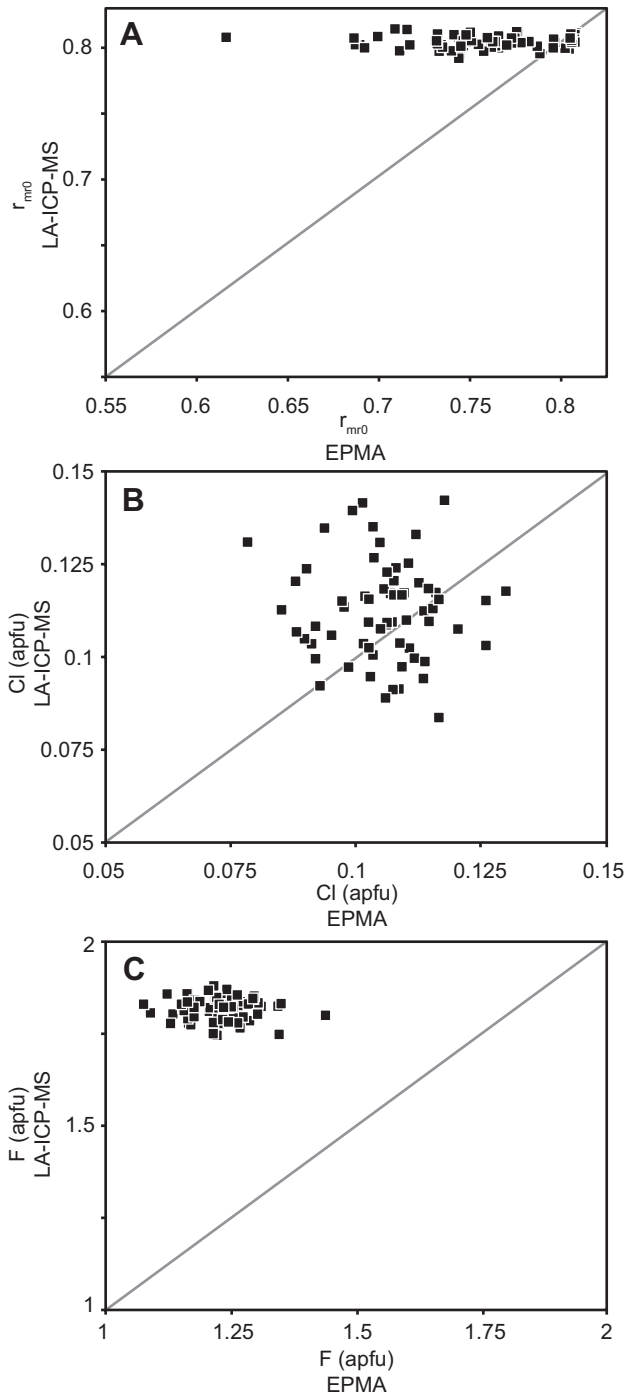

Fig. 10: A-C) Comparisons of kinetic parameters and chemistry calculated from LA-ICP-MS analyses with those that incorporate F, Cl, Ca, and P measurements from EPMA analyses. A) r_{mr0} [*Ketcham et al.*, 2007], B) Cl content (apfu), and C) F content (apfu). Gray lines illustrate the expected 1:1 between r_{mr0} and elemental measurements.

Appendix to

CHAPTER 3: Application of multi-kinetic apatite fission track and (U-Th)/He thermochronology to source rock thermal history: A case study from the Mackenzie Plain, NWT, Canada

Jeremy Powell[1], David Schneider[1], Dale Issler[2]
1. Department of Earth & Environmental Sciences, University of Ottawa, Ottawa, Canada
2. Natural Resources Canada, Geological Survey of Canada, Calgary, Canada

Contents
• Sampling and Methods
• Expanded description of forward modeling
• Figures A1 to A4
• Tables A1 to A6

Introduction

This Appendix incorporates text and figures that describes our sampling strategy, analytical methods, particulars of elemental analyses from LA-ICP-MS and EPMA approaches, and a more elaborate description of the AHe forward models (Fig. 7). Figures in the Appendix explore the relationships between AFT date/track length and Cl content, address how sensitive kinetic populations are to the r_{mr0} value of the kinetic boundary, and show the magnitude of [U] zoning required to yield the old ages. Additionally, we include six tables that include AFT data, apatite geochemistry, AHe data, calculations on the effect of zoning on AFT date, and a comparison of r_{mr0} values calculated for grains that were measured twice for D_{par}.

Text A1. Sampling and Methods

A.1.1. Sampling strategy

Our study focuses on a single Slater River Formation sample collected from an outcrop along the Imperial River in the foothills of the Mackenzie Mountains (Fig. 1; 65.152˚N, 127.822˚W). At this outcrop location, twelve bentonite layers are intercalated amongst shale. In an effort to better understand the effects of variable chemistry and provenance on the apatite fission track and apatite (U-Th)/He system, we avoided sampling siliciclastic units that possess detrital mineral phases, and instead opted to sample one of the bentonite layers exposed near the base of the Slater River Formation. These layers have previously been dated via U-Pb zircon geochronology at 97.6 ± 1.0 Ma (via ID-TIMS; Fallas et al. 2013; T. Hadlari pers. comm. 2016). The bentonite was poorly consolidated and did not require crushing. Apatite grains were separated using standard sieving, heavy liquid and magnetic separation techniques.

A.1.2 Apatite Geochemistry and Fission Track Analysis

In an effort to understand the uranium content and range of chemistry present in our sample suite, all 84 grains (38 AFT age-grains; 46 AFT length-grains) analyzed for AFTA were measured for major, minor and REE geochemistry (Fig. 2). Analyses were conducted via LA-ICP-MS methods at Apatite to Zircon Inc. (Viola, USA) using a Resonetics M-50-LR 193 nm ArF Excimer laser ablation system coupled to an Agilent 7700x quadrupole inductively coupled mass spectrometer (ICP-MS). Laser ablation was conducted using a 26 mm spot and a 7 Hz laser

repetition rate with the laser set in constant energy mode. Chemistries were calculated from isotopic counts per second (cps) summed from the seven of thirty scans that exhibited the highest background-corrected signal intensity. A conversion factor of (summed isotope cps/^{43}Ca cps) was smoothed using a load-specific running median method. These data were calibrated to a well characterized Durango apatite to determine elemental concentrations. In addition to the LA-ICP-MS data, major elements and halogens were analyzed at the University of Ottawa (Ottawa, Canada) using the JEOL JXA-8230 SuperProbe which operates with an accelerating voltage of 10 kV and beam current of 3.8 nA to focus and concentrate the electron beam to a minimum of 1 μm. These conditions were employed to better determine the halogen content. All REE are presented as C1 chondrite normalized plots. We use stoichiometric relationships (Ketcham, 2015) to convert measured weight% oxide values to atoms per formula unit (apfu), and later use these values to calculate grain-specific r_{mr0} values.

Apatite fission track analysis was conducted by P. O'Sullivan at Apatite to Zircon Inc. (Viola, USA) using the LA-ICP-MS method (Donelick et al., 2005; Hasebe et al., 2004). Apatite were mounted in an epoxy resin, cured at 90°C for 1 hour, and polished to expose internal surfaces of the apatite grains. After polishing, mounts were immersed in 5.5N HNO_3 for 20.0 seconds (± 0.5 seconds) at 21°C (± 1°C) to reveal all natural fission tracks that intersected the polished grain surfaces. D_{par} measurements were calculated from one to four etch pit diameters, and spontaneous (natural) fission-track densities were counted for each grain considered suitable for dating. Grains were then revisited using the LA-ICP-MS to make spot analyses to determine U, Th, and Sm concentrations of each apatite. Durango (DR) was used as the apatite FT zeta age calibration standard. During each LA-ICP-MS session containing samples of unknown FT age, clusters of ~10 zeta spots were analyzed during the session for purposes of calibrating ^{238}U/^{43}Ca. Ratios of primary zeta (original zeta LA-ICP-MS session) to secondary zeta (current LA-ICP-MS session) ^{238}U/^{43}Ca were determined for each zeta calibration spot and smoothed using a load-specific running-median method. Only spots visited during the primary, original zeta LA-ICP-MS session were revisited during the secondary, current LA-ICP-MS session for this purpose. This method is analogous to using ^{235}U-doped glass standards in the external detector method of fission track analysis (Donelick et al., 2005); in this study, specific DR grains from the primary standard LA-ICP-MS session serve as ^{235}U-doped standards.

Included in this document are figures and tables that address: 1) the lack of relationship between Cl content and AFT date and length (Fig. A1); 2) the effect of the r_{mr0} value of the boundary between kinetic populations on pooled ages, mean track length and chi-square statistics (Fig. A2); 3) an illustration of the effects of uranium zoning on AFT dates (Fig. A3; Table A5); 4) pictures of the apatite with the oldest and youngest AFT dates, showing no major difference in morphology or heterogeneities in track density (Fig. A4); and 5) a table (Table A6) that summarizes the change in closure temperatures expected for an apatite when r_{mr0} is calculated using D_{par} values from age and length grain measurements, and for different conversions and annealing models of *Carlson et al.* [1999] and *Ketcham et al.* [2007, 1999].

1.3 Apatite (U-Th)/He Analysis

Apatite (U-Th)/He analyses were conducted at the University of Texas Geo-Thermochronometry Lab (Austin, USA), and follow common (U-Th)/He dating conventions (Stockli et al., 2000). Following standard mineral separation, apatites were handpicked using binocular microscope and measured for length and width. In an effort to pick inclusion-free apatite, all grains analyzed were carefully screened for inclusions in isopropanol at 180x

magnification. Apatite grains were wrapped in Pt foil and degassed using in-vacuo diode laser heating at 1050°C and 1300°C, respectively. ^{4}He was measured via quadrupole ultra-high vacuum noble gas extraction and mass-spectrometry system with a cryogenic trap. A ^{3}He spike was used for isotope dilution. All apatites were degassed twice to ensure complete degassing. Degassed single grains were dissolved for ^{238}U, ^{232}Th, ^{149}Sm determinations by isotope dilution using an Element 2 ICP-MS. HNO_3 was used for apatite dissolution. All data were corrected for the effects of helium ejection (Farley et al., 1996). AHe dates are reported with a standard error of 6% respectively, which are reflective of the standard deviation of a population of analyzed standards.

Given that dispersion amongst AHe dates is common (Brown et al., 2013; Flowers et al., 2009; Murray et al., 2014), especially in rocks with protracted cooling histories (Ault et al., 2013; Fitzgerald et al., 2006) the 6% error applied to the AHe dates is likely not reflective of the true reproducibility of an analysis and may be too restrictive for modeling the AHe dates in this dataset. Additionally, since these data were collected in 2012/2013 and reduced using older methodolgy, recent grain-specific variables, including the effect of variable geometry (Beucher et al., 2013; Brown et al., 2013) and more recent methods for calculating Ft corrections (Ketcham et al., 2011) were not factored into data reduction. Nor were the dimensions in a second crystallographic width, as Ft corrections were generated under the assumption that the crystallographic a- and b-axes are equidimensional. This could be problematic, as many apatite grains exhibit differing widths, and as a result the crystal volume and mass derived from the apatite geometry may be an overestimate.

Due to the above reasons, ages and eU concentrations used in modeling were recalculated from the original data to test the effect of broken crystals, varying grain morphologies, different methods for calculating the Ft correction and a b-axis that is 75% the diameter of the A-axis. The modeled date, error and eU concentrations average the difference between our original corrected dates and the recalculated values. Whereas these modeled ages do not represent a "truer" AHe date than those reported, they are perhaps a more true representation of plausible variability in AHe dates than the standard 6% error. Original eU concentrations and recalculated AHe dates and errors were used for inverse modeling (Fig. 6). The recalculated eU concentrations are purely a visual aid for interpreting forward models (Fig. 8).

Text A2. Expanded AHe forward modeling

Because our AHe inverse thermal history model results are only based on two apatite grains and assume a fixed composition of 0.75 r_{mr0}, we use forward modeling of three candidate temperature-time histories to illustrate how radiation damage, grain size and compositional variance may be manifested in our AHe data (Fig. 8). These three forward models test for a range of maximum temperatures and burial and exhumation rates. Additionally, given the older AFT kinetic population #1 (154.3 ± 10.2 Ma), each model shows the expected AHe date-eU trend for an apatite with a predepositional history that began accumulating radiation damage at 150 Ma. Fig. 8a shows the expected AHe date-eU relationship for strata that experience a constant burial history from deposition and reach a maximum temperature of 65°C at 60 Ma. Due to the limited time spent at maximum temperature, this model predicts a strongly positive date-eU trend, with increased radiation damage resulting in lower helium diffusivity in apatite and older ages compared to the lower eU values. Although these date-eU curves account for some of the AHe date dispersion in our dataset, it cannot explain the younger, higher eU AHe date or the oldest AHe date. In comparison, the date-eU curve that factors in inherited helium

and radiation damage predicts substantially older dates than observed. The AHe date-eU relationships in Fig. 8b and c are produced from thermal histories with similarly rapid Late Cretaceous heating but variable maximum burial temperatures (65°C and 90°C, respectively). The date-eU trends for both these forward models more closely approximate the three younger AHe dates than Fig. 8a, and Fig. 8c predicts slightly younger dates than 8**b** due to heating at temperatures >65 °C. The date-eU curve produced with a predepositional history is within error of the oldest age in Fig. 8b, and slightly younger in Fig. 8c: the 20°C difference in maximum temperature between Fig. 8b and c is sufficient to anneal much of the inherited radiation damage and results in a less dramatic date-eU trend.

Tentatively, these models suggest a thermal history somewhere between b and c would best explain the observed AHe date dispersion. However, this interpretation requires a similar predepositional assumption for the c. 57 Ma AHe date as presented for AFT kinetic population #2. However, it is entirely possible that the older age of this grain is due to U-Th-Sm rich mineral inclusions (Vermeesch et al., 2007), strongly zoned apatite (Ault and Flowers, 2012) or ^{4}He implantation from neighbouring U-Th-Sm bearing minerals (Gautheron et al., 2012). For these reasons, we avoid interpreting the average AHe date (48.4 ± 7.2 Ma) as it may incorporate spurious age data, and removes useful AHe kinetic information (eU, ESR).

References

Ault, A.K., Flowers, R.M., 2012. Is apatite U-Th zonation information necessary for accurate interpretation of apatite (U-Th)/He thermochronometry data? Geochim. Cosmochim. Acta 79, 60–78. doi:10.1016/j.gca.2011.11.037

Ault, A.K., Flowers, R.M., Bowring, S.A., 2013. Phanerozoic surface history of the Slave craton. Tectonics 32, 1066–1083. doi:10.1002/tect.20069

Beucher, R., Brown, R.W., Roper, S., Stuart, F., Persano, C., 2013. Natural age dispersion arising from the analysis of broken crystals. Part II: Practical application to apatite (U-Th)/He thermochronometry. Geochim. Cosmochim. Acta 120, 395–416. doi:10.1016/j.gca.2013.05.041

Brown, R.W., Beucher, R., Roper, S., Persano, C., Stuart, F., Fitzgerald, P., 2013. Natural age dispersion arising from the analysis of broken crystals. Part I: Theoretical basis and implications for the apatite (U-Th)/He thermochronometer. Geochim. Cosmochim. Acta 122, 478–497. doi:10.1016/j.gca.2013.05.041

Carlson, W.D., Donelick, R.A., Ketcham, R.A., 1999. Variability of apatite fission-track annealing kinetics: I. Experimental results. Am. Mineral. 84, 1213–1223. doi:10.2138/am-1999-0901

Donelick, R.A., O'Sullivan, P.B., Ketcham, R.A., 2005. Apatite Fission-Track Analysis. Rev. Mineral. Geochemistry 58, 49–94. doi:10.2138/rmg.2005.58.3

Fallas, K.M., MacNaughton, R.B., MacLean, B.C., Hadlari, T., 2013. Geology, Norman Wells (southwest), Northwest Territories. Geol. Surv. Canada, Can. Geosci. Map 101. doi:10.4095/292293

Farley, K.A., Wolf, R.A., Silver, L.T., 1996. The effects of long alpha-stopping distances on (U-Th)/He ages. Geochim. Cosmochim. Acta 60, 4223–4229.

Fitzgerald, P.G., Baldwin, S.L., Webb, L.E., O'Sullivan, P.., 2006. Interpretation of (U–Th)/He single grain ages from slowly cooled crustal terranes: A case study from the Transantarctic Mountains of southern Victoria Land. Chem. Geol. 225, 91–120.

doi:10.1016/j.chemgeo.2005.09.001
Flowers, R.M., Ketcham, R.A., Shuster, D.L., Farley, K.A., 2009. Apatite (U-Th)/He thermochronometry using a radiation damage accumulation and annealing model. Geochim. Cosmochim. Acta 73, 2347–2365. doi:10.1016/j.gca.2009.01.015
Gautheron, C., Tassan-Got, L., Ketcham, R.A., Dobson, K.J., 2012. Accounting for long alpha-particle stopping distances in (U-Th-Sm)/He geochronology: 3D modeling of diffusion, zoning, implantation, and abrasion. Geochim. Cosmochim. Acta 96, 44–56. doi:10.1016/j.gca.2012.08.016
Hasebe, N., Barbarand, J., Jarvis, K., Carter, A., Hurford, A.J., 2004. Apatite fission-track chronometry using laser ablation ICP-MS. Chem. Geol. 207, 135–145. doi:10.1016/j.chemgeo.2004.01.007
Ketcham, R.A., 2015. Technical Note: Calculation of stoichiometry from EMP data for apatite and other phases with mixing on monovalent anion sites. Am. Mineral. 100, 1620–1623. doi:10.2138/am-2015-5171
Ketcham, R.A., Carter, A., Donelick, R.A., Barbarand, J., Hurford, A.J., 2007. Improved modeling of fission-track annealing in apatite. Am. Mineral. 92, 799–810. doi:10.2138/am.2007.2281
Ketcham, R.A., Donelick, R.A., Carlson, W.D., 1999. Variability of apatite fission-track anneling kinetics: III. Extrapolation to geological time scales. Am. Mineral. 84, 1235–1255.
Ketcham, R.A., Gautheron, C., Tassan-Got, L., 2011. Accounting for long alpha-particle stopping distances in (U-Th-Sm)/He geochronology: Refinement of the baseline case. Geochim. Cosmochim. Acta 75, 7779–7791. doi:10.1016/j.gca.2011.10.011
Murray, K.E., Orme, D.A., Reiners, P.W., 2014. Effects of U-Th-rich grain boundary phases on apatite helium ages. Chem. Geol. 390, 135–151. doi:10.1016/j.chemgeo.2014.09.023
Stockli, D.F., Farley, K.A., Dumitru, T.A., 2000. Calibration of the apatite (U-Th)/He thermochronometer on an exhumed fault block, White Mountains, California. Geology 28, 983. doi:10.1130/0091-7613(2000)28<983:COTAHT>2.0.CO;2
Vermeesch, P., Seward, D., Latkoczy, C., Wipf, M., Gunther, D., Baur, H., 2007. α-Emitting mineral inclusions in apatite, their effect on (U-Th)/He ages, and how to reduce it. Geochim. Cosmochim. Acta 71, 1737–1746. doi:10.1016/j.gca.2006.09.020

Table A1. Summary of AFT age data for sample JP005, Slater River Formation bentonite, Imperial River Section, NWT, Canada

A2Z Sample No.	N_s	Ω_i (cm^2)	P_i (dmnls)	$P_i\Omega_i$	one sigma (dmnls)	$\sigma P_i^2\Omega_i^2$	FT age (Ma)	one sigma (Ma)	Etch Figs.	D_{par} (µm)	U (ppm)	meas. F (apfu)	meas. Cl (apfu)	calc. OH (apfu)	r_{mr0}
Kinetic population #1 (rmr0 < 0.73)															
P1392_017_Ap_A_1_POS_32	20	4.368E-05	0.028	1.204E-06	0.001	8.952E-16	136.0	30.7	4	2.30	3	1.21	0.11	0.68	0.75
P1392_017_Ap_A_1_POS_37	38	4.854E-05	0.043	2.108E-06	0.001	4.661E-15	147.4	24.5	4	2.14	5	1.22	0.13	0.65	0.80
P1392_017_Ap_A_1_POS_17	26	4.368E-05	0.033	1.420E-06	0.001	1.148E-15	149.7	29.7	4	2.31	4	1.24	0.11	0.65	0.75
P1392_017_Ap_A_1_POS_15	25	2.815E-05	0.049	1.379E-06	0.001	1.665E-15	148.3	30.1	4	2.44	5	1.21	0.12	0.67	0.73
P1392_017_Ap_A_1_POS_0	21	4.854E-05	0.025	1.193E-06	0.001	6.776E-16	144.0	31.7	4	1.87	3	1.16	0.09	0.75	0.72
P1392_017_Ap_A_1_POS_3	31	4.854E-05	0.026	1.253E-06	0.001	1.676E-15	201.5	36.9	4	2.19	3	1.21	0.11	0.69	0.71
P1392_017_Ap_A_1_POS_27	44	4.854E-05	0.049	2.356E-06	0.001	2.896E-15	152.7	23.4	3	2.24	5	1.16	0.11	0.73	0.69
P1392_017_Ap_A_1_POS_36	43	3.883E-05	0.057	2.227E-06	0.001	2.113E-15	157.8	24.4	4	2.50	6	1.18	0.11	0.71	0.69
pooled (8) Q =90.2%	**248**	**0**		**0**		**0**	**154.3**	**10.2**		**2.25**		**1.20**	**0.11**	**0.69**	**0.73**
Kinetic population #2 (0.73 < rmr0 < 0.83)															
P1392_017_Ap_A_1_POS_2	17	4.3682E-05	0.029	1.274E-06	0.001	1.221E-15	109.4	26.8	4	2.35	3	1.26	0.10	0.64	0.81
P1392_017_Ap_A_1_POS_4	22	4.8535E-05	0.041	2.007E-06	0.001	2.649E-15	90.0	19.4	4	2.35	4	1.31	0.11	0.58	0.81
P1392_017_Ap_A_1_POS_21	33	4.3682E-05	0.056	2.426E-06	0.001	1.930E-15	111.6	19.6	4	2.20	5	1.34	0.11	0.55	0.81
P1392_017_Ap_A_1_POS_30	23	4.8535E-05	0.034	1.655E-06	0.001	1.339E-15	114.0	24.0	4	2.13	3	1.22	0.11	0.67	0.80
P1392_017_Ap_A_1_POS_29	50	4.8535E-05	0.116	5.634E-06	0.002	8.895E-15	73.0	10.5	4	2.30	12	1.29	0.09	0.63	0.79
P1392_017_Ap_A_1_POS_7	26	4.8535E-05	0.042	2.023E-06	0.001	1.734E-15	105.5	20.9	4	2.14	4	1.44	0.11	0.45	0.78
P1392_017_Ap_A_1_POS_11	7	4.8535E-05	0.011	5.300E-07	0.000	5.282E-16	108.4	41.3	2	2.12	1	1.27	0.09	0.64	0.78
P1392_017_Ap_A_1_POS_14	18	4.8535E-05	0.038	1.832E-06	0.001	2.013E-15	80.8	19.2	4	2.50	4	1.23	0.09	0.68	0.77
P1392_017_Ap_A_1_POS_13	8	4.8535E-05	0.024	1.158E-06	0.001	1.809E-15	56.9	20.3	4	2.21	3	1.34	0.09	0.56	0.77
P1392_017_Ap_A_1_POS_18	36	3.8828E-05	0.123	4.787E-06	0.002	6.267E-15	61.9	10.4	4	2.26	14	1.09	0.11	0.80	0.77
P1392_017_Ap_A_1_POS_1	17	4.8535E-05	0.033	1.620E-06	0.001	1.195E-15	86.2	21.0	4	2.45	4	1.23	0.09	0.68	0.77
P1392_017_Ap_A_1_POS_35	31	4.8535E-05	0.059	2.847E-06	0.001	4.798E-15	89.4	16.3	4	2.22	6	1.16	0.09	0.75	0.76
P1392_017_Ap_A_1_POS_26	18	4.8535E-05	0.036	1.740E-06	0.001	7.615E-16	85.0	20.1	4	2.34	4	1.22	0.11	0.68	0.76
P1392_017_Ap_A_1_POS_12	41	4.8535E-05	0.074	3.582E-06	0.002	5.332E-15	94.0	14.9	4	2.13	7	1.21	0.11	0.69	0.76
P1392_017_Ap_A_1_POS_24	43	4.8535E-05	0.081	3.911E-06	0.001	4.831E-15	90.3	14.0	4	2.25	9	1.13	0.11	0.75	0.75
P1392_017_Ap_A_1_POS_6	38	3.1062E-05	0.104	3.226E-06	0.001	2.119E-15	96.7	15.8	4	2.05	11	1.17	0.15	0.68	0.75
P1392_017_Ap_A_1_POS_10	19	4.8535E-05	0.041	1.975E-06	0.001	3.147E-15	79.1	18.3	4	2.50	4	1.27	0.11	0.61	0.75
P1392_017_Ap_A_1_POS_25	21	4.8535E-05	0.047	2.261E-06	0.001	4.159E-15	76.4	16.9	4	1.94	5	1.25	0.11	0.63	0.74
P1392_017_Ap_A_1_POS_33	75	4.8535E-05	0.099	4.823E-06	0.002	1.097E-14	127.4	15.1	4	2.31	11	1.15	0.10	0.75	0.74
P1392_017_Ap_A_1_POS_34	19	4.3682E-05	0.034	1.490E-06	0.001	1.407E-15	104.6	24.2	4	1.85	3	1.13	0.10	0.77	0.74
P1392_017_Ap_A_1_POS_5	17	4.3682E-05	0.035	1.526E-06	0.001	6.533E-16	91.5	22.3	4	2.19	4	1.16	0.11	0.72	0.74
P1392_017_Ap_A_1_POS_38	12	3.8828E-05	0.024	9.139E-07	0.001	1.801E-15	107.7	31.6	4	2.18	3	1.27	0.13	0.61	0.74
P1392_017_Ap_A_1_POS_23	28	4.8535E-05	0.044	2.120E-06	0.001	3.402E-15	108.3	20.8	4	1.88	5	1.24	0.10	0.66	0.73
P1392_017_Ap_A_1_POS_20	19	4.8535E-05	0.043	2.094E-06	0.001	2.662E-15	74.6	17.3	4	2.57	5	1.30	0.11	0.59	0.73
P1392_017_Ap_A_1_POS_39	46	4.8535E-05	0.112	5.445E-06	0.002	7.005E-15	69.5	10.4	4	2.37	12	1.17	0.09	0.75	0.73
P1392_017_Ap_A_1_POS_22	14	4.8535E-05	0.032	1.547E-06	0.001	2.934E-15	74.4	20.1	4	1.80	3	1.22	0.12	0.67	0.71
P1392_017_Ap_A_1_POS_28	21	4.8535E-05	0.040	1.932E-06	0.001	1.695E-15	89.3	19.6	4	2.35	4	1.23	0.12	0.66	0.62
pooled (27) Q =27.2%	**719**	**0**		**0**		**0**	**89.0**	**3.7**		**2.22**		**1.23**	**0.11**	**0.66**	**0.76**
Kinetic population #3															
P1392_017_Ap_A_1_POS_31	34	3.398E-05	0.148	5.036E-06	0.002	5.841E-15	55.6	9.6	4	2.02	15	1.24	0.11	0.65	0.79
P1392_017_Ap_A_1_POS_16	15	4.854E-05	0.054	2.626E-06	0.002	6.256E-15	47.1	12.3	3	2.02	6	1.27	0.13	0.61	0.72
P1392_017_Ap_A_1_POS_8	20	3.398E-05	0.087	2.963E-06	0.001	1.727E-15	55.6	12.5	4	2.33	9	1.25	0.10	0.65	0.71
pooled (3) Q = -	**69**	**0**	**0**	**0**	**0**	**0**	**53.5**	**6.5**		**2.12**		**1.25**	**0.11**	**0.64**	**0.74**

Note: Ns is the number of spontaneous fission tracks for each apatite. Ω_i is the area overwhich tracks are counted, whereas P_i is the $^{238}U/^{43}Ca$ ratio. Q represents the chi-squared probability for each population. A population passes the chi-squared test if Q > 5%. D_{par} is the diameter of the etch figure parallel to the c axis. F, Cl and OH concentrations were calculated from weight % oxide using the stoichiometric relationships of *Ketcham* [2015], and r_{mr0} was determined using the calculations of *Ketcham et al*. [2007]

modified zeta	8.2727
s.e. (zeta)	0.1407
total decay const.	1.55125E-10
g	1

Table A2. Summary of AFT length data for sample JP005, Slater River Formation bentonite, Imperial River Section, NWT, Canada

A2Z Sample No.	confined length (μm)	angle to c-axis (degrees)	etch figs.	D_{par} (μm)	meas. F (apfu)	meas. Cl (apfu)	calc. OH (apfu)	r_{mr0}
Kinetic Pop #1 (rmr0 < 0.73)								
P1392_017_Ap_A_2_POS_27	12.72	69.24	4	2.83	1.16	0.10	0.74	0.73
P1392_017_Ap_A_2_POS_27	14.45	35.67	4	2.83	1.16	0.10	0.74	0.73
P1392_017_Ap_A_2_POS_35	14.67	80.04	4	2.58	1.29	0.10	0.61	0.72
P1392_017_Ap_A_2_POS_35	15.37	61.66	4	2.58	1.29	0.10	0.61	0.72
P1392_017_Ap_A_2_POS_35	16.03	69.62	4	2.58	1.29	0.10	0.61	0.72
P1392_017_Ap_A_2_POS_0	12.60	53.56	4	2.31	1.16	0.09	0.75	0.72
P1392_017_Ap_A_2_POS_0	14.28	40.65	4	2.31	1.16	0.09	0.75	0.72
P1392_017_Ap_A_2_POS_0	11.97	87.31	4	2.31	1.16	0.09	0.75	0.72
P1392_017_Ap_A_2_POS_31	13.56	23.12	4	2.46	1.35	0.10	0.55	0.70
P1392_017_Ap_A_2_POS_19	16.79	22.37	4	2.54	1.12	0.12	0.76	0.69
P1392_017_Ap_A_2_POS_19	14.81	62.97	4	2.54	1.12	0.12	0.76	0.69
P1392_017_Ap_A_2_POS_19	14.65	76.38	4	2.54	1.12	0.12	0.76	0.69
P1392_017_Ap_A_2_POS_43	15.22	49.20	4	2.40	1.23	0.11	0.66	0.69
P1392_017_Ap_A_2_POS_43	15.17	89.51	4	2.40	1.23	0.11	0.66	0.69
P1392_017_Ap_A_2_POS_43	14.38	62.22	4	2.40	1.23	0.11	0.66	0.69
P1392_017_Ap_A_2_POS_43	14.01	81.14	4	2.40	1.23	0.11	0.66	0.69
P1392_017_Ap_A_2_POS_14	13.79	39.06	3	1.86	1.44	0.12	0.44	0.62
P1392_017_Ap_A_2_POS_14	14.37	59.28	3	1.86	1.44	0.12	0.44	0.62
P1392_017_Ap_A_2_POS_21	15.22	47.80	4	2.41	1.20	0.10	0.70	0.58
P1392_017_Ap_A_2_POS_21	15.59	38.70	4	2.41	1.20	0.10	0.70	0.58
P1392_017_Ap_A_2_POS_21	14.56	84.35	4	2.41	1.20	0.10	0.70	0.58
P1392_017_Ap_A_2_POS_21	13.32	54.10	4	2.41	1.20	0.10	0.70	0.58
P1392_017_Ap_A_2_POS_21	16.46	32.67	4	2.41	1.20	0.10	0.70	0.58
P1392_017_Ap_A_2_POS_21	16.81	7.12	4	2.41	1.20	0.10	0.70	0.58
Ave	**14.62**			**2.42**	**1.23**	**0.11**	**0.67**	**0.67**
SD	**1.26**			**0.22**	**0.09**	**0.01**	**0.09**	**0.06**
Kinetic Pop #2 (0.73 < rmr0 < 0.83								
P1392_017_Ap_A_2_POS_8	15.87	56.59	4	2.36	1.19	0.09	0.72	0.81
P1392_017_Ap_A_2_POS_8	13.59	86.93	4	2.36	1.19	0.09	0.72	0.81
P1392_017_Ap_A_2_POS_8	13.88	23.18	4	2.36	1.19	0.09	0.72	0.81
P1392_017_Ap_A_2_POS_8	13.69	34.40	4	2.36	1.19	0.09	0.72	0.81
P1392_017_Ap_A_2_POS_38	13.88	33.22	4	2.55	1.34	0.11	0.55	0.81
P1392_017_Ap_A_2_POS_38	11.89	80.13	4	2.55	1.34	0.11	0.55	0.81
P1392_017_Ap_A_2_POS_6	13.81	43.54	4	2.77	1.31	0.11	0.58	0.81
P1392_017_Ap_A_2_POS_6	15.49	16.71	4	2.77	1.31	0.11	0.58	0.81
P1392_017_Ap_A_2_POS_6	13.32	59.15	4	2.77	1.31	0.11	0.58	0.81
P1392_017_Ap_A_2_POS_6	11.91	40.78	4	2.77	1.31	0.11	0.58	0.81
P1392_017_Ap_A_2_POS_6	14.20	36.34	4	2.77	1.31	0.11	0.58	0.81
P1392_017_Ap_A_2_POS_6	10.89	76.29	4	2.77	1.31	0.11	0.58	0.81
P1392_017_Ap_A_2_POS_6	13.76	86.22	4	2.77	1.31	0.11	0.58	0.81
P1392_017_Ap_A_2_POS_25	14.88	87.76	4	2.61	1.25	0.11	0.64	0.81
P1392_017_Ap_A_2_POS_25	13.58	82.04	4	2.61	1.25	0.11	0.64	0.81
P1392_017_Ap_A_2_POS_2	11.99	70.99	4	2.37	1.20	0.10	0.70	0.81
P1392_017_Ap_A_2_POS_2	15.03	72.76	4	2.37	1.20	0.10	0.70	0.81
P1392_017_Ap_A_2_POS_2	16.75	62.23	4	2.37	1.20	0.10	0.70	0.81
P1392_017_Ap_A_2_POS_2	12.72	69.73	4	2.37	1.20	0.10	0.70	0.81
P1392_017_Ap_A_2_POS_2	13.84	50.49	4	2.37	1.20	0.10	0.70	0.81
P1392_017_Ap_A_2_POS_2	14.69	63.89	4	2.37	1.20	0.10	0.70	0.81
P1392_017_Ap_A_2_POS_2	14.55	44.88	4	2.37	1.20	0.10	0.70	0.81

A2Z Sample No.	confined length (μm)	angle to c-axis (degrees)	etch figs.	D_{par} (μm)	meas. F (apfu)	meas. Cl (apfu)	calc. OH (apfu)	r_{mr0}
P1392_017_Ap_A_2_POS_2	14.87	34.90	4	2.37	1.20	0.10	0.70	0.81
P1392_017_Ap_A_2_POS_2	15.78	39.53	4	2.37	1.20	0.10	0.70	0.81
P1392_017_Ap_A_2_POS_2	13.30	41.65	4	2.37	1.20	0.10	0.70	0.81
P1392_017_Ap_A_2_POS_2	13.12	84.31	4	2.37	1.20	0.10	0.70	0.81
P1392_017_Ap_A_2_POS_2	13.76	36.65	4	2.37	1.20	0.10	0.70	0.81
P1392_017_Ap_A_2_POS_2	12.96	65.06	4	2.37	1.20	0.10	0.70	0.81
P1392_017_Ap_A_2_POS_24	13.73	31.10	4	2.37	1.25	0.11	0.64	0.81
P1392_017_Ap_A_2_POS_24	15.40	57.46	4	2.37	1.25	0.11	0.64	0.81
P1392_017_Ap_A_2_POS_24	15.79	29.78	4	2.37	1.25	0.11	0.64	0.81
P1392_017_Ap_A_2_POS_24	14.15	33.59	4	2.37	1.25	0.11	0.64	0.81
P1392_017_Ap_A_2_POS_24	15.34	67.21	4	2.37	1.25	0.11	0.64	0.81
P1392_017_Ap_A_2_POS_24	10.71	71.23	4	2.37	1.25	0.11	0.64	0.81
P1392_017_Ap_A_2_POS_24	10.50	50.40	4	2.37	1.25	0.11	0.64	0.81
P1392_017_Ap_A_2_POS_24	14.92	77.31	4	2.37	1.25	0.11	0.64	0.81
P1392_017_Ap_A_2_POS_24	14.18	69.56	4	2.37	1.25	0.11	0.64	0.81
P1392_017_Ap_A_2_POS_12	12.47	65.91	4	2.73	1.25	0.11	0.64	0.81
P1392_017_Ap_A_2_POS_12	12.54	52.33	4	2.73	1.25	0.11	0.64	0.81
P1392_017_Ap_A_2_POS_29	12.34	83.85	4	2.44	1.23	0.11	0.65	0.81
P1392_017_Ap_A_2_POS_29	14.64	41.88	4	2.44	1.23	0.11	0.65	0.81
P1392_017_Ap_A_2_POS_28	15.40	36.67	4	2.57	1.22	0.10	0.68	0.81
P1392_017_Ap_A_2_POS_28	14.27	66.90	4	2.57	1.22	0.10	0.68	0.81
P1392_017_Ap_A_2_POS_28	14.40	49.80	4	2.57	1.22	0.10	0.68	0.81
P1392_017_Ap_A_2_POS_28	11.61	84.41	4	2.57	1.22	0.10	0.68	0.81
P1392_017_Ap_A_2_POS_1	15.81	35.90	4	2.69	1.26	0.10	0.64	0.80
P1392_017_Ap_A_2_POS_1	14.65	23.45	4	2.69	1.26	0.10	0.64	0.80
P1392_017_Ap_A_2_POS_1	11.42	47.81	4	2.69	1.26	0.10	0.64	0.80
P1392_017_Ap_A_2_POS_1	14.23	36.33	4	2.69	1.26	0.10	0.64	0.80
P1392_017_Ap_A_2_POS_1	13.13	55.23	4	2.69	1.26	0.10	0.64	0.80
P1392_017_Ap_A_2_POS_1	11.91	60.09	4	2.69	1.26	0.10	0.64	0.80
P1392_017_Ap_A_2_POS_9	14.87	57.89	4	2.70	1.30	0.12	0.58	0.80
P1392_017_Ap_A_2_POS_9	15.82	58.37	4	2.70	1.30	0.12	0.58	0.80
P1392_017_Ap_A_2_POS_9	13.46	47.40	4	2.70	1.30	0.12	0.58	0.80
P1392_017_Ap_A_2_POS_9	12.65	81.07	4	2.70	1.30	0.12	0.58	0.80
P1392_017_Ap_A_2_POS_9	15.30	42.93	4	2.70	1.30	0.12	0.58	0.80
P1392_017_Ap_A_2_POS_37	14.67	68.52	4	2.27	1.24	0.10	0.66	0.80
P1392_017_Ap_A_2_POS_37	14.19	61.94	4	2.27	1.24	0.10	0.66	0.80
P1392_017_Ap_A_2_POS_37	14.90	34.64	4	2.27	1.24	0.10	0.66	0.80
P1392_017_Ap_A_2_POS_37	13.65	79.40	4	2.27	1.24	0.10	0.66	0.80
P1392_017_Ap_A_2_POS_22	15.72	19.46	4	2.83	1.22	0.10	0.68	0.80
P1392_017_Ap_A_2_POS_22	12.95	73.74	4	2.83	1.22	0.10	0.68	0.80
P1392_017_Ap_A_2_POS_22	15.21	25.58	4	2.83	1.22	0.10	0.68	0.80
P1392_017_Ap_A_2_POS_22	13.20	77.18	4	2.83	1.22	0.10	0.68	0.80
P1392_017_Ap_A_2_POS_13	13.92	29.99	4	2.40	1.26	0.10	0.63	0.80
P1392_017_Ap_A_2_POS_13	13.96	31.87	4	2.40	1.26	0.10	0.63	0.80
P1392_017_Ap_A_2_POS_13	13.79	55.34	4	2.40	1.26	0.10	0.63	0.80
P1392_017_Ap_A_2_POS_13	13.57	41.57	4	2.40	1.26	0.10	0.63	0.80
P1392_017_Ap_A_2_POS_13	14.92	42.03	4	2.40	1.26	0.10	0.63	0.80
P1392_017_Ap_A_2_POS_13	13.54	49.30	4	2.40	1.26	0.10	0.63	0.80
P1392_017_Ap_A_2_POS_13	13.50	36.88	4	2.40	1.26	0.10	0.63	0.80
P1392_017_Ap_A_2_POS_13	12.22	52.77	4	2.40	1.26	0.10	0.63	0.80
P1392_017_Ap_A_2_POS_41	15.87	24.17	4	2.41	1.23	0.10	0.67	0.79
P1392_017_Ap_A_2_POS_41	14.18	50.55	4	2.41	1.23	0.10	0.67	0.79
P1392_017_Ap_A_2_POS_41	14.21	45.59	4	2.41	1.23	0.10	0.67	0.79
P1392_017_Ap_A_2_POS_17	14.26	44.87	4	2.46	1.25	0.12	0.63	0.78
P1392_017_Ap_A_2_POS_17	13.89	52.54	4	2.46	1.25	0.12	0.63	0.78

A2Z Sample No.	confined length (μm)	angle to c-axis (degrees)	etch figs.	D_{par} (μm)	meas. F (apfu)	meas. Cl (apfu)	calc. OH (apfu)	r_{mr0}
P1392_017_Ap_A_2_POS_20	16.35	60.40	4	2.61	1.21	0.11	0.68	0.78
P1392_017_Ap_A_2_POS_20	13.79	20.45	4	2.61	1.21	0.11	0.68	0.78
P1392_017_Ap_A_2_POS_20	13.95	44.27	4	2.61	1.21	0.11	0.68	0.78
P1392_017_Ap_A_2_POS_20	12.23	78.12	4	2.61	1.21	0.11	0.68	0.78
P1392_017_Ap_A_2_POS_20	15.58	24.50	4	2.61	1.21	0.11	0.68	0.78
P1392_017_Ap_A_2_POS_32	14.79	44.04	4	2.48	1.16	0.08	0.77	0.78
P1392_017_Ap_A_2_POS_32	10.69	65.12	4	2.48	1.16	0.08	0.77	0.78
P1392_017_Ap_A_2_POS_32	14.03	59.90	4	2.48	1.16	0.08	0.77	0.78
P1392_017_Ap_A_2_POS_42	13.98	40.41	4	2.44	1.18	0.11	0.72	0.77
P1392_017_Ap_A_2_POS_42	16.01	35.86	4	2.44	1.18	0.11	0.72	0.77
P1392_017_Ap_A_2_POS_42	16.49	43.82	4	2.44	1.18	0.11	0.72	0.77
P1392_017_Ap_A_2_POS_42	12.75	59.83	4	2.44	1.18	0.11	0.72	0.77
P1392_017_Ap_A_2_POS_43	14.15	50.35	4	2.40	1.18	0.11	0.72	0.77
P1392_017_Ap_A_2_POS_15	14.93	52.47	4	2.41	1.22	0.13	0.65	0.77
P1392_017_Ap_A_2_POS_15	11.49	54.02	4	2.41	1.22	0.13	0.65	0.77
P1392_017_Ap_A_2_POS_15	15.67	33.92	4	2.41	1.22	0.13	0.65	0.77
P1392_017_Ap_A_2_POS_15	11.65	68.79	4	2.41	1.22	0.13	0.65	0.77
P1392_017_Ap_A_2_POS_15	13.75	43.77	4	2.41	1.22	0.13	0.65	0.77
P1392_017_Ap_A_2_POS_10	12.35	57.08	4	2.23	1.23	0.10	0.68	0.76
P1392_017_Ap_A_2_POS_10	13.52	29.34	4	2.23	1.23	0.10	0.68	0.76
P1392_017_Ap_A_2_POS_10	14.28	35.65	4	2.23	1.23	0.10	0.68	0.76
P1392_017_Ap_A_2_POS_10	10.38	59.76	4	2.23	1.23	0.10	0.68	0.76
P1392_017_Ap_A_2_POS_4	13.47	65.36	4	2.05	1.29	0.11	0.60	0.76
P1392_017_Ap_A_2_POS_4	15.09	33.23	4	2.05	1.29	0.11	0.60	0.76
P1392_017_Ap_A_2_POS_4	12.42	46.80	4	2.05	1.29	0.11	0.60	0.76
P1392_017_Ap_A_2_POS_4	11.51	74.38	4	2.05	1.29	0.11	0.60	0.76
P1392_017_Ap_A_2_POS_4	13.86	42.83	4	2.05	1.29	0.11	0.60	0.76
P1392_017_Ap_A_2_POS_4	14.93	55.93	4	2.05	1.29	0.11	0.60	0.76
P1392_017_Ap_A_2_POS_4	15.33	41.79	4	2.05	1.29	0.11	0.60	0.76
P1392_017_Ap_A_2_POS_36	13.80	70.55	4	2.55	1.26	0.11	0.62	0.76
P1392_017_Ap_A_2_POS_36	13.17	46.96	4	2.55	1.26	0.11	0.62	0.76
P1392_017_Ap_A_2_POS_36	13.68	53.22	4	2.55	1.26	0.11	0.62	0.76
P1392_017_Ap_A_2_POS_36	13.83	82.90	4	2.55	1.26	0.11	0.62	0.76
P1392_017_Ap_A_2_POS_36	12.99	73.19	4	2.55	1.26	0.11	0.62	0.76
P1392_017_Ap_A_2_POS_36	14.67	27.86	4	2.55	1.26	0.11	0.62	0.76
P1392_017_Ap_A_2_POS_36	12.19	24.37	4	2.55	1.26	0.11	0.62	0.76
P1392_017_Ap_A_2_POS_36	14.58	26.10	4	2.55	1.26	0.11	0.62	0.76
P1392_017_Ap_A_2_POS_11	12.88	68.28	4	2.39	1.08	0.11	0.81	0.75
P1392_017_Ap_A_2_POS_11	13.10	58.09	4	2.39	1.08	0.11	0.81	0.75
P1392_017_Ap_A_2_POS_11	13.60	50.84	4	2.39	1.08	0.11	0.81	0.75
P1392_017_Ap_A_2_POS_11	13.43	69.25	4	2.39	1.08	0.11	0.81	0.75
P1392_017_Ap_A_2_POS_11	12.94	67.27	4	2.39	1.08	0.11	0.81	0.75
P1392_017_Ap_A_2_POS_23	15.05	66.87	4	2.51	1.20	0.09	0.70	0.75
P1392_017_Ap_A_2_POS_23	11.86	67.57	4	2.51	1.20	0.09	0.70	0.75
P1392_017_Ap_A_2_POS_23	15.75	82.64	4	2.51	1.20	0.09	0.70	0.75
P1392_017_Ap_A_2_POS_23	13.41	34.37	4	2.51	1.20	0.09	0.70	0.75
P1392_017_Ap_A_2_POS_23	14.75	47.08	4	2.51	1.20	0.09	0.70	0.75
P1392_017_Ap_A_2_POS_23	15.55	26.15	4	2.51	1.20	0.09	0.70	0.75
P1392_017_Ap_A_2_POS_23	11.28	49.34	4	2.51	1.20	0.09	0.70	0.75
P1392_017_Ap_A_2_POS_33	14.10	78.51	4	2.83	1.30	0.10	0.60	0.75
P1392_017_Ap_A_2_POS_33	12.59	28.96	4	2.83	1.30	0.10	0.60	0.75
P1392_017_Ap_A_2_POS_33	13.65	33.39	4	2.83	1.30	0.10	0.60	0.75
P1392_017_Ap_A_2_POS_26	14.77	68.28	4	2.37	0.08	0.11	1.81	0.75
P1392_017_Ap_A_2_POS_7	14.03	76.44	4	2.54	1.17	0.15	0.68	0.75
P1392_017_Ap_A_2_POS_7	13.17	43.47	4	2.54	1.17	0.15	0.68	0.75

A2Z Sample No.	confined length (μm)	angle to c-axis (degrees)	etch figs.	D_{par} (μm)	meas. F (apfu)	meas. Cl (apfu)	calc. OH (apfu)	r_{mr0}
P1392_017_Ap_A_2_POS_7	14.74	48.84	4	2.54	1.17	0.15	0.68	0.75
P1392_017_Ap_A_2_POS_7	14.33	34.02	4	2.54	1.17	0.15	0.68	0.75
P1392_017_Ap_A_2_POS_7	12.96	46.43	4	2.54	1.17	0.15	0.68	0.75
P1392_017_Ap_A_2_POS_7	14.01	66.39	4	2.54	1.17	0.15	0.68	0.75
P1392_017_Ap_A_2_POS_18	14.42	25.04	4	2.34	1.28	0.12	0.60	0.75
P1392_017_Ap_A_2_POS_18	14.17	47.30	4	2.34	1.28	0.12	0.60	0.75
P1392_017_Ap_A_2_POS_18	14.44	56.37	4	2.34	1.28	0.12	0.60	0.75
P1392_017_Ap_A_2_POS_18	15.79	37.81	4	2.34	1.28	0.12	0.60	0.75
P1392_017_Ap_A_2_POS_18	13.98	32.42	4	2.34	1.28	0.12	0.60	0.75
P1392_017_Ap_A_2_POS_5	15.47	64.08	4	2.15	1.16	0.11	0.72	0.74
P1392_017_Ap_A_2_POS_5	13.57	53.82	4	2.15	1.16	0.11	0.72	0.74
P1392_017_Ap_A_2_POS_30	12.67	75.53	4	2.30	1.24	0.10	0.65	0.73
P1392_017_Ap_A_2_POS_30	16.09	33.73	4	2.30	1.24	0.10	0.65	0.73
P1392_017_Ap_A_2_POS_39	14.23	56.61	4	2.52	1.30	0.11	0.59	0.73
P1392_017_Ap_A_2_POS_39	12.83	66.15	4	2.52	1.30	0.11	0.59	0.73
P1392_017_Ap_A_2_POS_39	13.63	51.80	4	2.52	1.30	0.11	0.59	0.73
P1392_017_Ap_A_2_POS_39	15.53	33.03	4	2.52	1.30	0.11	0.59	0.73
P1392_017_Ap_A_2_POS_39	14.09	32.53	4	2.52	1.30	0.11	0.59	0.73
P1392_017_Ap_A_2_POS_39	14.15	59.96	4	2.52	1.30	0.11	0.59	0.73
P1392_017_Ap_A_2_POS_39	15.59	70.00	4	2.52	1.30	0.11	0.59	0.73
P1392_017_Ap_A_2_POS_39	13.92	53.07	4	2.52	1.30	0.11	0.59	0.73
P1392_017_Ap_A_2_POS_39	15.17	30.13	4	2.52	1.30	0.11	0.59	0.73
P1392_017_Ap_A_2_POS_39	11.73	68.96	4	2.52	1.30	0.11	0.59	0.73
P1392_017_Ap_A_2_POS_34	13.50	44.30	4	2.44	1.15	0.10	0.75	0.73
P1392_017_Ap_A_2_POS_34	13.09	32.78	4	2.44	1.15	0.10	0.75	0.73
P1392_017_Ap_A_2_POS_34	15.33	47.96	4	2.44	1.15	0.10	0.75	0.73
P1392_017_Ap_A_2_POS_34	13.96	42.66	4	2.44	1.15	0.10	0.75	0.73
P1392_017_Ap_A_2_POS_34	16.16	54.63	4	2.44	1.15	0.10	0.75	0.73
P1392_017_Ap_A_2_POS_34	15.02	45.98	4	2.44	1.15	0.10	0.75	0.73
P1392_017_Ap_A_2_POS_34	10.17	72.44	4	2.44	1.15	0.10	0.75	0.73
P1392_017_Ap_A_2_POS_34	13.93	50.00	4	2.44	1.15	0.10	0.75	0.73
P1392_017_Ap_A_2_POS_34	12.87	70.92	4	2.44	1.15	0.10	0.75	0.73
P1392_017_Ap_A_2_POS_34	13.58	46.02	4	2.44	1.15	0.10	0.75	0.73
P1392_017_Ap_A_2_POS_34	14.13	24.11	4	2.44	1.15	0.10	0.75	0.73
P1392_017_Ap_A_2_POS_34	14.04	50.49	4	2.44	1.15	0.10	0.75	0.73
P1392_017_Ap_A_2_POS_34	13.98	89.50	4	2.44	1.15	0.10	0.75	0.73
P1392_017_Ap_A_2_POS_34	13.74	54.89	4	2.44	1.15	0.10	0.75	0.73
P1392_017_Ap_A_2_POS_34	14.26	31.88	4	2.44	1.15	0.10	0.75	0.73
P1392_017_Ap_A_2_POS_34	16.11	56.78	4	2.44	1.15	0.10	0.75	0.73
Ave	**13.89**			**2.47**	**1.22**	**0.11**	**0.67**	**0.77**
SD	**1.33**			**0.17**	**0.10**	**0.01**	**0.11**	**0.03**

Note: D_{par} is the diameter of the etch figure parallel to the c axis. F, Cl and OH concentrations were calculated from weight % oxide using the stoichiometric relationships of *Ketcham* [2015], and r_{mr0} was determined using the calculations of *Ketcham et al*. [2007]

Table A3. Apatite chemistry for all AFT age and length grains, sample JP005, Slater River Formation bentonite, Imperial River section, NWT, Canada

A2Z Sample No.	Na (apfu)	Mg (apfu)	P (apfu)	S (apfu)	Ca (apfu)	Mn (apfu)	Fe (apfu)	Sr (apfu)	Y (apfu)	La (apfu)	Ce (apfu)	K (apfu)	F (apfu)	Cl (apfu)	OH (apfu)	total (apfu)	r_{mr0} Ketcham et al. 2007	r_{mr0} Ketcham et al. 1999	Ca site 10	P site 6	F+Cl+OH 2	TOTAL wt% ox
AFT Age-Grains																						
1392-17-a1-0	0.013	0.016	5.979	0.034	9.718	0.017	0.104	0.003	0.005	0.004	0.011	0.000	1.162	0.093	0.745	17.9	0.716	0.614	9.89	6.04	2	97.95
1392-17-a1-1	0.013	0.016	5.975	0.034	9.799	0.017	0.059	0.003	0.005	0.005	0.012	0.000	1.227	0.090	0.684	18	0.766	0.721	9.93	6.02	2	98.84
1392-17-a1-2	0.013	0.016	6.058	0.034	9.639	0.017	0.000	0.003	0.005	0.004	0.011	0.000	1.265	0.099	0.637	17.8	0.808	0.809	9.71	6.11	2	96.90
1392-17-a1-3	0.013	0.016	6.012	0.035	9.556	0.017	0.106	0.004	0.005	0.005	0.014	0.007	1.207	0.106	0.687	17.9	0.709	0.610	9.74	6.11	2	95.25
1392-17-a1-4	0.013	0.016	6.083	0.034	9.529	0.017	0.000	0.003	0.005	0.005	0.011	0.000	1.309	0.109	0.582	17.8	0.808	0.810	9.6	6.16	2	97.76
1392-17-a1-5	0.013	0.016	5.993	0.035	9.721	0.017	0.076	0.003	0.008	0.006	0.016	0.003	1.163	0.114	0.724	17.9	0.741	0.678	9.88	6.04	2	96.05
1392-17-a1-6	0.014	0.017	5.913	0.036	9.871	0.018	0.062	0.003	0.009	0.007	0.019	0.000	1.170	0.150	0.680	18	0.746	0.697	10.02	5.99	2	94.53
1392-17-a1-7	0.014	0.017	6.274	0.036	9.045	0.018	0.047	0.003	0.006	0.004	0.011	0.000	1.437	0.111	0.453	17.5	0.776	0.751	9.16	6.33	2	92.04
1392-17-a1-8	0.013	0.016	5.886	0.035	9.963	0.017	0.105	0.003	0.011	0.007	0.021	0.004	1.252	0.097	0.650	18.1	0.712	0.616	10.16	5.93	2	97.23
1392-17-a1-10	0.013	0.016	6.032	0.034	9.598	0.017	0.076	0.003	0.006	0.005	0.013	0.000	1.273	0.112	0.615	17.8	0.746	0.685	9.75	6.1	2	97.33
1392-17-a1-11	0.014	0.017	6.264	0.037	9.112	0.018	0.048	0.003	0.003	0.003	0.007	0.000	1.268	0.092	0.641	17.5	0.776	0.741	9.23	6.3	2	89.69
1392-17-a1-12	0.013	0.016	5.900	0.035	9.835	0.017	0.061	0.003	0.007	0.006	0.017	0.009	1.206	0.108	0.686	18	0.758	0.712	9.98	6.01	2	96.41
1392-17-a1-13	0.013	0.016	6.110	0.034	9.430	0.017	0.059	0.003	0.006	0.005	0.014	0.000	1.342	0.094	0.564	17.7	0.767	0.728	9.56	6.17	2	96.91
1392-17-a1-14	0.013	0.016	5.932	0.034	9.846	0.017	0.045	0.003	0.007	0.006	0.018	0.010	1.226	0.091	0.683	18	0.775	0.743	9.98	6.01	2	97.82
1392-17-a1-15	0.013	0.016	6.019	0.034	9.596	0.017	0.087	0.003	0.006	0.005	0.013	0.001	1.214	0.116	0.671	17.9	0.731	0.655	9.76	6.1	2	99.50
1392-17-a1-16	0.013	0.016	6.012	0.035	9.477	0.017	0.091	0.003	0.008	0.007	0.018	0.007	1.265	0.128	0.607	17.8	0.722	0.644	9.66	6.15	2	94.93
1392-17-a1-17	0.013	0.016	6.136	0.034	9.324	0.017	0.075	0.003	0.006	0.005	0.013	0.005	1.244	0.109	0.647	17.7	0.746	0.689	9.48	6.21	2	96.33
1392-17-a1-18	0.014	0.017	6.009	0.036	9.578	0.018	0.047	0.003	0.011	0.007	0.021	0.001	1.089	0.110	0.801	17.8	0.766	0.727	9.72	6.12	2	92.94
1392-17-a1-20	0.013	0.016	5.977	0.034	9.777	0.017	0.090	0.003	0.005	0.004	0.012	0.000	1.303	0.106	0.591	18	0.734	0.660	9.94	6.02	2	97.22
1392-17-a1-21	0.014	0.016	6.015	0.035	9.647	0.018	0.000	0.003	0.005	0.005	0.014	0.007	1.345	0.107	0.548	17.8	0.807	0.811	9.73	6.12	2	94.36
1392-17-a1-22	0.013	0.016	5.913	0.033	9.900	0.017	0.104	0.004	0.006	0.005	0.013	0.000	1.219	0.116	0.665	18	0.711	0.616	10.08	5.96	2	100.85
1392-17-a1-23	0.013	0.016	5.978	0.034	9.712	0.017	0.089	0.003	0.006	0.005	0.014	0.000	1.240	0.097	0.663	17.9	0.735	0.658	9.87	6.05	2	99.41
1392-17-a1-24	0.013	0.016	5.936	0.035	9.816	0.017	0.061	0.003	0.007	0.005	0.015	0.008	1.134	0.114	0.753	18	0.755	0.704	9.96	6.02	2	95.91
1392-17-a1-25	0.013	0.016	6.066	0.034	9.448	0.017	0.074	0.003	0.009	0.007	0.022	0.003	1.253	0.113	0.634	17.8	0.745	0.689	9.61	6.16	2	97.38
1392-17-a1-26	0.013	0.016	5.976	0.034	9.787	0.017	0.059	0.003	0.007	0.006	0.016	0.000	1.215	0.106	0.679	17.9	0.762	0.717	9.92	6.02	2	98.97
1392-17-a1-27	0.013	0.016	5.983	0.034	9.634	0.017	0.118	0.003	0.007	0.004	0.013	0.000	1.163	0.107	0.730	17.9	0.690	0.559	9.83	6.07	2	97.28
1392-17-a1-28	0.013	0.016	5.999	0.035	9.590	0.017	0.150	0.003	0.007	0.005	0.015	0.005	1.228	0.117	0.656	17.9	0.616	0.374	9.82	6.07	2	96.55
1392-17-a1-29	0.013	0.016	5.901	0.034	9.853	0.017	0.030	0.003	0.009	0.007	0.021	0.003	1.286	0.088	0.626	18	0.788	0.771	9.97	6.02	2	97.80
1392-17-a1-30	0.013	0.016	6.065	0.034	9.502	0.017	0.000	0.003	0.006	0.005	0.014	0.008	1.221	0.111	0.668	17.8	0.805	0.804	9.58	6.17	2	96.63
1392-17-a1-31	0.013	0.016	6.064	0.034	9.542	0.017	0.015	0.003	0.010	0.008	0.023	0.000	1.240	0.109	0.651	17.8	0.795	0.787	9.65	6.14	2	98.41
1392-17-a1-32	0.013	0.016	5.944	0.033	9.820	0.017	0.072	0.003	0.005	0.004	0.011	0.008	1.214	0.110	0.676	18	0.748	0.688	9.97	6.01	2	100.92
1392-17-a1-33	0.013	0.016	5.850	0.035	0.021	0.018	0.077	0.003	0.011	0.005	0.014	0.000	1.153	0.098	0.749	18.1	0.744	0.680	10.18	5.93	2	95.76
1392-17-a1-34	0.013	0.016	5.861	0.035	0.067	0.017	0.075	0.004	0.004	0.005	0.013	0.006	1.129	0.103	0.768	18.1	0.744	0.676	10.22	5.91	2	97.87
1392-17-a1-35	0.013	0.016	5.977	0.034	9.726	0.017	0.059	0.003	0.006	0.004	0.012	0.001	1.164	0.088	0.747	17.9	0.764	0.717	9.86	6.06	2	98.49
1392-17-a1-36	0.015	0.018	5.754	0.038	0.110	0.019	0.116	0.003	0.009	0.006	0.018	0.000	1.177	0.112	0.711	18.2	0.687	0.567	10.31	5.9	2	89.34
1392-17-a1-37	0.013	0.016	5.906	0.034	9.996	0.017	0.000	0.003	0.006	0.005	0.012	0.011	1.223	0.126	0.651	18	0.802	0.802	10.08	5.97	2	97.75
1392-17-a1-38	0.014	0.017	5.906	0.035	9.927	0.018	0.077	0.004	0.008	0.006	0.016	0.000	1.267	0.126	0.607	18	0.740	0.678	10.09	5.96	2	95.41
1392-17-a1-39	0.013	0.016	5.908	0.035	9.873	0.017	0.091	0.003	0.008	0.003	0.010	0.003	1.169	0.085	0.746	18	0.733	0.650	10.04	5.99	2	96.77
AFT Length-Grains																						
1392-17-a2-0	0.013	0.016	5.978	0.034	9.717	0.017	0.104	0.004	0.006	0.005	0.012	0.000	1.162	0.093	0.745	17.9	0.715	0.614	9.89	6.04	2	97.98
1392-17-a2-1	0.013	0.016	6.043	0.034	9.615	0.017	0.000	0.025	0.018	0.014	0.015	0.000	1.261	0.098	0.640	17.8	0.804	0.809	9.73	6.1	2	97.48
1392-17-a2-2	0.013	0.016	5.939	0.034	9.915	0.017	0.000	0.004	0.006	0.005	0.012	0.001	1.199	0.104	0.697	18	0.806	0.805	9.99	6	2	97.67
1392-17-a2-4	0.013	0.016	6.057	0.034	9.580	0.017	0.059	0.003	0.005	0.005	0.012	0.013	1.293	0.105	0.602	17.8	0.763	0.722	9.72	6.11	2	98.15
1392-17-a2-5	0.013	0.016	5.993	0.035	9.720	0.017	0.076	0.004	0.008	0.006	0.016	0.003	1.163	0.114	0.724	17.9	0.741	0.678	9.88	6.04	2	96.07
1392-17-a2-6	0.013	0.016	6.080	0.034	9.525	0.017	0.000	0.003	0.006	0.006	0.016	0.000	1.308	0.109	0.583	17.8	0.807	0.810	9.6	6.16	2	97.87
1392-17-a2-7	0.014	0.017	5.909	0.036	9.866	0.018	0.062	0.003	0.012	0.008	0.024	0.000	1.169	0.150	0.680	18	0.745	0.697	10.02	5.99	2	94.66
1392-17-a2-8	0.013	0.016	6.139	0.034	9.397	0.017	0.000	0.004	0.006	0.005	0.014	0.001	1.187	0.090	0.723	17.7	0.808	0.806	9.47	6.21	2	96.85
1392-17-a2-9	0.014	0.017	5.977	0.036	9.720	0.018	0.000	0.004	0.010	0.008	0.022	0.001	1.301	0.122	0.577	17.9	0.803	0.807	9.81	6.08	2	93.04
1392-17-a2-10	0.013	0.016	5.964	0.034	9.789	0.017	0.059	0.004	0.007	0.006	0.017	0.000	1.226	0.095	0.679	18	0.764	0.720	9.93	6.03	2	99.01
1392-17-a2-11	0.013	0.016	5.986	0.035	9.638	0.017	0.061	0.004	0.010	0.008	0.024	0.008	1.076	0.115	0.810	17.9	0.751	0.700	9.8	6.08	2	95.84
1392-17-a2-12	0.013	0.016	6.062	0.035	9.600	0.017	0.000	0.003	0.005	0.004	0.013	0.000	1.250	0.114	0.636	17.8	0.805	0.806	9.67	6.13	2	96.27
1392-17-a2-13	0.013	0.016	6.035	0.034	9.599	0.017	0.015	0.003	0.008	0.007	0.021	0.008	1.262	0.104	0.635	17.8	0.796	0.789	9.71	6.12	2	98.50
1392-17-a2-14	0.016	0.020	5.705	0.043	0.269	0.021	0.149	0.004	0.001	0.009	0.014	0.000	1.437	0.121	0.441	18.3	0.624	0.423	10.5	5.8	2	79.49
1392-17-a2-15	0.013	0.016	5.987	0.034	9.712	0.017	0.044	0.003	0.006	0.005	0.014	0.001	1.225	0.130	0.645	17.9	0.770	0.738	9.83	6.07	2	99.22
1392-17-a2-17	0.013	0.016	6.023	0.034	9.714	0.017	0.030	0.003	0.007	0.005	0.016	0.004	1.250	0.121	0.630	17.9	0.783	0.763	9.82	6.06	2	98.06
1392-17-a2-18	0.013	0.016	6.035	0.034	9.532	0.017	0.074	0.003	0.010	0.007	0.023	0.000	1.284	0.117	0.600	17.8	0.745	0.689	9.69	6.12	2	98.18
1392-17-a2-19	0.014	0.017	5.825	0.036	0.040	0.018	0.110	0.004	0.009	0.007	0.022	0.000	1.122	0.118	0.760	18.1	0.692	0.577	10.24	5.9	2	93.47
1392-17-a2-20	0.014	0.017	5.972	0.036	9.705	0.018	0.031	0.004	0.009	0.008	0.023	0.000	1.215	0.106	0.680	17.9	0.782	0.763	9.83	6.07	2	93.60
1392-17-a2-21	0.013	0.016	6.090	0.034	9.386	0.017	0.162	0.003	0.006	0.005	0.014	0.004	1.202	0.101	0.696	17.8	0.585	0.787	9.62	6.15	2	98.48
1392-17-a2-22	0.013	0.016	5.864	0.034	9.998	0.017	0.015	0.004	0.007	0.006	0.018	0.000	1.220	0.104	0.676	18.1	0.796	0.691	10.09	5.97	2	98.09
1392-17-a2-23	0.013	0.016	5.962	0.034	9.713	0.017	0.074	0.003	0.006	0.005	0.014	0.000	1.204	0.092	0.704	17.9	0.750	0.807	9.86	6.07	2	97.98
1392-17-a2-24	0.013	0.016	6.041	0.034	9.631	0.017	0.000	0.003	0.007	0.006	0.017	0.000	1.253	0.109	0.639	17.8	0.806	0.807	9.71	6.11	2	98.76
1392-17-a2-25	0.013	0.016	5.875	0.035	0.099	0.017	0.000	0.004	0.006	0.004	0.015	0.000	1.247	0.108	0.645	18.1	0.806	0.599	10.17	5.92	2	96.96
1392-17-a2-27	0.013	0.016	5.817	0.034	9.984	0.017	0.088	0.003	0.005	0.004	0.013	0.000	1.162	0.103	0.735	18.1	0.732	0.652	10.14	5.95	2	98.60
1392-17-a2-28	0.013	0.016	6.000	0.033	9.732	0.017	0.000	0.003	0.011	0.008	0.027	0.000	1.218	0.102	0.680	17.9	0.805	0.806	9.83	6.06	2	100.69
1392-17-a2-29	0.013	0.016	6.017	0.034	9.701	0.017	0.000	0.003	0.006	0.004	0.014	0.000	1.234	0.114	0.652	17.9	0.805	0.805	9.77	6.09	2	99.56
1392-17-a2-30	0.013	0.016	5.827	0.034	0.043	0.017	0.088	0.003	0.004	0.003	0.009	0.004	1.244	0.105	0.651	18.1	0.735	0.661	10.2	5.93	2	99.51
1392-17-a2-31	0.013	0.016	5.850	0.034	0.073	0.017	0.118	0.003	0.006	0.005	0.015	0.000	1.349	0.103	0.549	18.2	0.699	0.587	10.27	5.89	2	99.59
1392-17-a2-32	0.013	0.016	6.052	0.034	9.645	0.017	0.044	0.003	0.005	0.004	0.014	0.000	1.156	0.078	0.766	17.8	0.778	0.742	9.76	6.09	2	97.10
1392-17-a2-33	0.013	0.016	6.077	0.034	9.489	0.017	0.074	0.003	0.010	0.007	0.024	0.003	1.295	0.102	0.603	17.8	0.748	0.695	9.66	6.13	2	97.19
1392-17-a2-34	0.013	0.015	6.064	0.033	9.507	0.016	0.088	0.003	0.005	0.004	0.012	0.005	1.151	0.103	0.747	17.8	0.732	0.652	9.67	6.13	2	100.57
1392-17-a2-35	0.013	0.016	6.118	0.034	9.395	0.017	0.103	0.004	0.007	0.005	0.017	0.006	1.293	0.099	0.608	17.7	0.717	0.628	9.58	6.16	2	97.94

A2Z Sample No.	Na (apfu)	Mg (apfu)	P (apfu)	S (apfu)	Ca (apfu)	Mn (apfu)	Fe (apfu)	Sr (apfu)	Y (apfu)	La (apfu)	Ce (apfu)	K (apfu)	F (apfu)	Cl (apfu)	OH (apfu)	total (apfu)	r_{mr0} Ketcham et al. 2007	r_{mr0} Ketcham et al. 1999	Ca site 10	P site 6	F+Cl+OH 2	TOTAL wt% ox
1392-17-a2-36	0.013	0.016	6.001	0.035	9.693	0.017	0.060	0.004	0.005	0.004	0.015	0.000	1.261	0.115	0.624	17.9	0.760	0.715	9.83	6.07	2	95.93
1392-17-a2-37	0.013	0.016	6.044	0.035	9.579	0.017	0.015	0.003	0.006	0.004	0.015	0.000	1.241	0.104	0.656	17.8	0.797	0.788	9.67	6.14	2	96.21
1392-17-a2-38	0.014	0.016	6.016	0.035	9.649	0.018	0.000	0.003	0.005	0.003	0.013	0.007	1.345	0.107	0.548	17.8	0.808	0.811	9.73	6.12	2	94.32
1392-17-a2-39	0.013	0.016	5.973	0.034	9.770	0.017	0.090	0.003	0.008	0.006	0.019	0.000	1.302	0.106	0.592	18.0	0.732	0.660	9.94	6.02	2	97.40
1392-17-a2-41	0.013	0.016	6.090	0.034	9.496	0.017	0.030	0.003	0.005	0.004	0.014	0.000	1.232	0.101	0.666	17.8	0.787	0.766	9.6	6.16	2	97.93
1392-17-a2-42	0.013	0.016	6.040	0.034	9.630	0.017	0.044	0.003	0.005	0.004	0.013	0.002	1.176	0.108	0.717	17.8	0.773	0.737	9.75	6.1	2	96.82
1392-17-a2-43	0.013	0.016	6.047	0.035	9.434	0.017	0.121	0.003	0.007	0.005	0.016	0.005	1.234	0.109	0.656	17.8	0.686	0.559	9.64	6.15	2	96.36

Note: Elemental concentrations in atoms per formula unit (apfu) were calculated from weight % oxide using the stoichiometric relationships of *Ketcham* [2015], and r_{mr0} was determined using the calculations of Ketcham 2007. Na, Mg, S, Mn, Fe, As, Sr, Y, La, Ce, and K were measured using LA-ICP-MS, whereas P, Ca, F and Cl were measured via EPMA.

Table A4. Single grain (U-Th)/He analyses of apatite from the Slater River Formation bentonite, Imperial River Section, NWT, Canada

sample	corr. age (Ma)	err. (Ma)	mod. age (Ma)	mod. err. (Ma)	U (ppm)	Th (ppm)	Sm (ppm)	eU (ppm)	mod. eU (ppm)	mod. err. (ppm)	Th/U	He (nmol/g)	mass (μg)	Ft	ESR (μm)
JP005-1	50.0	3.0	48.5	4.5	19.8	54.9	75.2	32.8	36.3	3.5	2.8	6.2	3.6	0.69	50.2
JP005-2	43.9	2.6	42.3	4.3	9.9	31.6	39.0	17.3	17.9	0.6	3.2	2.8	2.7	0.68	48.3
JP005-3	42.0	2.5	40.4	4.1	21.1	60.9	100.4	35.6	39.7	4.1	2.9	5.1	1.7	0.62	39.6
JP005-4	57.9	3.5	57.2	4.2	12.3	46.6	61.8	23.3	29.1	5.8	3.8	5.2	3.7	0.70	52.2

Note: Corr. Age is the measured (U-Th)/He age, corrected for the effects of alpha ejection (Ft correction; *Farley et al.*, 1996). Err. is the 6% error. Modified age and error account for different alpha ejection caluclations [*Ketcham et al.*, 2011] and variable morphology [*Beucher et al*., 2013; *Brown et al.*, 2013]. eU = [U]+(0.235*[Th]). Modified eU and error investigate the range of eU concentrations expected if the width of the crystallographic b axis was 75% the width of the a axis. ESR is the equivalent radius of a sphere with the same SA/V ratio of the measured apatite grain

Table A5. Assessing the magnitude of [U] zonation required to yield the old AFT dates in kinetic population #1 from apatite in kinetic population #2

Ns	area (cm^2)	zoning of $^{238}U/^{43}Ca$	$^{238}U/^{43}Ca$ (dmnls)	calculated U (ppm)	$P_i\Omega_i$	1 σ (dmnls)	$\sigma P_i^2\Omega_i^2$	FT age (Ma)	1 σ (Ma)
P1392_017_Ap_A_1_POS_35									
31	4.854E-05	1/5 depleted	0.029	3.0	1.424E-06	1.427E-03	4.798E-15	177.7	33.2
31	4.854E-05	4/5 depleted	0.033	3.4	1.582E-06	1.427E-03	4.798E-15	160.1	29.7
31	4.854E-05	3/5 depleted	0.037	3.8	1.780E-06	1.427E-03	4.798E-15	142.5	26.3
31	4.854E-05	2/5 depleted	0.042	4.4	2.034E-06	1.427E-03	4.798E-15	124.9	22.9
31	4.854E-05	1/5 depleted	0.049	5.1	2.373E-06	1.427E-03	4.798E-15	107.2	19.6
31	4.854E-05	Original Value	0.059	6.0	2.847E-06	1.427E-03	4.798E-15	89.4	16.2
31	4.854E-05	1/5 enriched	0.070	7.5	3.417E-06	1.427E-03	4.798E-15	74.6	13.5
31	4.854E-05	2/5 enriched	0.082	8.8	3.986E-06	1.427E-03	4.798E-15	64.0	11.6
31	4.854E-05	3/5 enriched	0.094	10.0	4.556E-06	1.427E-03	4.798E-15	56.0	10.1
31	4.854E-05	4/5 enriched	0.106	11.3	5.125E-06	1.427E-03	4.798E-15	49.8	9.0
31	4.854E-05	5/5 enriched	0.117	12.6	5.695E-06	1.427E-03	4.798E-15	44.9	8.1
P1392_017_Ap_A_1_POS_11									
7	4.854E-05	1/5 depleted	0.005	0.4	2.650E-07	1.427E-03	4.798E-15	214.9	98.8
7	4.854E-05	4/5 depleted	0.006	0.5	2.944E-07	1.427E-03	4.798E-15	193.7	86.3
7	4.854E-05	3/5 depleted	0.007	0.6	3.312E-07	1.427E-03	4.798E-15	172.5	74.6
7	4.854E-05	2/5 depleted	0.008	0.7	3.785E-07	1.427E-03	4.798E-15	151.2	63.5
7	4.854E-05	1/5 depleted	0.009	0.8	4.416E-07	1.427E-03	4.798E-15	129.8	53.2
7	4.854E-05	Original Value	0.011	1.0	5.300E-07	4.735E-04	5.282E-16	108.4	41.3
7	4.854E-05	1/5 enriched	0.013	1.3	6.359E-07	1.427E-03	4.798E-15	90.4	35.6
7	4.854E-05	2/5 enriched	0.015	1.5	7.419E-07	1.427E-03	4.798E-15	77.6	30.2
7	4.854E-05	3/5 enriched	0.017	1.7	8.479E-07	1.427E-03	4.798E-15	67.9	26.3
7	4.854E-05	4/5 enriched	0.020	2.0	9.539E-07	1.427E-03	4.798E-15	60.4	23.3
7	4.854E-05	5/5 enriched	0.022	2.2	1.060E-06	1.427E-03	4.798E-15	54.4	20.9
P1392_017_Ap_A_1_POS_29									
50	4.854E-05	1/5 depleted	0.058	6.1	2.817E-06	1.427E-03	4.798E-15	145.2	21.0
50	4.854E-05	4/5 depleted	0.064	6.8	3.130E-06	1.427E-03	4.798E-15	130.8	18.9
50	4.854E-05	3/5 depleted	0.073	7.7	3.521E-06	1.427E-03	4.798E-15	116.4	16.7
50	4.854E-05	2/5 depleted	0.083	8.8	4.024E-06	1.427E-03	4.798E-15	102.0	14.6
50	4.854E-05	1/5 depleted	0.097	10.3	4.695E-06	1.427E-03	4.798E-15	87.5	12.5
50	4.854E-05	Original Value	0.116	12.4	5.634E-06	1.943E-03	8.895E-15	73.0	10.5
50	4.854E-05	1/5 enriched	0.139	15.0	6.761E-06	1.427E-03	4.798E-15	60.9	8.7
50	4.854E-05	2/5 enriched	0.163	17.5	7.888E-06	1.427E-03	4.798E-15	52.2	7.5
50	4.854E-05	3/5 enriched	0.186	20.0	9.014E-06	1.427E-03	4.798E-15	45.7	6.5
50	4.854E-05	4/5 enriched	0.209	22.5	1.014E-05	1.427E-03	4.798E-15	40.7	5.8
50	4.854E-05	5/5 enriched	0.232	25.1	1.127E-05	1.427E-03	4.798E-15	36.6	5.2

Table A6. Comparison of r_{mt0} values calculated from duplicate D_{par} values measured on the same grain, and their corresponding closure temperature

A2Z Sample No. (age grain)	A2Z Sample No. (length grain)	r_{mt0}[1]	kinetic population no.	measured D_{par} (age grain)	measured D_{par} (length grain)	calc. r_{mt0} (age D_{par})[1]	calc. r_{mt0} (length D_{par})[1]	closure temp. (°C) age D_{par} calc r_{mt0}[1]	closure temp. (°C) length D_{par} calc r_{mt0}[1]	difference	calc. r_{mt0} (age D_{par})[2]	calc. r_{mt0} (length D_{par})[2]	closure temp. (°C) age D_{par} calc r_{mt0}[2]	closure temp. (°C) length D_{par} calc r_{mt0}[2]	difference
P1392_017_Ap_A_1_POS_0	P1392_017_Ap_A_2_POS_0	0.72	1	1.87	2.31	0.82	0.79	105	113	8.00	0.83	0.77	111	128	17.00
P1392_017_Ap_A_1_POS_4	P1392_017_Ap_A_2_POS_6	0.81	2	2.35	2.77	0.79	0.76	112	119	7.00	0.76	0.69	130	143	13.00
P1392_017_Ap_A_1_POS_21	P1392_017_Ap_A_2_POS_38	0.81	2	2.2	2.55	0.80	0.77	110	118	8.00	0.79	0.73	124	136	12.00
P1392_017_Ap_A_1_POS_20	P1392_017_Ap_A_2_POS_39	0.73	2	2.57	2.52	0.77	0.78	116	115	-1.00	0.73	0.74	137	134	-3.00
P1392_017_Ap_A_1_POS_2	P1392_017_Ap_A_2_POS_1	0.81	2	2.35	2.69	0.79	0.76	113	119	6.00	0.76	0.71	129	139	10.00
P1392_017_Ap_A_1_POS_5	P1392_017_Ap_A_2_POS_5	0.74	2	2.19	2.15	0.80	0.80	112	112	0.00	0.79	0.79	123	123	0.00
P1392_017_Ap_A_1_POS_6	P1392_017_Ap_A_2_POS_7	0.75	2	2.05	2.54	0.81	0.78	109	115	6.00	0.81	0.73	117.3	135	17.70
P1392_017_Ap_A_1_POS_19	P1392_017_Ap_A_2_POS_40	-	-	1.93	2.28	0.82	0.80	105	111	6.00	0.82	0.77	115	129	14.00
P1392_017_Ap_A_1_POS_1	P1392_017_Ap_A_2_POS_2	0.77	2	2.45	2.69	0.78	0.76	115	118	3.00	0.75	0.71	131	139	8.00

[1]Multi-compositional calculations of r_{mt0} and conversions from D_{par} to r_{mt0} derived from the annealing kinetics of *Ketcham et al*. [2007]

[2]Conversions from D_{par} to r_{mt0} derived from the annealing kinetics of *Ketcham et al*. [1999]

Closure temperatures calculated for apatites that cool from temperatures >200 °C at a cooling rate of 10 °C/Ma

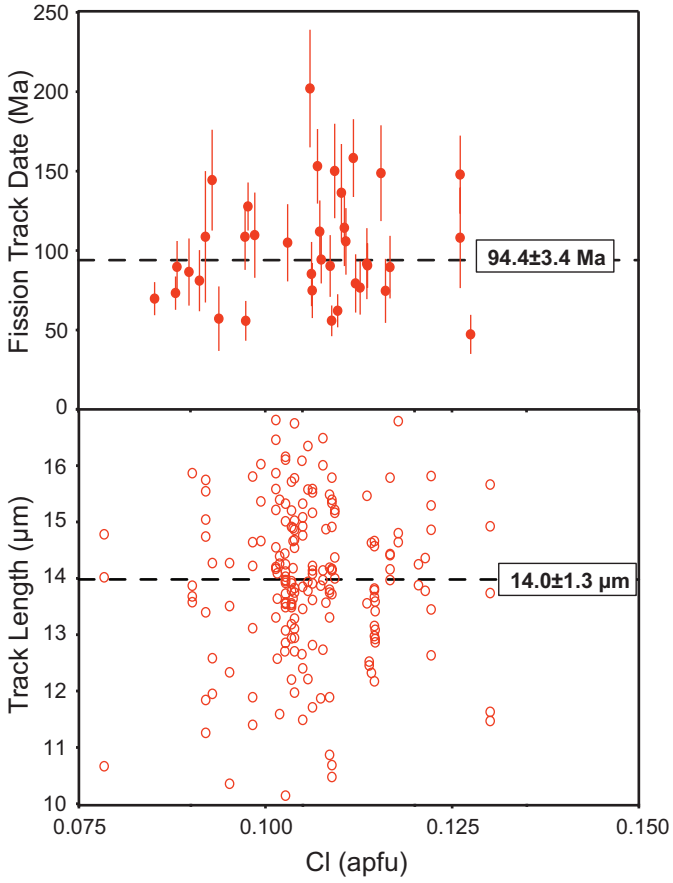

Fig. A1: Apatite fission track date and individual track length data plotted as a function of the kinetic parameter Cl content. Horizontal dashed lines indicate the pooled age (top) and mean track length (bottom) of a population.

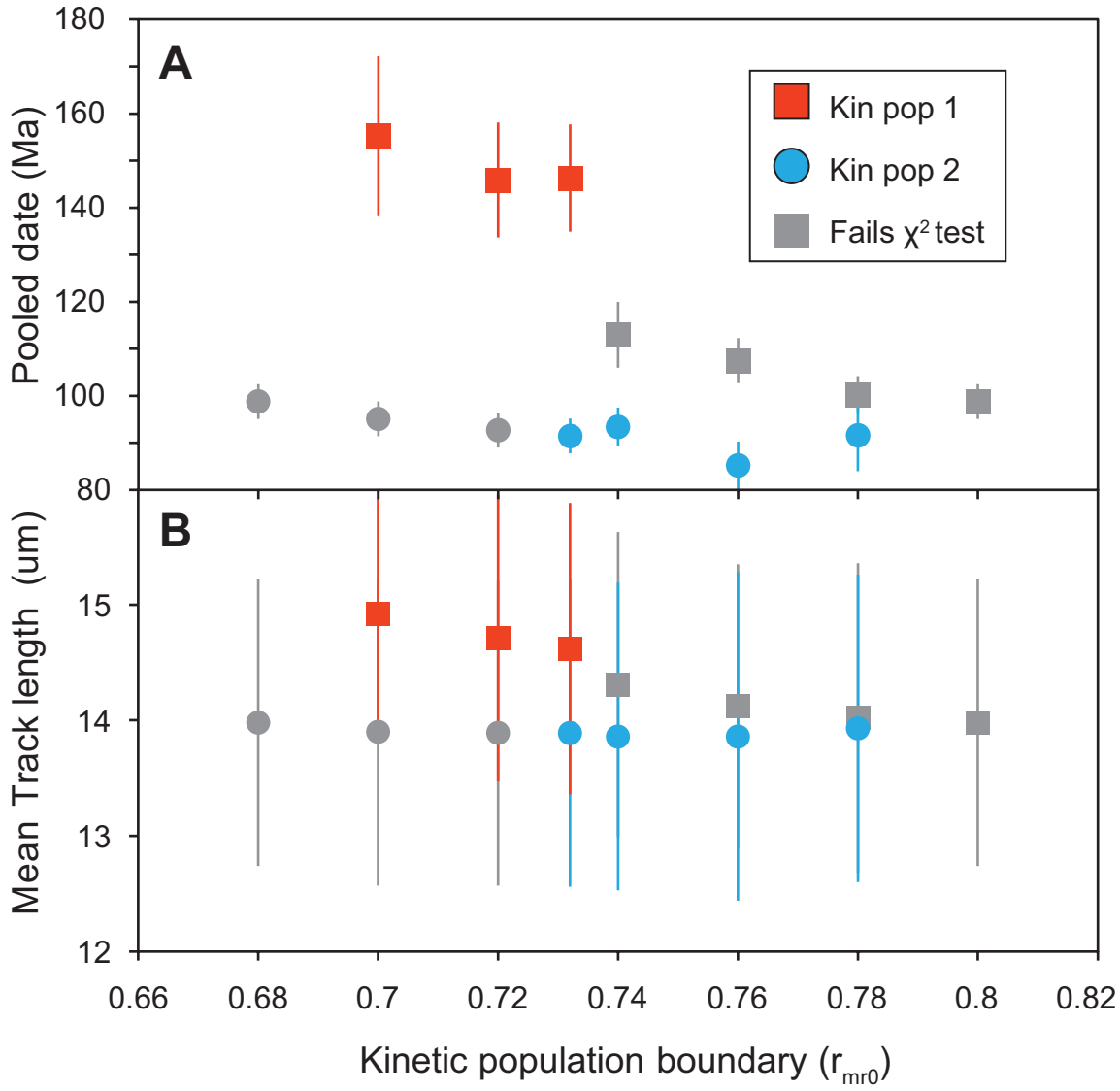

Fig. A2: Diagram assessing the sensitivity of AFT kinetic populations to the r_{mr0} value selected as the kinetic boundary. For each value of r_{mr0}, A) pooled dates, and B) mean track length is calculated from the data with r_{mr0} values less than the boundary (kin pop #1) and greater than the boundary (kin pop #2). Populations that pass the chi-squared test ($\chi^2 > 5\%$) are shown in colour, whereas those that fail are shown in gray. Valid kinetic boundaries require both AFT populations to pass the chi-square test. Dates from AFT population #3 (Fig. 3) were excluded from this test.

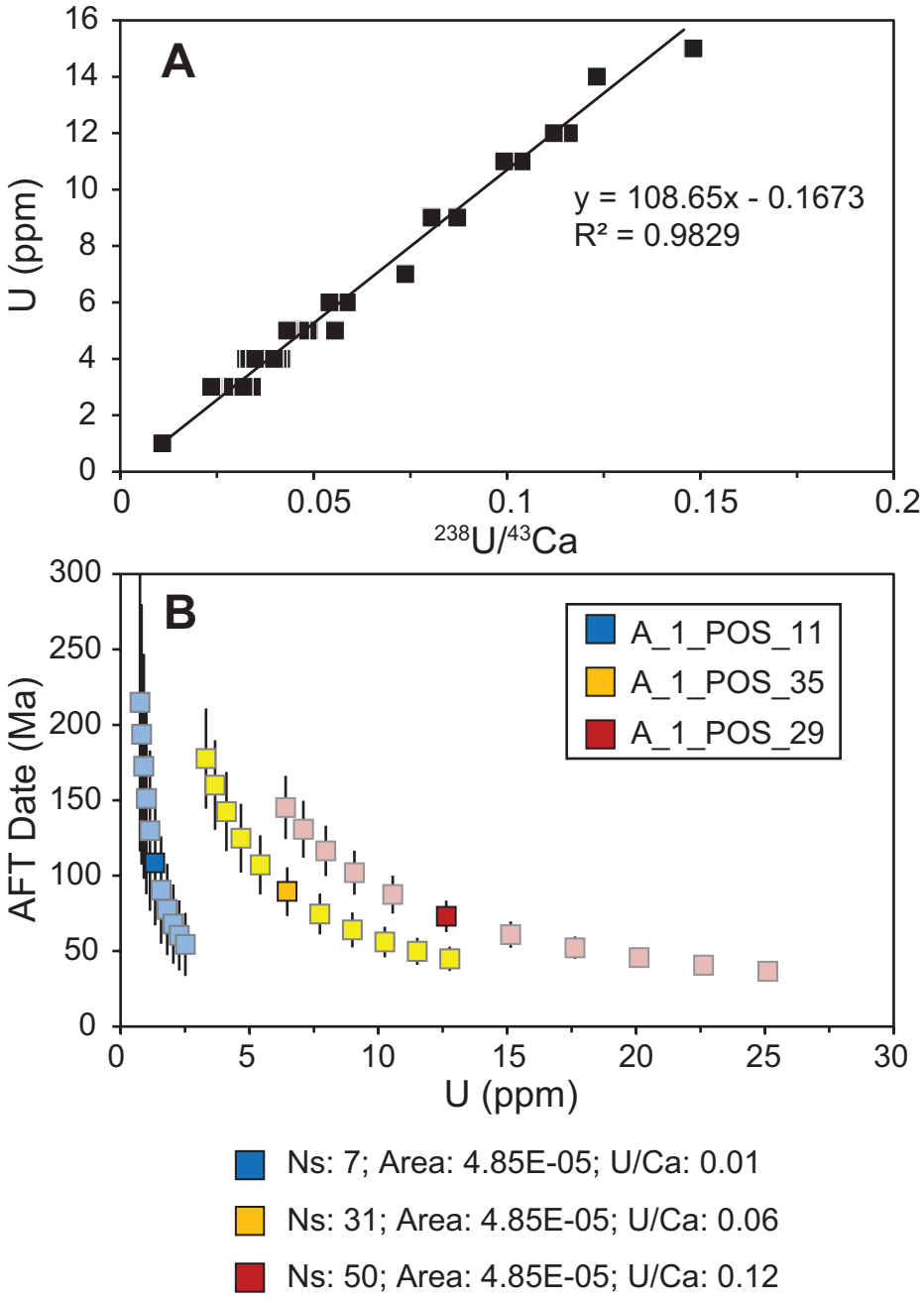

Fig. A3: A) plot of the cation ratio ($^{238}U/^{43}Ca$) used in AFT age determination against apatite-specific uranium concentration. B) diagram showing the effects of uranium zonation on AFT date for 3 grains with varying track densities and uranium content (A_1_POS_11; A_1_POS_35;A_1_POS_29; Table A1). For each apatite, the darker shaded data point outlined in black represents the original AFT date and composition, and lighter shaded data points represent the change in expected AFT date for changing uranium concentrations. Each simulation shows the magnitude of uranium zonation required to change the AFT date of an apatite belonging to kinetic population #2 (89.0 ± 3.7 Ma) to kinetic population #1 (154.3 ± 10.2 Ma) or kinetic population #3 (53.5 ± 6.5 Ma).

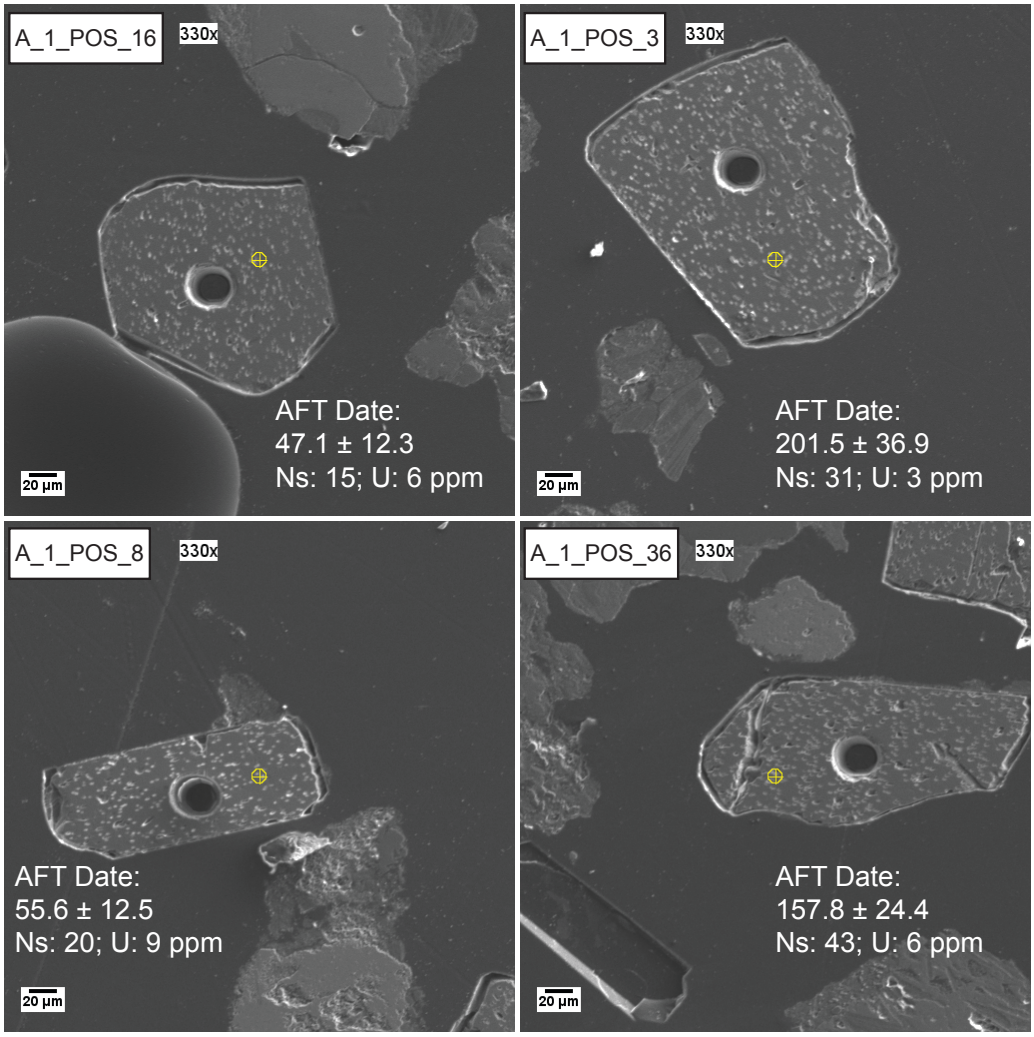

Fig. A4: Images of the grains corresponding to the youngest and oldest AFT dates in this study. Sample numbers correspond with the A2Z sample numbers in Table A1. Yellow spot indicates location of EPMA spot used for chemistry analysis. 330 x magnification.

CHAPTER 4

Thermal history of the Mackenzie Plain, NWT, Canada: insights from low-temperature thermochronology of the Devonian Imperial Formation

Jeremy Powell[1], Dale Issler[2], David Schneider[1], Karen Fallas[2], Daniel Stockli[3]
1. Department of Earth & Environmental Sciences, University of Ottawa, Ottawa, Canada
2. Natural Resources Canada, Geological Survey of Canada, Calgary, Canada
3. Jackson School of Geoscience, University of Texas at Austin, Austin, USA

Submitted to *Chemical Geology*

Abstract

Devonian strata from the Mackenzie Plain of the northern Canadian Cordillera have undergone two major burial and unroofing events since deposition, providing an excellent natural laboratory to assess the effects of protracted cooling history on low-temperature thermochronometers in sedimentary basins. Apatite and zircon (U-Th)/He (AHe, ZHe) and apatite fission track (AFT) thermochronology data were collected from six samples that span the hydrocarbon-bearing plain. Sixteen ZHe dates range from 415 ± 33 Ma to 40 ± 3 Ma, and AHe dates from 53 analyses vary from 225 ± 14 Ma to 3 ± 0.2 Ma. Whereas several samples exhibit correlations between date and radiation damage (eU), all samples demonstrate varying degrees of intra-sample date dispersion. AFT single grain dates from four samples are scattered between the Cambrian and Miocene (485 ± 118 Ma to 9 ± 7 Ma). Although there are no correlations between D_{par} and AFT date or track length distribution, a relationship exists between grain chemistry and age. We calculate the parameter r_{mr0} from apatite chemistry and distinguish up to four discrete kinetic populations per sample, with consistent Triassic-Jurassic, Cretaceous, and Cenozoic pooled ages. Thermal history modeling of AFT and AHe samples reveals that the Devonian strata reached maximum burial temperatures (~120°C–190°C) before Paleozoic to Mesozoic unroofing. Strata were reheated to lower temperatures in the Cretaceous to Paleogene (~100°C), and have a protracted, two-phase Cenozoic. This thermal information is compared with borehole organic thermal

maturity profiles to assess the regional burial history. Ultimately, these data reflect the complications, and possibilities, of low-temperature thermochronology in sedimentary rocks where detrital variance results in a broad range of diffusion and annealing kinetics. We use chemistry-dependent fission track annealing kinetics to explain dispersion in both our AFT and AHe datasets and detail the thermal history of strata that have experienced a protracted cooling history through the uppermost crust.

1. Introduction

Meaningful information on the temperatures experienced by strata during burial is essential in sedimentary basin analysis and petroleum system modeling. Whereas traditional methods of assessing burial history can estimate paleotemperature and eroded thickness, for example shale compaction profiles and organic thermal maturity parameters such as vitrinite reflectance (%Ro) and Rock-Eval pyrolysis (Tmax), these methods cannot directly evaluate the timing of thermal events in the basin. Unconformities further complicate the interpretation of these data, as the thermal effect of multiple packages of eroded material is difficult to quantify [*Feinstein et al.*, 1996]. Low-temperature thermochronology is a useful complement to these traditional methods, as recent advances in the understanding of diffusion and annealing kinetics [*Ketcham et al.*, 1999, 2007; *Flowers et al.*, 2009; *Gautheron et al.*, 2009; *Guenthner et al.*, 2013] allows for the interpretation of a rock's thermal history over a temperature window in accord with sedimentary basin processes [*Armstrong*, 2005].

Sedimentary strata from the Mackenzie Plain of northwestern Canada (Fig. 1) record a dynamic geologic history from the Paleozoic through the Paleogene. Although the Mackenzie Plain is presently covered by foreland basin strata related to Late Cretaceous to Paleogene

evolution of the adjacent Mackenzie Mountains [*Hadlari et al.*, 2014], the unconformities throughout the Cambrian to Paleocene sedimentary succession indicate that episodic burial and exhumation are a common theme through deep time [*MacLean et al.*, 2014]. Understanding the duration and magnitude of these events is especially critical in the hydrocarbon-bearing foreland basin, where the timing of maturation for the Devonian source rock is a major uncertainty for oil and gas exploration [*Issler et al.*, 2005]. However, quantitative thermochronology studies for the region are sparse, and limited to Neoproterozoic strata from the Mackenzie Mountains [*Powell et al.*, 2016], an outcrop sample of an Early Cretaceous bentonite [*Powell et al.*, 2017] and from a single well in the Mackenzie Plain [*Issler et al.*, 2005]. In an effort to better understand the tectonic and thermal evolution of the Mackenzie Plain, samples were collected for zircon and apatite (U-Th)/He (ZHe, AHe) and apatite fission track (AFT) thermochronometry. A strategic sampling transect followed the Mackenzie Mountains deformation front and across the Mackenzie Plain, and targeted outcrops of the Devonian Imperial Formation. This formation is the youngest Paleozoic strata beneath a regional sub-Cretaceous unconformity, and these analyses allow for quantification of the magnitude of the late Paleozoic to early Mesozoic thermal history in comparison with the Late Cretaceous to Paleocene thermal event related to foreland basin development. Moreover, this study illustrates the ways in which pre-depositional history, radiation damage and grain chemistry are manifest in thermochronometer dates from sedimentary strata.

2. Geological Setting

2.1. Stratigraphy

Phanerozoic strata of the Canadian Cordilleran Miogeocline unconformably overlie the Neoproterozoic stratigraphy across the Mackenzie Mountains and Plain of the Northwest

Territories, Canada [*Narbonne and Aitken*, 1995]. These strata record a complex geologic history, including deposition of early to middle Cambrian clastics in rift grabens [*MacLean*, 2011], and the subsequent subsidence and development of a westward-thickening, regional carbonate platform from the late Cambrian to Middle Devonian [*Fritz et al.*, 1991]. The sharp transition between carbonates of the Hume Formation and the basinal siliciclastics of the Horn River Group (Fig. 1) denotes rapid transgression and drowning of the regional carbonate platform [*Gal et al.*, 2009].

The clastic Upper Devonian Imperial Formation records the arrival of thick packages of fine- and coarse-grained detritus from uplifted regions northeast and east of the platform [*Lemieux et al.*, 2011]. In the Mackenzie Plain, these siltstones are thought to represent laterally extensive, southwestwardly prograding, fan-slope deposits. Palynomorph and conodont assemblages indicate that the Imperial Formation is Frasnian-Famennian [*Hadlari et al.*, 2009] and detrital zircon U-Pb analysis shows significant input of c. 500–700 Ma zircons, with additional contribution from Mesoproterozoic, Paleoproterozoic and Archean sources [*Lemieux et al.*, 2011]. Detrital muscovite $^{40}Ar/^{39}Ar$ ages from Imperial Formation are largely between 400–500 Ma, with a smaller population of 575–675 Ma ages, and few Paleoproterozoic grains [*Powell and Schneider*, 2013].

The Imperial Formation is the youngest Paleozoic unit in the Mackenzie Plain, and is separated from overlying Cretaceous strata by a significant regional unconformity [*Feinstein et al.*, 1991b, 1996; *Issler et al.*, 2005]. Cretaceous to Paleocene strata in the Mackenzie Plain can be separated into a locally-eroded Albian package deposited in the flexural margin of the ancestral Mackenzie Mountains foreland basin [*Hadlari et al.*, 2014], and two coarsening-upwards packages deposited in the Cenomanian–Paleocene foredeep of the propagating

Mackenzie Mountains fold-thrust belt [*Thomson et al.*, 2011; *Hadlari et al.*, 2014; *Powell et al.*, 2016].

2.2. Structural geology

The Keele Tectonic Zone [*Maclean and Cook*, 1999] defines a region of crustal instability that extends from north of the Franklin Mountains, through to the Mackenzie Plain and Brackett Basin. This feature, including the Keele Arch, began as a chain of Cambrian grabens and has experienced multiple episodes of subsidence and inversion throughout time, resulting in regional sub-Devonian, sub-Cretaceous and mid-Cretaceous unconformities [*MacLean et al.*, 2014]. Albian to Cenomanian uplift of the Keele Arch has resulted in differential erosion of Albian and underlying Paleozoic strata across the Mackenzie Plain [*Issler et al.*, 2005; *Thomson et al.*, 2011]. Late Campanian to Paleocene deposition in the Brackett Basin (Fig. 1), which is bounded on the west by the Gambill Fault and its subsurface expression as the northeast-trending Gambill Diapir [*Maclean and Cook*, 1999], marks the final phase of enhanced subsidence in the Keele Tectonic Zone [*MacLean et al.*, 2014]. The southern terminus of the Keele Tectonic zone is poorly defined, but likely coincides with the location of the Root Basin (Fig. 1), as this basin subsided to a greater degree throughout the middle and late Paleozoic, and the Keele Tectonic Zone later underwent several episodes of subsidence and uplift not recorded in the Root Basin [*Feinstein et al.*, 1991b].

Present day structures are a product of northeast–southwest Cordilleran compression. Zircon (U-Th)/He thermochronology from Neoproterozoic strata in the Mackenzie Mountains [*Powell et al.*, 2016], and analysis of Cretaceous tectonostratigraphy in the Mackenzie Plain [*Hadlari et al.*, 2014] tracks the propagation of the Mackenzie Mountains fold-thrust belt deformation front to its present location during the Albian/Cenomanian to the Paleocene.

Although low temperature thermochronology resolves the onset of cooling at the Mackenzie Mountains deformation front to 60–55 Ma [*Powell et al.*, 2016], the only constraint on the timing of cooling on Cordilleran structures to the north, such as the Imperial Anticline or Franklin Mountains, is the presence of folded Paleocene strata in the Brackett Basin [*Gordey et al.*, 2011]. Consequently, the temporal connection between ongoing Cordilleran shortening and the transition from deep detachment levels in the Mackenzie Mountains to a shallower level in the Upper Cambrian Saline River Formation in the Franklin Mountains [*Lawton and Isaac*, 2005] remains unclear.

2.3. Thermal history and petroleum potential

Numerous potential hydrocarbon source rocks and petroleum systems exist across the Mackenzie Plain [*Hannigan et al.*, 2011]. Regionally extensive, organic-rich shales include the Middle to Late Devonian Bluefish Member and Canol Formation of the Horn River Group, and the Cenomanian to Coniacian Slater River Formation [*Feinstein et al.*, 1988a, 1991a; *Pyle and Gal*, 2014]. However, the timing of hydrocarbon maturation is a significant regional uncertainty due to the unknown thermal history across sub-Cretaceous and post-Paleocene unconformities. Studies that use organic thermal maturity and shale compaction profiles to resolve the timing of generation suggest that, with exception of the Root Basin, maximum temperatures of Devonian source rocks were achieved in the Cenozoic, with between 1 and 3.5 km of eroded strata [*Feinstein et al.*, 1991a, 1996]. A more significant discontinuity between Cretaceous to Cenozoic and Paleozoic organic thermal maturity profiles in the Root Basin indicates a Paleozoic to Mesozoic thermal maximum. However, such an interpretation requires a spatially and temporally transient geothermal gradient, elevated to 55–65 °C/km in only the Paleozoic Root Basin [*Feinstein et al.*, 1991b], which relaxes to present day values of ~30–40 °C/km [*Majorowicz and*

Morrow, 1998] prior to the Late Cretaceous [*Feinstein et al.*, 1991b]. Contrary to this interpretation, a single apatite fission track study that sampled the Devonian Imperial Formation from a well in the northern Brackett Basin suggested a Triassic to Jurassic thermal maximum of 124 ± 10 °C, followed by Paleocene to Eocene burial to 97 ± 9 °C [*Issler et al.*, 2005].

3. Methods and Results

Six samples were collected from outcrops of the Upper Devonian Imperial Formation within the Mackenzie Plain, along the frontal range of the Mackenzie Mountains in the south, through the Imperial anticline to the Norman Range in the north (Fig. 1). Apatite and zircon grains were separated from the fine-grained siliciclastic rocks using standard mineral separation techniques. Apatite and zircon (U-Th)/He analyses were performed at the University of Texas at Austin following standard laboratory procedures [*Stockli et al.*, 2000; *Wolfe and Stockli*, 2010]. Apatite fission track analyses were conducted using the LA-ICP-MS method [*Hasebe et al.*, 2004; *Donelick et al.*, 2005; *Chew and Donelick*, 2012] by Apatite to Zircon, Inc. Major, minor, trace and rare earth element (REE) apatite chemistry data were collected for each AFT grain using both LA-ICP-MS and EPMA methods, and were used to calculate apatite-specific r_{mr0} values from published relationships between stoichiometric chemical formula and annealing kinetics [*Carlson et al.*, 1999; *Ketcham et al.*, 1999]. Full analytical conditions are described in detail in the Appendix to the Chapter.

3.1. Apatite and zircon (U-Th)/He thermochronology

Apatite and zircon (U-Th)/He thermochronology measures radiogenic ^{4}He produced during the decay of ^{238}U, ^{235}U, ^{232}Th and ^{147}Sm. Diffusion of helium in apatite and zircon is thermally controlled, occurring readily at high temperatures. These minerals become increasingly

retentive of radiogenic helium as they cool through low-temperatures in the uppermost crust [*Harrison and Zeitler*, 2005]. Although many studies invoke closure temperatures of ~70 °C [*Farley*, 2000] and ~185 °C [*Reiners et al.*, 2002; *Wolfe and Stockli*, 2010] for the AHe and ZHe systems, respectively, this concept requires a monotonic cooling history from open to closed system [*Reiners and Brandon*, 2006]. As a result, the closure temperature concept, and the idea of an AHe or ZHe cooling age, is not of much use when applied to thermochronology of sedimentary basins, where strata reside for long durations at temperatures below 200 °C, in which apatite and zircon may be partially retentive of radiogenic helium.

In addition to cooling rates, grain size and radiation damage also control diffusion kinetics of helium in apatite and zircon [*Farley*, 2002]. In apatite, the accumulation of radiation damage in the crystal structure results in an AHe system that is increasingly retentive of radiogenic helium [*Shuster et al.*, 2006; *Flowers et al.*, 2009; *Gautheron et al.*, 2009]. In the ZHe system, zircon becomes more retentive of helium with increasing radiation damage, until a threshold amount of damage is reached. Beyond this threshold, progressive radiation damage to the crystal structure results in a substantial decrease in the retention of radiogenic helium [*Guenthner et al.*, 2013]. A relative proxy for radiation damage is the grain-specific effective uranium concentration (eU = [U] + 0.235 • [Th]; Flowers et al., 2009), which is integrated over the time spent below temperatures corresponding with fission track annealing in apatite and zircon [*Flowers et al.*, 2009; *Guenthner et al.*, 2013] to assess the effect of damage accumulation on helium diffusion. Since apatite fission track annealing kinetics vary with composition [*Green et al.*, 1986; *Carlson et al.*, 1999; *Barbarand et al.*, 2003], apatite chemistry must be understood to quantify relationships between AHe date and eU [*Gautheron et al.*, 2013]. Interpretation of AHe and ZHe dates from sedimentary rocks is complicated due to intra-sample variability of

grain size [*Beucher et al.*, 2013; *Brown et al.*, 2013], chemistry [*Gautheron et al.*, 2013; *Djimbi et al.*, 2015] and radiation damage, compounded with the effects of an unknown pre-depositional thermal history of the accessory minerals [*Guenthner et al.*, 2015].

A suite of 53 single-grain AHe dates was collected from six Imperial Formation samples. Sixteen ZHe dates were acquired from three Imperial Formation samples in which zircon grains were present (Table 1). ZHe dates for the Imperial Formation span 39.9 ± 3.2 Ma to 414.7 ± 33.2 Ma. The four ZHe dates in sample JPCPC3 appear to form two disparate populations (39.9 ± 3.2 to 49.7 ± 4.0 Ma; 271.9 ± 21.8 to 300.7 ± 24.1 Ma). However, this observation may be a function of the limited number of grains, since ZHe dates from samples 10FNA066 and Husky6 are more broadly distributed (Fig. 2). Although AHe dates from all samples range from 3.2 ± 0.2 Ma to 224.9 ± 13.5 Ma, a majority of dates fall between 15.0 ± 0.9 Ma and 67.2 ± 5.4 Ma (Table 1). Samples 10FNA066 and 10FNARL008 both exhibit positive correlations between AHe date and radiation damage, as AHe dates systematically increase with eU concentration. Relationships between AHe date and eU are equivocal to non-existent for the other four samples in the dataset (Fig. 2). In general, the apatite grains analyzed for this study were relatively small, with equivalent spherical radii (ESR) between 26.1 and 44.7 μm. No correlations were observed between AHe date and crystal size (Table 1).

3.2. Apatite fission track thermochronology

Apatite fission-track thermochronology is a technique that measures the density and length of linear damage zones in the apatite crystal lattice that form continuously from the spontaneous fission of ^{238}U [*Donelick et al.*, 2005]. Thermal annealing of damage zones in the apatite crystal lattice results in the shortening of track length and decrease in fission track density with increasing temperature [*Green*, 1988]. The kinetics of fission track annealing are known to

be heavily influenced by apatite chemistry, with fission tracks in fluorapatite being less resistant to thermal annealing than fission tracks in chlorapatite [*Green et al.*, 1986]. Additionally, both the presence of hydroxyl and cation substitutions may result in an increase in fission track retentivity [*Carlson et al.*, 1999; *Barbarand et al.*, 2003]. Apatite fission track thermochronology is particularly useful when applied to sedimentary basin analysis, as patterns in AFT date, track length distribution and annealing kinetics can be quantified to evince the thermal history of rocks through ~50–150 °C, temperatures that span the oil and gas generation window [*Armstrong*, 2005; *Donelick et al.*, 2005; *Issler et al.*, 2005].

Fission track annealing kinetics are most commonly characterized through kinetic parameter D_{par}, which is an optical measurement of mean maximum diameter of the fission track etch pit [*Burtner et al.*, 1994]. D_{par} and resistance to thermal annealing are thought to be positively correlated [*Donelick et al.*, 2005], however this relation can be spurious, as apatite with D_{par} greater 1.75 μm are not always more resistant to thermal annealing than those with lower values [*Carlson et al.*, 1999; *Donelick et al.*, 2005]. The kinetic parameter r_{mr0}, a measurement of the relative resistance to thermal annealing of any apatite to that of the most-resistant apatite within a dataset [*Ketcham et al.*, 1999], is a possible alternative to characterizing annealing kinetics with D_{par} (Powell et al., 2017). This parameter becomes increasingly useful when apatite specimens with well-characterized chemistry and annealing kinetics are fitted to the most resistant apatite in laboratory studies, the B2 apatite of Bamble, Norway [*Ketcham et al.*, 1999]. Doing so creates a multi-kinetic model that allows annealing kinetics of any analyzed apatite to be quantified on the basis of its chemistry [*Carlson et al.*, 1999; *Ketcham et al.*, 2007].

Of the six samples analyzed for apatite (U-Th)/He analysis, four yielded sufficient apatite for fission track analysis (Table 2). Single grain AFT dates from the Imperial Formation vary

from 9.2 ± 6.5 Ma to 484.9 ± 118.4 Ma. Additionally, we report four 0 Ma ages, as these grains have chemistry consistent of apatite (Table A3) but no observed spontaneous tracks (Table A1). Each sample exhibits substantial dispersion in AFT dates, and fails the c^2 test, indicating that the data do not comprise a single, statistically significant kinetic population [*Green*, 1981]. Different kinetic populations cannot be separated on a basis of AFT date, track length and D_{par}. Instead, we identify kinetic populations for each sample on a basis of relationships between AFT date, track length and the kinetic parameter r_{mr0} (Fig. 3) and by examining grain age distributions on radial plots (Figs. A1-A4). Apatite-specific r_{mr0} values were calculated from grain chemistry (Table A3) following the relationship of *Carlson et al.* [1999], and vary from 0.48 to 0.87 in this dataset. In general, AFT dates decrease with increasing r_{mr0}, and boundary r_{mr0} values between kinetic populations were selected on a basis of major changes in AFT date within a sample. Each of these kinetic populations pass the c^2 test (Q > 5%) and have corresponding pooled ages and track length distributions (Table 2, Fig. 3).

Overlap between kinetic populations is present in varying degrees in each sample, especially near the boundary between kinetic populations, due to the accuracy to which r_{mr0} values can be calculated and to uncertainties with application of the kinetic annealing model to apatite from natural settings. AFT dates that overlap with different kinetic populations than predicted are incorporated with similar age grains when calculating pooled ages and χ^2 statistics. Overall, two to four kinetic populations were identified for each sample with consistent Triassic to Jurassic (170.1 ± 24.7 Ma; 224.1 ± 14.5 Ma; 225.4 ± 31.0 Ma; 240.7 ± 21.5), Cretaceous (85.9 ± 6.9; 100.6 ± 10.1 Ma), Eocene (50.2 ± 2.9 Ma; 45.7 ± 4.1 Ma; 46.0 ± 3.1 Ma; 55.0 ± 6.8 Ma) and Oligocene to Miocene (11.2 ± 6.5 Ma; 26.6 ± 5.7 Ma) pooled ages (Table 2). AFT date, track length and chemistry data are available in the Appendix to this Chapter.

4. Thermal History Modeling

Interpretation of geologic and thermal histories from low temperature thermochronology datasets is complicated by the variation in detrital grain chemistry, radiation damage, size and pre-depositional thermal history. These factors are compounded by the unknown magnitude of material deposited and eroded across several unconformities and their influence on fission track annealing and helium diffusion. Whereas a modeling approach that combines all data would be preferable, too many unconstrained variables prevent marrying the datasets. Instead, we follow an approach that uses the unique temperature sensitivity and kinetics of each system to address pertinent questions on thermal history. Our approach uses the ZHe system to test plausible maximum temperatures across the Mackenzie Plain. Multi-kinetic AFT modeling addresses sample-specific thermal history, and evaluates the magnitude of heating and cooling related to Late Devonian-Albian burial and unroofing in comparison with the Cretaceous to Paleocene thermal event. Finally, AHe modeling refines the thermal history from the Cretaceous to present, and addresses the timing and rates of the most recent cooling episode.

4.1. ZHe thermal history modeling

Due to the relatively small number of analyses and similar range of dates, we combine all three ZHe samples together to test plausible maximum temperatures experienced by the Imperial Formation throughout the Mackenzie Plain (Fig. 4). Whereas the zircon radiation damage and annealing model predicts that the thermal history of a sample should produce a diagnostic trend between ZHe date and eU concentration [*Guenthner et al.*, 2013, 2014], ZHe date-eU trends from sedimentary samples with diverse provenance may be complex due to the effects of varied pre-depositional histories and the unknown amount of inherited radiation damage accumulated prior to deposition (Guenthner et al., 2015; Powell et al., 2016). In an effort to isolate these

variables and assess probable post-depositional thermal history, we follow the "inheritance envelope" approach of *Guenthner et al.* [2015]. In this method, ZHe date-eU curves are generated for a given post-depositional thermal history from a range of pre-depositional inheritance histories (zero inheritance = depositional age; maximum inheritance = oldest U-Pb age). The inheritance envelope describes the region of date-eU space bounded by these curves.

We use the thermochronology modeling software HeFTy (Ketcham, 2005; version 1.9.1) to evaluate the *Issler et al.* [2005] model of a Devonian to Jurassic thermal maximum to determine whether our ZHe data are best explained by 100 °C, 150 °C, or 200 °C maximum burial temperatures (Fig. 4). In all three models, maximum Paleocene temperatures attain 100 °C [*Issler et al.*, 2005]. The zero-inheritance (375 Ma) and maximum inheritance (2750 Ma) curves illustrate the extremely variable relationship between temperature, pre-depositional history and predicted ZHe dates. At 100 °C (Fig. 4a), zircon with no pre-depositional history (blue curve) are only partially reset and exhibit a very rapid increase between ZHe date and radiation damage, reaching an age plateau at c. 350 Ma. Comparatively, zircon that have been accumulating radiation damage for the maximum duration allotted from U-Pb studies (red curve) exhibit a negative correlation between ZHe date and eU. Predicted ZHe dates in the red curve are older than deposition until ~300 ppm eU and then rapidly decrease with increasing radiation damage. Temperatures of 200 °C (Fig. 4c) are sufficient to fully reset zircon with zero-inheritance, yielding a c. 250 Ma date. However, these temperatures are not sufficient to fully reset all of the ZHe dates in the maximum inheritance curve. This model predicts that zircon will be very retentive of helium until a threshold amount of radiation damage is reached (~50 ppm) at which point increasing radiation damage results in progressively more diffuse zircon and younger ages.

These time-temperature histories are considered plausible if the observed ZHe date-eU variability falls within the modeled inheritance envelope. Based on the three time-temperature histories, our modeling suggest regional maximum temperatures were closer to 150 °C (Fig. 4b), as the inheritance envelopes for 100 °C (Fig. 4a) and 200 °C (Fig. 4c) cannot account for much of the observed ZHe date dispersion. Although three ZHe dates are younger than predicted from any of the inheritance envelopes, it is plausible that these zircons are chemically zoned. Parent zonation in zircon may result in systematically younger ZHe dates than predicted by date-eU modeling [*Guenthner et al.*, 2013].

4.2. AFT thermal history modeling

Multi-kinetic fission track inverse thermal history modeling provides the unique opportunity to derive plausible time-temperature histories from different statistical AFT kinetic populations within a single sample. Since each population has its own diagnostic relationships between fission track date, track length and kinetic parameter r_{mr0} (Fig. 3), individual populations serve as separate thermochronometers that are sensitive to different temperature regimes. This is particularly useful for our study, as different populations will resolve the thermal history between the Devonian and Albian and from the Late Cretaceous to present. We used an updated version of the software AFTINV [*Issler*, 1996] to quantify the time-temperature implications of these relationships.

For every sample, an r_{mr0} value was selected to represent the overall annealing kinetics of each AFT population. In all cases, the least retentive AFT populations were modeled with r_{mr0} values between 0.87 and 0.89. This range of kinetics predicts annealing at significantly lower temperatures than standard fluorapatite (0.83 r_{mr0}). Comparatively, the oldest populations in each sample were modeled with very retentive kinetics (JPCPC3, JPCPC4, 10FNARL008: 0.69-0.74

r_{mr0}; Husky7: 0.43 r_{mr0}) which allow for fission track stability at much higher temperatures than predicted by standard annealing kinetics [*Ketcham et al.*, 1999]. All models search for a random pre-depositional cooling history from 500 Ma to the time of deposition at 375 Ma. Following deposition, the model searches for: 1) a single heating and cooling event between 375 Ma and 110 Ma, to account for material deposited and eroded across the Devonian to Albian unconformity; 2) a heating and cooling event related to deposition and erosion of Albian to Cenomanian strata (110 Ma–95 Ma); 3) a heating and cooling event between 95 Ma to 0 Ma associated with burial and unroofing of the foreland basin in front of the emerging Mackenzie Mountains. Our model limits heating and cooling rates to 10 °C/m.y. (375 Ma–110 Ma; 110 Ma–95 Ma) and 15 °C/m.y. (95 Ma–0 Ma) to rule out geologically inadmissible thermal histories and randomizes these rates over 2.5 m.y. intervals.

Inverse thermal history modeling of sample JPCPC3 (Fig. 5) yields peak temperatures of 135 °C to 157 °C between the Permian and Early Cretaceous. The long track lengths of the most retentive AFT population suggest limited thermal annealing during Cretaceous to Paleocene burial, constraining peak temperatures of this thermal event to 65 °C to 85 °C. Model retention ages, which denote the age of the oldest track length, indicate that the younger kinetic population was fully annealed by both thermal events and began to retain fission tracks at 60 Ma, whereas the older population was only partially annealed during both burial episodes. Although the modeled %Ro (0.83 ± 0.08) is greater than the measured value for this sample (0.70 %Ro; Table A4), the sample was organically lean and the value was based on a small number of measurements. Instead, the modeled value is closer to the 0.87 %Ro equivalent calculated from Rock-Eval Tmax values from the underlying Horn River Group at the same location [*Jiang et*

al., 2014], and in agreement with regional trends in the Mackenzie Plain [*Feinstein et al.*, 1991b].

Despite the identification of three kinetic populations in sample JPCPC4 (Fig. 3), only two are incorporated in the model. Although inverse thermal history modeling can satisfy any two of these populations with one another, the track length, AFT date and r_{mr0} range of the three are incompatible, possibly related to the mixing of apatite grains between populations. We opt to model the better resolved oldest and youngest kinetic populations, as similarly pooled ages are present in all of our AFT samples. Our model (Fig. 5) indicates that JPCPC4 reached maximum temperatures of 119 °C to 153 °C sometime between the Mississippian and Late Jurassic/Early Cretaceous, and was reheated to temperatures between 80 °C and 97 °C in the Late Cretaceous to Paleocene. Retention ages indicate that the youngest AFT population was totally reset and began to retain fission tracks at 50 Ma, whereas the oldest population was only partially annealed following deposition. Although the intermediate age population was not modeled, it is probable that these grains were totally reset by the pre-Cretaceous thermal maximum and only partially annealed during the second thermal event. The modeled 0.74 ± 0.04 %Ro is just above the 0.66 %Ro equivalent calculated from bitumen reflectance (Table A4**)**.

Model results for sample 10FNARL008 indicate less of a difference between the relative magnitude of pre-Cretaceous and Late Cretaceous–to-present thermal maxima (Fig. 5). In this model, burial continues following the Devonian and reaches temperatures of 100 °C to 154 °C between the Mississippian and Middle Triassic, and 109 °C to 137 °C in the Late Cretaceous to Eocene. Retention ages for the youngest population indicate that the sample had only cooled to temperatures sufficient to retain fission tracks by 25 Ma. The 70 Ma retention age for the intermediate AFT date (46.0 ± 3.1 Ma) population indicates that the population was totally

annealed by burial in the Cretaceous to Paleocene foreland basin. The modeled retention age for the oldest population suggests only partial thermal annealing following deposition. The modeled %Ro value of 0.74 ± 0.05 agrees with the 0.74% Ro equivalent measured from bitumen reflectance (Table A4).

The four kinetic populations in sample Husky7 yield the most tightly constrained thermal history (Fig. 5). Inverse thermal history modeling of this sample reveals a thermal maximum of 165 °C to 190 °C between the Late Pennsylvanian and Late Triassic, and temperatures of 92 °C to 108 °C during Late Cretaceous to Eocene reheating. Retention ages indicate that the youngest two populations were fully annealed during both thermal events. The intermediate AFT date population (100.6 ± 10.1 Ma) has shortened track lengths and a retention age (174 Ma) that suggests total annealing during the pre-Cretaceous thermal maximum, and partial annealing during subsequent heating. The most retentive population (240.7 ± 21.5 Ma) was only partially annealed following deposition. The modeled 1.75 ± 0.18 %Ro is in good agreement with the 1.67 %Ro measured from nearby Husky6 sample.

4.3. AHe thermal history modeling

Whereas multi-kinetic AFT modeling provides critical information on the relative magnitude of each thermal event, the temperature sensitivity of the AHe system allows for a greater resolution on the most recent thermal history of the Imperial Formation throughout the Mackenzie Plain. To understand this history, we performed inverse and forward thermal history modeling using HeFTy (Ketcham, 2005; version 1.9.1). Each inverse history model has specified time-temperature constraints through which the generated time-temperature paths must pass. These constraints are defined using independent geologic information from preserved Cretaceous and Paleocene stratigraphy and known unconformities across the region [*Yorath and Cook*, 1981;

Dixon, 1999; *Thomson et al.*, 2011; *Hadlari et al.*, 2013], and thermal history information from AFT modeling (Fig. 5). Two to three grains were chosen for modeling from each sample. These grains were selected to capture the realm of AHe date, eU and grain size variations within a given sample. Since the chemistry of each apatite is unknown, radiation damage annealing was modeled assuming a standard fluorapatite composition and r_{mr0} value of 0.83. Organic thermal maturity data for each sample were incorporated into modeling to constrain maximum temperatures.

Inverse thermal history modeling for samples JPCPC3 and JPCPC4 (Fig. 6) requires Cretaceous to Paleocene burial temperatures in excess of 80 °C and 70 °C, respectively, in the foreland basin to explain the observed AHe date-eU variation in the modeled apatite. Good fit data from both models indicate that cooling began at latest by the end of the Paleocene, and that the strata had cooled to temperatures below resolution of the AHe data by c. 40 Ma. No AFT data exists to constrain the realm of plausible Cretaceous to Paleocene temperatures for samples 10FNA066 and JP019 from the Imperial anticline and Norman Range, so the AHe-modeled ~130 °C maximum are the only data on Cretaceous to Paleocene temperatures for this part of the Mackenzie Plain (Fig. 6). Inverse thermal history models for 10FNA066 and JP019 are similar to JPCPC3 and JPCPC4 in that they resolve the onset of cooling to be at latest in the Paleocene. However, they exhibit a more protracted cooling history, residing at temperatures between ~40 °C–80 °C during most of the Paleogene. In comparison, model results for sample 10FNARL008 and Husky7 reveal a two-phased cooling history, recording an initial Paleocene cooling event, followed by isothermal conditions throughout the Eocene and a final cooling event beginning in the Oligocene to Miocene (Fig. 6).

Since the inverse thermal history models (Fig. 6) were generated using a small subset of apatite grains from each sample and an assumed fluorapatite chemistry, we use forward modeling to understand whether these time-temperature solutions can account for the observed variation between AHe date, eU, grain size and radiation damage annealing kinetics. To increase the amount of grains per forward model, we grouped proximal samples from similar structural settings (Fig. 7). To simplify the forward models, timing of maximum Cretaceous to Paleocene burial is assumed to be 60 Ma, on the basis of Paleocene strata of the Summit Creek Formation [*Yorath and Cook*, 1981] and the modeled onset of cooling from this study (Fig. 6) and at the Mackenzie Mountains deformation front [*Powell et al.*, 2016]. Additionally, each model presumes a Permian to Triassic thermal maximum of 135 °C (Fig. 7a) and 120 °C (Fig. 7b) on the basis of AFT and AHe inverse history models and an overall decrease in Devonian %Ro from <1.0% from the Mackenzie Mountains to ~0.6% in the Norman Range [*Feinstein et al.*, 1991b]. Samples JPCPC3 and JPCPC4 are grouped together due to their position on the northern limb of the Stony anticline. Since maximum Cretaceous to Paleocene temperatures for these samples were constrained to <95 °C (Figs. 5, 6), forward models assess the effect of variable initial cooling rate on predicted AHe date-eU trends (Fig. 7a). These models suggest that with broad variations of apatite chemistry, and accounting for fission track and radiation damage annealing kinetics (r_{mr0}), lower cooling rates of 1.9 °C/m.y. and 2.8 °C/m.y. better match the observed dispersion in the data than do more moderate cooling rates of 5.5 °C/m.y. as the longer time spent at temperatures above ~40 °C results in younger AHe dates from the least retentive grains (0.83–0.86 r_{mr0}). Samples 10FNA066 and JP019 were grouped together due to their position on structural features to the north and east of the Mackenzie Mountains deformation front (Fig. 7b). Since inverse thermal history models for these samples predict a more protracted

cooling history compared to JPCPC3 and JPCPC4 (Fig. 6), forward modeling was used to evaluate the effect of increasing maximum burial temperatures from 95 °C to 105 °C. All three time-temperature histories account for the bulk of the observed data when accounting for a wide range of annealing kinetics (0.6–0.86 r_{mr0}). However, the model with 100 °C Paleocene thermal maximum better addresses the AHe dates with a standard fluorapatite chemistry (0.83 r_{mr0}) than do the 95 °C and 105 °C models, which require radiation damage annealing kinetics of apatite chemistries that are less common in the dataset to explain the observed AHe date-eU dispersion. Whereas these samples were grouped together due to similar modeled cooling histories (Fig. 6), we note that the burial temperatures may be slightly different due to depositional thinning of Cretaceous deposits towards the Keele Arch in the northeast [*Thomson et al.*, 2011]. This may explain why lower temperatures (Fig. 7bi, ii) appear to better fit the data for JP019 compared to 10FNA066, where the dates are satisfied by burial between 100–105 °C (Fig. 7bii, iii).

Samples JPCPC4, JP019 and 10FNA066 contain AHe dates significantly older than the remainder of the dataset and cannot be explained via forward modeling of date-eU trends (Fig. 7a, b). It is plausible that similar to the ZHe system (Fig. 4), the older AHe dates are a result of apatite with anomalous diffusion kinetics [*Guenthner et al.*, 2015]. Fig. 7c examines the effects of long-term radiation damage accumulation in apatite on predicted AHe date-eU trends. These models illustrate that older-than-predicted AHe dates can be explained in a similar way to the ZHe system [*Guenthner et al.*, 2015], where apatite with chemistries that are the most resistant to thermal annealing (low r_{mr0} values) retain pre-depositional radiation damage and helium even when heated to temperatures in excess of 120 °C during their post-depositional thermal history.

Forward models for sample 10FNARL008 (Fig. 8a) examine the effect of maximum Paleocene burial temperature on predicted AHe date. Whereas both 100 °C and 110 °C thermal

maxima can account for the observed AHe dispersion when a wide range of r_{mr0} values are justified, the 100 °C model explains a majority of the data for a standard fluorapatite chemistry (0.83 r_{mr0}) over the range of grain sizes exhibited in the sample. This temperature is slightly lower than the range of temperatures indicated by AFT inverse thermal history modeling (>109 ° C), highlighting the difference in low-temperature thermal histories quantified by AHe diffusion kinetics and those predicted from r_{mr0}-derived annealing kinetics of the least retentive AFT populations. Although no trends are observed between AHe date and eU or grain size for sample Husky7, forward models that consider the rate of initial Paleocene cooling on predicted AHe dates (Fig. 8b) indicate that with a range of radiation damage annealing kinetics, lower cooling rates (5.3–3.3 °C/m.y.) explain the observed AHe date dispersion. However, the quantitative power of AHe data dispersion in this sample is limited by the very small grain size (27.1 μm–31.0 μm). F_t-corrections for these grains indicate that as much as 50% of the radiogenic helium has been lost due to alpha ejection from the crystal, which decreases the precision of the corrected AHe dates [*Farley et al.*, 1996; *Ketcham et al.*, 2011].

5. Discussion

5.1. Low temperature thermochronology of sedimentary basins

Interpretation of dispersion in low temperature thermochronometer dates from siliciclastic rocks is complicated due to the wide variation of grain size, chemistry and radiation damage expected in a detrital population, and a pre-depositional history that is unique for each grain and cannot be constrained *a priori* [*Guenthner et al.*, 2015]. Thermal history modeling of dispersed low temperature thermochronology data from sedimentary rocks must consider the potential sources of this variation and follow an appropriate strategy to quantify the thermal

implications of the data. For example, given the presence of Precambrian detrital zircon and muscovite grains in the Imperial Formation [*Lemieux et al.*, 2011; *Powell and Schneider*, 2013], we use forward thermal history modeling of ZHe data (Fig. 4) to account for radiation damage accumulation for a wide range of pre-depositional histories [*Guenthner et al.*, 2015]. Likewise, the scatter in AFT dates can be explained using the chemically defined kinetic parameter r_{mr0}, and modeling of the multiple statistically significant kinetic populations within a single sample has significant interpretive power for determining the thermal history (Fig. 5). This approach has very important ramifications for the use of AFT thermochronology in sedimentary basin analysis, as samples that fail the χ^2 test may in fact host a tremendous amount of time-temperature information, and ignoring this complexity will bias interpretations towards samples with limited detrital variability or less complex thermal histories.

In turn, an understanding of the range of fission track annealing kinetics is essential in explaining AHe dispersion in this dataset (Figs. 6, 7, 8), as radiation damage is retained during burial in apatite that are more resistant to thermal annealing, resulting in exaggerated AHe date-eU trends when compared with less retentive chemistries. In the case of this dataset, AHe date-eU dispersion is essential in thermal history interpretation, as the scatter is quantifiable on the basis of maximum Paleocene burial temperatures, cooling rates and known annealing kinetics. Although other studies have recognized the importance of fission track annealing kinetics on natural dispersion in AHe datasets [*Gautheron et al.*, 2013], these results highlight that pre-depositional history should be considered in samples that are sourced from ancient terranes and contain apatite with very retentive fission track annealing kinetics (Fig. 7c), as the accumulation of radiation damage over geologic timescales will result in apatite that is extremely retentive of radiogenic helium.

5.2. Application of thermal models to Mackenzie Plain burial history

In an effort to ground truth our thermal history models, we perform simple 1D burial history modeling of wells from the Mackenzie Plain to determine whether %Ro profiles calculated using thermochronometer-derived burial temperatures match the observed trends in organic thermal maturity data (Fig. 9). Four wells were selected for this investigation on the basis of their proximity to outcrop samples and availability of published vitrinite reflectance and Rock-Eval pyrolysis data [*Feinstein et al.*, 1988b; *Snowdon*, 1990]. Rock-Eval Tmax data were converted to %Ro equivalent values using relationships derived from the Barnett Shale [*Jarvie et al.*, 2001]. Although there are issues associated with using a Tmax-Ro conversion that is not calibrated to Mackenzie Plain strata [*Wust et al.*, 2013], the wells selected for this investigation either contained natural vitrinite data to compare with values calculated from Rock-Eval Tmax (e.g. K-71, A-28), or had robust Tmax datasets with small sampling intervals to compare reproducibility of measured data and assess trends with depth (e.g. N-22, K-53). Whereas no organic thermal maturity data exists for the Lower Cretaceous section in N-22, proximal outcrops of Slater River Formation have %Ro equivalents between 0.47–0.54 (Table A5). Estimates on the magnitude of the Paleozoic to Mesozoic and Cretaceous to Paleocene eroded sections for each well were based on the difference between current stratigraphic thickness, and maximum thicknesses calculated from modeled temperatures derived of adjacent outcrop samples (Figs. 5, 7, 8), and a time-invariant geothermal gradient equivalent to the present-day value. Projected profiles of %Ro were calculated using both the EASY%Ro [*Sweeney and Burnham*, 1990] and basin%Ro calibrations [*Nielsen et al.*, 2015].

Whereas the %Ro profiles created using the EASY%Ro calibration can only account for the thermal history in A-28, the projected profiles from the basin%Ro calibration are able to recreate the observed trends between maturity and depth in all four wells. Although these forward models are simplistic, the basin%Ro organic thermal maturity profiles support the interpretation of a regional Paleozoic to early Mesozoic thermal maximum modeled using low temperature thermochronometers from the Imperial Formation. These results are contrary to existing interpretations of organic thermal maturity profiles from the region [*Feinstein et al.*, 1991b, 1996], which suggest that with the exception of the Root Basin in the southeast, the maturity trends across the Mackenzie Plain were dictated by Cenozoic thermal conditions. Our burial models indicate that the Imperial Formation across the Mackenzie Plain reached maximum burial depths of 3.3–3.4 km, which are near identical to the 3.6 km predicted from AFT modeling of the Imperial Formation in well I-77 of the Brackett Basin [*Issler et al.*, 2005]. The forward model predictions of maximum burial thicknesses from wells are similar to the range of plausible burial depths (2.2–4.1 km) indicated from multi-kinetic AFT modeling of outcrop samples (Fig. 9b). Both the outcrop sample and well A-28 from the Root Basin indicate substantially deeper pre-Cretaceous maximum burial depths (5.5–6.3 km) than the Mackenzie Plain to the north. Although the northern boundary of the Paleozoic Root Basin is ambiguous, a substantial increase in organic thermal maturity of Devonian strata of ~0.7 %Ro over a 10 km distance in the southern Brackett Basin [*Feinstein et al.*, 1988b] indicates that the north to south increase in Imperial Formation maximum burial temperatures is geographically abrupt, supporting earlier hypotheses of the Root Basin as a region with a pre-Cretaceous thermal history that differs from the Keele Tectonic Zone and Mackenzie Plain to the north [*Williams*, 1989; *Feinstein et al.*, 1991b].

Previous interpretations of vitrinite reflectance and Rock-Eval pyrolysis data from the Cretaceous section have been complicated by the recycling of higher maturity organic material from Devonian and Carboniferous sources [*Issler et al.*, 2005]. Possible examples of this phenomenon include the %Ro data converted from Rock-Eval Tmax values for K-53 (Fig. 9), where the lower %Ro of some Little Bear Formation samples (<0.5%) might be a more accurate estimation of the true thermal maturity than the 0.5–0.65 %Ro values observed throughout the Cretaceous section. To that extent, previous calculations of post-Paleoene erosion that rely on the slope of these data [*Feinstein et al.*, 1991b, 1996] may over estimate the total thickness of eroded material. Comparatively, the estimates of Cretaceous to Paleocene stratigraphic thicknesses for well and outcrop samples for this study are extrapolated from Paleocene temperatures indicated through AHe forward models (Figs. 7, 8) and present day geothermal gradients. Cretaceous organic thermal maturity profiles from wells K-71 and K-53 can be reconciled with maximum Cretaceous to Paleocene burial thicknesses of 2.2 km, in accord with the 2.2–2.4 km modeled from Imperial Formation outcrops along the Mackenzie Mountains front, Imperial Anticline and Norman Range. These burial models suggest 1 km of post-Paleocene erosion from well K-53 and 1.6 km of erosion in well K-71. Both erosional amounts are similar to the estimate of ~1.2–1.8 km of post-Summit Creek Formation erosion from AFT modeling and shale compaction profiles in the proximal I-77 well in the Brackett Basin [*Issler et al.*, 2005]. Estimates for Cretaceous to Paleocene burial in the Root Basin include 3.3 km from the outcrop sample and 3.8 km from well A-28. Although it is possible that the 500 m thickening of the Cretaceous to Paleocene package represents deepening of the foreland away from the emerging Mackenzie Mountains and into the Brackett Basin, it is more probable that the apparent maturity trends the Cretaceous section in well A-28 is a product of organic material recycling and is not reflective of true paleothermal conditions.

We note that the minimum vitrinite reflectance value for all Cretaceous samples varied from 0.44–0.47 %Ro, compared to the maximum values of 0.64–0.74 %Ro [*Feinstein et al.*, 1988a]. To that extent, if well A-28 had a similarly thick foreland basin package as modeled in the adjacent outcrop sample, only 2.1 km of material would have been removed during post-Paleocene erosion as compared to the 2.6 km suggested from forward modeling of the organic thermal maturity profile. This modified erosion estimate is similar to the 1.9 ± 0.4 km of erosion estimated from shale compaction curves for the same well [*Feinstein et al.*, 1996].

Our interpretation of a regional Paleozoic to early Mesozoic thermal maximum are comparable to findings from organic thermal maturity data in the Root Basin [*Feinstein et al.*, 1991a, 1996] and the only other thermochronology study in the Mackenzie Plain [*Issler et al.*, 2005]. Our results, however, diverge from the existing interpretation that Devonian strata in the Mackenzie Plain and Brackett Basin achieved peak thermal maturity due to burial in the Cretaceous to Paleocene foreland basin [*Feinstein et al.*, 1991b, 1996]. The significant differences between vitrinite reflectance calibrations used in forward modeling may explain this disparity between previous interpretations and those presented in this study. Forward modeling in previous studies [*Feinstein et al.*, 1991b, 1996] used the EASY%Ro calibration [*Sweeney and Burnham*, 1990], and interpreted organic thermal maturity profiles that were relatively continuous across the sub-Cretaceous unconformity to represent the influence of Cenozoic thermal maturation. However, the new basin%Ro calibration [*Nielsen et al.*, 2015] predicts that the EASY%Ro calibration systematically overestimates vitrnite reflectance by as much as 0.35 %Ro in the 0.5–1.7 %Ro reflectance window. Coincidentally, the sub-Cretaceous unconformity in wells across the Mackenzie Plain lies within this vitrinite reflectance range, indicating that EASY%Ro accurately predicts maturity trends in the overlying Cretaceous section, but over

estimates reflectance values in the underlying Devonian strata. This relationship is paramount in the K-71 and K-53 wells, where the curve generated using the basin%Ro calibration predicts a small offset in reflectance values across the unconformity and can account for the relatively continuous maturity profile, whereas EASY%Ro predicts reflectance values that are substantially more mature than the observed data.

Burial thicknesses extrapolated from thermal history models indicate a uniformly thick Cretaceous to Paleocene foreland basin (~2.2–2.5 km) in the northern portion of the study area, and between 3 km [*Issler et al.*, 2005] and 3.8 km in the Brackett Basin. Whereas this trend could represent a deeper foreland basin to the east of the Mackenzie Mountains in comparison to the northern Mackenzie Plain, we acknowledge our calculation of stratigraphic thickness is strongly affected by the variable present day geothermal gradient, which is in excess of 40 °C/km in the northern portion of the study area, and ~30 °C/km in the Brackett Basin [*Majorowicz and Morrow*, 1998]. Given the fact that forward modeling of AHe data indicate regional Paleocene temperatures of ~100 °C (Figs. 7, 8), it is possible that the foreland basin strata had little lateral variation, but matured under a different gradient than the present day thermal regime. Likewise, it is plausible that the timing of regional maximum burial depth for Paleozoic strata was the Cenozoic as suggested by shale compaction studies [*Feinstein et al.*, 1996] and that our modeled Paleozoic–Mesozoic thermal maximum recognized in this study occurred under a much higher geothermal gradient. An elevated Paleozoic geothermal gradient of 53–65 °C/km has previously been speculated for the Root Basin [*Feinstein et al.*, 1991b, 1996]. However, it is unclear what mechanism could result in such a dramatic change in regional heat flow, given that the high values for present day geothermal gradients are in part related to

higher than average basement heat generation [*Majorowicz et al.*, 2005], and basement conditions have remained unchanged since the Devonian.

5.3. Implications for Mackenzie Plain unroofing history and petroleum systems

Thermal histories derived from multi-kinetic AFT modeling (Fig. 5) suggest that the Imperial Formation across the Mackenzie Plain reached peak temperatures due to burial beneath a Carboniferous to pre-Cretaceous stratigraphic package that has since been eroded. The two models that provide the best resolution on the Paleozoic to Mesozoic thermal history (Fig. 5; 10FNARL008, Husky7) refine the timing of this thermal maximum to Carboniferous to Late Triassic, overlapping with the Triassic to Jurassic thermal maximum modeled from AFT data in the I-77 well [*Issler et al.*, 2005]. Although Lower Carboniferous strata exist in the Peel Plain directly to the west of the study area [*Lemieux et al.*, 2011], no Permian to Triassic strata are preserved for hundreds of kilometers from the study area, so ongoing deposition during this time interval is conjectural. Other low-temperature thermochronology datasets from the Mackenzie Mountains [*Powell et al.*, 2016] and Slave craton to the east [*Ault et al.*, 2009, 2013] report similar magnitudes of late Paleozoic to early Mesozoic burial and erosion, potentially in response to subsidence and uplift of long-wavelength dynamic topography, a consequence of changing mantle flow dynamics at plate boundaries. To that extent, the Triassic cooling signature common to the AFT models from this dataset (Fig. 5) and other studies in the Mackenzie Mountains and Plain (Powell et al., 2016; Powell et al., 2017; Issler et al., 2005) may represent the continuation of the 340–225 Ma westward migrating cooling front modeled in the Slave craton [*Ault et al.*, 2013].

AHe thermal history models (Figs. 6, 7, 8) suggest that the timing of Cretaceous foreland basin inversion recorded by the Imperial Formation along the Mackenzie Mountains deformation

front, Imperial Anticline and Franklin Mountains are indistinguishable, commencing sometime between the Paleocene and earliest Eocene. These results are similar to the 60–55 Ma cooling history modeled in the frontal anticlines of the Mackenzie Mountains [*Powell et al.*, 2016], suggesting that the final pulse of deformation in the fold-thrust belt is contemporaneous with the initiation of movement on Cordilleran structures to the northeast in the Franklin Mountains. It is probable that other major basin structures, including the latest movements along the Gambill Fault, formed at this time as well. However, unlike the moderate cooling rates predicted in the Mackenzie Mountains [*Powell et al.*, 2016] some AHe models (Figs. 6, 7, 8) evince a protracted, two-phase Cenozoic cooling history. These results are similar to unpublished AFT data from the region [*Green et al.*, 2005]. Presently, the source of the poorly defined Oligocene/Miocene cooling event is unknown. It is possible that this cooling history represents reactivation of Cordilleran structures; indeed, the Mackenzie Mountains are presently seismically active and undergoing shortening at a rate of 1.8–3.9 mm/a [*Leonard et al.*, 2008], potentially due to far field strain accommodation resulting from the collision of the Yakutat block with North America [*Hyndman et al.*, 2005]. Additionally, it is possible that a change in Cenozoic weather patterns may have impacted the feedback between climate and tectonic or erosional processes [*Reiners and Brandon*, 2006]. The Eocene to Oligocene transition marks a major global transition from greenhouse to icehouse conditions, which at northern latitudes is manifested by cooler winter temperatures, and an increase in seasonality and aridity [*Eldrett et al.*, 2009]. Such a change in climate, and the corresponding variation in precipitation rates and fluvial systems, may be responsible for the increased erosion rates observed over this period in the Mackenzie Plain.

Ultimately, the results of this study suggest that the burial and unroofing history of Devonian source rocks across the Mackenzie Plain is not conducive to the preservation of major

conventional petroleum systems: hydrocarbons would have been generated from source rocks during burial and unroofing in the late Paleozoic to early Mesozoic, well before the establishment of Paleocene to early Eocene trapping structures in the foreland basin. The oil hosted in Devonian reefs in the prolific Norman Wells oil field may be an exception to this trend, as studies link its source to the Canol Formation [*Snowdon et al.*, 1987]. Due to the low thermal maturity (0.51–0.69 %Ro) of the Norman Wells field [*Feinstein et al.*, 1991b] and absence of AFT data from the Norman Range, the timing of hydrocarbon generation in the northern Mackenzie Plain remains unclear. Either the Devonian strata achieved peak burial temperatures in the late Paleozoic to Mesozoic as suggested for the rest of the Mackenzie Plain, or during the Paleocene when Devonian sources were reburied to ~100 °C (Fig. 7). Alternatively, it is possible that the source to this system matured prior to the Cretaceous but was charged through Cenozoic unroofing and shallow fracture-induced oil migration from the Canol Formation [*Hadlari*, 2015].

There remains some potential for petroleum systems sourced from the organic-rich shales of the Cretaceous Slater River Formation. However, since AHe data point towards relatively uniform maximum Cretaceous burial temperatures of ~100 °C across the Mackenzie Plain, undiscovered systems are, at best, marginally mature and likely behave similar to existing plays, where hydrocarbons are generated and trapped locally [*Feinstein et al.*, 1988a]. Whereas these results are not promising for conventional petroleum systems, significant potential still exists for unconventional shale gas and shale oil plays from Devonian source rocks. Our data indicate that these sources have matured to temperatures within, but not exceeding, the oil and gas window across much of the Mackenzie Plain.

6. Conclusions

ZHe, AHe and AFT data from the Devonian Imperial Formation exhibits significant intra-sample dispersion due to episodic burial and unroofing and a protracted residence at low-temperatures in the uppermost crust. We invoke the effects of pre-depositional history, radiation damage and mineralogical chemistry on fission track annealing to explain the dispersion, and quantify thermal histories that are consistent with the observed data scatter. As a result, our models trace the thermal evolution of Devonian strata over two major episodes of regional burial and unroofing. Results from AFT modeling suggest that Devonian Imperial Formation achieved maximum temperatures of 120–160 °C in the Mackenzie Plain and 165–190 °C in the Root Basin between the late Paleozoic and Mesozoic. Our ZHe forward modeling results support these temperatures. Thermal history models that account for chemical influence on radiation damage annealing in the AHe system suggest that the observed AHe date-eU dispersion is consistent with Cretaceous to Paleocene temperatures of ~100 °C across the entire study region.

In the present day basin, maturation profiles generated using the new basin%Ro calibration and maximum burial temperatures derived from outcrop thermal histories closely match observed organic thermal maturity data, whereas profiles calculated using the standard EASY%Ro calibration over estimate the degree of maturation. These results support the contention that EASY%Ro systematically over estimates %Ro in the 80–190 °C window, which has significant implications for thermochronolgy studies that incorporate vitrinite reflectance data into thermal history models. Assuming a fixed geothermal gradient equivalent to present values, these results indicate Imperial Formation maximum burial depths of 2.2–4 km in the Mackenzie Plain and 5.5–6.3 km in the Root Basin. Maximum Cretaceous to Paleocene burial depths were determined to be between 2.2 to 3.8 km across the study area.

AHe thermal history models suggest that the Imperial Formation experienced a protracted Cenozoic cooling history. Data from the Mackenzie Mountains deformation front, Imperial anticline and Norman Range indicate that basin inversion occurred coevally throughout the region in the Paleocene to early Eocene. This cooling event likely coincides with initiation of movement on other regional structures in Mackenzie Plain and Franklin Mountains, and potential trapping structures in the basin. Some samples evince an increase in cooling rate of varying magnitude later in the Cenozoic.

The results of this study do not appear promising for conventional petroleum systems that rely on hydrocarbon generation from Devonian sources and Paleocene trapping structures. Though petroleum systems charged from Cretaceous source rocks may exist, our models suggest that they will be only marginally mature across the study area. Whereas these data are not favourable for regional petroleum exploration, they provide an excellent case study on the sources of intra-sample dispersion in thermochronometers from sedimentary rocks, and methods to quantify meaningful thermal histories from outwardly confusing datasets.

Acknowledgments

Funding for this project was provided by an NSERC-CRD grant to DAS, with contributions from ConocoPhillips Canada and Chevron Canada. Additional financial and logistical support was generously made possible by the Geo-mapping for Energy and Minerals (GEM) program at Natural Resources Canada. We thank Julito Reyes (GSC) for organic thermal maturity assessments, Paul O'Sullivan and Apatite to Zircon Incorporated for assistance with the apatite fission track data collection, the University of Texas at Austin thermochronology laboratory for their analytical support, Glenn Poirier (Canadian Museum of Nature) for assistance with EPMA

data collection, and the kind assistance of Justin MacDonald, Trevor Gray and Louise Klatzel-Mudry from ConocoPhillips Canada and Husky Energy for providing outcrop samples for thermochronology studies.

References

Armstrong, P. A. (2005), Thermochronometers in Sedimentary Basins, *Rev. Mineral. Geochemistry*, *58*(1), 499–525, doi:10.2138/rmg.2005.58.19.

Ault, A. K., R. M. Flowers, and S. A. Bowring (2009), Phanerozoic burial and unroofing history of the western Slave craton and Wopmay orogen from apatite (U–Th)/He thermochronometry, *Earth Planet. Sci. Lett.*, *284*(1-2), 1–11, doi:10.1016/j.epsl.2009.02.035.

Ault, A. K., R. M. Flowers, and S. A. Bowring (2013), Phanerozoic surface history of the Slave craton, *Tectonics*, *32*(5), 1066–1083, doi:10.1002/tect.20069.

Barbarand, J., A. Carter, I. Wood, and T. Hurford (2003), Compositional and structural control of fission-track annealing in apatite, *Chem. Geol.*, *198*(1-2), 107–137, doi:10.1016/S0009-2541(02)00424-2.

Beucher, R., R. W. Brown, S. Roper, F. Stuart, and C. Persano (2013), Natural age dispersion arising from the analysis of broken crystals. Part II: Practical application to apatite (U-Th)/He thermochronometry, *Geochim. Cosmochim. Acta*, *120*, 395–416, doi:10.1016/j.gca.2013.05.041.

Brown, R. W., R. Beucher, S. Roper, C. Persano, F. Stuart, and P. Fitzgerald (2013), Natural age dispersion arising from the analysis of broken crystals. Part I: Theoretical basis and implications for the apatite (U-Th)/He thermochronometer, *Geochim. Cosmochim. Acta*, *122*(120), 478–497, doi:10.1016/j.gca.2013.05.041.

Burtner, R. L., A. Nigrini, and R. a. Donelick (1994), Thermochronology of Lower Cretaceous source rocks in the Idaho-Wyoming thrust belt., *Am. Assoc. Pet. Geol. Bull.*, *78*(10), 1613–1636, doi:10.1306/A25FF233-171B-11D7-8645000102C1865D.

Carlson, W. D., R. A. Donelick, and R. A. Ketcham (1999), Variability of apatite fission-track annealing kinetics: I. Experimental results, *Am. Mineral.*, *84*(9), 1213–1223, doi:10.2138/am-1999-0901.

Chew, D. M., and R. A. Donelick (2012), Combined apatite fission track and U-Pb dating by LA–ICP–MS and its application in apatite provenance analysis, *Mineral. Assoc. Canada Short Course 42*, 219–247.

Dixon, J. (1999), Mesozoic-Cenozoic stratigraphy of the northern Interior Plains and Plateaux, Northwest Territories, *Geol. Surv. Canada, Bull.*, *536*, 56 p.

Djimbi, M. D., C. Gautheron, J. Roques, L. Tassan-Got, C. Gerin, and E. Simoni (2015), Impact of apatite chemical composition on (U-Th)/He thermochronometry: An atomistic point of view, *Geochim. Cosmochim. Acta*, *167*, 162–176, doi:10.1016/j.gca.2015.06.017.

Donelick, R. A., P. B. O'Sullivan, and R. A. Ketcham (2005), Apatite Fission-Track Analysis, *Rev. Mineral. Geochemistry*, *58*(1), 49–94, doi:10.2138/rmg.2005.58.3.

Eldrett, J. S., D. R. Greenwood, I. C. Harding, and M. Huber (2009), Increased seasonality through the Eocene to Oligocene transition in northern high latitudes., *Nature*, *459*, 969–973, doi:10.1038/nature08069.

Fallas, K. M., and R. B. MacNaughton (2014a), Geology, Carcajou Canyon (northwest), Northwest Territories, *Geol. Surv. Canada, Can. Geosci. Map*, (94), doi:10.4095/292286.

Fallas, K. M., and R. B. MacNaughton (2014b), Geology, Carcajou Canyon (southeast), Northwest Territories, *Geol. Surv. Canada, Can. Geosci. Map*, (96), doi:10.4095/292288.

Fallas, K. M., and R. B. MacNaughton (2014c), Geology, Carcajou Canyon (southwest), Northwest Territories, *Geol. Surv. Canada, Can. Geosci. Map*, *97*, doi:10.4095/292289.

Fallas, K. M., T. Hadlari, and B. C. MacLean (2013a), Geology, Carcajou Canyon (northeast), Northwest Territories, *Geol. Surv. Canada, Geosci. Map*, *95*, doi:10.4095/292287.

Fallas, K. M., B. C. Maclean, and T. Proks (2013b), Geology, Fort Norman (northwest), Northwest Territories, *Geol. Surv. Canada, Can. Geosci. Map*, *92*, doi:10.4095/292284.

Fallas, K. M., R. B. MacNaughton, B. C. MacLean, and T. Hadlari (2013c), Geology, Norman Wells (southwest), Northwest Territories, *Geol. Surv. Canada, Can. Geosci. Map*, *101*, doi:10.4095/292293.

Farley, K. A. (2000), Helium diffusion from apatite: General behavior as illustrated by Durango fluorapatite, *J. Geophys. Res.*, *105*(B2), 2903–2914, doi:10.1029/1999JB900348.

Farley, K. A. (2002), (U-Th)/He Dating: Techniques, Calibrations, and Applications, *Rev. Mineral. Geochemistry*, *47*(1), 819–844, doi:10.2138/rmg.2002.47.18.

Farley, K. A., R. A. Wolf, and L. T. Silver (1996), The effects of long alpha-stopping distances on (U-Th)/He ages, *Geochim. Cosmochim. Acta*, *60*(21), 4223–4229.

Feinstein, S., P. W. Brooks, M. G. Fowler, L. R. Snowdon, and G. K. Williams (1988a), Families of oils and source rocks in the central Mackenzie corridor: a geochemical oil-oil and oil-source rock correlation, *Can. Soc. Pet. Geol. Mem.*, *15*, 543–552.

Feinstein, S., P. W. Brooks, T. Gentzis, F. Goodarzi, L. R. Snowdon, and G. K. Williams (1988b), Thermal maturity in the Mackenzie Corridor, Northwest and Yukon Territories, Canada, *Geol. Surv. Canada, Open File 1944*, 65 p., doi:10.4095/130457.

Feinstein, S., G. K. Williams, L. R. Snowdon, P. W. Brooks, M. G. Fowler, F. Goodarzi, and T. Gentzis (1991a), Organic geochemical characterization and hydrocarbon generation potential of mid-Late Devonian Horn River bituminous shales, southern Northwest

Territories, *Bull. Can. Pet. Geol.*, *39*(2), 192–202.

Feinstein, S., G. K. Williams, L. R. Snowdon, F. Goodarzi, and T. Gentzis (1991b), Thermal maturation of organic matter in the Middle Devonian to Tertiary section, Fort Norman area (central Mackenzie Plain), *Can. J. Earth Sci.*, *28*(7), 1009–1018, doi:10.1139/e91-092.

Feinstein, S., D. R. Issler, L. R. Snowdon, and G. K. Williams (1996), Characterization of major unconformities by paleothermometric and paleobarometric methods: application to the Mackenzie Plain, Northwest Territories, Canada, *Bull. Can. Pet. Geol.*, *44*(1), 55–71.

Flowers, R. M., R. A. Ketcham, D. L. Shuster, and K. A. Farley (2009), Apatite (U-Th)/He thermochronometry using a radiation damage accumulation and annealing model, *Geochim. Cosmochim. Acta*, *73*(8), 2347–2365, doi:10.1016/j.gca.2009.01.015.

Fritz, W. H., M. P. Cecile, B. S. Norford, D. Morrow, and H. H. J. Geldsetzer (1991), Cambrian to Middle Devonian assemblages, in *Geology of the Cordilleran Orogen in Canada*, edited by H. Gabrielse and C. J. Yorath, pp. 151–218, Geological Survey of Canada, Geology of Canada, no. 4.

Gal, L. P., L. J. Pyle, T. Hadlari, and T. L. Allen (2009), Chapter 6 - Lower to Upper Devonian strata, Arnica-Landry play, and Kee Scarp play, in *Regional Geoscience Studies and Petroleum Potential, Peel Plateau and Plain, Northwest Territories and Yukon: Project Volume, Northwest Territories Geoscience Office and Yukon Geological Survey, NWT Open FIle 2009-002 and YGS Open File 2009-25*, edited by L. J. Pyle and A. Jones.

Gautheron, C., L. Tassan-Got, J. Barbarand, and M. Pagel (2009), Effect of alpha-damage annealing on apatite (U-Th)/He thermochronology, *Chem. Geol.*, *266*(3-4), 166–179, doi:10.1016/j.chemgeo.2009.06.001.

Gautheron, C., J. Barbarand, R. A. Ketcham, L. Tassan-Got, P. Van Der Beek, M. Pagel, R. Pinna-Jamme, F. Couffignal, and M. Fialin (2013), Chemical influence on α-recoil damage annealing in apatite: Implications for (U-Th)/He dating, *Chem. Geol.*, *351*(August 2013), 257–267, doi:10.1016/j.chemgeo.2013.05.027.

Gordey, S. P., J. D. Macdonald, E. C. Turner, and D. G. F. Long (2011), Chapter 5. Structural Geology of the Central Mackenzie Mountains, in *Geology of the Central Mackenzie Mountains of the Northern Canadian Cordillera, Sekwi Mountain (105P), Mount Eduni (106A), and the northwestern Wrigley Lake (95M) Map Areas, Northwest Territories*, edited by E. Martel, E. C. Turner, and B. J. Fischer, pp. 215 – 250, NWT Geoscience Office.

Green, P. F. (1981), A new look at statistics in fission-track dating, *Nucl. Tracks*, *5*(1-2), 77–86, doi:10.1016/0191-278X(81)90029-9.

Green, P. F. (1988), The relationship between track shortening and fission track age reduction in apatite: combined influences of inherent instability, annealing anisotropy, length bias and system calibration, *Earth Planet. Sci. Lett.*, *89*(3-4), 335–352, doi:10.1016/0012-821X(88)90121-5.

Green, P. F., I. R. Duddy, A. J. W. Gleadow, P. R. Tingate, and G. M. Laslett (1986), Thermal

annealing of fission tracks in apatite 1. Variable temperature behaviour, *Chem. Geol. Isot. Geosci. Sect.*, *59*, 237–253, doi:10.1016/0168-9622(88)90019-X.

Green, P. F., I. R. Duddy, L. Slind, and F. Rayer (2005), Multiple paleo-thermal episodes in Mackenzie Corridor, Northwest Territory, Canada revealed by apatite fission trak analysis (AFTA): Implications for hydrocarbon prospectivity, in *AAPG Search and Discovery*, Calgary, Alberta.

Guenthner, W. R., P. W. Reiners, R. A. Ketcham, L. Nasdala, and G. Giester (2013), Helium diffusion in natural zircon: Radiation damage, anisotropy, and the interpretation of zircon (U-Th)/He thermochronology, *Am. J. Sci.*, *313*(3), 145–198, doi:10.2475/03.2013.01.

Guenthner, W. R., P. W. Reiners, and Y. Tian (2014), Interpreting date–eU correlations in zircon (U-Th)/He datasets: A case study from the Longmen Shan, China, *Earth Planet. Sci. Lett.*, *403*, 328–339, doi:10.1016/j.epsl.2014.06.050.

Guenthner, W. R., P. W. Reiners, P. G. DeCelles, and J. Kendall (2015), Sevier belt exhumation in central Utah constrained from complex zircon (U-Th)/He data sets: Radiation damage and He inheritance effects on partially reset detrital zircons, *Geol. Soc. Am. Bull.*, *127*(3-4), 1–26, doi:10.1130/B31032.1.

Hadlari, T. (2015), Oil migration driven by exhumation of the Canol Formation oil shale: A new conceptual model for the Norman Wells oil field, northwestern Canada, *Mar. Pet. Geol.*, *65*(May), 172–177, doi:10.1016/j.marpetgeo.2015.03.027.

Hadlari, T., L. P. Gal, W. G. Zantvoort, S. A. Tylosky, T. L. Allen, T. A. Fraser, Y. Lemieux, and O. Catuneanu (2009), Chapter 7 - Upper Devonian to Carboniferous strata I - Imperial Formation Play, in *Regional Geoscience Studies and Petroleum Potential, Peel Plateau and Plain, Northwest Territories and Yukon: Project Volume, Northwest Territories Geoscience Office and Yukon Geological Survey, NWT Open FIle 2009-002 and YGS Open File 2009-25*.

Hadlari, T., D. Midwinter, B. C. MacLean, K. M. Fallas, and J. Dixon (2013), Formation tops and isopach maps of Cretaceous strata of Mackenzie Plain and parts of Peel Plain, Northwest Territories, *Geol. Surv. Canada, Open File 7326*, 4 p., doi:10.4095/293112.

Hadlari, T., B. C. MacLean, J. M. Galloway, A. R. Sweet, J. M. White, D. Thomson, J. Gabites, and C. J. Schröder-Adams (2014), The flexural margin, the foredeep, and the orogenic margin of a northern Cordilleran foreland basin: Cretaceous tectonostratigraphy and detrital zircon provenance, northwestern Canada, *Mar. Pet. Geol.*, *57*, 173–186, doi:10.1016/j.marpetgeo.2014.05.019.

Hannigan, P. K., D. W. Morrow, and B. C. MacLean (2011), Petroleum resource potential of the northern mainland of Canada (Mackenzie Corridor), *Geol. Surv. Canada, Open File 6757*, 271 p., doi:289095.

Harrison, T. M., and P. K. Zeitler (2005), Fundamentals of Noble Gas Thermochronometry, *Rev. Mineral. Geochemistry*, *58*(1), 123–149, doi:10.2138/rmg.2005.58.5.

Hasebe, N., J. Barbarand, K. Jarvis, A. Carter, and A. J. Hurford (2004), Apatite fission-track chronometry using laser ablation ICP-MS, *Chem. Geol.*, *207*(3-4), 135–145, doi:10.1016/j.chemgeo.2004.01.007.

Hyndman, R. D., P. Flück, S. Mazzotti, T. J. Lewis, J. Ristau, and L. Leonard (2005), Current tectonics of the northern Canadian Cordillera, *Can. J. Earth Sci.*, *42*(6), 1117–1136, doi:10.1139/e05-023.

Issler, D. R. (1996), An inverse model for extracting thermal histories from apatite fission track data: instructions and software for the Windows 95 environment, *Geol. Surv. Canada, Open File 2325*, 85 p.

Issler, D. R. D., A. Grist, and L. Stasiuk (2005), Post-Early Devonian thermal constraints on hydrocarbon source rock maturation in the Keele Tectonic Zone, Tulita area, NWT, Canada, from multi-kinetic apatite fission track thermochronology, vitrinite reflectance and shale compaction, *Bull. Can. Pet. Geol.*, *53*(4), 405–431, doi:10.2113/53.4.405.

Jarvie, D. M., B. L. Claxton, F. Henk, and J. T. Breyer (2001), Oil and shale gas from the Barnett Shale, Fort Worth basin, Texas, *AAPG Natl. Conv. June 3-6, 2001, Denver, CO, AAPG Bull.*, *85*(13 (supplement)), A100.

Jiang, C., L. J. Pyle, and L. P. Gal (2014), Organic geochemistry of petroleum hydrocarbons in Middle to Upper Devonian outcrop samples from Mackenzie Plain area, *Northwest Territ. Geosci. Off. NWT Open Rep. 2014-05*.

Ketcham, R. A. (2005), Forward and Inverse Modeling of Low-Temperature Thermochronometry Data, *Rev. Mineral. Geochemistry*, *58*(1), 275–314, doi:10.2138/rmg.2005.58.11.

Ketcham, R. A., R. A. Donelick, and W. D. Carlson (1999), Variability of apatite fission-track anneling kinetics: III. Extrapolation to geological time scales, *Am. Mineral.*, *84*, 1235–1255.

Ketcham, R. A., A. Carter, R. A. Donelick, J. Barbarand, and A. J. Hurford (2007), Improved modeling of fission-track annealing in apatite, *Am. Mineral.*, *92*(5-6), 799–810, doi:10.2138/am.2007.2281.

Ketcham, R. A., C. Gautheron, and L. Tassan-Got (2011), Accounting for long alpha-particle stopping distances in (U-Th-Sm)/He geochronology: Refinement of the baseline case, *Geochim. Cosmochim. Acta*, *75*(24), 7779–7791, doi:10.1016/j.gca.2011.10.011.

Lawton, D. C., and J. H. Isaac (2005), Geophysical evidence for thin-skinned structural deformation in the Norman Range, Northwest Territories, *Bull. Can. Pet. Geol.*, *53*(2), 200–209.

Lemieux, Y., T. Hadlari, and A. Simonetti (2011), Detrital zircon geochronology and provenance of Devono-Mississippian strata in the northern Canadian Cordilleran miogeocline, *Can. J. Earth Sci.*, *48*(2), 515–541, doi:10.1139/E10-056.

Leonard, L. J., S. Mazzotti, and R. D. Hyndman (2008), Deformation rates estimated from earthquakes in the northern Cordillera of Canada and eastern Alaska, *J. Geophys. Res.*,

113(B8), B08406, doi:10.1029/2007JB005456.

MacLean, B. C. (2011), Tectonic and stratigraphic evolution of the Cambrian basin of northern Northwest Territories, *Bull. Can. Pet. Geol.*, *59*(2), 172–194, doi:10.2113/gscpgbull.59.2.172.

Maclean, B. C., and D. G. Cook (1999), Salt tectonism in the Fort Norman area, Northwest Territories, Canada, *Bull. Can. Pet. Geol.*, *47*(2), 104–135.

MacLean, B. C., K. M. Fallas, and T. Hadlari (2014), The multi-phase Keele Arch, central Mackenzie Corridor, Northwest Territories, *Bull. Can. Pet. Geol.*, *62*(2), 68–104, doi:10.2113/gscpgbull.62.2.68.

Majorowicz, J. A., and D. W. Morrow (1998), Subsurface temperature and heat flow - Yukon and Northwest Territories, *Geol. Surv. Canada, Open File 3626*, 6 p.

Majorowicz, J. A., A. M. Jessop, and L. S. Lane (2005), Regional heat flow pattern and lithospheric geotherms in northeastern British Columbia and adjacent Northwest Territories, Canada, *Bull. Can. Pet. Geol*, *53*(1), 51–66.

Narbonne, G. M., and J. D. Aitken (1995), Neoproterozoic of the Mackenzie Mountains, northwestern Canada, *Precambrian Res.*, *73*, 101-121.

Nielsen, S. B., O. R. Clausen, and E. Mcgregor (2015), Basin%Ro: A vitrinite reflectance model derived from basin and laboratory data, *Basin Res.*, 1–22, doi:10.1111/bre.12160.

Powell, J., and D. A. Schneider (2013), Preliminary results of 40Ar/39Ar geochronology from the eastern Mackenzie Mountains and Mackenzie Plain, Northwest Territories, *Geol. Surv. Canada Curr. Res.*, *2013-18*, 16 p.

Powell, J., D. Schneider, D. Stockli, and K. Fallas (2016), Zircon (U-Th)/He thermochronology of Neoproterozoic strata from the Mackenzie Mountains, Canada: Implications for the Phanerozoic exhumation and deformation history of the northern Canadian Cordillera, *Tectonics*, *35*(3), 663–689, doi:10.1002/2015TC003989.

Powell, J., D. A. Schneider, and D. R. Issler (2017), Application of multi-kinetic apatite fission track and (U-Th)/He thermochronology to source rock thermal history: a case study from the Mackenzie Plain, NWT, Canada, *Basin Res.*, doi:10.1111/bre.12233.

Pyle, L. J., and L. P. Gal (2014), Analytical Results from Cretaceous and Devonian Studies in Mackenzie Plain, *Northwest Territ. Geosci. Off. NWT Open Rep. 2014-006*, 28 p.

Reiners, P. W., and M. T. Brandon (2006), Using Thermochronology To Understand Orogenic Erosion, *Annu. Rev. Earth Planet. Sci.*, *34*(1), 419–466, doi:10.1146/annurev.earth.34.031405.125202.

Reiners, P. W., K. A. Farley, and H. J. Hickes (2002), He diffusion and (U-Th)/He thermochronometry of zircon: Initial results from Fish Canyon Tuff and Gold Butte, *Tectonophysics*, *349*(1-4), 297–308, doi:10.1016/S0040-1951(02)00058-6.

Shuster, D. L., R. M. Flowers, and K. A. Farley (2006), The influence of natural radiation damage on helium diffusion kinetics in apatite, *Earth Planet. Sci. Lett.*, *249*(3-4), 148–161, doi:10.1016/j.epsl.2006.07.028.

Snowdon, L. R. (1990), Rock-Eval/TOC data for 55 Northwest and Yukon Territories wells [60°- 69°N], *Geol. Surv. Canada, Open File 2327*, 164, doi:10.4095/131489.

Snowdon, L. R., P. W. Brooks, G. K. Williams, and F. Goodarzi (1987), Correlation of the Canol Formation source rock with oil from Norman Wells, *Org. Geochem.*, *11*(6), 529–548, doi:10.1016/0146-6380(87)90008-8.

Stockli, D. F., K. A. Farley, and T. A. Dumitru (2000), Calibration of the apatite (U-Th)/He thermochronometer on an exhumed fault block, White Mountains, California, *Geology*, *28*(11), 983, doi:10.1130/0091-7613(2000)28<983:COTAHT>2.0.CO;2.

Sweeney, J. J., and A. K. Burnham (1990), Evaluation of a simple model of vitrinite reflectance based on chemical kinetics, *Am. Assoc. Pet. Geol. Bull.*, *74*(10), 1559–1570.

Thomson, D., C. J. Schröder-Adams, T. Hadlari, G. Dix, and W. J. Davis (2011), Albian to Turonian stratigraphy and palaeoenvironmental history of the northern Western Interior Sea in the Peel Plateau Region, Northwest Territories, Canada, *Palaeogeogr. Palaeoclimatol. Palaeoecol.*, *302*(3-4), 270–300, doi:10.1016/j.palaeo.2011.01.017.

Vermeesch, P. (2009), RadialPlotter: A Java application for fission track, luminescence and other radial plots, *Radiat. Meas.*, *44*(4), 409–410, doi:10.1016/j.radmeas.2009.05.003.

Wheeler, J. O., P. F. Hoffman, K. D. Card, A. Davidson, B. V. Sanford, A. V. Okulitch, and W. R. Roest (1996), Geological map of Canada, *Geol. Surv. Canada, "A" Ser. Map*, *1860A*, doi:10.4095/208175.

Williams, G. K. (1989), The Root Basin, *Geol. Surv. Canada, Open File 2129*, 47.

Wolfe, M. R., and D. F. Stockli (2010), Zircon (U–Th)/He thermochronometry in the KTB drill hole, Germany, and its implications for bulk He diffusion kinetics in zircon, *Earth Planet. Sci. Lett.*, *295*(1-2), 69–82, doi:10.1016/j.epsl.2010.03.025.

Wust, R. A. J., P. C. Hackley, B. R. Nassichuk, N. Willment, and R. Brezovski (2013), Vitrinite reflectance versus pyrolysis Tmax data: Assessing thermal maturity in shale plays with special reference to the Duvernay shale play of the Western Canadian Sedimentary Basin, Alberta, Canada, *Soc. Pet. Eng. Unconv. Resour. Conf. Exhib. Pacific*, (October), 1–11, doi:10.2118/167031-MS.

Yorath, C. J., and D. G. Cook (1981), Cretaceous and Tertiary Stratigraphy and Paleogeography, Northern Interior Plains, District of Mackenzie, *Geol. Surv. Canada, Mem.*, *398*, 1–76, doi:10.1017/CBO9781107415324.004.

Table 1. Single grain (U-Th)/He analyses of apatite and zircon, Imperial Formation, Mackenzie Plain, NWT

	Corr. Age (Ma)	Err. (Ma)	Mod. Age (Ma)	Mod. Err. (Ma)	U (ppm)	Th (ppm)	^{147}Sm (ppm)	eU (ppm)	Mod. eU (ppm)	Mod. Err. (ppm)	Th/U	He (nmol/g)	mass (µg)	Ft	ESR (µm)
JPCPC3, Imperial Fm. (siltstone) Powell River section, ~0.70 %Ro, 65.277 N, 128.774 W															
a1	50.5	3.0	48.2	5.3	4.7	143.5	31.3	37.9	39.4	1.5	30.6	6.0	1.0	0.56	34.9
a2	37.0	2.2	35.1	4.1	7.3	186.0	45.6	50.3	52.7	2.4	25.6	5.8	1.0	0.56	35.0
a3	43.5	2.6	42.0	4.1	29.1	214.9	63.6	78.9	77.6	1.3	7.4	10.4	0.8	0.55	33.5
a4	44.5	2.7	43.5	3.7	18.6	131.8	42.0	49.2	51.1	2.0	7.1	6.9	1.0	0.57	35.3
a5	48.2	2.9	47.4	3.7	9.2	103.2	49.8	33.2	34.6	1.4	11.2	4.7	0.8	0.53	32.1
a6	47.8	2.9	47.3	3.4	5.5	145.0	72.8	39.3	44.0	4.8	26.3	5.7	1.0	0.55	33.8
a7	55.3	3.3	54.0	4.6	30.6	148.2	53.4	65.0	68.3	3.2	4.8	11.4	1.2	0.58	36.0
z1	39.9	3.2	-	-	550.3	262.8	41.4	611.0	-	-	0.5	87.9	1.6	0.67	33.8
z2	300.7	24.1	-	-	180.2	18.6	0.8	184.5	-	-	0.1	224.6	3.3	0.74	42.7
z3	271.9	21.8	-	-	347.6	217.0	4.8	397.5	-	-	0.6	409.9	2.3	0.69	37.0
z5	49.7	4.0	-	-	4.2	72.0	38.4	21.0	-	-	17.0	4.1	2.9	0.70	41.7
JPCPC4, Imperial Fm. (siltstone) Imperial River section, ~0.66 %Ro, 65.116 N, 127.859 W															
a1	38.2	2.3	37.4	3.1	19.8	74.3	13.4	37.0	38.4	1.5	3.8	5.1	2.1	0.65	44.7
a2	132.9	8.0	129.8	11.1	5.0	53.5	34.9	17.5	18.2	0.7	10.7	7.4	1.0	0.57	35.5
a3	52.1	3.1	51.7	3.6	4.3	81.4	91.8	23.5	24.5	1.0	19.0	4.2	1.7	0.62	41.1
a4	52.3	3.1	51.2	4.3	8.8	40.2	20.3	18.2	18.9	0.7	4.6	3.4	2.0	0.65	44.2
a5	41.0	2.5	40.7	2.7	25.3	47.7	25.3	36.4	49.9	13.5	1.9	5.3	1.8	0.65	42.8
a6	52.8	3.2	50.6	5.3	4.7	59.7	47.9	18.7	19.4	0.7	12.7	3.0	1.0	0.55	33.8
a7	47.9	2.9	46.8	4.0	7.5	52.1	38.5	19.7	20.4	0.8	7.0	2.9	1.1	0.56	34.8
a8	71.6	4.3	67.9	8.0	10.4	80.2	36.6	29.1	30.2	1.1	7.7	6.4	0.9	0.56	34.4
a9	94.1	5.6	93.2	6.6	10.1	128.7	69.3	40.1	41.7	1.7	12.7	11.2	0.8	0.54	32.5
a10	50.8	3.0	48.2	5.6	9.3	88.7	36.9	29.9	31.2	1.2	9.5	4.8	1.0	0.57	35.4
10FNA066, Imperial Fm. (lithic arenite) Imperial Anticline, ~0.81 %Ro, 65.359 N, 127.956 W															
a1	19.3	1.2	18.9	1.5	6.3	87.6	44.5	26.7	27.7	1.0	13.9	1.8	1.6	0.62	40.7
a2	32.2	1.9	30.5	3.7	19.5	68.1	48.5	35.4	36.7	1.2	3.5	3.8	1.2	0.60	38.3
a3	40.3	2.4	39.2	3.5	42.3	263.2	47.8	103.1	107.2	4.1	6.2	12.0	0.8	0.52	31.3
a4	46.7	2.8	43.3	6.2	0.8	0.9	0.5	1.0	1.0	0.0	1.2	0.1	0.4	0.47	26.1
a5	32.6	2.0	31.9	2.7	8.8	102.5	35.4	32.5	33.9	1.3	11.7	3.3	1.1	0.57	35.4
a6	34.6	2.1	33.5	3.2	33.5	85.6	96.9	53.7	55.7	2.0	2.6	5.6	0.8	0.55	32.8
a7	18.2	1.1	17.3	2.0	5.6	170.7	67.2	45.3	47.1	1.8	30.3	2.9	1.7	0.63	42.1
a8	34.9	2.1	34.1	2.8	13.9	152.3	65.0	49.3	51.3	2.0	10.9	5.6	1.2	0.58	36.9
a9	3.2	0.2	3.1	0.3	5.9	2.0	0.5	6.4	6.6	0.2	0.3	0.1	0.8	0.57	32.6
a10	47.7	2.9	45.2	5.4	74.3	193.6	63.5	119.2	124.1	4.9	2.6	18.6	1.2	0.60	37.6
z1	234.3	18.7	-	-	212.4	113.5	2.3	238.6	-	-	0.5	213.2	2.2	0.70	37.7
z2	305.2	24.4	-	-	146.4	21.5	1.0	151.3	-	-	0.1	178.0	2.4	0.70	37.4
z3	390.4	31.2	-	-	135.8	48.4	1.0	146.9	-	-	0.4	217.9	1.9	0.69	36.0
z4	169.9	13.6	-	-	149.9	36.1	3.3	158.2	-	-	0.2	105.7	2.7	0.72	40.7
z6	297.5	23.8	-	-	74.4	21.4	1.0	79.3	-	-	0.3	82.4	1.1	0.64	30.2
z7	277.1	22.2	-	-	63.0	14.6	0.5	66.4	-	-	0.2	64.5	1.1	0.64	30.5
JP019, Imperial Fm. (siltstone) Norman Wells Quarry section, ~0.73 %Ro, 65.266 N 126.738 W															
a1	23.0	1.4	22.4	2.0	4.0	47.7	24.3	15.1	15.7	0.5	11.8	1.0	0.7	0.52	31.3
a2	224.9	13.5	219.7	18.7	4.0	43.7	38.0	14.2	14.7	0.5	11.0	10.0	1.0	0.56	34.4
a3	37.1	2.2	36.2	3.1	2.7	49.3	21.4	14.1	14.6	0.5	18.5	1.5	0.6	0.50	29.9
a4	37.2	2.2	35.8	3.6	29.1	89.3	18.7	49.8	52.0	2.2	3.1	5.2	0.6	0.51	30.1
a6	17.0	1.0	16.1	2.0	3.9	76.2	54.0	21.7	24.8	3.1	19.5	0.9	0.4	0.44	25.9
10FNARL008, Imperial Fm. (lithic arenite) Carcajou River section, ~0.74 %Ro, 64.752 N, 126.778 W															
a1	21.4	1.3	21.0	1.7	1.2	122.0	16.9	29.4	30.6	1.2	101.7	1.9	0.9	0.55	33.9
a2	26.4	1.6	24.9	3.1	3.9	233.7	68.6	58.0	60.4	2.3	60.0	4.6	0.8	0.54	32.8
a3	40.4	2.4	38.7	4.2	22.7	262.2	18.8	83.1	86.9	3.7	11.6	11.7	1.7	0.63	42.6
a4	42.0	2.5	41.0	3.6	38.6	313.2	58.6	111.0	115.4	4.4	8.1	13.1	0.7	0.51	30.3
a5	47.9	2.9	46.3	4.4	71.6	230.9	39.0	125.0	129.6	4.7	3.2	17.7	0.8	0.54	32.1
a6	15.0	0.9	14.7	1.2	2.1	119.9	35.3	29.9	31.2	1.3	56.2	1.3	0.7	0.51	31.0
a7	22.7	1.4	22.1	1.9	23.1	114.7	20.3	49.6	51.5	1.9	5.0	3.7	1.3	0.60	38.4
a8	17.1	1.0	17.0	1.1	2.2	119.3	31.5	29.8	36.4	6.6	53.4	1.5	1.0	0.54	32.8
a9	24.9	1.5	23.1	3.2	28.7	219.5	31.6	79.4	82.9	3.5	7.6	5.1	0.5	0.47	27.6
a10	33.3	2.0	32.6	2.7	0.9	104.5	59.9	25.3	26.4	1.1	115.6	2.4	0.6	0.50	30.3
Husky7, Imperial Fm. (fine grain sandstone) Redstone River section, ~1.67 %Ro, 63.916 N, 125.198W															
a1	44.8	2.7	42.0	5.5	9.7	110.9	62.2	35.6	36.8	1.3	11.4	4.4	0.6	0.50	29.9
a2	56.5	3.4	54.2	5.7	38.9	119.1	27.3	66.4	69.0	2.6	3.1	9.8	0.4	0.48	27.4
a3	28.3	2.3	27.8	2.7	5.0	169.0	63.7	44.2	46.2	1.9	33.7	3.3	0.5	0.47	27.7
a4	25.0	1.5	24.3	2.2	15.8	258.1	130.4	75.9	79.1	3.2	16.3	5.0	0.5	0.48	28.1
a5	12.7	1.0	12.4	1.3	12.0	189.1	52.1	55.8	58.3	2.6	15.8	1.7	0.4	0.44	26.0
a6	39.5	2.4	38.7	3.2	1.9	135.3	40.2	33.2	38.6	1.4	71.9	3.6	0.5	0.49	29.0
a7	43.1	2.6	41.5	4.2	53.1	176.3	28.2	93.9	97.3	3.5	3.3	11.2	0.6	0.51	29.6
a8	41.0	2.5	39.8	3.7	21.7	164.6	31.9	59.7	62.9	3.2	7.6	7.0	0.7	0.52	31.0
a9	67.2	5.4	66.0	6.6	8.2	99.4	27.6	31.2	32.6	1.3	12.1	5.9	0.6	0.51	30.5
a10	32.7	2.6	32.0	3.2	6.5	60.5	31.9	20.6	21.5	0.9	9.3	1.9	0.7	0.52	31.0
a11	32.9	2.6	30.9	4.7	13.4	214.7	36.2	63.0	65.2	2.3	16.1	5.3	0.5	0.47	27.5
Husky6, Imperial Fm. (siltstone), Redstone River section, ~1.67 %Ro, 63.954 N, 125.047 W															
z1	414.7	33.2	-	-	136.7	58.7	1.1	150.3	-	-	0.4	254.2	3.9	0.73	43.5
z2	96.7	7.7	-	-	441.7	127.7	0.7	471.1	-	-	0.3	197.7	11.3	0.80	58.3
z4	97.9	7.8	-	-	469.8	227.2	1.7	522.2	-	-	0.5	221.0	10.0	0.79	57.8
z5	101.7	8.1	-	-	150.5	27.2	0.4	156.7	-	-	0.2	73.7	23.7	0.85	79.7
z6	372.4	29.8	-	-	127.7	77.1	11.4	145.5	-	-	0.6	209.2	2.4	0.70	38.0
z8	233.0	18.6	-	-	316.4	66.2	59.2	331.9	-	-	0.2	303.6	2.8	0.72	39.8

Note: Corr. Age is the measured (U-Th)/He age, corrected for the effects of alpha ejection (Ft correction; *Farley et al*., 1996). Err. is the 6% error for apatite and 8% error for zircon. Modified age and error account for different alpha ejection caluclations [*Ketcham et al*., 2011] and variable morphology [*Beaucher et al*., 2013; *Brown et al*., 2013]. eU = [U]+(0.235*[Th]). Modified eU and error investigate the range of eU concentrations expected if the width of the crystallographic b axis was 75% the width of the a axis. ESR is the equivalent radius of a sphere with the same SA/V ratio of the measured apatite grain. Organic thermal maturity data (%Ro) for each sample can be retrieved from the supporting information document

Table 2. Apatite fission track data, Imperial Formation, Mackenzie Plains, NWT

Sample (kinetic population)	*n*	$\sum N_s$	$\sum P_i\Omega_i$	$\sum\sigma_{Pi}^2\Omega^2$	Q (%)	Pooled AFT date (Ma)	one sigma (Ma)	MTL ± st. dev (*n*)	D_{par} (μm)	r_{mr0}
JPCPC3, Imperial Fm. (siltstone) Powell River section, ~0.70 %Ro, 65.277 N, 128.774 W										
JPCPC3-1	24	343	5.6E-05	7.9E-13	27	50.2	2.9	13.6 ± 1.8 (104)	2.2	0.90-0.76
JPCPC3-2	4	50	2.4E-06	4.3E-15	62	170.1	24.7	14.1 ± 2.2 (17)	2.6	0.76-0.64
JPCPC4, Imperial Fm. (siltstone) Imperial River section, ~0.66 %Ro, 65.116 N, 127.859 W										
JPCPC4-1	7	137	2.5E-05	1.7E-13	34	45.7	4.1	13.9 ± 1.5 (92)	2	0.90-0.82
JPCPC4-2	14	175	1.7E-05	1.3E-13	53	85.9	6.9	13.3 ± 2.1 (39)	2.1	0.82-0.76
JPCPC4-3	13	291	1.1E-05	5.1E-14	13	224.1	14.5	13.0 ± 2.4 (28)	2.4	0.76-0.62
10FNARL008, Imperial Fm. (lithic arenite) Carcajou River section, ~0.74 %Ro, 64.752 N, 126.778 W										
10FNARL008-1	4	3	2.2E-06	1.2E-15	21	11.2	6.5	11.4 ± 0.1 (3)	1.8	0.90-0.86
10FNARL008-2	18	230	4.1E-05	5.7E-14	84	46.0	3.1	13.6 ± 1.4 (35)	2	0.86-0.76
10FNARL008-3	4	54	1.9E-06	5.9E-16	12	225.4	31.0	12.2 ± 1.6 (10)	2.3	0.76-0.47
Husky7, Imperial Fm. (fine grain sandstone) Redstone River section, ~1.67 %Ro, 63.916 N, 125.198W										
Husky7-1	5	24	5.8E-06	1.1E-13	50	26.6	5.7	13.4 ± 1.0 (10)	1.5	0.90-0.86
Husky7-2	8	79	9.2E-06	1.1E-13	52	55.0	6.8	13.0 ± 1.7 (42)	1.7	0.86-0.84
Husky7-3	10	129	8.2E-06	7.0E-14	98	100.6	10.1	11.7 ± 2.5 (133)	2.0	0.84-0.76
Husky7-4	10	182	4.8E-06	2.6E-14	65	240.7	21.5	12.5 ± 2.0 (13)	2.5	0.76-0.70

Note: $\sum N_s$ is the sum of the number of spontaneous fission tracks for each kinetic population. $\sum P_i\Omega_i$ is the sum of the product of $^{238}U/^{43}Ca$ ratio (P_i) and corresponding track count area (Ω_i) for each apatite in the population. $\sum\sigma_{Pi}^2\Omega_i^2$ is the error for $\sum P_i\Omega_i$ and is used for calculating the error on the pooled AFT age. Q represents the chi-squared probability for each population. A population passes the chi-squared test if Q > 5%. D_{par} is the diameter of the etch figure parallel to the c axis. MTL is the mean track length for each population. Zeta factors differ between Husky7 and the other samples, in part, due to differences in the geometry factor (g). Whereas g = 0.5 in Husky7, it it set at 1 for the other samples as it was combined with the other constants and as such does not appear in the age equation

	JPCPC3; JPCPC4; 10FNARL008	Husky7
modified zeta	8.2727	12.92353
s.e. (zeta)	0.1407	0.4752371
total decay const.	1.55125E-10	1.55125E-10
geometry factor (g)	1	0.5

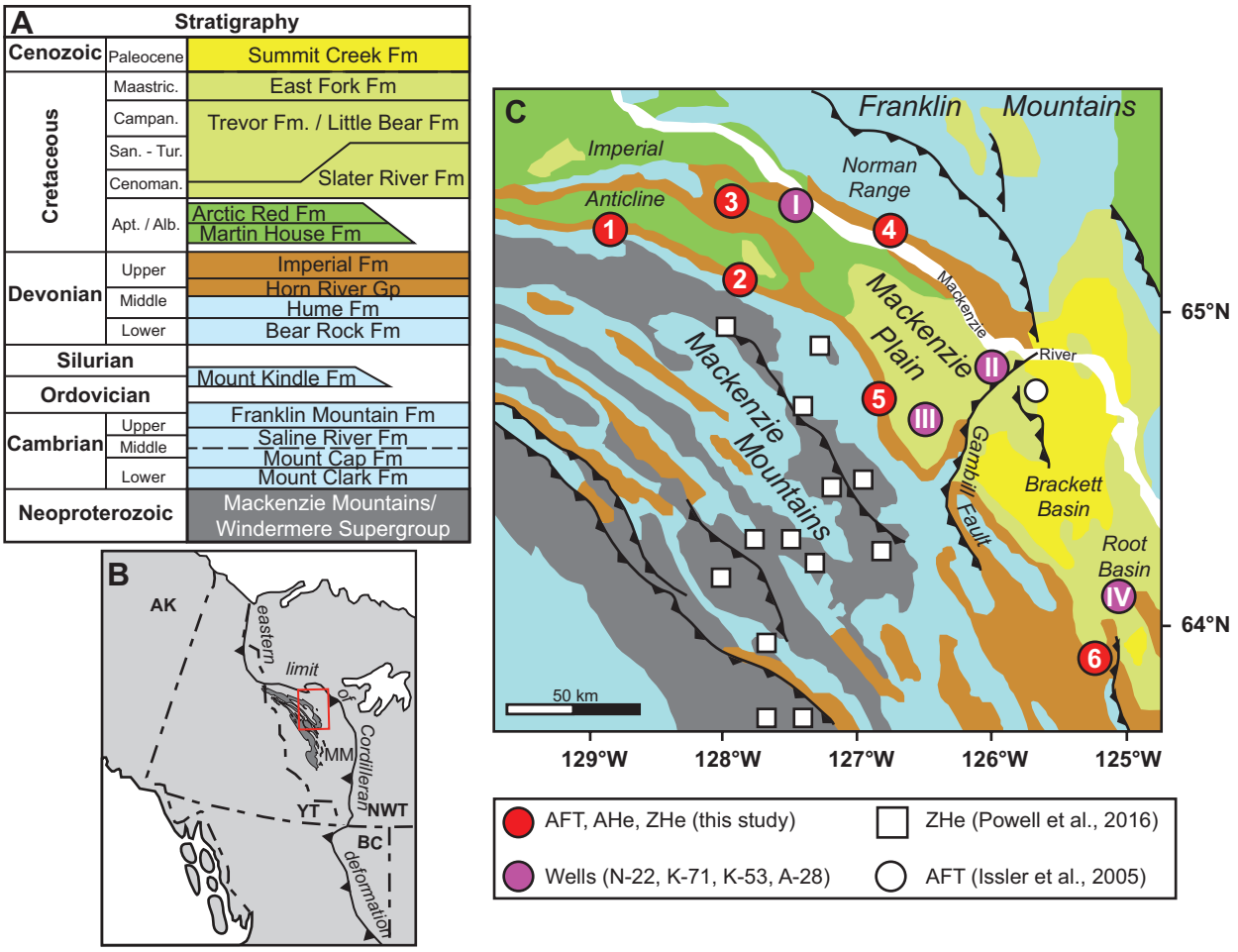

Fig. 1: A) Stratigraphic column for the Mackenzie Mountains and Plain, Northwest Territories, Canada (modified after Maclean and Cook, 1999 and Thomson et al., 2011). B) Simplified map of northwestern Canada and Alaska (modified after Powell et al., 2016) showing the location of the Mackenzie Mountains (MM; dark gray). Study area is denoted by the red box. C) Generalized geologic map highlighting the Neoproterozoic to Cenozoic bedrock geology of the study area [*Wheeler et al.*, 1996; *Fallas et al.*, 2013a, 2013b, 2013c; *Fallas and MacNaughton*, 2014a, 2014b, 2014c]. The colours of the map units correspond with the stratigraphy detailed in A. The locations of published thermochronology samples are shown as white circles and squares. Location of study samples shown by red circles: 1) JPCPC3; 2) JPCPC4; 3) 10FNA066; 4) JP019; 5) 10FNARL008; 6) Husky6 and Husky7. Purple circles indicate wells with organic thermal maturity data that are incorporated into this study: I) N-22; II) K-71; III) K-53; IV) A-28.

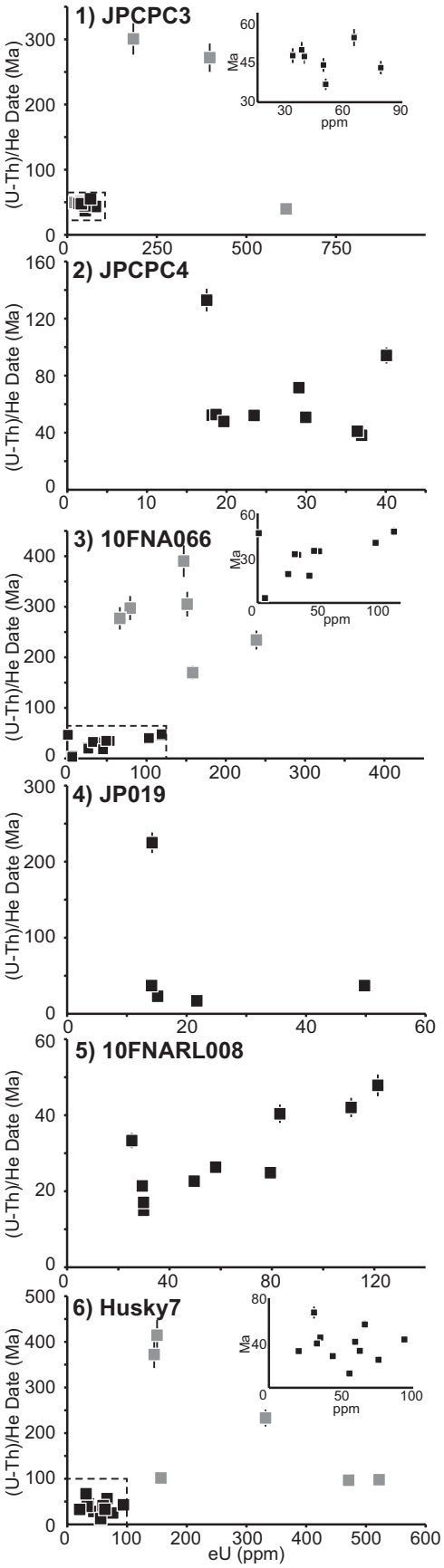

Fig 2: Single grain apatite (black squares) and zircon (gray squares) (U-Th)/He dates plotted against the effective uranium concentration (eU). For samples with both AHe and ZHe data (JPCPC3, 10FNA066, Husky7), the date-eU space outlined by a dashed box is expanded into an inset graph to show AHe date-eU relationships. Analytical errors for AHe and ZHe data are 6% and 8%, respectively.

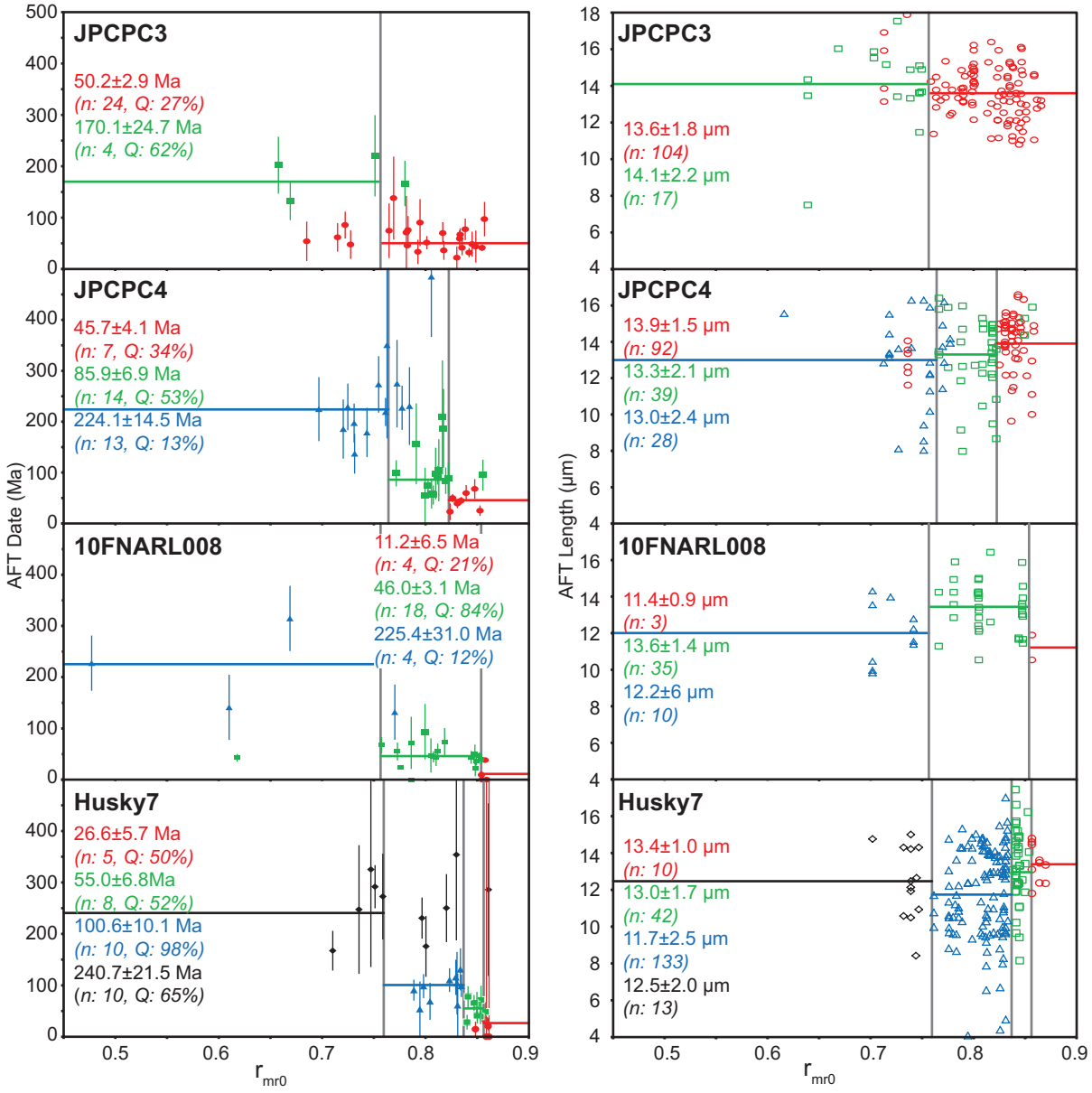

Fig. 3: AFT date and track length distribution for the four samples examined in this study, plotted against the kinetic parameter r_{mr0}. Data define distinct kinetic populations on the basis of date and kinetic parameter. Horizontal lines and the correspondingly coloured text indicate the pooled ages and mean track length for each kinetic population. Vertical grey lines indicate the boundaries between kinetic populations. All kinetic populations pass the χ^2-test ($Q > 0.05$) indicating that they represent statistically significant groups of data. Errors on AFT dates are 1 S.D. Corresponding tables showing AFT date, track length and chemistry and figures that display radial plots [*Vermeesch*, 2009] of AFT dates and peak ages can be retrieved in the Appendix.

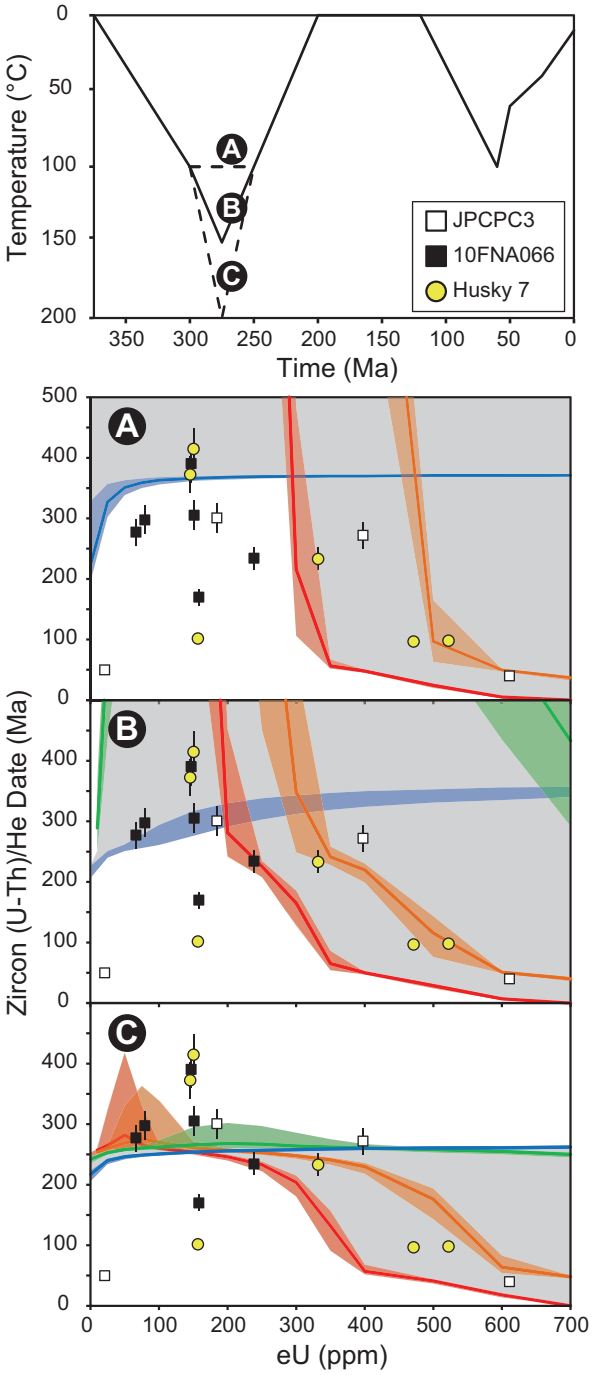

Fig. 4: Forward thermal history models showing the predicted date-eU relationships for three (A, B, C) candidate burial histories with varying Paleozoic maximum temperatures (100°C, 150°C, 200°C) and a single Cretaceous 100°C heating and cooling event. Coloured curves indicate ZHe inheritance date-eU trends for 30-60 µm zircons (solid line: 45 µm) with variable pre-depositional histories (red: 2750 Ma; orange: 2000 Ma; green: 1000 Ma; blue: 375 Ma). The gray shaded area bounded by the coloured inheritance date-eU curves denotes the inheritance envelope, or the realm of plausible ZHe date-eU relationships for the candidate post-depositional history, given the unknown pre-depositional history for each zircon.

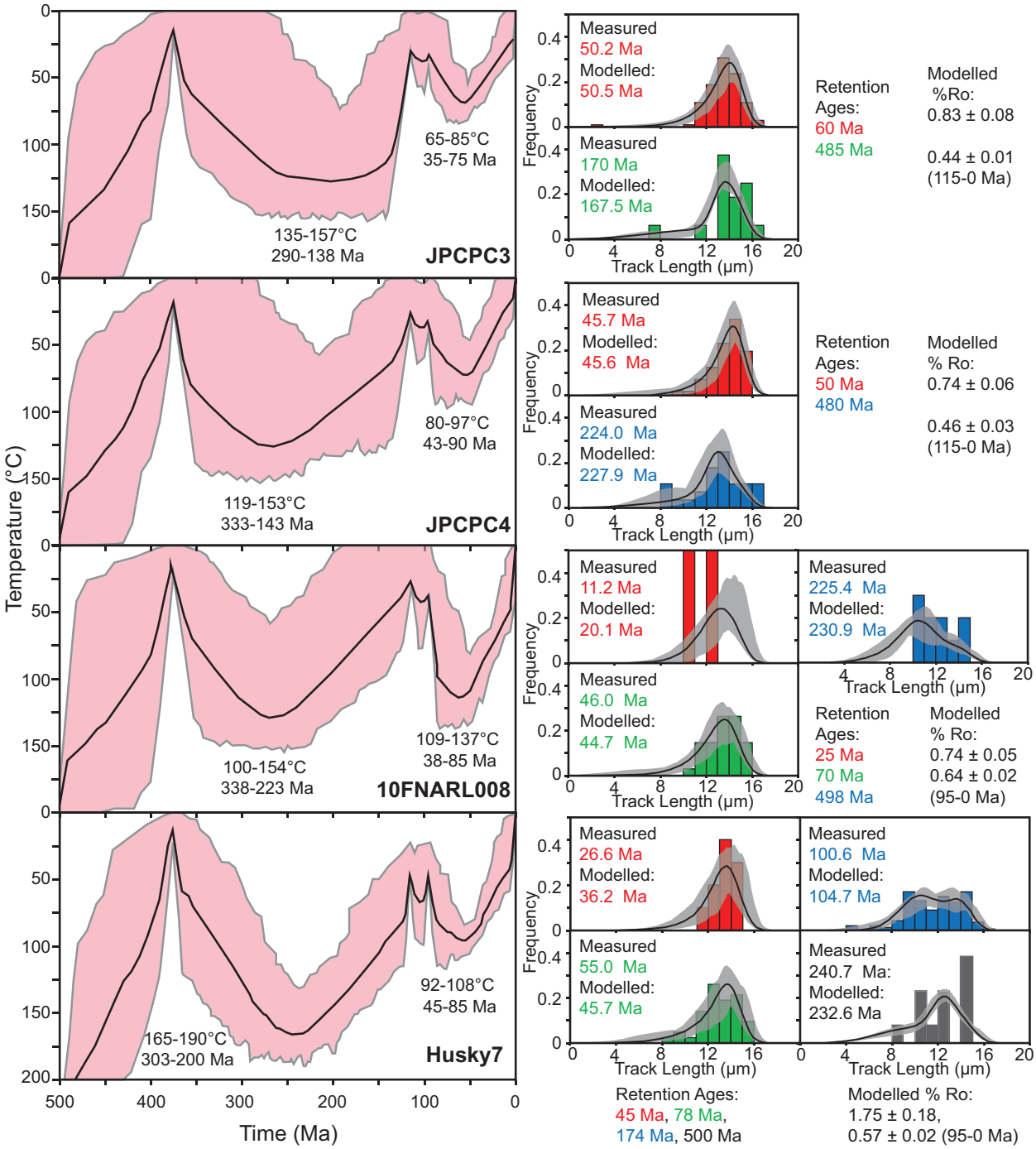
Temperature (°C)
Time (Ma)
65-85°C
35-75 Ma
135-157°C
290-138 Ma
JPCPC3
80-97°C
43-90 Ma
119-153°C
333-143 Ma
JPCPC4
109-137°C
38-85 Ma
100-154°C
338-223 Ma
10FNARL008
92-108°C
45-85 Ma
165-190°C
303-200 Ma
Husky7
Measured
50.2 Ma
Modelled:
50.5 Ma
Measured
170 Ma
Modelled:
167.5 Ma
Retention Ages:
60 Ma
485 Ma
Modelled %Ro:
0.83 ± 0.08
0.44 ± 0.01
(115-0 Ma)
Measured
45.7 Ma
Modelled:
45.6 Ma
Measured
224.0 Ma
Modelled:
227.9 Ma
Retention Ages:
50 Ma
480 Ma
Modelled % Ro:
0.74 ± 0.06
0.46 ± 0.03
(115-0 Ma)
Measured
11.2 Ma
Modelled:
20.1 Ma
Measured
46.0 Ma
Modelled:
44.7 Ma
Measured
225.4 Ma
Modelled:
230.9 Ma
Retention Ages:
25 Ma
70 Ma
498 Ma
Modelled % Ro:
0.74 ± 0.05
0.64 ± 0.02
(95-0 Ma)
Measured
26.6 Ma
Modelled:
36.2 Ma
Measured
55.0 Ma
Modelled:
45.7 Ma
Measured
100.6 Ma
Modelled:
104.7 Ma
Measured
240.7 Ma:
Modelled:
232.6 Ma
Retention Ages:
45 Ma, 78 Ma,
174 Ma, 500 Ma
Modelled % Ro:
1.75 ± 0.18,
0.57 ± 0.02 (95-0 Ma)
Frequency
Track Length (μm)

Fig. 5 (previous page): Four inverse thermal history models derived from AFT kinetic populations (identified in Figure 3) using the software AFTINV [*Issler*, 1996]. The pink envelope indicates the solution boundary of 300 statistically significant Monte Carlo solutions. The black curve is the exponential mean of all 300 solutions. For each inverse thermal history model, coloured histograms show measured track length distribution for each kinetic population (colours correspond to kinetic populations in Figure 3). Black curves represent the probability density functions of predicted track lengths for the exponential mean thermal history. The light gray shaded regions show the solution bounds for probability density functions calculated from all 300 Monte Carlo solutions. For each kinetic population, both the measured (pooled) and modeled (from the exponential mean solution) AFT dates are shown. The retention age is derived from the exponential mean solution and indicates the oldest track length greater than 2 microns for each kinetic population. Additionally, each calculated %Ro value predicts the resulting thermal maturity for the sample from both deposition (375 Ma) to present and Cretaceous (115, 95 Ma) to present. The inverse thermal history model was run in conventional track length mode to compare calculated length distributions with observed length distributions.

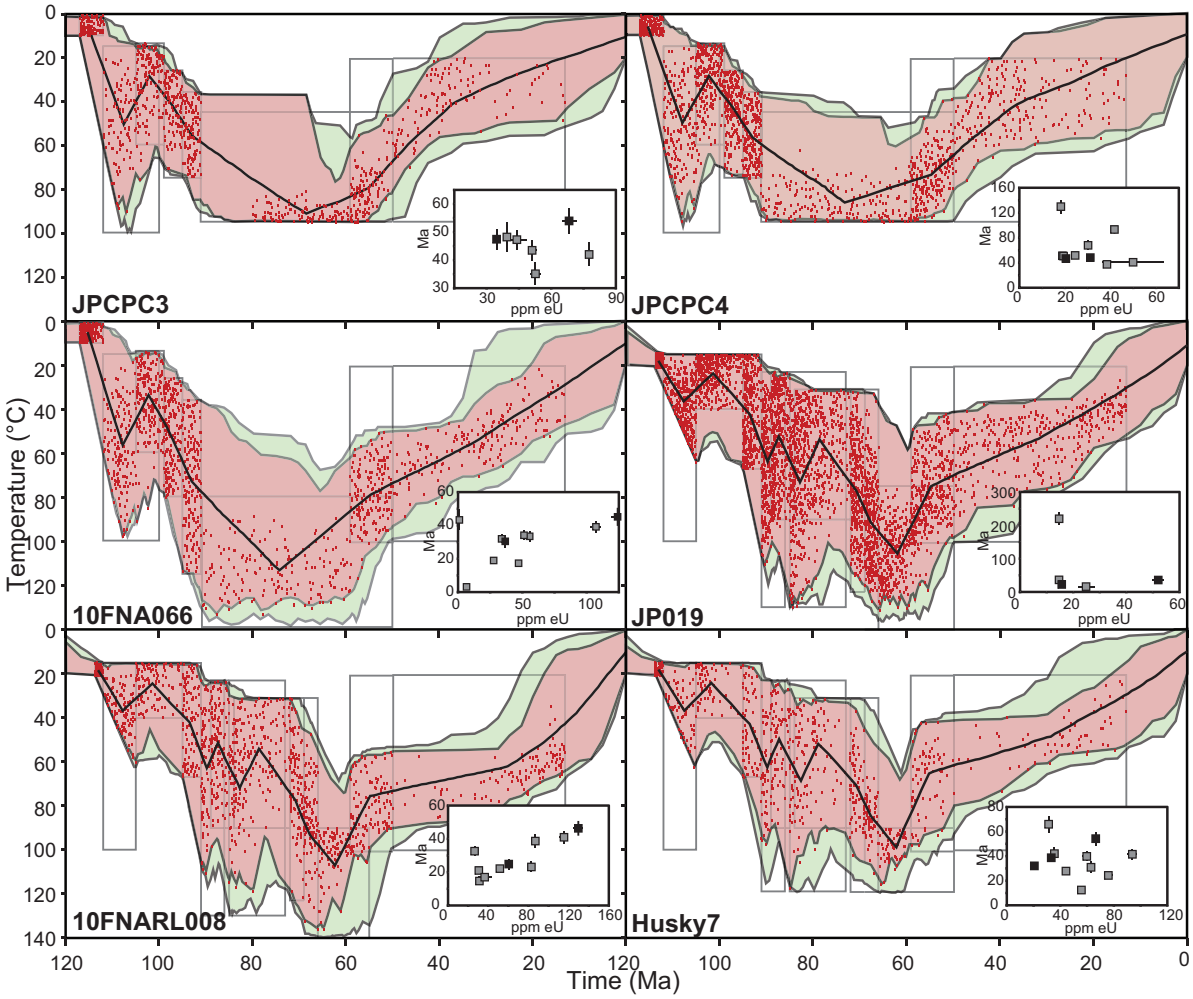

Fig. 6: Inverse thermal history model incorporating AHe data created using HeFTy (Ketcham, 2005). Light green and pink envelopes indicate the realm of t-T solutions for acceptable and good paths, respectively. Red dots indicate the inflection points of good t-T paths. Gray outlined rectangles represent independent time-temperature constraints based on preserved stratigraphic section, unconformities, plausible geothermal gradients, and the range of maximum temperatures as indicated by AFT modeling (Fig. 5). The black curve indicates the weighted mean t-T path of all acceptable and good solutions. Inset graph shows AHe dates, modified from Figure 2 to account for variable geometries and broken grains. AHe grains in black were incorporated into the inverse model. Although these figures only display the modeled Cretaceous thermal history, expanded models (Devonian to present) are available in the Appendix to this Chapter, as is a table that summarizes age and thickness of Cretaceous stratigraphy incorporated into the models as t-T constraints.

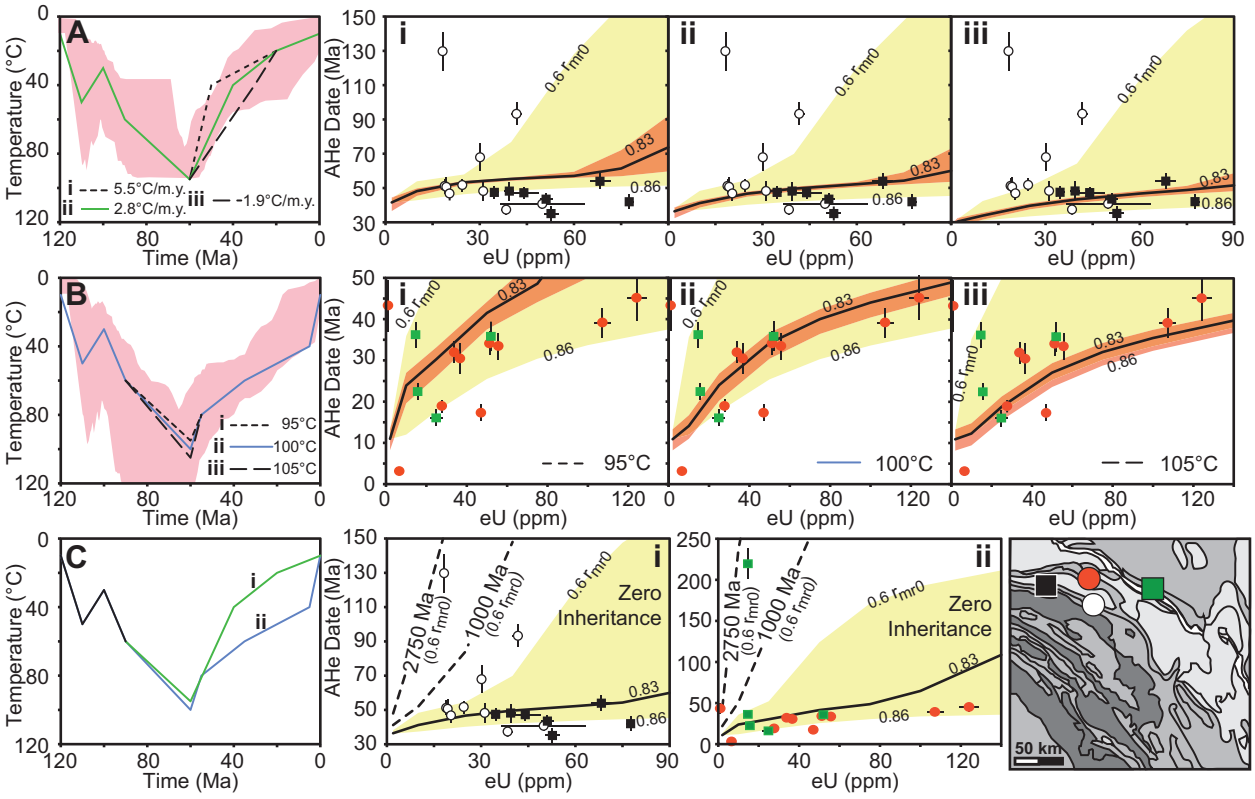

Fig. 7: Forward models assessing three different thermal histories for samples A) JPCPC3 and JPCPC4, and B) 10FNA066 and JP019. Pink polygons outline the envelope of good paths from the JPCPC3 and 10FNA066 inverse thermal history model. Inset map shows the sample location for the data points of corresponding symbol. For each forward model, the orange envelope highlights the expected date-eU relationships for fluorapatite (0.83 r_{mr0}) with grain sizes between 25-45 µm (solid line: 35 µm). The yellow envelope outlines the realm of plausible AHe date-eU relationships for variable apatite chemistry and damage-annealing kinetics (35 µm; 0.60-0.86 r_{mr0}). C) Forward thermal history models for Aii and Bii, accounting for predepositional histories and inherited radiation damage. The yellow envelope indicates the expected date-eU relationship for apatite with zero inheritance (35 µm; 0.60-0.86 r_{mr0}). Dashed lines show date-eU trends for retentive apatite (0.6 r_{mr0}) with variable pre-depositional histories (2750 Ma, 1000 Ma).

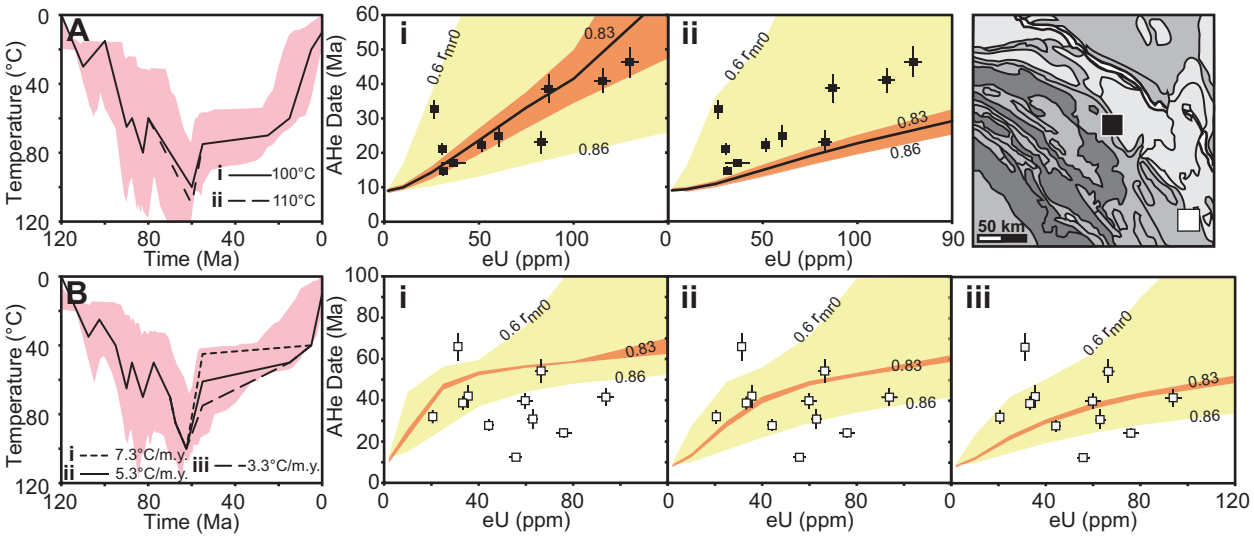

Fig. 8: A) Forward thermal history models assessing two different maximum Cretaceous-Cenozoic temperatures for sample 10FNARL008. Pink polygon outlines the envelope of good paths from the 10FNARL008 inverse thermal history model. For each forward model, the orange envelope highlights the expected date-eU relationships for fluorapatite (0.83 r_{mr0}) with grain sizes between 25-45 µm (solid line: 35 µm). The yellow envelope outlines the realm of plausible AHe date-eU relationships for variable apatite chemistry and damage-annealing kinetics (35 µm; 0.60-0.86 r_{mr0}). B) Forward thermal history models assessing three different cooling histories for sample Husky7. Pink polygon outlines the envelope of good paths from the 10FNARL008 inverse thermal history model. For each forward model, the orange envelope highlights the expected date-eU relationships for fluorapatite (0.83 r_{mr0}) with grain sizes between 25-35 µm. The yellow envelope outlines the realm of plausible AHe date-eU relationships for variable apatite chemistry and damage-annealing kinetics (30 µm; 0.60-0.86 r_{mr0}). Inset map shows the sample location for the data points of corresponding symbol.

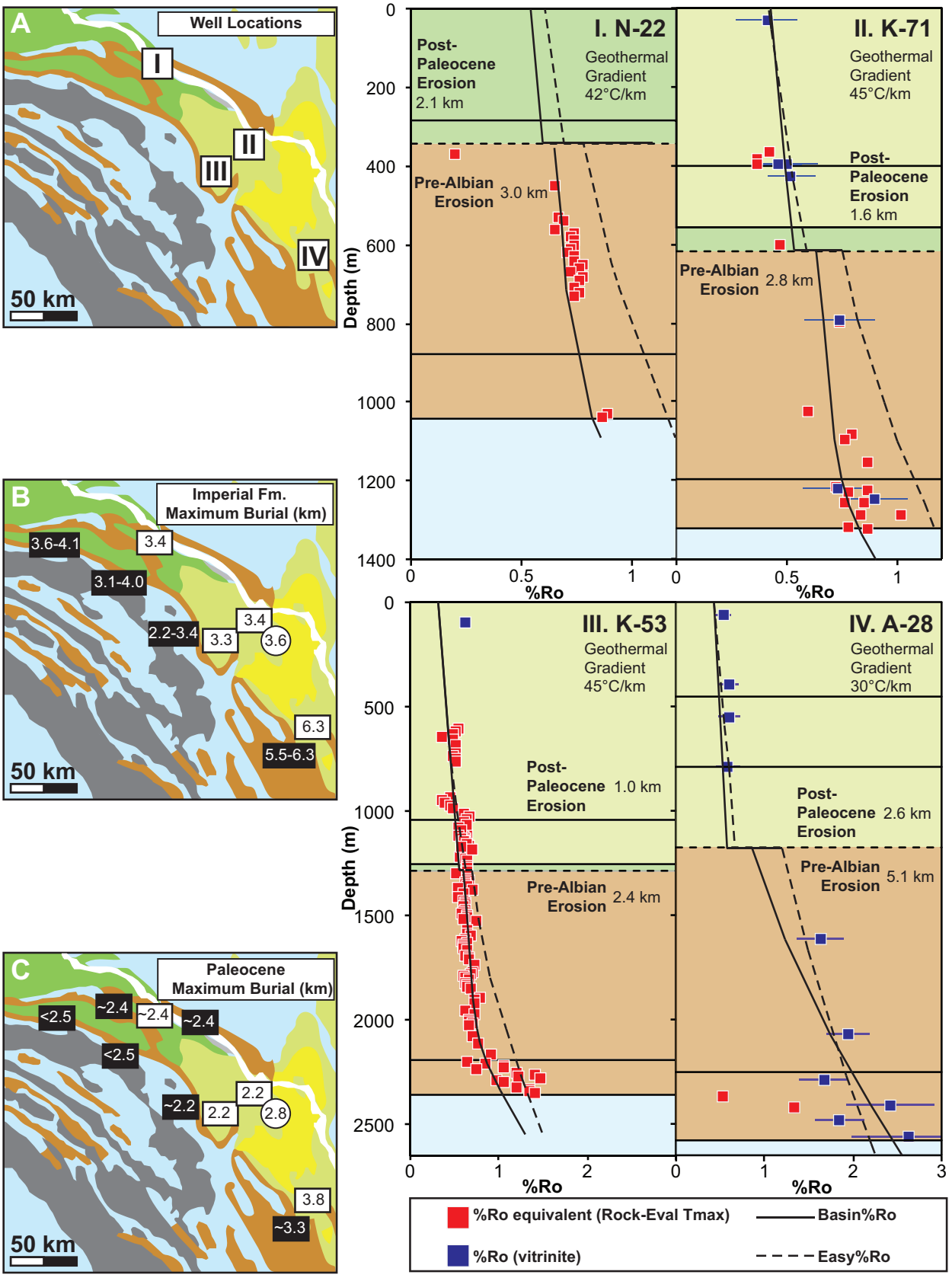
A
Well Locations
I
II
III
IV
50 km
B
Imperial Fm.
Maximum Burial (km)
3.6-4.1
3.4
3.1-4.0
2.2-3.4
3.3
3.4
3.6
6.3
5.5-6.3
50 km
C
Paleocene
Maximum Burial (km)
<2.5
~2.4
~2.4
~2.4
<2.5
~2.2
2.2
2.2
2.8
3.8
~3.3
50 km
I. N-22
Geothermal Gradient 42°C/km
Post-Paleocene Erosion 2.1 km
Pre-Albian Erosion 3.0 km
II. K-71
Geothermal Gradient 45°C/km
Post-Paleocene Erosion 1.6 km
Pre-Albian Erosion 2.8 km
III. K-53
Geothermal Gradient 45°C/km
Post-Paleocene Erosion 1.0 km
Pre-Albian Erosion 2.4 km
IV. A-28
Geothermal Gradient 30°C/km
Post-Paleocene Erosion 2.6 km
Pre-Albian Erosion 5.1 km
Depth (m)
%Ro
%Ro equivalent (Rock-Eval Tmax)
%Ro (vitrinite)
Basin%Ro
Easy%Ro

Fig. 9 (previous page): A) Location of selected wells (I-IV) and their corresponding organic thermal maturity profiles. An expanded methodology on the treatment of Rock-Eval pyrolysis data is available in the Appendix. Coloured stratigraphy for each well corresponds to map units (Fig. 1), and horizontal lines delineate formation tops. Estimates of pre-Albian and post-Cretaceous erosion for each well were based on the difference between preserved stratigraphic thickness and the maximum burial depth indicated from thermal history modeling of proximal outcrop samples assuming a constant geothermal gradient equivalent to the present day value. Predicted vitrinite reflectance profiles were generated for each well using both the basin%Ro model (solid black line; Nielsen et al., 2015) and EASY%Ro model (dashed line; Sweeney and Burnham, 1990). Vitrinite reflectance values (blue squares) are an averaged value, with error bars corresponding to the total range of measurements for each sample. Rock-Eval pyrolysis Tmax values were converted to a vitrinite reflectance equivalent using the relationship of *Jarvie et al*. [2001]. B, C) Suggested maximum burial thicknesses of B) Devonian Imperial Formation, and C) Cretaceous – Paleocene strata overlying the sub-Cretaceous unconformity for outcrop samples (black box), wells shown in A (white box), and the I-77 well (white circle; Issler et al., 2005). Outcrop-specific burial depth estimates were generated from temperatures indicated from AFT and AHe thermal history models (Fig. 5, 7, 8) and the present day geothermal gradients of adjacent wells.

Appendix to

CHAPTER 4: Thermal history of the Mackenzie Plain, NWT, Canada: insights from low-temperature thermochronology of the Devonian Imperial Formation

Jeremy Powell[1], Dale Issler[2], David Schneider[1], Karen Fallas[2], Daniel Stockli[3]
1. Department of Earth & Environmental Sciences, University of Ottawa, Ottawa, Canada
2. Natural Resources Canada, Geological Survey of Canada, Calgary, Canada
3. Jackson School of Geoscience, University of Texas at Austin, Austin, USA

Contents

- Expanded AHe, ZHe and AFT methods and results
- Expanded organic thermal maturity methods and results
- Comment on AFTINV software
- Tables A1 – A6
- Figures A1 – A10

Introduction

This Appendix incorporates text on analytical methods, expanded results figures that illustrate the apatite (U-Th)/He inverse thermal history models, and radial plots for all fission track samples. Additionally, it includes tables that show fission track age, track length distribution and chemistry for the four samples discussed in the Chapter 4, organic thermal maturity data used in thermal history modeling, and Cretaceous stratigraphic thicknesses used in AHe inverse history modeling.

Text A1. Analytical methods and results

A.1.1. Apatite and zircon (U-Th)/He method

Apatite and zircon (U-Th)/He analyses were conducted at the University of Texas Geo-Thermochronometry Lab (Austin, USA), and follow common (U-Th)/He dating conventions [*Stockli et al.*, 2000; *Wolfe and Stockli*, 2010]. Following standard mineral separation, apatite and zircon were handpicked using a customized Nikon SMZ-U/100 stereomicroscope, and photographed using Nikon digital ColorView® camera. Grain dimensions were measured using the AnalySIS® software. In an effort to pick inclusion-free apatite, all grains analyzed were carefully screened for inclusions in isopropanol at 180x magnification. Apatite and zircon grains were wrapped in Pt foil and degassed using in-vacuo diode laser heating at 1050°C and 1300°C, respectively. ^{4}He was measured via quadrupole ultra-high vacuum noble gas extraction and mass-spectrometry system with a cryogenic trap. A ^{3}He spike was used for isotope dilution. All apatites were degassed twice to ensure complete degassing, and zircons were repeatedly heated until He yields were <1%. Degassed single grains were dissolved for ^{238}U, ^{232}Th, ^{149}Sm determinations by isotope dilution using an Element 2 ICP-MS. HNO_3 was used for apatite dissolution, whereas zircon were dissolved using a HF-HCl two-step pressure vessel procedure. All data were corrected for the effects of helium ejection [*Farley et al.*, 1996]. AHe and ZHe dates are reported with a standard error of 6% and 8%, respectively, which are reflective of the standard deviation of a population of analyzed standards.

Given that dispersion amongst AHe dates is common [*Flowers et al.*, 2009; *Brown et al.*, 2013; *Murray et al.*, 2014], especially in rocks with protracted cooling histories [*Fitzgerald et*

al., 2006; *Ault et al.*, 2013] the 6% error applied to the AHe dates is likely not reflective of the true reproducibility of an analysis and may be too restrictive for modeling of the young AHe dates in this dataset. Additionally, since many of these data were collected from 2012 through 2014, more recent grain-specific variables, including the effect of variable geometry [*Beucher et al.*, 2013; *Brown et al.*, 2013] and more recent methods for calculating Ft corrections [*Ketcham et al.*, 2011] were not factored into data reduction. Nor were the dimensions in a second crystallographic width, as Ft corrections were generated under the assumption that the crystallographic A- and B-axes are equidimensional. This could be problematic, as most detrital apatite are beveled to some degree, and as a result the crystal volume and mass derived from the apatite geometry may be an overestimate.

Due to the above reasons, ages and eU concentrations used in modeling were recalculated from the original data to test the effect of broken crystals, varying grain morphologies, different methods for calculating the Ft correction and a B-axis that is 75% the diameter of the A-axis. The modeled date, error and eU concentrations are an average of the difference between our original corrected dates and the recalculated values. Overall, the modeled AHe date is <5% different than the original corrected date, and the errors used in modeling are ~10% the modeled date. Modeled eU concentrations are mostly within 5% of the original values, but can be substantially larger when the mass of the recalculated grain is substantially less than the original value. This is especially evident in grain JPCPC4-5, where the mass of the bipyramidal grain with a smaller second width is much less than initially calculated (1.05 μg vs 1.89 μg). Whereas these modeled ages do not represent a "truer" AHe date than those reported, they are perhaps a better representation of plausible variability in detrital AHe dates than the standard 6% error.

A suite of 53 single-grain AHe dates was collected from the six Imperial Formation samples. Sixteen ZHe dates were acquired from three Imperial Formation samples in which zircon grains were present (Table 1). Sample JPCPC3 has seven AHe dates that range from 37.0 ± 2.2 to 55.3 ± 3.3 Ma and four ZHe dates that form two disparate populations younger than the depositional age (39.9 ± 3.2 to 49.7 ± 4.0 Ma; 271.9 ± 21.8 to 300.7 ± 24.1 Ma). The eU concentrations for apatite and zircon grains lie between 33 and 79 ppm and 21 to 611 ppm, respectively. Ten apatite grains from sample JPCPC4 yield AHe dates between 38.2 ± 2.3 to 132.9 ± 8.0 Ma. AHe dates have no obvious trend with respect to eU concentration, which varies from 18 to 40 ppm in the sample. Ten apatite and six zircon (U-Th)/He dates were acquired from the Imperial anticline sample 10FNA066. AHe dates range from 3.2 ± 0.2 to 47.7 ± 2.9 Ma and are positively correlated with increasing eU concentration (1 to 119 ppm). ZHe dates span 169.9 ± 13.6 to 390.4 ± 31.2 Ma over an eU range of 66 to 239 ppm. Sample JP019 from Norman Wells had few apatite grains and only yielded five AHe dates. Four of these dates are between 17.0 ± 1.0 and 37.2 ± 2.2 Ma, with the fifth grain yielding a much older 224.9 ± 13.5 Ma. This large range in AHe dates does not correspond with increases in the eU concentration from 14 to 50 ppm. The ten AHe dates from sample 10FNARL008 are positively correlated with eU concentration, increasing gradually from 15.0 ± 0.9 to 47.9 ± 2.9 Ma as eU increases 25 to 125 ppm. The furthest southeast sample, Husky7, has eleven AHe dates that range from 12.7 ± 1.0 to 67.2 ± 5.4 Ma. Dispersion within the sample cannot be explained with respect to increasing eU concentrations (21 to 94 ppm). Six ZHe dates from the adjacent sample, Husky6, are broadly scattered from 96.7 ± 7.7 to 414.7 ± 33.2 Ma. With the exception of a single data point, the ZHe dates are negatively correlated with eU concentration.

A.1.2 LA-ICP-MS fission track method

The four samples processed for apatite fission track thermochronology were analyzed using the laser ablation inductively coupled plasma mass spectrometry method (LA-ICP-MS) method [*Hasebe et al.*, 2004; *Donelick et al.*, 2005; *Chew and Donelick*, 2012] and the modified zeta calibration [*Hurford and Green*, 1983; *Hasebe et al.*, 2004]. Samples were analyzed by Paul O'Sullivan at Apatite to Zircon, Incorporated (Viola, USA) using a Resonetics M-50 193 nm ArF Eximer laser-ablation system coupled to an Agilent 7700x quadrupole ICP-MS. Laser ablation was conducted using a 26 mm spot and a 7 Hz laser repetition rate with the laser set in constant energy mode. Fission tracks were viewed and counted or measured at 2000x (Zeiss Axioplan microscope) dry magnification using unpolarized, transmitted light with or without reflected light. All AFT age (Table A1) and length grains (Table A2) were selected to sample the greatest range of observable characteristics (size, degree of roundness, color, etch figure size, etc.). Durango (DR) was used as the apatite FT zeta age calibration standard. During each LA-ICP-MS session containing samples of unknown FT age, clusters of ~10 zeta spots were analyzed during the session for purposes of calibrating $^{238}U/^{43}Ca$. Ratios of primary zeta (original zeta LA-ICP-MS session) to secondary zeta (current LA-ICP-MS session) $^{238}U/^{43}Ca$ were determined for each zeta calibration spot and smoothed using a load-specific running-median method. Only spots visited during the primary, original zeta LA-ICP-MS session were revisited during the secondary, current LA-ICP-MS session for this purpose. This method is analogous to using ^{235}U-doped glass standards in the external detector method of fission track analysis (Donelick et al., 2005); in this study, specific DR grains from the primary standard LA-ICP-MS session serve as ^{235}U-doped standards.

In an effort to understand the uranium content and range of chemistry present in our sample suite, all grains analyzed for AFTA were measured for major, minor and REE geochemistry. Analyses were conducted via LA-ICP-MS methods at Apatite to Zircon, Inc. (Viola, USA) using a Resonetics M-50-LR 193 nm ArF Excimer laser ablation system coupled to an Agilent 7700x quadrupole inductively coupled mass spectrometer (ICP-MS). The laser was operated at a repetition rate of 10 Hz, with a lateral spot size of 10 μm, and pulse energy of 0.422 mJ. In addition to the LA-ICP-MS data, major elements and halogens were analyzed at the University of Ottawa (Ottawa, Canada) to recalculate r_{mr0} values for samples that exhibited substantial kinetic overlap using r_{mr0} values from LA-ICP-MS derived chemistry. EPMA chemistry was measured using the JEOL JXA-8230 SuperProbe which operates with an accelerating voltage of 10 kV and beam current of 3.8 nA to focus and concentrate the electron beam to a minimum of 1 μm. These conditions were employed to better determine the halogen content in JPCPC3, JPCPC4 and Husky7, and in particular, to assess the effect of hydroxyl on calculated r_{mr0} values. Additionally, Husky7 was analyzed using the microprobe at Washington State University (Pullman, USA). We use the stoichiometric relationships [*Ketcham*, 2015] to convert measured weight% oxide values to atoms per formula unit (apfu), and later use these values to calculate grain-specific r_{mr0} values (Table A3). We opt to use the original r_{mr0} calculation [*Carlson et al.*, 1999] over the more recent derivation [*Ketcham et al.*, 2007], as the newer equation is based on combined annealing experiments from different labs, which may introduce systematic error to the calculated values.

Of the six samples analyzed for apatite (U-Th)/He analysis, four yielded sufficient apatite for apatite fission track analysis. Each sample exhibits substantial dispersion in AFT dates, and fails the c^2 test, indicating that the data do not comprise single kinetic populations. We use the kinetic parameter r_{mr0} [*Ketcham et al.*, 1999] to isolate statistically significant AFT populations

and report their pooled age and mean track length (Table 2). Twenty-eight AFT dates for sample JPCPC3 span 22.0 ± 22.1 to 220.3 ± 79.1 Ma. Two kinetic populations were identified on the basis of their r_{mr0} values (50.2 ± 2.9 Ma, 13.6 ± 1.8 μm; 170.1 ± 24.7 Ma, 14.1 ± 2.2 μm). Sample JPCPC4 has thirty-four AFT dates that range from 23.1 ± 16.4 to 484.9 ± 118.4 Ma. These dates were separated into three statistically significant populations (45.7 ± 4.1 Ma, 13.9 ± 1.5 μm; 85.9 ± 6.9 Ma, 13.3 ± 2.1 μm; 224.1 ± 14.5 Ma, 13.0 ± 2.4 μm). Sample 10FNARL008 yielded 26 AFT dates between 314.6 ± 63.6 and 9.2 ± 6.5 Ma and three discrete kinetic populations (11.2 ± 6.5 Ma, 11.4 ± 0.9 μm; 46.0 ± 3.1 Ma, 13.6 ± 1.4 μm; 225.4 ± 31.0 Ma, 12.2 ± 1.6 μm). Finally, the 33 AFT dates from sample Husky7 are between 353.94 ± 166.6 and 14.6 ± 14.8 Ma. These AFT data were separated into four distinct kinetic populations on the basis of their date and r_{mr0} values (26.6 ± 5.7 Ma, 13.4 ± 1.0 μm; 55.0 ± 6.8 Ma, 13.0 ± 1.7 μm; 100.6 ± 10.1 Ma, 11.7 ± 2.5 μm; 240.7 ± 21.5 Ma, 12.5 ± 2.0 μm).

Comparatively, Figs. A1 through A4 show radial plots [*Vermeesch*, 2009] for all four fission track samples. These plots graphically compare AFT dates with different precisions and can identify different AFT date populations within a single sample. Overall, there is good agreement between AFT kinetic populations recognized on the basis of r_{mr0} and those identified graphically.

A.1.3. Vitrinite Reflectance and Rock Eval

Vitrinite reflectance and Rock-Eval pyrolysis analyses were undertaken at the Geological Survey of Canada (Calgary, Canada). A short discussion on the techniques is included below, but is expanded upon in many GSC open file reports [*Issler et al.*, 2012, 2016].

Vitrinite reflectance is based on the percentage of incident light reflected from polished vitrinite macerals and is commonly used in sedimentary basin thermal history analysis. Kinetic models that account for the increase of vitrinite reflectance values with increasing burial temperature include the EASY%Ro calibration [*Sweeney and Burnham*, 1990] and the basin%Ro calibration [*Nielsen et al.*, 2015]. Crushed rock material between 1 and 10 mm in size is mounted into epoxy, ground using carborundum and diamond grit, and polished using a cloth and an alumina-water slurry. Microscopes used for study include a Zeiss UMSP microscope fitted with a UMP photometer and a Leitz MPM II with a PC-controller system. Organic material was observed under magnification (up to 2000x) with white and fluorescent light sources and oil, air and water immersion objectives. %Ro values were measured for several organic macerals and compared with glass standards of known refractive indices.

Rock-Eval pyrolysis was conducted on four samples using the Rock-Eval 6 machine at the GSC Calgary office. Rock-Eval pyrolysis is a technique that assesses the abundance, quality and thermal maturity of organic matter in sedimentary rocks. In this method, rock material is crushed into a powder, separated into ~70 mg aliquots and placed into stainless steel crucibles. Samples undergo non-isothermal pyrolysis in an inert atmosphere (nitrogen) to yield hydrocarbons (S1 and S2 curves) and oxidized carbon from organics and mineral sources (S3). Following the pyrolysis, samples are heated in an oxidation oven to determine the weight percent of total organic carbon (TOC).

Samples JPCPC3, JPCPC4, 10FNA066 and 10FNARL008 were organically-lean sandstones and were analyzed for both organic thermal maturity and Rock-Eval pyrolysis (Table A4). Organic petrology measured the reflectance of bitumen, vitrinite and recycled vitrinite. Due to the low number of measurements of natural vitrnite, the thermal maturity indicated from these reflectance data should be considered as broad estimates. Likewise, %Ro equivalents from

bitumen reflectance may be measuring migrated bitumen, and as a result reflects the lower boundary of the true maturity. Thermal maturity as indicated by Rock-Eval pyrolysis Tmax data from the same samples are in many cases spurious due to the low weight % TOC values and S2 values. Table A5 is comprised of pertinent Rock-Eval data for Cretaceous and Devonian outcrop samples proximal to 10FNA066, JP019 and well N-22.

In manuscript Figure 9, Rock-Eval pyrolysis data from wells in the Mackenzie Plain [*Feinstein et al.*, 1988] were deemed suspect if total organic carbon was <0.5 wt% or if the value corresponding to the S2 curve was <0.5 mg HC/g of initial rock [*Issler et al.*, 2012, 2016], and egregious data were not converted to %Ro equivalents. The depth of stratigraphic formation tops were taken from publically available databases [*Hadlari et al.*, 2013; *NEB*, 2013] and used to determine stratigraphic ages and thicknesses (Table A6). Present day geothermal gradients were calculated from borehole logging and drillstem test data [*Geotech*, 1984; *Majorowicz and Morrow*, 1998] assuming a surface temperature of 0 °C due to regional permafrost.

A.1.4. AFTINV thermal history modeling software

AFTINV[*Issler*, 1996] [*Issler*, 1996; *Issler et al.*, 2005] is an AFT inverse model that extracts thermal history information from multi-kinetic AFT data. AFTINV uses a non-directed Monte Carlo method to search parameter space for a user-specified set of (typically 300) unique thermal histories that 1) provide a statistical fit between modeled and observed track length distribution using the Kolmogorov-Smirnov (KS) statistic, and 2) have calculated AFT dates within two standard deviations of the measured data. Additionally, the program has been upgraded to incorporate multi-kinetic annealing equations [*Ketcham et al.*, 1999, 2007] and the basin%Ro kinetic vitrinite reflectance model [*Nielsen et al.*, 2015].

References

Ault, A. K., R. M. Flowers, and S. A. Bowring (2013), Phanerozoic surface history of the Slave craton, *Tectonics*, *32*(5), 1066–1083, doi:10.1002/tect.20069.

Beucher, R., R. W. Brown, S. Roper, F. Stuart, and C. Persano (2013), Natural age dispersion arising from the analysis of broken crystals. Part II: Practical application to apatite (U-Th)/He thermochronometry, *Geochim. Cosmochim. Acta*, *120*, 395–416, doi:10.1016/j.gca.2013.05.041.

Brown, R. W., R. Beucher, S. Roper, C. Persano, F. Stuart, and P. Fitzgerald (2013), Natural age dispersion arising from the analysis of broken crystals. Part I: Theoretical basis and implications for the apatite (U-Th)/He thermochronometer, *Geochim. Cosmochim. Acta*, *122*(120), 478–497, doi:10.1016/j.gca.2013.05.041.

Carlson, W. D., R. A. Donelick, and R. A. Ketcham (1999), Variability of apatite fission-track annealing kinetics: I. Experimental results, *Am. Mineral.*, *84*(9), 1213–1223, doi:10.2138/am-1999-0901.

Chew, D. M., and R. A. Donelick (2012), Combined apatite fission track and U-Pb dating by LA–ICP–MS and its application in apatite provenance analysis, *Mineral. Assoc. Canada Short Course 42*, 219–247.

Donelick, R. A., P. B. O'Sullivan, and R. A. Ketcham (2005), Apatite Fission-Track Analysis, *Rev. Mineral. Geochemistry*, *58*(1), 49–94, doi:10.2138/rmg.2005.58.3.

Farley, K. A., R. A. Wolf, and L. T. Silver (1996), The effects of long alpha-stopping distances on (U-Th)/He ages, *Geochim. Cosmochim. Acta*, *60*(21), 4223–4229.

Feinstein, S., P. W. Brooks, T. Gentzis, F. Goodarzi, L. R. Snowdon, and G. K. Williams (1988), Thermal maturity in the Mackenzie Corridor, Northwest and Yukon Territories, Canada, *Geol. Surv. Canada, Open File 1944*, 6, doi:10.4095/130457.

Fitzgerald, P. G., S. L. Baldwin, L. E. Webb, and P. . O'Sullivan (2006), Interpretation of (U–Th)/He single grain ages from slowly cooled crustal terranes: A case study from the Transantarctic Mountains of southern Victoria Land, *Chem. Geol.*, *225*(1-2), 91–120, doi:10.1016/j.chemgeo.2005.09.001.

Flowers, R. M., R. A. Ketcham, D. L. Shuster, and K. A. Farley (2009), Apatite (U-Th)/He thermochronometry using a radiation damage accumulation and annealing model, *Geochim. Cosmochim. Acta*, *73*(8), 2347–2365, doi:10.1016/j.gca.2009.01.015.

Geotech (1984), *Subsurface Temperature Data from Wells North of Sixty Yukon - Northwest Territories*.

Hadlari, T., D. Midwinter, B. C. MacLean, K. M. Fallas, and J. Dixon (2013), Formation tops and isopach maps of Cretaceous strata of Mackenzie Plain and parts of Peel Plain, Northwest Territories, *Geol. Surv. Canada, Open File 7326*, 4, doi:10.4095/293112.

Hasebe, N., J. Barbarand, K. Jarvis, A. Carter, and A. J. Hurford (2004), Apatite fission-track chronometry using laser ablation ICP-MS, *Chem. Geol.*, *207*(3-4), 135–145, doi:10.1016/j.chemgeo.2004.01.007.

Hurford, A. J., and P. F. Green (1983), The zeta age calibration of fission-track dating, *Chem. Geol.*, *41*, 285–317, doi:10.1016/S0009-2541(83)80026-6.

Issler, D. R. (1996), An inverse model for extracting thermal histories from apatite fission track data: instructions and software for the Windows 95 environment, *Geol. Surv. Canada, Open File 2325*, 85.

Issler, D. R., M. Obermajer, J. Reyes, and M. Li (2012), Integrated analysis of vitrinite reflectance, Rock-Eval 6, gas chromatography, and gas chromatography-mass spectrometry data for the Mallik A-06, Parsons N-10 and Kugaluk N-02 wells, Beaufort-Mackenzie Basin, northern Canada, *Geol. Surv. Canada, Open File 6978*, 78, doi:10.4095/289672.

Issler, D. R., C. Jiang, J. Reyes, and M. Obermajer (2016), Integrated analysis of vitrinite reflectance, Rock-Eval 6, gas chromatography, and gas chromatography-mass spectrometry data for the Reindeer D-27 and Tununuk K-10 wells, Beaufort-Mackenzie Basin, northern Canada, *Geol. Surv. Canada, Open File 8047*, 94, doi:10.4095/297905.

Issler, D. R. D., A. Grist, and L. Stasiuk (2005), Post-Early Devonian thermal constraints on

hydrocarbon source rock maturation in the Keele Tectonic Zone, Tulita area, NWT, Canada, from multi-kinetic apatite fission track thermochronology, vitrinite reflectance and shale compaction, *Bull. Can. Pet. Geol.*, *53*(4), 405–431, doi:10.2113/53.4.405.

Ketcham, R. A. (2015), Technical Note: Calculation of stoichiometry from EMP data for apatite and other phases with mixing on monovalent anion sites, *Am. Mineral.*, *100*(7), 1620–1623, doi:10.2138/am-2015-5171.

Ketcham, R. A., R. A. Donelick, and W. D. Carlson (1999), Variability of apatite fission-track anneling kinetics: III. Extrapolation to geological time scales, *Am. Mineral.*, *84*, 1235–1255.

Ketcham, R. A., A. Carter, R. A. Donelick, J. Barbarand, and A. J. Hurford (2007), Improved modeling of fission-track annealing in apatite, *Am. Mineral.*, *92*(5-6), 799–810, doi:10.2138/am.2007.2281.

Ketcham, R. A., C. Gautheron, and L. Tassan-Got (2011), Accounting for long alpha-particle stopping distances in (U-Th-Sm)/He geochronology: Refinement of the baseline case, *Geochim. Cosmochim. Acta*, *75*(24), 7779–7791, doi:10.1016/j.gca.2011.10.011.

Majorowicz, J. A., and D. W. Morrow (1998), Subsurface temperature and heat flow - Yukon and Northwest Territories, *Geol. Surv. Canada, Open File 3626*, 6.

Murray, K. E., D. A. Orme, and P. W. Reiners (2014), Effects of U-Th-rich grain boundary phases on apatite helium ages, *Chem. Geol.*, *390*, 135–151, doi:10.1016/j.chemgeo.2014.09.023.

NEB (2013), Table of Formation Tops, Available from: https://www.neb-one.gc.ca/nrth/pblctn/tbfrmtntp-eng.html (Accessed 16 September 2015)

Nielsen, S. B., O. R. Clausen, and E. Mcgregor (2015), Basin%Ro: A vitrinite reflectance model derived from basin and laboratory data, *Basin Res.*, 1–22, doi:10.1111/bre.12160.

Stockli, D. F., K. A. Farley, and T. A. Dumitru (2000), Calibration of the apatite (U-Th)/He thermochronometer on an exhumed fault block, White Mountains, California, *Geology*, *28*(11), 983, doi:10.1130/0091-7613(2000)28<983:COTAHT>2.0.CO;2.

Sweeney, J. J., and A. K. Burnham (1990), Evaluation of a simple model of vitrinite reflectance based on chemical kinetics, *Am. Assoc. Pet. Geol. Bull.*, *74*(10), 1559–1570.

Vermeesch, P. (2009), RadialPlotter: A Java application for fission track, luminescence and other radial plots, *Radiat. Meas.*, *44*(4), 409–410, doi:10.1016/j.radmeas.2009.05.003.

Wolfe, M. R., and D. F. Stockli (2010), Zircon (U–Th)/He thermochronometry in the KTB drill hole, Germany, and its implications for bulk He diffusion kinetics in zircon, *Earth Planet. Sci. Lett.*, *295*(1-2), 69–82, doi:10.1016/j.epsl.2010.03.025.

Table A1. Summary of AFT age data, Imperial Formation, Mackenzie Plain, NWT, Canada

A2Z Sample No.	N_s	Ω_i (cm^2)	P_i (dmnls)	$P_i\Omega_i$	one sigma (dmnls)	$\sigma P_i^2\Omega_i^2$	FT age (Ma)	one sigma (Ma)	Etch Figs.	D_{par} (µm)	U (ppm)	meas. F (apfu)	meas. Cl (apfu)	calc. OH (apfu)	r_{mr0}
JPCPC3, Imperial Fm. (siltstone) Powell River section, ~0.70 %Ro, 65.277 N, 128.774 W															
Kinetic population #1 (r_{mr0} > 0.76)															
P1420_003_Ap_A_1_POS_36	9	3.398E-05	0.022	7.614E-07	0.002	4.723E-15	97.1	33.6	2	1.76	2	1.98	0.01	0.01	0.86
P1420_003_Ap_A_1_POS_9	44	2.330E-05	0.377	8.786E-06	0.012	7.731E-14	41.3	6.4	4	2.07	50	2.03	0.00	0.00	0.85
P1420_003_Ap_A_1_POS_37	2	3.398E-05	0.011	3.778E-07	0.001	1.667E-15	43.6	31.2	2	1.92	1	2.06	0.00	0.00	0.85
P1420_003_Ap_A_1_POS_17	4	1.699E-05	0.040	6.823E-07	0.003	1.845E-15	48.3	24.4	3	2.29	5	1.72	0.01	0.27	0.85
P1420_003_Ap_A_1_POS_10	13	1.941E-05	0.173	3.361E-06	0.007	2.060E-14	31.9	9.0	4	2.04	24	1.57	0.00	0.42	0.84
P1420_003_Ap_A_1_POS_29	14	2.184E-05	0.068	1.489E-06	0.003	4.120E-15	77.3	21.0	4	2.20	7	1.62	0.02	0.36	0.84
P1420_003_Ap_A_1_POS_34	8	1.747E-05	0.091	1.595E-06	0.003	3.077E-15	41.4	14.7	2	2.02	11	1.82	0.06	0.12	0.84
P1420_003_Ap_A_1_POS_5	32	3.883E-05	0.101	3.936E-06	0.005	4.301E-14	66.9	12.4	4	2.16	12	1.51	0.02	0.47	0.83
P1420_003_Ap_A_1_POS_24	14	2.378E-05	0.082	1.950E-06	0.004	8.324E-15	59.1	16.1	4	1.94	11	1.87	0.02	0.11	0.83
P1420_003_Ap_A_1_POS_14	1	2.330E-05	0.016	3.753E-07	0.001	5.941E-16	22.0	22.1	2	2.85	2	1.75	0.04	0.21	0.83
P1420_003_Ap_A_1_POS_39	4	2.718E-05	0.034	9.113E-07	0.002	2.984E-15	36.2	18.2	2	1.87	4	1.72	0.07	0.21	0.82
P1420_003_Ap_A_1_POS_20	11	9.707E-06	0.133	1.294E-06	0.004	1.750E-15	69.9	21.2	2	1.94	17	1.16	0.03	0.81	0.82
P1420_003_Ap_A_1_POS_16	16	2.330E-05	0.110	2.565E-06	0.003	5.875E-15	51.4	13.0	3	2.20	13	0.62	0.12	1.26	0.80
P1420_003_Ap_A_1_POS_7	4	2.427E-05	0.015	3.640E-07	0.001	9.020E-16	90.3	45.8	2	1.90	2	1.81	0.05	0.14	0.79
P1420_003_Ap_A_1_POS_15	2	1.747E-05	0.028	4.940E-07	0.003	2.024E-15	33.4	23.8	2	2.33	3	1.73	0.08	0.19	0.79
P1420_003_Ap_A_1_POS_33	8	2.912E-05	0.030	8.703E-07	0.003	5.857E-15	75.6	27.6	3	2.32	4	1.93	0.10	0.00	0.78
P1420_003_Ap_A_1_POS_19	130	3.106E-05	0.756	2.347E-05	0.025	6.007E-13	45.7	4.3	2	2.71	83	1.18	0.18	0.64	0.78
P1420_003_Ap_A_1_POS_25	1	2.912E-05	0.004	1.159E-07	0.000	1.836E-16	71.0	71.5	1	2.52	0	1.31	0.03	0.66	0.78
P1420_003_Ap_A_1_POS_11	3	2.427E-05	0.007	1.779E-07	0.001	2.678E-16	138.0	80.7	2	1.82	1	1.78	0.15	0.07	0.77
P1420_003_Ap_A_1_POS_6	2	1.941E-05	0.011	2.207E-07	0.001	4.825E-16	74.5	53.2	4	2.39	1	1.39	0.05	0.56	0.76
P1420_003_Ap_A_1_POS_8	3	2.330E-05	0.022	5.187E-07	0.002	2.138E-15	47.7	27.9	2	3.09	3	1.40	0.42	0.17	0.73
P1420_003_Ap_A_1_POS_0	11	1.941E-05	0.054	1.056E-06	0.002	1.891E-15	85.6	26.1	3	2.75	6	1.00	0.16	0.85	0.72
P1420_003_Ap_A_1_POS_35	5	3.106E-05	0.021	6.674E-07	0.001	1.736E-15	61.7	27.9	3	2.58	3	1.11	0.21	0.68	0.72
P1420_003_Ap_A_1_POS_28	2	1.747E-05	0.017	3.053E-07	0.001	6.764E-16	54.0	38.4	1	2.46	3	1.14	0.34	0.52	0.69
pooled (24) Q=27%	**343**	**5.790E-04**		**5.635E-05**		**7.927E-13**	**50.2**	**2.9**		**2.26**		**1.55**	**0.09**	**0.36**	**0.80**
Kinetic population #2 (r_{mr0} < 0.76)															
P1420_003_Ap_A_1_POS_2	15	1.747E-05	0.042	7.357E-07	0.002	1.796E-15	166.5	44.1	4	2.18	5	1.21	0.14	0.65	0.78
P1420_003_Ap_A_1_POS_27	8	1.165E-05	0.025	2.953E-07	0.002	3.166E-16	220.3	79.1	4	~~20.37~~	3	1.73	0.19	0.08	0.75
P1420_003_Ap_A_1_POS_21	13	1.699E-05	0.047	8.042E-07	0.002	1.162E-15	132.4	37.2	1	2.40	6	0.97	0.32	0.70	0.67
P1420_003_Ap_A_1_POS_22	14	1.941E-05	0.029	5.639E-07	0.002	1.052E-15	202.2	55.4	4	3.18	3	1.05	0.35	0.60	0.66
pooled (4) Q=62%	**50**	**6.552E-05**		**2.399E-06**		**4.327E-15**	**170.1**	**24.7**		**2.59**		**1.24**	**0.25**	**0.51**	**0.71**
JPCPC4, Imperial Fm. (siltstone) Imperial River section, ~0.66 %Ro, 65.116 N, 127.859 W															
Kinetic population #1 (r_{mr0} > 0.82)															
P1420_004_Ap_A_1_POS_16	6	2.912E-05	0.068	1.981E-06	0.003	7.010E-15	25.0	10.3	1	1.47	8	1.89	0.00	0.11	0.85
P1420_004_Ap_A_1_POS_6	13	2.718E-05	0.058	1.579E-06	0.004	1.005E-14	67.8	19.3	4	2.17	7	2.06	0.01	0.00	0.85
P1420_004_Ap_A_1_POS_33	15	2.912E-05	0.071	2.076E-06	0.005	2.096E-14	59.5	15.9	4	2.25	8	1.72	0.01	0.27	0.84
P1420_004_Ap_A_1_POS_39	39	3.106E-05	0.231	7.186E-06	0.007	5.415E-14	44.7	7.3	4	1.90	26	2.10	0.01	0.00	0.83
P1420_004_Ap_A_1_POS_12	20	2.912E-05	0.145	4.220E-06	0.005	2.483E-14	39.1	8.9	4	2.48	17	1.64	0.04	0.32	0.83
P1420_004_Ap_A_1_POS_4	42	1.747E-05	0.398	6.947E-06	0.013	5.008E-14	49.8	7.9	4	1.79	43	1.66	0.01	0.33	0.83
P1420_004_Ap_A_1_POS_9	2	1.747E-05	0.041	7.156E-07	0.002	1.873E-15	23.1	16.4	1	1.90	5	1.97	0.05	0.00	0.82
pooled (7) Q=34%	**137**	**1.806E-04**		**2.470E-05**		**1.689E-13**	**45.7**	**4.1**		**1.99**		**1.86**	**0.02**	**0.15**	**0.84**
Kinetic population #2 (0.76 < r_{mr0} < 0.82)															
P1420_004_Ap_A_1_POS_14	11	4.368E-05	0.022	9.500E-07	0.002	9.753E-15	95.1	30.4	3	1.85	2	1.94	0.00	0.06	0.86
P1420_004_Ap_A_1_POS_17	9	1.747E-05	0.048	8.304E-07	0.003	2.566E-15	89.0	30.2	2	1.66	6	1.76	0.06	0.18	0.82
P1420_004_Ap_A_1_POS_3	11	2.330E-05	0.046	1.075E-06	0.003	4.494E-15	84.1	25.9	3	2.17	6	1.22	0.02	0.76	0.82
P1420_004_Ap_A_1_POS_18	6	3.398E-05	0.008	2.616E-07	0.001	2.914E-16	187.0	77.4	1	2.27	1	1.94	0.08	0.00	0.82
P1420_004_Ap_A_1_POS_0	8	3.398E-05	0.009	3.122E-07	0.004	1.571E-14	208.6	111.6	2	2.62	1	2.04	0.08	0.00	0.82
P1420_004_Ap_A_1_POS_2	3	3.106E-05	0.008	2.356E-07	0.001	4.075E-16	104.5	61.0	1	2.31	1	1.30	0.05	0.65	0.81
P1420_004_Ap_A_1_POS_5	28	1.747E-05	0.139	2.428E-06	0.005	7.634E-15	94.7	18.3	4	1.90	18	1.51	0.02	0.47	0.81
P1420_004_Ap_A_1_POS_29	4	2.912E-05	0.011	3.342E-07	0.001	1.778E-15	98.3	50.7	2	2.22	1	1.23	0.00	0.77	0.81
P1420_004_Ap_A_1_POS_30	9	2.912E-05	0.046	1.326E-06	0.001	1.842E-15	55.9	18.7	4	2.11	5	1.98	0.04	0.00	0.81
P1420_004_Ap_A_1_POS_7	4	2.378E-05	0.024	5.601E-07	0.001	9.253E-16	58.8	29.6	2	1.88	3	2.01	0.11	0.00	0.81
P1420_004_Ap_A_1_POS_15	62	2.912E-05	0.234	6.827E-06	0.010	7.819E-14	74.7	10.0	4	2.17	27	1.08	0.06	0.86	0.80
P1420_004_Ap_A_1_POS_20	1	1.747E-05	0.009	1.511E-07	0.001	2.895E-16	54.5	54.9	1	1.84	1	1.68	0.04	0.28	0.80
P1420_004_Ap_A_1_POS_34	4	3.106E-05	0.007	2.089E-07	0.001	3.602E-16	156.5	79.6	2	2.48	1	1.20	0.16	0.64	0.79
P1420_004_Ap_A_1_POS_32	15	1.747E-05	0.072	1.249E-06	0.003	1.948E-15	98.6	25.7	2	2.36	8	0.85	0.13	1.02	0.77
pooled (14) Q=53%	**175**	**3.781E-04**		**1.675E-05**		**1.262E-13**	**85.9**	**6.9**		**2.13**		**1.55**	**0.06**	**0.41**	**0.81**
Kinetic population #3 (r_{mr0} < 0.76)															
P1420_004_Ap_A_1_POS_31	20	3.106E-05	0.011	3.285E-07	0.001	1.011E-15	484.9	118.4	3	3.06	2	0.62	0.02	1.36	0.81
P1420_004_Ap_A_1_POS_11	11	2.912E-05	0.013	3.875E-07	0.002	2.806E-15	230.6	76.5	3	1.92	1	1.44	0.08	0.48	0.78
P1420_004_Ap_A_1_POS_28	32	4.854E-05	0.024	1.144E-06	0.002	6.478E-15	227.3	43.4	4	2.13	3	1.43	0.05	0.52	0.78
P1420_004_Ap_A_1_POS_8	12	2.427E-05	0.015	3.537E-07	0.002	1.803E-15	274.8	86.0	3	2.23	2	1.35	0.08	0.57	0.77
P1420_004_Ap_A_1_POS_36	4	2.912E-05	0.003	9.188E-08	0.000	1.933E-16	350.5	183.2	2	1.95	1	1.54	0.05	0.41	0.76
P1420_004_Ap_A_1_POS_24	73	3.883E-05	0.070	2.710E-06	0.003	1.351E-14	219.1	27.6	4	2.50	9	1.15	0.16	0.69	0.76
P1420_004_Ap_A_1_POS_10	26	1.747E-05	0.044	7.705E-07	0.002	1.493E-15	273.3	55.5	3	2.40	5	0.60	0.19	1.20	0.75
P1420_004_Ap_A_1_POS_38	16	3.398E-05	0.021	7.302E-07	0.002	5.636E-15	178.8	48.4	3	2.51	2	1.05	0.06	0.90	0.74
P1420_004_Ap_A_1_POS_25	13	2.912E-05	0.027	7.765E-07	0.002	2.531E-15	137.0	39.1	2	2.39	3	1.22	0.03	0.75	0.73
P1420_004_Ap_A_1_POS_35	31	3.398E-05	0.038	1.280E-06	0.003	7.775E-15	197.3	38.1	4	2.38	5	1.11	0.13	0.76	0.73
P1420_004_Ap_A_1_POS_22	28	3.883E-05	0.026	9.937E-07	0.002	4.073E-15	229.0	45.9	3	2.72	3	0.80	0.18	1.03	0.72
P1420_004_Ap_A_1_POS_1	11	2.718E-05	0.018	4.836E-07	0.001	1.637E-15	185.5	58.1	3	2.27	2	0.60	0.13	1.27	0.72
P1420_004_Ap_A_1_POS_13	14	3.398E-05	0.015	5.067E-07	0.001	1.651E-15	224.6	62.8	2	3.11	2	0.75	0.22	1.02	0.70
pooled (13) Q=13%	**291**	**4.155E-04**		**1.056E-05**		**5.059E-14**	**224.1**	**14.5**		**2.43**		**1.05**	**0.11**	**0.84**	**0.75**
10FNARL008, Imperial Fm. (lithic arenite) Carcajou River section, ~0.74 %Ro, 64.752 N, 126.778 W															
Kinetic population #1 (r_{mr0} > 0.86)															
P1392_015_Ap_A_1_POS_16	0	1.213E-05	0.009	1.098E-07	0.000	2.109E-17	0.0		1	1.67	1	1.86	0.03	-	0.86
P1392_015_Ap_A_1_POS_23	1	1.747E-05	0.012	2.172E-07	0.001	8.908E-17	38.0	38.0	1	2.11	1	1.94	0.03	-	0.86
P1392_015_Ap_A_1_POS_22	0	1.213E-05	0.007	8.750E-08	0.000	1.857E-17	0.0		1	1.59	1	1.91	0.03	-	0.85

A2Z Sample No.	N_s	Ω_i (cm^2)	P_i (dmnls)	$P_i\Omega_i$	one sigma (dmnls)	$\sigma P_i^2\Omega_i^2$	FT age (Ma)	one sigma (Ma)	Etch Figs.	D_{par} (µm)	U (ppm)	meas. F (apfu)	meas. Cl (apfu)	calc. OH (apfu)	r_{mr0}
P1392_015_Ap_A_1_POS_7	2	2.427E-05	0.074	1.794E-06	0.001	1.073E-15	9.2	6.5	3	1.83	7	1.89	0.02	-	0.85
pooled (4) Q=21%	**3**	**6.601E-05**		**2.209E-06**		**1.202E-15**	**11.2**	**6.5**		**1.80**		**1.90**	**0.03**		**0.86**
Kinetic population #2 (0.76 < r_{mr0} < 0.86)															
P1392_015_Ap_A_1_POS_10	17	1.456E-05	0.241	3.511E-06	0.003	2.418E-15	39.9	9.7	3	1.81	27	1.90	0.04	-	0.85
P1392_015_Ap_A_1_POS_5	56	2.330E-05	0.423	9.844E-06	0.006	2.291E-14	46.9	6.4	4	2.29	51	1.97	0.03	-	0.85
P1392_015_Ap_A_1_POS_27	20	1.165E-05	0.398	4.639E-06	0.007	6.811E-15	35.6	8.0	4	1.92	42	1.90	0.05	-	0.85
P1392_015_Ap_A_1_POS_18	2	9.707E-06	0.076	7.364E-07	0.001	1.724E-16	22.4	15.9	1	2.37	9	1.95	0.05	-	0.85
P1392_015_Ap_A_1_POS_24	7	2.330E-05	0.050	1.164E-06	0.001	3.999E-16	49.6	18.8	3	1.90	6	1.98	0.01	-	0.85
P1392_015_Ap_A_1_POS_0	12	1.747E-05	0.130	2.277E-06	0.002	1.864E-15	43.4	12.6	4	1.92	14	1.86	0.06	-	0.84
P1392_015_Ap_A_1_POS_25	7	1.747E-05	0.045	7.874E-07	0.001	2.117E-16	73.1	27.7	2	1.80	5	1.95	0.05	-	0.82
P1392_015_Ap_A_1_POS_21	16	3.398E-05	0.069	2.342E-06	0.001	2.213E-15	56.3	14.1	4	1.81	7	1.80	0.17	-	0.81
P1392_015_Ap_A_1_POS_26	7	1.213E-05	0.111	1.342E-06	0.002	5.146E-16	43.0	16.3	4	1.78	13	1.79	0.21	-	0.81
P1392_015_Ap_A_1_POS_9	17	3.106E-05	0.102	3.154E-06	0.002	5.199E-15	44.4	10.9	4	1.90	11	1.75	0.18	-	0.81
P1392_015_Ap_A_1_POS_15	2	9.707E-06	0.036	3.490E-07	0.001	9.136E-17	47.2	33.4	2	2.36	4	1.94	0.06	-	0.81
P1392_015_Ap_A_1_POS_17	3	9.707E-06	0.027	2.633E-07	0.001	9.824E-17	93.6	54.2	2	2.32	3	1.82	0.16	-	0.80
P1392_015_Ap_A_1_POS_4	0	1.941E-05	0.008	1.540E-07	0.000	4.101E-17	0.0		1	1.80	1	1.82	0.16	-	0.79
P1392_015_Ap_A_1_POS_1	2	9.707E-06	0.024	2.289E-07	0.001	4.968E-17	71.9	50.9	1	1.84	3	1.85	0.15	-	0.79
P1392_015_Ap_A_1_POS_3	1	1.456E-05	0.024	3.567E-07	0.001	1.674E-16	23.2	23.2	1	1.78	3	1.83	0.17	-	0.78
P1392_015_Ap_A_1_POS_11	10	3.106E-05	0.048	1.500E-06	0.002	2.261E-15	54.9	17.5	4	2.04	5	1.83	0.10	-	0.77
P1392_015_Ap_A_1_POS_19	18	9.707E-06	0.227	2.202E-06	0.006	3.248E-15	67.3	16.0	4	2.08	28	1.64	0.36	-	0.76
P1392_015_Ap_A_1_POS_2	33	2.330E-05	0.274	6.381E-06	0.004	8.714E-15	42.6	7.5	4	2.20	35	1.86	0.14	-	0.62
pooled (18) Q=84%	**230**	**3.218E-04**		**4.123E-05**		**5.738E-14**	**46.0**	**3.1**		**2.00**		**1.86**	**0.12**		**0.80**
Kinetic population # 3 (r_{mr0} < 0.76)															
P1392_015_Ap_A_1_POS_8	6	1.553E-05	0.024	3.729E-07	0.001	6.395E-17	131.8	53.9	3	1.98	3	1.80	0.18	-	0.77
P1392_015_Ap_A_1_POS_6	25	1.456E-05	0.044	6.415E-07	0.001	2.347E-16	314.6	63.6	3	2.80	6	1.57	0.43	-	0.67
P1392_015_Ap_A_1_POS_12	5	1.165E-05	0.025	2.898E-07	0.001	2.088E-16	141.2	63.6	4	1.95	3	1.41	0.59	-	0.61
P1392_015_Ap_A_1_POS_20	18	1.213E-05	0.053	6.435E-07	0.001	8.750E-17	227.4	53.8	3	2.27	7	1.59	0.41	-	0.48
pooled (4) Q=12%	**54**	**5.387E-05**		**1.948E-06**		**5.950E-16**	**225.4**	**31.0**		**2.25**		**1.59**	**0.40**		**0.63**
Husky7, Imperial Fm. (fine grain sandstone) Redstone River section, ~1.67 %Ro, 63.916 N, 125.198W															
Kinetic population #1 (r_{mr0} > 0.86)															
P943_07_AP_A_1_POS_21	0	7.766E-06	0.001	1.020E-08	0.000	1.732E-18	0.0	832.6	1	1.48	1	1.88	0.00	0.12	0.86
P943_07_AP_A_1_POS_34	7	1.699E-05	0.130	2.201E-06	0.011	3.434E-14	20.5	8.0	2	1.34	57	2.00	0.00	0.00	0.86
P943_07_AP_A_1_POS_23	0	1.747E-05	0.000	1.433E-09	0.000	3.071E-19	0.0	3645.0	1	1.58	0	2.00	0.00	0.00	0.86
P943_07_AP_A_1_POS_37	1	7.766E-06	0.057	4.433E-07	0.010	5.462E-15	14.6	14.8	1	1.18	25	2.00	0.00	0.00	0.85
P943_07_AP_A_1_POS_32	16	1.359E-05	0.233	3.172E-06	0.020	7.143E-14	32.5	8.7	2	1.33	102	1.98	0.02	0.00	0.86
pooled (5) Q=50%	**24**	**6.358E-05**		**5.828E-06**		**1.112E-13**	**26.6**	**5.7**		**1.36**		**1.99**	**0.01**	**0.00**	**0.86**
Kinetic population #2 (0.84 < r_{mr0} < 0.86)															
P943_07_AP_A_1_POS_33	7	1.941E-05	0.048	9.356E-07	0.004	5.487E-15	48.2	18.7	2	0.95	21	1.96	0.01	0.03	0.86
P943_07_AP_A_1_POS_22	7	7.766E-06	0.081	6.309E-07	0.008	3.773E-15	71.3	28.0	2	1.26	36	1.99	0.01	0.00	0.85
P943_07_AP_A_1_POS_38	8	1.941E-05	0.068	1.319E-06	0.008	2.248E-14	39.1	14.6	2	1.16	30	2.00	0.00	0.00	0.85
P943_07_AP_A_1_POS_25	8	1.019E-05	0.124	1.265E-06	0.011	1.258E-14	40.7	14.9	4	1.35	54	1.83	0.00	0.17	0.85
P943_07_AP_A_1_POS_11	7	5.824E-06	0.123	7.157E-07	0.009	2.682E-15	62.9	24.3	2	1.21	54	1.74	0.02	0.24	0.85
P943_07_AP_A_1_POS_24	21	7.766E-06	0.264	2.054E-06	0.022	2.874E-14	65.7	15.5	4	1.37	116	1.89	0.02	0.09	0.85
P943_07_AP_A_1_POS_6	17	7.766E-06	0.181	1.409E-06	0.021	2.573E-14	77.5	21.0	2	1.64	80	1.63	0.02	0.35	0.84
P943_07_AP_A_1_POS_26	4	1.165E-05	0.078	9.124E-07	0.007	5.960E-15	28.3	14.4	2	1.58	34	1.61	0.01	0.38	0.84
pooled (8) Q=52%	**79**	**8.979E-05**		**9.240E-06**		**1.074E-13**	**55.0**	**6.8**		**1.31**		**1.83**	**0.01**	**0.16**	**0.85**
Kinetic population #3 (0.76 < r_{mr0} < 0.86)															
P943_07_AP_A_1_POS_28	24	1.941E-05	0.080	1.558E-06	0.006	1.207E-14	98.8	21.6	3	1.30	35	1.85	0.06	0.08	0.83
P943_07_AP_A_1_POS_1	11	7.766E-06	0.069	5.369E-07	0.005	1.531E-15	131.1	40.9	2	1.13	30	1.78	0.04	0.18	0.83
P943_07_AP_A_1_POS_4	1	7.766E-06	0.014	1.049E-07	0.001	3.649E-17	61.3	61.4	1	1.35	6	1.43	0.04	0.53	0.83
P943_07_AP_A_1_POS_35	3	7.766E-06	0.024	1.848E-07	0.002	1.992E-16	104.0	60.7	2	1.79	10	1.46	0.05	0.49	0.83
P943_07_AP_A_1_POS_15	12	1.456E-05	0.046	6.648E-07	0.002	1.188E-15	115.6	34.2	2	1.53	20	1.52	0.03	0.45	0.83
P943_07_AP_A_1_POS_31	30	1.359E-05	0.128	1.745E-06	0.012	2.818E-14	110.1	23.1	2	1.26	56	0.33	0.08	1.59	0.82
P943_07_AP_A_1_POS_5	4	1.699E-05	0.022	3.737E-07	0.003	3.241E-15	68.8	36.0	2	1.54	10	1.21	0.01	0.78	0.80
P943_07_AP_A_1_POS_12	20	1.019E-05	0.128	1.302E-06	0.009	8.078E-15	98.5	23.3	4	1.66	56	1.51	0.16	0.33	0.80
P943_07_AP_A_1_POS_20	1	1.165E-05	0.010	1.199E-07	0.001	7.171E-17	53.7	53.8	2	1.78	5	1.36	0.08	0.56	0.79
P943_07_AP_A_1_POS_13	23	7.766E-06	0.210	1.628E-06	0.016	1.542E-14	90.7	20.4	2	1.58	92	0.28	0.04	1.68	0.79
pooled (10) Q=98%	**129**	**1.175E-04**		**8.218E-06**		**7.001E-14**	**100.6**	**10.1**		**1.49**		**1.27**	**0.06**	**0.67**	**0.82**
Kinetic population #4 (r_{mr0} < 0.76)															
P943_07_AP_A_1_POS_40	3	2.427E-05	0.003	6.630E-08	0.000	4.368E-17	286.0	167.9	2	1.40	1	1.96	0.00	0.04	0.86
P943_07_AP_A_1_POS_36	5	1.941E-05	0.005	8.880E-08	0.001	1.587E-16	353.9	166.6	2	1.44	2	1.71	0.08	0.21	0.83
P943_07_AP_A_1_POS_2	23	9.707E-06	0.060	5.827E-07	0.009	8.499E-15	250.1	66.1	4	1.57	26	1.51	0.05	0.44	0.82
P943_07_AP_A_1_POS_30	10	1.941E-05	0.019	3.626E-07	0.002	1.568E-15	175.8	59.2	4	2.15	8	1.69	0.10	0.20	0.80
P943_07_AP_A_1_POS_27	46	1.941E-05	0.065	1.266E-06	0.005	1.112E-14	230.7	40.0	4	1.67	29	1.06	0.14	0.80	0.80
P943_07_AP_A_1_POS_7	11	9.707E-06	0.026	2.553E-07	0.001	1.067E-16	272.5	83.5	3	1.92	12	1.13	0.17	0.69	0.76
P943_07_AP_A_1_POS_8	56	7.766E-06	0.156	1.213E-06	0.006	2.174E-15	291.7	42.0	2	1.93	69	1.48	0.45	0.07	0.75
P943_07_AP_A_1_POS_10	3	9.707E-06	0.006	5.813E-08	0.000	1.830E-17	325.1	189.6	2	1.83	3	1.07	0.07	0.86	0.75
P943_07_AP_A_1_POS_16	4	1.213E-05	0.008	1.025E-07	0.001	4.640E-17	247.4	125.1	2	1.99	4	1.33	0.30	0.37	0.74
P943_07_AP_A_1_POS_39	21	1.747E-05	0.046	8.004E-07	0.003	2.625E-15	167.3	38.5	4	2.27	20	1.13	0.32	0.56	0.71
pooled (10) Q=65%	**182**	**1.490E-04**		**4.795E-06**		**2.636E-14**	**240.7**	**21.5**		**1.81**		**1.41**	**0.17**	**0.43**	**0.78**

Note: Ns is the number of spontaneous fission tracks for each apatite. Ω_i is the area overwhich tracks are counted, whereas P_i is the $^{238}U/^{43}Ca$ ratio. Q represents the chi-squared probability for each population. A population passes the chi-squared test if Q > 5%. D_{par} is the diameter of the etch figure parallel to the c axis. F, Cl and OH concentrations were calculated from weight % oxide using the stoichiometric relationships of *Ketcham* [2015], and r_{mr0} was determined using the calculations of *Carlson et al.* [1999]. Zeta factors differ between Husky7 and the other samples, in part, due to differences in the geometry factor (g). Whereas g = 0.5 in Husky7, it it set at 1 for the other samples as it was combined with the other constants and as such does not appear in the age equation

	JPCPC3; JPCPC4; 10FNARL008	HUSKY7
modified zeta	8.2727	12.92353
s.e. (zeta)	0.1407	0.4752371
total decay const.	1.55125E-10	1.55125E-10
g	1	0.5

Table A2. Summary of AFT length data, Imperial Formation, Mackenzie Plain, NWT, Canada

A2Z Sample No.	Confined length (mm)	angle to C-axis (degrees)	Etch Figs.	D_{par} (µm)	meas. F (apfu)	meas. Cl (apfu)	calc. OH (apfu)	r_{mr0}
JPCPC3, Imperial Fm. (siltstone) Powell River section, ~0.70 %Ro, 65.277 N, 128.774 W								
Kinetic population #1 (rmr0 > 0.76)								
P1420_003_Ap_A_2_POS_40	13.20	45.20	2	2.68	1.98	0.01	0.01	0.87
P1420_003_Ap_A_2_POS_40	12.90	66.77	2	2.68	1.98	0.01	0.01	0.87
P1420_003_Ap_A_2_POS_48	13.24	39.08	4	2.50	2.09	0.00	0.00	0.86
P1420_003_Ap_A_2_POS_48	12.76	65.83	4	2.50	2.09	0.00	0.00	0.86
P1420_003_Ap_A_2_POS_27	14.53	57.21	3	2.25	1.98	0.01	0.01	0.86
P1420_003_Ap_A_2_POS_27	14.62	55.33	3	2.25	1.98	0.01	0.01	0.86
P1420_003_Ap_A_2_POS_27	11.05	51.98	3	2.25	1.98	0.01	0.01	0.86
P1420_003_Ap_A_2_POS_41	12.17	51.05	2	2.44	1.83	0.01	0.16	0.85
P1420_003_Ap_A_2_POS_41	12.95	57.70	2	2.44	1.83	0.01	0.16	0.85
P1420_003_Ap_A_2_POS_41	12.57	81.05	2	2.44	1.83	0.01	0.16	0.85
P1420_003_Ap_A_2_POS_23	11.49	59.92	2	2.60	1.81	0.03	0.16	0.85
P1420_003_Ap_A_2_POS_23	2.14	27.06	2	2.60	1.81	0.03	0.16	0.85
P1420_003_Ap_A_2_POS_33	14.60	49.24	3	2.38	2.08	0.03	0.00	0.85
P1420_003_Ap_A_2_POS_44	14.84	24.20	2	2.62	1.81	0.01	0.18	0.85
P1420_003_Ap_A_2_POS_44	15.29	63.26	2	2.62	1.81	0.01	0.18	0.85
P1420_003_Ap_A_2_POS_44	16.02	31.37	2	2.62	1.81	0.01	0.18	0.85
P1420_003_Ap_A_2_POS_45	11.04	55.12	4	2.53	1.72	0.01	0.27	0.85
P1420_003_Ap_A_2_POS_45	11.98	82.05	4	2.53	1.72	0.01	0.27	0.85
P1420_003_Ap_A_2_POS_45	13.02	47.78	4	2.53	1.72	0.01	0.27	0.85
P1420_003_Ap_A_2_POS_45	16.11	66.41	4	2.53	1.72	0.01	0.27	0.85
P1420_003_Ap_A_2_POS_45	13.56	75.22	4	2.53	1.72	0.01	0.27	0.85
P1420_003_Ap_A_2_POS_37	10.79	58.65	4	2.90	1.66	0.01	0.33	0.84
P1420_003_Ap_A_2_POS_37	12.53	79.73	4	2.90	1.66	0.01	0.33	0.84
P1420_003_Ap_A_2_POS_37	11.70	72.66	4	2.90	1.66	0.01	0.33	0.84
P1420_003_Ap_A_2_POS_1	14.14	70.09	4	2.22	1.62	0.02	0.36	0.84
P1420_003_Ap_A_2_POS_19	13.26	37.56	3	2.37	1.57	0.00	0.42	0.84
P1420_003_Ap_A_2_POS_19	13.60	51.81	3	2.37	1.57	0.00	0.42	0.84
P1420_003_Ap_A_2_POS_19	12.10	79.70	3	2.37	1.57	0.00	0.42	0.84
P1420_003_Ap_A_2_POS_58	14.97	26.60	3	2.35	1.61	0.02	0.36	0.84
P1420_003_Ap_A_2_POS_13	15.04	30.28	3	2.50	1.59	0.02	0.39	0.84
P1420_003_Ap_A_2_POS_13	11.00	60.85	3	2.50	1.59	0.02	0.39	0.84
P1420_003_Ap_A_2_POS_13	11.24	58.46	3	2.50	1.59	0.02	0.39	0.84
P1420_003_Ap_A_2_POS_30	13.92	56.69	4	3.07	1.58	0.03	0.39	0.84
P1420_003_Ap_A_2_POS_30	12.13	67.98	4	3.07	1.58	0.03	0.39	0.84
P1420_003_Ap_A_2_POS_30	15.30	80.97	4	3.07	1.58	0.03	0.39	0.84
P1420_003_Ap_A_2_POS_30	13.13	78.28	4	3.07	1.58	0.03	0.39	0.84
P1420_003_Ap_A_2_POS_30	14.02	56.52	4	3.07	1.58	0.03	0.39	0.84

A2Z Sample No.	Confined length (mm)	angle to C-axis (degrees)	Etch Figs.	D_{par} (µm)	meas. F (apfu)	meas. Cl (apfu)	calc. OH (apfu)	r_{mr0}
P1420_003_Ap_A_2_POS_30	13.55	54.69	4	3.07	1.58	0.03	0.39	0.84
P1420_003_Ap_A_2_POS_30	15.20	42.64	4	3.07	1.58	0.03	0.39	0.84
P1420_003_Ap_A_2_POS_51	11.80	65.39	4	2.66	1.51	0.03	0.46	0.83
P1420_003_Ap_A_2_POS_51	11.94	73.12	4	2.66	1.51	0.03	0.46	0.83
P1420_003_Ap_A_2_POS_51	14.52	77.90	4	2.66	1.51	0.03	0.46	0.83
P1420_003_Ap_A_2_POS_51	14.42	56.96	4	2.66	1.51	0.03	0.46	0.83
P1420_003_Ap_A_2_POS_8	13.19	78.45	4	2.46	1.72	0.06	0.22	0.83
P1420_003_Ap_A_2_POS_8	13.54	88.95	4	2.46	1.72	0.06	0.22	0.83
P1420_003_Ap_A_2_POS_8	12.53	39.01	4	2.46	1.72	0.06	0.22	0.83
P1420_003_Ap_A_2_POS_62	13.73	64.10	2	2.73	1.50	0.06	0.44	0.83
P1420_003_Ap_A_2_POS_21	13.44	64.95	3	2.75	1.89	0.09	0.02	0.82
P1420_003_Ap_A_2_POS_21	14.95	39.01	3	2.75	1.89	0.09	0.02	0.82
P1420_003_Ap_A_2_POS_22	15.94	30.85	1	2.91	1.33	0.10	0.57	0.82
P1420_003_Ap_A_2_POS_22	11.15	69.54	1	2.91	1.33	0.10	0.57	0.82
P1420_003_Ap_A_2_POS_56	12.13	76.56	4	2.44	1.72	0.05	0.24	0.82
P1420_003_Ap_A_2_POS_56	12.12	47.03	4	2.44	1.72	0.05	0.24	0.82
P1420_003_Ap_A_2_POS_25	14.47	55.16	4	2.60	1.63	0.08	0.29	0.82
P1420_003_Ap_A_2_POS_25	12.87	86.62	4	2.60	1.63	0.08	0.29	0.82
P1420_003_Ap_A_2_POS_46	13.03	69.61	4	2.51	1.72	0.07	0.21	0.82
P1420_003_Ap_A_2_POS_46	16.39	12.33	4	2.51	1.72	0.07	0.21	0.82
P1420_003_Ap_A_2_POS_46	11.12	86.09	4	2.51	1.72	0.07	0.21	0.82
P1420_003_Ap_A_2_POS_7	15.28	13.38	2	2.68	1.73	0.02	0.24	0.81
P1420_003_Ap_A_2_POS_59	12.51	74.33	4	2.72	1.43	0.10	0.47	0.81
P1420_003_Ap_A_2_POS_64	14.10	59.64	4	2.34	2.02	0.13	0.00	0.80
P1420_003_Ap_A_2_POS_61	14.80	65.78	2	1.88	0.96	0.01	1.04	0.80
P1420_003_Ap_A_2_POS_14	15.20	31.21	4	2.85	0.96	0.08	0.96	0.80
P1420_003_Ap_A_2_POS_14	15.94	28.13	4	2.85	0.96	0.08	0.96	0.80
P1420_003_Ap_A_2_POS_14	14.24	55.33	4	2.85	0.96	0.08	0.96	0.80
P1420_003_Ap_A_2_POS_14	14.56	37.05	4	2.85	0.96	0.08	0.96	0.80
P1420_003_Ap_A_2_POS_14	14.93	21.37	4	2.85	0.96	0.08	0.96	0.80
P1420_003_Ap_A_2_POS_14	14.82	34.16	4	2.85	0.96	0.08	0.96	0.80
P1420_003_Ap_A_2_POS_14	14.18	24.68	4	2.85	0.96	0.08	0.96	0.80
P1420_003_Ap_A_2_POS_14	12.15	59.74	4	2.85	0.96	0.08	0.96	0.80
P1420_003_Ap_A_2_POS_14	13.97	38.10	4	2.85	0.96	0.08	0.96	0.80
P1420_003_Ap_A_2_POS_14	16.22	22.71	4	2.85	0.96	0.08	0.96	0.80
P1420_003_Ap_A_2_POS_52	15.03	31.25	4	2.68	2.07	0.03	0.00	0.80
P1420_003_Ap_A_2_POS_52	12.95	80.33	4	2.68	2.07	0.03	0.00	0.80
P1420_003_Ap_A_2_POS_36	13.09	47.22	2	2.17	1.66	0.18	0.17	0.80
P1420_003_Ap_A_2_POS_36	13.68	63.82	2	2.17	1.66	0.18	0.17	0.80
P1420_003_Ap_A_2_POS_65	14.66	68.77	3	1.86	0.96	0.01	1.04	0.80
P1420_003_Ap_A_2_POS_5	14.52	81.03	4	3.32	0.96	0.08	0.97	0.79
P1420_003_Ap_A_2_POS_42	13.16	52.60	3	2.71	1.24	0.23	0.53	0.79

A2Z Sample No.	Confined length (mm)	angle to C-axis (degrees)	Etch Figs.	D_{par} (µm)	meas. F (apfu)	meas. Cl (apfu)	calc. OH (apfu)	r_{mr0}
P1420_003_Ap_A_2_POS_42	13.10	61.07	3	2.71	1.24	0.23	0.53	0.79
P1420_003_Ap_A_2_POS_42	13.89	74.89	3	2.71	1.24	0.23	0.53	0.79
P1420_003_Ap_A_2_POS_42	13.48	51.41	3	2.71	1.24	0.23	0.53	0.79
P1420_003_Ap_A_2_POS_42	13.69	78.24	3	2.71	1.24	0.23	0.53	0.79
P1420_003_Ap_A_2_POS_49	14.85	43.14	3	2.97	1.16	0.16	0.68	0.79
P1420_003_Ap_A_2_POS_49	13.85	42.37	3	2.97	1.16	0.16	0.68	0.79
P1420_003_Ap_A_2_POS_50	13.33	79.66	3	2.89	1.24	0.16	0.60	0.79
P1420_003_Ap_A_2_POS_57	12.51	57.01	4	2.68	1.23	0.20	0.57	0.78
P1420_003_Ap_A_2_POS_57	13.78	54.47	4	2.68	1.23	0.20	0.57	0.78
P1420_003_Ap_A_2_POS_26	12.39	48.69	4	3.63	1.38	0.22	0.40	0.78
P1420_003_Ap_A_2_POS_63	15.34	51.44	4	2.61	1.37	0.20	0.43	0.77
P1420_003_Ap_A_2_POS_63	13.36	59.82	4	2.61	1.37	0.20	0.43	0.77
P1420_003_Ap_A_2_POS_63	14.05	73.70	4	2.61	1.37	0.20	0.43	0.77
P1420_003_Ap_A_2_POS_34	13.20	60.76	2	3.13	1.01	0.16	0.83	0.77
P1420_003_Ap_A_2_POS_28	14.48	72.13	4	3.09	1.42	0.15	0.43	0.76
P1420_003_Ap_A_2_POS_28	12.82	58.00	4	3.09	1.42	0.15	0.43	0.76
P1420_003_Ap_A_2_POS_28	13.36	80.77	4	3.09	1.42	0.15	0.43	0.76
P1420_003_Ap_A_2_POS_28	13.78	43.41	4	3.09	1.42	0.15	0.43	0.76
P1420_003_Ap_A_2_POS_2	11.37	41.12	4	3.25	1.20	0.23	0.57	0.76
P1420_003_Ap_A_2_POS_3	14.23	59.64	4	2.58	1.43	0.10	0.48	0.76
P1420_003_Ap_A_2_POS_39	17.87	35.17	2	3.22	1.11	0.21	0.68	0.74
P1420_003_Ap_A_2_POS_10	13.85	76.96	4	3.53	0.99	0.16	0.85	0.71
P1420_003_Ap_A_2_POS_10	16.91	47.19	4	3.53	0.99	0.16	0.85	0.71
P1420_003_Ap_A_2_POS_10	13.14	56.31	4	3.53	0.99	0.16	0.85	0.71
P1420_003_Ap_A_2_POS_10	15.92	67.93	4	3.53	0.99	0.16	0.85	0.71
Ave	**13.55**			**2.72**	**1.50**	**0.08**	**0.43**	**0.81**
SD	**1.82**			**0.33**	**0.33**	**0.07**	**0.29**	**0.04**
Kinetic population #2 (rmr0 < 0.76)								
P1420_003_Ap_A_2_POS_18	14.89	64.11	4	2.70	1.34	0.09	0.57	0.75
P1420_003_Ap_A_2_POS_18	13.68	71.97	4	2.70	1.34	0.09	0.57	0.75
P1420_003_Ap_A_2_POS_11	15.10	55.54	4	3.23	0.80	0.17	1.02	0.75
P1420_003_Ap_A_2_POS_11	13.63	50.63	4	3.23	0.80	0.17	1.02	0.75
P1420_003_Ap_A_2_POS_11	13.60	65.21	4	3.23	0.80	0.17	1.02	0.75
P1420_003_Ap_A_2_POS_11	11.46	50.20	4	3.23	0.80	0.17	1.02	0.75
P1420_003_Ap_A_2_POS_9	14.88	49.91	3	3.15	1.34	0.24	0.42	0.74
P1420_003_Ap_A_2_POS_9	13.32	50.54	3	3.15	1.34	0.24	0.42	0.74
P1420_003_Ap_A_2_POS_43	17.53	15.81	3	3.91	1.02	0.19	0.79	0.73
P1420_003_Ap_A_2_POS_43	13.41	56.02	3	3.91	1.02	0.19	0.79	0.73
P1420_003_Ap_A_2_POS_54	15.16	38.81	4	3.67	0.83	0.18	0.98	0.72
P1420_003_Ap_A_2_POS_17	15.51	41.04	1	4.00	1.23	0.50	0.27	0.70
P1420_003_Ap_A_2_POS_17	15.87	75.71	1	4.00	1.23	0.50	0.27	0.70
P1420_003_Ap_A_2_POS_31	16.02	31.62	2	4.17	0.97	0.32	0.70	0.67

A2Z Sample No.	Confined length (mm)	angle to C-axis (degrees)	Etch Figs.	D_{par} (µm)	meas. F (apfu)	meas. Cl (apfu)	calc. OH (apfu)	r_{mr0}
P1420_003_Ap_A_2_POS_29	13.46	49.98	2	3.92	1.05	0.35	0.60	0.64
P1420_003_Ap_A_2_POS_29	14.34	58.04	2	3.92	1.05	0.35	0.60	0.64
P1420_003_Ap_A_2_POS_29	7.50	81.29	2	3.92	1.05	0.35	0.60	0.64
Ave	**14.08**			**3.53**	**1.06**	**0.25**	**0.69**	**0.71**
SD	**2.19**			**0.48**	**0.21**	**0.12**	**0.26**	**0.04**
JPCPC4, Imperial Fm. (siltstone) Imperial River section, ~0.66 %Ro, 65.116 N, 127.859 W								
Kinetic population #1 (rmr0 > 0.82)								
P1420_004_Ap_A_2_POS_6	14.57	50.65	1	2.05	1.99	0.05	0.00	0.86
P1420_004_Ap_A_2_POS_6	14.89	51.21	1	2.05	1.99	0.05	0.00	0.86
P1420_004_Ap_A_2_POS_43	12.94	52.12	2	2.56	1.92	0.00	0.08	0.86
P1420_004_Ap_A_2_POS_43	10.00	71.22	2	2.56	1.92	0.00	0.08	0.86
P1420_004_Ap_A_2_POS_43	11.10	58.74	2	2.56	1.92	0.00	0.08	0.86
P1420_004_Ap_A_2_POS_21	12.12	56.09	4	2.17	1.85	0.01	0.15	0.85
P1420_004_Ap_A_2_POS_4	13.52	70.02	4	2.73	2.06	0.01	0.00	0.85
P1420_004_Ap_A_2_POS_4	16.33	40.44	4	2.73	2.06	0.01	0.00	0.85
P1420_004_Ap_A_2_POS_4	14.37	36.17	4	2.73	2.06	0.01	0.00	0.85
P1420_004_Ap_A_2_POS_39	15.09	52.42	2	2.82	1.71	0.01	0.28	0.85
P1420_004_Ap_A_2_POS_39	14.77	30.06	2	2.82	1.71	0.01	0.28	0.85
P1420_004_Ap_A_2_POS_39	14.52	17.55	2	2.82	1.71	0.01	0.28	0.85
P1420_004_Ap_A_2_POS_51	15.03	70.88	4	3.25	2.02	0.03	0.00	0.84
P1420_004_Ap_A_2_POS_51	15.33	40.73	4	3.25	2.02	0.03	0.00	0.84
P1420_004_Ap_A_2_POS_41	16.59	54.09	2	2.66	1.79	0.04	0.17	0.84
P1420_004_Ap_A_2_POS_41	13.05	52.54	2	2.66	1.79	0.04	0.17	0.84
P1420_004_Ap_A_2_POS_41	14.07	41.80	2	2.66	1.79	0.04	0.17	0.84
P1420_004_Ap_A_2_POS_41	16.47	21.63	2	2.66	1.79	0.04	0.17	0.84
P1420_004_Ap_A_2_POS_35	13.81	70.35	3	2.77	1.72	0.01	0.27	0.84
P1420_004_Ap_A_2_POS_35	13.40	54.71	3	2.77	1.72	0.01	0.27	0.84
P1420_004_Ap_A_2_POS_35	14.52	41.37	3	2.77	1.72	0.01	0.27	0.84
P1420_004_Ap_A_2_POS_35	13.08	30.90	3	2.77	1.72	0.01	0.27	0.84
P1420_004_Ap_A_2_POS_24	15.43	60.84	3	2.47	1.51	0.03	0.47	0.84
P1420_004_Ap_A_2_POS_24	11.49	56.01	3	2.47	1.51	0.03	0.47	0.84
P1420_004_Ap_A_2_POS_24	12.18	65.35	3	2.47	1.51	0.03	0.47	0.84
P1420_004_Ap_A_2_POS_24	15.53	58.63	3	2.47	1.51	0.03	0.47	0.84
P1420_004_Ap_A_2_POS_46	14.00	74.34	0	2.58	2.10	0.01	0.00	0.84
P1420_004_Ap_A_2_POS_46	14.71	46.68	0	2.58	2.10	0.01	0.00	0.84
P1420_004_Ap_A_2_POS_46	15.03	8.89	0	2.58	2.10	0.01	0.00	0.84
P1420_004_Ap_A_2_POS_46	14.74	73.58	0	2.58	2.10	0.01	0.00	0.84
P1420_004_Ap_A_2_POS_46	14.64	71.72	0	2.58	2.10	0.01	0.00	0.84
P1420_004_Ap_A_2_POS_46	11.30	79.79	0	2.58	2.10	0.01	0.00	0.84
P1420_004_Ap_A_2_POS_46	14.31	49.64	0	2.58	2.10	0.01	0.00	0.84
P1420_004_Ap_A_2_POS_45	9.63	50.95	2	2.58	2.10	0.01	0.00	0.84

A2Z Sample No.	Confined length (mm)	angle to C-axis (degrees)	Etch Figs.	D_{par} (µm)	meas. F (apfu)	meas. Cl (apfu)	calc. OH (apfu)	r_{mr0}
P1420_004_Ap_A_2_POS_12	15.42	34.75	2	2.74	1.86	0.00	0.14	0.83
P1420_004_Ap_A_2_POS_12	14.87	45.61	2	2.74	1.86	0.00	0.14	0.83
P1420_004_Ap_A_2_POS_12	12.16	69.41	2	2.74	1.86	0.00	0.14	0.83
P1420_004_Ap_A_2_POS_12	15.10	32.78	2	2.74	1.86	0.00	0.14	0.83
P1420_004_Ap_A_2_POS_12	13.43	78.62	2	2.74	1.86	0.00	0.14	0.83
P1420_004_Ap_A_2_POS_12	15.60	21.12	2	2.74	1.86	0.00	0.14	0.83
P1420_004_Ap_A_2_POS_38	14.74	62.37	1	1.90	2.14	0.00	0.00	0.83
P1420_004_Ap_A_2_POS_38	13.77	40.19	1	1.90	2.14	0.00	0.00	0.83
P1420_004_Ap_A_2_POS_14	14.92	53.96	4	2.43	1.64	0.04	0.32	0.83
P1420_004_Ap_A_2_POS_14	13.99	36.48	4	2.43	1.64	0.04	0.32	0.83
P1420_004_Ap_A_2_POS_14	13.87	66.02	4	2.43	1.64	0.04	0.32	0.83
P1420_004_Ap_A_2_POS_14	13.70	29.78	4	2.43	1.64	0.04	0.32	0.83
P1420_004_Ap_A_2_POS_14	13.83	57.16	4	2.43	1.64	0.04	0.32	0.83
P1420_004_Ap_A_2_POS_14	14.49	34.95	4	2.43	1.64	0.04	0.32	0.83
P1420_004_Ap_A_2_POS_49	15.07	62.02	3	2.22	1.77	0.08	0.15	0.83
P1420_004_Ap_A_2_POS_34	14.98	51.77	4	3.20	1.31	0.01	0.68	0.83
P1420_004_Ap_A_2_POS_34	12.72	53.89	4	3.20	1.31	0.01	0.68	0.83
P1420_004_Ap_A_2_POS_1	14.70	60.29	3	2.99	2.17	0.03	0.00	0.82
P1420_004_Ap_A_2_POS_1	13.80	67.59	3	2.99	2.17	0.03	0.00	0.82
P1420_004_Ap_A_2_POS_3	12.61	70.82	2	2.23	1.34	0.01	0.65	0.74
P1420_004_Ap_A_2_POS_3	12.30	55.15	2	2.23	1.34	0.01	0.65	0.74
P1420_004_Ap_A_2_POS_3	11.61	57.45	2	2.23	1.34	0.01	0.65	0.74
P1420_004_Ap_A_2_POS_3	13.55	80.79	2	2.23	1.34	0.01	0.65	0.74
P1420_004_Ap_A_2_POS_3	13.35	51.00	2	2.23	1.34	0.01	0.65	0.74
P1420_004_Ap_A_2_POS_3	14.05	48.33	2	2.23	1.34	0.01	0.65	0.74
Ave	**13.92**			**2.58**	**1.79**	**0.02**	**0.22**	**0.83**
SD	**1.48**			**0.30**	**0.26**	**0.02**	**0.22**	**0.03**
Kinetic population #2 (0.76 < rmr0 < 0.82)								
P1420_004_Ap_A_2_POS_13	15.90	39.28	2	2.50	1.94	0.00	0.06	0.86
P1420_004_Ap_A_2_POS_23	14.37	78.39	2	2.72	1.77	0.06	0.17	0.85
P1420_004_Ap_A_2_POS_23	15.29	39.39	2	2.72	1.77	0.06	0.17	0.85
P1420_004_Ap_A_2_POS_15	8.66	49.29	2	3.11	1.58	0.01	0.40	0.82
P1420_004_Ap_A_2_POS_15	10.83	43.44	2	3.11	1.58	0.01	0.40	0.82
P1420_004_Ap_A_2_POS_15	13.58	51.95	2	3.11	1.58	0.01	0.40	0.82
P1420_004_Ap_A_2_POS_48	14.73	76.44	2	2.16	1.41	0.07	0.52	0.82
P1420_004_Ap_A_2_POS_48	13.02	56.66	2	2.16	1.41	0.07	0.52	0.82
P1420_004_Ap_A_2_POS_48	14.92	52.97	2	2.16	1.41	0.07	0.52	0.82
P1420_004_Ap_A_2_POS_48	14.95	72.25	2	2.16	1.41	0.07	0.52	0.82
P1420_004_Ap_A_2_POS_48	9.48	81.89	2	2.16	1.41	0.07	0.52	0.82
P1420_004_Ap_A_2_POS_48	14.55	27.63	2	2.16	1.41	0.07	0.52	0.82
P1420_004_Ap_A_2_POS_2	14.47	71.75	2	2.78	1.22	0.02	0.76	0.82
P1420_004_Ap_A_2_POS_2	12.03	62.26	2	2.78	1.22	0.02	0.76	0.82

A2Z Sample No.	Confined length (mm)	angle to C-axis (degrees)	Etch Figs.	D_{par} (µm)	meas. F (apfu)	meas. Cl (apfu)	calc. OH (apfu)	r_{mr0}
P1420_004_Ap_A_2_POS_2	13.67	55.11	2	2.78	1.22	0.02	0.76	0.82
P1420_004_Ap_A_2_POS_26	12.85	60.12	3	2.73	1.08	0.06	0.86	0.82
P1420_004_Ap_A_2_POS_26	12.22	75.66	3	2.73	1.08	0.06	0.86	0.82
P1420_004_Ap_A_2_POS_26	13.40	58.12	3	2.73	1.08	0.06	0.86	0.82
P1420_004_Ap_A_2_POS_26	13.96	43.39	3	2.73	1.08	0.06	0.86	0.82
P1420_004_Ap_A_2_POS_0	15.00	29.77	2	2.97	2.04	0.08	0.00	0.81
P1420_004_Ap_A_2_POS_0	14.70	38.93	2	2.97	2.04	0.08	0.00	0.81
P1420_004_Ap_A_2_POS_42	12.27	62.91	4	3.22	1.51	0.06	0.43	0.81
P1420_004_Ap_A_2_POS_42	12.75	57.08	4	3.22	1.51	0.06	0.43	0.81
P1420_004_Ap_A_2_POS_42	10.46	76.24	4	3.22	1.51	0.06	0.43	0.81
P1420_004_Ap_A_2_POS_42	15.29	36.65	4	3.22	1.51	0.06	0.43	0.81
P1420_004_Ap_A_2_POS_5	12.70	55.43	2	2.34	2.01	0.11	0.00	0.80
P1420_004_Ap_A_2_POS_44	15.97	68.02	1	2.94	1.35	0.19	0.46	0.79
P1420_004_Ap_A_2_POS_44	14.69	58.64	1	2.94	1.35	0.19	0.46	0.79
P1420_004_Ap_A_2_POS_44	12.64	48.73	1	2.94	1.35	0.19	0.46	0.79
P1420_004_Ap_A_2_POS_44	7.97	57.84	1	2.94	1.35	0.19	0.46	0.79
P1420_004_Ap_A_2_POS_17	9.14	49.27	4	3.27	1.58	0.06	0.36	0.79
P1420_004_Ap_A_2_POS_17	13.99	64.30	4	3.27	1.58	0.06	0.36	0.79
P1420_004_Ap_A_2_POS_17	11.85	70.27	4	3.27	1.58	0.06	0.36	0.79
P1420_004_Ap_A_2_POS_31	15.89	44.37	1	3.07	1.62	0.09	0.29	0.78
P1420_004_Ap_A_2_POS_31	12.58	77.30	1	3.07	1.62	0.09	0.29	0.78
P1420_004_Ap_A_2_POS_19	15.79	86.87	3	3.60	1.23	0.17	0.59	0.77
P1420_004_Ap_A_2_POS_19	16.40	43.66	3	3.60	1.23	0.17	0.59	0.77
P1420_004_Ap_A_2_POS_19	13.28	76.58	3	3.60	1.23	0.17	0.59	0.77
P1420_004_Ap_A_2_POS_19	13.46	54.00	3	3.60	1.23	0.17	0.59	0.77
Ave	**13.33**			**2.89**	**1.46**	**0.08**	**0.46**	**0.81**
SD	**2.10**			**0.43**	**0.26**	**0.06**	**0.23**	**0.02**
Kinetic population #3 (rmr0 < 0.76)								
P1420_004_Ap_A_2_POS_16	14.17	59.78	4	2.35	1.44	0.08	0.48	0.78
P1420_004_Ap_A_2_POS_16	13.92	22.44	4	2.35	1.44	0.08	0.48	0.78
P1420_004_Ap_A_2_POS_7	12.88	81.75	2	3.06	0.61	0.19	1.20	0.76
P1420_004_Ap_A_2_POS_32	16.20	81.03	4	2.95	1.22	0.03	0.75	0.77
P1420_004_Ap_A_2_POS_32	12.87	68.70	4	2.95	1.22	0.03	0.75	0.77
P1420_004_Ap_A_2_POS_18	11.42	29.98	4	2.74	1.35	0.08	0.57	0.77
P1420_004_Ap_A_2_POS_18	14.92	64.17	4	2.74	1.35	0.08	0.57	0.77
P1420_004_Ap_A_2_POS_18	13.74	47.74	4	2.74	1.35	0.08	0.57	0.77
P1420_004_Ap_A_2_POS_7	11.30	-1.00	2	3.06	0.61	0.19	1.20	0.76
P1420_004_Ap_A_2_POS_7	10.18	73.61	2	3.06	0.61	0.19	1.20	0.76
P1420_004_Ap_A_2_POS_7	12.25	33.17	2	3.06	0.61	0.19	1.20	0.76
P1420_004_Ap_A_2_POS_7	12.20	56.55	2	3.06	0.61	0.19	1.20	0.76
P1420_004_Ap_A_2_POS_7	15.91	27.65	2	3.06	0.61	0.19	1.20	0.76
P1420_004_Ap_A_2_POS_37	16.29	25.43	3	2.62	1.11	0.13	0.76	0.75

A2Z Sample No.	Confined length (mm)	angle to C-axis (degrees)	Etch Figs.	D_{par} (µm)	meas. F (apfu)	meas. Cl (apfu)	calc. OH (apfu)	r_{mr0}
P1420_004_Ap_A_2_POS_37	9.42	42.30	3	2.62	1.11	0.13	0.76	0.75
P1420_004_Ap_A_2_POS_37	8.54	66.67	3	2.62	1.11	0.13	0.76	0.75
P1420_004_Ap_A_2_POS_37	8.03	63.26	3	2.62	1.11	0.13	0.76	0.75
P1420_004_Ap_A_2_POS_50	16.29	42.54	1	4.39	0.84	0.20	0.96	0.74
P1420_004_Ap_A_2_POS_50	13.69	70.91	1	4.39	0.84	0.20	0.96	0.74
P1420_004_Ap_A_2_POS_10	8.11	63.63	2	3.31	0.61	0.13	1.27	0.73
P1420_004_Ap_A_2_POS_10	13.62	43.15	2	3.31	0.61	0.13	1.27	0.73
P1420_004_Ap_A_2_POS_40	13.32	41.85	2	3.35	1.02	0.21	0.77	0.72
P1420_004_Ap_A_2_POS_40	13.39	57.77	2	3.35	1.02	0.21	0.77	0.72
P1420_004_Ap_A_2_POS_40	14.43	50.43	2	3.35	1.02	0.21	0.77	0.72
P1420_004_Ap_A_2_POS_40	15.52	70.55	2	3.35	1.02	0.21	0.77	0.72
P1420_004_Ap_A_2_POS_40	13.14	54.62	2	3.35	1.02	0.21	0.77	0.72
P1420_004_Ap_A_2_POS_25	12.84	73.61	2	4.65	0.75	0.22	1.02	0.71
P1420_004_Ap_A_2_POS_33	15.55	56.11	1	4.33	0.90	0.38	0.72	0.62
Ave	**13.01**			**3.17**	**0.97**	**0.16**	**0.87**	**0.74**
SD	**2.42**			**0.61**	**0.29**	**0.07**	**0.25**	**0.03**

10FNARL008, Imperial Fm. (lithic arenite) Carcajou River section, ~0.74 %Ro, 64.752 N, 126.778 W

Kinetic population #1 (rmr0 > 0.86)								
P1392_015_Ap_A_1_POS_4	12.08	52.19	4	2.41	2	0	-	0.86
P1392_015_Ap_A_1_POS_4	10.76	62.76	4	2.41	2	0	-	0.86
Kinetic population #2 (0.76 < rmr0 < 0.86)								
P1392_015_Ap_A_1_POS_3	13.07	81.75	4	2.63	1.94	0.06	-	0.85
P1392_015_Ap_A_1_POS_3	14.05	84.27	4	2.63	1.94	0.06	-	0.85
P1392_015_Ap_A_1_POS_3	11.85	37.49	4	2.63	1.94	0.06	-	0.85
P1392_015_Ap_A_1_POS_3	14.67	59.71	4	2.63	1.94	0.06	-	0.85
P1392_015_Ap_A_1_POS_3	11.64	60.73	4	2.63	1.94	0.06	-	0.85
P1392_015_Ap_A_1_POS_12	13.18	79.65	4	2.21	1.96	0.04	-	0.85
P1392_015_Ap_A_1_POS_12	15.93	75.77	4	2.21	1.96	0.04	-	0.85
P1392_015_Ap_A_1_POS_12	13.72	58.43	4	2.21	1.96	0.04	-	0.85
P1392_015_Ap_A_1_POS_12	13.35	31.74	4	2.21	1.96	0.04	-	0.85
P1392_015_Ap_A_1_POS_12	13.59	63.72	4	2.21	1.96	0.04	-	0.85
P1392_015_Ap_A_1_POS_10	11.85	47.37	4	2.82	1.97	0.03	-	0.84
P1392_015_Ap_A_1_POS_10	11.93	51.23	4	2.82	1.97	0.03	-	0.84
P1392_015_Ap_A_1_POS_8	16.47	42.93	4	2.58	1.85	0.15	-	0.82
P1392_015_Ap_A_1_POS_8	12.77	42.34	4	2.58	1.85	0.15	-	0.82
P1392_015_Ap_A_1_POS_5	15.09	57.63	4	2.34	1.80	0.20	-	0.81
P1392_015_Ap_A_1_POS_5	10.76	69.86	4	2.34	1.80	0.20	-	0.81
P1392_015_Ap_A_1_POS_5	12.40	47.70	4	2.34	1.80	0.20	-	0.81
P1392_015_Ap_A_1_POS_5	13.00	38.41	4	2.34	1.80	0.20	-	0.81
P1392_015_Ap_A_1_POS_5	14.18	60.45	4	2.34	1.80	0.20	-	0.81
P1392_015_Ap_A_1_POS_5	13.55	77.03	4	2.34	1.80	0.20	-	0.81

A2Z Sample No.	Confined length (mm)	angle to C-axis (degrees)	Etch Figs.	D_{par} (µm)	meas. F (apfu)	meas. Cl (apfu)	calc. OH (apfu)	r_{mr0}
P1392_015_Ap_A_1_POS_5	13.38	77.81	4	2.34	1.80	0.20	-	0.81
P1392_015_Ap_A_1_POS_5	12.28	46.57	4	2.34	1.80	0.20	-	0.81
P1392_015_Ap_A_1_POS_11	14.03	56.02	4	2.34	1.96	0.04	-	0.80
P1392_015_Ap_A_1_POS_11	14.27	53.64	4	2.34	1.96	0.04	-	0.80
P1392_015_Ap_A_1_POS_11	14.35	58.82	4	2.34	1.96	0.04	-	0.80
P1392_015_Ap_A_1_POS_11	14.36	70.47	4	2.34	1.96	0.04	-	0.80
P1392_015_Ap_A_1_POS_11	15.02	61.27	4	2.34	1.96	0.04	-	0.80
P1392_015_Ap_A_1_POS_11	12.58	49.46	4	2.34	1.96	0.04	-	0.80
P1392_015_Ap_A_1_POS_2	15.96	45.77	4	2.55	1.83	0.17	-	0.78
P1392_015_Ap_A_1_POS_6	15.03	75.70	4	2.33	1.68	0.32	-	0.78
P1392_015_Ap_A_1_POS_6	14.35	33.77	4	2.33	1.68	0.32	-	0.78
P1392_015_Ap_A_1_POS_6	13.70	65.69	4	2.33	1.68	0.32	-	0.78
P1392_015_Ap_A_1_POS_6	13.00	89.33	4	2.33	1.68	0.32	-	0.78
P1392_015_Ap_A_1_POS_0	11.49	64.10	4	2.31	1.79	0.21	-	0.77
P1392_015_Ap_A_1_POS_0	14.35	73.95	4	2.31	1.79	0.21	-	0.77
Ave	**13.58**			**2.41**	**1.87**	**0.13**		**0.81**
SD	**1.35**			**0.17**	**0.10**	**0.10**		**0.03**
Kinetic population # 3 (rmr0 < 0.76)								
P1392_015_Ap_A_1_POS_7	12.95	64.94	4	3.18	1.59	0.41	-	0.74
P1392_015_Ap_A_1_POS_7	11.74	39.58	4	3.18	1.59	0.41	-	0.74
P1392_015_Ap_A_1_POS_7	11.59	81.84	4	3.18	1.59	0.41	-	0.74
P1392_015_Ap_A_1_POS_7	12.42	54.34	4	3.18	1.59	0.41	-	0.74
P1392_015_Ap_A_1_POS_9	14.10	61.10	4	2.33	1.73	0.27	-	0.72
P1392_015_Ap_A_1_POS_1	14.42	42.43	4	2.42	1.90	0.10	-	0.70
P1392_015_Ap_A_1_POS_1	10.69	82.33	4	2.42	1.90	0.10	-	0.70
P1392_015_Ap_A_1_POS_1	13.69	57.02	4	2.42	1.90	0.10	-	0.70
P1392_015_Ap_A_1_POS_1	10.08	56.80	4	2.42	1.90	0.10	-	0.70
P1392_015_Ap_A_1_POS_1	10.21	72.16	4	2.42	1.90	0.10	-	0.70
Ave	**12.19**			**2.72**	**1.76**	**0.24**		**0.72**
SD	**1.59**			**0.40**	**0.15**	**0.15**		**0.02**

Husky7, Imperial Fm. (fine grain sandstone) Redstone River section, ~1.67 %Ro, 63.916 N, 125.198W

Kinetic population #1 (rmr0 > 0.86)								
P943_07_AP_A_2_POS_52	12.35	31.53	3	1.54	2.35	0.00	0.00	0.87
P943_07_AP_A_2_POS_52	13.35	51.09	3	1.54	2.35	0.00	0.00	0.87
P943_07_AP_A_2_POS_49	13.46	57.78	4	1.85	2.05	0.00	0.00	0.86
P943_07_AP_A_2_POS_49	12.37	36.65	4	1.85	2.05	0.00	0.00	0.86
P943_07_AP_A_2_POS_49	13.60	39.54	4	1.85	2.05	0.00	0.00	0.86
P943_07_AP_A_2_POS_53	11.80	41.95	4	1.18	2.15	0.02	0.00	0.86
P943_07_AP_A_2_POS_53	14.46	51.43	4	1.18	2.15	0.02	0.00	0.86
P943_07_AP_A_2_POS_53	14.59	73.36	4	1.18	2.15	0.02	0.00	0.86

A2Z Sample No.	Confined length (mm)	angle to C-axis (degrees)	Etch Figs.	D_{par} (µm)	meas. F (apfu)	meas. Cl (apfu)	calc. OH (apfu)	r_{mr0}
P943_07_AP_A_2_POS_53	13.10	38.96	4	1.18	2.15	0.02	0.00	0.86
P943_07_AP_A_2_POS_53	14.79	19.47	4	1.18	2.15	0.02	0.00	0.86
Ave	**13.39**			**1.45**	**2.16**	**0.01**	**0.00**	**0.86**
SD	**1.02**			**0.31**	**0.11**	**0.01**	**0.00**	**0.01**
Kinetic population #2 (0.84 < rmr0 < 0.86)								
P943_07_AP_A_2_POS_57	14.05	47.86	4	1.37	2.11	0.01	0.00	0.85
P943_07_AP_A_2_POS_25	16.22	76.95	3	1.39	1.82	0.02	0.16	0.85
P943_07_AP_A_2_POS_58	11.86	50.98	4	1.72	1.94	0.06	0.00	0.85
P943_07_AP_A_2_POS_58	13.42	38.12	4	1.72	1.94	0.06	0.00	0.85
P943_07_AP_A_2_POS_2	12.53	69.60	2	1.48	2.23	0.01	0.00	0.85
P943_07_AP_A_2_POS_46	8.15	79.65	4	1.57	1.78	0.00	0.21	0.84
P943_07_AP_A_2_POS_46	13.32	36.41	4	1.57	1.78	0.00	0.21	0.84
P943_07_AP_A_2_POS_60	14.90	22.21	4	2.14	1.68	0.01	0.31	0.84
P943_07_AP_A_2_POS_60	11.09	57.92	4	2.14	1.68	0.01	0.31	0.84
P943_07_AP_A_2_POS_60	9.41	67.06	4	2.14	1.68	0.01	0.31	0.84
P943_07_AP_A_2_POS_60	13.29	46.57	4	2.14	1.68	0.01	0.31	0.84
P943_07_AP_A_2_POS_60	11.05	61.46	4	2.14	1.68	0.01	0.31	0.84
P943_07_AP_A_2_POS_67	14.81	36.57	4	1.67	1.73	0.02	0.25	0.84
P943_07_AP_A_2_POS_51	13.96	78.29	4	1.36	1.85	0.06	0.10	0.84
P943_07_AP_A_2_POS_51	12.40	75.75	4	1.36	1.85	0.06	0.10	0.84
P943_07_AP_A_2_POS_51	14.89	54.66	4	1.36	1.85	0.06	0.10	0.84
P943_07_AP_A_2_POS_51	12.34	46.10	4	1.36	1.85	0.06	0.10	0.84
P943_07_AP_A_2_POS_35	12.33	39.22	4	1.65	1.89	0.06	0.05	0.84
P943_07_AP_A_2_POS_35	14.88	78.76	4	1.65	1.89	0.06	0.05	0.84
P943_07_AP_A_2_POS_35	12.34	45.73	4	1.65	1.89	0.06	0.05	0.84
P943_07_AP_A_2_POS_35	14.21	74.10	4	1.65	1.89	0.06	0.05	0.84
P943_07_AP_A_2_POS_35	14.34	79.79	4	1.65	1.89	0.06	0.05	0.84
P943_07_AP_A_2_POS_59	12.27	50.29	3	1.51	1.99	0.04	0.00	0.84
P943_07_AP_A_2_POS_59	15.19	23.19	3	1.51	1.99	0.04	0.00	0.84
P943_07_AP_A_2_POS_59	12.40	23.96	3	1.51	1.99	0.04	0.00	0.84
P943_07_AP_A_2_POS_18	12.29	43.13	4	1.58	0.16	0.03	1.80	0.84
P943_07_AP_A_2_POS_50	11.92	31.76	4	1.61	1.63	0.03	0.33	0.84
P943_07_AP_A_2_POS_50	12.99	21.14	4	1.61	1.63	0.03	0.33	0.84
P943_07_AP_A_2_POS_50	12.78	66.77	4	1.61	1.63	0.03	0.33	0.84
P943_07_AP_A_2_POS_50	10.22	49.18	4	1.61	1.63	0.03	0.33	0.84
P943_07_AP_A_2_POS_50	15.72	17.53	4	1.61	1.63	0.03	0.33	0.84
P943_07_AP_A_2_POS_50	16.62	52.00	4	1.61	1.63	0.03	0.33	0.84
P943_07_AP_A_2_POS_50	13.14	64.77	4	1.61	1.63	0.03	0.33	0.84
P943_07_AP_A_2_POS_50	9.65	57.48	4	1.61	1.63	0.03	0.33	0.84
P943_07_AP_A_2_POS_33	13.84	63.80	4	1.61	1.75	0.01	0.25	0.84
P943_07_AP_A_2_POS_33	15.62	18.97	4	1.61	1.75	0.01	0.25	0.84

A2Z Sample No.	Confined length (mm)	angle to C-axis (degrees)	Etch Figs.	D_{par} (µm)	meas. F (apfu)	meas. Cl (apfu)	calc. OH (apfu)	r_{mr0}
P943_07_AP_A_2_POS_33	14.63	51.32	4	1.61	1.75	0.01	0.25	0.84
P943_07_AP_A_2_POS_11	17.44	48.03	4	2.24	1.83	0.01	0.16	0.84
P943_07_AP_A_2_POS_11	11.88	46.18	4	2.24	1.83	0.01	0.16	0.84
P943_07_AP_A_2_POS_11	12.77	57.79	4	2.24	1.83	0.01	0.16	0.84
P943_07_AP_A_2_POS_11	14.44	18.30	4	2.24	1.83	0.01	0.16	0.84
P943_07_AP_A_2_POS_11	15.19	55.58	4	2.24	1.83	0.01	0.16	0.84
P943_07_AP_A_2_POS_7	13.81	83.33	2	1.39				
P943_07_AP_A_2_POS_7	11.05	61.70	2	1.39				
P943_07_AP_A_2_POS_40	13.07	51.91	3	1.44	1.76	0.01	0.23	0.84
Ave	**13.22**			**1.69**	**1.77**	**0.03**	**0.22**	**0.84**
SD	**1.93**			**0.29**	**0.29**	**0.02**	**0.28**	**0.00**
Kinetic population #3 (0.76 < rmr0 < 0.86)								
P943_07_AP_A_2_POS_68	13.93	76.08	4	1.63	1.85	0.04	0.10	0.83
P943_07_AP_A_2_POS_68	10.33	67.29	4	1.63	1.85	0.04	0.10	0.83
P943_07_AP_A_2_POS_22	15.70	74.95	4	1.92	1.58	0.04	0.38	0.83
P943_07_AP_A_2_POS_23	15.26	23.18	4	1.92	1.58	0.04	0.38	0.83
P943_07_AP_A_2_POS_54	14.88	52.33	4	1.65	1.41	0.04	0.55	0.83
P943_07_AP_A_2_POS_54	9.96	76.16	4	1.65	1.41	0.04	0.55	0.83
P943_07_AP_A_2_POS_54	9.72	39.68	4	1.65	1.41	0.04	0.55	0.83
P943_07_AP_A_2_POS_38	14.73	49.28	2	1.79	1.48	0.04	0.48	0.83
P943_07_AP_A_2_POS_38	4.95	72.77	2	1.79	1.48	0.04	0.48	0.83
P943_07_AP_A_2_POS_38	13.82	68.47	2	1.79	1.48	0.04	0.48	0.83
P943_07_AP_A_2_POS_62	13.60	54.73	3	1.40	1.56	0.01	0.43	0.83
P943_07_AP_A_2_POS_62	12.88	76.60	3	1.40	1.56	0.01	0.43	0.83
P943_07_AP_A_2_POS_54	9.64	47.86	3	1.62	1.41	0.04	0.55	0.83
P943_07_AP_A_2_POS_54	17.01	30.48	3	1.62	1.41	0.04	0.55	0.83
P943_07_AP_A_2_POS_54	13.27	83.57	3	1.62	1.41	0.04	0.55	0.83
P943_07_AP_A_2_POS_54	13.14	40.60	3	1.62	1.41	0.04	0.55	0.83
P943_07_AP_A_2_POS_69	12.61	75.58	4	1.85	1.60	0.03	0.37	0.83
P943_07_AP_A_2_POS_69	14.33	72.02	4	1.85	1.60	0.03	0.37	0.83
P943_07_AP_A_2_POS_1	10.94	74.82	4	1.46	1.54	0.03	0.44	0.83
P943_07_AP_A_2_POS_1	12.86	78.22	4	1.46	1.54	0.03	0.44	0.83
P943_07_AP_A_2_POS_1	11.10	19.20	4	1.46	1.54	0.03	0.44	0.83
P943_07_AP_A_2_POS_1	11.83	80.57	4	1.46	1.54	0.03	0.44	0.83
P943_07_AP_A_2_POS_34	12.85	57.37	4	2.01	1.75	0.05	0.21	0.83
P943_07_AP_A_2_POS_34	10.82	50.88	4	2.01	1.75	0.05	0.21	0.83
P943_07_AP_A_2_POS_34	14.63	35.12	4	2.01	1.75	0.05	0.21	0.83
P943_07_AP_A_2_POS_34	8.29	60.61	4	2.01	1.75	0.05	0.21	0.83
P943_07_AP_A_2_POS_19	9.48	66.39	4	2.15	2.52	0.02	0.00	0.83
P943_07_AP_A_2_POS_19	9.79	51.43	4	2.15	2.52	0.02	0.00	0.83
P943_07_AP_A_2_POS_19	13.12	29.14	4	2.15	2.52	0.02	0.00	0.83
P943_07_AP_A_2_POS_19	12.75	67.89	4	2.15	2.52	0.02	0.00	0.83

A2Z Sample No.	Confined length (mm)	angle to C-axis (degrees)	Etch Figs.	D_{par} (µm)	meas. F (apfu)	meas. Cl (apfu)	calc. OH (apfu)	r_{mr0}
P943_07_AP_A_2_POS_19	9.99	40.30	4	2.15	2.52	0.02	0.00	0.83
P943_07_AP_A_2_POS_19	7.99	66.55	4	2.15	2.52	0.02	0.00	0.83
P943_07_AP_A_2_POS_28	12.99	81.72	4	1.54	1.67	0.08	0.25	0.83
P943_07_AP_A_2_POS_48	13.57	52.80	4	1.67	2.06	0.07	0.00	0.83
P943_07_AP_A_2_POS_48	4.40	76.29	4	1.67	2.06	0.07	0.00	0.83
P943_07_AP_A_2_POS_48	6.70	51.71	4	1.67	2.06	0.07	0.00	0.83
P943_07_AP_A_2_POS_47	13.84	67.72	4	1.67	1.56	0.04	0.40	0.83
P943_07_AP_A_2_POS_47	10.45	81.48	4	1.67	1.56	0.04	0.40	0.83
P943_07_AP_A_2_POS_47	8.81	52.13	4	1.67	1.56	0.04	0.40	0.83
P943_07_AP_A_2_POS_32	15.49	32.91	4	1.36	1.26	0.01	0.74	0.83
P943_07_AP_A_2_POS_42	12.95	50.11	4	1.46	1.50	0.03	0.47	0.82
P943_07_AP_A_2_POS_8	9.61	84.34	4	1.95	2.13	0.08	0.00	0.82
P943_07_AP_A_2_POS_8	13.88	56.25	4	1.95	2.13	0.08	0.00	0.82
P943_07_AP_A_2_POS_7	13.55	78.27	4	1.40	0.08	0.06	1.86	0.82
P943_07_AP_A_2_POS_70	14.10	54.51	4	1.97	1.39	0.03	0.58	0.82
P943_07_AP_A_2_POS_71	13.78	32.13	4	1.97	1.39	0.03	0.58	0.82
P943_07_AP_A_2_POS_74	11.64	32.88	4	1.81	1.65	0.11	0.24	0.82
P943_07_AP_A_2_POS_74	12.96	46.17	4	1.81	1.65	0.11	0.24	0.82
P943_07_AP_A_2_POS_74	9.68	73.63	4	1.81	1.65	0.11	0.24	0.82
P943_07_AP_A_2_POS_63	10.98	79.75	4	1.58	1.50	0.05	0.47	0.82
P943_07_AP_A_2_POS_27	12.96	62.50	4	1.98	1.40	0.07	0.53	0.82
P943_07_AP_A_2_POS_27	13.98	27.97	4	1.98	1.40	0.07	0.53	0.82
P943_07_AP_A_2_POS_43	9.57	44.64	4	1.51	1.23	0.02	0.75	0.82
P943_07_AP_A_2_POS_43	13.89	16.27	4	1.51	1.23	0.02	0.75	0.82
P943_07_AP_A_2_POS_43	12.85	65.14	4	1.51	1.23	0.02	0.75	0.82
P943_07_AP_A_2_POS_43	14.09	41.45	4	1.51	1.23	0.02	0.75	0.82
P943_07_AP_A_2_POS_10	11.00	36.55	3	2.26	1.36	0.05	0.59	0.81
P943_07_AP_A_2_POS_10	13.93	78.88	3	2.26	1.36	0.05	0.59	0.81
P943_07_AP_A_2_POS_9	12.57	37.34	4	1.97	1.94	0.06	1.92	0.81
P943_07_AP_A_2_POS_9	14.61	34.45	4	1.97	1.94	0.06	1.92	0.81
P943_07_AP_A_2_POS_9	8.63	56.55	4	1.97	1.94	0.06	1.92	0.81
P943_07_AP_A_2_POS_9	10.51	62.13	4	1.97	1.94	0.06	1.92	0.81
P943_07_AP_A_2_POS_5	10.65	83.80	4	1.79	1.24	0.10	0.66	0.81
P943_07_AP_A_2_POS_5	9.17	85.15	4	1.79	1.24	0.10	0.66	0.81
P943_07_AP_A_2_POS_5	6.55	39.89	4	1.79	1.24	0.10	0.66	0.81
P943_07_AP_A_2_POS_5	10.28	73.66	4	1.79	1.24	0.10	0.66	0.81
P943_07_AP_A_2_POS_5	7.88	70.23	4	1.79	1.24	0.10	0.66	0.81
P943_07_AP_A_2_POS_73	12.73	77.15	4	1.90	1.34	0.06	0.60	0.81
P943_07_AP_A_2_POS_73	9.46	51.52	4	1.90	1.34	0.06	0.60	0.81
P943_07_AP_A_2_POS_44	12.84	74.86	4	2.14	1.30	0.08	0.62	0.81
P943_07_AP_A_2_POS_44	14.12	86.16	4	2.14	1.30	0.08	0.62	0.81
P943_07_AP_A_2_POS_44	14.44	56.28	4	2.14	1.30	0.08	0.62	0.81

A2Z Sample No.	Confined length (mm)	angle to C-axis (degrees)	Etch Figs.	D_{par} (µm)	meas. F (apfu)	meas. Cl (apfu)	calc. OH (apfu)	r_{mr0}
P943_07_AP_A_2_POS_55	14.14	42.54	4	2.18	1.27	0.07	0.65	0.81
P943_07_AP_A_2_POS_55	14.40	87.39	4	2.18	1.27	0.07	0.65	0.81
P943_07_AP_A_2_POS_55	14.82	42.00	4	2.18	1.27	0.07	0.65	0.81
P943_07_AP_A_2_POS_61	9.54	52.30	4	2.18	1.72	0.18	0.10	0.81
P943_07_AP_A_2_POS_61	10.05	74.17	4	2.18	1.72	0.18	0.10	0.81
P943_07_AP_A_2_POS_39	14.81	40.02	4	1.93	1.24	0.06	0.70	0.81
P943_07_AP_A_2_POS_39	14.72	32.12	4	1.93	1.24	0.06	0.70	0.81
P943_07_AP_A_2_POS_17	14.55	24.73	3	2.07	1.43	0.14	0.43	0.81
P943_07_AP_A_2_POS_17	11.36	52.35	3	2.07	1.43	0.14	0.43	0.81
P943_07_AP_A_2_POS_17	9.66	57.47	3	2.07	1.43	0.14	0.43	0.81
P943_07_AP_A_2_POS_14	12.41	67.38	4	1.68	1.43	0.14	0.43	0.80
P943_07_AP_A_2_POS_14	15.04	34.21	4	1.68	1.43	0.14	0.43	0.80
P943_07_AP_A_2_POS_66	9.34	34.90	4	1.75	1.64	0.23	0.13	0.80
P943_07_AP_A_2_POS_66	14.29	50.22	4	1.75	1.64	0.23	0.13	0.80
P943_07_AP_A_2_POS_12	14.82	70.98	3	1.66	1.98	0.02	0.00	0.80
P943_07_AP_A_2_POS_12	13.62	15.26	3	1.66	1.98	0.02	0.00	0.80
P943_07_AP_A_2_POS_72	12.39	26.69	4	1.69	1.63	0.19	0.17	0.79
P943_07_AP_A_2_POS_72	12.36	53.00	4	1.69	1.63	0.19	0.17	0.79
P943_07_AP_A_2_POS_72	14.41	32.48	4	1.69	1.63	0.19	0.17	0.79
P943_07_AP_A_2_POS_72	4.09	54.10	4	1.69	1.63	0.19	0.17	0.79
P943_07_AP_A_2_POS_24	9.60	70.60	2	1.74				
P943_07_AP_A_2_POS_24	9.43	79.94	2	1.74				
P943_07_AP_A_2_POS_24	6.84	70.67	2	1.74				
P943_07_AP_A_2_POS_24	14.97	49.94	2	1.74				
P943_07_AP_A_2_POS_56	15.33	17.80	4	1.90	0.86	0.06	1.08	0.79
P943_07_AP_A_2_POS_64	14.29	69.19	4	1.60	1.31	0.13	0.55	0.79
P943_07_AP_A_2_POS_64	10.29	63.82	4	1.60	1.31	0.13	0.55	0.79
P943_07_AP_A_2_POS_26	11.09	54.29	4	1.93	0.10	0.04	1.86	
P943_07_AP_A_2_POS_26	16.06	23.05	4	1.93	0.10	0.04	1.86	
P943_07_AP_A_2_POS_26	9.21	89.68	4	1.93	0.10	0.04	1.86	
P943_07_AP_A_2_POS_26	12.74	42.29	4	1.93	0.10	0.04	1.86	
P943_07_AP_A_2_POS_26	11.32	56.81	4	1.93	0.10	0.04	1.86	
P943_07_AP_A_2_POS_37	8.90	48.46	4	1.68	0.71	0.03	1.25	
P943_07_AP_A_2_POS_37	12.63	80.99	4	1.68	0.71	0.03	1.25	
P943_07_AP_A_2_POS_71	14.30	54.94	3	2.04	0.77	0.11	1.12	0.79
P943_07_AP_A_2_POS_21	10.51	43.71	4	2.20	1.46	0.24	0.30	0.79
P943_07_AP_A_2_POS_22	11.04	69.37	4	2.20	1.46	0.24	0.30	0.79
P943_07_AP_A_2_POS_23	10.85	51.09	4	2.20	1.46	0.24	0.30	0.79
P943_07_AP_A_2_POS_24	12.24	45.82	4	2.20	1.46	0.24	0.30	0.79
P943_07_AP_A_2_POS_76	13.63	46.55	4	1.78	1.45	0.17	0.38	0.78
P943_07_AP_A_2_POS_76	9.59	79.43	4	1.78	1.45	0.17	0.38	0.78
P943_07_AP_A_2_POS_76	11.72	38.97	4	1.78	1.45	0.17	0.38	0.78

A2Z Sample No.	Confined length (mm)	angle to C-axis (degrees)	Etch Figs.	D_{par} (µm)	meas. F (apfu)	meas. Cl (apfu)	calc. OH (apfu)	r_{mr0}
P943_07_AP_A_2_POS_76	8.67	84.88	4	1.78	1.45	0.17	0.38	0.78
P943_07_AP_A_2_POS_29	11.21	55.00	4	2.13	1.43	0.04	0.53	0.78
P943_07_AP_A_2_POS_73	9.62	76.43	4	1.96	1.29	0.18	0.52	0.78
P943_07_AP_A_2_POS_73	10.53	55.42	4	1.96	1.29	0.18	0.52	0.78
P943_07_AP_A_2_POS_45	10.50	87.94	4	2.06	1.11	0.19	0.70	0.78
P943_07_AP_A_2_POS_45	12.21	65.09	4	2.06	1.11	0.19	0.70	0.78
P943_07_AP_A_2_POS_45	9.69	76.11	4	2.06	1.11	0.19	0.70	0.78
P943_07_AP_A_2_POS_45	9.95	76.18	4	2.06	1.11	0.19	0.70	0.78
P943_07_AP_A_2_POS_4	10.62	57.15	4	2.34	1.09	0.11	0.81	0.78
P943_07_AP_A_2_POS_4	8.82	83.93	4	2.34	1.09	0.11	0.81	0.78
P943_07_AP_A_2_POS_4	14.77	57.01	4	2.34	1.09	0.11	0.81	0.78
P943_07_AP_A_2_POS_4	11.35	82.34	4	2.34	1.09	0.11	0.81	0.78
P943_07_AP_A_2_POS_4	13.05	75.29	4	2.34	1.09	0.11	0.81	0.78
P943_07_AP_A_2_POS_3	9.98	42.54	4	1.72	1.61	0.19	0.20	0.76
P943_07_AP_A_2_POS_3	10.77	32.81	4	1.72	1.61	0.19	0.20	0.76
P943_07_AP_A_2_POS_3	11.71	39.67	4	1.72	1.61	0.19	0.20	0.76
P943_07_AP_A_2_POS_36	10.47	40.47	4	2.11				
P943_07_AP_A_2_POS_36	9.29	80.40	4	2.11				
P943_07_AP_A_2_POS_36	11.24	53.27	4	2.34				
P943_07_AP_A_2_POS_36	14.18	28.84	4	2.34				
Ave	**11.78**			**1.87**	**1.45**	**0.09**	**0.56**	**0.81**
SD	**2.49**			**0.25**	**0.46**	**0.06**	**0.47**	**0.02**
Kinetic population #4 (rmr0 < 0.76)								
P943_07_AP_A_2_POS_65	10.93	51.77	4	3.44	1.18	0.02	0.80	0.75
P943_07_AP_A_2_POS_65	14.30	43.42	4	3.44	1.18	0.02	0.80	0.75
P943_07_AP_A_2_POS_16	12.65	76.63	4	1.71	0.71	0.04	1.25	0.74
P943_07_AP_A_2_POS_6	8.42	73.58	3	3.12	1.08	0.06	0.86	0.74
P943_07_AP_A_2_POS_31	12.13	74.57	4	2.56	1.03	0.26	0.70	0.74
P943_07_AP_A_2_POS_32	12.47	59.93	4	2.56	1.03	0.26	0.70	0.74
P943_07_AP_A_2_POS_33	15.00	84.53	4	2.56	1.03	0.26	0.70	0.74
P943_07_AP_A_2_POS_34	10.49	59.24	4	2.56	1.03	0.26	0.70	0.74
P943_07_AP_A_2_POS_35	14.21	40.54	4	2.56	1.03	0.26	0.70	0.74
P943_07_AP_A_2_POS_36	11.93	70.50	4	2.56	1.03	0.26	0.70	0.74
P943_07_AP_A_2_POS_39	10.58	77.97	4	2.56	1.04	0.19	0.77	0.73
P943_07_AP_A_2_POS_39	14.30	42.88	4	2.56	1.04	0.19	0.77	0.73
P943_07_AP_A_2_POS_75	14.76	21.10	4	2.27	1.14	0.27	0.59	0.70
Ave	**12.47**			**2.65**	**1.04**	**0.18**	**0.77**	**0.74**
SD	**2.00**			**0.46**	**0.12**	**0.11**	**0.16**	**0.01**

Note: D_{par} is the diameter of the etch figure parallel to the c axis. F, Cl and OH concentrations were caluclated from weight % oxide using the stoichiometric relationships of *Ketcham* [2015], and r_{mr0} was determined using the calculations of *Carlson et al*. [1999]

Table A3. Apatite chemistry for all AFT age and length grains, Imperial Formation, Mackenzie Plain, NWT, Canada

A2Z Sample No.	Na (apfu)	Mg (apfu)	P (apfu)	S (apfu)	Ca (apfu)	Mn (apfu)	Fe (apfu)	As (apfu)	Sr (apfu)	Y (apfu)	La (apfu)	Ce (apfu)	F (apfu)	Cl (apfu)	OH (apfu)	TOTAL (apfu)	r_{mr0}	Ca SITE 10	P SITE 6	F+Cl+OH 2	TOTAL WT% OX
JPCPC3, Imperial Fm. (siltstone) Powell River section, ~0.70 %Ro, 65.277 N, 128.774 W																					
AFT Age-Grains																					
P1420_003_Ap_A_1_POS_0	0.034	0.026	6.063	-	9.683	0.017	0.038	0.000	0.008	0.005	0.008	0.021	0.996	0.156	0.848	17.900	0.722	9.84	6.06	2.00	92.93
P1420_003_Ap_A_1_POS_2	0.038	0.011	5.931	-	10.050	0.026	0.010	0.000	0.003	0.004	0.010	0.022	1.215	0.137	0.648	18.100	0.780	10.17	5.93	2.00	94.89
P1420_003_Ap_A_1_POS_5	0.000	0.000	6.169	-	9.543	0.011	0.003	0.000	0.015	0.001	0.001	0.002	1.507	0.022	0.471	17.700	0.834	9.58	6.17	2.00	89.59
P1420_003_Ap_A_1_POS_6	0.014	0.078	6.068	-	9.660	0.010	0.043	0.000	0.007	0.006	0.003	0.007	1.385	0.053	0.562	17.900	0.765	9.83	6.07	2.00	96.27
P1420_003_Ap_A_1_POS_7	0.072	0.086	5.882	-	10.040	0.007	0.034	0.000	0.040	0.002	0.010	0.025	1.813	0.048	0.139	18.200	0.795	10.31	5.88	2.00	91.76
P1420_003_Ap_A_1_POS_8	0.126	0.012	5.911	-	10.010	0.012	0.015	0.000	0.014	0.004	0.018	0.043	1.403	0.424	0.173	18.200	0.728	10.25	5.91	2.00	93.05
P1420_003_Ap_A_1_POS_9	0.012	0.002	5.958	-	9.980	0.009	0.004	0.000	0.002	0.015	0.013	0.040	2.026	0.000	0.000	18.100	0.855	10.08	5.96	2.03	94.55
P1420_003_Ap_A_1_POS_10	0.030	0.000	5.864	-	10.278	0.003	0.001	0.000	0.030	0.001	0.002	0.007	1.574	0.002	0.424	18.200	0.842	10.35	5.86	2.00	97.14
P1420_003_Ap_A_1_POS_11	0.009	0.071	6.061	-	9.681	0.009	0.044	0.000	0.012	0.005	0.004	0.009	1.779	0.151	0.070	17.900	0.769	9.84	6.06	2.00	94.60
P1420_003_Ap_A_1_POS_13	0.000	0.000	6.007	-	9.981	0.000	0.000	0.000	0.000	0.000	0.000	0.000	1.286	0.113	0.602	18.000	0.820	9.98	6.01	2.00	94.66
P1420_003_Ap_A_1_POS_14	0.024	0.008	6.093	-	9.681	0.012	0.011	0.000	0.005	0.006	0.005	0.014	1.752	0.042	0.206	17.900	0.830	9.77	6.09	2.00	95.25
P1420_003_Ap_A_1_POS_15	0.019	0.090	5.956	-	9.912	0.009	0.031	0.000	0.037	0.003	0.004	0.009	1.733	0.080	0.187	18.100	0.793	10.11	5.96	2.00	89.25
P1420_003_Ap_A_1_POS_16	0.012	0.003	6.006	-	9.953	0.008	0.004	0.000	0.002	0.001	0.002	0.004	0.620	0.121	1.260	18.000	0.801	9.99	6.01	2.00	100.34
P1420_003_Ap_A_1_POS_17	0.020	0.001	5.974	-	10.007	0.006	0.004	0.000	0.016	0.001	0.004	0.009	1.725	0.008	0.267	18.000	0.845	10.07	5.97	2.00	94.43
P1420_003_Ap_A_1_POS_19	0.030	0.003	6.025	-	9.799	0.016	0.005	0.006	0.010	0.007	0.012	0.030	1.180	0.183	0.637	17.900	0.783	9.91	6.03	2.00	90.44
P1420_003_Ap_A_1_POS_20	0.007	0.000	6.017	-	9.878	0.005	0.002	0.001	0.027	0.004	0.005	0.018	1.156	0.030	0.815	18.000	0.817	9.95	6.02	2.00	89.91
P1420_003_Ap_A_1_POS_21	0.114	0.030	5.950	-	9.830	0.031	0.031	0.000	0.031	0.005	0.020	0.052	0.974	0.325	0.701	18.100	0.669	10.14	5.95	2.00	89.15
P1420_003_Ap_A_1_POS_22	0.098	0.101	5.920	-	9.833	0.014	0.039	0.000	0.054	0.004	0.019	0.052	1.052	0.348	0.600	18.100	0.658	10.21	5.92	2.00	90.37
P1420_003_Ap_A_1_POS_24	0.023	0.002	6.078	-	9.663	0.013	0.013	0.000	0.003	0.010	0.017	0.040	1.868	0.023	0.109	17.900	0.833	9.78	6.08	2.00	94.74
P1420_003_Ap_A_1_POS_25	0.021	0.082	6.185	-	9.351	0.008	0.030	0.000	0.033	0.002	0.003	0.010	1.307	0.028	0.664	17.700	0.782	9.54	6.19	2.00	86.50
P1420_003_Ap_A_1_POS_27	0.063	0.078	5.858	-	10.080	0.010	0.043	0.000	0.016	0.005	0.018	0.043	1.733	0.191	0.077	18.200	0.751	10.35	5.86	2.00	89.28
P1420_003_Ap_A_1_POS_28	0.119	0.038	5.893	-	10.006	0.024	0.032	0.001	0.013	0.005	0.015	0.043	1.141	0.342	0.517	18.200	0.685	10.29	5.89	2.00	92.73
P1420_003_Ap_A_1_POS_29	0.005	0.002	5.964	-	10.067	0.010	0.005	0.000	0.000	0.002	0.000	0.001	1.621	0.017	0.362	18.100	0.838	10.09	5.96	2.00	97.15
P1420_003_Ap_A_1_POS_33	0.006	0.015	6.036	-	9.792	0.013	0.047	0.000	0.004	0.010	0.003	0.011	1.927	0.099	0.000	18.000	0.783	9.90	6.04	2.03	91.64
P1420_003_Ap_A_1_POS_34	0.040	0.005	5.975	-	9.912	0.009	0.005	0.000	0.008	0.003	0.019	0.047	1.822	0.063	0.115	18.000	0.835	10.05	5.98	2.00	93.25
P1420_003_Ap_A_1_POS_35	0.058	0.033	6.014	-	9.787	0.024	0.037	0.000	0.009	0.003	0.007	0.021	1.111	0.206	0.683	18.000	0.715	9.98	6.01	2.00	92.71
P1420_003_Ap_A_1_POS_36	0.005	0.001	5.915	-	10.183	0.011	0.003	0.000	0.001	0.006	0.000	0.001	1.982	0.007	0.012	18.100	0.857	10.21	5.91	2.00	95.72
P1420_003_Ap_A_1_POS_37	0.021	0.000	6.042	-	9.812	0.021	0.007	0.000	0.001	0.028	0.000	0.001	2.055	0.000	0.000	18.000	0.849	9.89	6.04	2.06	96.78
P1420_003_Ap_A_1_POS_39	0.043	0.010	5.999	-	9.865	0.018	0.012	0.000	0.005	0.006	0.011	0.031	1.722	0.072	0.206	18.000	0.818	10.00	6.00	2.00	95.27
AFT Length-Grains																					
P1420_003_Ap_A_2_POS_1	0.020	0.001	5.868	-	10.298	0.007	0.001	0.000	0.001	0.008	0.000	0.000	1.621	0.015	0.364	18.200	0.844	10.34	5.87	2.00	96.10
P1420_003_Ap_A_2_POS_2	0.030	0.020	5.975	-	9.903	0.009	0.016	0.000	0.016	0.005	0.015	0.036	1.201	0.232	0.567	18.000	0.761	10.05	5.98	2.00	101.25
P1420_003_Ap_A_2_POS_3	0.034	0.054	6.017	-	9.772	0.018	0.039	0.000	0.008	0.007	0.007	0.019	1.426	0.097	0.477	18.000	0.759	9.96	6.02	2.00	93.32
P1420_003_Ap_A_2_POS_5	0.013	0.000	6.138	-	9.594	0.018	0.005	0.000	0.005	0.003	0.004	0.010	0.960	0.075	0.965	17.800	0.792	9.65	6.14	2.00	92.95
P1420_003_Ap_A_2_POS_7	0.057	0.059	6.003	-	9.755	0.006	0.019	0.000	0.077	0.004	0.008	0.021	1.733	0.022	0.245	18.000	0.815	10.01	6.00	2.00	93.20
P1420_003_Ap_A_2_POS_8	0.029	0.003	5.983	-	9.898	0.016	0.004	0.000	0.007	0.010	0.013	0.043	1.718	0.058	0.225	18.000	0.829	10.02	5.98	2.00	94.51
P1420_003_Ap_A_2_POS_9	0.029	0.058	6.008	-	9.789	0.009	0.033	0.000	0.007	0.006	0.012	0.029	1.340	0.243	0.417	18.000	0.739	9.97	6.01	2.00	95.64
P1420_003_Ap_A_2_POS_10	0.060	0.030	6.055	-	9.670	0.018	0.041	0.000	0.010	0.004	0.009	0.028	0.995	0.156	0.849	17.900	0.713	9.87	6.06	2.00	93.17
P1420_003_Ap_A_2_POS_11	0.014	0.006	5.977	-	9.905	0.017	0.016	0.000	0.010	0.003	0.021	0.040	0.803	0.173	1.024	18.000	0.748	10.03	5.98	2.00	101.47
P1420_003_Ap_A_2_POS_13	0.007	0.002	6.080	-	9.772	0.012	0.003	0.001	0.002	0.001	0.000	0.001	1.587	0.021	0.392	17.900	0.838	9.80	6.08	2.00	93.78
P1420_003_Ap_A_2_POS_14	0.009	0.001	6.145	-	9.605	0.009	0.003	0.001	0.012	0.001	0.000	0.001	0.961	0.075	0.964	17.800	0.800	9.64	6.15	2.00	92.71
P1420_003_Ap_A_2_POS_16	0.000	0.000	6.088	-	9.779	0.000	0.000	0.000	0.000	0.000	0.000	0.000	1.029	0.345	0.626	17.900	0.769	9.78	6.09	2.00	90.16
P1420_003_Ap_A_2_POS_17	0.107	0.007	6.042	-	9.680	0.013	0.012	0.000	0.015	0.003	0.020	0.054	1.226	0.499	0.275	18.000	0.703	9.91	6.04	2.00	86.15
P1420_003_Ap_A_2_POS_18	0.007	0.040	5.967	-	9.939	0.014	0.047	0.000	0.006	0.008	0.004	0.011	1.339	0.089	0.572	18.000	0.750	10.07	5.97	2.00	97.25
P1420_003_Ap_A_2_POS_19	0.030	0.002	5.865	-	10.280	0.004	0.002	0.000	0.023	0.001	0.001	0.006	1.575	0.002	0.424	18.200	0.842	10.35	5.87	2.00	97.07
P1420_003_Ap_A_2_POS_21	0.028	0.012	5.932	-	10.035	0.015	0.012	0.000	0.008	0.002	0.018	0.030	1.889	0.093	0.019	18.100	0.825	10.16	5.93	2.00	92.06
P1420_003_Ap_A_2_POS_22	0.000	0.000	5.964	-	10.089	0.000	0.000	0.000	0.000	0.000	0.000	0.000	1.331	0.098	0.572	18.100	0.824	10.09	5.96	2.00	99.69
P1420_003_Ap_A_2_POS_23	0.028	0.000	6.099	-	9.695	0.007	0.001	0.000	0.004	0.001	0.006	0.013	1.806	0.029	0.165	17.900	0.848	9.76	6.10	2.00	92.88
P1420_003_Ap_A_2_POS_25	0.006	0.005	6.044	-	9.825	0.010	0.010	0.000	0.005	0.002	0.006	0.014	1.632	0.077	0.292	17.900	0.823	9.88	6.04	2.00	91.65
P1420_003_Ap_A_2_POS_26	0.048	0.000	5.991	-	9.869	0.025	0.008	0.000	0.007	0.007	0.013	0.039	1.384	0.219	0.397	18.000	0.777	10.02	5.99	2.00	88.17

A2Z Sample No.	Na (apfu)	Mg (apfu)	P (apfu)	S (apfu)	Ca (apfu)	Mn (apfu)	Fe (apfu)	As (apfu)	Sr (apfu)	Y (apfu)	La (apfu)	Ce (apfu)	F (apfu)	Cl (apfu)	OH (apfu)	TOTAL (apfu)	r_{mr0}	Ca SITE 10	P SITE 6	F+Cl+OH 2	TOTAL WT% OX
P1420_003_Ap_A_2_POS_27	0.009	0.000	6.042	-	9.855	0.007	0.002	0.000	0.002	0.017	0.000	0.001	1.983	0.010	0.007	17.900	0.859	9.89	6.04	2.00	92.18
P1420_003_Ap_A_2_POS_28	0.040	0.069	5.849	-	10.165	0.010	0.030	0.000	0.020	0.004	0.010	0.029	1.424	0.147	0.429	18.200	0.764	10.38	5.85	2.00	92.01
P1420_003_Ap_A_2_POS_29	0.112	0.132	5.908	-	9.814	0.015	0.043	0.000	0.055	0.004	0.019	0.054	1.050	0.347	0.603	18.200	0.639	10.25	5.91	2.00	90.60
P1420_003_Ap_A_2_POS_30	0.012	0.000	6.058	-	9.784	0.009	0.003	0.000	0.007	0.004	0.007	0.020	1.584	0.029	0.388	17.900	0.835	9.84	6.06	2.00	90.71
P1420_003_Ap_A_2_POS_31	0.155	0.032	5.943	-	9.819	0.033	0.028	0.000	0.024	0.005	0.022	0.059	0.973	0.324	0.703	18.100	0.669	10.18	5.94	2.00	89.33
P1420_003_Ap_A_2_POS_33	0.003	0.000	5.930	-	10.089	0.007	0.008	0.000	0.002	0.005	0.010	0.030	2.080	0.030	0.000	18.200	0.848	10.15	5.93	2.11	95.68
P1420_003_Ap_A_2_POS_34	0.066	0.010	6.278	-	9.147	0.009	0.010	0.000	0.039	0.002	0.010	0.025	1.005	0.161	0.834	17.600	0.768	9.32	6.28	2.00	94.51
P1420_003_Ap_A_2_POS_36	0.015	0.003	5.965	-	9.883	0.022	0.009	0.000	0.003	0.017	0.022	0.068	1.659	0.175	0.166	18.000	0.799	10.04	5.97	2.00	90.94
P1420_003_Ap_A_2_POS_37	0.000	0.001	6.056	-	9.831	0.010	0.002	0.000	0.005	0.001	0.002	0.004	1.662	0.012	0.326	17.900	0.844	9.86	6.06	2.00	95.75
P1420_003_Ap_A_2_POS_39	0.025	0.033	6.020	-	9.798	0.026	0.026	0.000	0.011	0.002	0.007	0.020	1.112	0.206	0.682	18.000	0.736	9.95	6.02	2.00	92.54
P1420_003_Ap_A_2_POS_40	0.000	0.000	5.922	-	10.195	0.000	0.000	0.000	0.000	0.000	0.000	0.000	1.984	0.007	0.009	18.100	0.866	10.20	5.92	2.00	95.51
P1420_003_Ap_A_2_POS_41	0.014	0.000	5.974	-	10.007	0.006	0.002	0.000	0.005	0.006	0.004	0.015	1.827	0.010	0.163	18.000	0.851	10.06	5.97	2.00	98.42
P1420_003_Ap_A_2_POS_42	0.000	0.000	5.994	-	9.975	0.008	0.003	0.002	0.005	0.001	0.003	0.008	1.235	0.232	0.533	18.000	0.790	10.00	6.00	2.00	95.41
P1420_003_Ap_A_2_POS_43	0.026	0.047	5.925	-	10.009	0.012	0.034	0.000	0.011	0.003	0.009	0.028	1.020	0.185	0.795	18.100	0.726	10.18	5.93	2.00	92.66
P1420_003_Ap_A_2_POS_44	0.015	0.002	6.073	-	9.720	0.010	0.003	0.000	0.003	0.047	0.000	0.001	1.811	0.010	0.179	17.900	0.847	9.80	6.07	2.00	97.14
P1420_003_Ap_A_2_POS_45	0.003	0.001	6.004	-	9.920	0.006	0.002	0.000	0.007	0.002	0.009	0.025	1.719	0.012	0.270	18.000	0.846	9.97	6.00	2.00	91.28
P1420_003_Ap_A_2_POS_46	0.060	0.007	5.995	-	9.859	0.021	0.010	0.000	0.004	0.007	0.012	0.036	1.721	0.072	0.207	18.000	0.817	10.02	6.00	2.00	95.41
P1420_003_Ap_A_2_POS_47	0.007	0.002	5.934	-	10.086	0.009	0.003	0.004	0.005	0.016	0.002	0.013	1.515	0.018	0.467	18.100	0.834	10.14	5.94	2.00	93.09
P1420_003_Ap_A_2_POS_48	0.008	0.000	6.075	-	9.742	0.005	0.002	0.011	0.004	0.002	0.006	0.010	2.090	0.000	0.000	18.000	0.862	9.78	6.09	2.09	96.76
P1420_003_Ap_A_2_POS_49	0.019	0.000	5.990	-	9.927	0.013	0.005	0.000	0.005	0.004	0.011	0.029	1.161	0.161	0.678	18.000	0.788	10.01	5.99	2.00	100.75
P1420_003_Ap_A_2_POS_50	0.005	0.007	5.823	-	10.343	0.018	0.009	0.000	0.004	0.004	0.010	0.024	1.238	0.162	0.600	18.200	0.785	10.43	5.82	2.00	94.67
P1420_003_Ap_A_2_POS_51	0.004	0.001	5.800	-	10.466	0.009	0.003	0.000	0.003	0.002	0.002	0.006	1.506	0.033	0.461	18.300	0.833	10.50	5.80	2.00	89.07
P1420_003_Ap_A_2_POS_52	0.044	0.108	5.873	-	10.055	0.010	0.038	0.000	0.018	0.003	0.011	0.031	2.074	0.034	0.000	18.300	0.799	10.32	5.87	2.11	98.61
P1420_003_Ap_A_2_POS_54	0.043	0.030	5.973	-	9.899	0.028	0.028	0.000	0.011	0.003	0.008	0.023	0.834	0.182	0.984	18.000	0.715	10.07	5.97	2.00	101.33
P1420_003_Ap_A_2_POS_56	0.027	0.003	5.835	-	10.199	0.019	0.007	0.001	0.003	0.018	0.021	0.074	1.716	0.049	0.235	18.200	0.824	10.37	5.84	2.00	92.97
P1420_003_Ap_A_2_POS_57	0.024	0.006	5.818	-	10.335	0.008	0.011	0.000	0.008	0.005	0.011	0.034	1.228	0.198	0.574	18.300	0.779	10.44	5.82	2.00	100.85
P1420_003_Ap_A_2_POS_58	0.003	0.000	5.996	-	9.974	0.007	0.004	0.000	0.005	0.009	0.001	0.003	1.611	0.025	0.364	18.000	0.839	10.01	6.00	2.00	93.65
P1420_003_Ap_A_2_POS_59	0.012	0.008	5.939	-	10.104	0.010	0.007	0.000	0.004	0.009	0.000	0.000	1.430	0.098	0.472	18.100	0.814	10.15	5.94	2.00	97.03
P1420_003_Ap_A_2_POS_61	0.028	0.002	5.984	-	9.918	0.030	0.003	0.001	0.001	0.004	0.012	0.031	0.958	0.005	1.037	18.000	0.801	10.03	5.98	2.00	100.86
P1420_003_Ap_A_2_POS_62	0.038	0.001	6.049	-	9.795	0.008	0.002	0.000	0.005	0.006	0.008	0.019	1.498	0.058	0.444	17.900	0.827	9.88	6.05	2.00	91.40
P1420_003_Ap_A_2_POS_63	0.030	0.001	5.897	-	10.075	0.018	0.016	0.000	0.004	0.008	0.020	0.058	1.373	0.197	0.431	18.100	0.773	10.23	5.90	2.00	91.17
P1420_003_Ap_A_2_POS_64	0.067	0.055	6.002	-	9.760	0.011	0.022	0.000	0.009	0.005	0.019	0.047	2.019	0.129	0.000	18.100	0.801	9.99	6.00	2.15	95.81
P1420_003_Ap_A_2_POS_65	0.031	0.003	5.986	-	9.921	0.031	0.005	0.000	0.001	0.003	0.009	0.026	0.958	0.005	1.036	18.000	0.798	10.03	5.99	2.00	100.74
JPCPC4, Imperial Fm. (siltstone) Imperial River section, ~0.66 %Ro, 65.116 N, 127.859 W																					
AFT Age-Grains																					
P1420_004_Ap_A_1_POS_0	0.020	0.073	6.056	-	9.659	0.007	0.020	0.000	0.057	0.002	0.005	0.015	2.036	0.082	0.000	18.000	0.816	9.86	6.06	2.12	94.62
P1420_004_Ap_A_1_POS_1	0.022	0.056	5.962	-	9.928	0.025	0.047	0.000	0.008	0.002	0.003	0.009	0.605	0.126	1.270	18.100	0.720	10.10	5.96	2.00	90.97
P1420_004_Ap_A_1_POS_2	0.018	0.010	6.012	-	9.904	0.008	0.008	0.000	0.012	0.003	0.002	0.008	1.299	0.051	0.651	18.000	0.813	9.97	6.01	2.00	92.97
P1420_004_Ap_A_1_POS_3	0.000	0.002	6.046	-	9.857	0.014	0.003	0.000	0.003	0.001	0.001	0.003	1.219	0.022	0.760	17.900	0.820	9.88	6.05	2.00	93.95
P1420_004_Ap_A_1_POS_4	0.000	0.000	5.853	-	10.277	0.011	0.015	0.000	0.001	0.025	0.002	0.013	1.661	0.014	0.326	18.200	0.826	10.35	5.85	2.00	81.83
P1420_004_Ap_A_1_POS_5	0.013	0.008	6.112	-	9.636	0.037	0.011	0.000	0.003	0.010	0.001	0.003	1.512	0.023	0.465	17.800	0.812	9.72	6.11	2.00	87.61
P1420_004_Ap_A_1_POS_6	0.038	0.022	5.896	-	10.056	0.011	0.003	0.000	0.012	0.003	0.021	0.067	2.063	0.012	0.000	18.200	0.848	10.23	5.90	2.07	94.39
P1420_004_Ap_A_1_POS_7	0.034	0.026	6.064	-	9.714	0.014	0.025	0.000	0.011	0.001	0.005	0.016	2.012	0.114	0.000	18.000	0.806	9.85	6.06	2.13	96.43
P1420_004_Ap_A_1_POS_8	0.022	0.001	5.970	-	9.914	0.031	0.026	0.000	0.004	0.016	0.011	0.033	1.347	0.081	0.572	18.000	0.772	10.06	5.97	2.00	88.61
P1420_004_Ap_A_1_POS_9	0.016	0.001	5.918	-	10.049	0.016	0.020	0.000	0.001	0.013	0.014	0.047	1.973	0.050	0.000	18.100	0.824	10.18	5.92	2.02	95.91
P1420_004_Ap_A_1_POS_10	0.079	0.014	5.965	-	9.886	0.016	0.011	0.001	0.011	0.003	0.015	0.054	0.605	0.194	1.202	18.100	0.755	10.09	5.97	2.00	101.94
P1420_004_Ap_A_1_POS_11	0.017	0.022	6.019	-	9.817	0.017	0.027	0.000	0.004	0.010	0.006	0.022	1.444	0.081	0.475	18.000	0.785	9.94	6.02	2.00	94.72
P1420_004_Ap_A_1_POS_12	0.017	0.002	6.115	-	9.623	0.012	0.007	0.000	0.001	0.022	0.003	0.015	1.639	0.038	0.323	17.800	0.831	9.70	6.11	2.00	88.56
P1420_004_Ap_A_1_POS_13	0.078	0.053	5.929	-	9.826	0.016	0.025	0.000	0.146	0.002	0.013	0.033	0.754	0.221	1.025	18.100	0.697	10.19	5.93	2.00	103.15
P1420_004_Ap_A_1_POS_14	0.007	0.000	6.035	-	9.886	0.003	0.006	0.000	0.006	0.001	0.001	0.003	1.936	0.000	0.064	17.900	0.856	9.91	6.03	2.00	92.04
P1420_004_Ap_A_1_POS_15	0.011	0.002	6.038	-	9.825	0.007	0.007	0.000	0.005	0.001	0.011	0.024	1.085	0.060	0.855	17.900	0.802	9.89	6.04	2.00	99.51
P1420_004_Ap_A_1_POS_16	0.002	0.000	5.894	-	10.233	0.013	0.003	0.000	0.002	0.004	0.001	0.004	1.886	0.000	0.114	18.200	0.853	10.26	5.89	2.00	99.64
P1420_004_Ap_A_1_POS_17	0.018	0.001	5.878	-	10.161	0.022	0.011	0.000	0.001	0.015	0.013	0.039	1.761	0.060	0.179	18.200	0.822	10.28	5.88	2.00	93.08

A2Z Sample No.	Na (apfu)	Mg (apfu)	P (apfu)	S (apfu)	Ca (apfu)	Mn (apfu)	Fe (apfu)	As (apfu)	Sr (apfu)	Y (apfu)	La (apfu)	Ce (apfu)	F (apfu)	Cl (apfu)	OH (apfu)	TOTAL (apfu)	r_{mr0}	Ca SITE 10	P SITE 6	F+Cl+OH 2	TOTAL WT% OX
P1420_004_Ap_A_1_POS_18	0.020	0.020	6.151	-	9.464	0.012	0.020	0.000	0.069	0.002	0.005	0.011	1.940	0.081	0.000	17.800	0.817	9.62	6.15	2.02	95.93
P1420_004_Ap_A_1_POS_20	0.034	0.033	6.026	-	9.749	0.008	0.029	0.000	0.076	0.002	0.005	0.009	1.677	0.043	0.280	18.000	0.800	9.94	6.03	2.00	94.88
P1420_004_Ap_A_1_POS_22	0.057	0.020	5.975	-	9.903	0.015	0.028	0.000	0.014	0.003	0.011	0.021	0.797	0.177	1.026	18.000	0.725	10.07	5.98	2.00	101.30
P1420_004_Ap_A_1_POS_24	0.036	0.013	5.909	-	10.071	0.021	0.018	0.001	0.003	0.007	0.016	0.032	1.147	0.164	0.688	18.100	0.761	10.22	5.91	2.00	86.78
P1420_004_Ap_A_1_POS_25	0.021	0.060	5.990	-	9.842	0.014	0.059	0.000	0.006	0.006	0.004	0.012	1.223	0.029	0.749	18.000	0.731	10.02	5.99	2.00	96.71
P1420_004_Ap_A_1_POS_8	0.022	0.045	6.023	-	9.785	0.018	0.034	0.000	0.008	0.008	0.007	0.014	1.434	0.048	0.518	18.000	0.777	9.94	6.02	2.00	99.29
P1420_004_Ap_A_1_POS_29	0.012	0.001	6.093	-	9.715	0.011	0.014	0.000	0.004	0.006	0.002	0.004	1.231	0.003	0.766	17.900	0.810	9.77	6.09	2.00	88.95
P1420_004_Ap_A_1_POS_30	0.019	0.075	5.944	-	9.953	0.006	0.036	0.000	0.016	0.003	0.008	0.019	1.981	0.042	0.000	18.100	0.807	10.13	5.94	2.02	97.72
P1420_004_Ap_A_1_POS_31	0.081	0.033	5.971	-	9.896	0.002	0.015	0.000	0.055	0.002	0.006	0.013	0.621	0.017	1.362	18.100	0.806	10.10	5.97	2.00	101.36
P1420_004_Ap_A_1_POS_32	0.004	0.004	5.991	-	9.962	0.013	0.013	0.000	0.004	0.002	0.005	0.010	0.853	0.126	1.021	18.000	0.772	10.02	5.99	2.00	91.33
P1420_004_Ap_A_1_POS_33	0.016	0.000	5.994	-	9.955	0.018	0.005	0.000	0.002	0.004	0.004	0.010	1.719	0.008	0.273	18.000	0.839	10.01	5.99	2.00	91.19
P1420_004_Ap_A_1_POS_34	0.014	0.004	5.943	-	10.041	0.004	0.007	0.000	0.056	0.003	0.004	0.009	1.201	0.163	0.636	18.100	0.791	10.14	5.94	2.00	89.75
P1420_004_Ap_A_1_POS_35	0.034	0.081	5.967	-	9.881	0.017	0.039	0.000	0.009	0.004	0.005	0.016	1.112	0.126	0.762	18.100	0.731	10.09	5.97	2.00	97.04
P1420_004_Ap_A_1_POS_36	0.000	0.063	6.108	-	9.577	0.008	0.053	0.000	0.006	0.006	0.003	0.007	1.537	0.052	0.411	17.800	0.763	9.72	6.11	2.00	96.48
P1420_004_Ap_A_1_POS_38	0.002	0.039	5.985	-	9.919	0.009	0.046	0.000	0.004	0.004	0.003	0.007	1.049	0.056	0.895	18.000	0.743	10.03	5.99	2.00	100.57
P1420_004_Ap_A_1_POS_39	0.016	0.017	6.036	-	9.804	0.015	0.019	0.001	0.010	0.003	0.006	0.014	2.096	0.014	0.000	18.100	0.835	9.90	6.04	2.11	94.11
AFT Length-Grains																					
P1420_004_Ap_A_2_POS_0	0.050	0.055	6.054	-	9.657	0.010	0.024	0.000	0.049	0.003	0.008	0.019	2.036	0.082	0.000	18.000	0.809	9.87	6.05	2.12	94.70
P1420_004_Ap_A_2_POS_1	0.042	0.055	5.983	-	9.780	0.012	0.019	0.000	0.028	0.006	0.023	0.058	2.171	0.030	0.000	18.200	0.824	10.02	5.98	2.20	91.04
P1420_004_Ap_A_2_POS_2	0.014	0.000	6.045	-	9.855	0.009	0.005	0.001	0.004	0.001	0.001	0.003	1.218	0.022	0.760	17.900	0.818	9.89	6.05	2.00	93.98
P1420_004_Ap_A_2_POS_3	0.012	0.004	5.979	-	9.910	0.009	0.068	0.000	0.002	0.022	0.002	0.011	1.340	0.011	0.649	18.000	0.736	10.04	5.98	2.00	100.65
P1420_004_Ap_A_2_POS_4	0.030	0.007	5.901	-	10.064	0.014	0.003	0.000	0.015	0.003	0.022	0.063	2.064	0.012	0.000	18.200	0.849	10.22	5.90	2.08	94.29
P1420_004_Ap_A_2_POS_5	0.039	0.021	6.060	-	9.708	0.016	0.027	0.000	0.019	0.001	0.005	0.020	2.011	0.114	0.000	18.000	0.802	9.86	6.06	2.12	96.62
P1420_004_Ap_A_2_POS_6	0.000	0.000	5.955	-	10.113	0.000	0.000	0.000	0.000	0.000	0.000	0.000	1.985	0.051	0.000	18.100	0.859	10.11	5.95	2.04	94.53
P1420_004_Ap_A_2_POS_7	0.086	0.004	5.968	-	9.891	0.016	0.010	0.000	0.010	0.003	0.019	0.049	0.605	0.194	1.201	18.100	0.758	10.09	5.97	2.00	101.87
P1420_004_Ap_A_2_POS_10	0.019	0.044	5.965	-	9.933	0.026	0.043	0.000	0.009	0.003	0.003	0.009	0.605	0.126	1.269	18.100	0.727	10.09	5.97	2.00	90.93
P1420_004_Ap_A_2_POS_12	0.013	0.003	5.967	-	9.989	0.036	0.011	0.000	0.002	0.017	0.001	0.005	1.860	0.002	0.138	18.000	0.831	10.08	5.97	2.00	94.10
P1420_004_Ap_A_2_POS_13	0.002	0.000	6.034	-	9.885	0.004	0.004	0.001	0.007	0.002	0.002	0.004	1.936	0.000	0.065	17.900	0.857	9.91	6.03	2.00	92.08
P1420_004_Ap_A_2_POS_14	0.010	0.005	6.116	-	9.625	0.012	0.007	0.000	0.002	0.021	0.003	0.014	1.639	0.038	0.323	17.800	0.831	9.70	6.12	2.00	88.52
P1420_004_Ap_A_2_POS_15	0.087	0.018	5.946	-	9.855	0.003	0.006	0.000	0.113	0.005	0.017	0.043	1.581	0.015	0.404	18.100	0.822	10.15	5.95	2.00	102.02
P1420_004_Ap_A_2_POS_16	0.028	0.032	6.014	-	9.809	0.022	0.029	0.000	0.004	0.012	0.006	0.018	1.443	0.081	0.477	18.000	0.777	9.96	6.01	2.00	94.82
P1420_004_Ap_A_2_POS_17	0.085	0.042	5.816	-	10.138	0.017	0.022	0.000	0.074	0.004	0.024	0.055	1.585	0.056	0.359	18.300	0.788	10.46	5.82	2.00	74.03
P1420_004_Ap_A_2_POS_18	0.018	0.014	5.963	-	9.902	0.034	0.026	0.000	0.006	0.016	0.014	0.039	1.346	0.081	0.573	18.000	0.770	10.07	5.96	2.00	88.82
P1420_004_Ap_A_2_POS_19	0.029	0.014	5.975	-	9.902	0.031	0.013	0.000	0.006	0.005	0.015	0.034	1.233	0.175	0.593	18.000	0.766	10.05	5.97	2.00	101.17
P1420_004_Ap_A_2_POS_21	0.014	0.000	5.949	-	10.070	0.005	0.003	0.000	0.002	0.007	0.005	0.015	1.847	0.008	0.145	18.100	0.852	10.12	5.95	2.00	94.61
P1420_004_Ap_A_2_POS_23	0.000	0.000	5.912	-	10.220	0.000	0.000	0.000	0.000	0.000	0.000	0.000	1.772	0.060	0.168	18.100	0.850	10.22	5.91	2.00	91.86
P1420_004_Ap_A_2_POS_24	0.000	0.001	5.921	-	10.163	0.004	0.001	0.000	0.004	0.003	0.004	0.010	1.508	0.026	0.466	18.100	0.839	10.19	5.92	2.00	92.52
P1420_004_Ap_A_2_POS_25	0.063	0.057	5.935	-	9.836	0.018	0.017	0.000	0.134	0.002	0.012	0.032	0.755	0.221	1.024	18.100	0.713	10.17	5.93	2.00	102.91
P1420_004_Ap_A_2_POS_26	0.000	0.000	6.013	-	9.966	0.000	0.000	0.000	0.000	0.000	0.000	0.000	1.080	0.060	0.860	18.000	0.818	9.97	6.01	2.00	99.76
P1420_004_Ap_A_2_POS_31	0.063	0.102	6.067	-	9.561	0.018	0.031	0.000	0.009	0.008	0.013	0.032	1.622	0.087	0.291	17.900	0.775	9.84	6.07	2.00	85.35
P1420_004_Ap_A_2_POS_32	0.010	0.059	5.997	-	9.852	0.015	0.033	0.000	0.006	0.007	0.005	0.013	1.224	0.029	0.748	18.000	0.772	10.00	6.00	2.00	96.55
P1420_004_Ap_A_2_POS_33	0.075	0.055	5.863	-	10.093	0.032	0.045	0.000	0.013	0.004	0.013	0.029	0.895	0.381	0.724	18.200	0.616	10.36	5.86	2.00	88.22
P1420_004_Ap_A_2_POS_34	0.008	0.002	5.985	-	10.009	0.006	0.005	0.000	0.006	0.001	0.000	0.002	1.307	0.014	0.679	18.000	0.825	10.04	5.99	2.00	91.61
P1420_004_Ap_A_2_POS_35	0.011	0.001	5.994	-	9.955	0.019	0.004	0.000	0.004	0.004	0.004	0.011	1.719	0.008	0.273	18.000	0.841	10.01	5.99	2.00	91.20
P1420_004_Ap_A_2_POS_37	0.017	0.040	5.980	-	9.902	0.024	0.027	0.000	0.011	0.004	0.006	0.017	1.114	0.127	0.759	18.000	0.752	10.05	5.98	2.00	96.82
P1420_004_Ap_A_2_POS_38	0.074	0.001	5.884	-	10.131	0.034	0.014	0.001	0.002	0.031	0.003	0.011	2.141	0.000	0.000	18.300	0.831	10.30	5.89	2.14	96.41
P1420_004_Ap_A_2_POS_39	0.010	0.000	5.900	-	10.222	0.009	0.002	0.000	0.004	0.001	0.001	0.004	1.709	0.014	0.277	18.200	0.846	10.25	5.90	2.00	96.61
P1420_004_Ap_A_2_POS_40	0.044	0.037	6.013	-	9.792	0.035	0.027	0.000	0.007	0.002	0.009	0.022	1.019	0.214	0.767	18.000	0.718	9.97	6.01	2.00	91.21
P1420_004_Ap_A_2_POS_41	0.013	0.001	5.924	-	10.143	0.010	0.004	0.000	0.003	0.002	0.004	0.010	1.789	0.038	0.174	18.100	0.843	10.19	5.92	2.00	93.10
P1420_004_Ap_A_2_POS_42	0.007	0.008	5.952	-	10.045	0.009	0.019	0.000	0.005	0.003	0.004	0.013	1.506	0.060	0.434	18.100	0.809	10.11	5.95	2.00	92.51
P1420_004_Ap_A_2_POS_43	0.005	0.000	5.982	-	10.020	0.006	0.003	0.000	0.004	0.001	0.002	0.004	1.920	0.003	0.077	18.000	0.857	10.04	5.98	2.00	98.11
P1420_004_Ap_A_2_POS_44	0.031	0.006	5.969	-	9.968	0.013	0.008	0.000	0.007	0.002	0.013	0.024	1.354	0.186	0.461	18.000	0.789	10.07	5.97	2.00	95.60
P1420_004_Ap_A_2_POS_45	0.013	0.016	6.040	-	9.810	0.017	0.016	0.000	0.013	0.002	0.004	0.009	2.097	0.014	0.000	18.000	0.837	9.90	6.04	2.11	94.00
P1420_004_Ap_A_2_POS_46	0.010	0.012	6.039	-	9.808	0.017	0.016	0.001	0.011	0.003	0.005	0.013	2.097	0.014	0.000	18.000	0.837	9.89	6.04	2.11	94.05

A2Z Sample No.	Na (apfu)	Mg (apfu)	P (apfu)	S (apfu)	Ca (apfu)	Mn (apfu)	Fe (apfu)	As (apfu)	Sr (apfu)	Y (apfu)	La (apfu)	Ce (apfu)	F (apfu)	Cl (apfu)	OH (apfu)	TOTAL (apfu)	r_{mr0}	Ca SITE 10	P SITE 6	F+Cl+OH 2	TOTAL WT% OX
P1420_004_Ap_A_2_POS_48	0.038	0.000	6.044	-	9.805	0.006	0.005	0.000	0.005	0.018	0.003	0.014	1.408	0.068	0.524	17.900	0.819	9.89	6.04	2.00	89.76
P1420_004_Ap_A_2_POS_49	0.000	0.004	5.887	-	10.208	0.011	0.010	0.008	0.004	0.002	0.006	0.009	1.770	0.078	0.152	18.100	0.829	10.25	5.90	2.00	97.98
P1420_004_Ap_A_2_POS_50	0.000	0.000	6.038	-	9.829	0.000	0.026	0.000	0.011	0.000	0.002	0.023	0.835	0.203	0.962	17.900	0.740	9.89	6.04	2.00	89.96
P1420_004_Ap_A_2_POS_51	0.046	0.000	5.860	-	10.223	0.012	0.006	0.001	0.040	0.002	0.009	0.019	2.016	0.030	0.000	18.300	0.844	10.36	5.86	2.05	91.14
10FNARL008, Imperial Fm. (lithic arenite) Carcajou River section, ~0.74 %Ro, 64.752 N, 126.778 W																					
AFT Age-Grains																					
P1392_015_Ap_A_1_POS_0	0.021	0.006	5.985	0.015	9.921	0.010	0.005	0.000	0.009	0.001	0.007	0.014	1.856	0.062	-	17.912	0.843	9.99	6.00	1.92	96.51
P1392_015_Ap_A_1_POS_1	0.012	0.014	5.967	0.033	9.892	0.007	0.041	0.000	0.003	0.005	0.001	0.006	1.853	0.147	-	17.982	0.783	9.98	6.00	2.00	96.25
P1392_015_Ap_A_1_POS_2	0.005	0.031	5.964	0.036	9.780	0.006	0.130	0.000	0.004	0.005	0.005	0.016	1.857	0.143	-	17.982	0.609	9.98	6.00	2.00	96.25
P1392_015_Ap_A_1_POS_3	0.059	0.142	5.955	0.045	9.691	0.007	0.040	0.000	0.019	0.003	0.008	0.020	1.829	0.171	-	17.987	0.763	9.99	6.00	2.00	96.44
P1392_015_Ap_A_1_POS_4	0.049	0.094	5.966	0.034	9.785	0.008	0.035	0.000	0.019	0.001	0.001	0.004	1.820	0.162	-	17.979	0.779	10.00	6.00	1.98	96.63
P1392_015_Ap_A_1_POS_5	0.007	0.005	5.949	0.051	9.941	0.006	0.006	0.000	0.002	0.003	0.006	0.015	1.972	0.028	-	17.991	0.851	9.99	6.00	2.00	96.22
P1392_015_Ap_A_1_POS_6	0.110	0.091	5.951	0.049	9.609	0.030	0.045	0.000	0.009	0.006	0.018	0.051	1.567	0.433	-	17.970	0.653	9.97	6.00	2.00	96.57
P1392_015_Ap_A_1_POS_7	0.018	0.002	5.978	0.021	9.942	0.008	0.005	0.000	0.002	0.008	0.000	0.002	1.886	0.020	-	17.893	0.853	9.99	6.00	1.91	96.34
P1392_015_Ap_A_1_POS_8	0.086	0.089	5.965	0.035	9.713	0.012	0.039	0.000	0.018	0.002	0.007	0.020	1.803	0.180	-	17.970	0.762	9.99	6.00	1.98	96.49
P1392_015_Ap_A_1_POS_9	0.042	0.005	5.971	0.029	9.842	0.012	0.014	0.000	0.005	0.009	0.012	0.034	1.745	0.181	-	17.899	0.805	9.97	6.00	1.93	96.40
P1392_015_Ap_A_1_POS_10	0.002	0.001	5.974	0.026	9.955	0.008	0.003	0.000	0.006	0.003	0.002	0.008	1.905	0.037	-	17.930	0.853	9.99	6.00	1.94	96.34
P1392_015_Ap_A_1_POS_11	0.011	0.088	5.965	0.035	9.797	0.011	0.057	0.000	0.006	0.005	0.003	0.010	1.830	0.096	-	17.913	0.764	9.99	6.00	1.93	96.45
P1392_015_Ap_A_1_POS_12	0.045	0.056	5.965	0.032	9.744	0.010	0.055	0.004	0.009	0.006	0.013	0.036	1.406	0.594	-	17.973	0.596	9.98	6.00	2.00	96.91
P1392_015_Ap_A_1_POS_15	0.051	0.144	5.970	0.030	9.671	0.009	0.034	0.000	0.017	0.004	0.011	0.033	1.936	0.064	-	17.975	0.793	9.98	6.00	2.00	96.05
P1392_015_Ap_A_1_POS_16	0.000	0.002	5.982	0.018	9.988	0.004	0.001	0.000	0.002	0.001	0.001	0.001	1.864	0.028	-	17.891	0.859	10.00	6.00	1.89	96.59
P1392_015_Ap_A_1_POS_17	0.026	0.134	5.983	0.017	9.723	0.006	0.026	0.000	0.039	0.002	0.008	0.021	1.825	0.157	-	17.967	0.789	9.99	6.00	1.98	96.42
P1392_015_Ap_A_1_POS_18	0.019	0.003	5.972	0.028	9.897	0.008	0.004	0.000	0.004	0.003	0.013	0.035	1.954	0.046	-	17.984	0.847	9.98	6.00	2.00	96.15
P1392_015_Ap_A_1_POS_19	0.017	0.016	5.986	0.014	9.873	0.008	0.024	0.000	0.007	0.004	0.009	0.023	1.640	0.360	-	17.983	0.754	9.98	6.00	2.00	96.66
P1392_015_Ap_A_1_POS_20	0.050	0.117	5.968	0.032	9.628	0.014	0.116	0.000	0.009	0.003	0.012	0.030	1.592	0.408	-	17.980	0.422	9.98	6.00	2.00	96.71
P1392_015_Ap_A_1_POS_21	0.023	0.011	5.980	0.019	9.887	0.015	0.012	0.000	0.010	0.003	0.007	0.020	1.796	0.175	-	17.958	0.810	9.99	6.00	1.97	96.51
P1392_015_Ap_A_1_POS_22	0.000	0.007	5.972	0.028	9.981	0.003	0.006	0.000	0.002	0.000	0.000	0.000	1.908	0.029	-	17.936	0.854	10.00	6.00	1.94	96.52
P1392_015_Ap_A_1_POS_23	0.012	0.000	5.959	0.041	9.962	0.006	0.001	0.000	0.001	0.011	0.000	0.000	1.939	0.027	-	17.959	0.857	9.99	6.00	1.97	96.36
P1392_015_Ap_A_1_POS_24	0.071	0.002	5.978	0.022	9.757	0.011	0.005	0.000	0.005	0.034	0.012	0.041	1.984	0.011	-	17.933	0.842	9.94	6.00	2.00	95.32
P1392_015_Ap_A_1_POS_25	0.059	0.075	5.968	0.032	9.614	0.006	0.019	0.000	0.141	0.002	0.016	0.042	1.946	0.054	-	17.974	0.811	9.97	6.00	2.00	96.01
P1392_015_Ap_A_1_POS_26	0.032	0.009	5.960	0.040	9.863	0.010	0.009	0.000	0.004	0.008	0.011	0.030	1.792	0.208	-	17.975	0.807	9.98	6.00	2.00	96.27
P1392_015_Ap_A_1_POS_27	0.007	0.002	5.976	0.024	9.937	0.009	0.003	0.000	0.007	0.005	0.003	0.011	1.897	0.054	-	17.935	0.848	9.98	6.00	1.95	96.27
AFT Length-Grains																					
P1392_015_Ap_A_2_POS_0	0.027	0.018	5.983	0.017	9.821	0.009	0.041	0.000	0.006	0.009	0.011	0.033	1.672	0.209	-	17.856	0.762	9.97	6.00	1.88	96.57
P1392_015_Ap_A_2_POS_1	0.004	0.002	5.974	0.026	9.851	0.007	0.100	0.000	0.004	0.003	0.005	0.014	1.895	0.105	-	17.989	0.700	9.99	6.00	2.00	96.35
P1392_015_Ap_A_2_POS_2	0.050	0.171	5.976	0.024	9.674	0.006	0.036	0.000	0.020	0.002	0.008	0.021	1.795	0.174	-	17.956	0.768	9.99	6.00	1.97	96.52
P1392_015_Ap_A_2_POS_3	0.004	0.008	5.988	0.012	9.943	0.006	0.005	0.000	0.003	0.002	0.006	0.014	1.916	0.060	-	17.966	0.847	9.99	6.00	1.98	96.34
P1392_015_Ap_A_2_POS_5	0.037	0.003	5.978	0.021	9.847	0.012	0.012	0.000	0.004	0.008	0.013	0.037	1.787	0.202	-	17.962	0.802	9.97	6.00	1.99	96.28
P1392_015_Ap_A_2_POS_6	0.012	0.005	5.958	0.041	9.927	0.010	0.015	0.001	0.006	0.003	0.002	0.008	1.679	0.321	-	17.989	0.779	9.99	6.00	2.00	96.71
P1392_015_Ap_A_2_POS_7	0.050	0.017	5.981	0.019	9.809	0.017	0.019	0.000	0.011	0.002	0.015	0.041	1.589	0.411	-	17.981	0.738	9.98	6.00	2.00	96.78
P1392_015_Ap_A_2_POS_8	0.019	0.007	5.982	0.018	9.887	0.015	0.012	0.000	0.011	0.003	0.008	0.025	1.766	0.149	-	17.901	0.815	9.99	6.00	1.91	96.57
P1392_015_Ap_A_2_POS_9	0.058	0.063	5.978	0.022	9.742	0.018	0.055	0.000	0.004	0.003	0.011	0.030	1.640	0.274	-	17.897	0.711	9.98	6.00	1.91	96.74
P1392_015_Ap_A_2_POS_10	0.030	0.011	5.980	0.020	9.899	0.020	0.007	0.000	0.002	0.001	0.011	0.014	1.831	0.027	-	17.854	0.843	10.00	6.00	1.86	96.58
P1392_015_Ap_A_2_POS_11	0.010	0.019	5.982	0.018	9.873	0.010	0.042	0.000	0.006	0.005	0.003	0.015	1.849	0.043	-	17.876	0.802	9.98	6.00	1.89	96.36
P1392_015_Ap_A_2_POS_12	0.016	0.003	5.976	0.024	9.919	0.007	0.007	0.000	0.001	0.016	0.001	0.007	1.816	0.044	-	17.837	0.845	9.98	6.00	1.86	96.34
Husky7, Imperial Fm. (fine grain sandstone) Redstone River section, ~1.67 %Ro, 63.916 N, 125.198W																					
AFT Age-Grains																					
P943_07_AP_A_1_POS_1	0.010	0.003	5.884	-0.001	10.167	0.012	0.011	-	0.007	0.003	-0.002	-0.003	1.775	0.040	0.185	17.905	0.834	10.21	5.88	2	99.235
P943_07_AP_A_1_POS_2	0.007	0.005	5.777	0.009	10.159	0.015	0.006	-	-0.005	0.004	0.031	0.050	1.513	0.049	0.438	17.620	0.820	10.27	5.79	2	94.863
P943_07_AP_A_1_POS_3	0.078	0.003	5.515	0.118	10.526	0.002	0.000	-	0.002	0.002	0.006	0.006	1.433	0.036	0.532	17.725	0.831	10.62	5.63	2	89.022
P943_07_AP_A_1_POS_4	0.000	0.008	5.783	0.001	10.086	0.006	0.018	-	0.004	0.006	0.005	0.007	1.212	0.009	0.780	17.145	0.804	10.14	5.78	2	99.453
P943_07_AP_A_1_POS_5	0.010	0.000	5.862	0.013	10.060	0.010	0.000	-	-0.001	0.016	0.010	0.015	1.630	0.023	0.347	17.647	0.841	10.12	5.87	2	98.442
P943_07_AP_A_1_POS_6	0.067	0.014	5.619	0.069	10.264	0.020	0.018	-	0.002	0.005	0.005	0.022	1.135	0.172	0.694	17.411	0.759	10.42	5.69	2	93.647
P943_07_AP_A_1_POS_7	0.028	0.003	5.930	-0.001	10.038	0.008	0.010	-	0.000	0.016	0.000	0.030	1.480	0.446	0.074	17.988	0.751	10.13	5.93	2	95.623

A2Z Sample No.	Na (apfu)	Mg (apfu)	P (apfu)	S (apfu)	Ca (apfu)	Mn (apfu)	Fe (apfu)	As (apfu)	Sr (apfu)	Y (apfu)	La (apfu)	Ce (apfu)	F (apfu)	Cl (apfu)	OH (apfu)	TOTAL (apfu)	r_{mr0}	Ca SITE 10	P SITE 6	F+Cl+OH 2	TOTAL WT% OX
P943_07_AP_A_1_POS_8	0.066	0.099	5.588	0.085	10.095	0.005	0.035	-	0.084	0.002	-0.009	0.002	1.070	0.067	0.863	17.188	0.747	10.38	5.67	2	93.917
P943_07_AP_A_1_POS_9	0.013	0.000	5.846	0.014	10.158	0.007	-0.001	-	0.004	0.004	0.011	0.019	1.745	0.017	0.238	17.836	0.850	10.21	5.86	2	99.945
P943_07_AP_A_1_POS_10	0.013	0.003	5.901	0.017	9.960	0.019	0.011	-	0.007	0.002	0.009	0.006	1.508	0.159	0.334	17.613	0.798	10.03	5.92	2	98.875
P943_07_AP_A_1_POS_11	0.003	0.003	5.712	0.015	9.759	0.006	0.044	-	0.001	0.001	0.004	0.009	0.277	0.043	1.681	15.876	0.789	9.83	5.73	2	98.115
P943_07_AP_A_1_POS_12	0.020	0.000	5.866	0.041	9.942	0.009	0.006	-	0.005	0.004	0.002	0.006	1.514	0.034	0.450	17.448	0.829	9.99	5.91	2	99.019
P943_07_AP_A_1_POS_13	0.013	0.049	5.854	0.005	9.984	0.006	0.029	-	0.056	0.002	0.011	0.008	1.326	0.300	0.374	17.643	0.736	10.16	5.86	2	98.693
P943_07_AP_A_1_POS_14	0.003	0.031	5.826	-0.001	10.004	0.004	0.019	-	0.031	0.006	0.023	0.016	1.355	0.083	0.562	17.399	0.795	10.14	5.83	2	97.019
P943_07_AP_A_1_POS_15	-0.007	0.000	5.945	0.000	10.083	0.001	0.000	-	0.006	0.001	-0.004	-0.002	1.880	0.003	0.117	17.907	0.861	10.08	5.94	2	98.95
P943_07_AP_A_1_POS_16	-0.007	0.005	5.928	0.000	10.104	0.003	0.010	-	0.008	0.006	0.001	0.001	2.081	0.006	0.000	18.145	0.854	10.13	5.93	2.09	100.199
P943_07_AP_A_1_POS_17	0.020	0.000	5.948	0.001	10.070	0.004	0.004	-	0.005	0.013	-0.002	-0.007	2.051	0.003	0.000	18.110	0.859	10.11	5.95	2.05	99.395
P943_07_AP_A_1_POS_18	0.007	0.003	5.908	0.023	10.043	0.014	0.004	-	0.006	0.005	0.018	0.004	1.885	0.020	0.094	17.940	0.847	10.1	5.93	2	99.629
P943_07_AP_A_1_POS_19	0.007	0.000	5.952	0.003	10.021	0.009	0.006	-	0.003	0.002	-0.004	-0.006	1.828	0.003	0.168	17.822	0.850	10.04	5.95	2	99.819
P943_07_AP_A_1_POS_20	0.016	0.002	5.989	0.011	9.747	0.012	0.001	-	0.007	0.015	-0.001	0.005	1.612	0.008	0.379	17.425	0.840	9.8	6	2	102.374
P943_07_AP_A_1_POS_21	0.028	0.005	5.706	0.016	10.217	0.003	0.002	-	0.009	0.002	-0.003	0.026	1.061	0.139	0.800	17.210	0.797	10.29	5.72	2	94.729
P943_07_AP_A_1_POS_22	0.020	0.003	5.894	0.000	10.099	0.007	0.009	-	0.004	0.006	0.022	0.034	1.853	0.064	0.083	18.014	0.835	10.2	5.89	2	98.573
P943_07_AP_A_1_POS_23	0.088	0.037	5.790	0.082	9.996	0.003	0.023	-	0.106	0.005	0.017	0.017	2.004	0.024	0.000	18.191	0.819	10.29	5.87	2.03	97.328
P943_07_AP_A_1_POS_24	0.106	0.010	5.749	0.133	9.946	0.012	0.019	-	0.028	0.004	0.013	0.022	1.692	0.104	0.204	17.837	0.800	10.16	5.88	2	98.999
P943_07_AP_A_1_POS_25	0.013	0.005	5.726	0.001	9.784	0.010	0.003	-	0.003	0.006	0.019	0.023	0.326	0.080	1.593	16.000	0.823	9.87	5.73	2	98.334
P943_07_AP_A_1_POS_26	0.010	0.003	5.994	0.000	9.929	0.003	0.003	-	0.002	0.007	0.009	0.011	2.045	0.017	0.000	18.032	0.858	9.98	5.99	2.06	99.84
P943_07_AP_A_1_POS_27	0.016	0.000	5.914	0.026	10.056	0.006	0.001	-	0.013	0.002	0.016	0.006	1.963	0.006	0.031	18.025	0.858	10.12	5.94	2	100.614
P943_07_AP_A_1_POS_28	0.007	0.000	5.836	0.003	10.143	0.010	0.000	-	0.002	0.021	0.001	0.003	2.411	0.003	0.000	18.439	0.861	10.19	5.84	2.41	98.042
P943_07_AP_A_1_POS_29	0.007	0.000	5.882	0.000	10.024	0.003	0.004	-	0.009	0.004	-0.009	0.009	1.460	0.046	0.495	17.437	0.830	10.05	5.88	2	99.561
P943_07_AP_A_1_POS_30	0.016	0.000	5.902	-0.001	10.059	0.007	0.007	-	0.003	0.005	0.010	0.024	1.711	0.078	0.211	17.821	0.830	10.13	5.9	2	99.67
P943_07_AP_A_1_POS_31	-0.003	0.003	5.905	0.000	10.124	-0.001	0.017	-	0.010	0.000	0.002	-0.001	2.165	0.003	0.000	18.224	0.848	10.15	5.91	2.17	98.769
P943_07_AP_A_1_POS_32	0.020	-0.003	5.971	0.001	9.938	0.009	0.007	-	0.004	0.021	0.000	0.003	2.135	0.003	0.000	18.109	0.853	10	5.97	2.14	98.796
P943_07_AP_A_1_POS_33	0.030	0.033	5.819	0.027	9.897	0.014	0.030	-	0.016	0.004	0.022	0.033	1.125	0.317	0.558	17.367	0.710	10.08	5.85	2	99.534
P943_07_AP_A_1_POS_34	0.010	0.003	5.920	0.009	10.116	0.006	0.000	-	0.003	0.002	0.010	0.002	1.958	0.003	0.040	18.040	0.861	10.15	5.93	2	98.398
AFT Length-Grains																					
P943_07_AP_A_2_POS_1	0.007	0.003	5.886	0.013	9.978	0.011	0.007	-	0.001	0.004	0.005	0.009	1.538	0.026	0.436	17.486	0.829	10.02	5.9	2	100.028
P943_07_AP_A_2_POS_2	0.040	-0.003	5.877	0.030	10.041	0.004	0.012	-	0.003	0.001	0.012	0.001	2.223	0.015	0.000	18.257	0.847	10.11	5.91	2.24	97.083
P943_07_AP_A_2_POS_3	0.036	0.000	5.875	0.026	9.996	0.012	0.039	-	0.000	0.005	0.019	0.024	1.613	0.188	0.200	17.831	0.761	10.13	5.9	2	99.346
P943_07_AP_A_2_POS_4	0.045	0.012	5.797	0.083	9.718	0.004	0.018	-	0.043	0.002	0.007	0.015	1.085	0.107	0.807	16.937	0.776	9.86	5.88	2	100.833
P943_07_AP_A_2_POS_5	0.022	0.002	5.884	0.043	9.798	0.008	0.001	-	0.001	0.003	-0.004	0.009	1.243	0.099	0.658	17.108	0.812	9.84	5.93	2	103.076
P943_07_AP_A_2_POS_6	0.186	0.090	5.704	0.092	9.746	0.004	0.032	-	0.051	0.001	0.005	0.003	1.076	0.063	0.862	17.055	0.744	10.12	5.8	2	99.454
P943_07_AP_A_2_POS_8	0.106	0.013	5.776	0.131	9.872	0.007	0.013	-	0.040	0.003	0.015	0.024	2.132	0.081	0.000	18.212	0.823	10.09	5.91	2.21	98.808
P943_07_AP_A_2_POS_9	0.010	0.008	5.829	0.003	9.387	0.003	0.038	-	0.021	0.001	-0.002	0.001	0.058	0.023	1.919	15.379	0.813	9.47	5.83	2	97.446
P943_07_AP_A_2_POS_10	0.096	0.005	5.749	0.108	9.828	0.003	0.004	-	0.058	0.002	0.021	0.017	1.365	0.046	0.590	17.303	0.814	10.03	5.86	2	99.055
P943_07_AP_A_2_POS_11	0.037	0.003	5.741	0.093	10.065	0.003	0.004	-	0.067	0.006	0.023	0.058	1.828	0.015	0.158	17.941	0.841	10.26	5.83	2	97.716
P943_07_AP_A_2_POS_12	0.017	0.080	5.020	0.000	10.409	0.007	0.065	-	-0.006	0.003	0.004	0.012	1.980	0.022	0.000	17.613	0.774	10.59	5.02	2	78.225
P943_07_AP_A_2_POS_13	0.013	0.062	5.622	0.000	9.606	0.006	0.050	-	-0.005	0.003	0.003	0.009	4.379	0.017	0.000	19.764	0.798	9.75	5.62	4.4	99.745
P943_07_AP_A_2_POS_14	0.034	0.003	5.826	0.034	9.999	0.012	0.007	-	0.006	0.002	0.017	0.029	1.426	0.139	0.435	17.534	0.802	10.11	5.86	2	96.653
P943_07_AP_A_2_POS_16	0.020	0.010	5.775	-0.001	9.866	0.004	0.057	-	0.002	0.003	-0.004	-0.004	0.707	0.041	1.253	16.474	0.745	9.95	5.77	2	97.5
P943_07_AP_A_2_POS_17	0.027	0.003	5.826	0.016	10.066	0.005	0.006	-	0.011	-0.003	0.025	0.025	1.431	0.144	0.426	17.582	0.807	10.17	5.84	2	95.786
P943_07_AP_A_2_POS_18	0.009	0.000	5.729	0.000	9.731	0.010	0.005	-	-0.003	0.003	0.006	0.010	0.163	0.033	1.804	15.696	0.842	9.77	5.73	2	102.591
P943_07_AP_A_2_POS_19	0.072	0.043	5.406	0.083	10.694	0.005	0.022	-	0.109	0.000	0.008	0.028	2.520	0.024	0.000	19.015	0.820	10.98	5.49	2.54	84.185
P943_07_AP_A_2_POS_20	0.039	0.000	5.594	0.019	10.854	0.003	0.017	-	0.006	0.002	0.002	0.017	1.676	0.272	0.052	18.501	0.788	10.94	5.61	2	87.281
P943_07_AP_A_2_POS_21	0.034	0.000	5.877	0.017	10.042	0.003	0.015	-	0.005	0.002	0.001	0.015	1.466	0.238	0.296	17.714	0.786	10.12	5.89	2	97.364
P943_07_AP_A_2_POS_22	0.000	0.000	5.882	0.012	10.049	0.010	0.006	-	0.006	0.002	-0.005	0.003	1.582	0.038	0.380	17.584	0.833	10.07	5.89	2	96.674
P943_07_AP_A_2_POS_23	0.000	0.000	5.882	0.012	10.049	0.010	0.006	-	0.006	0.002	-0.005	0.003	1.582	0.038	0.380	17.584	0.833	10.07	5.89	2	96.674
P943_07_AP_A_2_POS_25	0.003	0.005	5.969	0.001	9.967	0.004	0.001	-	0.008	0.005	-0.003	0.003	1.819	0.017	0.163	17.799	0.853	9.99	5.97	2	99.757
P943_07_AP_A_2_POS_26	0.009	0.222	5.433	0.005	9.283	0.001	1.044	-	-0.088	0.003	-0.002	0.001	0.096	0.041	1.864	16.049		10.47	5.44	2	105.569
P943_07_AP_A_2_POS_27	0.033	0.000	5.939	0.030	9.710	0.007	0.007	-	0.001	0.008	0.004	0.025	1.404	0.066	0.531	17.233	0.816	9.79	5.97	2	98.903
P943_07_AP_A_2_POS_28	0.017	0.010	5.928	-0.001	9.951	0.009	0.006	-	0.007	0.011	0.020	0.016	1.671	0.084	0.246	17.726	0.827	10.04	5.93	2	99.31
P943_07_AP_A_2_POS_29	0.058	0.084	5.655	0.023	10.276	0.008	0.028	-	0.049	0.003	0.017	0.017	1.431	0.041	0.529	17.690	0.782	10.54	5.68	2	90.851
P943_07_AP_A_2_POS_30	0.030	0.026	5.637	0.023	10.412	0.015	0.021	-	0.019	0.001	0.020	0.014	1.145	0.294	0.561	17.654	0.736	10.56	5.66	2	89.868
P943_07_AP_A_2_POS_31	0.027	0.023	5.810	0.021	9.928	0.013	0.019	-	0.017	0.001	0.018	0.013	1.031	0.265	0.704	17.184	0.739	10.06	5.83	2	98.255
P943_07_AP_A_2_POS_32	0.003	-0.003	5.901	-0.001	9.871	0.004	0.006	-	0.008	-0.001	-0.004	0.002	1.255	0.006	0.739	17.046	0.825	9.89	5.9	2	100.263
P943_07_AP_A_2_POS_34	0.016	-0.003	5.887	0.014	10.049	0.013	0.011	-	0.002	0.003	0.019	0.015	1.747	0.046	0.208	17.820	0.829	10.13	5.9	2	99.688
P943_07_AP_A_2_POS_35	0.010	0.003	5.908	0.017	10.102	0.013	0.004	-	0.006	0.001	0.000	0.013	1.892	0.055	0.053	18.024	0.843	10.15	5.92	2	98.244
P943_07_AP_A_2_POS_37	0.008	0.188	5.502	0.018	9.856	0.003	0.606	-	-0.029	0.003	-0.006	0.005	0.834	0.039	1.126	17.026		10.63	5.52	2	87.892
P943_07_AP_A_2_POS_38	0.003	-0.003	5.905	0.006	9.975	0.009	0.004	-	0.001	0.003	-0.009	0.001	1.482	0.040	0.479	17.417	0.831	9.98	5.91	2	100.285
P943_07_AP_A_2_POS_39	0.020	0.000	5.804	0.021	9.990	0.013	0.006	-	0.005	0.005	0.013	0.019	1.241	0.061	0.699	17.197	0.808	10.07	5.82	2	98.542
P943_07_AP_A_2_POS_40	0.028	0.000	5.762	0.028	10.341	0.014	0.009	-	0.006	0.002	0.005	0.001	1.759	0.009	0.233	17.963	0.838	10.4	5.79	2	95.438
P943_07_AP_A_2_POS_41	0.014	0.000	5.804	0.016	10.132	0.009	-0.002	-	0.007	0.003	0.007	0.001	1.406	0.045	0.549	17.441	0.831	10.17	5.82	2	96.167
P943_07_AP_A_2_POS_42	0.007	0.015	5.937	0.001	9.867	0.003	0.013	-	0.009	0.002	-0.003	0.007	1.504	0.029	0.468	17.390	0.824	9.92	5.94	2	98.774
P943_07_AP_A_2_POS_43	0.000	0.000	5.657	0.000	10.458	0.006	0.009	-	0.007	0.014	-0.012	-0.001	1.226	0.022	0.753	17.386	0.816	10.48	5.66	2	91.251
P943_07_AP_A_2_POS_44	0.046	0.000	5.779	0.068	9.957	0.010	0.004	-	0.007	0.006	0.012	0.006	1.298	0.078	0.624	17.271	0.811	10.05	5.85	2	98.132

A2Z Sample No.	Na (apfu)	Mg (apfu)	P (apfu)	S (apfu)	Ca (apfu)	Mn (apfu)	Fe (apfu)	As (apfu)	Sr (apfu)	Y (apfu)	La (apfu)	Ce (apfu)	F (apfu)	Cl (apfu)	OH (apfu)	TOTAL (apfu)	r_{mr0}	Ca SITE 10	P SITE 6	F+Cl+OH 2	TOTAL WT% OX
P943_07_AP_A_2_POS_45	0.003	-0.003	5.926	0.000	9.755	0.018	0.008	-	0.003	0.001	0.013	0.023	1.114	0.189	0.697	17.050	0.776	9.82	5.93	2	100.723
P943_07_AP_A_2_POS_46	0.003	0.005	5.904	0.004	10.087	0.006	0.009	-	0.003	0.006	-0.001	0.002	1.783	0.003	0.215	17.813	0.845	10.12	5.91	2	98.168
P943_07_AP_A_2_POS_47	0.007	0.003	5.772	0.019	10.230	0.009	0.009	-	0.005	0.008	0.013	0.016	1.563	0.040	0.398	17.694	0.825	10.3	5.79	2	93.599
P943_07_AP_A_2_POS_48	0.010	0.005	5.904	0.000	9.925	0.013	0.012	-	-0.005	0.029	0.035	0.083	2.055	0.075	0.000	18.141	0.826	10.11	5.9	2.13	96.84
P943_07_AP_A_2_POS_49	0.003	-0.005	5.898	0.040	10.105	-0.002	0.003	-	0.005	0.002	-0.003	0.000	2.054	0.003	0.000	18.103	0.864	10.11	5.94	2.06	97.7
P943_07_AP_A_2_POS_50	0.003	0.003	5.840	0.022	10.138	0.012	0.000	-	0.004	0.003	-0.004	0.006	1.633	0.033	0.334	17.693	0.841	10.16	5.86	2	95.857
P943_07_AP_A_2_POS_51	0.017	0.005	5.941	0.015	10.007	0.016	0.001	-	0.002	0.012	-0.004	0.001	1.846	0.055	0.098	17.914	0.844	10.06	5.96	2	98.243
P943_07_AP_A_2_POS_52	0.000	0.000	5.857	0.039	10.070	-0.001	-0.003	-	0.002	0.004	-0.005	-0.002	2.352	0.003	0.000	18.315	0.870	10.06	5.9	2.35	99.561
P943_07_AP_A_2_POS_53	0.027	0.003	5.785	0.060	10.207	0.005	0.002	-	0.004	0.004	0.007	0.018	2.146	0.021	0.000	18.287	0.857	10.28	5.84	2.17	96.153
P943_07_AP_A_2_POS_54	0.010	0.000	5.881	0.016	9.953	0.004	0.001	-	0.003	0.001	-0.001	0.006	1.410	0.043	0.548	17.326	0.831	9.98	5.9	2	99.857
P943_07_AP_A_2_POS_55	0.033	0.003	5.782	0.094	9.827	0.006	0.006	-	0.022	0.002	0.023	0.014	1.274	0.075	0.651	17.159	0.809	9.93	5.88	2	99.002
P943_07_AP_A_2_POS_56	-0.003	-0.003	5.845	0.000	9.806	0.019	0.013	-	0.008	0.001	-0.001	0.005	0.864	0.058	1.078	16.611	0.789	9.84	5.85	2	97.941
P943_07_AP_A_2_POS_57	0.004	-0.003	5.758	0.001	10.469	0.009	0.005	-	0.002	0.008	0.007	0.023	2.109	0.013	0.000	18.404	0.854	10.52	5.76	2.12	92.747
P943_07_AP_A_2_POS_58	0.017	0.003	5.879	0.044	10.115	0.004	0.003	-	0.003	0.002	0.010	0.010	1.940	0.055	0.005	18.084	0.850	10.17	5.92	2	98.698
P943_07_AP_A_2_POS_59	0.020	0.003	5.924	0.030	9.992	0.028	0.003	-	-0.004	0.006	0.010	0.022	1.989	0.038	0.000	18.060	0.843	10.08	5.95	2.03	97.432
P943_07_AP_A_2_POS_60	0.073	-0.003	5.861	0.086	9.772	0.006	-0.004	-	0.057	0.005	0.010	0.034	1.683	0.009	0.307	17.588	0.844	9.95	5.95	2	98.957
P943_07_AP_A_2_POS_61	-0.003	0.008	5.893	0.003	10.149	0.019	0.010	-	0.006	0.007	-0.001	0.007	1.725	0.175	0.101	17.997	0.809	10.2	5.9	2	96.599
P943_07_AP_A_2_POS_62	0.010	0.005	5.953	0.004	9.826	0.013	0.007	-	0.010	0.009	0.005	0.005	1.563	0.011	0.426	17.420	0.831	9.89	5.96	2	100.806
P943_07_AP_A_2_POS_63	0.010	-0.007	5.947	0.012	9.814	0.011	0.011	-	0.006	0.004	-0.002	0.010	1.479	0.047	0.475	17.342	0.819	9.86	5.96	2	101.45
P943_07_AP_A_2_POS_64	0.014	0.003	5.748	0.007	10.194	0.021	0.010	-	0.003	0.007	0.025	0.033	1.310	0.134	0.555	17.507	0.789	10.31	5.75	2	96.822
P943_07_AP_A_2_POS_65	0.134	0.066	5.794	0.020	9.767	0.018	0.037	-	0.061	0.004	0.007	0.018	1.181	0.024	0.795	17.129	0.747	10.11	5.81	2	95.011
P943_07_AP_A_2_POS_66	0.027	0.003	5.936	0.001	10.021	0.016	0.009	-	0.007	0.006	0.006	0.005	1.645	0.227	0.128	17.907	0.799	10.1	5.94	2	98.491
P943_07_AP_A_2_POS_67	0.003	0.000	5.879	0.026	10.063	0.010	0.003	-	0.005	0.003	0.009	0.001	1.727	0.023	0.251	17.750	0.844	10.1	5.9	2	98.942
P943_07_AP_A_2_POS_68	0.000	0.003	5.772	0.027	10.281	0.012	0.011	-	0.002	0.005	0.042	0.040	1.854	0.043	0.104	18.090	0.833	10.39	5.8	2	95.129
P943_07_AP_A_2_POS_69	0.013	0.005	5.878	0.035	9.929	0.012	0.006	-	0.003	0.003	0.016	0.019	1.602	0.032	0.366	17.553	0.831	10.01	5.91	2	98.239
P943_07_AP_A_2_POS_70	0.023	-0.005	5.876	0.041	9.822	0.008	0.007	-	0.002	0.003	0.009	0.022	1.386	0.034	0.581	17.228	0.821	9.89	5.92	2	100.75
P943_07_AP_A_2_POS_71	-0.010	0.000	5.828	0.001	9.826	0.009	0.011	-	0.011	0.004	0.002	0.003	0.767	0.109	1.123	16.560	0.787	9.85	5.83	2	98.787
P943_07_AP_A_2_POS_72	0.035	0.000	5.797	0.034	10.141	0.015	0.012	-	0.004	0.004	0.027	0.054	1.635	0.191	0.174	17.950	0.795	10.29	5.83	2	94.178
P943_07_AP_A_2_POS_73	0.029	0.008	5.931	0.009	9.790	0.011	0.014	-	0.014	0.005	0.004	0.014	1.295	0.184	0.521	17.307	0.780	9.89	5.94	2	100.326
P943_07_AP_A_2_POS_75	0.117	0.046	5.706	0.149	9.761	0.013	0.036	-	0.013	0.001	0.016	0.028	1.139	0.275	0.586	17.300	0.702	10.03	5.85	2	97.767
P943_07_AP_A_2_POS_76	0.020	0.003	5.827	0.032	10.029	0.018	0.017	-	0.000	0.003	0.018	0.027	1.450	0.172	0.377	17.616	0.783	10.13	5.86	2	98.152

Note: Elemental concentrations in atoms per formula unit (apfu) were caluclated from weight % oxide using the stoichiometric relationships of *Ketcham* [2015], and r_{mr0} was determined using the calculations of *Carlson et al.* [1999]. For samples JPCPC3 and JPCPC4 Na, Mg, Mn, Fe, As, Sr, Y, La, and Ce were measured using LA-ICP-MS, whereas P, Ca, F and Cl were measured via EPMA. LA-ICPMS apatite chemistry was used for sample 10FNARL008. Chemistry for sample Husky7 was analyzed using EPMA. Negative values represent weight % oxide measurements that were below detection limits and fell below the baseline.

Table A4. Organic thermal maturity for four Imperial Formation samples from the Mackenzie Plain, NWT

Sample	Petrology							Rock Eval										
	Bitumen reflectance	StDev	%Ro Equiv (bitumen)	%Ro	StDev	% Ro (recycled)	StDev	Qty (g)	S1 (mg HC/g rock)	S2 (mg HC/g rock)	PI (S1/(S1+S2))	S3 (mg CO2/g rock)	Tmax (°C)	Tpeak (°C)	TOC (wt %)	HI (mg HC/g TOC)	%Ro Equiv (GSC)	%Ro Equiv (Jarvie et al, 2001)
10FNA066	0.41 *(n: 3)*	0.050	0.65	0.81 *(n: 3)*	0.033	1.11 *(n: 3)*	0.025	71.0	0.01	0.07	0.12	0.38	447	486	0.15	47	0.99	0.89
						1.85 *(n: 3)*	0.013										(Type III	
10FNARL008	0.55 *(n: 2)*	0.053	0.74			1.11 *(n: 4)*	0.065	70.4	0.03	0.09	0.26	0.27	444	483	0.13	69	0.92	0.83
						1.39 *(n: 4)*	0.092										(Type III	
						1.84 *(n: 1)*	0.000										OM)	
JPCPC3	0.44 *(n: 5)*	0.027	0.67	0.70 *(n: 4)*	0.028			70.7	0.39	0.99	0.28	0.18	366	405	0.38	261		0.00
JPCPC4	0.43 *(n: 14)*	0.04	0.66					70.3	0.03	0.09	0.22	0.30	432	471	0.07	129	0.62	0.62
	0.36 *(n: 2)*	0.00																

Petrology measurements for Bitumen, natural vitrinite (%Ro), recycled vitrnite (%Ro recycled). Bitumen reflectance values are converted to %Ro equivalent

%Ro equiv calculated from Rock Eval Tmax data following the equation of *Jarvie et al*. [2001]

%Ro values for Husky7 (1.67 %Ro equivalent) and JP019 (0.73 %Ro) after Issler (unpublished)

Table A5. Rock-Eval data for Devonian and Cretaceous outcrop samples proximal to samples 10FNA066, JP019, and well N-22, Mackenzie Plain, NWT, Canada

Sample ID	Tmax	TOC	S2	%Ro Equiv (Jarvie et al, 2001)	Map Unit	Comments	Latitude	Longitude	Datum
10FNA067	434	3.55	10.25	0.65	Canol	sampled at next outcrop below 10FNA066, 3 km along creek	65.338885	-127.91221	NAD83
10FNA063	428	1.99	1.00	0.54	Slater River	10 km east of N-22	65.353125	-127.376864	NAD83
10FNA061	424	1.89	1.49	0.47	Slater River	20 km SE of N-22	65.292678	-127.197699	NAD83
10FNA002	430	0.95	3.77	0.58	Canol	at base of Canol, 3.5 km N of JP019	65.297061	-126.726424	NAD83
09FNA150	443	6.24	20.34	0.81	Hare Indian	at base of Hare Indian, 16 km E of JP019	65.24219	-126.392981	NAD83
10FNA038	428	4.4	16	0.54	Canol	upper Canol, 20 km E of JP019	65.221445	-126.344097	NAD83
09FNA140	435	7.86	26.3	0.67	Canol	upper Canol, 25 km ESE of JP019	65.184134	-126.237776	NAD83
10FNA266	439	0.51	0.22	0.74	Imperial	33 km SE of JP 019	65.086263	-126.171554	NAD83

%Ro equiv calculated from Rock Eval Tmax data following the equation of *Jarvie et al.* [2001]

Table A6. Summary of Cretaceous stratigraphic age and thickness for the Mackenzie Plain, NWT

Formation	Description	Stage	Age (Ma)	Minimum Thickness (m)	Maximum Thickness (m)
Western Mackenzie Plain (JPCPC3, JPCPC4, 10FNA066)					
Martin House	siltstone/shale/minor glauconite sand	Late Aptian to Albian	~112	100	160
Arctic Red	shale with minor bentonite	Early to late Albian	~110 - 100	350	>1000
		unconformity			
Slater River	shale interbedded with sandstone	Early Cenomanian	~99 - 95	400	500
Trevor	fine to coarse grained (locally conglomeratic) sandstone. Shale interbeds	Late Cenomanian to Middle Turonian	~95 -91	350	800
		unconformity			
Eastern Mackenzie Plain (JP019, 10FNARL008)					
Martin House	siltstone/shale/minor glauconite sand	Late Aptian to Albian	~112	20	40
Arctic Red	shale with minor bentonite	Early to late Albian	~110 - 105	150	>400
		unconformity			
Slater River	shale interbedded with minor sandstone and bentonite	Cenomanian to Coniacian	99-86	350	720
Little Bear	shale coarsening upwards to sand	Late Coniacian to Santonian	~87 - 83?	285	500
		unconformity?			
	more developed sand bodies	Santonian to Campanian	~83 - 70 ?		
		unconformity? Gradational contact?			
East Fork	shale and siltstone	Late Campanian to Maastrichtian	~72 - 66	0	200
		unconformity			
Keele Arch/Brackett Basin (Husky7)					
Martin House	siltstone/shale/minor glauconite sand	Late Aptian to Albian	~112	0	?
Arctic Red	shale with minor bentonite	Early to late Albian	~110 - 105	0	?
		unconformity			
Slater River	shale interbedded with sandstone	Turonian to Coniacian	~94 - 86	250	400
Little Bear	shale coarsening upwards to sand	Late Coniacian to Santonian	~87 - 83?	285	500
		unconformity			
	more developed sand bodies	Santonian to Campanian	~83 - 70 ?		
		unconformity? Gradational contact?			
East Fork	shale and siltstone	Late Campanian to Maastrichtian	~72 - 66	500	850
Summit Creek	coarsening upwards deltaic depostis followed by fining upwards fluvial systems	Maastrichtian to Paleocene	~66 - ?	200	470
		unconformity			

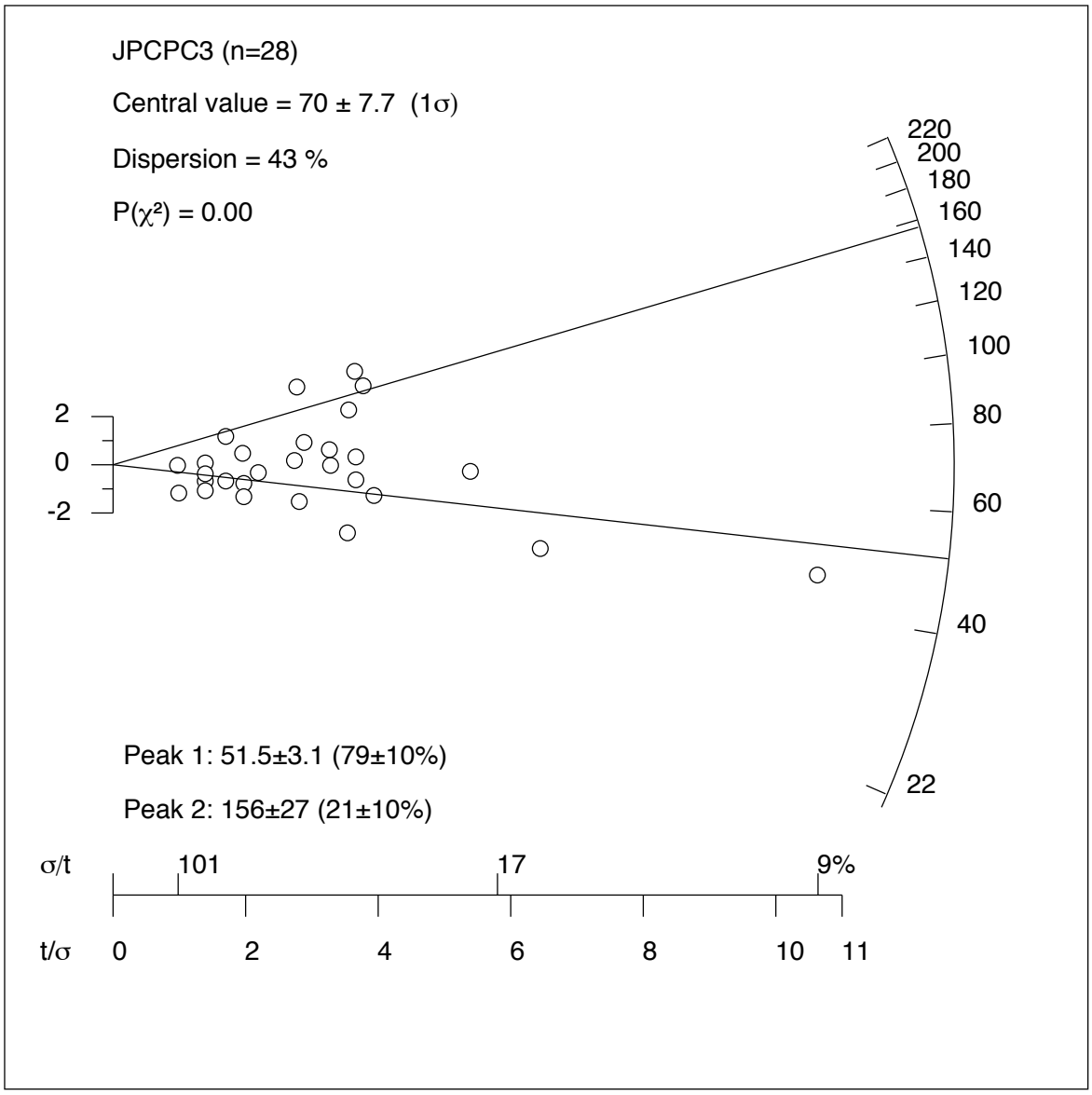

Fig. A1: Radial plot of the apatite fission track data for JPCPC3 using RadialPlotter [*Vermeesch*, 2009]. Fission track dates and their associated error are plotted as a function of the degree of rotation along, and distance from, the curved axis. Pooled ages from proposed kinetic populations (Table 2, S1) are within error of the peak ages predicted from the radial plot.

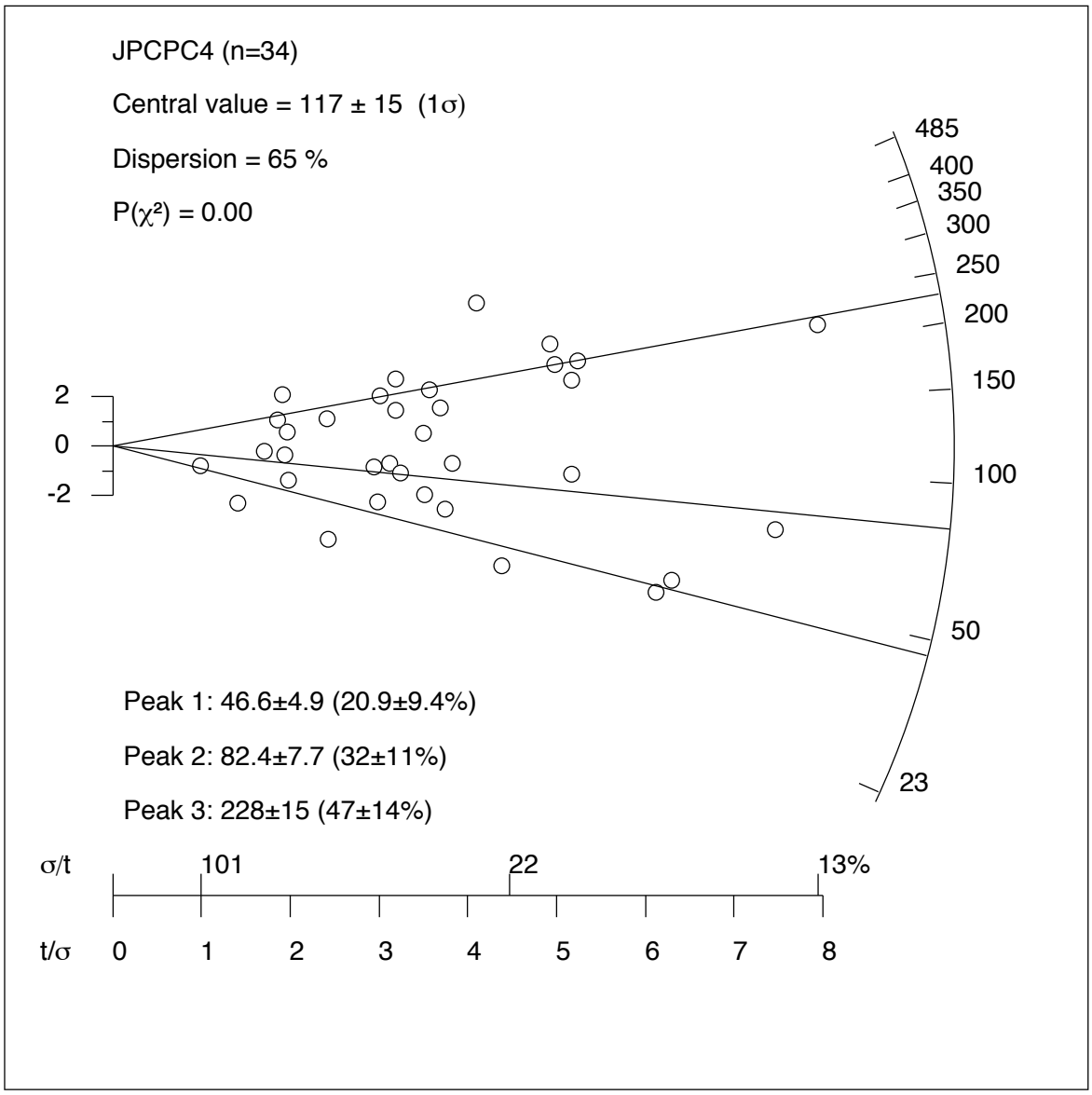

Fig. A2: Radial plot of the apatite fission track data for JPCPC4 using RadialPlotter [*Vermeesch*, 2009]. Fission track dates and their associated error are plotted as a function of the degree of rotation along, and distance from, the curved axis. Pooled ages from proposed kinetic populations (Table 2, S1) are within error of the peak ages predicted from the radial plot.

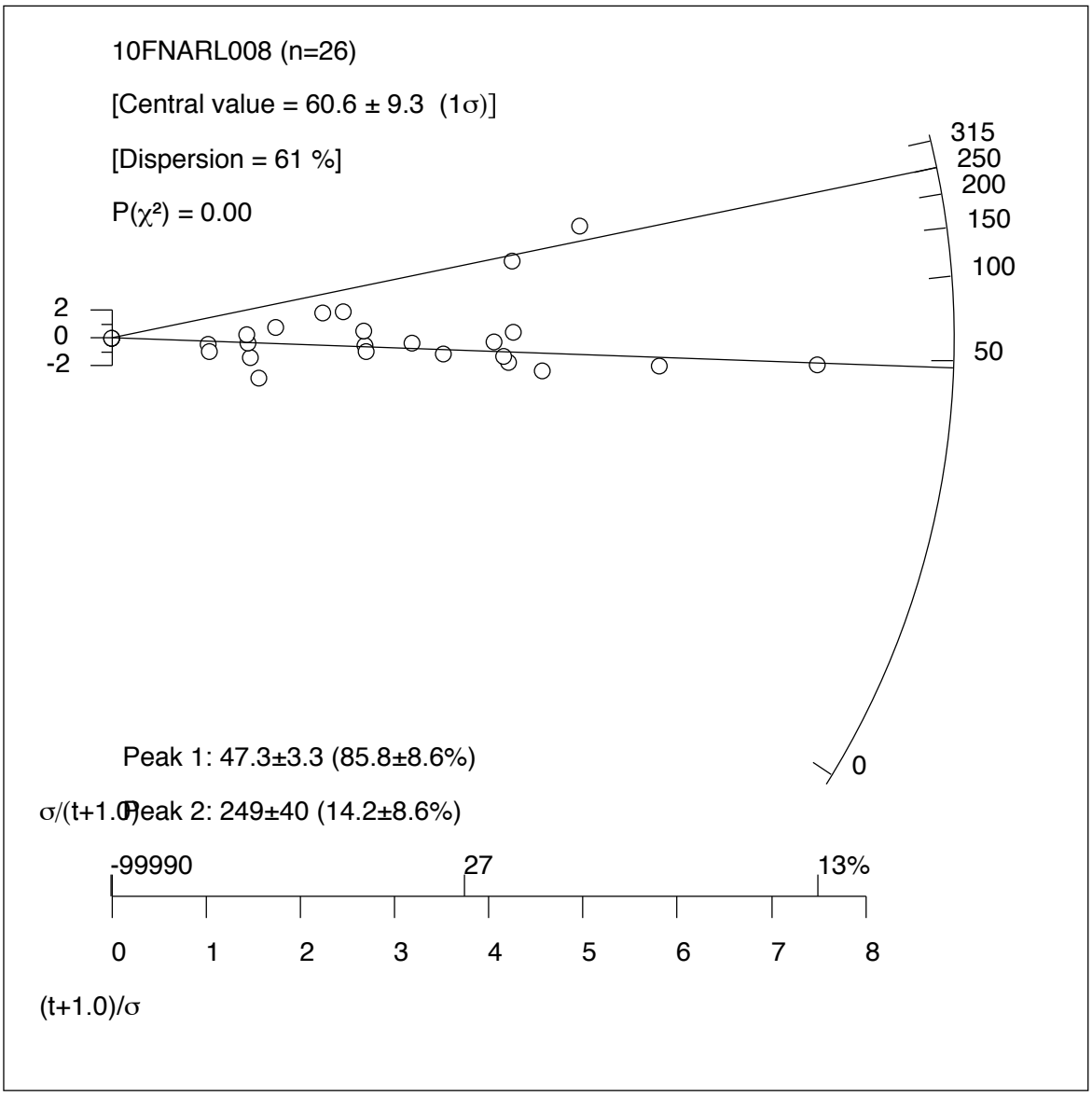

Fig. A3: Radial plot of the apatite fission track data for 10FNARL008 using RadialPlotter [*Vermeesch*, 2009]. Fission track dates and their associated error are plotted as a function of the degree of rotation along, and distance from, the curved axis. Pooled ages from two of the three proposed kinetic populations (Table 2, S1) are within error of the peak ages predicted from the radial plot. However, the radial plot is not able to identify the third population recognized based on r_{mr0} values (11.2 ± 6.5 Ma).

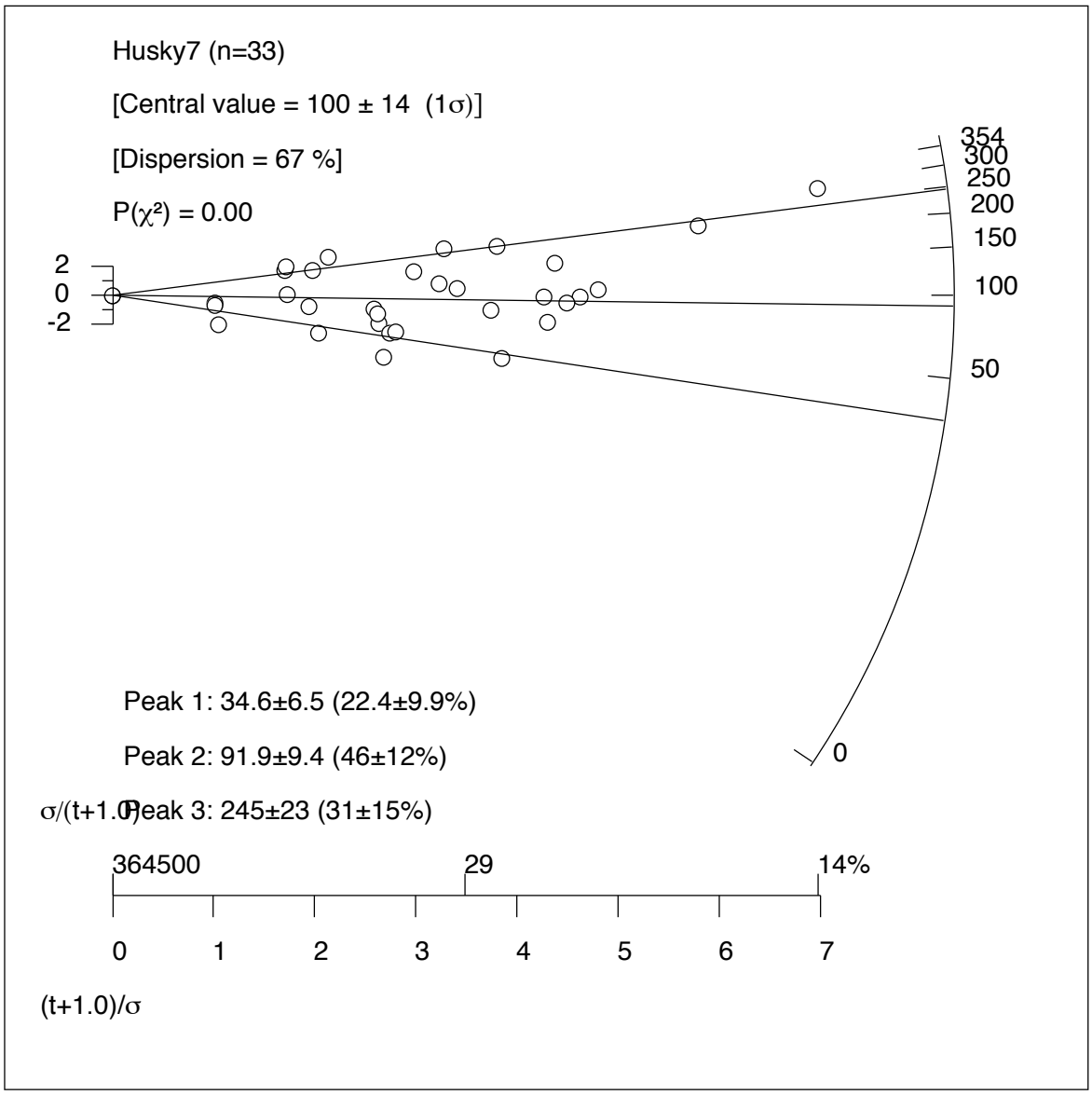

Fig. A4: Radial plot of the apatite fission track data for Husky7 using RadialPlotter [*Vermeesch*, 2009]. Fission track dates and their associated error are plotted as a function of the degree of rotation along, and distance from, the curved axis. Pooled ages from two of the four proposed kinetic populations (Table 2, S1) are within error of the peak ages predicted from the radial plot. However, the radial plot does not recognize the two youngest kinetic r_{mr0} populations (26.6 ± 5.7 Ma; 55.0 ± 6.8 Ma; Table 2, S1), and instead combines these AFT dates into a single peak age (34.6 ± 6.5 Ma).

Fig. A5: Inverse thermal model for AHe dates from the Imperial Formation sample JPCPC3. 'Good fit' thermal histories are summarized by the purple envelope, whereas 'acceptable' solutions are highlighted in green. The blue line represents the weighted mean of all good and acceptable time-temperature solutions. X-axis is from 375 – 0 Ma, and Y-axis is from 0 – 200 °C. The Albian to present thermal history is expanded in Chapter 4 (Fig. 6).

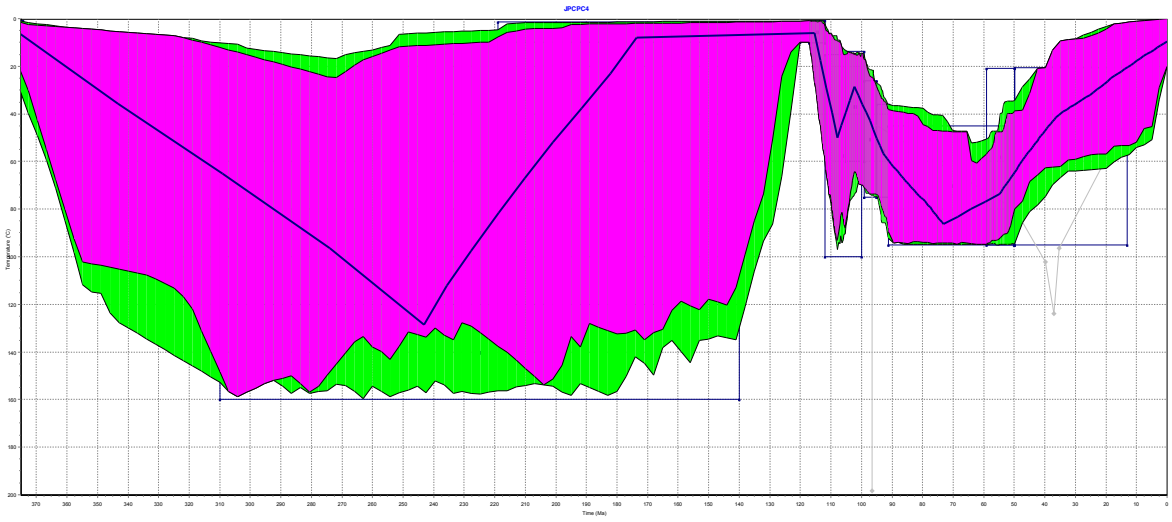

Fig. A6: Inverse thermal model for AHe dates from the Imperial Formation sample JPCPC4. 'Good fit' thermal histories are summarized by the purple envelope, whereas 'acceptable' solutions are highlighted in green. The blue line represents the weighted mean of all good and acceptable time-temperature solutions. X-axis is from 375 – 0 Ma, and Y-axis is from 0 – 200 °C. The Albian to present thermal history is expanded in Chapter 4 (Fig. 6).

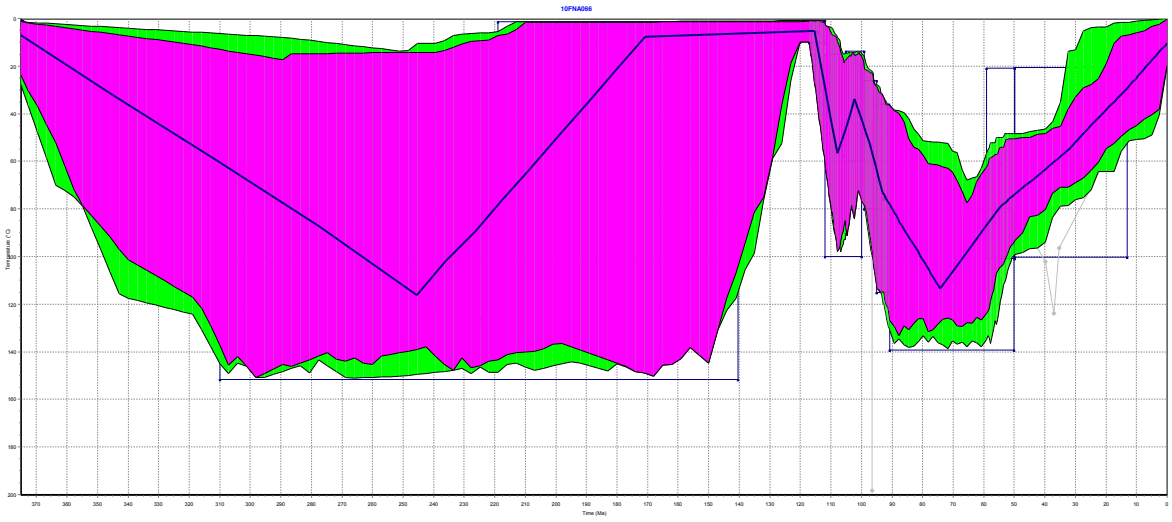

Fig. A7: Inverse thermal model for AHe dates from the Imperial Formation sample 10FNA066. 'Good fit' thermal histories are summarized by the purple envelope, whereas 'acceptable' solutions are highlighted in green. The blue line represents the weighted mean of all good and acceptable time-temperature solutions. X-axis is from 375 – 0 Ma, and Y-axis is from 0 – 200 °C. The Albian to present thermal history is expanded in Chapter 4 (Fig. 6).

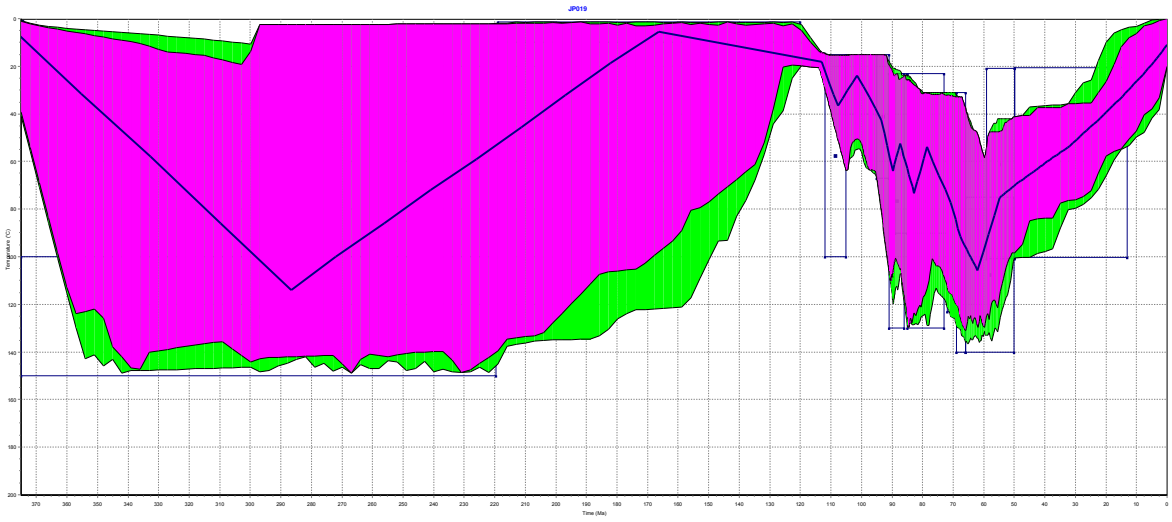

Fig. A8: Inverse thermal model for AHe dates from the Imperial Formation sample JP019. 'Good fit' thermal histories are summarized by the purple envelope, whereas 'acceptable' solutions are highlighted in green. The blue line represents the weighted mean of all good and acceptable time-temperature solutions. X-axis is from 375 – 0 Ma, and Y-axis is from 0 – 200 °C. The Albian to present thermal history is expanded in Chapter 4 (Fig. 6).

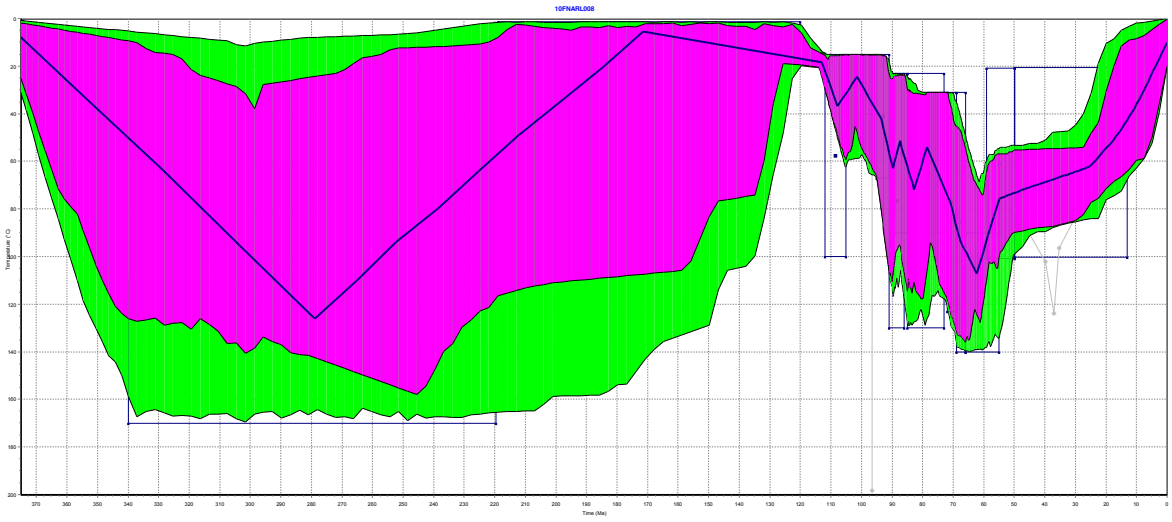

Fig. A9: Inverse thermal model for AHe dates from the Imperial Formation sample 10FNARL008. 'Good fit' thermal histories are summarized by the purple envelope, whereas 'acceptable' solutions are highlighted in green. The blue line represents the weighted mean of all good and acceptable time-temperature solutions. X-axis is from 375 – 0 Ma, and Y-axis is from 0 – 200 °C. The Albian to present thermal history is expanded in Chapter 4 (Fig. 6).

Fig. A10: Inverse thermal model for AHe dates from the Imperial Formation sample Husky7. 'Good fit' thermal histories are summarized by the purple envelope, whereas 'acceptable' solutions are highlighted in green. The blue line represents the weighted mean of all good and acceptable time-temperature solutions. X-axis is from 375 – 0 Ma, and Y-axis is from 0 – 200 °C. The Albian to present thermal history is expanded in Chapter 4 (Fig. 6).

CHAPTER 5

Low-temperature thermochronology of Anticosti Island: a case study on the application of conodont (U-Th)/He thermochronology to carbonate basin analysis

Jeremy Powell[1], David Schneider[1], André Desrochers[1], Rebecca Flowers[2], James Metcalf[2], Fred Gaides[3], Daniel Stockli[4]

1. Department of Earth & Environmental Sciences, University of Ottawa, Ottawa, Canada
2. Department of Geological Sciences, University of Colorado, Boulder, USA
3. Department of Earth Sciences, Carleton University, Ottawa, Canada
4. Jackson School of Geosciences, University of Texas at Austin, Austin, USA

Submitted to *Marine and Petroleum Geology*

Abstract

The Ordovician to Silurian carbonate succession preserved on Anticosti Island is a near continuous record of the changing depositional and tectonic history of the Early Paleozoic Laurentian margin. These strata are a prime natural laboratory to test the applicability of conodont apatite (U-Th)/He thermochronology (CAHe) for carbonate basin analysis in a setting with a well-understood burial history and paleotemperatures. We report 63 CAHe dates from seven samples collected from two boreholes. X-ray micro-computed tomography (MicroCT) was used to assess individual conodont element size, volume and alpha ejection correction. CAHe dates are negatively correlated with effective uranium concentration (eU), with single conodont dates enigmatically older than the age of deposition to conodont dates as young as 2.7 ± 0.2 Ma. We rationalize this dispersion as a product of several factors, including diagenetic processes and pervasive conodont crystalline porosity and permeability. Additionally, one basement and two sandstone samples were collected for apatite and zircon (U-Th)/He (AHe, ZHe) and apatite fission track (AFT) thermochronology. In the Precambrian basement, ZHe dates range from 581.7 ± 46.5 Ma to 761.2 ± 60.9 Ma (n: 4) and AHe dates range from 26.7 ± 1.6 to 48.4 ± 2.9 Ma (n: 4). AHe dates from two Lower Ordovician sandstones (n: 8) are positively correlated with eU, increasing from 13.7 ± 0.8 Ma to 105.2 ± 6.3 Ma over a range of 186 ppm eU. Thermal

history modeling of these data suggests two plausible thermal histories, both of which are novel as they imply that far-field effects related to the opening of the Atlantic Ocean have influenced the thermal history of Anticosti Island. Ultimately, these data highlight the complexities associated with, and necessity of, low-temperature thermochronology in carbonate basins.

1. Introduction

All carbonate basins present significant challenges for thermochronology due to the paucity of accessory minerals required in apatite fission track (AFT) and apatite and zircon (U-Th)/He (AHe, ZHe) analyses. In an effort to address this discrepancy, recent studies have tested various novel thermochronometers applicable to carbonate basins [e.g., *Copeland et al.*, 2007, 2015; *Cros et al.*, 2014]. Perhaps the most promising of these techniques is conodont apatite (U-Th)/He (CAHe) thermochronology [*Peppe and Reiners*, 2007; *Landman et al.*, 2016]. Conodonts are phosphatic microfossils that are common in Cambrian through Triassic strata [*Sweet and Donoghue*, 2001]. Whereas previous studies have outlined the similarities between CAHe and AHe [*Peppe and Reiners*, 2007; *Landman et al.*, 2016], more work is required to understand complexities associated with the system. In this study, samples were collected from two boreholes on Anticosti Island (Fig. 1), a thick succession of Ordovician to Silurian carbonate rocks in the Gulf of the St. Lawrence. We compare CAHe dates from Ordovician to Silurian carbonate rocks with AFT, AHe and ZHe analyses from the Precambrian basement and two Ordovician sandstone sequences.

The Gulf of the St. Lawrence is a geologically complex region that is comprised of several discrete tectonostratigraphic domains including the Proterozoic Grenville Province of the Canadian Shield, undeformed Paleozoic strata of the St. Lawrence platform, and the strongly

deformed strata of the Appalachian Orogen [*Pinet et al.*, 2012; *Pinet*, 2016; Fig 1]. The Cambrian to Devonian strata of the Anticosti Basin (Fig. 1) are unique in that they preserve a near-complete stratigraphic record of the Laurentian margin from the opening of the Iapetus Ocean following the breakup of Rodinia [*Williams and Hiscott*, 1987] to its subsequent closing during Appalachian events including the mid-Ordovician Taconic and Devonian Acadian orogenies [*Stockmal et al.*, 1990; *Dubé et al.*, 1995]. Conversely, the absence of post-Paleozoic strata in the region result in a poor understanding on the regional implications of regional Mesozoic tectonics, such as the breakup of Pangea and creation of the Atlantic basin [*Faure et al.*, 2006]. Although a low-temperature thermochronology study has documented the Mesozoic thermal history elsewhere along the St. Lawrence [*Tremblay et al.*, 2013], no similar study exists that constrains the Mesozoic evolution of the platform carbonates of the Anticosti Basin.

The data presented is this study are an innovative approach to conodont (U-Th)/He thermochronology, as they calibrate CAHe dates against borehole-specific thermal histories. Ultimately, these data serve to resolve the Neoproterozoic to present day thermal history of Anticosti Island and elucidate problems and potential of the CAHe thermochronometer.

2. Regional Geology

Sedimentary strata of the Anticosti Basin, the eastern component to the St. Lawrence platform (Fig. 1a), developed autochthonously along the Laurentian margin throughout the Paleozoic [*Pinet et al.*, 2012]. The Anticosti Basin itself can be further divided into western and eastern sub-basins that are separated by the north-south trending Beaugé Arch. Unlike the eastern Anticosti Basin, in which Lower Cambrian to Devonian sediments are preserved, strata of the western Anticosti Basin span the Early Ordovician through Upper Silurian [*Desrochers et al.*,

2012]. These strata onlap the Canadian Shield to the north, and dip gently towards their southern boundary at the Appalachian deformation front [*Pinet et al.*, 2012]. Although the western Anticosti Basin is mostly submerged under the Gulf of the St. Lawrence [*Marillier and Verhoef*, 1989; *Hayward et al.*, 2001], strata are exposed at the surface in a few locations, including Anticosti Island (Fig. 1b) [*Desrochers and Gauthier*, 2009].

On Anticosti Island, hydrocarbon exploration wells indicate that the Ordovician to Silurian succession thickens from ~900 m in the northeast to >3800 m in the southwest [*Bertrand*, 1990; *Bordet et al.*, 2010]. At the base of the section, peritidal carbonates of the Lower to Middle Ordovician Romaine Formation directly overly the Precambrian basement (Fig 2) and were deposited along the passive margin of Laurentia [*Desrochers et al.*, 2012]. The Middle Ordovician to Silurian carbonate record spans the Taconic Orogeny, and strata document the depositional transition from a tectonically subsiding foreland basin to a post-Taconic successor basin [*Lavoie*, 2008; *Desrochers et al.*, 2012]. These foreland basin deposits include the Mingan Formation, where a basal transgressive sandstone is overlain by peritidal to open marine carbonates [*Desrochers*, 1985], the Macasty Formation, an organic-rich marine shale [*Lavoie et al.*, 2005], and the shallow, open marine carbonates of the Vauréal and Ellis Bay formations and the overlying Becsie, Merrimack, Gun River, Jupiter and Chicotte Formations that comprise the Silurian Anticosti Group [*Long*, 2007].

Structurally, the island is cross-cut by a series of Middle to Late Ordovician normal faults related to Taconic extensional stresses [*Bordet et al.*, 2010]. Folds observed in Silurian strata onshore and in the post-Lower Silurian strata offshore are interpreted to be a product of the Middle Devonian Acadian Orogeny [*Bordet et al.*, 2010; *Pinet*, 2016]. The youngest structural

elements on Anticosti Island are NW-SE striking Jurassic quartz-tholeiite dikes [*Bédard*, 1992; *Faure et al.*, 2006].

Whereas Anticosti Island, both in surface and subsurface, preserve a near complete record of the Lower Ordovician to Lower Silurian strata, the post-Early Silurian geologic history is ambiguous. High resolution seismic data have identified another ~1140 m of sediment younger than the Silurian Anticosti Group offshore [*Pinet et al.*, 2012], and organic thermal maturity profiles indicate differential erosion of 2.3 to 3.5 km across Anticosti Island [*Bertrand*, 1990]. It is plausible that burial in the western Anticosti Basin continued into the Devonian, with the deposition of time-equivalent strata to the Clam Bank and Red Island Road formations that are preserved in the eastern Anticosti Basin [*Burden et al.*, 2002; *Quinn et al.*, 2004]. However, unpublished thermochronology from Anticosti Island [*Lynch and Grist*, 2002] and western Newfoundland [*Stockmal et al.*, 2008] suggest that burial may have continued into the Carboniferous or Permian.

Organic thermal maturity data from hydrocarbon exploration wells suggest an increase in maximum burial temperatures from 112 °C in the northeast of Anticosti Island to 168 °C in the southwest, and estimate spatially variable geothermal gradients between ~20 – 26 °C/km [*Bertrand*, 1990]. In addition to heating due to burial, hydrothermal dolomites of the Romaine and Mingan formations suggest that multiple episodes of hot, dolomitizing fluids affected diagenesis of the Lower to Middle Ordovician strata [*Lavoie et al.*, 2005; *Lavoie and Chi*, 2010]. Although the present understanding of regional exhumation suggests that the ~3.5 km of post-Lower Silurian sediment was rapidly eroded in the Middle Devonian [*Bertrand*, 1990], the only corroborating evidence of this hypothesis is the relative chronology of fracture sets [*Bordet et al.*,

2010] and comparisons with deformation patterns in the Appalachians of the Gaspé belt and western Newfoundland [*Cooper et al.*, 2001; *Pinet*, 2016].

3. Conodont Bioapatite

Conodont elements are the phosphatic, biomineralized skeletal remains forming a bilaterally symmetrical array in the head of eel-shaped marine animals that were common from the Cambrian to Triassic [*Sweet and Donoghue*, 2001]. These elements range in size from 0.1 to 3.0 mm in length and are composed of carbonate fluorapatite with a general chemical composition of $Ca_5Na_{0.14}(PO_4)_{3.01}(CO_3)_{0.16}F_{0.73}(H_2O)_{0.85}$ [*Pietzner et al.*, 1968]. The morphology of conodont elements varies substantially between conodont taxa and with the functional position in the feeding apparatus [*Dzik*, 1976; *Purnell et al.*, 2000]. Despite variable morphologies, all conodont elements share similar histologic components, including a crown made of translucent hyaline and opaque albid tissues, and the hardly preserved basal body [*Trotter and Eggins*, 2006]. Transmission electron microscopy of the conodont crowns shows that the albid tissue is composed of apatite crystals that are hundreds of microns in size [*Trotter et al.*, 2007]. Comparatively, the hyaline tissue has a lamellar structure that is defined by elongate microcrystals of apatite that range from ~100 nm to several microns [*Pietzner et al.*, 1968; *Trotter et al.*, 2007]. The basal body of conodont elements is composed of basal tissue, which is a matrix of irregularly arranged, fine-grained polycrystalline apatite [*Donoghue*, 1998].

Conodont bioapatite is a porous and permeable medium, with each tissue exhibiting varying degrees of inter- and intra-crystalline porosity [*Wright*, 1989]. In the albid tissue, porosity ranges from nanometer subspherical pores to microns scale intra-crystalline porosity; even larger macro-pores between apatite crystals are locally present. Intra-crystalline nano-

porosity is extensively developed in the hyaline crown tissue, whereas inter-crystalline porosity is less common and mostly observed along growth cavities [*Trotter et al.*, 2007]. Although porosity is well documented in conodont tissues, it is unclear as to the degree of interconnectivity between pores. Diagenetic iron-oxide precipitates within hyaline crown tissue indicate some degree of interconnectivity [*Trotter and Eggins*, 2006], and the resistance of albid tissue to acid etching relative to hyaline tissue may be indicative of lower permeability [*Trotter et al.*, 2007]. Pore spaces in basal tissues are likely interconnected, as evinced by their poor preservation potential relative to the crown tissues [*Sanz-López and Blanco-Ferrera*, 2012].

Many major, minor and trace element cation species substitute for Ca in conodont apatite [*Wright*, 1989]. Some of these are incorporated biologically during growth, whereas others, such as U, Th and REE, are concentrated post-mortem [*Trotter and Eggins*, 2006]. Following the death of the conodont organism, U from the surrounding water is incorporated into the apatite crystal lattice through diffusion-adsorption processes in which uranyl ions are adsorbed onto the element surface through cation exchange with Ca [*Millard and Hedges*, 1996; *Pike and Hedges*, 2001]. The concentration of U and Th varies between tissues for a given element, with U as low as <1 ppm in the albid tissue, to <10 ppm in the hyaline tissue and as high as 100 ppm in the basal tissue [*Trotter and Eggins*, 2006]. This difference in concentration is possibly attributed to the variable permeability and apatite crystal size, where fluids have access to significantly more surface area for chemical exchange in the basal, and to a lesser extent, hyaline tissues compared to the larger apatite crystals in the albid tissue [*Trotter et al.*, 2007].

The colour of conodont elements changes systematically with increasing temperature, gradually transitioning from pale yellow to black. The Conodont Alteration Index (CAI), which parameterizes the relationship between colour and temperature, is a useful tool for assessing the

maximum paleotemperatures experienced by strata [*Epstein et al.*, 1977]. Changes to conodont colour are also attributed to oxidizing hydrothermal fluids [*Rejebian et al.*, 1987] and elements that have been in contact with these fluids exhibit textures that are indicative of recrystallization [*Königshof*, 2003; *Sanz-López and Blanco-Ferrera*, 2012].

The two studies that have attempted to date conodont elements using the (U-Th)/He (CAHe) method yielded some promising results [*Peppe and Reiners*, 2007; *Landman et al.*, 2016]. Cycled step-heating diffusion experiments suggest that conodont ^{4}He diffusion is similar to abioitic apatite, with a closure temperature of ~60 – 70 °C [*Peppe and Reiners*, 2007]. Both studies reported a subset of CAHe dates consistent with known regional thermal events, but also found other samples yield irreproducible dates of equivocal geologic significance [*Peppe and Reiners*, 2007; *Landman et al.*, 2016]. Both the *Landman et al.* [2016] and *Peppe and Reiners* [2007] investigations suggest that spurious CAHe dates are a function of post-depositional U-Th leaching from conodont elements.

4. Methods and Results

4.1. Sampling and separation

Sampling for this study targeted two hydrocarbon exploration wells, Princeton Lake (LGPL) or D002 and New Associated Consolidated Paper (NACP) or D003 (Fig. 1b). Strata from these wells achieved maximum paleotemperatures of ~146 °C and ~135 °C, respectively [*Bertrand*, 1990]. In addition to heating due to burial, fluid inclusions within calcite from the D003 well indicate that the Romaine and Mingan formations were subject to circulation of hot (<138 °C) hydrothermal fluids throughout their burial history [*Lavoie et al.*, 2005]. Although present day geothermal gradients are between 15 °C/km – 23 °C/km [*Marcil et al.*, 2014], strata

from the study wells matured under steeper geothermal gradients and a higher average surface temperature [*Bertrand*, 1990; *Chi et al.*, 2010].

We sampled both the Grenvillian basement and the directly overlying Romaine Formation in the D002 well (Fig. 2) to compare the behaviour of the CAHe system with abiotic accessory minerals (apatite, zircon) under similar thermal conditions. To test the effect of increasing burial temperature on the CAHe system, we collected samples from core at regular (~300 m) intervals in the D003 well (Fig. 2). Additionally, we sampled the basal sandstone of the Mingan Formation from both D002 and D003 wells to provide another independent thermochronometer (AHe) to calibrate borehole thermal history.

Apatite and zircon were separated from drill core using standard mineral separation techniques. Conodonts were dissolved from ~2 kg carbonate samples via buffered acetic acid [*Jeppsson et al.*, 1999]. Of the seven carbonate horizons sampled (Fig. 2), three had very good conodont yields (13JP02, 13JP06, 13JP07), two had moderate yields (13JP01, 13JP03), one had a very poor yield (13JP05) and one sample yielded no conodont elements (13JP04).

4.2. AFT thermochronology

Apatite fission-track analysis is a widely used thermochronometer in sedimentary basin analysis as the method is sensitive to a temperature window (~50 – 150 °C) that coincides with the thermal conditions required for hydrocarbon generation [*Armstrong*, 2005]. Fission tracks are damage zones in the crystal lattice produced via the spontaneous fission of ^{238}U [*Naeser*, 1967]. These tracks undergo thermal annealing at elevated temperatures, resulting in shortening of track lengths and a decrease in their density [*Green*, 1988]. Measurements of fission track density and length distribution are used to model the time-temperature history of a sample [*Donelick et al.*, 2005].

Apatite chemistry has a first order control over the kinetics of fission track annealing, with cation substitutions (namely Cl) increasing the resistance to thermal annealing from end-member fluorapatite [*Green et al.*, 1986; *Carlson et al.*, 1999; *Barbarand et al.*, 2003]. Whereas parameters such as D_{par}, a measurement of the mean-maximum diameter of the fission track etch pit, have traditionally been used to assess annealing kinetics [*Burtner et al.*, 1994], the kinetic parameter r_{mr0} [*Carlson et al.*, 1999] may be a better tool. Compared to D_{par}, r_{mr0} parameterizes the chemistry of an individual apatite to predict its annealing kinetics relative to laboratory-defined annealing experiments [*Carlson et al.*, 1999; *Ketcham et al.*, 2007]. Recent studies have reported the utility of r_{mr0} in separating multiple kinetic populations from single AFT samples (*Powell et al.*, 2017, submitted).

We analyzed a single AFT sample from the Grenville basement of D002. Fission track dates were acquired using the LA-ICP-MS method [*Hasebe et al.*, 2004; *Donelick et al.*, 2005; *Chew and Donelick*, 2012]. Full analytical conditions are available in the Appendix to this Chapter. We report 39 AFT dates between 81.6 ± 12.1 Ma to 216.1 ± 35.8 Ma (Table A1), and track lengths that span 8.4 μm to 16.3 μm (Table A2). We used LA-ICP-MS and EPMA chemistry (Table A3) to calculate r_{mr0} values following the relationship defined by *Carlson et al.* [1999]. These values span 0.787 to 0.829 r_{mr0} for the AFT age grains and 0.558 to 0.825 r_{mr0} for the AFT length grains. AFT dates have a central age of 125.1 ± 2.9 Ma but fail the χ^2 test (Fig. 3a) indicating that the AFT data do not compose a single, statistically significant population [*Green*, 1981]. However, two populations are differentiated when AFT dates are plotted against their corresponding r_{mr0} value. A retentive population with a pooled age of 126.2 ± 6.7 Ma that passes the χ^2 test ($P(\chi^2) = 0.84$) is characterized by r_{mr0} <0.813. In contrast, a less retentive population has r_{mr0} values >0.813, a pooled age of 121.3 ± 3.7 Ma, and fails the χ^2 test ($P(\chi^2) = 0.00$) due to the presence of six high precision AFT dates between

81.6 ± 12.1 Ma and 94.2 ± 14.2 Ma (Fig. 3b). The track length distributions for each population indicate significant track shortening, with near identical mean track lengths of 12.4 ± 1.6 μm and 12.4 ± 1.7 μm, respectively (Fig. 3c). We interpret these data to represent a single AFT population of ca. 125 Ma, in which a small subset of the less retentive, higher r_{mr0} apatite is partially annealed to young AFT dates. In this sense, we submit that the more retentive, lower r_{mr0} population is a statistically significant record of the thermal history experienced by the sample.

4.3. AHe and ZHe thermochronology

In both AHe and ZHe thermochronology, radiogenic ^{4}He is produced via alpha decay of ^{238}U, ^{235}U, ^{232}Th, and ^{147}Sm and undergoes thermally activated diffusion through the apatite and zircon crystal lattice [*Farley*, 2002]. When ^{4}He is produced during alpha decay, the associated energy causes the particle to travel ~20 μm through the crystal lattice before stopping. This long stopping distance is problematic when parent radionuclides are close to the grain boundary, as ^{4}He may be ejected from the crystal [*Farley et al.*, 1996]. An alpha ejection correction (F_t) is commonly applied to measured (U-Th)/He dates to correct for ejected ^{4}He [*Farley et al.*, 1996; *Ketcham et al.*, 2011]. The F_t correction is a function of the surface area to volume ratio of a grain, and is geometrically calculated using mineral-specific dimensions [*Farley et al.*, 1996].

Helium diffusion is an open system at elevated temperatures, and apatite and zircon become increasingly retentive of radiogenic helium as they cool through temperatures in the uppermost crust [*Ehlers and Farley*, 2003]. Classically, this partial retention zone corresponds to ~130 – 200 °C in zircon [*Wolfe and Stockli*, 2010] and ~40 – 85 °C in apatite [*Wolf et al.*, 1998]. However, these temperature regimes are also dependent on cooling rate, grain size and radiation damage [*Farley*, 2002]. In particular, recent studies have illustrated the first order control that

radiation damage has on the diffusivity of helium in apatite [*Shuster et al.*, 2006; *Flowers et al.*, 2009; *Gautheron et al.*, 2009] and zircon [*Guenthner et al.*, 2013; *Powell et al.*, 2016]

In the AHe system, radiation damage is thought to result in crystal lattice dislocations in which helium can be "trapped." Once trapped, helium requires a higher activation energy to re-enter the crystal compared to the activation energy needed for volume diffusion through the undamaged structure [*Shuster et al.*, 2006]. For some thermal histories this relationship is manifest as a positive correlation between AHe date and radiation damage. The apatite radiation damage accumulation and annealing model (RDAAM) predicts that radiation damage undergoes thermal annealing following the same kinetics as fission tracks, and calculates apatite specific radiation damage by proxy of the effective fission track density ($e\rho_s$) [*Flowers et al.*, 2009]. The $e\rho_s$ of apatite can be calculated by integrating the effective uranium concentration (eU), a measure of the alpha decay productivity of U and Th (eU = [U] + 0.235 • [Th]; *Shuster et al.,* 2006; Flowers et al., 2007), over the time spent at thermal regimes corresponding with apatite fission track annealing [*Flowers et al.*, 2009]. Given that the parameter r_{mr0} suggests that annealing temperatures can vary widely between apatite [*Carlson et al.*, 1999; *Ketcham et al.*, 1999, 2007], the temperature sensitivity of helium diffusion kinetics in apatite should also vary with apatite chemistry.

A suite of twelve apatite grains from three samples and four zircon grains from one sample were handpicked under a binocular microscope and analyzed for (U-Th)/He thermochronology and are reported with 6% and 8% (2σ) analytical uncertainty for apatite and zircon, respectively (Table 1). Full methodology is available in the Appendix to this Chapter. Of the four ZHe dates analyzed from the Grenvillian basement of D002, three are within errors of each other (581.7 ± 46.5 to 638.7 ± 51.1) whereas a fourth grain is older (761.2 ± 60.9 Ma). No

obvious relationships between grain size (ESR: equivalent spherical radius), or radiation damage (eU) exist to explain the dispersion in ZHe dates.

Eleven single grain AHe dates from the three samples analyzed in this study span 13.7 ± 0.8 Ma to 105.2 ± 6.3 Ma (Table 1) and exhibit a positive correlation between AHe date and eU (Fig. 4). Although every effort was made to select apatite grains free of visible inclusions, the apatite yield from the Mingan Formation of D002 (13JP08; Table 1) was poor, and non-ideal grains were analyzed. In particular, the 194.5 ± 11.7 Ma date contained a large fluid inclusion, which may contain a parentless ^{4}He component that would account for its old date and low eU concentration. In the same well, three of the four AHe dates from the Grenvillian basement (13JP10; Table 1) are between 26.7 ± 1.6 Ma and 32.0 ± 1.9 Ma, whereas the fourth is 48.4 ± 2.9 Ma. No obvious relationships exist between AHe date and eU or ESR (Fig. 4). In the D003 well, four AHe dates from the Mingan Formation (13JP09; Table 1) span 17.7 ± 1.1 Ma to 63.6 ± 3.8 Ma (Fig. 4), and are positively correlated with eU (16.3 ppm – 54.9 ppm) and ESR (29.2 μm – 46.3 μm).

4.4. CAHe thermochronology

Following digestion and separation, conodont genera were classified via comparison with other Anticosti Island conodont studies [*McCracken and Barnes*, 1981; *Nowlan and Barnes*, 1981; *Zhang and Barnes*, 2002]. Conodont elements were grouped into five types on the basis of their morphology and genera (Fig. 5). Type 1 elements (e.g. *Panderodus*) exhibit elongate, conic forms. Type 2 elements (e.g. *Drepanostoidus*) differ from type 1 by their broad, hollow basal cavities. Type 3 elements (e.g. *Belodina* and *Phragmodus*) are characterized by the flattest morphologies of our studied suite. Type 4 elements correspond to fragments of the S_1 to S_4 anatomical groups [*Purnell et al.*, 2000] with a distinctive "bar" morphology [*Landman et al.*,

2016]. Type 5 conodont elements type match the ornate, S_0 anatomical morphology [*Purnell et al.*, 2000].

A simple geometric assessment of volume, surface area, mass and F_t correction is intrinsically more complicated in conodonts than abiotic apatite due to the complex morphologies associated with elements. We therefore employed X-ray micro-computed tomography (MicroCT) to measure these variables. MicroCT is a volumetric imaging technique that allows for 3D reconstruction of discrete objects [*Ketcham*, 2005a]. In this technique, conodonts are rotated in front of an X-ray source, and a linear array of detectors measures the decrease in intensity of X-rays as they pass through the elements [*Ketcham*, 2005c]. Data from the sensors is reconstructed into 2D slices, and then rendered into 3D objects using the program Blob3D [*Ketcham*, 2005a; version 1.4]. Whereas other studies have derived methods for calculating F_t corrections using MicroCT [*Herman et al.*, 2007; *Evans et al.*, 2008], Blob3D has a built-in tool that processes F_t corrections for each isotope given the 3D shape of the element following the methods of Ketcham et al. [2011].

We analyzed a suite of 63 single conodont elements from seven samples for CAHe thermochronology (Table 2). The number of individual aliquots per sample depended on the conodont yield and overall diversity of elements: only three conodonts were analyzed from sample 13JP05, whereas twenty were analyzed in sample 13JP02 due to the wide diversity in morphology and size. Eighteen CAHe dates were analyzed prior to the MicroCT work. We derive volume, mass, ESR and F_t corrections for these elements using their measured dimensions and volumetric relationships for each conodont type calculated from our large MicroCT database (154 Ordovician to Silurian conodont elements; Table A4; Appendix).

Table 2 and Fig. 6 display the CAHe dates from both wells. We report CAHe data from Becsie and Vauréal formations (Fig. 6a) separately from Romaine Formation samples (Fig. 6b) as conodonts from the Romaine Formation exhibit textures consistent with recrystallization due to hydrothermal fluids. We note that U-Th concentrations are very low, with eU concentrations of <1 ppm in eighteen elements. The CAHe dates are broadly dispersed, with 32 CAHe dates that are greater than stratigraphic ages. F_t-corrected CAHe dates from the Becsie and Vauréal formations (Fig. 6a) are negatively correlated with eU concentration, ranging from significantly older than deposition to 2.7 ± 0.2 Ma as eU increases from 0 ppm. In general, older than depositional ages from the Vauréal, Macasty and Becsie Formation occur when CAHe eU concentration is less than 1 ppm. Such a correlation is less clear in samples from the Romaine Formation (Fig. 6b), where some CAHe dates with high eU concentrations (< 30 ppm) are older than the stratigraphic age. No obvious relationships exist between CAHe date and ESR in any of the seven samples, and with the exception of a single data point, CAHe date and Th/U ratio are negatively correlated. Perhaps the only evidence of reproducible CAHe dates in our dataset comes from the Becsie Formation (13JP01) of the NACP D002 well. Of the five CAHe dates from this sample, four have F_t-corrected dates younger than deposition and three dates span 40.8 ± 5.2 Ma to 51.3 ± 6.8 Ma. This age range is similar to the 17.7 ± 1.1 Ma to 63.6 ± 3.8 Ma AHe dates from the Mingan Formation of the same well (Fig 4). Even the youngest CAHe date from the Romaine Formation of D002 (266.6 ± 19.6 Ma; Fig. 6b) is significantly older than AHe dates from the Grenvillian basement (26.7 ± 1.6 Ma to 48.4 ± 2.9 Ma; Fig. 4) despite only 15 m of stratigraphic separation (Fig. 2).

5. Thermal History Modeling

5.1. AFT, AHe and ZHe modeling

We performed inverse and forward thermal history modeling to understand the implications of our thermochronology data for the time-temperature history of Anticosti Island. We used the software HeFTy [*Ketcham*, 2005b; version 1.9.1] to model our AFT, AHe and ZHe data for sample 13JP10 from the Grenvillian basement of well LGPL D002 (Fig. 7). HeFTy uses a Monte Carlo approach to generate time-temperature paths, and assesses the agreement between modeled and empirical AFT, AHe and ZHe data. Users select independent geological time-temperature constraints through which the generated time-temperature paths must pass, and HeFTy uses a combined merit function to evaluate how well the model results compare with observed data. Paths are deemed as "acceptable" or "good" should they meet certain statistical precision limits.

Our modeling incorporates a mean ZHe date with dates and track lengths from AFT population 1 (Fig. 3b, c) and two AHe dates (Fig. 4). The mean ZHe data was modeled using the helium diffusion kinetics of the ZRDAAM [*Guenthner et al.*, 2013]. Since these dates were not reset following deposition, they constrain the pre-Ordovician cooling history of the Grenvillian basement. We model the AFT population 1 using the annealing kinetics of *Ketcham et al.* [2007] with an r_{mr0} value of 0.775, which represents the average value for the date and length grains (Fig. 3b, 3c). AHe data were modeled using the helium diffusion kinetics of the RDAAM and an r_{mr0} value of 0.83. This value was selected due to the AFT chemistry (Table A3), which suggests the majority of apatite in the dataset to be near-end member fluorapatite. Our inverse thermal history modeling tests two plausible burial histories for Anticosti Island: 1) a single heating and cooling event with maximum burial in the Devonian (Fig. 7a; model 1); and 2) two heating and cooling events, with maximum burial in the Devonian and a second heating event in the Jurassic

– Cretaceous due to a change in heat flow related to the opening of the Atlantic Ocean and igneous dike emplacement (Fig. 7a; model 2). Ordovician to Devonian time-temperature constraints were selected on the basis of the preserved thickness in the D002 well, the estimated 2.8 km of eroded Silurian – Devonian strata, and a range of present and paleogeothermal gradients [*Bertrand*, 1990; *Marcil et al.*, 2014].

Inverse modeling results show that either burial history hypothesis can satisfy the observed thermochronology data. In the first scenario, the basement is reheated to temperatures >120 °C in the Devonian and experiences a protracted thermal history through the Paleozoic and early Mesozoic, with cooling to temperatures <100 °C in the Late Jurassic to Early Cretaceous. In the second scenario, the basement is cooled to <80 °C by the Late Devonian, and is reheated to temperatures between 120 °C to 150 °C in the Jurassic.

Since these models were derived using only a subset of the thermochronology data from the D002 well, we use forward modeling of AFT and AHe data (Fig. 7b, c, d) to test whether the predicted thermal histories can satisfy the remainder of the observed data. Forward modeled time-temperature paths (Fig. 7a) follow a heating path consistent with the depositional history of the strata and a paleogeothermal gradient of 26 °C/km [*Bertrand*, 1990], whereas the cooling history is consistent with inverse models and the stratigraphic separation between the Grenvillian basement and Mingan Formation sample.

Fig. 7b illustrates the observed and modeled track length distributions for both apatite fission track populations. The track length distributions generated from both time-temperature histories yield goodness-of-fit (GOF) statistics >0.05 suggesting that they fit the observed data. Additionally, the model results predict a younger AFT pooled age in AFT population 2. Figure 7c shows expected AHe date-eU trends for a range of annealing kinetics observed in the AFT

population (Fig. 3b, c). Since the r_{mr0} values of AHe grains are unknown, it is possible that the date-dispersion is related to the range of expected chemistry for the population. Fig. 7d illustrates the predicted AHe date-eU trends for the Mingan sample. A broad range of r_{mr0} values are investigated to simulate the potentially varied provenance of apatite in the sandstone. These results demonstrate that despite appearing very dispersed, the AHe dates are in the realm of expected results. Particularly the 105.2 ± 6.3 Ma, high eU AHe date from the Mingan Formaiton is within the expected date-eU trend for fluorapatite of similar size.

We follow a similar modeling approach for the Mingan Formation sample (13JP09) from the NACP D003 well (Fig. 8). The Paleozoic to Mesozoic history thermal (Fig. 8a) is poorly resolved from inverse thermal history modeling since only AHe data were available for this sample. However, the model results suggest a similar Cretaceous to Recent cooling history as highlighted in Fig. 7a. Forward models were generated using a time-temperature history consistent with the burial history of NACP D003, a paleogeothermal gradient of 22 °C/km [*Bertrand*, 1990] and a cooling history that is constrained by inverse modeling results. The forward models illustrate that the majority of the AHe dates for this sample follow date-eU trends predicted for the observed range of grain size and a standard fluorapatite chemistry (Fig. 8b). The one AHe date that does not match this trend can be explained by less retentive diffusion kinetics.

5.2. CAHe forward modeling

In this section, we evaluate whether abundant nano- and micro-porosity in conodont elements can account for the observed CAHe date dispersion without invoking other external causes (e.g. U-Th leaching: Landman et al., 2016; Peppe and Reiners, 2007; Common He: Copeland et al., 2015). We posit that inter and intracrystalline porosity in bioapatite tissues may

have a similar effect on the kinetics of helium diffusion as radiation damage, serving as dislocations in the crystal lattice in which helium can be trapped [*Shuster et al.*, 2006]. Since porosity was not measured directly in conodont elements analyzed in this study, we use forward modeling to compare CAHe dates with predicted AHe dates for a broad range of radiation damage, as measured by the effective fission track density (Fig. 9). The candidate time-temperature paths used for forward modeling of the Romaine Formation follow the same thermal history as the basement forward models in Fig. 7. Time-temperature paths for the Becsie and Vauréal formations were generated using the stratigraphic separation between then 13JP01 and 13JP02 samples relative to the forward thermal history models from the Mingan 13JP09 sample (Fig. 8a).

In Fig. 9, both measured and F_t-corrected CAHe dates are plotted as a function of their ESR and conodont type. AHe dates predicted from forward modeling are plotted as a relationship between ESR and effective fission track density ($e\rho_s$); these curves were generated using the RDAAM and a range of eU concentrations (1, 10, 100, 1000 ppm). Because conodont porosity is not observed to thermally anneal at the temperatures experienced by these strata [*Rejebian et al.*, 1987; *Königshof*, 2003], annealing kinetics were set to 0.4 r_{mr0} to ensure that the modeled radiation damage was unannealed during burial. Values for $e\rho_s$ were calculated using the relationship described by Flowers et al. [2009]. The calculated $e\rho_s$ ($1.5 \times 10^4 - 1.7 \times 10^7$ tracks/cm^2) span the values used to calibrate the RDAAM. According to the *Flowers et al.* [2009], $e\rho_s$ values between $1 \times 10^4 - 1 \times 10^5$ tracks/cm^2 correspond with effective closure temperatures < 60 °C, whereas $1 \times 10^6 - 1 \times 10^7$ are substantially more retentive systems with closure temperatures between ~80 °C to >140 °C [*Flowers et al.*, 2009].

Forward models for the Becksie Formation show that 40.8 ± 5.2 Ma to 51.3 ± 6.8 Ma dates are substantially younger than predicted by either of the modeled thermal histories (Fig. 9b; Type 1 CAHe dates). Forward modeled t-T paths for the Vauréal Formation (Fig. 9a) predict that this stratigraphic horizon has experienced a protracted thermal history with maximum paleotemperatures of <110 °C in the Devonian. Forward models results (Fig. 9c) show that while CAHe dates from the Vauréal Formation may appear dispersed, much of the dates are within the realm of expected data for apatite with $e\rho_s$ values less than 1.5 x 10^6 tracks/cm^2 and closure temperatures < 80 °C. Near depositional CAHe ages from the Vauréal Formation can be explained by very porous conodont elements, as the projected 140 °C closure temperature for very damaged apatite is substantially higher than the maximum temperatures experienced by strata. The Vauréal Formation also exhibits two dates that are younger than predicted (2.7 ± 0.2 Ma, 47.1 ± 3.2 Ma). The CAHe dates from the Romaine Formation, which are much older than AHe dates from the underlying Grenvillian basement and the stratigraphically higher Mingan Formation, provide another example of how retentive kinetics due to tissue porosity may affect CAHe date (Fig. 9d). Forward models for the Romaine Formation illustrate that much of the CAHe data are similar to predicted AHe dates with $e\rho_s$ values between 1.5 x 10^6 and 1.5 x 10^7 tracks/cm^2 and closure temperatures ~80 °C - 140 °C. Whereas these forward model results suggest that helium trapping within conodont tissue porosity may be a significant contributor to CAHe dispersion, it is probable that other processes contribute as well. Alternative hypotheses as to the source of CAHe date dispersion are addressed in the following discussion.

6. Discussion

6.1. CAHe dispersion

Conodont (U-Th)/He data from the Ordovician subsurface of Anticosti Island are widely dispersed, with many spurious dates older than the stratigraphic age of each unit (Fig. 6). Many of these dates have extremely low U concentrations that are near the detection limits of the instrumentation (Table 2). It is plausible that analytical errors in the U-Th measurement may explain some CAHe dates that are older than the deposition age. Likewise, we note that of the 32 spuriously old CAHe dates, 24 are older than the stratigraphic ages when uncorrected for alpha ejection. It is unclear how applicable F_t corrections are for conodont thermochronology, as the order of magnitude difference in U-Th concentration between conodont tissues within a single element violates one of the central assumptions of the alpha ejection correction, which requires a spatially homogeneous chemical composition [*Farley et al.*, 1996].

Although the combination of low U-Th values and the ambiguity of F_t-corrections may account for some of the spurious dates, they cannot explain all of the older-than-deposition CAHe dates, nor the negative trends between date and eU. Similar inverse correlations between CAHe date and eU have been reported in other studies [*Peppe and Reiners*, 2007; *Landman et al.*, 2016] and attributed to leaching of U-Th from conodont elements. Those interpretations were supported by the observation that the most dispersed data were characterized by highly variable Th/U ratios, suggesting U, and to a lesser extent Th, loss. In contrast, the subset of reproducible dates were associated with lower and less variable Th/U. In comparison, Th/U ratios in this study are negatively correlated with CAHe date, and many of the lowest Th/U values in this dataset correspond with CAHe dates that are older than the stratigraphic age of the unit (Fig. 6b).

Peppe and Reiners [2007] and *Landman et al.* [2016] suggested U-Th leaching might be a product of primary diagenetic processes or acid leaching during limestone digestion. Given that U-Th uptake in fossil bone is related to attaining an equilibrium with the concentration of U in

groundwater, it is plausible that a change in groundwater geochemistry may result in diffusion of U from the conodont element [*Pike and Hedges*, 2001]. If diagentic radionuclide leaching is responsible for the older-than-deposition ages, then it must be a recent phenomenon as the conodonts in question contain as much, or substantially more, helium than the AHe in this study (Tables 1, 2). To that extent, we do not believe that the old CAHe dates are related solely to acid digestion, as that process would surely leach helium as well [*Peppe and Reiners*, 2007].

Whereas the recent study did not find evidence to support ^{4}He implantation and common helium as the primary causes of the negative date-eU trends in conodonts [*Landman et al.*, 2016], we believe that these factors may be significant contributors in our results. We posit that ^{4}He implantation is either a result of conodont tissues that have broken from the element following separation, or dissolved during burial and diagenesis [*Sanz-López and Blanco-Ferrera*, 2012]. Basal tissues are perhaps the most likely contributor of implanted He, as the tissue can contain U concentrations greater than 100 ppm [*Trotter and Eggins*, 2006] and are poorly preserved, either dislocating from the conodont crown post-mortem, or dissolving during burial and heating [*Sanz-López and Blanco-Ferrera*, 2012]. Given the large concentrations of U-Th, basal would generate most of the radiogenic helium in a conodont element. Any ^{4}He that diffused or implanted into the surrounding hyaline and albid crown tissues during burial are now parentless if the basal body separated from the crown prior to (U-Th)/He analysis.

Hydrothermally-mediated recrystallization of conodont bioapatite [*Rejebian et al.*, 1987; *Königshof*, 2003] may be another source for ^{4}He implantation. The Sanz-López and Blanco-Ferrera [2012] study suggests that hydrothermal fluids cause preferential dissolution of some bioapatite, such as the basal body, and its subsequent reprecipitation as blocky authigenic crystals along the crown. These authigenic crystals would behave similarly to other U-Th-rich

grain boundary phases, which implant helium into the host phase via alpha ejection from adjoining phases and are prone to removal from the grain boundary prior to dating [*Murray et al.*, 2014]. The CAHe dates from the Romaine Formation (Table 2; Figs. 6, 9) are perhaps an example of this process: the observed textures and colours of these conodonts suggest recrystallization due to the well-documented hydrothermal events in the formation [*Lavoie et al.*, 2005; *Lavoie and Chi*, 2010]. This observation may explain why high eU conodont elements yield older-than-deposition CAHe dates in the Romaine Formation but not in the overlying Vauréal and Becsie formations, as these units have not been subject to similar hydrothermal alteration.

Copeland et al. [2015] hypothesized that a common He component was responsible for older-than-deposition (U-Th)/He dates in their low-U crinoids. Whereas conodont diffusion studies [*Peppe and Reiners*, 2007] indicate that the temperature regime Ordovician to Silurian strata of Anticosti Island have been subject to should be sufficient liberate non-radiogenic helium, our modeling results (Fig. 9) suggest that retentive helium diffusion kinetics can be expected in conodonts, provided that unconnected nano- and micro-porosity are as pervasive in the tissue as dislocations are in the crystal lattice of radiation damaged apatite [*Flowers et al.*, 2009]. It is possible that the very low U, older than deposition CAHe dates in this study contain common He that was trapped in porosity and retained in the conodont tissue throughout burial.

If it is an increase in tissue permeability that allows for post-mortem U-Th enrichments in the high eU conodonts [*Trotter and Eggins*, 2006; *Trotter et al.*, 2007], then this permeability may also serve as fast diffusion pathways, creating poorly retentive CAHe systems and explaining the younger than expected dates in the Becsie and Vauréal formations (Fig. 9). To

that extent, porosity and permeability may explain the inverse CAHe date-eU correlations noted in this dataset and others [*Peppe and Reiners*, 2007; *Landman et al.*, 2016].

6.2. Precambrian cooling history of Anticosti Island

Interpretation of seismic reflection profiles from Anticosti Island by Pinet [2016] suggests that the Precambrian basement is characterized by broad folds and is correlative with the Wakeham Group of the eastern Grenville Province. ZHe data collected from these rocks in the subsurface of the D002 well (581.7 ± 46.5 to 638.7 ± 51.1; 761.2 ± 60.9 Ma; Table 1) are some of the only quantitative records of Proterozoic cooling for the region. Relative to the timing of rifting of Rodinia and opening of the Iapetus Ocean, the youngest dates ZHe dates in this dataset overlap with $^{40}Ar/^{39}Ar$ dates from pre-breakup mafic dikes in western Newfoundland (602 ± 10 Ma) and the 550 – 570 Ma rift-to-drift transition in the Cambrian strata of the eastern Anticosti Basin [*Williams and Hiscott*, 1987]. These dates reveal that cooling through temperatures <200 °C in the western Anticosti Basin was synchronous with the opening of the Iapetus Ocean. These data corroborate interpretations of the Beaugé Arch as an active geologic structure throughout the Precambrian [*Hayward et al.*, 2001], with rift shoulder uplift and erosion in the western Anticosti Basin, and down dropping and deposition of Cambrian strata in the eastern Anticosti Basin [*Desrochers et al.*, 2012]. Stratigraphic interpretations of Desrochers et al. [2012] suggests that the Beaugé Arch remained an active structure through the Middle Ordovician.

6.3. Anticosti Basin thermal history

The traditional opinion on the time-temperature history of the Ordovician to Silurian strata on Anticosti Island assumed a single heating event related to continuous deposition, attaining maximum temperatures just prior to rapid exhumation in the Middle Devonian

[*Bertrand*, 1990]. However, numerous studies on the structural geology [*Bordet et al.*, 2010], diagenetic history [*Lavoie et al.*, 2005; *Lavoie and Chi*, 2010] and igneous activity [*Faure et al.*, 2006] of Anticosti Island elucidate a more complicated thermal history. Even though our data are unable to distinguish between two plausible time-temperature models (Figs. 7a, 8a), both datasets contrast the exhumation history established by Bertrand [1990], as our models require that the carbonate strata in the LGPL D002 and NACP D003 wells resided at significantly higher temperatures than expected in the Mesozoic to recent. Below we examine evidence for each scenario and discuss their implications on the regional geologic history.

In the first thermal model (Figs. 7a, 8a; Model 1), strata experience a protracted cooling history following Devonian maximum temperatures, with a final cooling phase commencing in the Jurassic to Early Cretaceous. The onset of this cooling is approximately coincident with the emplacement of the 178 ± 8 Ma Jurassic dikes on Anticosti Island [*Bédard*, 1992; *Faure et al.*, 2006]. These dikes are some of the only direct evidence in Quebec of Jurassic intraplate extension related to the opening of the Atlantic Ocean [*Faure et al.*, 2006]. Indirectly, AFT thermochronology of normal faults along the St. Lawrence rift system records a complex Triassic to Jurassic cooling history [*Tremblay et al.*, 2013]. Tremblay et al. [2013] attribute these dates to normal faulting and subsequent tectonic inversion produced via far-field stresses associated with the breakup of Pangea and opening of the Atlantic Ocean. Unroofing of the region may have followed similar processes as suggested for the St. Lawrence rift system [*Tremblay et al.*, 2013], and have been facilitated by the reactivation of pre-existing faults. Evidence for this hypothesis includes the Jurassic dikes on Anticosti Island, which along with coeval dikes in eastern Canada, are speculated to be controlled by Mesozoic reactivation of Proterozoic basement structures [*Faure et al.*, 2006]. Additionally, the structural lineament analyses of Bordet et al. [2010]

determined that surface and subsurface faults on Anticosti Island had been reactivated by a post-Early Silurian deformation event, which they tentatively associated with the emplacement of Jurassic dikes. Supporting this interpretation are observations that the dikes run parallel with major fault systems, and are associated with a regional fracture set [*Bordet et al.*, 2010]. Alternatively, Mesozoic unroofing may not have been tectonic, but a function of rising topography due to thermal arching during the emplacement of Jurassic plutons in New England [*Faure et al.*, 2006].

Comparatively, the second model (Figs. 7a, 8a; Model 2) follows the Middle Devonian cooling history predicted by Bertrand [1990], but includes a brief increase in Mesozoic heat flow due to extension and the emplacement of Jurassic dikes [*Pe-Piper and Piper*, 1999; *Faure et al.*, 2006]. This model is similar to Model 1 in that it invokes the opening of the Atlantic Ocean, but different in that the subsequent cooling represents a relaxation of the geothermal gradient, as opposed to tectonic cooling or landscape development. A caveat to this model is that temperatures experienced by strata during Mesozoic heating must have been less than maximum burial temperatures, as the slope of the organic thermal maturity curves from the Anticosti Island subsurface indicate continual burial and not punctuated thermal events [*Bertrand*, 1990]. A similar process has been invoked in the Gulf of the St. Lawrence, where 1D modeling of organic thermal maturity profiles requires a Late Jurassic heat-flow anomaly in a subset of hydrocarbon exploration wells [*Wielens and Avery*, 2009]. Although our dataset is equally well resolved by either of the two disparate time-temperature scenarios, both modeled histories are similar in that they connect Mesozoic rifting of Pangea and opening of the Atlantic Ocean with the thermal history of Anticosti Island and the Gulf of the St. Lawrence.

6.4. Implications for petroleum systems

Anticosti Island has long been the subject of hydrocarbon exploration due to the presence of a regionally extensive, oil-prone source rock in the Macasty Formation [*Bertrand*, 1991], and potential reservoir units in the hydrothermal dolomites of the Romaine and Mingan formations [*Lavoie et al.*, 2005; *Lavoie and Chi*, 2010]. Renewed interest in the hydrocarbon potential of Anticosti Island has been fuelled by discoveries in western Newfoundland [*Cooper et al.*, 2001] and the identification of the Macasty Formation as a potential unconventional target [*Duchesne et al.*, 2016]. Our thermochronology data and the derived thermal history models are sure to have major implications on how the regional hydrocarbon system is viewed, as modeling of hydrocarbon generation and migration for Anticosti Island has classically assumed a much shorter residence at temperatures within the oil and gas window [*Chi et al.*, 2010]. These interpretations have significant ramifications on the timing of structural trap development relative to hydrocarbon generation, on the pressures under which hydrocarbons generated and migrated and on the volume of resources produced and remaining in the Macasty shale.

6.5. Thermochronology in carbonate basins

Carbonate sequences compose almost a quarter of all global hydrocarbon reservoirs [*Ehrenberg and Nadeau*, 2005] and information on the time-temperature history of these basins is an essential vector for petroleum exploration and exploitation. Recent studies have explored the potential of calcite [*Copeland et al.*, 2007; *Cros et al.*, 2014], crinoid [*Copeland et al.*, 2015], and conodont [*Peppe and Reiners*, 2007; *Landman et al.*, 2016] (U-Th)/He thermochronology to constrain the thermal history of carbonate sequences and found that potential complications of these methods include low U-Th concentrations, common helium, and U-Th mobility. This study additionally suggests that conodont element-specific variables that cannot be constrained *a*

priori, including tissue porosity, permeability, and diagenetic history, may greatly influence helium diffusion and CAHe date. As a result, we suspect that conodont (U-Th)/He may be most applicable to geologic structures or terranes that have cooled rapidly, as corroborated by the reproducible dates from the Nevada and Colorado samples of Peppe and Reiners [2007]. However, CAHe dates from rapidly cooled terranes may still be subject to issues related to low U-Th, U-Th mobility and common He.

Comparatively, advances in the understanding of the diffusion and annealing kinetics of the AHe, ZHe, and AFT systems [*Ketcham et al.*, 1999, 2007; *Flowers et al.*, 2009; *Guenthner et al.*, 2013] and practical ways in which they are integrated [*Gautheron et al.*, 2013; *Powell et al.*, 2017], allow for a tremendous amount of time-temperature information to be extracted from the apatite and zircon analyzed in this dataset. We suggest that thermochronology studies in carbonate basins target the few available horizons that contain accessory minerals, characterize their samples with respect to chemistry and annealing kinetics, and integrate available thermochronometers. Although siliciclastic units may be few and far between in most carbonate basins, modeling of the thermochronometers they contain elicits a comprehensive thermal history over a broad temperature window.

7. Conclusions

This dataset presents a first-of-its-kind comparison between AHe, AFT, ZHe and CAHe thermochronometers from the same borehole. ZHe dates from the Grenvillian basement of the LGPG D002 well record cooling synchronous with the rifting of Rodinia and opening of the Iapetus Ocean. We propose that these data explain the differential preservation of Cambrian strata in the Anticosti Basin, as they indicate that the basement to the west of the Beaugé Arch

was undergoing rift-shoulder uplift at approximately the same time that the eastern basin was subsiding and preserving Cambrian strata. Cretaceous AFT and AHe dates from both the LGPL D002 and NACP D003 wells are significantly younger than anticipated given the long-standing model of regional Devonian exhumation. Thermal history modeling indicates that these data can be resolved by two separate time-temperature histories. In either scenario, these models require that the Lower Ordovician strata of Anticosti Island resided at temperatures >80 °C throughout most of the Mesozoic prior to cooling to present day temperatures. We rectify these model results by invoking far-field effects of the Triassic to Jurassic rifting of Pangea and opening of the Atlantic Ocean.

CAHe dates are dispersed, ranging from near-zero at high eU concentrations to dates that are artificially older than the stratigraphic age at very low concentrations of eU. Whereas our results may support earlier interpretations on diagenetic U-Th leaching, we performed forward thermal history modeling to test whether this dispersion is explainable via the present understanding of helium diffusion in apatite. Our modeling suggests that given the protracted thermal history of Anticosti Island, porosity of conodont element tissues may explain the observed irreproducibility in CAHe dates. Such an interpretation requires that conodont element tissue porosity is pervasive, unconnected, and has the same effects on the kinetics of helium diffusion as radiation damage does to crystalline apatite. These findings have significant implications for the retention of common He in low-U conodonts. Likewise, we suggest that recrystallization and He implantation may be another vector for anomalous CAHe dates.

These data highlight the complexities associated with thermochronology studies in carbonate basins. Although conodont (U-Th)/He thermochronology may be a viable tool in some geologic scenarios, our results suggest it has limited application in sedimentary basins with

protracted burial and unroofing histories through temperatures corresponding with the oil and gas window. Conversely, advances in fission track and (U-Th)/He thermochronology allow for a tremendous amount of time-temperature information to be gleaned from single samples. In the case of this study, relatively few apatite and zircon grains elucidate a novel thermal history with significant tectonic and economic implications for carbonate strata in the Gulf of the St. Lawrence.

Acknowledgments

Funding for this project was provided by an NSERC-CRD grant to DAS, with contributions from ConocoPhillips Canada and Chevron Canada. We thank the Ministère de l'Énergie et des Ressources naturelles for facilitating core sampling. We are grateful to Alyssa Bancroft and Charles Henderson for their assistance with conodont separation, and Stephen Leslie for sending example Ordovician conodont specimens. We thank Paul O'Sullivan and Apatite to Zircon Inc. for assistance with the apatite fission track data collection and Glenn Poirier (Canadian Museum of Nature) for assistance with EPMA data collection.

References

Armstrong, P. A. (2005), Thermochronometers in Sedimentary Basins, *Rev. Mineral. Geochemistry*, *58*(1), 499–525, doi:10.2138/rmg.2005.58.19.

Barbarand, J., A. Carter, I. Wood, and T. Hurford (2003), Compositional and structural control of fission-track annealing in apatite, *Chem. Geol.*, *198*(1-2), 107–137, doi:10.1016/S0009-2541(02)00424-2.

Bédard, J. (1992), Jurassic quartz-normative tholeiite dikes from Anticosti Island, Quebec, *Geol. Soc. Am. Spec. Pap.*, *268*, 161–168.

Bertrand, R. (1990), Maturation thermique et histoire de l'enfouissement et de la génération des hydrocarbures du bassin Mingan-Anticosti, *Can. J. Earth Sci.*, *27*, 731–741.

Bertrand, R. (1991), Maturation thermique des roches mères dans les bassins des basses-terres du Saint-Laurent et dans quelques buttes témoins au sud-est du Bouclier canadien, *Int. J. Coal Geol.*, *19*(1–4), 359–383, doi:10.1016/0166-5162(91)90027-G.

Bordet, E., M. Malo, and D. Kirkwood (2010), A structural study of western Anticosti Island, St.

Lawrence platform, Québec: A fracture analysis that integrates surface and subsurface structural data, *Bull. Can. Pet. Geol.*, *58*(1), 36–55, doi:10.2113/gscpgbull.58.1.36.

Burden, E. T., L. Quinn, G. S. Nowlan, and L. A. Bailey-Nill (2002), Palynology and Micropaleontology of the Clam Bank Formation (Lower Devonian) of Western Newfoundland, Canada, *Palynology*, *26*(1), 185–215, doi:10.2113/0260185.

Burtner, R. L., A. Nigrini, and R. a. Donelick (1994), Thermochronology of Lower Cretaceous source rocks in the Idaho-Wyoming thrust belt., *Am. Assoc. Pet. Geol. Bull.*, *78*(10), 1613–1636, doi:10.1306/A25FF233-171B-11D7-8645000102C1865D.

Carlson, W. D., R. A. Donelick, and R. A. Ketcham (1999), Variability of apatite fission-track annealing kinetics: I. Experimental results, *Am. Mineral.*, *84*(9), 1213–1223, doi:10.2138/am-1999-0901.

Chew, D. M., and R. A. Donelick (2012), Combined apatite fission track and U-Pb dating by LA–ICP–MS and its application in apatite provenance analysis, *Mineral. Assoc. Canada Short Course 42*, 219–247.

Chi, G., D. Lavoie, R. Bertrand, and M.-K. Lee (2010), Downward hydrocarbon migration predicted from numerical modeling of fluid overpressure in the Paleozoic Anticosti Basin, eastern Canada, *Geofluids*, *10*(3), 334–350, doi:10.1111/j.1468-8123.2010.00280.x.

Cooper, M. et al. (2001), Basin evolution in western Newfoundland: New insights from hydrocarbon exploration, *Am. Assoc. Pet. Geol. Bull.*, *85*(3), 393–418.

Copeland, P., E. B. Watson, S. C. Urizar, D. Patterson, and T. J. Lapen (2007), Alpha thermochronology of carbonates, *Geochim. Cosmochim. Acta*, *71*(18), 4488–4511, doi:10.1016/j.gca.2007.07.004.

Copeland, P., K. Cox, and E. B. Watson (2015), The potential of crinoids as (U+Th+Sm)/He thermochronometers, *Earth Planet. Sci. Lett.*, *422*(July), 1–10, doi:10.1016/j.epsl.2015.04.007.

Cros, A., C. Gautheron, M. Pagel, P. Berthet, L. Tassan-Got, E. Douville, R. Pinna-Jamme, and P. Sarda (2014), 4He behavior in calcite filling viewed by (U-Th)/He dating, 4He diffusion and crystallographic studies, *Geochim. Cosmochim. Acta*, *125*, 414–432, doi:10.1016/j.gca.2013.09.038.

Desrochers, A. (1985), The Lower and Middle Ordovician platform carbonates of the Mingan Islads, Quebec: Stratigraphy, sedimentology, paleokarst, and limestone diagenesis, Memorial University of Newfoundland.

Desrochers, A., and É. L. Gauthier (2009), Carte géologique synthèse de l´´île d'Anticosti, *Ministère des Ressources Nat. la Faune, Québec,*, *DV 2009-03*.

Desrochers, A., P. Brennan-Alpert, D. Lavoie, and G. Chi (2012), Regional stratigraphic, depositional and diagenetic patterns of the interior of St. Lawrence Platform: the Lower Ordovician Romain Formation, Western Anticosti Basin, Quebec, in *The great American carbonate bank: The geology of economic resources of the Cambrian - Ordovician Sauk meagasequence of Laurentia: AAPG Memoir 98*, vol. 98, edited by J. R. Derby, R. D. Fritz, S. A. Longacre, W. A. Morgan, and C. A. Sternbach, pp. 525–543.

Donelick, R. A., P. B. O'Sullivan, and R. A. Ketcham (2005), Apatite Fission-Track Analysis, *Rev. Mineral. Geochemistry*, *58*(1), 49–94, doi:10.2138/rmg.2005.58.3.

Donoghue, P. C. J. (1998), Growth and patterning in the conodont skeleton, *Philos. Trans. R. Soc. London B*, *353*(1368), 633–666, doi:10.1098/rstb.1998.0231.

Dubé, B., G. R. Dunning, K. Lauziere, and J. C. Roddick (1995), New insights into the Appalachian Orogen from geology and geochronology along the Cape Ray fault zone, SW

Newfoundland, *Geol. Soc. Am. Bull.*, (1), 101–116.
Duchesne, M. J., Z. Chen, and D. Lavoie (2016), Seismic imaging of a thin unconventional reservoir in highly attenuating media: the case of the Macasty Formation, Anticosti Island, Canada, *Soc. Explor. Geophys. Tech. Progr. Expand. Abstr. 2016*, 2775–2779.
Dzik, J. (1976), Remarks on the evolution of Ordovician conodonts, *Acta Palaeontol. Pol.*, *21*(4), 395–455.
Ehlers, T. A., and K. A. Farley (2003), Apatite (U-Th)/He thermochronometry: Methods and applications to problems in tectonic and surface processes, *Earth Planet. Sci. Lett.*, *206*(1-2), 1–14, doi:10.1016/S0012-821X(02)01069-5.
Ehrenberg, S. N., and P. H. Nadeau (2005), Sandstone vs. carbonate petroleum reservoirs: A global perspective on porosity-depth and porosity-permeability relationships, *Am. Assoc. Pet. Geol. Bull.*, *89*(4), 435–445, doi:10.1306/11230404071.
Epstein, A. G., J. B. Epstein, and L. D. Harris (1977), Conodont color alteration - an index to organic metamorphism, *USGS Prof. Pap.*, *995*, 27pp, doi:10.1130/0016-7606(1987)99<471:CCATAA>2.0.CO;2.
Evans, N. J., B. I. A. McInnes, A. P. Squelch, P. J. Austin, B. J. McDonald, and Q. Wu (2008), Application of X-ray micro-computed tomography in (U-Th)/He thermochronology, *Chem. Geol.*, *257*(1-2), 101–113, doi:10.1016/j.chemgeo.2008.08.021.
Farley, K. A. (2002), (U-Th)/He Dating: Techniques, Calibrations, and Applications, *Rev. Mineral. Geochemistry*, *47*(1), 819–844, doi:10.2138/rmg.2002.47.18.
Farley, K. A., R. A. Wolf, and L. T. Silver (1996), The effects of long alpha-stopping distances on (U-Th)/He ages, *Geochim. Cosmochim. Acta*, *60*(21), 4223–4229.
Faure, S., A. Tremblay, M. Malo, and J. Angelier (2006), Paleostress analysis of Atlantic crustal extension in the Quebec Appalachians, *J. Geol.*, *114*(4), 435–448, doi:10.1086/504178.
Flowers, R. M., D. L. Shuster, B. P. Wernicke, and K. A. Farley (2007), Radiation damage control on apatite (U-Th)/He dates from the Grand Canyon region, Colorado Plateau, *Geol.,* 35, 447-450.
Flowers, R. M., R. A. Ketcham, D. L. Shuster, and K. A. Farley (2009), Apatite (U-Th)/He thermochronometry using a radiation damage accumulation and annealing model, *Geochim. Cosmochim. Acta*, *73*(8), 2347–2365, doi:10.1016/j.gca.2009.01.015.
Gautheron, C., L. Tassan-Got, J. Barbarand, and M. Pagel (2009), Effect of alpha-damage annealing on apatite (U-Th)/He thermochronology, *Chem. Geol.*, *266*(3-4), 166–179, doi:10.1016/j.chemgeo.2009.06.001.
Gautheron, C., J. Barbarand, R. A. Ketcham, L. Tassan-Got, P. Van Der Beek, M. Pagel, R. Pinna-Jamme, F. Couffignal, and M. Fialin (2013), Chemical influence on α-recoil damage annealing in apatite: Implications for (U-Th)/He dating, *Chem. Geol.*, *351*(August 2013), 257–267, doi:10.1016/j.chemgeo.2013.05.027.
Green, P. F. (1981), A new look at statistics in fission-track dating, *Nucl. Tracks*, *5*(1-2), 77–86, doi:10.1016/0191-278X(81)90029-9.
Green, P. F. (1988), The relationship between track shortening and fission track age reduction in apatite: combined influences of inherent instability, annealing anisotropy, length bias and system calibration, *Earth Planet. Sci. Lett.*, *89*(3-4), 335–352, doi:10.1016/0012-821X(88)90121-5.
Green, P. F., I. R. Duddy, A. J. W. Gleadow, P. R. Tingate, and G. M. Laslett (1986), Thermal annealing of fission tracks in apatite 1. Variable temperature behaviour, *Chem. Geol. Isot. Geosci. Sect.*, *59*, 237–253, doi:10.1016/0168-9622(88)90019-X.

Guenthner, W. R., P. W. Reiners, R. A. Ketcham, L. Nasdala, and G. Giester (2013), Helium diffusion in natural zircon: Radiation damage, anisotropy, and the interpretation of zircon (U-Th)/He thermochronology, *Am. J. Sci.*, *313*(3), 145–198, doi:10.2475/03.2013.01.

Hasebe, N., J. Barbarand, K. Jarvis, A. Carter, and A. J. Hurford (2004), Apatite fission-track chronometry using laser ablation ICP-MS, *Chem. Geol.*, *207*(3-4), 135–145, doi:10.1016/j.chemgeo.2004.01.007.

Hayward, N., S. A. Dehler, and G. N. Oakey (2001), The structure of the northeastern Gulf of St . Lawrence, Canada: new insight from geophysical data analysis, *Can. J. Earth Sci.*, *38*, 1495–1516, doi:10.1139/cjes-38-11-1495.

Herman, F., J. Braun, T. J. Senden, and W. J. Dunlap (2007), (U-Th)/He thermochronometry: Mapping 3D geometry using micro-X-ray tomography and solving the associated production-diffusion equation, *Chem. Geol.*, *242*(1-2), 126–136, doi:10.1016/j.chemgeo.2007.03.009.

Jeppsson, L., R. Anehus, and D. Fredholm (1999), The optimal acetate buffered acetic acid Technique for extracting phosphatic fossils, *J. Paleontol.*, *73*(5), 964–972.

Ketcham, R. A. (2005a), Computational methods for quantitative analysis of three-dimensional features in geological specimens, *Geosphere*, *1*(1), 32–41, doi:10.1130/GES00001.1.

Ketcham, R. A. (2005b), Forward and Inverse Modeling of Low-Temperature Thermochronometry Data, *Rev. Mineral. Geochemistry*, *58*(1), 275–314, doi:10.2138/rmg.2005.58.11.

Ketcham, R. A. (2005c), Three-dimensional grain fabric measurements using high-resolution X-ray computed tomography, *J. Struct. Geol.*, *27*(7), 1217–1228, doi:10.1016/j.jsg.2005.02.006.

Ketcham, R. A., R. A. Donelick, and W. D. Carlson (1999), Variability of apatite fission-track anneling kinetics: III. Extrapolation to geological time scales, *Am. Mineral.*, *84*, 1235–1255.

Ketcham, R. A., A. Carter, R. A. Donelick, J. Barbarand, and A. J. Hurford (2007), Improved modeling of fission-track annealing in apatite, *Am. Mineral.*, *92*(5-6), 799–810, doi:10.2138/am.2007.2281.

Ketcham, R. A., C. Gautheron, and L. Tassan-Got (2011), Accounting for long alpha-particle stopping distances in (U-Th-Sm)/He geochronology: Refinement of the baseline case, *Geochim. Cosmochim. Acta*, *75*(24), 7779–7791, doi:10.1016/j.gca.2011.10.011.

Königshof, P. (2003), Conodont deformation patterns and textural alteration in Paleozoic conodonts: examples from Germany and France, *Senckenbergiana lethaea*, *83*, 149–156, doi:10.1007/BF03043310.

Landman, R. L., R. M. Flowers, N. A. Rosenau, and J. Powell (2016), Conodont (U-Th)/He thermochronology: A case study from the Illinois Basin, *Earth Planet. Sci. Lett.*, *456*, 55–65, doi:10.1016/j.epsl.2016.10.003.

Lavoie, D. (2008), Appalachian foreland basin of Canada, in *Sedimentary Basins of the World, Vol 5, The Sedimentary Basins of the United States and Canada*, edited by A. D. Miall, pp. 65–103, Elsevier, Amsterdam.

Lavoie, D., and G. Chi (2010), Lower Paleozoic foreland basins in eastern Canada: Tectono-thermal events recorded by faults, fluids and hydrothermal dolomites, *Bull. Can. Pet. Geol.*, *58*(1), 17–35, doi:10.2113/gscpgbull.58.1.17.

Lavoie, D., G. Chi, P. Brennan-Alpert, A. Desrochers, and R. Bertrand (2005), Hydrothermal dolomitization in the Lower Ordovician Romaine Formation of the Anticosti Basin: Significance for hydrocarbon exploration, *Bull. Can. Pet. Geol.*, *53*(4), 454–472,

doi:10.2113/53.4.454.
Long, D. G. F. (2007), Tempestite frequency curves: a key to Late Ordovician and Early Silurian subsidence, sea-level change and orbital forcing in the Anticosti forelans basin, Quebec, Canada, *Can. J. Earth Sci.*, *44*, 413–431.
Lynch, G., and A. M. Grist (2002), Thermal Modelling of the Laurentian Margin Beneath Anticosti Island using AFTA , 1D Well Profiles , and Bulk Fluid Inclusions, in *Canadian Society of Petroleum Geologists, Diamond Jubilee Convention, Calgary 2002. Programs with Abstracts*, p. 210.
Marcil, J. S., P. K. Dorrins, J. Lavoie, and N. Mechti (2014), Anticosti Island, Quebec: Compelling data for a deep fairway Utica-equivalent oil, in *Unconventional Resources Technology Conference (URTeC), Denver*.
Marillier, F., and J. Verhoef (1989), Crustal thickness under the Gulf of St. Lawrence, Northern Appalachians, from gravity and deep seismic data, *Can. J. Earth Sci.*, *26*(8), 1517–1532.
McCracken, A. D., and C. R. Barnes (1981), Conodont biostratigraphy and paleoecology of the Ellis Bay Formation, Anticosti Island, Quebec, *Geol. Surv. Canada Bull.*, *329*, 51–134.
McLaughlin, P. I. et al. (2016), Refining 2 km of ordovician chronostratigraphy beneath anticosti island utilizing integrated chemostratigraphy, *Can. J. Earth Sci.*, *53*(8), 1–10, doi:10.1139/cjes-2015-0242.
Millard, A. R., and R. E. M. Hedges (1996), A diffusion-adsorption model of uranium uptake by archaeological bone, *Geochim. Cosmochim. Acta*, *60*(12), 2139–2152, doi:10.1016/0016-7037(96)00050-6.
Murray, K. E., D. A. Orme, and P. W. Reiners (2014), Effects of U-Th-rich grain boundary phases on apatite helium ages, *Chem. Geol.*, *390*, 135–151, doi:10.1016/j.chemgeo.2014.09.023.
Naeser, C. W. (1967), The use of apatite and sphene for fission track age determinations, *Bull. Geol. Soc. Am.*, *78*, 1523–1526.
Nowlan, G. S., and C. R. Barnes (1981), Late Ordovician conodonts from the Vauréal Formation, Anticosti Island, Quebec, *Geol. Surv. Canada Bull.*, *329*, 1–49.
Ogg, J. G., G. M. Ogg, and F. M. Gradstein (2016), Ordovician, in *A Concise Geologic Time Scale 2016*, edited by J. G. Ogg, G. M. Ogg, and F. M. Gradstein, pp. 57–69, Elsevier B.V.
Pe-Piper, G., and D. J. W. Piper (1999), Were Jurassic tholeiitic lavas originally widespread in southeastern Canada?: a test of the broad terrane hypothesis, *Can. J. Earth Sci.*, *36*, 1509–1516, doi:10.1139/cjes-36-9-1509.
Peppe, D. J., and P. W. Reiners (2007), Conodont (U–Th)/He thermochronology: Initial results, potential, and problems, *Earth Planet. Sci. Lett.*, *258*(3-4), 569–580, doi:10.1016/j.epsl.2007.04.022.
Pietzner, H., J. Vahl, H. Werner, and W. Ziegler (1968), Zur chemischen zusammensetzung und mikromorphologie der Conodonten, *Paleontographica*, *128*(A), 115–152.
Pike, A. W. G., and R. E. M. Hedges (2001), Sample geometry and U uptake in archaeological teeth: Implications for U-series and ESR dating, *Quat. Sci. Rev.*, *20*(5-9), 1021–1025, doi:10.1016/S0277-3791(00)00063-9.
Pinet, N. (2016), Southern continuation of the Wakeham Group and Robe-Noire mafic suite (eastern Grenville Province) from hydrocarbon-targeted seismic reflection data on Anticosti Island, Quebec, Canada 1, *Can. J. Earth Sci.*, *53*(9), 875–882, doi:10.1139/cjes-2016-0011.
Pinet, N., P. Keating, D. Lavoie, J. Dietrich, M. J. Duchesne, and V. Brake (2012), Revisiting the Appalachian structural front and offshore Anticosti Basin (northern Gulf of St. Lawrence,

Canada) by integrating old and new geophysical datasets, *Mar. Pet. Geol.*, *32*(1), 50–62, doi:10.1016/j.marpetgeo.2011.12.004.

Powell, J., D. Schneider, D. Stockli, and K. Fallas (2016), Zircon (U-Th)/He thermochronology of Neoproterozoic strata from the Mackenzie Mountains, Canada: Implications for the Phanerozoic exhumation and deformation history of the northern Canadian Cordillera, *Tectonics*, *35*(3), 663–689, doi:10.1002/2015TC003989.

Powell, J., D. A. Schneider, and D. R. Issler (2017), Application of multi-kinetic apatite fission track and (U-Th)/He thermochronology to source rock thermal history: a case study from the Mackenzie Plain, NWT, Canada, *Basin Res.*, doi:10.1111/bre.12233.

Powell, J., D. Issler, D. Schneider, and K. Fallas (n.d.), Thermal history of the Mackenzie Plain, NWT, Canada: insights from low-temperature thermochronology of the Devonian Imperial Formation, *Basin Res.*

Purnell, M., P. Donoghue, and R. Aldridge (2000), Orientation and anatomical notation in conodonts, *J. Paleontol.*, *74*(1), 113–122, doi:10.1666/0022-3360(2000)074<0113:OAANIC>2.0.CO;2.

Quinn, L., A. R. Bashforth, E. T. Burden, H. Gillespie, R. K. Springer, and S. H. Williams (2004), The Red Island Road Formation: Early Devonian terrestrial fill in the Anticosti Foreland Basin, western Newfoundland, *Can. J. Earth Sci.*, *41*(5), 587–602, doi:10.1139/e04-021.

Rejebian, V. A., A. G. Harris, and J. S. Huebner (1987), Conodont color and textural alteration: an index To regional metamorphism, contact metamorphism, and hydrothermal alteration, *Bull. Geol. Soc. Am.*, *99*(4), 471–479, doi:10.1130/0016-7606(1987)99<471:CCATAA>2.0.CO;2.

Sanz-López, J., and S. Blanco-Ferrera (2012), Overgrowths of large authigenic apatite crystals on the surface of conodonts from Cantabrian limestones (Spain), *Facies*, *58*(4), 707–726, doi:10.1007/s10347-012-0295-3.

Shuster, D. L., R. M. Flowers, and K. A. Farley (2006), The influence of natural radiation damage on helium diffusion kinetics in apatite, *Earth Planet. Sci. Lett.*, *249*(3-4), 148–161, doi:10.1016/j.epsl.2006.07.028.

Stockmal, G. S., S. P. Colman-sadd, C. E. Keen, F. Marillier, S. J. O'Brien, and G. M. Quinlan (1990), Deep seismic structure and plate tectonic evolution of the Canadian Appalachians, *Tectonics*, *9*(1), 45–62.

Stockmal, G. S., D. R. Issler, and A. M. Grist (2008), Proceedings from the 11th International Conference on Thermochronometry, in *Proceedings from the 11th International Conference on Thermochronometry*, edited by J. I. Garver and M. J. Montario, pp. 217–218.

Sweet, W. C., and P. C. J. Donoghue (2001), Conodonts: past, present, future, *J. Paleontol.*, *75*(6), 1174–1184, doi:10.1666/0022-3360(2001)075<1174:CPPF>2.0.CO;2.

Tremblay, A., M. K. Roden-Tice, J. A. Brandt, and T. W. Megan (2013), Mesozoic fault reactivation along the st. Lawrence rift system, eastern canada: Thermochronologic evidence from apatite fission-track dating, *Bull. Geol. Soc. Am.*, *125*(5-6), 794–810, doi:10.1130/B30703.1.

Trotter, J. a., and S. M. Eggins (2006), Chemical systematics of conodont apatite determined by laser ablation ICPMS, *Chem. Geol.*, *233*(3-4), 196–216, doi:10.1016/j.chemgeo.2006.03.004.

Trotter, J. A., J. D. Fitz Gerald, H. Kokkonen, and C. R. Barnes (2007), New insights into the ultrastructure, permeability, and integrity of conodont apatite determined by transmission

electron microscopy, *Lethaia*, *40*(2), 97–110, doi:10.1111/j.1502-3931.2007.00024.x.
Vermeesch, P. (2009), RadialPlotter: A Java application for fission track, luminescence and other radial plots, *Radiat. Meas.*, *44*(4), 409–410, doi:10.1016/j.radmeas.2009.05.003.
Wielens, H., and M. Avery (2009), Gulf of St. Lawrence: Source rock data and results of 1D modelling of well data, *Geol. Surv. Canada Open File*.
Williams, H., and R. N. Hiscott (1987), Definition of the Iapetus rift-drift transition in western Newfoundland, *Geology*, *15*(11), 1044, doi:10.1130/0091-7613(1987)15<1044:DOTLRT>2.0.CO;2.
Wolf, R. A., K. A. Farley, and D. M. Kass (1998), Modeling of the temperature sensitivity of the apatite (U–Th/He) thermochronometer, *Chem. Geol.*, (148), 105–114, doi:http://dx.doi.org/10.1016/S0009-2541(98)00024-2.
Wolfe, M. R., and D. F. Stockli (2010), Zircon (U–Th)/He thermochronometry in the KTB drill hole, Germany, and its implications for bulk He diffusion kinetics in zircon, *Earth Planet. Sci. Lett.*, *295*(1-2), 69–82, doi:10.1016/j.epsl.2010.03.025.
Wright, J. (1989), Conodont Apatite: Structure and Geochemistry, *Skelet. Biominer. Patterns, Process. Evol. Trends*, *5*(13821), 149–163, doi:10.1029/SC005p0149.
Zhang, S. X., and C. R. Barnes (2002), A new Llandovery (Early Silurian) conodont biozonation and conodonts from the Becscie, Merrimack, and Gun River formations, Anticosti Island, Quebec, *J. Paleontol.*, *76*(2), 1–46, doi:10.1666/0022-3360(2002)76[1:ANLESC]2.0.CO;2.

Table 1. Single grain (U-Th)/He analyses of apatite and zircon from subsurface samples, Anticosti Island, QC

Sample	Mineral	ESR (μm)	mass (μg)	U (ppm)	Th (ppm)	Sm (ppm)	eU (ppm)	Th/U	He (nmol/g)	Ft	Meas. Age (Ma)	± (Ma)	Corr. Age (Ma)	± (Ma)
D002 LGPL Core														
13JP08, ~1300 m, Mingan Formation sandstone														
a1	apatite	42.1	1.7	2.4	77.6	37.9	20.4	32.7	1.0	0.63	8.6	0.5	13.7	0.8
a2	apatite	32.9	0.8	178.5	29.9	33.6	185.5	0.2	61.5	0.58	61.1	3.7	105.2	6.3
a3	apatite	31.9	0.8	1.5	21.5	22.9	6.5	14.8	0.6	0.53	15.2	0.9	28.8	1.7
a4	apatite	41.9	1.6	1.7	0.3	15.9	1.8	0.2	1.3	0.66	128.5	7.7	194.5	11.7
13JP10, ~1700 m, Grenvillian basement														
a1	apatite	49.8	3.3	10.1	40.3	81.4	19.8	4.0	2.1	0.69	19.3	1.2	28.1	1.7
a2	apatite	53.4	4.0	10.5	38.4	67.4	19.6	3.7	3.7	0.70	34.1	2.0	48.4	2.9
a3	apatite	48.6	2.9	12.9	65.7	70.9	28.4	5.1	2.8	0.68	18.1	1.1	26.7	1.6
a4	apatite	39.8	1.8	19.4	70.7	127.5	36.3	3.7	4.0	0.62	19.7	1.2	32.0	1.9
z1	zircon	64.6	13.4	62.0	31.1	0.5	69.2	0.5	185.5	0.82	474.1	37.9	581.7	46.5
z2	zircon	43.2	4.1	85.0	45.9	1.2	95.6	0.5	252.0	0.73	466.5	37.3	638.3	51.1
z3	zircon	55.5	9.3	76.5	42.1	0.6	86.1	0.6	295.8	0.79	598.4	47.9	761.2	60.9
z4	zircon	48.9	5.0	111.9	54.8	0.4	124.5	0.5	342.4	0.76	485.6	38.8	638.7	51.1
D003 NACP Core														
13JP09, 1520 m, Mingan Formaiton sandstone														
a1	apatite	29.2	0.7	3.5	54.7	48.4	16.3	15.8	0.8	0.49	8.7	0.5	17.7	1.1
a2	apatite	36.7	1.2	2.7	53.7	89.9	15.5	20.2	2.2	0.58	24.7	1.5	42.6	2.6
a3	apatite	37.4	1.3	13.1	41.8	42.1	22.9	3.2	3.0	0.60	23.5	1.4	39.5	2.4
a4	apatite	46.3	2.2	13.8	177.0	54.2	54.9	12.8	12.7	0.66	41.9	2.5	63.6	3.8

Note: Corr. Age is the measured (U-Th)/He age, corrected for the effects of alpha ejection (Ft correction; Farley 1996). Error Is the 6% error for apatite and 8% err for zircon. eU = [U]+(0.235*[Th]). ESR is the equivalent radius of a sphere with the same SA/V ratio of the measured apatite grain

Table 2. Single grain (U-Th)/He analyses of conodonts from subsurface samples, Anticosti Island, QC

Sample	Morphology Type	ESR (μm)	mass (μg)	U (ppm)	±	Th (ppm)	±	Sm (ppm)	±	eU (ppm)	Th/U	He (nmol/g)	±	Meas. Age (Ma)	±	Micro CT	Ft	Corr. Age (Ma)	±
D002 LGPL Core																			
13JP07, ~1685 m, Romaine Formation																			
c1	Type 2	63.2	13.4	1.71	0.07	5.94	0.06	0.00	0.00	3.1	3.5	13.10	0.02	743.9	17.1	y	0.77	963.9	71.0
c2	Type 1	53.7	10.7	0.24	0.08	4.06	0.06	0.00	0.00	1.2	17.2	33.31	0.21	4344.6	303.3	y	0.72	6060.1	683.0
c3	Type 2	56.8	7.6	1.16	0.12	4.84	0.06	0.00	0.00	2.3	4.2	16.14	0.02	1205.8	63.3	y	0.74	1621.1	279.1
c4	Type 1	69.0	17.5	0.00	0.00	0.00	0.00	0.00	0.00	0.0	0.0	15.82	0.01	0.0	0.0	y	0.80	-	-
c5	Type 2	26.1	1.3	5.46	0.73	45.43	0.79	0.00	0.00	16.1	8.3	37.92	0.10	424.5	19.0	y	0.45	939.0	78.1
c6	Type 1	42.4	5.4	1.20	0.10	4.25	0.18	0.23	0.34	2.2	3.5	6.93	0.01	563.0	27.6	-	0.62	902.6	106.4
c7	Type 1	54.0	13.7	7.64	0.20	5.06	0.05	1.35	0.14	8.8	0.7	9.32	0.01	192.4	4.2	-	0.72	266.6	19.6
c8	Type 1	49.5	9.5	23.97	0.44	17.79	0.21	3.71	0.25	28.2	0.7	29.89	0.02	193.5	3.0	-	0.68	283.1	20.3
c9	Type 5	79.7	36.3	1.45	0.02	0.98	0.01	0.44	0.05	1.7	0.7	9.78	0.01	989.5	14.0	-	0.81	1216.2	86.9
c10	Type 1	90.6	11.1	8.53	0.25	1.75	0.06	0.54	0.19	8.9	0.2	35.86	0.03	697.9	18.9	-	0.88	791.5	59.4
c11	Type 1	92.3	142.3	1.37	0.04	3.42	0.04	0.23	0.02	2.2	2.5	5.14	0.00	424.3	8.3	-	0.89	476.7	34.6
c12	Type 2	45.4	11.4	18.83	0.33	40.51	0.69	5.00	0.22	28.4	2.2	73.03	0.04	460.7	5.9	-	0.67	692.2	49.2
c13	Type 2	68.1	44.1	14.29	0.17	15.36	0.20	1.20	0.06	17.9	1.1	26.42	0.02	267.7	2.6	-	0.76	352.4	24.9
c14	Type 1	56.1	11.2	1.88	0.06	3.82	0.12	0.56	0.13	2.8	2.0	15.809	0.02	976.1	23.7	y	0.75	1274.6	95.6
c15	Type 1	46.4	7.5	0.41	0.03	0.59	0.02	0.04	0.09	0.6	1.4	8.588	0.01	2317.2	110.9	y	0.70	3028.0	265.0
D003 NACP Core																			
13JP01, 35 m, Becksie Formation																			
c1	Type 1	32.0	2.8	4.05	0.13	74.29	1.10	5.60	0.40	21.5	18.4	2.84	0.01	24.2	0.3	y	0.57	42.7	5.4
c2	Type 4	39.3	6.8	0.17	0.02	2.15	0.07	0.49	0.08	0.7	12.3	1.56	0.00	412.3	15.3	y	0.64	643.0	51.0
c3	Type 4	35.5	3.3	0.97	0.04	4.02	0.10	0.78	0.27	1.9	4.1	0.76	0.01	72.6	1.7	y	0.62	117.6	13.2
c4	Type 1	35.4	2.7	1.40	0.07	6.69	0.06	0.64	0.37	3.0	4.8	0.52	0.01	32.1	0.8	y	0.62	51.3	6.8
c5	Type 1	31.5	2.9	3.93	0.15	64.23	0.91	6.71	0.27	19.0	16.3	2.41	0.01	23.2	0.3	y	0.57	40.8	5.2
13JP02, 320 m, Vaureal Formation																			
c1	Type 1	58.8	16.2	2.24	0.06	9.83	0.08	3.97	2.49	4.6	4.4	1.44	0.00	57.9	0.9	y	0.75	77.2	5.5
c2	Type 2	72.2	50.2	0.42	0.02	0.29	0.01	0.00	0.00	0.5	0.7	1.38	0.00	504.5	22.7	y	0.81	624.5	52.0
c3	type 1	123.4	108.8	0.08	0.01	0.42	0.00	0.00	0.00	0.2	5.1	0.73	0.00	707.4	32.5	y	0.88	803.8	67.3
c4	Type 1	97.2	31.8	0.02	0.03	0.44	0.00	0.00	0.00	0.1	21.3	2.30	0.00	3023.4	655.7	y	0.84	3601.0	820.6
c5	Type 3	64.2	28.3	1.84	0.05	6.92	0.09	1.84	1.42	3.5	3.8	2.87	0.01	151.3	2.4	y	0.77	196.2	14.1

Sample	Morphology Type	ESR (μm)	mass (μg)	U (ppm)	±	Th (ppm)	±	Sm (ppm)	±	eU (ppm)	Th/U	He (nmol/g)	±	Meas. Age (Ma)	±	Micro CT	Ft	Corr. Age (Ma)	±
c6	Type 5	85.6	60.4	0.02	0.02	0.40	0.01	0.00	0.00	0.1	18.6	1.15	0.00	1734.5	220.3	y	0.82	2112.7	306.4
c7	Type 4	58.0	12.2	0.00	0.00	0.19	0.00	0.00	0.00	0.0	0.0	2.69	0.06	8897.8	14191.2	y	0.70	-	-
c8	Type 1	33.1	1.7	2.81	0.53	23.27	0.35	0.00	0.00	8.3	8.3	3.16	0.02	70.2	4.4	y	0.56	125.8	11.8
c9	Type 5	73.2	20.1	0.01	0.05	1.68	0.02	0.00	0.00	0.4	167.2	1.38	0.00	616.2	66.6	y	0.78	785.5	101.1
c10	Type 1	74.0	9.0	0.84	0.10	6.78	0.09	0.00	0.00	2.4	8.0	2.46	0.01	184.8	7.8	y	0.80	232.1	19.0
c11	Type 3	30.3	2.3	3.23	0.24	35.17	0.77	5.66	0.81	11.5	10.9	5.47	0.02	87.0	2.2	-	0.55	158.9	50.7
c12	Type 1	40.0	1.5	1.20	0.27	12.73	0.29	8.57	1.34	4.2	10.6	3.25	0.02	139.6	8.9	-	0.60	231.5	32.4
c13	Type 4	63.7	29.6	0.11	0.01	0.58	0.02	0.19	0.07	0.3	5.0	0.36	0.00	261.5	13.4	-	0.80	325.6	28.3
c14	Type 1	30.3	5.7	0.81	0.10	15.71	0.19	8.58	0.57	4.5	19.5	1.64	0.01	65.9	1.6	-	0.53	123.8	31.4
c15	Type 4	52.0	11.6	0.20	0.04	0.30	0.01	0.52	0.17	0.3	1.5	1.16	0.00	749.1	93.8	-	0.70	1063.8	152.6
c16	Type 4	34.1	2.8	0.05	0.13	2.52	0.06	1.08	0.65	0.6	50.2	0.29	0.01	82.6	16.1	-	0.55	149.1	39.8
c17	Type 5	94.5	43.5	1.10	0.03	27.47	0.40	5.54	0.07	7.6	25.1	1.634	0.00	39.5	0.5	y	0.84	47.1	3.2
c18	Type 2	74.7	39.0	0.69	0.02	0.53	0.01	1.17	0.10	0.8	0.8	1.300	0.00	284.6	6.1	y	0.81	347.4	24.1
c19	Type 5	81.8	22.8	0.51	0.02	1.28	0.02	0.76	0.05	0.8	2.5	2.663	0.00	579.2	15.6	y	0.82	695.2	49.7
c20	Type 5	60.2	14.2	0.35	0.02	1.20	0.02	1.00	0.03	0.6	3.4	3.109	0.00	847.6	24.1	y	0.76	1094.2	77.0
13JP03, 620 m, Vaureal Formation																			
c1	Type 1	34.6	4.8	1.09	0.03	5.43	0.07	3.56	0.31	2.4	5.0	1.74	0.00	133.3	2.0	y	0.60	223.3	36.9
c2	Type 4	53.7	11.9	0.41	0.02	3.95	0.10	1.62	0.26	1.3	9.6	3.11	0.00	415.0	8.8	y	0.73	568.8	41.6
c3	Type 3	36.1	5.0	0.28	0.02	3.55	0.06	1.02	0.14	1.1	12.8	2.82	0.01	454.0	10.4	y	0.61	746.3	70.8
c4	Type 1	37.8	4.5	0.82	0.06	9.74	0.10	3.80	0.29	3.1	11.9	1.79	0.01	104.6	2.0	y	0.62	168.9	33.1
c5	Type 5	50.9	11.7	0.05	0.01	0.67	0.02	0.11	0.05	0.2	12.2	0.67	0.01	564.3	22.0	y	0.71	794.0	79.9
c6	Type 5	53.5	10.7	1.14	0.02	16.22	0.32	10.82	0.19	4.9	14.3	2.37	0.00	86.4	1.4	y	0.72	119.2	8.6
c7	Type 3	59.9	18.9	0.00	0.00	4.52	0.08	0.09	0.03	1.1	0.0	2.75	0.00	470.0	8.6	y	0.78	605.4	43.8
c8	Type 1	58.8	25.3	1.67	0.06	14.60	0.32	5.02	0.25	5.1	8.8	2.044	0.00	73.1	1.4	y	0.75	96.8	6.6
c9	Type 1	70.7	53.1	0.24	0.01	0.70	0.02	0.59	0.05	0.4	2.9	1.642	0.00	711.6	14.5	y	0.80	875.9	61.8
c10	Type 4	57.1	12.8	2.09	0.06	80.94	1.30	21.30	0.36	21.1	38.7	0.227	0.00	2.0	0.0	y	0.74	2.7	0.2
13JP05, 1240 m, Mingan Formation																			
c1	Type 1	78.4	10.7	0.00	0.00	4.86	0.04	0.02	0.02	1.1	0.0	3.59	0.01	570.0	5.8	y	0.82	696.1	49.2
c2	Type 1	45.5	6.9	0.00	0.00	0.09	0.00	0.03	0.10	0.0	0.0	0.05	0.00	424.3	136.5	y	0.65	652.9	217.6
c3	Type 1	34.8	0.4	42.75	1.08	107.59	1.80	156.88	11.45	68.0	2.5	2.41	0.04	6.4	0.1	y	0.56	11.4	2.2

Sample	Morphology Type	ESR (μm)	mass (μg)	U (ppm)	±	Th (ppm)	±	Sm (ppm)	±	eU (ppm)	Th/U	He (nmol/g)	±	Meas. Age (Ma)	±	Micro CT	Ft	Corr. Age (Ma)	±
13JP06, 1580 m, Romaine Formation																			
c1	Type 5	84.1	53.4	1.39	0.02	10.03	0.09	1.84	0.03	3.7	7.2	13.91	0.01	659.1	4.8	y	0.82	803.7	56.6
c2	Type 1	65.3	22.0	2.45	0.05	23.91	0.17	2.26	0.09	8.1	9.8	9.25	0.01	208.7	1.6	y	0.77	271.0	19.1
c3	Type 1	78.4	26.8	0.01	0.00	1.41	0.03	0.11	0.03	0.3	126.9	7.76	0.01	3707.2	72.8	y	0.80	-	-
c4	Type 1	93.7	22.3	0.17	0.01	9.73	0.13	5.80	0.15	2.5	56.3	0.29	0.00	21.1	0.3	y	0.83	25.3	1.8
c5	Type 1	44.6	1.6	9.61	0.31	184.45	3.08	38.61	1.73	53.0	19.2	22.00	0.03	75.8	1.1	-	0.64	117.6	16.6
c6	Type 1	56.2	23.0	1.41	0.04	27.70	0.44	3.07	0.21	7.9	19.7	10.82	0.01	248.5	3.5	-	0.72	345.0	24.6
c7	Type 4	30.0	2.0	3.87	0.23	35.62	0.49	7.93	0.99	12.2	9.2	17.31	0.02	256.4	5.2	-	0.52	494.3	112.9
c8	Type 1	28.5	6.9	1.17	0.08	9.81	0.35	1.83	0.28	3.5	8.4	7.12	0.01	369.4	12.1	-	0.52	711.8	200.3
c9	Type 3	69.3	21.4	1.63	0.05	61.51	1.34	10.22	0.39	16.1	37.6	11.838	0.04	134.0	2.7	y	0.78	172.2	12.5
c10	Type 1	70.0	18.4	3.31	0.09	48.07	0.69	4.62	0.09	14.6	14.5	11.141	0.02	139.3	1.8	y	0.78	177.5	12.0

Note: Morphology type relates to the ways in which conodont elements were grouped (Fig. A1). MicroCT indicates whether or not x-ray micro-computed tomography was utilized to calculate volume, size and Ft correction. If conodonts were not analyzed via MicroCT, these values were estimated on the basis of MicroCT-derived relationships for varying morphologies (see Appendix). Corr. Age is the measured (U-Th)/He age, corrected for the effects of alpha ejection. eU = [U]+(0.235*[Th]). ESR is the equivalent radius of a sphere with the same SA/V ratio of the measured conodont

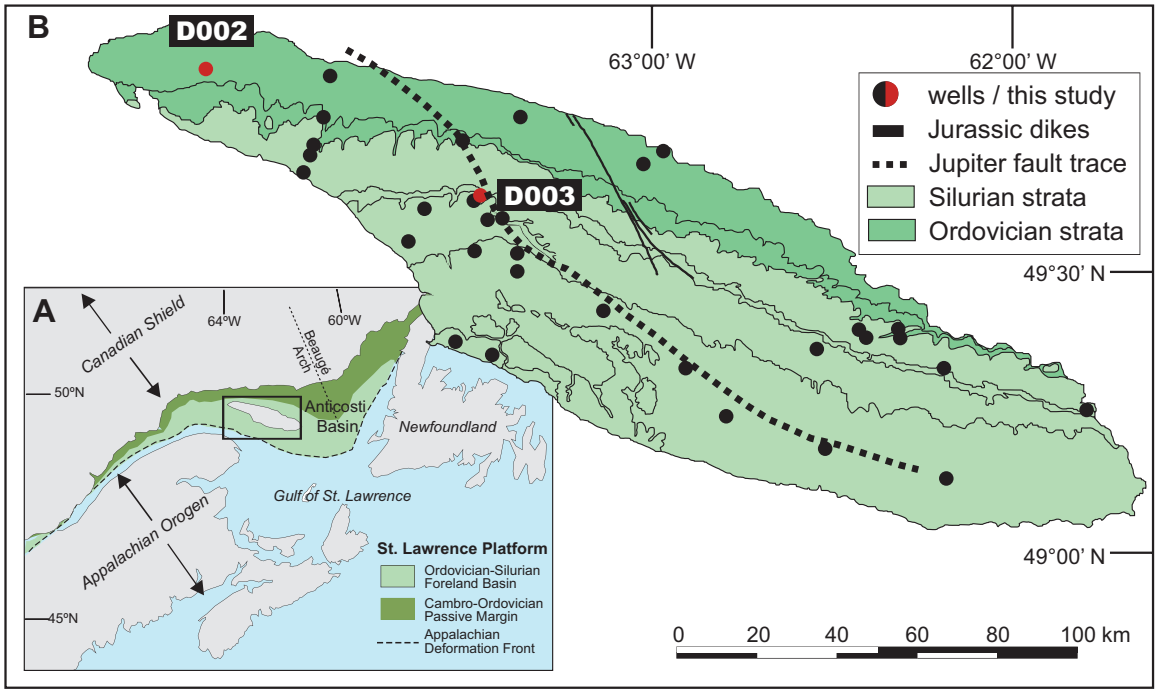

Fig. 1: **A)** Map highlighting the geologic framework of the Gulf of the St. Lawrence. All landmasses are shown in gray. Study area (black box) is expanded in B. **B)** Bedrock geology of Anticosti Island (modified after *Desrochers and Gauthier*, 2010). Wells sampled in this study are highlighted in red. See Fig. 2 for the color scheme of the bedrock.

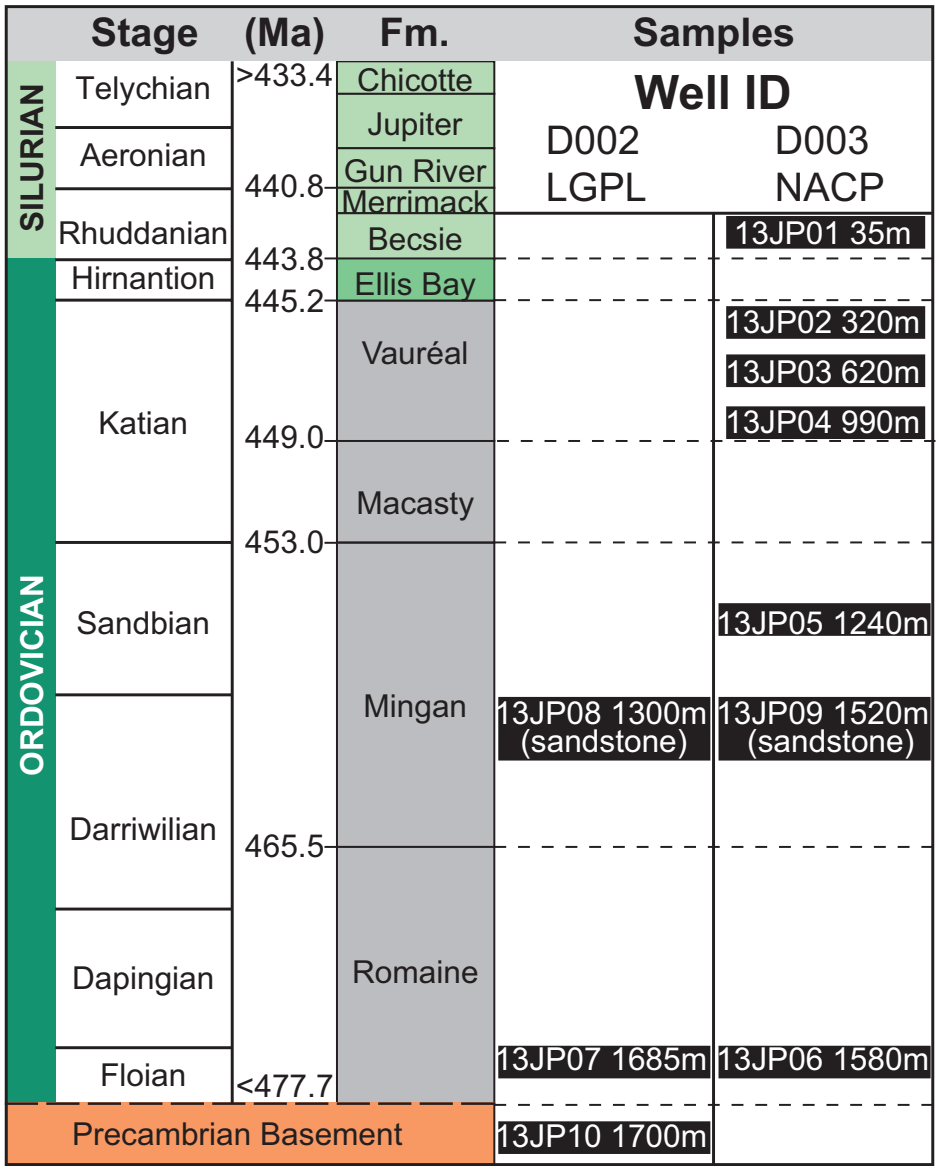

Fig. 2: Anticosti Island stratigraphic column [*McLaughlin et al.*, 2016; *Ogg et al.*, 2016]. Formation colours in green correspond to bedrock geology map of Fig. 1B, whereas those coloured gray are only present in the Anticosti Island subsurface. Sample names, depths and their corresponding wells are highlighted in the right-hand columns.

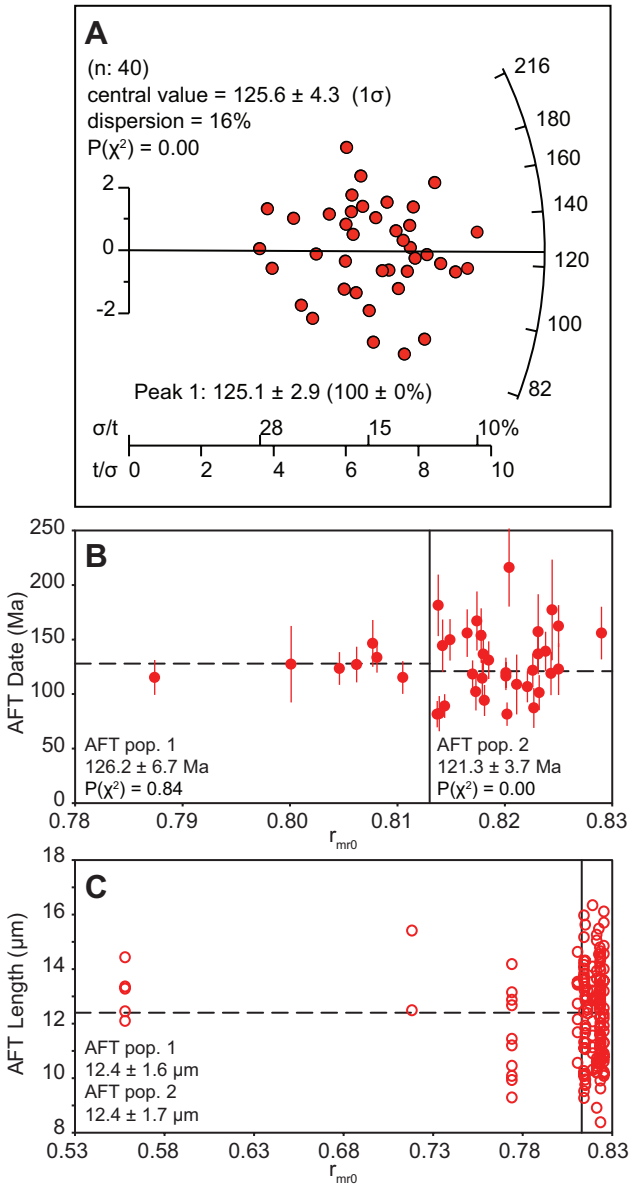

Fig. 3: AFT data for sample 13JP10 from the Grenvillian basement of well LGPL D002. **A)** radial plot of the AFT dates created using RadialPlotter [*Vermeesch*, 2009]. Fission track dates and errors are plotted as a function of the degree of rotation along, and distance from, the curved axis. AFT data fail the χ^2 test ($P(\chi^2) < 0.05$) indicating that the data do not comprise a single, statistically significant population. **B)** AFT dates as a function of the kinetic parameter r_{mr0}. Solid black line indicates the kinetic boundary (0.813 r_{mr0}) that separates an AFT population that passes the χ^2test (AFT population 1), from one that fails (AFT population 2). Dashed line indicates the pooled age for each population. **C)** AFT lengths as a function of kinetic parameter r_{mr0}. Dashed line indicates the mean track length for both populations. Note the x-axis scale is different from B. Tables containing the AFT dates, lengths and chemistry can be retrieved from the Appendix to this Chapter.

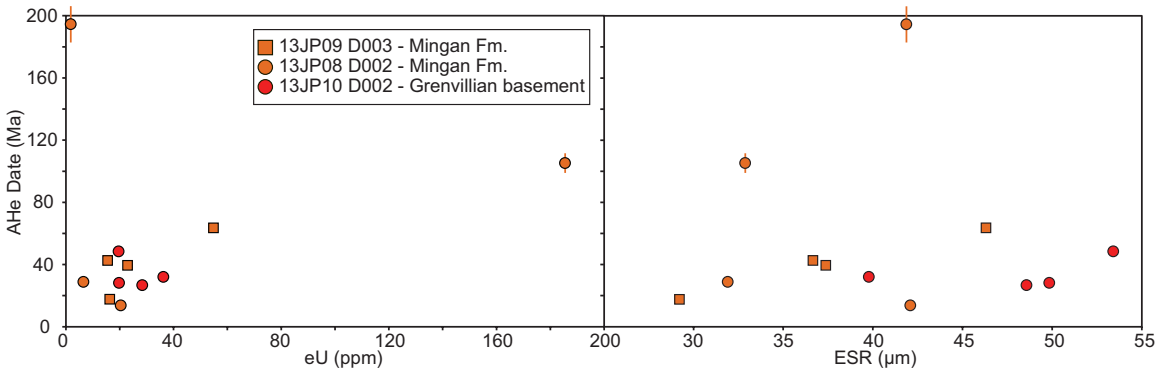

Fig. 4: Alpha ejection-corrected AHe data plotted against effective uranium concentration (eU) and equivalent spherical radius (ESR).

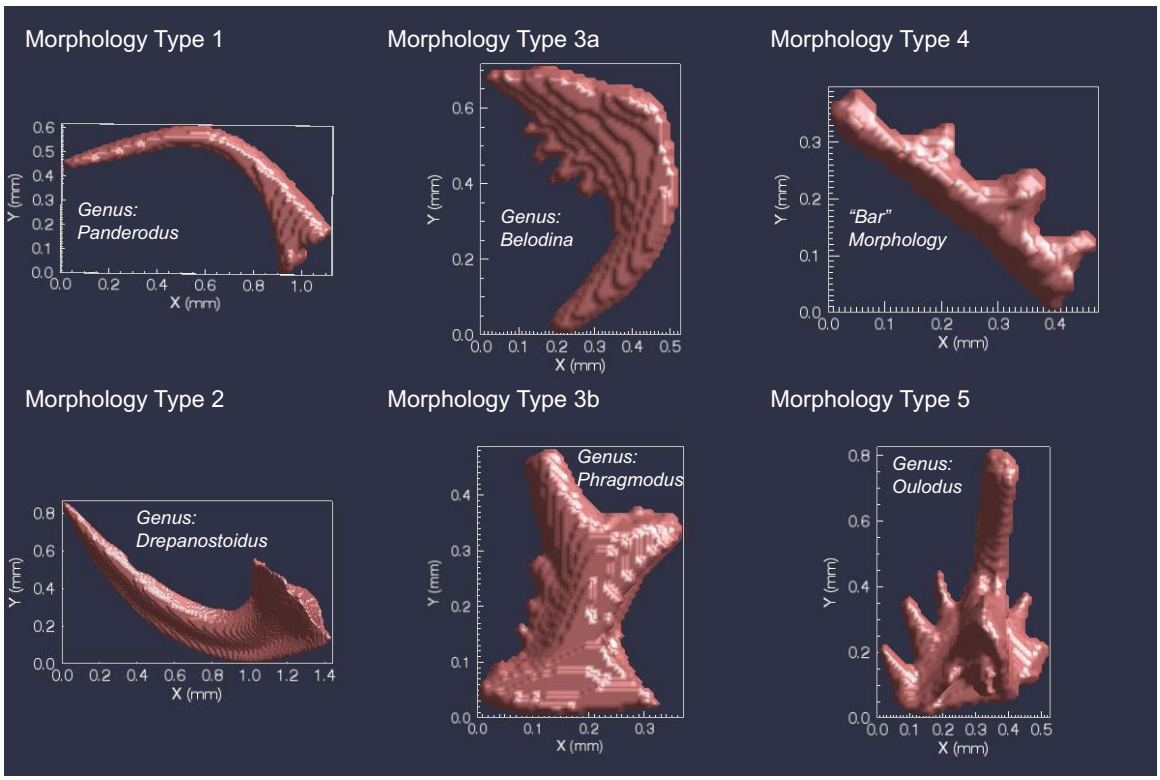

Fig. 5: Examples of conodont morphologies and corresponding genera utilized in this study. Images created from microCT data using the program Blob3D [*Ketcham*, 2005a]. Corresponding MicroCT data available in the Appendix to this Chapter (Table A4; Figs. A1 – A9).

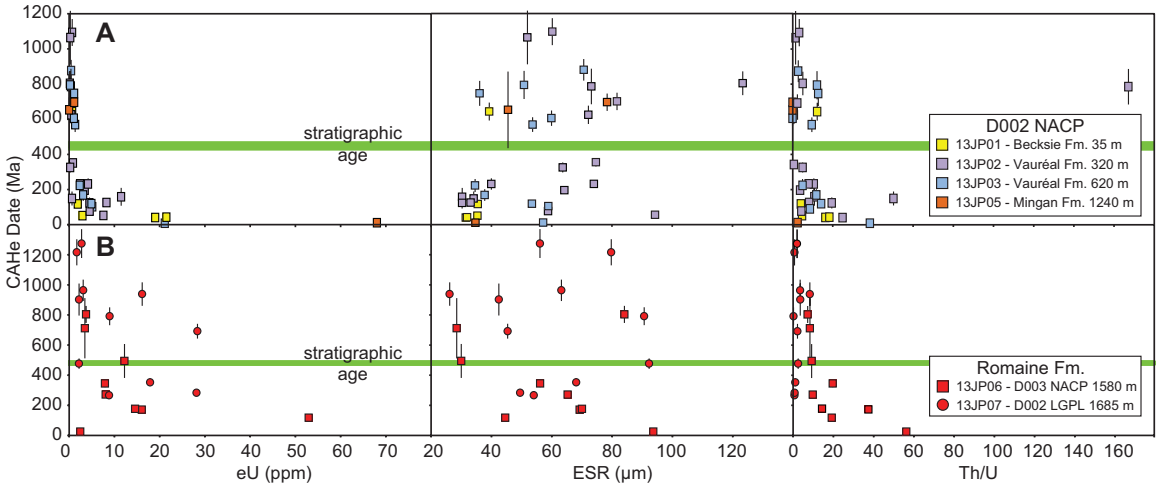

Fig. 6: Alpha ejection-corrected CAHe dates as a function of effective uranium concentration (eU), equivalent spherical radius (ESR) and Th/U for **A)** Becsie, Vauréal and Mingan formation samples, and **B)** Romaine Formation samples. Horizontal green line indicates the stratigraphic age of the units. CAHe dates older than 1400 Ma are not displayed.

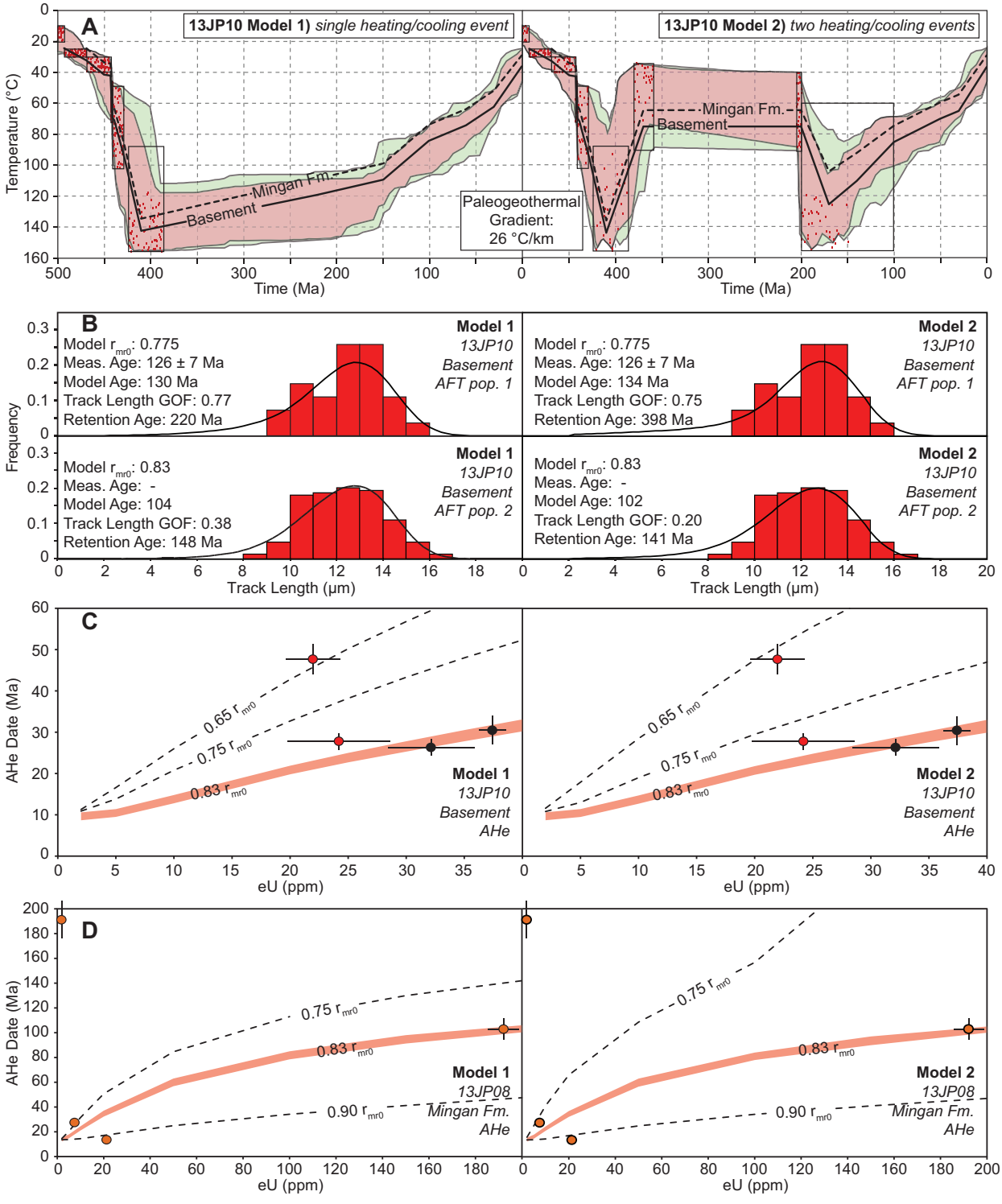
A
13JP10 Model 1) single heating/cooling event
13JP10 Model 2) two heating/cooling events
Temperature (°C)
Time (Ma)
Mingan Fm.
Basement
Paleogeothermal Gradient: 26 °C/km
B
Model 1
13JP10
Basement
AFT pop. 1
Model r$_{mr0}$: 0.775
Meas. Age: 126 ± 7 Ma
Model Age: 130 Ma
Track Length GOF: 0.77
Retention Age: 220 Ma
Model 2
13JP10
Basement
AFT pop. 1
Model r$_{mr0}$: 0.775
Meas. Age: 126 ± 7 Ma
Model Age: 134 Ma
Track Length GOF: 0.75
Retention Age: 398 Ma
Model 1
13JP10
Basement
AFT pop. 2
Model r$_{mr0}$: 0.83
Meas. Age: -
Model Age: 104
Track Length GOF: 0.38
Retention Age: 148 Ma
Model 2
13JP10
Basement
AFT pop. 2
Model r$_{mr0}$: 0.83
Meas. Age: -
Model Age: 102
Track Length GOF: 0.20
Retention Age: 141 Ma
Frequency
Track Length (µm)
C
0.65 r$_{mr0}$
0.75 r$_{mr0}$
0.83 r$_{mr0}$
Model 1
13JP10
Basement
AHe
Model 2
13JP10
Basement
AHe
AHe Date (Ma)
eU (ppm)
D
0.75 r$_{mr0}$
0.83 r$_{mr0}$
0.90 r$_{mr0}$
Model 1
13JP08
Mingan Fm.
AHe
Model 2
13JP08
Mingan Fm.
AHe
AHe Date (Ma)
eU (ppm)

Fig. 7 (previous page): Thermal history models for samples from the D002 well. **A)** Inverse thermal history models created using HeFTy [*Ketcham*, 2005b]. Models incorporate subsets of the AHe, ZHe and AFT data. Light green and pink envelopes indicate the realm of time-temperature solutions for acceptable and good paths, respectively. Red dots indicate inflection points of good time-temperature paths. Black boxes correspond to time-temperature constraints used in thermal history modeling. The solid black line indicates a candidate temperature-time path used for forward modeling of the basement sample (B, C), whereas the dashed line indicates the corresponding thermal history used for forward modeling of the Mingan Formation sample (D). **B)** Forward modeling of AFT data following the cooling history illustrated in A. Track length GOF details the goodness-of-fit statistic between measured and modeled track length distributions and retention age signifies the modeled age of the oldest fission track that has not been fully annealed. **C, D)** Forward modeling of AHe date-eU trends given a range of r_{mr0} values and the candidate temperature time histories indicated in A. Red shaded curve illustrates the expected date-eU trends for grains with an r_{mr0} value of 0.83 and grain sizes between 40 – 50 μm (C) and 30 – 40 μm (D). Dashed lines show expected AHe date-eu trends for a range of plausible r_{mro} values and grain sizes of 50 μm (C) and 40 μm (D). Black data points indicate AHe dates incorporated into the inverse thermal history model (A).

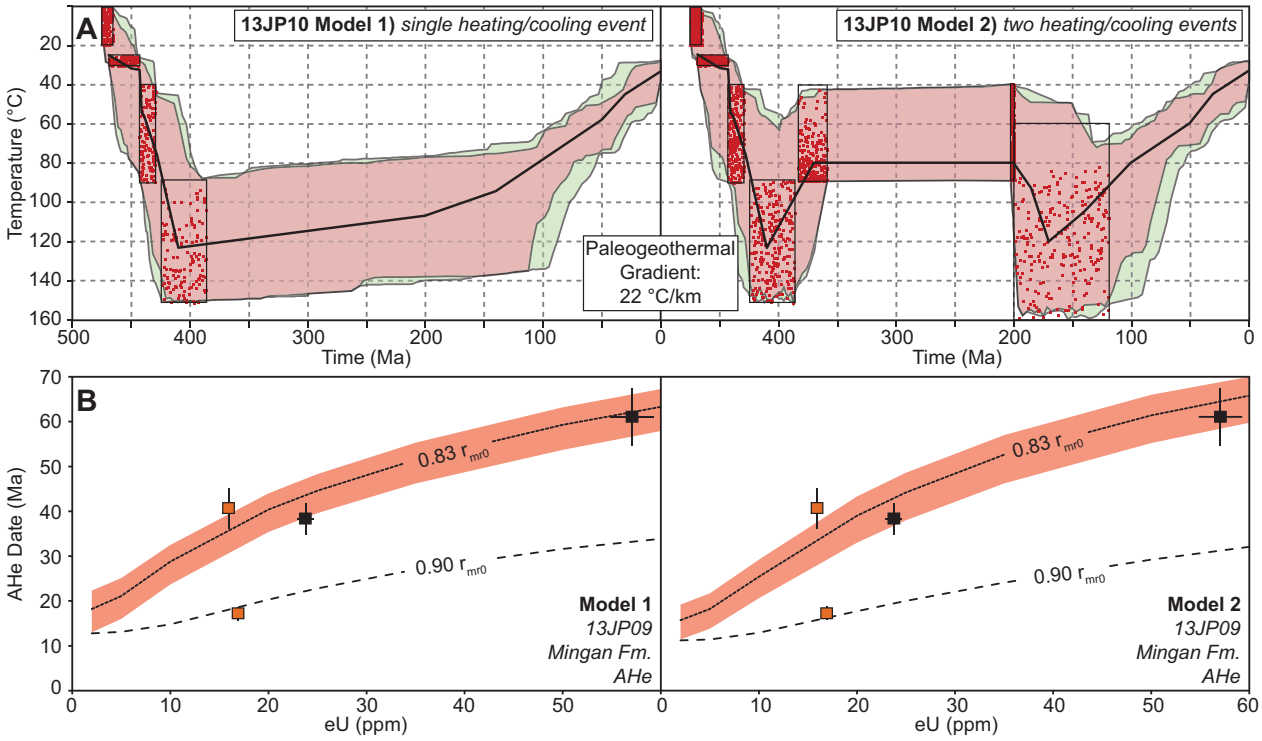

Fig 8: Thermal history models for the Mingan Formation sample from the NACP D003 well. **A)** Inverse thermal history models created using HeFTy [*Ketcham*, 2005b]. Models incorporate subsets of the AHe data. Light green and pink envelopes indicate the realm of time-temperature solutions for acceptable and good paths, respectively. Red dots indicate inflection points of good time-temperature paths. Black boxes correspond to time-temperature constraints used in thermal history modeling. The solid black line indicates a candidate temperature-time path used for forward modeling of AHe data. **B)** Forward modeling of AHe date-eU trends given a range of r_{mr0} values and the candidate temperature time histories indicated in A. Red shaded curve illustrates the expected date-eU trends for grains with an r_{mr0} value of 0.83 and grain sizes between 25 – 45 µm (dotted line = 35 µm). Dashed lines show expected AHe date-eU trends for an r_{mro} value of 0.90 and grain sizes of 35 µm. Black data points indicate AHe dates incorporated into the inverse thermal history model (A).

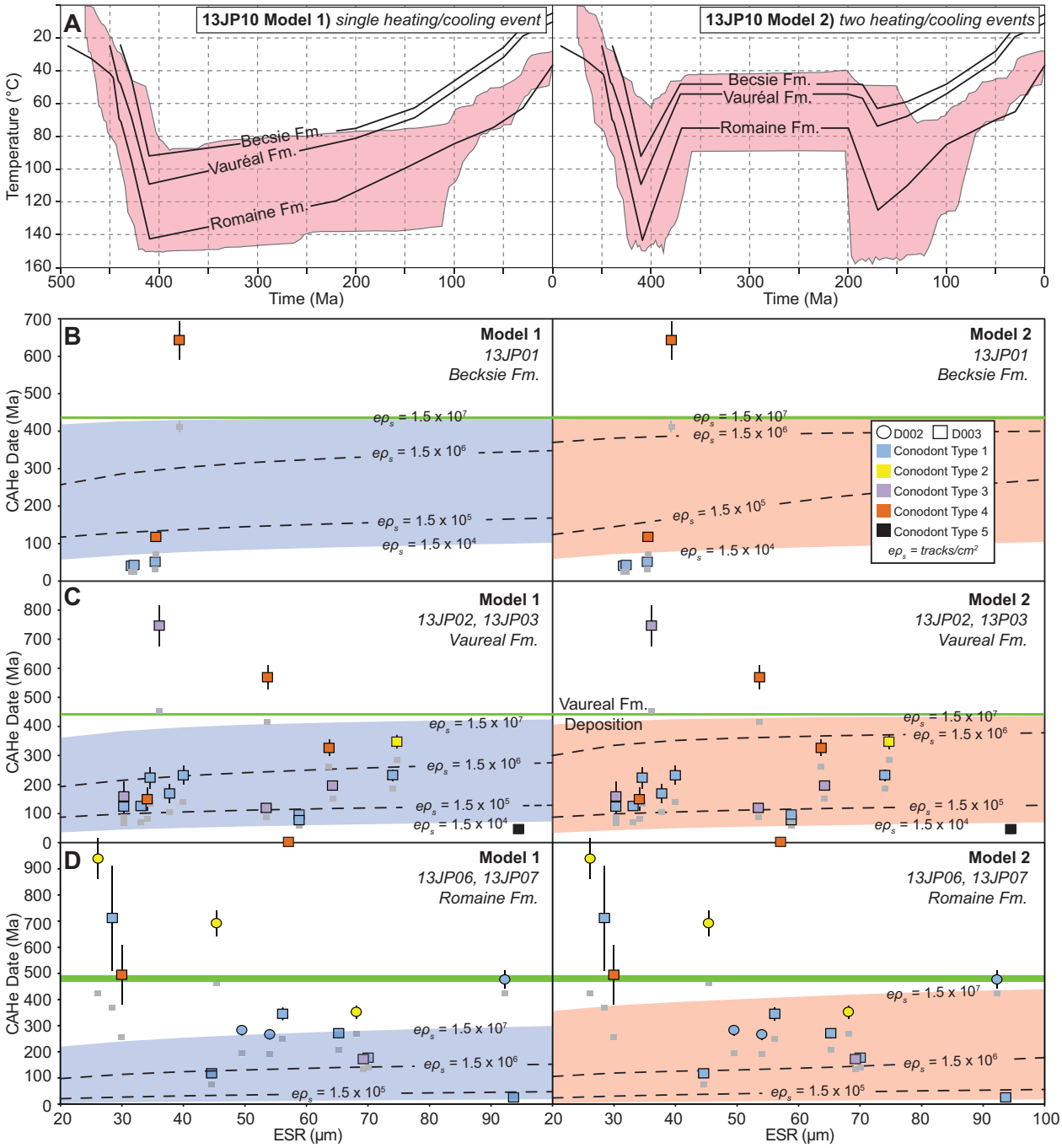
A
13JP10 Model 1) single heating/cooling event
13JP10 Model 2) two heating/cooling events
Temperature (°C)
Becsie Fm.
Vauréal Fm.
Romaine Fm.
Time (Ma)
B
Model 1
13JP01
Becksie Fm.
Model 2
13JP01
Becksie Fm.
CAHe Date (Ma)
$e\rho_s$ = 1.5 x 10^7
$e\rho_s$ = 1.5 x 10^6
$e\rho_s$ = 1.5 x 10^5
$e\rho_s$ = 1.5 x 10^4
D002 D003
Conodont Type 1
Conodont Type 2
Conodont Type 3
Conodont Type 4
Conodont Type 5
$e\rho_s$ = tracks/cm²
C
Model 1
13JP02, 13JP03
Vaureal Fm.
Model 2
13JP02, 13JP03
Vaureal Fm.
Vaureal Fm.
Deposition
D
Model 1
13JP06, 13JP07
Romaine Fm.
Model 2
13JP06, 13JP07
Romaine Fm.
ESR (µm)

Fig. 9 (previous page): Forward models showing expected CAHe date vs ESR (equivalent spherical radius) trends for each formation given a range of effective fission track densities ($e\rho_s$ = tracks/cm^2). **A)** Candidate time-temperature paths used for forward modeling of Becsie, Vauréal and Romaine formation samples (B, C, D). Pink envelopes indicate the realm of good fit thermal history solutions from inverse modeling of Mingan Formation AHe from well D003 (Fig. 7a). **B, C, D)** Expected CAHe date-ESR (equivalent spherical radius) trends for each formation given a range of effective fission track densities. Trends are derived from the candidate cooling histories in A. Coloured data points represent F_t corrected CAHe data of varying morphology type (Fig. 5), whereas gray data are the corresponding uncorrected dates. Horizontal green line indicates the stratigraphic age of each formation. Only CAHe dates with measured dates less than, or within the error of, the depositional age are shown.

Appendix to

Low-temperature thermochronology of Anticosti Island: a case study on the application of conodont (U-Th)/He thermochronology to carbonate basin analysis

Jeremy Powell[1], David Schneider[1], André Desrochers[1], Rebecca Flowers[2], James Metcalf[2], Fred Gaides[3], Daniel Stockli[4]

1. Department of Earth & Environmental Sciences, University of Ottawa, Ottawa, Canada
2. Department of Geological Sciences, University of Colorado, Boulder, USA
3. Department of Earth Sciences, Carleton University, Ottawa, Canada
4. Jackson School of Geosciences, University of Texas at Austin, Austin, USA

Contents

- Expanded AFT, AHe, ZHe and MicroCT methods and results
- Tables A1 – A4
- Figures A1 – A9

Introduction

This Appendix incorporates text on analytical methods, figures that expand on the the conodont X-ray micro-computed tomography dataset, tables that show fission track age, track length distribution and chemistry for the four samples discussed in Chapter 5.

Text A1. Analytical methods and results

A.1.1. LA-ICP-MS fission track method

AFT data for sample 13JP10 from the Grenvillian basement of LGPL D002 was analyzed using the laser ablation inductively coupled plasma mass spectrometry method (LA-ICP-MS) method [*Hasebe et al.*, 2004; *Donelick et al.*, 2005; *Chew and Donelick*, 2012] and the modified zeta calibration [*Hurford and Green*, 1983; *Hasebe et al.*, 2004]. Apatite were mounted in an epoxy resin, cured at 90°C for 1 hour, and polished to expose internal surfaces of the apatite grains. After polishing, mounts were immersed in 5.5N HNO_3 for 20.0 seconds (± 0.5 seconds) at 21°C (± 1°C) to reveal all natural fission tracks that intersected the polished grain surfaces. D_{par} measurements were calculated from one to four etch pit diameters, and spontaneous (natural) fission-track densities were counted for each grain considered suitable for dating. Samples were analyzed by Paul O'Sullivan at Apatite to Zircon, Incorporated (Viola, USA) using a Resonetics M-50 193 nm ArF Eximer laser-ablation system coupled to an Agilent 7700x quadrupole ICP-MS. Laser ablation was conducted a 26 mm spot and a 7 Hz laser repetition rate with the laser set in constant energy mode. Fission tracks were viewed and counted or measured at 2000x (Zeiss Axioplan microscope) dry magnification using unpolarized, transmitted light with or without reflected light. All AFT age (Table A1) and length grains (Table A2) were selected to sample the greatest range of observable characteristics (size, degree of roundness, color, etch figure size, etc.). Durango (DR) was used as the apatite FT zeta age calibration standard. During each LA-ICP-MS session containing samples of unknown FT age, clusters of ~10 zeta spots were analyzed during the session for purposes of calibrating $^{238}U/^{43}Ca$. Ratios of primary zeta (original zeta LA-ICP-MS session) to secondary zeta (current LA-ICP-MS session) $^{238}U/^{43}Ca$ were determined for each zeta calibration spot and smoothed using a load-specific

running-median method. Only spots visited during the primary, original zeta LA-ICP-MS session were revisited during the secondary, current LA-ICP-MS session for this purpose. This method is analogous to using ^{235}U-doped glass standards in the external detector method of fission track analysis (Donelick et al., 2005); in this study, specific DR grains from the primary standard LA-ICP-MS session serve as ^{235}U-doped standards.

In an effort to understand the uranium content and range of chemistry present in our sample suite, all grains analyzed for AFTA were measured for major, minor and REE geochemistry. Analyses were conducted via LA-ICP-MS methods at Apatite to Zircon, Inc. (Viola, USA) using a Resonetics M-50-LR 193 nm ArF Excimer laser ablation system coupled to an Agilent 7700x quadrupole inductively coupled mass spectrometer (ICP-MS). The laser was operated at a repetition rate of 10 Hz, with a lateral spot size of 10 μm, and pulse energy of 0.422 mJ. In addition to the LA-ICP-MS data, major elements and halogens were analyzed at the University of Ottawa (Ottawa, Canada) to recalculate r_{mr0} values for samples that exhibited substantial kinetic overlap using r_{mr0} values from LA-ICP-MS derived chemistry. EPMA chemistry was measured using the JEOL JXA-8230 SuperProbe which operates with an accelerating voltage of 10 kV and beam current of 3.8 nA to focus and concentrate the electron beam to a minimum of 1 μm. EPMA methods were employed to better determine the halogen content. We use the stoichiometric relationships of *Ketcham* (2015) to convert measured weight% oxide values to atoms per formula unit (apfu), and later use these values to calculate grain-specific r_{mr0} values (**Table A3**). We opt to use the original r_{mr0} calculation [*Carlson et al.*, 1999] over the more recent derivation [*Ketcham et al.*, 2007], as the newer equation is based on combined annealing experiments from different labs, which may introduce systematic error to the calculated values.

Included in this document are tables for: 1) the fission track age data (Table A1); 2) fission track length data (Table A2); and 3) fission track chemistry (Table A3).

A.1.2. Apatite and zircon (U-Th)/He method

Apatite and zircon (U-Th)/He analyses were conducted at the University of Texas Geo-Thermochronometry Lab (Austin, USA), and follow common (U-Th)/He dating conventions [*Stockli et al.*, 2000; *Wolfe and Stockli*, 2010]. Following standard mineral separation, apatite and zircon were handpicked using a customized Nikon SMZ-U/100 steremicroscope, and photographed using Nikon digital ColorView® camera. Grain dimensions were measured using the AnalySIS® software. In an effort to pick inclusion-free apatite, all grains analyzed were carefully screened for inclusions in isopropanol at 180x magnification. Apatite and zircon grains were wrapped in Pt foil and degassed using in-vacuo diode laser heating at 1050°C and 1300°C, respectively. ^{4}He was measured via quadrupole ultra-high vacuum noble gas extraction and mass-spectrometry system with a cryogenic trap. A ^{3}He spike was used for isotope dilution. All apatites were degassed twice to ensure complete degassing, and zircons were repeatedly heated until He yields were <1%. Degassed single grains were dissolved for ^{238}U, ^{232}Th, ^{149}Sm determinations by isotope dilution using an Element 2 ICP-MS. HNO_3 was used for apatite dissolution, whereas zircon were dissolved using a HF-HCl two-step pressure vessel procedure. All data were corrected for the effects of helium ejection [*Farley et al.*, 1996]. AHe and ZHe dates are reported with a standard error of 6% and 8%, respectively, which are reflective of the standard deviation of a population of analyzed standards.

Conodont (U-Th)/He analyses were conducted at the University of Colorado at Boulder TRaIL facility. Individual conodont elements were placed into Nb tubes and loaded into an ASI

Alphachron helium extraction line. Helium was extracted from individual aliquots via diode laser heating to temperatures of ~800-1100 °C. This degassed helium was spiked with 133 ncc of ^{3}He, cleaned with two SAES getters and analyzed with a Balzers PrimaPlus QME 220 quadrupole mass spectrometer. Nb tubes were then removed from the line, spiked with a ^{235}U-^{230}Th tracer in HNO_3 and baked in an 80 °C oven for two hours. Following this dissolution, aliquots are diluted with doubly-deionized water and analyzed for U, Th, Sm using a Thermo Element 2 magnetic sector mass spectrometer.

Given that dispersion amongst AHe dates is common [*Flowers et al.*, 2009; *Brown et al.*, 2013; *Murray et al.*, 2014], especially in rocks with protracted cooling histories [*Fitzgerald et al.*, 2006; *Ault et al.*, 2013] the 6% error applied to the AHe dates is likely not reflective of the true reproducibility of an analysis and may be too restrictive for modeling of the young AHe dates in this dataset. Additionally, since many of these data were collected from 2012 through 2014, more recent grain-specific variables, including the effect of variable geometry [*Beucher et al.*, 2013; *Brown et al.*, 2013] and more recent methods for calculating Ft corrections [*Ketcham et al.*, 2011] were not factored into data reduction. Nor were the dimensions in a second crystallographic width, as Ft corrections were generated under the assumption that the crystallographic A- and B-axes are equidimensional. This could be problematic, as most detrital apatite are beveled to some degree, and as a result the crystal volume and mass derived from the apatite geometry may be an overestimate.

Due to the above reasons, ages and eU concentrations used in modeling were recalculated from the original data to test the effect of broken crystals, varying grain morphologies, different methods for calculating the Ft correction and a B-axis that is 75% the diameter of the A-axis. The modeled date, error and eU concentrations average difference between our original corrected dates and the recalculated values. Overall, the modeled AHe date is <5% different than the original corrected date, and the errors used in modeling are ~10% the modeled date. Modeled eU concentrations are mostly within 5% of the original values, but can be substantial larger when the mass of the recalculated grain is substantially less than the original value. Whereas these modeled ages do not represent a "truer" AHe date than those reported, they are perhaps a more accurate representation of plausible variability in AHe dates than the standard 6% error.

A.1.3. Conodont X-ray micro-computed tomography

Volumetric data were collected for individual conodont elements using the Skyscan 117S ultra-high resolution X-ray micro-computed tomography laboratory at Carleton University (Ottawa, Canada). Dozens of conodont elements from the same sample were mounted on a 6 mm wide circle of double-sided sticky tape and analyzed at an 80kV voltage and 100 mA current. The sample stage was rotated counterclockwise in 0.15° intervals for a total of 180°, and image pixel size ranged between 9.95 μm to 6.40 μm depending on the number of samples analyzed at once and the distance between sample holder and source. Images were constructed into 3D volumes using the program Blob3D [*Ketcham*, 2005]. Volumetric data for each conodont was separated from the volume using a gray scale cut-off of 140.

Since volumes, F_t corrections and grain size were not available for 18 CAHe dates (Table 2), we calculate these values via geometric measurements taken using a binocular microscope and CT derived relationships for each conodont morphology type (Fig. 5). Conodonts in this study were grouped into 5 types on the basis of their morphology and genera (Fig. 5). Type 1 included coniform elements such as Panderodus, which generally exhibit elongate, conic morphologies. In comparison, type 2 elements are typified by Drepanostoidus, which differ from

type 1 due to broad, hollow basal cavities. Example genera of type 3 conodonts include Belodina and Phragmodus, which are significantly more flat than the others. Type 4 elements consist of fragments of S_1 to S_4 conodonts [*Purnell et al.*, 2000] and are the "bar" morphologies described by *Landman et al.* [2016]. Conodont elements of type 5 consist of ornate, S_0 morphologies [*Purnell et al.*, 2000]. These relationships (conodont morphology type vs volume, F_t correction and ESR) were calculated for the Ordovician to Silurian elements from this dataset, as well as Ordovician elements from the Iowa, Kentucky and Minnesota ("Leslie" samples; Table A4). This method assumes that conodont element volume, F_t corrections and ESR scale systematically for a given morphology. Relationships were calculated using either the maximum or minimum lengths of the best fitting ellipsoid generated by Blob3D. Because the coniform elements (type 1, type 2) are prone to breaking, we distinguish between fractured and whole elements for our calculations. These data and the derived relationships are shown in Figs. A1 – A6. In Figs. A7 – A9 we compare the CT-measured parameters, with those calculated via the derived relationships.

References

Ault, A. K., R. M. Flowers, and S. A. Bowring (2013), Phanerozoic surface history of the Slave craton, *Tectonics*, *32*(5), 1066–1083, doi:10.1002/tect.20069.

Beucher, R., R. W. Brown, S. Roper, F. Stuart, and C. Persano (2013), Natural age dispersion arising from the analysis of broken crystals. Part II: Practical application to apatite (U-Th)/He thermochronometry, *Geochim. Cosmochim. Acta*, *120*, 395–416, doi:10.1016/j.gca.2013.05.041.

Brown, R. W., R. Beucher, S. Roper, C. Persano, F. Stuart, and P. Fitzgerald (2013), Natural age dispersion arising from the analysis of broken crystals. Part I: Theoretical basis and implications for the apatite (U-Th)/He thermochronometer, *Geochim. Cosmochim. Acta*, *122*(120), 478–497, doi:10.1016/j.gca.2013.05.041.

Carlson, W. D., R. A. Donelick, and R. A. Ketcham (1999), Variability of apatite fission-track annealing kinetics: I. Experimental results, *Am. Mineral.*, *84*(9), 1213–1223, doi:10.2138/am-1999-0901.

Chew, D. M., and R. A. Donelick (2012), Combined apatite fission track and U-Pb dating by LA–ICP–MS and its application in apatite provenance analysis, *Mineral. Assoc. Canada Short Course 42*, 219–247.

Donelick, R. A., P. B. O'Sullivan, and R. A. Ketcham (2005), Apatite Fission-Track Analysis, *Rev. Mineral. Geochemistry*, *58*(1), 49–94, doi:10.2138/rmg.2005.58.3.

Farley, K. A., R. A. Wolf, and L. T. Silver (1996), The effects of long alpha-stopping distances on (U-Th)/He ages, *Geochim. Cosmochim. Acta*, *60*(21), 4223–4229.

Fitzgerald, P. G., S. L. Baldwin, L. E. Webb, and P. . O'Sullivan (2006), Interpretation of (U–Th)/He single grain ages from slowly cooled crustal terranes: A case study from the Transantarctic Mountains of southern Victoria Land, *Chem. Geol.*, *225*(1-2), 91–120, doi:10.1016/j.chemgeo.2005.09.001.

Flowers, R. M., R. A. Ketcham, D. L. Shuster, and K. A. Farley (2009), Apatite (U-Th)/He thermochronometry using a radiation damage accumulation and annealing model, *Geochim. Cosmochim. Acta*, *73*(8), 2347–2365, doi:10.1016/j.gca.2009.01.015.

Hasebe, N., J. Barbarand, K. Jarvis, A. Carter, and A. J. Hurford (2004), Apatite fission-track chronometry using laser ablation ICP-MS, *Chem. Geol.*, *207*(3-4), 135–145, doi:10.1016/j.chemgeo.2004.01.007.

Hurford, A. J., and P. F. Green (1983), The zeta age calibration of fission-track dating, *Chem. Geol.*, *41*, 285–317, doi:10.1016/S0009-2541(83)80026-6.

Ketcham, R. A. (2005), Computational methods for quantitative analysis of three-dimensional features in geological specimens, *Geosphere*, *1*(1), 32–41, doi:10.1130/GES00001.1.

Ketcham, R. A., A. Carter, R. A. Donelick, J. Barbarand, and A. J. Hurford (2007), Improved modeling of fission-track annealing in apatite, *Am. Mineral.*, *92*(5-6), 799–810, doi:10.2138/am.2007.2281.

Ketcham, R. A., C. Gautheron, and L. Tassan-Got (2011), Accounting for long alpha-particle stopping distances in (U-Th-Sm)/He geochronology: Refinement of the baseline case, *Geochim. Cosmochim. Acta*, *75*(24), 7779–7791, doi:10.1016/j.gca.2011.10.011.

Murray, K. E., D. A. Orme, and P. W. Reiners (2014), Effects of U-Th-rich grain boundary phases on apatite helium ages, *Chem. Geol.*, *390*, 135–151, doi:10.1016/j.chemgeo.2014.09.023.

Purnell, M., P. Donoghue, and R. Aldridge (2000), Orientation and anatomical notation in conodonts, *J. Paleontol.*, *74*(1), 113–122, doi:10.1666/0022-3360(2000)074<0113:OAANIC>2.0.CO;2.

Stockli, D. F., K. A. Farley, and T. A. Dumitru (2000), Calibration of the apatite (U-Th)/He thermochronometer on an exhumed fault block, White Mountains, California, *Geology*, *28*(11), 983–986, doi:10.1130/0091-7613(2000)28<983:COTAHT>2.0.CO;2.

Wolfe, M. R., and D. F. Stockli (2010), Zircon (U–Th)/He thermochronometry in the KTB drill hole, Germany, and its implications for bulk He diffusion kinetics in zircon, *Earth Planet. Sci. Lett.*, *295*(1-2), 69–82, doi:10.1016/j.epsl.2010.03.025.

Table A1. Summary of AFT age data for sample 13JP10, Grenvillian basement, D002 LGPL core, Anticosti Island

A2Z Sample No.	N_s	Ω_i (cm^2)	P_i (dmnls)	$P_i\Omega_i$	one sigma (dmnls)	$\sigma P_i^2\Omega_i^2$	FT age (Ma)	one sigma (Ma)	Etch Figs.	D_{par} (µm)	U (ppm)	meas. F (apfu)	meas. Cl (apfu)	calc. OH (apfu)	r_{mr0}
Kinetic population #1 (rmr0 < 0.813)															
P1420_006_Ap_A_1_POS_30	57	4.854E-05	0.084	4.055E-06	0.003	2.483E-14	115.3	16.0	4	1.74	9	1.63	0.16	0.21	0.787
P1420_006_Ap_A_1_POS_18	16	3.398E-05	0.030	1.029E-06	0.003	1.396E-14	127.4	35.1	3	1.99	4	1.78	0.15	0.07	0.800
P1420_006_Ap_A_1_POS_9	77	4.854E-05	0.105	5.108E-06	0.004	3.721E-14	123.5	15.0	4	2.37	10	1.76	0.16	0.08	0.805
P1420_006_Ap_A_1_POS_17	71	4.854E-05	0.094	4.576E-06	0.004	4.499E-14	127.1	16.3	4	1.97	8	1.74	0.17	0.10	0.806
P1420_006_Ap_A_1_POS_19	50	2.912E-05	0.096	2.792E-06	0.003	8.987E-15	146.5	21.5	4	2.07	10	1.72	0.17	0.12	0.808
P1420_006_Ap_A_1_POS_24	107	3.398E-05	0.193	6.561E-06	0.007	5.016E-14	133.5	13.9	3	2.07	16	1.72	0.15	0.12	0.808
P1420_006_Ap_A_1_POS_36	65	4.854E-05	0.095	4.626E-06	0.003	2.588E-14	115.2	15.0	4	2.04	10	1.77	0.18	0.05	0.811
pooled (7) Q = 84%	**443**	**0**		**0**		**0**	**126.2**	**6.7**		**2.04**		**1.73**	**0.16**	**0.11**	**0.804**
Kinetic population #2 (rmr0 > 0.813)															
P1420_006_Ap_A_1_POS_13	57	4.3682E-05	0.132	5.745E-06	0.008	1.322E-13	81.6	12.1	4	1.97	11	1.82	0.15	0.03	0.814
P1420_006_Ap_A_1_POS_27	46	4.8535E-05	0.043	2.069E-06	0.002	9.424E-15	181.4	28.2	4	1.81	4	1.89	0.18	0.00	0.814
P1420_006_Ap_A_1_POS_26	28	4.8535E-05	0.058	2.804E-06	0.003	2.037E-14	82.1	16.1	3	2.13	4	1.81	0.15	0.04	0.814
P1420_006_Ap_A_1_POS_15	44	4.8535E-05	0.051	2.493E-06	0.004	2.972E-14	144.4	24.1	4	2.05	5	1.73	0.16	0.11	0.814
P1420_006_Ap_A_1_POS_22	75	3.8828E-05	0.178	6.923E-06	0.006	6.341E-14	89.0	10.9	4	2.16	18	1.79	0.15	0.07	0.814
P1420_006_Ap_A_1_POS_11	73	4.3682E-05	0.091	3.986E-06	0.004	3.433E-14	149.7	19.0	4	2.22	10	1.84	0.14	0.02	0.815
P1420_006_Ap_A_1_POS_14	59	4.8535E-05	0.064	3.093E-06	0.003	2.243E-14	155.9	21.8	4	1.76	4	1.81	0.13	0.06	0.817
P1420_006_Ap_A_1_POS_1	109	4.3682E-05	0.173	7.554E-06	0.008	1.103E-13	118.3	12.6	4	2.17	17	1.80	0.12	0.08	0.817
P1420_006_Ap_A_1_POS_23	38	4.8535E-05	0.063	3.052E-06	0.003	1.517E-14	102.2	17.2	2	1.89	7	1.79	0.16	0.05	0.817
P1420_006_Ap_A_1_POS_34	48	4.8535E-05	0.048	2.346E-06	0.003	2.857E-14	167.1	27.1	4	2.09	5	1.79	0.15	0.06	0.817
P1420_006_Ap_A_1_POS_31	49	4.8535E-05	0.054	2.607E-06	0.004	3.847E-14	153.7	24.9	4	2.06	6	1.91	0.16	0.00	0.818
P1420_006_Ap_A_1_POS_32	60	4.8535E-05	0.089	4.295E-06	0.005	6.296E-14	114.5	16.3	4	1.86	10	1.84	0.14	0.02	0.818
P1420_006_Ap_A_1_POS_28	44	4.8535E-05	0.054	2.637E-06	0.003	2.090E-14	136.6	22.0	4	2.14	6	1.80	0.13	0.07	0.818
P1420_006_Ap_A_1_POS_5	49	4.8535E-05	0.088	4.274E-06	0.004	3.647E-14	94.2	14.2	3	1.65	8	1.83	0.13	0.04	0.818
P1420_006_Ap_A_1_POS_37	65	4.8535E-05	0.084	4.060E-06	0.003	2.807E-14	131.1	17.3	4	2.01	8	1.83	0.11	0.06	0.819
P1420_006_Ap_A_1_POS_39	82	4.8535E-05	0.116	5.620E-06	0.004	3.081E-14	119.6	13.9	4	2.01	12	1.85	0.15	0.00	0.820
P1420_006_Ap_A_1_POS_33	92	4.8535E-05	0.133	6.473E-06	0.004	4.669E-14	116.5	12.9	3	2.04	13	1.91	0.14	0.00	0.820
P1420_006_Ap_A_1_POS_35	65	4.8535E-05	0.135	6.550E-06	0.005	6.562E-14	81.6	10.7	4	1.97	15	1.93	0.13	0.00	0.820
P1420_006_Ap_A_1_POS_10	47	4.8535E-05	0.036	1.769E-06	0.003	1.857E-14	216.1	35.8	4	1.86	3	1.87	0.13	0.00	0.820
P1420_006_Ap_A_1_POS_7	18	3.3975E-05	0.040	1.357E-06	0.004	1.456E-14	108.8	27.5	3	1.93	3	1.88	0.16	0.00	0.821
P1420_006_Ap_A_1_POS_21	62	3.8828E-05	0.123	4.766E-06	0.005	3.622E-14	106.7	14.3	3	2.32	12	1.88	0.15	0.00	0.822
P1420_006_Ap_A_1_POS_6	82	4.8535E-05	0.114	5.520E-06	0.007	1.065E-13	121.7	15.4	4	2.02	10	1.88	0.15	0.00	0.823
P1420_006_Ap_A_1_POS_25	24	4.3682E-05	0.052	2.259E-06	0.002	1.018E-14	87.3	18.3	4	2.14	6	1.80	0.14	0.06	0.823
P1420_006_Ap_A_1_POS_20	26	3.8828E-05	0.035	1.352E-06	0.003	1.694E-14	157.2	34.5	4	1.93	4	1.79	0.14	0.07	0.823
P1420_006_Ap_A_1_POS_29	66	4.8535E-05	0.081	3.952E-06	0.004	4.523E-14	136.7	18.5	4	2.02	9	1.89	0.13	0.00	0.823
P1420_006_Ap_A_1_POS_12	48	4.8535E-05	0.080	3.889E-06	0.005	6.333E-14	101.3	16.1	3	2.02	8	1.90	0.13	0.00	0.823
P1420_006_Ap_A_1_POS_16	74	4.8535E-05	0.090	4.349E-06	0.005	5.288E-14	139.2	17.9	4	1.94	10	1.84	0.11	0.05	0.824
P1420_006_Ap_A_1_POS_8	46	4.854E-05	0.065	3.172E-06	0.005	5.839E-14	118.9	19.8	4	2.04	7	1.79	0.14	0.07	0.824
P1420_006_Ap_A_1_POS_0	17	3.398E-05	0.023	7.826E-07	0.002	5.338E-15	177.2	46.2	4	2.12	3	1.84	0.14	0.02	0.824
P1420_006_Ap_A_1_POS_3	31	4.368E-05	0.047	2.068E-06	0.003	1.959E-14	122.8	23.7	3	1.67	4	1.82	0.11	0.06	0.825
P1420_006_Ap_A_1_POS_38	84	4.854E-05	0.087	4.227E-06	0.004	3.223E-14	162.3	19.2	3	1.78	10	1.88	0.14	0.00	0.825
P1420_006_Ap_A_1_POS_4	46	3.883E-05	0.062	2.410E-06	0.003	1.105E-14	156.0	24.1	3	2.07	8	2.03	0.11	0.00	0.829
pooled (32) Q = 0 %	**1754**	**0**	**3**	**0**	**0**	**0**	**121.3**	**3.7**		**2.00**		**1.85**	**0.14**	**0.03**	**0.820**

Note: Ns is the number of spontaneous fission tracks for each apatite. Ω_i is the area overwhich tracks are counted, whereas P_i is the $^{238}U/^{43}Ca$ ratio. Q represents the chi-squared probability for each population. A population passes the chi-squared test if Q > 5%. D_{par} is the diameter of the etch figure parallel to the c axis. F, Cl and OH concentrations were calculated from weight % oxide using the stoichiometric relationships of *Ketcham* [2015], and r_{mr0} was determined using the calculations of *Carlson et al.* [1999].

modified zeta	8.2727
s.e. (zeta)	0.1407
total decay const.	1.55125E-10
g	1

Table A2. Summary of AFT length data for sample 13JP10, Grenvillian basement, D002 LGPL core, Anticosti Island

A2Z Sample No.	confined length (µm)	angle to c-axis (degrees)	etch figs.	D_{par} (µm)	meas. F (apfu)	meas. Cl (apfu)	calc. OH (apfu)	r_{mr0}
Kinetic Pop #1 (rmr0 < 0.81)								
P1420_006_Ap_A_2_POS_5	12.10	61.54	4	2.52	1.98	0.15	0.00	0.56
P1420_006_Ap_A_2_POS_5	14.43	34.87	4	2.52	1.98	0.15	0.00	0.56
P1420_006_Ap_A_2_POS_5	12.45	59.10	4	2.52	1.98	0.15	0.00	0.56
P1420_006_Ap_A_2_POS_5	13.28	42.14	4	2.52	1.98	0.15	0.00	0.56
P1420_006_Ap_A_2_POS_5	13.36	28.53	4	2.52	1.98	0.15	0.00	0.56
P1420_006_Ap_A_2_POS_3	12.49	47.00	2	2.67	2.00	0.16	0.00	0.72
P1420_006_Ap_A_2_POS_3	15.41	33.03	2	2.67	2.00	0.16	0.00	0.72
P1420_006_Ap_A_2_POS_15	12.67	59.53	4	2.93	1.79	0.13	0.08	0.77
P1420_006_Ap_A_2_POS_15	10.45	49.65	4	2.93	1.79	0.13	0.08	0.77
P1420_006_Ap_A_2_POS_15	9.29	56.33	4	2.93	1.79	0.13	0.08	0.77
P1420_006_Ap_A_2_POS_15	11.44	84.60	4	2.93	1.79	0.13	0.08	0.77
P1420_006_Ap_A_2_POS_15	13.15	36.50	4	2.93	1.79	0.13	0.08	0.77
P1420_006_Ap_A_2_POS_15	14.18	44.77	4	2.93	1.79	0.13	0.08	0.77
P1420_006_Ap_A_2_POS_15	10.08	57.14	4	2.93	1.79	0.13	0.08	0.77
P1420_006_Ap_A_2_POS_15	12.87	61.46	4	2.93	1.79	0.13	0.08	0.77
P1420_006_Ap_A_2_POS_15	11.20	85.43	4	2.93	1.79	0.13	0.08	0.77
P1420_006_Ap_A_2_POS_15	9.93	49.08	4	2.93	1.79	0.13	0.08	0.77
P1420_006_Ap_A_2_POS_1	13.53	18.65	4	2.64	1.62	0.14	0.24	0.81
P1420_006_Ap_A_2_POS_1	13.47	46.48	4	2.64	1.62	0.14	0.24	0.81
P1420_006_Ap_A_2_POS_1	12.73	53.88	4	2.64	1.62	0.14	0.24	0.81
P1420_006_Ap_A_2_POS_1	14.63	35.35	4	2.64	1.62	0.14	0.24	0.81
P1420_006_Ap_A_2_POS_1	13.49	71.61	4	2.64	1.62	0.14	0.24	0.81
P1420_006_Ap_A_2_POS_1	12.16	46.69	4	2.64	1.62	0.14	0.24	0.81
P1420_006_Ap_A_2_POS_1	11.68	77.40	4	2.64	1.62	0.14	0.24	0.81
P1420_006_Ap_A_2_POS_1	10.56	39.24	4	2.64	1.62	0.14	0.24	0.81
P1420_006_Ap_A_2_POS_1	13.43	50.67	4	2.64	1.62	0.14	0.24	0.81
P1420_006_Ap_A_2_POS_0	10.14	64.43	4	2.46	1.89	0.13	0.00	0.81
Ave	**12.39**			**2.72**	**1.79**	**0.14**	**0.11**	**0.74**
SD	**1.58**			**0.17**	**0.14**	**0.01**	**0.10**	**0.09**
Kinetic Pop #2 (rmr0 > 0.81								
P1420_006_Ap_A_2_POS_0	14.30	60.65	4	2.46	1.89	0.13	0.00	0.81
P1420_006_Ap_A_2_POS_0	13.83	76.07	4	2.46	1.89	0.13	0.00	0.81
P1420_006_Ap_A_2_POS_0	13.58	56.08	4	2.46	1.89	0.13	0.00	0.81
P1420_006_Ap_A_2_POS_10	15.97	56.29	4	2.28	1.83	0.15	0.02	0.81
P1420_006_Ap_A_2_POS_10	10.07	69.98	4	2.28	1.83	0.15	0.02	0.81
P1420_006_Ap_A_2_POS_10	14.15	43.98	4	2.28	1.83	0.15	0.02	0.81
P1420_006_Ap_A_2_POS_10	11.10	48.97	4	2.28	1.83	0.15	0.02	0.81
P1420_006_Ap_A_2_POS_10	14.02	36.74	4	2.28	1.83	0.15	0.02	0.81
P1420_006_Ap_A_2_POS_10	12.44	59.64	4	2.28	1.83	0.15	0.02	0.81
P1420_006_Ap_A_2_POS_10	9.52	68.17	4	2.28	1.83	0.15	0.02	0.81
P1420_006_Ap_A_2_POS_10	15.17	50.39	4	2.28	1.83	0.15	0.02	0.81
P1420_006_Ap_A_2_POS_10	13.70	60.72	4	2.28	1.83	0.15	0.02	0.81
P1420_006_Ap_A_2_POS_10	11.32	69.10	4	2.28	1.83	0.15	0.02	0.81

A2Z Sample No.	confined length (µm)	angle to c-axis (degrees)	etch figs.	D_{par} (µm)	meas. F (apfu)	meas. Cl (apfu)	calc. OH (apfu)	r_{mr0}
P1420_006_Ap_A_2_POS_10	10.26	49.82	4	2.28	1.83	0.15	0.02	0.81
P1420_006_Ap_A_2_POS_10	9.27	74.55	4	2.28	1.83	0.15	0.02	0.81
P1420_006_Ap_A_2_POS_9	13.60	34.01	3	2.50	1.88	0.18	0.00	0.81
P1420_006_Ap_A_2_POS_9	11.10	50.37	3	2.50	1.88	0.18	0.00	0.81
P1420_006_Ap_A_2_POS_9	13.22	42.32	3	2.50	1.88	0.18	0.00	0.81
P1420_006_Ap_A_2_POS_9	13.47	50.23	3	2.50	1.88	0.18	0.00	0.81
P1420_006_Ap_A_2_POS_6	15.63	27.65	4	2.26	1.76	0.17	0.06	0.82
P1420_006_Ap_A_2_POS_6	14.31	26.91	4	2.26	1.76	0.17	0.06	0.82
P1420_006_Ap_A_2_POS_6	14.28	23.42	4	2.26	1.76	0.17	0.06	0.82
P1420_006_Ap_A_2_POS_6	11.65	62.25	4	2.26	1.76	0.17	0.06	0.82
P1420_006_Ap_A_2_POS_16	10.16	80.27	3	2.44	1.81	0.15	0.04	0.82
P1420_006_Ap_A_2_POS_16	9.74	53.76	3	2.44	1.81	0.15	0.04	0.82
P1420_006_Ap_A_2_POS_16	11.06	60.91	3	2.44	1.81	0.15	0.04	0.82
P1420_006_Ap_A_2_POS_16	11.09	43.44	3	2.44	1.81	0.15	0.04	0.82
P1420_006_Ap_A_2_POS_16	11.92	74.47	3	2.44	1.81	0.15	0.04	0.82
P1420_006_Ap_A_2_POS_16	13.02	42.34	3	2.44	1.81	0.15	0.04	0.82
P1420_006_Ap_A_2_POS_16	11.82	69.81	3	2.44	1.81	0.15	0.04	0.82
P1420_006_Ap_A_2_POS_16	9.95	62.37	3	2.44	1.81	0.15	0.04	0.82
P1420_006_Ap_A_2_POS_16	11.28	64.25	3	2.44	1.81	0.15	0.04	0.82
P1420_006_Ap_A_2_POS_16	11.82	56.34	3	2.44	1.81	0.15	0.04	0.82
P1420_006_Ap_A_2_POS_16	12.96	45.27	3	2.44	1.81	0.15	0.04	0.82
P1420_006_Ap_A_2_POS_16	12.85	68.52	3	2.44	1.81	0.15	0.04	0.82
P1420_006_Ap_A_2_POS_16	13.34	70.40	3	2.44	1.81	0.15	0.04	0.82
P1420_006_Ap_A_2_POS_16	9.78	59.98	3	2.44	1.81	0.15	0.04	0.82
P1420_006_Ap_A_2_POS_13	13.21	69.38	4	2.36	1.82	0.15	0.03	0.82
P1420_006_Ap_A_2_POS_13	12.59	50.88	4	2.36	1.82	0.15	0.03	0.82
P1420_006_Ap_A_2_POS_13	12.51	51.74	4	2.36	1.82	0.15	0.03	0.82
P1420_006_Ap_A_2_POS_13	12.38	49.90	4	2.36	1.82	0.15	0.03	0.82
P1420_006_Ap_A_2_POS_8	10.31	54.20	4	2.57	1.89	0.13	0.00	0.82
P1420_006_Ap_A_2_POS_8	11.13	61.15	4	2.57	1.89	0.13	0.00	0.82
P1420_006_Ap_A_2_POS_8	14.09	39.58	4	2.57	1.89	0.13	0.00	0.82
P1420_006_Ap_A_2_POS_8	13.53	42.14	4	2.57	1.89	0.13	0.00	0.82
P1420_006_Ap_A_2_POS_8	11.56	77.49	4	2.57	1.89	0.13	0.00	0.82
P1420_006_Ap_A_2_POS_8	12.91	40.26	4	2.57	1.89	0.13	0.00	0.82
P1420_006_Ap_A_2_POS_8	16.34	28.26	4	2.57	1.89	0.13	0.00	0.82
P1420_006_Ap_A_2_POS_8	12.08	73.49	4	2.57	1.89	0.13	0.00	0.82
P1420_006_Ap_A_2_POS_8	13.21	56.09	4	2.57	1.89	0.13	0.00	0.82
P1420_006_Ap_A_2_POS_8	10.91	59.91	4	2.57	1.89	0.13	0.00	0.82
P1420_006_Ap_A_2_POS_8	12.85	57.52	4	2.57	1.89	0.13	0.00	0.82
P1420_006_Ap_A_2_POS_7	15.26	32.68	4	2.59	1.98	0.12	0.00	0.82
P1420_006_Ap_A_2_POS_7	10.20	65.72	4	2.59	1.98	0.12	0.00	0.82
P1420_006_Ap_A_2_POS_7	12.85	58.54	4	2.59	1.98	0.12	0.00	0.82
P1420_006_Ap_A_2_POS_7	15.05	54.77	4	2.59	1.98	0.12	0.00	0.82
P1420_006_Ap_A_2_POS_7	13.93	45.47	4	2.59	1.98	0.12	0.00	0.82
P1420_006_Ap_A_2_POS_7	8.91	55.90	4	2.59	1.98	0.12	0.00	0.82
P1420_006_Ap_A_2_POS_7	10.35	67.07	4	2.59	1.98	0.12	0.00	0.82
P1420_006_Ap_A_2_POS_7	12.98	64.00	4	2.59	1.98	0.12	0.00	0.82

A2Z Sample No.	confined length (µm)	angle to c-axis (degrees)	etch figs.	D_{par} (µm)	meas. F (apfu)	meas. Cl (apfu)	calc. OH (apfu)	r_{mr0}
P1420_006_Ap_A_2_POS_7	10.59	61.12	4	2.59	1.98	0.12	0.00	0.82
P1420_006_Ap_A_2_POS_7	13.65	48.24	4	2.59	1.98	0.12	0.00	0.82
P1420_006_Ap_A_2_POS_7	10.23	64.53	4	2.59	1.98	0.12	0.00	0.82
P1420_006_Ap_A_2_POS_7	10.44	51.02	4	2.59	1.98	0.12	0.00	0.82
P1420_006_Ap_A_2_POS_7	10.72	58.50	4	2.59	1.98	0.12	0.00	0.82
P1420_006_Ap_A_2_POS_7	12.89	49.24	4	2.59	1.98	0.12	0.00	0.82
P1420_006_Ap_A_2_POS_11	13.15	46.96	4	2.85	1.81	0.12	0.07	0.82
P1420_006_Ap_A_2_POS_11	15.48	33.90	4	2.85	1.81	0.12	0.07	0.82
P1420_006_Ap_A_2_POS_11	12.75	46.46	4	2.85	1.81	0.12	0.07	0.82
P1420_006_Ap_A_2_POS_11	10.71	70.51	4	2.85	1.81	0.12	0.07	0.82
P1420_006_Ap_A_2_POS_11	14.54	44.45	4	2.85	1.81	0.12	0.07	0.82
P1420_006_Ap_A_2_POS_2	11.20	50.82	4	2.42	1.95	0.13	0.00	0.82
P1420_006_Ap_A_2_POS_2	12.23	64.83	4	2.42	1.95	0.13	0.00	0.82
P1420_006_Ap_A_2_POS_2	12.74	37.35	4	2.42	1.95	0.13	0.00	0.82
P1420_006_Ap_A_2_POS_2	13.19	32.69	4	2.42	1.95	0.13	0.00	0.82
P1420_006_Ap_A_2_POS_2	12.92	59.23	4	2.42	1.95	0.13	0.00	0.82
P1420_006_Ap_A_2_POS_2	12.55	38.96	4	2.42	1.95	0.13	0.00	0.82
P1420_006_Ap_A_2_POS_2	12.69	81.58	4	2.42	1.95	0.13	0.00	0.82
P1420_006_Ap_A_2_POS_2	11.10	47.49	4	2.42	1.95	0.13	0.00	0.82
P1420_006_Ap_A_2_POS_2	11.83	70.35	4	2.42	1.95	0.13	0.00	0.82
P1420_006_Ap_A_2_POS_2	13.42	25.36	4	2.42	1.95	0.13	0.00	0.82
P1420_006_Ap_A_2_POS_2	14.79	57.08	4	2.42	1.95	0.13	0.00	0.82
P1420_006_Ap_A_2_POS_2	12.67	67.70	4	2.42	1.95	0.13	0.00	0.82
P1420_006_Ap_A_2_POS_2	14.25	41.71	4	2.42	1.95	0.13	0.00	0.82
P1420_006_Ap_A_2_POS_2	13.63	25.93	4	2.42	1.95	0.13	0.00	0.82
P1420_006_Ap_A_2_POS_2	11.62	82.93	4	2.42	1.95	0.13	0.00	0.82
P1420_006_Ap_A_2_POS_2	14.07	43.33	4	2.42	1.95	0.13	0.00	0.82
P1420_006_Ap_A_2_POS_2	12.50	44.99	4	2.42	1.95	0.13	0.00	0.82
P1420_006_Ap_A_2_POS_2	13.60	67.61	4	2.42	1.95	0.13	0.00	0.82
P1420_006_Ap_A_2_POS_14	12.91	47.36	4	2.64	1.78	0.13	0.09	0.82
P1420_006_Ap_A_2_POS_14	14.46	25.75	4	2.64	1.78	0.13	0.09	0.82
P1420_006_Ap_A_2_POS_14	10.69	46.75	4	2.64	1.78	0.13	0.09	0.82
P1420_006_Ap_A_2_POS_14	9.91	82.23	4	2.64	1.78	0.13	0.09	0.82
P1420_006_Ap_A_2_POS_14	13.65	51.99	4	2.64	1.78	0.13	0.09	0.82
P1420_006_Ap_A_2_POS_14	12.02	43.14	4	2.64	1.78	0.13	0.09	0.82
P1420_006_Ap_A_2_POS_14	12.22	51.01	4	2.64	1.78	0.13	0.09	0.82
P1420_006_Ap_A_2_POS_14	13.40	57.62	4	2.64	1.78	0.13	0.09	0.82
P1420_006_Ap_A_2_POS_4	10.66	40.78	4	2.56	1.88	0.14	0.00	0.82
P1420_006_Ap_A_2_POS_4	10.92	69.64	4	2.56	1.88	0.14	0.00	0.82
P1420_006_Ap_A_2_POS_4	14.65	41.42	4	2.56	1.88	0.14	0.00	0.82
P1420_006_Ap_A_2_POS_4	11.55	72.36	4	2.56	1.88	0.14	0.00	0.82
P1420_006_Ap_A_2_POS_4	14.38	57.48	4	2.56	1.88	0.14	0.00	0.82
P1420_006_Ap_A_2_POS_4	13.38	39.61	4	2.56	1.88	0.14	0.00	0.82
P1420_006_Ap_A_2_POS_4	8.38	63.88	4	2.56	1.88	0.14	0.00	0.82
P1420_006_Ap_A_2_POS_4	11.30	71.30	4	2.56	1.88	0.14	0.00	0.82
P1420_006_Ap_A_2_POS_4	13.96	36.58	4	2.56	1.88	0.14	0.00	0.82
P1420_006_Ap_A_2_POS_4	11.90	61.11	4	2.56	1.88	0.14	0.00	0.82

A2Z Sample No.	confined length (µm)	angle to c-axis (degrees)	etch figs.	D_{par} (µm)	meas. F (apfu)	meas. Cl (apfu)	calc. OH (apfu)	r_{mr0}
P1420_006_Ap_A_2_POS_4	11.56	73.08	4	2.56	1.88	0.14	0.00	0.82
P1420_006_Ap_A_2_POS_4	10.59	50.95	4	2.56	1.88	0.14	0.00	0.82
P1420_006_Ap_A_2_POS_4	13.21	78.31	4	2.56	1.88	0.14	0.00	0.82
P1420_006_Ap_A_2_POS_4	10.75	64.58	4	2.56	1.88	0.14	0.00	0.82
P1420_006_Ap_A_2_POS_4	13.30	72.40	4	2.56	1.88	0.14	0.00	0.82
P1420_006_Ap_A_2_POS_4	11.46	78.75	4	2.56	1.88	0.14	0.00	0.82
P1420_006_Ap_A_2_POS_4	11.39	77.87	4	2.56	1.88	0.14	0.00	0.82
P1420_006_Ap_A_2_POS_4	12.77	45.91	4	2.56	1.88	0.14	0.00	0.82
P1420_006_Ap_A_2_POS_4	10.86	51.52	4	2.56	1.88	0.14	0.00	0.82
P1420_006_Ap_A_2_POS_4	10.92	58.20	4	2.56	1.88	0.14	0.00	0.82
P1420_006_Ap_A_2_POS_4	13.08	60.50	4	2.56	1.88	0.14	0.00	0.82
P1420_006_Ap_A_2_POS_4	12.23	64.14	4	2.56	1.88	0.14	0.00	0.82
P1420_006_Ap_A_2_POS_4	11.28	51.87	4	2.56	1.88	0.14	0.00	0.82
P1420_006_Ap_A_2_POS_4	12.27	60.55	4	2.56	1.88	0.14	0.00	0.82
P1420_006_Ap_A_2_POS_4	9.62	48.80	4	2.56	1.88	0.14	0.00	0.82
P1420_006_Ap_A_2_POS_12	14.85	82.80	4	2.63	1.85	0.13	0.02	0.83
P1420_006_Ap_A_2_POS_12	11.29	63.34	4	2.63	1.85	0.13	0.02	0.83
P1420_006_Ap_A_2_POS_12	16.11	41.03	4	2.63	1.85	0.13	0.02	0.83
P1420_006_Ap_A_2_POS_12	13.58	52.46	4	2.63	1.85	0.13	0.02	0.83
P1420_006_Ap_A_2_POS_12	13.56	40.06	4	2.63	1.85	0.13	0.02	0.83
P1420_006_Ap_A_2_POS_12	14.00	74.60	4	2.63	1.85	0.13	0.02	0.83
P1420_006_Ap_A_2_POS_12	13.19	73.18	4	2.63	1.85	0.13	0.02	0.83
P1420_006_Ap_A_2_POS_12	10.23	76.24	4	2.63	1.85	0.13	0.02	0.83
P1420_006_Ap_A_2_POS_12	14.56	68.36	4	2.63	1.85	0.13	0.02	0.83
P1420_006_Ap_A_2_POS_12	11.31	66.77	4	2.63	1.85	0.13	0.02	0.83
P1420_006_Ap_A_2_POS_12	10.08	72.65	4	2.63	1.85	0.13	0.02	0.83
P1420_006_Ap_A_2_POS_12	11.72	79.08	4	2.63	1.85	0.13	0.02	0.83
P1420_006_Ap_A_2_POS_12	10.91	75.76	4	2.63	1.85	0.13	0.02	0.83
P1420_006_Ap_A_2_POS_12	10.82	77.14	4	2.63	1.85	0.13	0.02	0.83
P1420_006_Ap_A_2_POS_12	10.73	40.63	4	2.63	1.85	0.13	0.02	0.83
P1420_006_Ap_A_2_POS_12	11.92	73.63	4	2.63	1.85	0.13	0.02	0.83
P1420_006_Ap_A_2_POS_12	12.20	38.65	4	2.63	1.85	0.13	0.02	0.83
P1420_006_Ap_A_2_POS_12	12.34	54.59	4	2.63	1.85	0.13	0.02	0.83
P1420_006_Ap_A_2_POS_12	15.70	29.91	4	2.63	1.85	0.13	0.02	0.83
P1420_006_Ap_A_2_POS_12	10.61	80.18	4	2.63	1.85	0.13	0.02	0.83
P1420_006_Ap_A_2_POS_12	10.16	62.47	4	2.63	1.85	0.13	0.02	0.83
P1420_006_Ap_A_2_POS_12	12.56	42.51	4	2.63	1.85	0.13	0.02	0.83
Ave	**12.36**			**2.52**	**1.87**	**0.14**	**0.02**	**0.82**
SD	**1.66**			**0.13**	**0.06**	**0.01**	**0.03**	**0.00**

Note: D_{par} is the diameter of the etch figure parallel to the c axis. F, Cl and OH concentrations were caluclated from weight % oxide using the stoichiometric relationships of *Ketcham* [2015], and r_{mr0} was determined using the calculations of *Carlson et al*. [1999]

Table A3. Apatite chemistry for all AFT age and length grains, sample 13JP10, Grenvillian basement, D002 LGPL core, Anticosti Island

A2Z Sample No.	Na (apfu)	Mg (apfu)	P (apfu)	Ca (apfu)	Mn (apfu)	Fe (apfu)	As (apfu)	Sr (apfu)	Y (apfu)	La (apfu)	Ce (apfu)	F (apfu)	Cl (apfu)	OH (apfu)	total (apfu)	r_{mr0} Carlson et al. 1999	Ca site 10	P site 6	F+Cl+OH 2	TOTAL wt% ox
AFT Age-Grains																				
P1420_006_Ap_A_1_POS_0	0.013	0.001	5.991	9.939	0.015	0.007	0.000	0.003	0.005	0.008	0.020	1.843	0.140	0.016	18	0.824	10.01	5.99	2	94.72
P1420_006_Ap_A_1_POS_1	0.012	0.006	6.018	9.794	0.020	0.009	0.001	0.003	0.011	0.019	0.047	1.801	0.121	0.079	17.9	0.817	9.92	6.02	2	90.27
P1420_006_Ap_A_1_POS_3	0.030	0.001	6.037	9.783	0.011	0.009	0.000	0.003	0.009	0.013	0.035	1.825	0.112	0.063	17.9	0.825	9.89	6.04	2	94.08
P1420_006_Ap_A_1_POS_4	0.029	0.003	5.973	9.947	0.013	0.007	0.001	0.002	0.014	0.011	0.028	2.027	0.108	0.000	18.2	0.829	10.05	5.97	2.14	94.33
P1420_006_Ap_A_1_POS_5	0.010	0.006	5.910	10.098	0.018	0.011	0.000	0.002	0.016	0.011	0.030	1.835	0.125	0.040	18.1	0.818	10.2	5.91	2	92.88
P1420_006_Ap_A_1_POS_6	0.000	0.000	5.925	10.065	0.014	0.007	0.000	0.003	0.017	0.011	0.037	1.875	0.147	0.000	18.1	0.823	10.15	5.93	2.02	96.02
P1420_006_Ap_A_1_POS_7	0.014	0.004	5.978	9.951	0.014	0.008	0.000	0.002	0.013	0.008	0.025	1.876	0.156	0.000	18	0.821	10.04	5.98	2.03	94.09
P1420_006_Ap_A_1_POS_8	0.018	0.006	6.034	9.797	0.009	0.005	0.002	0.002	0.009	0.015	0.030	1.791	0.141	0.069	17.9	0.824	9.89	6.04	2	92.92
P1420_006_Ap_A_1_POS_9	0.018	0.002	6.072	9.636	0.015	0.013	0.000	0.002	0.026	0.021	0.049	1.759	0.163	0.079	17.9	0.805	9.78	6.07	2	94.96
P1420_006_Ap_A_1_POS_10	0.037	0.007	6.017	9.822	0.012	0.011	0.000	0.002	0.009	0.014	0.034	1.873	0.132	0.000	18	0.820	9.95	6.02	2	94.89
P1420_006_Ap_A_1_POS_11	0.033	0.007	5.989	9.818	0.014	0.010	0.000	0.003	0.022	0.023	0.061	1.843	0.141	0.016	18	0.815	9.99	5.99	2	91.72
P1420_006_Ap_A_1_POS_12	0.032	0.000	6.013	9.812	0.012	0.009	0.000	0.002	0.015	0.018	0.044	1.899	0.125	0.000	18	0.823	9.94	6.01	2.02	93.80
P1420_006_Ap_A_1_POS_13	0.017	0.006	6.003	9.806	0.013	0.011	0.000	0.002	0.017	0.022	0.059	1.825	0.148	0.028	18	0.814	9.95	6	2	91.09
P1420_006_Ap_A_1_POS_14	0.026	0.005	6.013	9.836	0.014	0.011	0.001	0.003	0.014	0.011	0.031	1.811	0.134	0.055	18	0.817	9.95	6.01	2	95.54
P1420_006_Ap_A_1_POS_15	0.009	0.000	5.971	9.988	0.012	0.009	0.001	0.002	0.006	0.009	0.023	1.729	0.164	0.107	18	0.814	10.06	5.97	2	90.43
P1420_006_Ap_A_1_POS_16	0.026	0.000	6.068	9.661	0.016	0.007	0.000	0.002	0.014	0.020	0.053	1.840	0.114	0.046	17.9	0.824	9.8	6.07	2	93.01
P1420_006_Ap_A_1_POS_17	0.025	0.004	6.089	9.626	0.015	0.011	0.000	0.003	0.011	0.017	0.043	1.736	0.166	0.098	17.8	0.806	9.75	6.09	2	95.37
P1420_006_Ap_A_1_POS_18	0.007	0.004	5.999	9.871	0.015	0.022	0.000	0.003	0.012	0.012	0.032	1.781	0.151	0.068	18	0.800	9.98	6	2	93.68
P1420_006_Ap_A_1_POS_19	0.020	0.004	6.030	9.758	0.013	0.010	0.000	0.003	0.016	0.019	0.049	1.718	0.166	0.116	17.9	0.808	9.89	6.03	2	87.82
P1420_006_Ap_A_1_POS_20	0.017	0.001	6.081	9.669	0.009	0.006	0.000	0.002	0.012	0.014	0.042	1.789	0.144	0.067	17.9	0.823	9.77	6.08	2	94.59
P1420_006_Ap_A_1_POS_21	0.009	0.004	6.023	9.810	0.011	0.007	0.000	0.002	0.020	0.012	0.038	1.876	0.151	0.000	18	0.822	9.91	6.02	2.03	95.96
P1420_006_Ap_A_1_POS_22	0.011	0.004	6.029	9.795	0.015	0.011	0.000	0.002	0.010	0.013	0.041	1.787	0.147	0.067	17.9	0.814	9.9	6.03	2	95.61
P1420_006_Ap_A_1_POS_23	0.018	0.004	5.986	9.897	0.012	0.008	0.000	0.004	0.016	0.013	0.040	1.790	0.156	0.054	18	0.817	10.01	5.99	2	93.96
P1420_006_Ap_A_1_POS_24	0.024	0.003	5.999	9.790	0.016	0.008	0.001	0.002	0.015	0.027	0.070	1.725	0.155	0.121	18	0.808	9.96	6	2	92.53
P1420_006_Ap_A_1_POS_25	0.023	0.001	5.922	10.055	0.010	0.006	0.000	0.003	0.015	0.014	0.044	1.799	0.140	0.060	18.1	0.823	10.17	5.92	2	93.29
P1420_006_Ap_A_1_POS_26	0.025	0.004	6.026	9.788	0.016	0.010	0.000	0.001	0.011	0.016	0.041	1.807	0.148	0.045	17.9	0.814	9.91	6.03	2	94.61
P1420_006_Ap_A_1_POS_27	0.027	0.005	6.029	9.783	0.011	0.009	0.000	0.002	0.011	0.016	0.043	1.885	0.179	0.000	18	0.814	9.91	6.03	2.06	94.99
P1420_006_Ap_A_1_POS_28	0.026	0.005	5.961	9.958	0.015	0.009	0.000	0.002	0.008	0.015	0.041	1.796	0.132	0.072	18	0.818	10.08	5.96	2	89.31
P1420_006_Ap_A_1_POS_29	0.025	0.004	5.953	9.952	0.014	0.007	0.000	0.002	0.015	0.020	0.049	1.890	0.129	0.000	18.1	0.823	10.09	5.95	2.02	90.09
P1420_006_Ap_A_1_POS_30	0.033	0.006	5.982	9.823	0.015	0.020	0.000	0.002	0.020	0.021	0.067	1.633	0.159	0.208	18	0.787	10.01	5.98	2	89.28
P1420_006_Ap_A_1_POS_31	0.020	0.003	5.984	9.913	0.012	0.009	0.000	0.002	0.012	0.012	0.037	1.909	0.162	0.000	18.1	0.818	10.02	5.98	2.07	92.31
P1420_006_Ap_A_1_POS_32	0.025	0.002	6.026	9.761	0.014	0.009	0.001	0.002	0.012	0.021	0.056	1.844	0.140	0.016	17.9	0.818	9.9	6.03	2	93.11
P1420_006_Ap_A_1_POS_33	0.017	0.004	6.012	9.784	0.011	0.009	0.000	0.002	0.015	0.021	0.064	1.909	0.140	0.000	18	0.820	9.93	6.01	2.05	94.87
P1420_006_Ap_A_1_POS_34	0.017	0.003	6.013	9.845	0.010	0.009	0.000	0.003	0.012	0.010	0.037	1.788	0.154	0.058	18	0.817	9.95	6.01	2	92.03
P1420_006_Ap_A_1_POS_35	0.024	0.003	5.973	9.856	0.012	0.008	0.001	0.003	0.016	0.025	0.074	1.927	0.134	0.000	18.1	0.820	10.02	5.97	2.06	89.32
P1420_006_Ap_A_1_POS_36	0.022	0.002	6.010	9.832	0.012	0.009	0.000	0.003	0.022	0.011	0.037	1.774	0.180	0.046	18	0.811	9.95	6.01	2	88.93
P1420_006_Ap_A_1_POS_37	0.026	0.002	6.030	9.754	0.015	0.011	0.000	0.002	0.011	0.022	0.054	1.827	0.113	0.060	17.9	0.819	9.9	6.03	2	94.80
P1420_006_Ap_A_1_POS_38	0.027	0.001	6.041	9.743	0.010	0.005	0.001	0.002	0.014	0.021	0.048	1.882	0.144	0.000	17.9	0.825	9.87	6.04	2.03	92.21
P1420_006_Ap_A_1_POS_39	0.019	0.001	5.994	9.864	0.012	0.008	0.001	0.002	0.011	0.019	0.048	1.851	0.151	0.000	18	0.820	9.98	6	2	92.03
AFT Length-Grains																				
P1420_006_Ap_A_2_POS_0	0.035	0.002	5.908	10.053	0.015	0.013	0.001	0.002	0.016	0.020	0.047	1.892	0.132	0.000	18.1	0.814	10.2	5.91	2.02	95.41
P1420_006_Ap_A_2_POS_1	0.023	0.002	6.090	9.651	0.015	0.008	0.001	0.002	0.011	0.014	0.030	1.621	0.137	0.242	17.8	0.811	9.76	6.09	2	91.57
P1420_006_Ap_A_2_POS_2	0.025	0.007	5.977	9.904	0.013	0.008	0.000	0.002	0.013	0.018	0.043	1.946	0.127	0.000	18.1	0.823	10.03	5.98	2.07	94.51
P1420_006_Ap_A_2_POS_3	0.050	0.061	5.937	9.879	0.013	0.071	0.000	0.002	0.014	0.017	0.040	1.999	0.159	0.000	18.2	0.718	10.15	5.94	2.16	94.00
P1420_006_Ap_A_2_POS_4	0.031	0.004	6.032	9.796	0.016	0.005	0.000	0.002	0.007	0.013	0.034	1.884	0.144	0.000	18	0.824	9.91	6.03	2.03	94.30
P1420_006_Ap_A_2_POS_5	0.026	0.011	5.887	9.758	0.010	0.133	0.001	0.002	0.016	0.073	0.148	1.984	0.148	0.000	18.2	0.558	10.18	5.89	2.13	97.17
P1420_006_Ap_A_2_POS_6	0.025	0.007	6.044	9.761	0.014	0.006	0.000	0.002	0.013	0.012	0.034	1.765	0.171	0.064	17.9	0.815	9.87	6.04	2	92.48
P1420_006_Ap_A_2_POS_7	0.028	0.004	5.928	9.985	0.017	0.008	0.001	0.002	0.014	0.024	0.061	1.980	0.124	0.000	18.2	0.821	10.14	5.93	2.1	92.88
P1420_006_Ap_A_2_POS_8	0.026	0.002	5.922	10.018	0.019	0.008	0.000	0.003	0.014	0.021	0.053	1.886	0.135	0.000	18.1	0.819	10.16	5.92	2.02	94.82
P1420_006_Ap_A_2_POS_9	0.017	0.014	5.988	9.886	0.016	0.006	0.001	0.002	0.011	0.017	0.038	1.882	0.180	0.000	18.1	0.815	10.01	5.99	2.06	95.65
P1420_006_Ap_A_2_POS_10	0.019	0.000	6.004	9.852	0.014	0.012	0.000	0.001	0.010	0.016	0.043	1.828	0.148	0.024	18	0.814	9.97	6	2	92.17
P1420_006_Ap_A_2_POS_11	0.008	0.007	6.111	9.638	0.014	0.010	0.000	0.002	0.008	0.007	0.017	1.807	0.119	0.074	17.8	0.823	9.71	6.11	2	94.94
P1420_006_Ap_A_2_POS_12	0.016	0.001	6.063	9.706	0.014	0.006	0.001	0.002	0.019	0.014	0.036	1.851	0.133	0.016	17.9	0.825	9.81	6.06	2	91.74
P1420_006_Ap_A_2_POS_13	0.028	0.004	5.978	9.883	0.018	0.006	0.000	0.002	0.015	0.020	0.051	1.820	0.153	0.028	18	0.816	10.03	5.98	2	92.01
P1420_006_Ap_A_2_POS_14	0.018	0.002	6.115	9.586	0.013	0.006	0.001	0.002	0.012	0.014	0.036	1.785	0.129	0.087	17.8	0.823	9.69	6.12	2	93.95
P1420_006_Ap_A_2_POS_15	0.018	0.058	5.937	9.974	0.016	0.041	0.000	0.002	0.011	0.006	0.022	1.792	0.131	0.077	18.1	0.774	10.15	5.94	2	93.93
P1420_006_Ap_A_2_POS_16	0.027	0.007	5.991	9.845	0.020	0.006	0.000	0.002	0.013	0.021	0.053	1.811	0.149	0.040	18	0.815	9.99	5.99	2	89.43

Note: Elemental concentrations in atoms per formula unit (apfu) were calculated from weight % oxide using the stoichiometric relationships of *Ketcham* [2015], and r_{mr0} was determined using the calculations of *Carlson et al.,* [1999]. Na, Mg, Mn, Fe, As, Sr, Y, La, Ce, and K were measured using LA-ICP-MS, whereas P, Ca, F and Cl were measured via EPMA.

Table A4. Conodont x-ray microcomputed tomography data

Blob Sample #	Genus	Max Length (µm)	Min Length (µm)	Volume ($µm^3$)	Surface Area ($µm^2$)	S/V	ESR (µm)	FT238	FT235	FT232	FT147	Simple Ft	Fragment
13JP02_14	Type 1	661.3	93.3	5405110	275711	0.051	58.8	0.77	0.74	0.73	0.91	0.74	-
13JP02_3	Type 1	2389.3	429.3	76589600	2010630	0.026	114.3	0.88	0.87	0.86	0.95	0.87	y
13JP02_22	Type 1	648.5	196.7	10592500	326856	0.031	97.2	0.86	0.84	0.84	0.94	0.84	y
13JP02_33	Type 1	301.9	53.0	575284	52117.2	0.091	33.1	0.60	0.55	0.54	0.84	0.56	-
13JP02_6	Type 1	555.7	82.0	2881340	150563	0.052	57.4	0.76	0.73	0.73	0.91	0.74	y
13JP02_16	Type 1	332.2	169.9	5134210	203749	0.040	75.6	0.82	0.80	0.79	0.93	0.80	y
13JP02_29	Type 1	238.0	65.5	528000	46952.5	0.089	33.7	0.61	0.55	0.55	0.84	0.56	-
13JP01_10	Type 1	355.6	72.0	918643	86191.2	0.094	32.0	0.61	0.56	0.56	0.85	0.59	-
13JP01_11	Type 1	389.6	71.6	969080	92242.7	0.095	31.5	0.61	0.57	0.56	0.84	0.59	-
13JP01_1	Type 1	297.2	82.7	850982	74980.8	0.088	34.0	0.63	0.58	0.58	0.85	0.61	-
13JP01_3	Type 1	323.9	60.5	497918	54873.4	0.110	27.2	0.55	0.49	0.48	0.82	0.52	-
13JP01_4	Type 1	753.2	105.6	3235700	295426	0.091	32.9	0.64	0.59	0.59	0.85	0.61	-
13JP03_2	Type 1	609.9	64.8	1613700	139924	0.087	34.6	0.63	0.58	0.57	0.86	0.57	-
13JP03_3	Type 1	321.7	67.6	610788	70043.9	0.115	26.2	0.53	0.48	0.47	0.81	0.47	-
13JP03_8	Type 1	984.1	114.7	7915950	403569	0.051	58.8	0.78	0.75	0.74	0.92	0.74	-
13JP03_9	Type 1	536.3	80.1	1492220	118478	0.079	37.8	0.66	0.61	0.61	0.87	0.61	-
13JP03_11	Type 1	512.8	42.0	632316	71192.6	0.113	26.6	0.53	0.46	0.45	0.82	0.45	-
13JP03_13	Type 1	507.2	57.3	1083490	98686.4	0.091	32.9	0.61	0.56	0.55	0.85	0.55	-
13JP03_17	Type 1	848.3	97.0	5461720	347950	0.064	47.1	0.72	0.68	0.68	0.90	0.68	-
13JP03_18	Type 1	426.7	66.4	1748100	123953	0.071	42.3	0.69	0.65	0.64	0.89	0.64	-
13JP03_20	Type 1	386.5	80.9	833452	92884.6	0.111	26.9	0.55	0.49	0.48	0.82	0.48	-
13JP03_21	Type 1	403.9	41.3	664916	69613.3	0.105	28.7	0.56	0.50	0.49	0.83	0.49	-
13JP03_24	Type 1	1486.0	110.3	16607200	705085	0.042	70.7	0.81	0.79	0.78	0.93	0.78	y
13JP03_25	Type 1	476.7	76.4	1726260	138571	0.080	37.4	0.65	0.61	0.60	0.87	0.60	-
13JP03_28	Type 1	527.6	49.6	958316	92659.9	0.097	31.0	0.59	0.53	0.53	0.85	0.53	-
13JP03_32	Type 1	484.4	45.6	960776	103670	0.108	27.8	0.55	0.49	0.49	0.83	0.49	-
13JP03_34	Type 1	382.4	47.6	956471	96349.5	0.101	29.8	0.58	0.52	0.51	0.84	0.51	-
13JP06_20	Type 1	975.8	126.5	7321120	336572	0.046	65.3	0.79	0.76	0.76	0.92	0.77	-
13JP06_4	Type 1	678.4	125.3	8938990	342159	0.038	78.4	0.83	0.80	0.80	0.93	0.81	y
13JP06_24	Type 1	379.9	136.6	5761560	246753	0.043	70.0	0.81	0.78	0.78	0.92	0.79	y
13JP06_5	Type 1	238.3	48.9	559008	50480.6	0.090	33.2	0.60	0.55	0.54	0.84	0.56	-
13JP06_7	Type 1	446.5	83.6	1464400	98901.1	0.068	44.4	0.70	0.66	0.65	0.88	0.66	y
13JP06_15	Type 1	1008.2	158.9	11385900	394410	0.035	86.6	0.84	0.82	0.82	0.94	0.82	-
13JP06_18	Type 1	245.6	61.1	468127	40705.4	0.087	34.5	0.61	0.56	0.55	0.85	0.57	-
13JP06_23	Type 1	1216.9	219.0	11522300	509223	0.044	67.9	0.80	0.77	0.77	0.92	0.78	-
13JP06_25	Type 1	448.5	60.3	1103440	80663.9	0.073	41.0	0.67	0.63	0.62	0.87	0.64	y
13JP06_26	Type 1	305.8	84.1	954258	64271.7	0.067	44.5	0.70	0.65	0.65	0.88	0.66	y
13JP07_9	Type 1	296.9	98.2	956830	76070.6	0.080	37.7	0.65	0.60	0.59	0.86	0.61	-
Leslie_8	Type 1	685.5	106.6	6846680	332544	0.049	61.8	0.79	0.76	0.75	0.92	0.76	-
Leslie_11	Type 1	692.5	123.1	7084440	327718	0.046	64.9	0.80	0.77	0.77	0.92	0.77	-
Leslie_13	Type 1	641.1	108.8	6463160	288406	0.045	67.2	0.80	0.78	0.77	0.93	0.78	-
Leslie_14	Type 1	500.8	92.6	4030460	215325	0.053	56.2	0.77	0.73	0.73	0.91	0.74	-
Leslie_16	Type 1	658.2	88.9	3656910	215031	0.059	51.0	0.74	0.71	0.70	0.90	0.71	-
Leslie_21	Type 1	545.4	71.4	1273230	115938	0.091	32.9	0.62	0.57	0.56	0.85	0.58	-
Leslie_25	Type 1	454.0	70.1	1143470	93762.6	0.082	36.6	0.65	0.60	0.60	0.87	0.61	-
Leslie_28	Type 1	454.2	90.5	3123970	244166	0.078	38.4	0.67	0.62	0.62	0.88	0.63	y
13JP01_9	Type 1	355.6	57.0	807003	71559.7	0.089	33.8	0.63	0.58	0.57	0.85	0.60	-
13JP07_4	Type 1	190.4	51.0	306940	28614.6	0.093	32.2	0.58	0.53	0.52	0.83	0.54	y
13JP07_6	Type 1	294.7	80.0	1289490	75291.3	0.058	51.4	0.74	0.70	0.69	0.90	0.71	y
13JP07_8	Type 1	349.5	90.1	1948810	102842	0.053	56.8	0.76	0.73	0.72	0.91	0.74	y
13JP07_12	Type 1	239.2	48.5	364384	33419	0.092	32.7	0.59	0.53	0.53	0.84	0.54	y
13JP02_8	Type 1	416.3	100.2	3042900	142931	0.047	63.9	0.79	0.76	0.75	0.92	0.76	y
13JP02_9	Type 1	457.7	70.5	1313100	103958	0.079	37.9	0.65	0.60	0.59	0.86	0.61	-
13JP02_21	Type 1	353.1	57.7	745702	61417	0.082	36.4	0.63	0.58	0.57	0.85	0.59	-
13JP02_24	Type 1	330.8	109.6	2070630	106726	0.052	58.2	0.77	0.73	0.73	0.91	0.74	y
13JP06_14	Type 1	408.3	111.7	2853340	165080	0.058	51.9	0.74	0.70	0.70	0.90	0.71	-
13JP06_17	Type 1	221.3	92.3	1179750	70381.7	0.060	50.3	0.73	0.69	0.69	0.89	0.70	-
13JP06_21	Type 1	413.3	46.6	536717	50490.7	0.094	31.9	0.58	0.52	0.52	0.84	0.53	-
13JP07_15	Type 1	508.1	139.5	5836150	253607	0.043	69.0	0.81	0.78	0.78	0.92	0.78	-
13JP07_14	Type 1	639.3	81.5	3505810	187428	0.053	56.1	0.76	0.73	0.72	0.91	0.73	-
13JP07_11	Type 1	680.3	64.9	2332060	150764	0.065	46.4	0.71	0.67	0.66	0.89	0.67	-
13JP07_1	Type 1	309.3	132.4	2367210	114977	0.049	61.8	0.78	0.75	0.75	0.92	0.76	-
13JP07_2	Type 1	145.3	39.0	170618	20708.2	0.121	24.7	0.47	0.41	0.40	0.78	0.42	-
13JP07_5	Type 1	169.8	47.5	277789	26708.5	0.096	31.2	0.57	0.51	0.50	0.83	0.52	y
13JP07_7	Type 1	172.3	63.3	486132	39765.8	0.082	36.7	0.64	0.59	0.58	0.86	0.60	-
13JP07_18	Type 1	523.6	149.7	8748650	294855	0.034	89.0	0.85	0.82	0.82	0.94	0.83	y
13JP07_16	Type 1	500.8	140.6	3564110	199075	0.056	53.7	0.75	0.71	0.71	0.90	0.72	-
13JP03_12	Type 1	510.2	50.3	1139460	111771	0.098	30.6	0.59	0.53	0.53	0.84	0.53	-
13JP01_7	Type 1	278.3	71.0	891886	75588.3	0.085	35.4	0.65	0.61	0.60	0.86	0.63	-
13JP02_30	Type 1	1010.9	203.2	36277400	882061	0.024	123.4	0.89	0.87	0.87	0.96	0.88	-
13JP02_2	Type 1	501.0	159.3	6579320	246515	0.037	80.1	0.83	0.80	0.80	0.93	0.81	y
13JP02_27	Type 1	856.2	104.7	9900000	457954	0.046	64.9	0.79	0.76	0.76	0.92	0.77	-

Blob Sample #	Genus	Max Length (µm)	Min Length (µm)	Volume ($µm^3$)	Surface Area ($µm^2$)	S/V	ESR (µm)	FT238	FT235	FT232	FT147	Simple Ft	Fragment
13JP02_26	Type 2	768.3	168.7	12203100	489965	0.040	74.7	0.82	0.79	0.79	0.93	0.80	y
13JP02_10	Type 2	1444.5	177.4	16746300	695890	0.042	72.2	0.81	0.79	0.78	0.93	0.79	-
13JP02_1	Type 2	1247.9	174.6	16048800	638714	0.040	75.4	0.82	0.79	0.79	0.93	0.80	-
13JP02_25	Type 2	372.9	113.0	3865430	166625	0.043	69.6	0.80	0.78	0.77	0.93	0.78	y
13JP02_32	Type 2	886.2	106.9	5477020	300164	0.055	54.7	0.75	0.72	0.71	0.90	0.72	-
13JP03_5	Type 2	362.5	95.3	2306600	161301	0.070	42.9	0.70	0.66	0.65	0.88	0.65	y
13JP03_23	Type 2	705.2	105.7	3097610	243001	0.078	38.2	0.66	0.62	0.61	0.87	0.61	-
13JP03_36	Type 2	836.7	119.5	6976390	388738	0.056	53.8	0.76	0.72	0.72	0.91	0.72	-
13JP07_13	Type 2	331.3	41.3	427830	49125.5	0.115	26.1	0.50	0.44	0.43	0.80	0.45	-
Leslie_1	Type 2	720.1	128.7	8157660	447529	0.055	54.7	0.76	0.73	0.72	0.91	0.74	-
Leslie_2	Type 2	1511.4	339.2	30806100	1248360	0.041	74.0	0.82	0.80	0.79	0.93	0.80	-
Leslie_3	Type 2	1016.1	168.9	4862250	352706	0.073	41.4	0.69	0.64	0.64	0.88	0.65	-
Leslie_10	Type 2	1191.4	391.1	35216400	1208180	0.034	87.4	0.85	0.83	0.82	0.94	0.83	y
Leslie_12	Type 2	1097.4	235.7	10381400	578930	0.056	53.8	0.75	0.72	0.71	0.91	0.73	-
Leslie_17	Type 2	778.7	130.1	4540600	310728	0.068	43.8	0.70	0.66	0.65	0.89	0.67	-
Leslie_22	Type 2	392.0	81.2	1212680	126393	0.104	28.8	0.57	0.51	0.50	0.83	0.52	Y
Leslie_24	Type 2	1024.6	215.2	14893400	672457	0.045	66.4	0.80	0.77	0.77	0.93	0.78	y
Leslie_26	Type 2	1141.1	185.0	8136690	457101	0.056	53.4	0.76	0.72	0.72	0.91	0.73	-
Leslie_29	Type 2	659.9	125.2	4527750	253166	0.056	53.7	0.76	0.72	0.71	0.91	0.73	-
Leslie_30	Type 2	1231.5	284.0	15117600	750100	0.050	60.5	0.79	0.75	0.75	0.92	0.76	-
Leslie_32	Type 2	720.0	141.1	8836870	378489	0.043	70.0	0.81	0.79	0.78	0.93	0.79	y
Leslie_34	Type 2	731.2	102.0	5157680	302613	0.059	51.1	0.75	0.71	0.70	0.91	0.72	-
Leslie_38	Type 2	685.0	176.5	4045670	301459	0.075	40.3	0.68	0.64	0.63	0.88	0.64	-
Leslie_39	Type 2	909.1	129.2	4839180	336486	0.070	43.1	0.70	0.66	0.65	0.89	0.66	-
Leslie_42	Type 2	524.9	135.0	4906550	305054	0.062	48.3	0.73	0.70	0.69	0.90	0.70	y
Leslie_44	Type 2	904.0	149.4	5670440	315334	0.056	53.9	0.76	0.72	0.72	0.91	0.73	-
13JP02_11	Type 2	623.6	140.1	8616450	343147	0.040	75.3	0.82	0.79	0.79	0.93	0.80	y
13JP07_17	Type 2	437.2	136.6	4453210	211445	0.047	63.2	0.79	0.76	0.75	0.92	0.76	-
13JP07_19	Type 2	374.2	132.1	2542970	134224	0.053	56.8	0.76	0.73	0.73	0.91	0.74	-
13JP02_18	Type 3a	805.1	96.9	9431110	440442	0.047	64.2	0.79	0.76	0.75	0.92	0.76	-
13JP07_10	Type 3a	273.2	49.6	631028	58724.5	0.093	32.2	0.59	0.54	0.53	0.84	0.55	-
Leslie_33	Type 3a	579.4	53.2	2328620	194384	0.083	35.9	0.64	0.59	0.58	0.87	0.60	-
Leslie_35	Type 3a	400.3	108.8	3668970	254909	0.069	43.2	0.70	0.66	0.65	0.89	0.67	-
Leslie_37	Type 3a	788.0	58.0	4270330	305577	0.072	41.9	0.69	0.65	0.64	0.89	0.66	-
Leslie_40	Type 3a	681.2	67.6	5219290	333444	0.064	47.0	0.73	0.69	0.68	0.90	0.69	-
13JP02_7	Type 3b	418.5	127.8	5536120	227451	0.041	73.0	0.81	0.79	0.78	0.93	0.79	y
13JP02_31	Type 3b	416.6	130.9	4308720	187909	0.044	68.8	0.80	0.78	0.77	0.92	0.78	-
13JP01_5	Type 3b	248.8	58.9	494228	59911.5	0.121	24.7	0.51	0.46	0.45	0.80	0.49	-
13JP03_4	Type 3b	411.7	59.5	1367350	129375	0.095	31.7	0.60	0.55	0.54	0.85	0.54	-
13JP03_30	Type 3b	468.4	43.9	822073	96482.7	0.117	25.6	0.52	0.46	0.45	0.81	0.45	-
13JP06_11	Type 3b	483.1	127.1	6702100	290312	0.043	69.3	0.81	0.78	0.77	0.92	0.78	-
13JP06_1	Type 3b	629.8	191.8	12702900	447039	0.035	85.2	0.84	0.82	0.82	0.94	0.82	-
13JP07_3	Type 3b	458.7	164.8	5989620	251300	0.042	71.5	0.81	0.78	0.78	0.93	0.79	-
Leslie_4	Type 3b	450.6	77.9	3169840	185894	0.059	51.2	0.74	0.71	0.70	0.91	0.71	-
Leslie_5	Type 3b	365.0	80.4	2674390	161670	0.060	49.6	0.74	0.70	0.69	0.90	0.71	-
Leslie_6	Type 3b	466.1	63.2	2078800	158158	0.076	39.4	0.67	0.63	0.62	0.88	0.63	-
Leslie_7	Type 3b	391.9	103.0	2298480	157720	0.069	43.7	0.70	0.66	0.66	0.89	0.67	-
Leslie_9	Type 3b	501.1	59.8	1860440	134072	0.072	41.6	0.69	0.64	0.64	0.88	0.65	-
Leslie_15	Type 3b	441.0	71.6	2834300	180602	0.064	47.1	0.72	0.68	0.67	0.90	0.69	-
Leslie_18	Type 3b	529.7	101.9	5586030	288174	0.052	58.2	0.77	0.74	0.73	0.92	0.75	-
Leslie_19	Type 3b	404.7	69.3	2587360	178105	0.069	43.6	0.70	0.66	0.66	0.89	0.67	-
Leslie_20	Type 3b	569.6	88.9	5124910	275449	0.054	55.8	0.77	0.73	0.73	0.91	0.74	-
Leslie_23	Type 3b	507.1	67.6	2457600	185552	0.076	39.7	0.67	0.63	0.62	0.88	0.64	-
Leslie_27	Type 3b	346.9	77.1	2323380	146234	0.063	47.7	0.73	0.69	0.69	0.90	0.70	-
Leslie_31	Type 3b	450.2	76.4	3321100	203939	0.061	48.9	0.74	0.70	0.69	0.90	0.70	-
13JP03_10	Type 3b	346.4	48.0	1102560	106856	0.097	31.0	0.59	0.53	0.53	0.85	0.53	-
13JP03_6	Type 3b	574.3	60.2	1650910	137159	0.083	36.1	0.65	0.60	0.60	0.87	0.60	-
13JP03_31	Type 3b	542.8	78.6	6294560	315021	0.050	59.9	0.78	0.75	0.74	0.92	0.74	-
13JP06_19	Type 3b	587.8	208.7	12984900	463310	0.036	84.1	0.84	0.82	0.81	0.94	0.82	-
13JP03_29	type 4	386.2	62.8	2103010	144376	0.069	43.7	0.70	0.66	0.66	0.89	0.66	-
13JP03_33	type 4	629.2	77.2	1590320	126114	0.079	37.8	0.66	0.61	0.60	0.87	0.60	-
13JP03_35	type 4	643.9	107.7	3989500	209552	0.053	57.1	0.77	0.74	0.73	0.91	0.73	-
13JP01_6	type 4	282.4	75.5	1092100	92278	0.084	35.5	0.65	0.60	0.59	0.86	0.62	y
13JP02_20	type 4	642.9	94.3	4066390	210461	0.052	58.0	0.77	0.73	0.73	0.91	0.74	y
13JP02_5	type 4	462.6	130.5	4433820	221074	0.050	60.2	0.78	0.74	0.74	0.91	0.75	y
13JP02_15	type 4	614.1	74.3	2579910	169439	0.066	45.7	0.71	0.67	0.66	0.89	0.67	-
13JP01_8	Type 4	430.8	91.0	2277380	173817	0.076	39.3	0.68	0.64	0.63	0.87	0.66	-
13JP03_7	type 4	425.2	77.5	1306770	107783	0.082	36.4	0.65	0.60	0.59	0.87	0.59	-
13JP03_14	type 4	536.6	80.3	3965510	221606	0.056	53.7	0.76	0.72	0.72	0.91	0.72	y
13JP03_22	type 4	363.1	51.5	509913	67613.6	0.133	22.6	0.46	0.40	0.40	0.79	0.40	-
13JP03_26	type 4	405.3	57.4	933712	97977.4	0.105	28.6	0.56	0.51	0.50	0.83	0.50	-
13JP06_9	Type 5	687.8	282.2	17797400	635031	0.036	84.1	0.84	0.81	0.81	0.94	0.82	-
13JP02_4	Type 5	559.1	191.0	13606800	432044	0.032	94.5	0.86	0.84	0.83	0.94	0.84	-

Blob Sample #	Genus	Max Length (µm)	Min Length (µm)	Volume ($µm^3$)	Surface Area ($µm^2$)	S/V	ESR (µm)	FT238	FT235	FT232	FT147	Simple Ft	Fragment
13JP03_19	Type 5	305.4	119.4	1256020	121960	0.097	30.9	0.59	0.53	0.52	0.84	0.52	-
13JP02_28	Type 5	815.4	301.9	20125100	705628	0.035	85.6	0.84	0.82	0.82	0.94	0.82	-
13JP02_13	Type 5	669.3	274.9	13978200	525706	0.038	79.8	0.83	0.81	0.80	0.93	0.81	-
13JP02_17	Type 5	310.0	116.8	2786780	130409	0.047	64.1	0.79	0.76	0.75	0.92	0.76	-
13JP02_23	Type 5	345.5	221.7	7113230	260997	0.037	81.8	0.84	0.81	0.81	0.94	0.82	-
13JP02_12	Type 5	384.1	193.6	6708360	274955	0.041	73.2	0.81	0.79	0.78	0.93	0.79	-
13JP03_15	Type 5	422.4	125.8	3906460	230435	0.059	50.9	0.74	0.71	0.70	0.90	0.70	-
13JP03_16	Type 5	242.5	34.1	326615	44871.9	0.137	21.8	0.43	0.37	0.36	0.78	0.36	-
13JP03_27	Type 5	388.4	144.5	3565080	200005	0.056	53.5	0.76	0.72	0.72	0.91	0.72	-

Blob3D derived volumetric data dor conodonts of Ordovician to Silurian age from Anticosti Island (13JP01, 13JP02, 13JP03, 13JP06, 13JP07) and Iowa, Kentucky, and Minnesota (Leslie). Max and min lengths refer to the dimensions of the longest and shortest axes of the best fitting ellipsoid generated by Blob3D [*Ketcham*, 2005]. Ft describes the alpha ejection correction for ^{238}U, ^{235}U, ^{232}Th and ^{147}Sm. Simple Ft summarizes a plausible Ft correction for each conodont assuming a fixed Th/U ratio of 10. Note that the true Ft correction for each analyzed conodont will differ depending on the proportions of U, Th and Sm. Fragment refers to whether or not the conodont is whole (-) or has been broken (y)

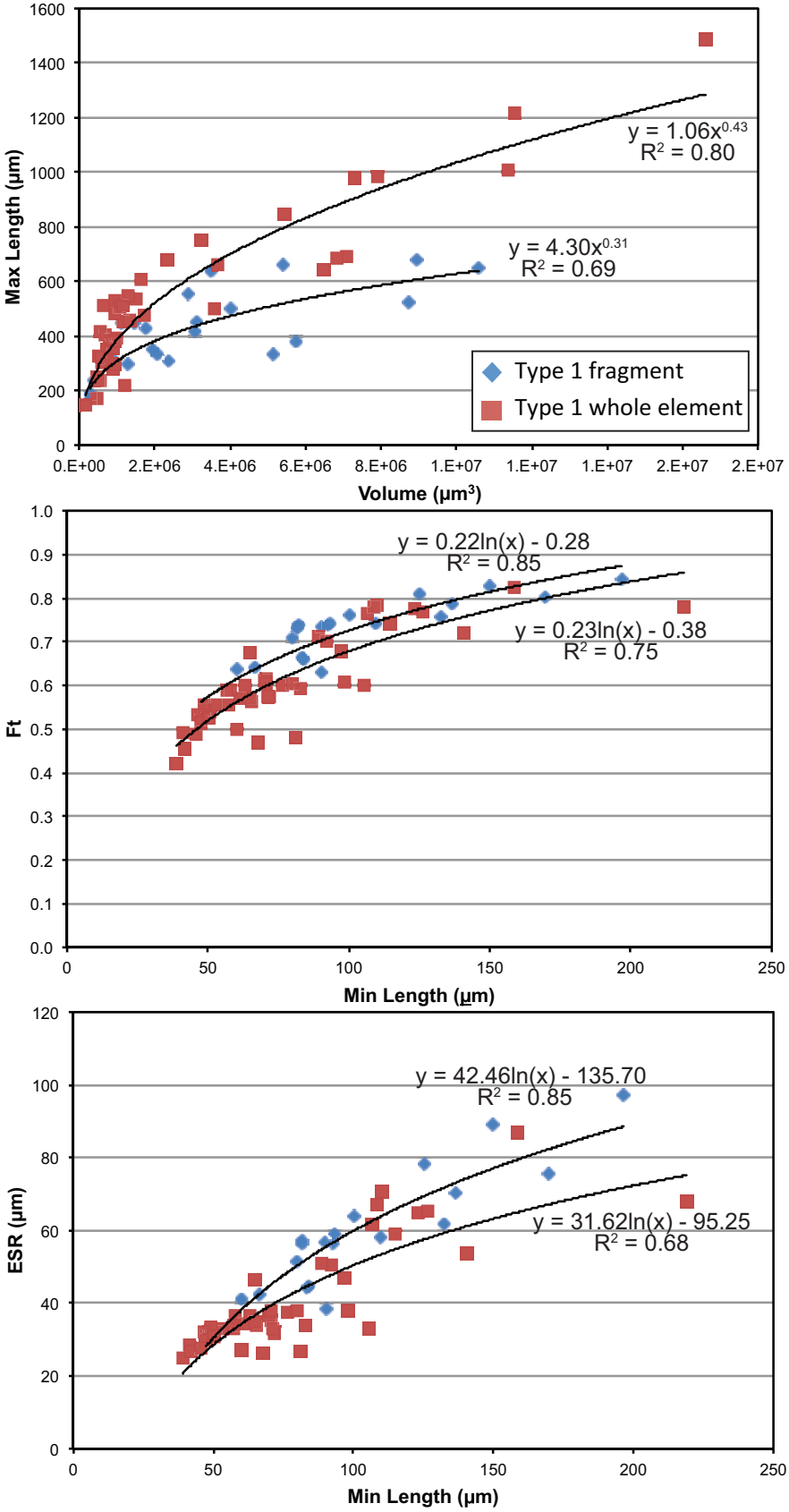

Fig. A1: X-Ray micro-computed CT relationships for Type 1 conodont elements

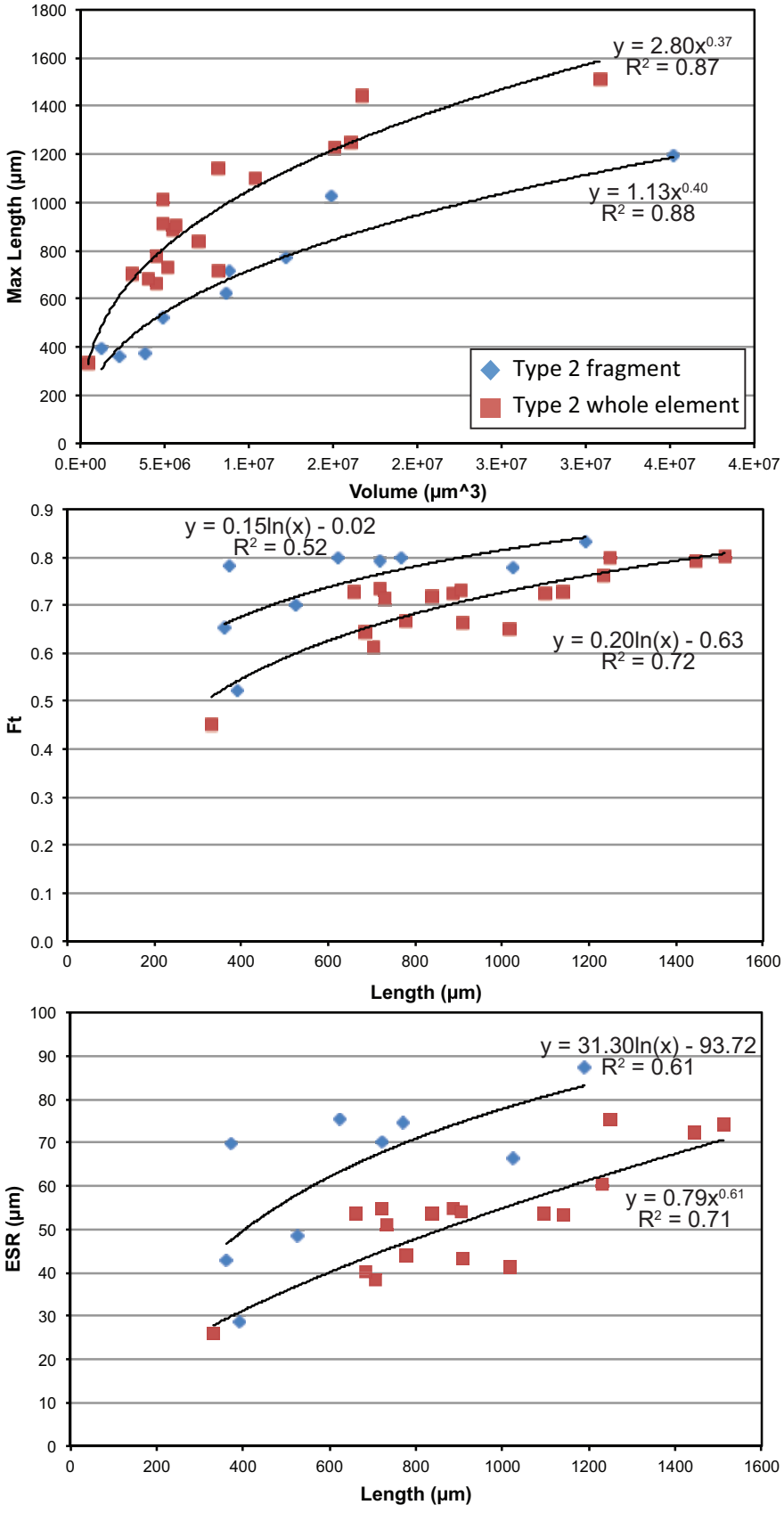

Fig. A2: X-Ray micro-computed CT relationships for Type 2 conodont elements

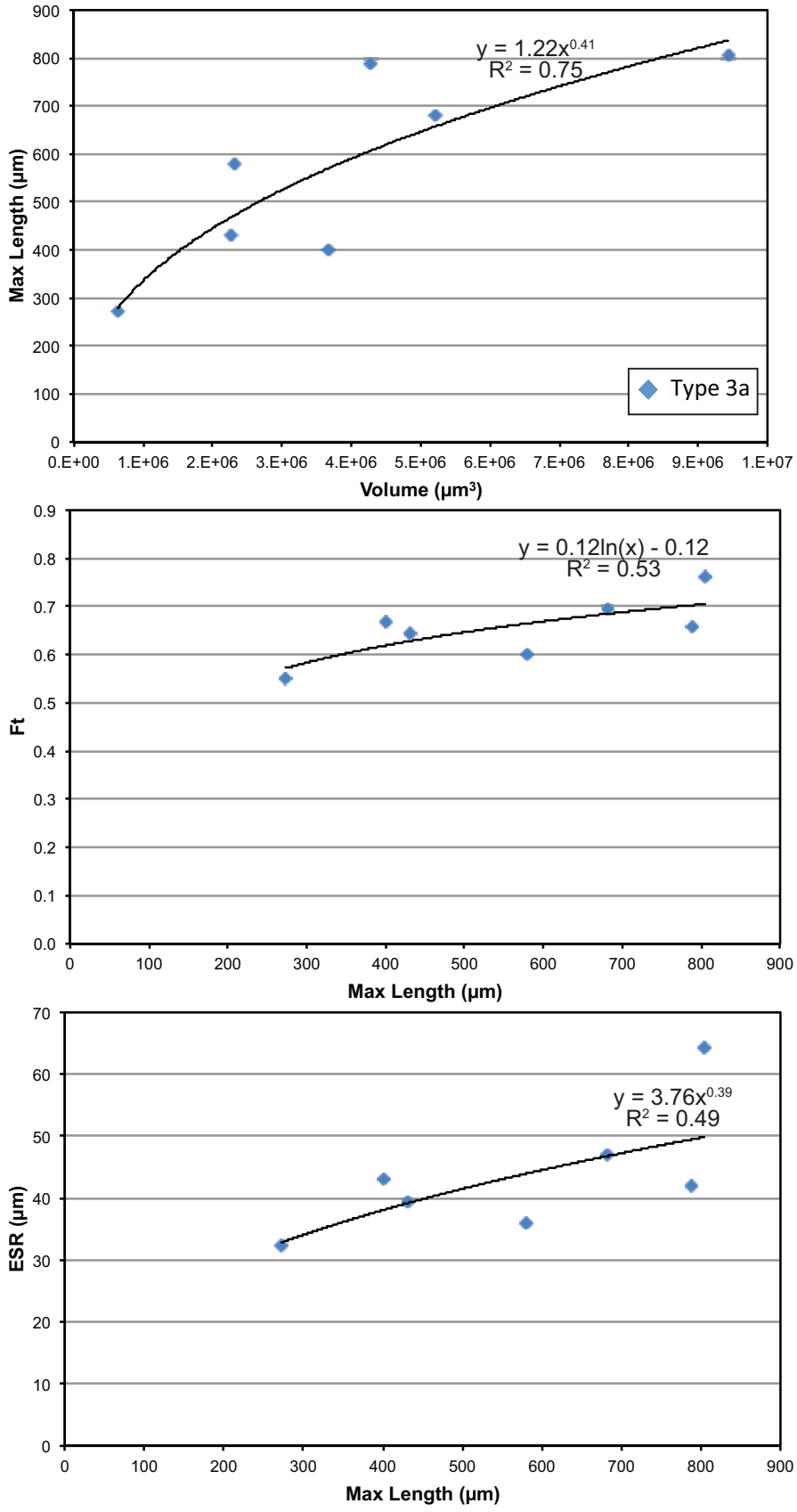

Fig. A3: X-Ray micro-computed CT relationships for Type 3a conodont elements

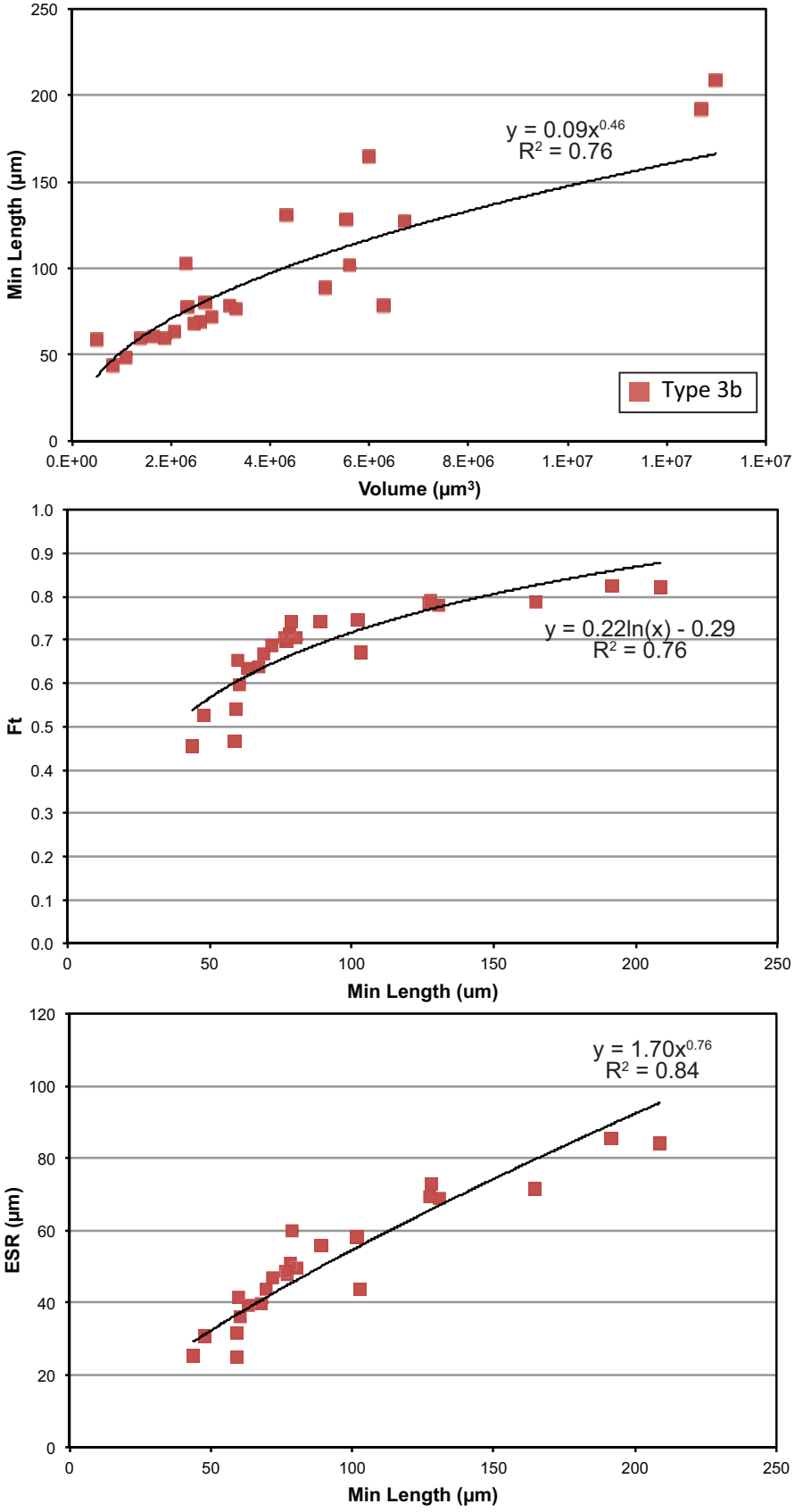

Fig. A4: X-Ray micro-computed CT relationships for Type 3b conodont elements

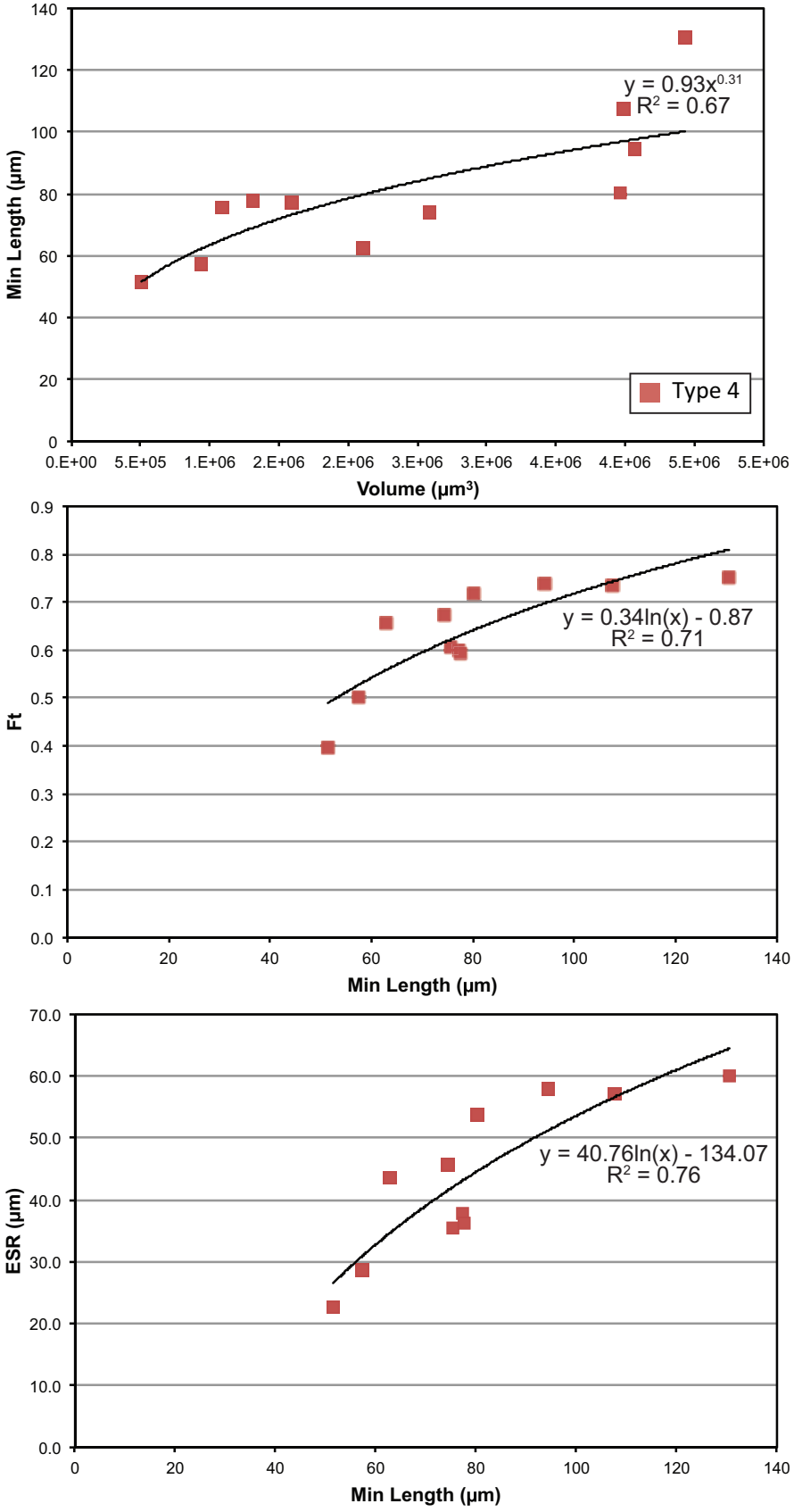

Fig. A5: X-Ray micro-computed CT relationships for Type 4 conodont elements

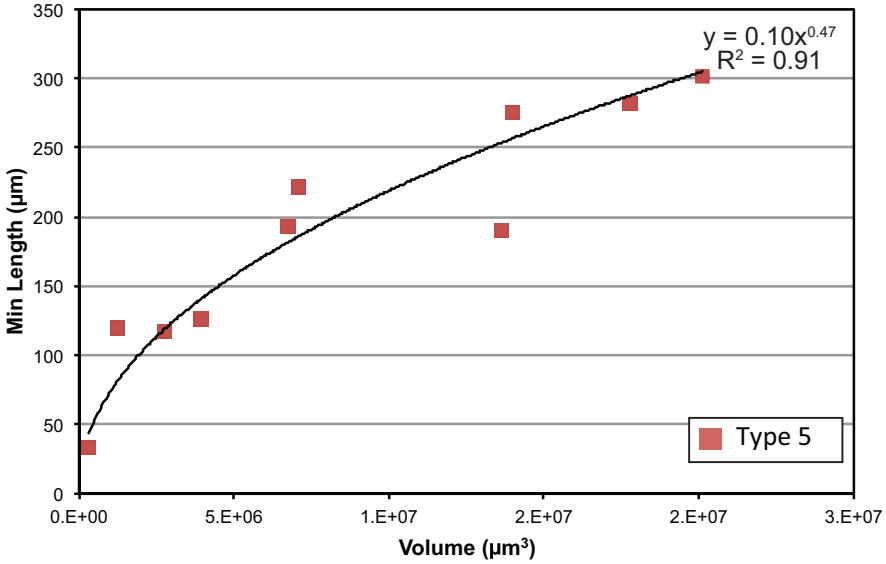

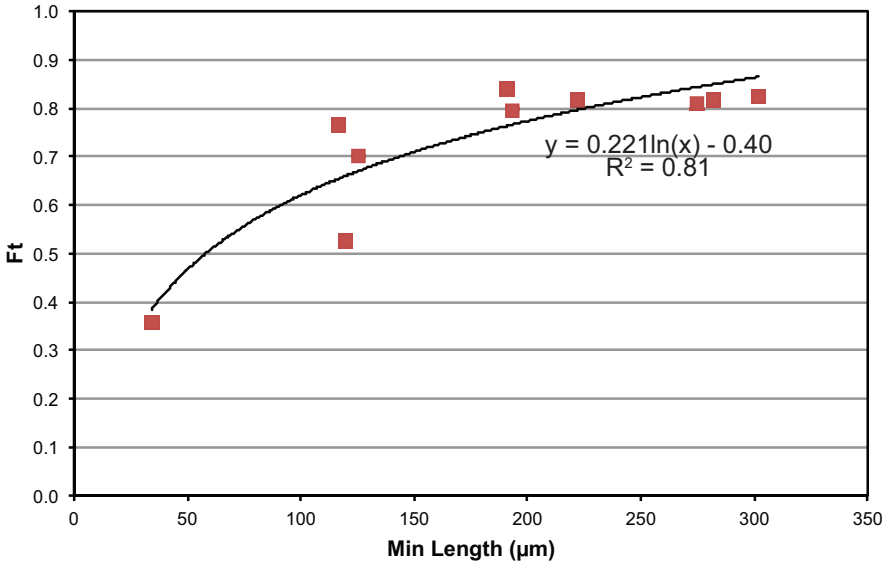

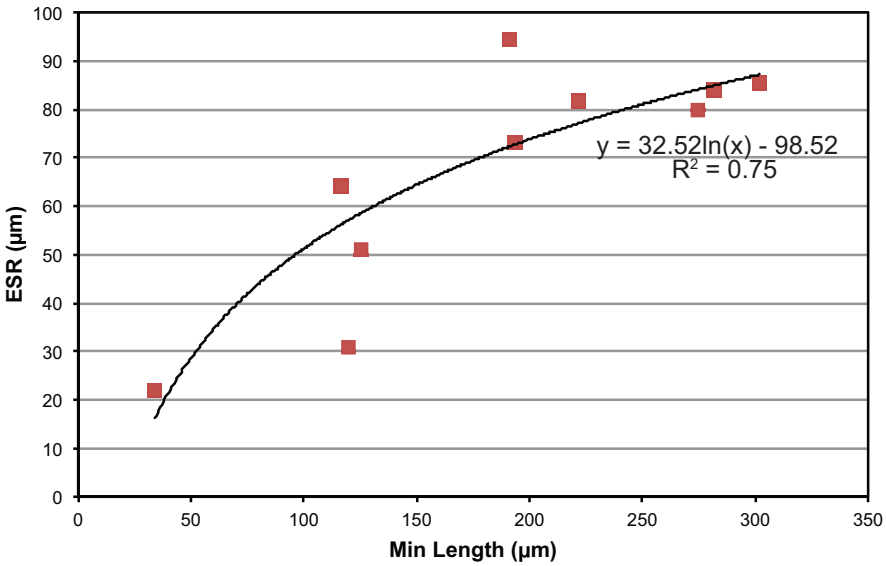

Fig. A6: X-Ray micro-computed CT relationships for Type 5 conodont elements

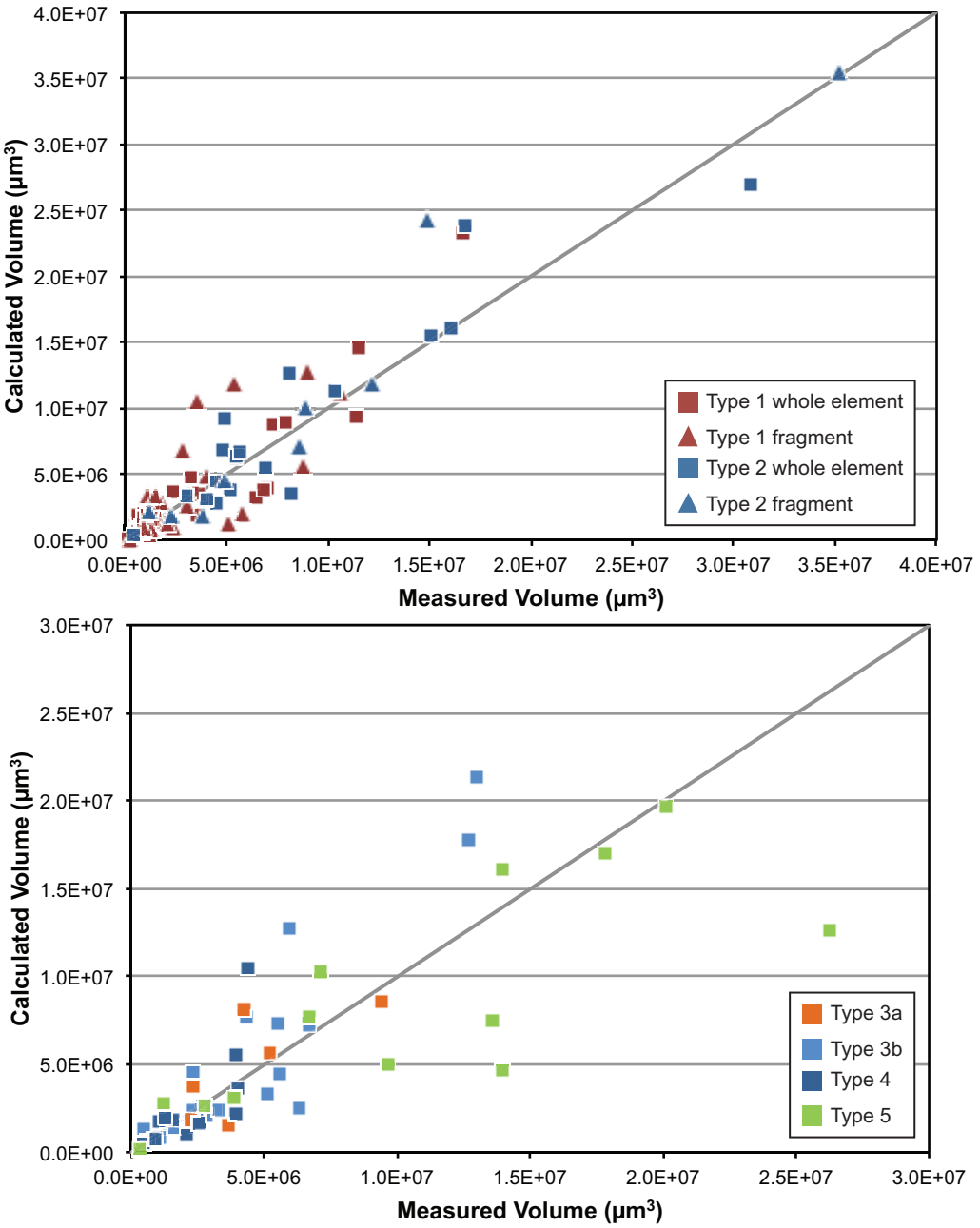

Fig. A7: Calculated vs measured volumes for all conodont morphology types. Gray line shows a 1:1 relationship for comparison

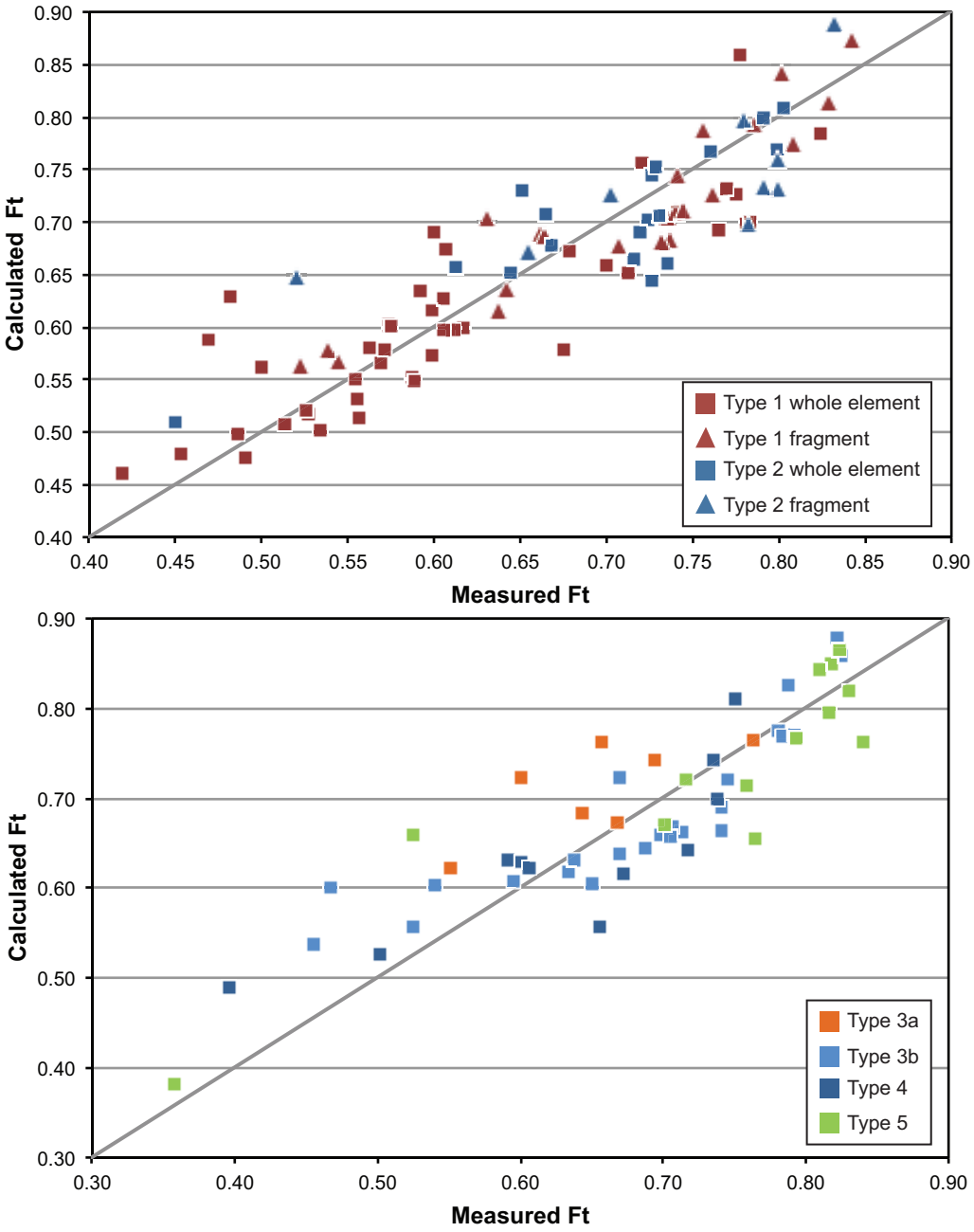

Fig. A8: Calculated vs measured F_t-corrections for all conodont morphology types. Gray line shows a 1:1 relationship for comparison

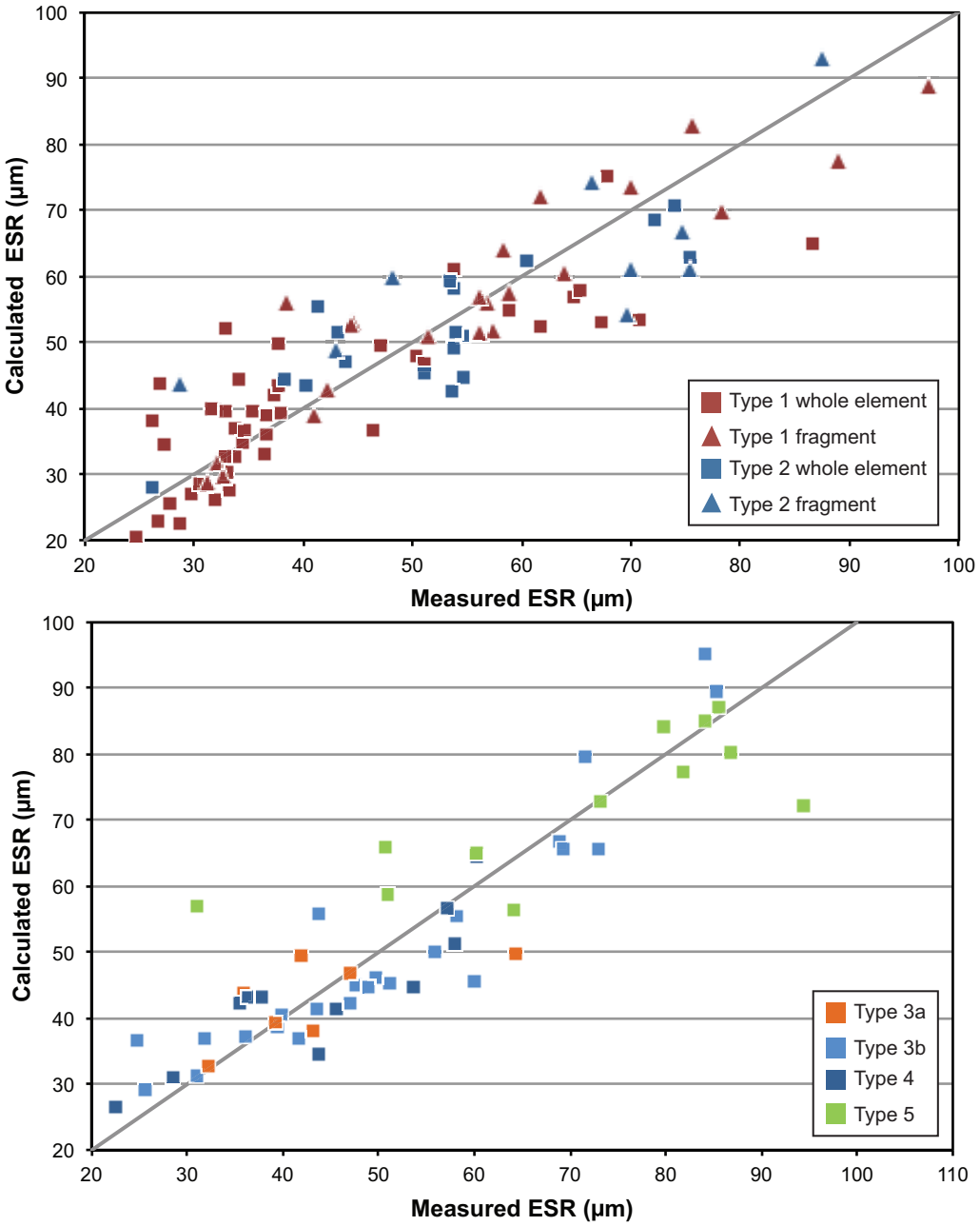

Fig. A9: Calculated vs measured equivalent spherical radius (ESR) for all conodont morphology types. Gray line shows a 1:1 relationship for comparison

CHAPTER 6

Conclusions

6.1. Unroofing and uplift history of the northern Canadian Cordillera foreland fold-thrust belt

Zircon and apatite (U-Th)/He (ZHe, AHe) and apatite fission track (AFT) thermochronology data presented in Chapters 2 and 4 are a significant improvement to the overall understanding of the northern Canadian Cordillera as they provide the first quantitative assessments of the exhumation history of its the foreland fold-thrust belt [*Powell et al.*, 2016]. Whereas many previous studies [e.g., *Dusel-Bacon et al*., 2002; *Mair et al.,* 2006; *Staples et al.,* 2016] have connected the timing of Mesozoic terrane accretion and Farallon plate subduction with northern Cordillera structural evolution (Fig. 1), similar relationships cannot be easily drawn with the Mackenzie Mountains due to the absence of a magmatic record and lack of syntectonic strata [*Gordey et al.*, 2011].

ZHe data presented in Chapter 2 span the Mackenzie Mountains from the hanging wall of the Plateau Fault in the south through each of the major anticlines to the deformation front in the north (Fig. 1 of Chapter 2). Results from this study track the Albian – Paleocene propagation of the fold-thrust belt towards the foreland. These data suggest that Early Cretaceous deformation in the Selwyn Basin resulted in subsidence in the study area and the deposition of a northeast-thinning Aptian – Albian stratigraphic package (Fig. 2). Cenomanian cooling in the southwest of the study area is the earliest evidence of Cordilleran deformation in the region (Fig. 3). Deformation in the fold-thrust belt continued throughout the Cretaceous, including movement along the Canyon Fault in the Maastrichtian and regional folding between the Paleocene and Eocene [*Powell et al.*, 2016].

Among the most important findings of this study are the constraints placed on the timing of movement along the Plateau and Canyon Faults. The Plateau Fault is a major regional thrust

fault with a strike length of ~270 km [*MacNaughton et al.*, 2008] that separates highly deformed and faulted strata in the hinterland from the broad, flat-topped anticlines that characterize the study area [*Gordey et al.*, 2011]. Whereas timing of movement along the Plateau Fault was loosely constrained to Early Cretaceous to Paleocene on the basis of deformed strata [*Blusson*, 1971; *Aitken et al.*, 1982], the ZHe data in Chapter 2 resolve its history to Cenomanian to Maastrichtian [*Powell et al.*, 2016]. These findings suggest that onset of deformation in the Mackenzie Mountains closely followed the waning stages of deformation in the Selwyn Basin [*Mair et al.*, 2006]. ZHe data exhibit a significant difference in cooling date over a short distance across the Canyon Fault, a thrust fault proximal to the Mackenzie Mountains deformation front. These results suggest discrete cooling histories for the Foran and Rouge Mountain anticlines on either side of the structure, and support recent remapping of the Canyon Fault as a thrust fault with significant displacement [*Fallas and MacNaughton*, 2014].

AHe and AFT data Devonian Imperial Formations along the Mackenzie Mountains front, Norman Range and the intermediate Imperial Anticline (Fig. 1 of Chapter 4) elucidate a similar Paleocene – Eocene cooling history as the ZHe data of Chapter 2, albeit with lower cooling rates than modeled from the cores of anticlines across the fold-thrust belt. These results indicate that the formation of Cordilleran structures to the north of the Mackenzie Mountains front was contemporaneous with the final pulse of exhumation in the fold thrust belt (Fig. 3). A subset of the AHe and AFT data presented in Chapter 4 elicit a two-phase Cenozoic cooling history, in which an Oligocene/Miocene cooling event follows isothermal conditions throughout the Late Paleocene and Eocene. The cause of this final cooling event is poorly understood, and is tentatively attributed to either a change in climate between the Eocene and Oligocene [*Eldrett et*

al., 2009] or far-field effects of the collision between the Yakutat block with North America [*Hyndman et al.*, 2005].

6.2. Burial history of the hydrocarbon-bearing Mackenzie Plain

A central objective of this project was to determine whether the burial history of Phanerozoic strata across the Mackenzie Plain was conducive to hydrocarbon generation. The thermal history of Devonian source rocks were of specific interest, as shales within the Horn River Group are organically-rich, oil-prone, aerially extensive [*Feinstein et al.*, 1988a] and are the known source rock for the Norman Wells oil field [*Snowdon et al.*, 1987]. However, determining the timing of their maturation is confounded by unknown amounts of material deposited and eroded across sub-Albian and post-Paleocene unconformities [*Feinstein et al.*, 1991, 1996; *Issler et al.*, 2005].

Thermochronology data presented in Chapter 4 suggest a pre-Albian thermal maximum across the Mackenzie Plain, with total burial thickness for the Imperial Formation ranging from 2.2 – 3.6 km in the northern Mackenzie Plain and 5.5 – 6.3 km in the Root Basin (Fig. 9 of Chapter 4). In comparison, results from AHe modeling suggest that Cretaceous to Paleocene strata achieved a maximum thickness of ~2.2 – 2.5 km in the northern Mackenzie Plain and 2.8 – 3.8 km in the Brackett Basin. The temperatures corresponding to this Cretaceous package are similar to those derived from multi-kinetic AFT and AHe modeling of the basal bentonite to the Cretaceous Slater River Formation (Chapter 3).

Whereas these results are supported by another thermochronology study in the region [*Issler et al.*, 2005], they are counter to the Cenozoic maximum predicted from shale compaction and organic thermal maturity profiles [*Feinstein et al.*, 1991, 1996]. A comparison of organic thermal maturity profiles modeled using the new basin%Ro calibration [*Nielsen et al.*, 2015]

with the earlier EASY%Ro [*Sweeney and Burnham*, 1990] suggests that discrepancy between modeled thermal maximums is due to the EASY%Ro calibration systematically over-predicting organic thermal maturity values through a key maturity window that coincides with the sub-Cretaceous unconformity across the northern Mackenzie Plain (Chapter 4).

Problematic to the interpretation of a pre-Albian thermal maximum is the absence of late Paleozoic to Early Cretaceous stratigraphy across the region. The nearest examples of similar age strata in the region are hundreds of kilometers distal from the study area and include Permian to Triassic strata that terminate abruptly at the Beaver River Structure in the southern Mackenzie Mountains [*Morrow and Miles*, 2000] and the Jurassic Husky Formation of the Anderson Plain in the Yukon [*Dixon*, 1999]. However, the conclusions of Chapter 4 are supported by other regional thermochronology studies, including the ZHe data presented in Chapter 2 and AHe data from the Slave craton to the east. These studies report heating and cooling due to the deposition and erosion of Paleozoic to Mesozoic strata of similar thickness as estimated in Chapter 4 [*Ault et al.*, 2009, 2013; *Powell et al.*, 2016].

ZHe data in Chapter 2 invoke heating across much of the present day fold-thrust belt due to burial of an Aptian to Albian sedimentary package (Fig. 2). These results suggest an aerially extensive Early Cretaceous basin connected the marine sediments of the Martin House and Arctic Red Formations in the Mackenzie Plain [*Dixon*, 1999; *Thomson et al.*, 2011] with the non-marine strata preserved in fault-bounded outliers in the hanging wall of the Plateau Fault [*Blusson*, 1971]. This package has been entirely eroded from the fold-thrust belt during folding and faulting (Fig. 3) and partially eroded from the Mackenzie Plain due to movement along the Keele Arch [*MacLean et al.*, 2014]. Likewise, the ZHe modeled cooling histories of structures within the fold-thrust belt coincide with periods of punctuated subsidence and increasingly

proximal sediment sources recorded in the Cretaceous stratigraphy of the Mackenzie Plain (Fig. 3).

Results from Chapters 2, 3 and 4 are not overly favourable for the preservation of conventional petroleum systems in the Mackenzie Plain: hydrocarbons that generated from Devonian sources likely migrated into reservoir units that were eroded prior to the Cretaceous. Some potential exists for Cretaceous hydrocarbon systems, given isolated hydrocarbon discoveries that are sourced from the Slater River Formation [*Feinstein et al.*, 1988a]. Thermal history modeling of apatite from the bentonite in Chapter 3 [*Powell et al.*, 2017] indicates that the Slater River Formation is perhaps marginally mature at the Imperial River section. These results support other studies [*Feinstein et al.*, 1988a] that suggest shales of the Slater River Formation may be of local significance across the Mackenzie Plain, charging proximal structural and stratigraphic traps. Such an interpretation has been suggested for the heavy oil recovered from the Cambrian-Ordovician Franklin Mountain Formation in the B-44 well of the Brackett Basin [*Feinstein et al.*, 1988a; *Hannigan et al.*, 2011]. Timing of structural trap formation in the Mackenzie Plain are likely coincident with either the Maastrichtian cooling modeled in the Foran anticline or the Paleocene cooling history of the deformation front, Imperial anticline and Norman Range (Fig. 3). Additionally, studies of salt-induced tectonism across the Mackenzie Plain suggest several phases of salt movement, including pre-Turonian, Late Cretaceous and post-Paleocene events, which may provide additional hydrocarbon trapping structures across the region [*Maclean and Cook*, 1999].

Results from this study do not preclude a Cenozoic thermal maximum for the northern Mackenzie Plain, as no AFT samples were analyzed from Devonian outcrops north of the deformation front, and organic thermal maturity data from Devonian strata suggest increasingly

lower maximum paleotemperatures towards the north of the study area [*Feinstein et al.*, 1988b]. As a result, this study is unable to resolve the timing of hydrocarbon charging in the Norman Wells oil field [*Hadlari*, 2015]. This thesis did not investigate earlier hydrocarbon systems across the Mackenzie Plain, including those hosted in Cambrian-Ordovician carbonates or basal Cambrian sandstones [*Hannigan et al.*, 2011].

6.3. Implications for low-temperature thermochronology

Prior to the onset of this study, it was uncommon to measure more than 4 single grains per sample for (U-Th)/He analysis [e.g., *Tian et al.*, 2012]. Whereas this study analyzed many more individual aliquots per sample (n: 20 for sample 13JP02 of Chapter 5), advances in mineral dissolution methods [*Metcalf et al.*, 2016] and in-situ LA-ICP-MS (U-Th)/He thermochronology [*Evans et al.*, 2015; *Pickering et al.*, 2015] are sure to substantially increase both the number of single-grain analyses as well as the practicality of analyzing many samples. However, the results of this research stress that proper sample characterization is essential to understand the time-temperature implication of thermochronometer date dispersion. In that sense, larger datasets that have been properly characterized with respect to diffusion and annealing kinetics will have the same interpretative challenges as those with fewer grains.

The presence of multi-kinetic fission track annealing kinetics in all detrital, igneous and metamorphic AFT samples in this dataset (Chapters 3 – 5) are among the most important observations of this study. These results suggest that small differences in apatite chemistry may have a significant effect on annealing kinetics in samples with protracted thermal histories. These findings have major implications for other AFT studies in sedimentary basins, as samples that fail the chi-squared test and show no relationship with D_{par} or wt% Cl kinetic parameters, may actually contain multiple kinetic populations when data are sorted by the multi-compositional

kinetic parameter r_{mr0}. Conversely, samples that pass the chi-square test as a single population might be amalgamations of separate kinetic populations, and models that do not acknowledge these relationships may yield spurious thermal histories.

This study also connects diffusion kinetics in the AHe system with variation in AFT annealing kinetics. Whereas this relationship has been previously discussed [*Gautheron et al.*, 2013], Chapters 3 to 5 are the first to use relationships between chemistry derived kinetics and AHe date dispersion from the same sample to quantify maximum temperatures and plausible cooling rates. Results from these three studies emphasize how the temperature sensitivity of the AHe system can vary by 10's of degrees Celsius given natural variation in apatite chemistry. Thermal history models that do not account for differences in annealing kinetics may generate inaccurate estimates of paleotemperatures and cooling history.

Chapters 2 to 4 highlight the effect of pre-depositional history on helium diffusion in detrital thermochronometers. Whereas the relationship between pre-depositional radiation damage accumulation and inherited helium on (U-Th)/He dates is well documented for the ZHe system [*Guenthner et al.*, 2015; *Powell et al.*, 2016], Chapter 4 is the first study to invoke a similar relationship in the AHe system. These results illustrate that apatite with retentive annealing kinetics may retain pre-depositional radiation damage during burial heating. Consequently, detrital apatite populations that include sources from ancient terranes, such as Archean crust, may produce older AHe dates than can be explained by traditional date-radiation damage relationships.

Whereas the study in Chapter 5 attempted to calibrate the conodont apatite (U-Th)/He system (CAHe), the results were complex due to low U-Th concentrations of the conodonts and issues stemming from some combination of diagenetic U-Th leaching, ^{4}He trapping in pore

spaces, and ^{4}He implantation from authigenic recrystallization of conodont bioapatite. Results from Chapter 5 suggest that the CAHe method may be applicable to quickly cooled geologic terranes, but is of limited utility in regions with protracted cooling histories. However, the other thermochronometers employed in the study highlight how modeling of well characterized ZHe, AHe and AFT samples reveal significantly more time-temperature information than techniques presently available for carbonate horizons [e.g., *Landman et al.*, 2016; *Copeland et al.*, 2015; *Cros et al.*, 2014]. To that extent, carbonate basin analysis would benefit from focusing on the few horizons that do contain accessory minerals. In the case of the Anticosti Island study, low-temperature thermochronology data reveal a Mesozoic cooling history previously undocumented in the basin.

The thermochronology data presented in this thesis emphasize just how few kinetic variables can be constrained *a priori*. Variables such as grain size, volume and U-Th concentrations can be measured during analysis, but information on the chemistry, annealing kinetics, and pre-depositional history are difficult, if not impossible, to constrain prior to destructive (U-Th)/He measurements. Whereas these variables can be accounted for separately via forward modeling, an inverse modeling approach that combines AFT, AHe, and ZHe data from detrital sources ignores the contemporary understanding of diffusion and annealing kinetics and are likely to misrepresent the time-temperature history of a sample. This discrepancy between variables that can and cannot be quantified *a priori* leads to the following observation: the recent advances in the field of thermochronology towards methods that increase "n" are encouraging, as intrasample data trends can be assessed more confidently with larger, statistically relevant sample sizes. However, more thermochronology data per sample do not necessarily equate better resolution on thermal history. Methodological advancements in data

acquisition should be matched by the refinement of helium diffusion and multi-compositional fission track annealing models, the development of techniques that quantify grain-specific variables prior to an analysis, and an improved understanding on the ways in which all techniques are integrated.

6.4. Future work

Whereas the results of this study provide insight into both the thermal history of the Mackenzie Plain and application of thermochronology to slowly cooled geologic terranes, they also reveal many avenues for future investigation. A complementary study to the ZHe traverse of the Mackenzie Mountains in Chapter 2 [*Powell et al.*, 2016] would be an investigation of along strike differences in cooling history for each of the anticlines. The Tawu anticline is of particular interest due to its similarity to the modeled cooling history of the deformation front compared with more proximal structures (Foran and Tigonankweine anticlines). The thermal history of the Ten Stone Ranges structural complex and Shattered Range anticline should be investigated, as these structures were not sampled in this study. The highly deformed Ten Stone Ranges structural complex marks the transition from the continuous southern Plateau Fault of this study with the en-echelon thrusts of its northern expression [*Gordey et al.*, 2011]. Determining its thermal history would constrain the timing of this structural transition and provide insight as to the exhumation history of the Plateau Fault. Similarly, a thermochronology study of the Shattered Range anticline, which lies in the footwall of the Plateau Fault along strike of the Tigonankweine anticline would reveal whether structures at similar positions in the fold-thrust belt have comparable exhumation histories.

A subset of the AHe and AFT data presented in Chapter 4 evoke a late Cenozoic cooling history. A low-temperature thermochronology study that spanned the Franklin Mountains,

Mackenzie Mountains and Selwyn basin may reveal the extent and source of this cooling signature. Similarly, a low-temperature thermochronology study of the Beaver River Structure in the southern Mackenzie Mountains would provide conclusive insight into the geologic history beneath the sub-Cretaceous unconformity. This structure marks the abrupt northern termination of Permian-Triassic strata at the Beaver Fault, and a multi-kinetic AFT and AHe study from either side of the fault would reveal the timing the erosional history of Paleozoic to Mesozoic strata.

Whereas low-temperature thermochronology data from the D002 and D003 wells of Anticosti Island were unable to distinguish between two plausible thermal histories (Chapter 5), a broader investigation into the low-temperature thermochronology of Anticosti Island would surely evince the regional cooling history and its ramifications for the Mesozoic geologic history of the Gulf of the St. Lawrence. Such a study would be similar to Chapter 4 and involve sampling the Mingan Formation sandstone from each exploration well, as well as samples from the Grenville basement where available. Due to the range of present day and paleotemperatures experienced by strata across Anticosti Island, the multi-kinetic detrital AFT modeling would resolve many regional geologic questions, including the timing of maximum burial, probable age of sediments in the basin offshore, the effect of Jurassic dike emplacement, and the overall unroofing history for the western Anticosti Basin.

References

Aitken, J. D., Cook. D. G., and C. J. Yorath (1982), Upper Ramparts River (106 G) and Sans Sault Rapids (106 H) map areas, district of Mackenzie, *Geol. Surv. Canada, Mem.*, *388*, 48 p.

Ault, A. K., R. M. Flowers, and S. A. Bowring (2009), Phanerozoic burial and unroofing history of the western Slave craton and Wopmay orogen from apatite (U–Th)/He thermochronometry, *Earth Planet. Sci. Lett.*, *284*(1-2), 1–11,

doi:10.1016/j.epsl.2009.02.035.
Ault, A. K., R. M. Flowers, and S. A. Bowring (2013), Phanerozoic surface history of the Slave craton, *Tectonics*, *32*(5), 1066–1083, doi:10.1002/tect.20069.
Blusson, S. (1971), Sekwi Mountain map-area, Yukon Territory and district of Mackenzie, *Geol. Surv. Canada, Pap. 71-22*, 17 p.
Copeland, P., K. Cox, and E. B. Watson (2015), The potential of crinoids as (U+Th+Sm)/He thermochronometers, *Earth Planet. Sci. Lett.*, *422*(July), 1–10, doi:10.1016/j.epsl.2015.04.007.
Cros, A., C. Gautheron, M. Pagel, P. Berthet, L. Tassan-Got, E. Douville, R. Pinna-Jamme, and P. Sarda (2014), 4He behavior in calcite filling viewed by (U-Th)/He dating, 4He diffusion and crystallographic studies, *Geochim. Cosmochim. Acta*, *125*, 414–432, doi:10.1016/j.gca.2013.09.038.
Dixon, J. (1999), Mesozoic-Cenozoic stratigraphy of the northern Interior Plains and Plateaux, Northwest Territories, *Geol. Surv. Canada, Bull.*, *536*, 56 p.
Dusel-bacon, C., M. A. Lanphere, W. D. Sharp, P. W. Layer, and V. L. Hansen (2002), Mesozoic thermal history and timing of structural events for the Yukon – Tanana Upland , east-central Alaska : ^{40}Ar / ^{39}Ar data from metamorphic and plutonic rocks, *Can. J. Earth Sci.*, *39*, 1013–1051, doi:10.1139/E02-018.
Eldrett, J. S., D. R. Greenwood, I. C. Harding, and M. Huber (2009), Increased seasonality through the Eocene to Oligocene transition in northern high latitudes., *Nature*, *459*, 969–973, doi:10.1038/nature08069.
Evans, N. J., B. I. A. McInnes, B. McDonald, M. Danišík, T. Becker, P. Vermeesch, M. Shelley, E. Marillo-Sialer, and D. B. Patterson (2015), An in situ technique for (U–Th–Sm)/He and U–Pb double dating, *J. Anal. At. Spectrom.*, *30*(7), 1636–1645, doi:10.1039/C5JA00085H.
Fallas, K. M., and R. B. MacNaughton (2014), Geology, Carcajou Canyon (northwest), Northwest Territories, *Geol. Surv. Canada, Can. Geosci. Map*, (94), doi:10.4095/292286.
Feinstein, S., P. W. Brooks, M. G. Fowler, L. R. Snowdon, and G. K. Williams (1988a), Families of oils and source rocks in the central Mackenzie corridor: a geochemical oil-oil and oil-source rock correlation, *Can. Soc. Pet. Geol. Mem.*, *15*, 543–552.
Feinstein, S., P. W. Brooks, T. Gentzis, F. Goodarzi, L. R. Snowdon, and G. K. Williams (1988b), Thermal maturity in the Mackenzie Corridor, Northwest and Yukon Territories, Canada, *Geol. Surv. Canada, Open File 1944*, 65 p., doi:10.4095/130457.
Feinstein, S., G. K. Williams, L. R. Snowdon, F. Goodarzi, and T. Gentzis (1991), Thermal maturation of organic matter in the Middle Devonian to Tertiary section, Fort Norman area (central Mackenzie Plain), *Can. J. Earth Sci.*, *28*(7), 1009–1018, doi:10.1139/e91-092.
Feinstein, S., D. R. Issler, L. R. Snowdon, and G. K. Williams (1996), Characterization of major unconformities by paleothermometric and paleobarometric methods: application to the Mackenzie Plain, Northwest Territories, Canada, *Bull. Can. Pet. Geol.*, *44*(1), 55–71.
Gautheron, C., J. Barbarand, R. A. Ketcham, L. Tassan-Got, P. Van Der Beek, M. Pagel, R. Pinna-Jamme, F. Couffignal, and M. Fialin (2013), Chemical influence on α-recoil damage annealing in apatite: Implications for (U-Th)/He dating, *Chem. Geol.*, *351*(August 2013), 257–267, doi:10.1016/j.chemgeo.2013.05.027.
Gordey, S. P., J. D. Macdonald, E. C. Turner, and D. G. F. Long (2011), Chapter 5. Structural Geology of the Central Mackenzie Mountains, in *Geology of the Central Mackenzie Mountains of the Northern Canadian Cordillera, Sekwi Mountain (105P), Mount Eduni (106A), and the northwestern Wrigley Lake (95M) Map Areas, Northwest Territories*, edited

by E. Martel, E. C. Turner, and B. J. Fischer, pp. 215 – 250, NWT Geoscience Office.
Guenthner, W. R., P. W. Reiners, P. G. DeCelles, and J. Kendall (2015), Sevier belt exhumation in central Utah constrained from complex zircon (U-Th)/He data sets: Radiation damage and He inheritance effects on partially reset detrital zircons, *Geol. Soc. Am. Bull.*, *127*(3-4), 1–26, doi:10.1130/B31032.1.
Hadlari, T. (2015), Oil migration driven by exhumation of the Canol Formation oil shale: A new conceptual model for the Norman Wells oil field, northwestern Canada, *Mar. Pet. Geol.*, *65*(May), 172–177, doi:10.1016/j.marpetgeo.2015.03.027.
Hannigan, P. K., D. W. Morrow, and B. C. MacLean (2011), Petroleum resource potential of the northern mainland of Canada (Mackenzie Corridor), *Geol. Surv. Canada, Open File 6757*, 271 p., doi:289095.
Hyndman, R. D., P. Flück, S. Mazzotti, T. J. Lewis, J. Ristau, and L. Leonard (2005), Current tectonics of the northern Canadian Cordillera, *Can. J. Earth Sci.*, *42*(6), 1117–1136, doi:10.1139/e05-023.
Issler, D. R. D., A. Grist, and L. Stasiuk (2005), Post-Early Devonian thermal constraints on hydrocarbon source rock maturation in the Keele Tectonic Zone, Tulita area, NWT, Canada, from multi-kinetic apatite fission track thermochronology, vitrinite reflectance and shale compaction, *Bull. Can. Pet. Geol.*, *53*(4), 405–431, doi:10.2113/53.4.405.
Landman, R. L., R. M. Flowers, N. A. Rosenau, and J. Powell (2016), Conodont (U-Th)/He thermochronology: A case study from the Illinois Basin, *Earth Planet. Sci. Lett.*, *456*, 55–65, doi:10.1016/j.epsl.2016.10.003.
Maclean, B. C., and D. G. Cook (1999), Salt tectonism in the Fort Norman area, Northwest Territories, Canada, *Bull. Can. Pet. Geol.*, *47*(2), 104–135.
MacLean, B. C., K. M. Fallas, and T. Hadlari (2014), The multi-phase Keele Arch, central Mackenzie Corridor, Northwest Territories, *Bull. Can. Pet. Geol.*, *62*(2), 68–104, doi:10.2113/gscpgbull.62.2.68.
MacNaughton, R. B., K. M. Fallas, and W. Zantvoort (2008), Qualitative assessment of the Plateau Fault (Mackenzie Mountains, NWT) as a conceptual hydrocarbon play, *Geol. Surv. Canada, Open File 5831*, 29 p..
Mair, J. L., C. J. R. Hart, and J. R. Stephens (2006), Deformation history of the northwestern Selwyn Basin, Yukon, Canada: Implications for orogen evolution and mid-Cretaceous magmatism, *Bull. Geol. Soc. Am.*, *118*(3-4), 304–323, doi:10.1130/B25763.1.
Metcalf, J. R., J. S. Baughman, and R. M. Flowers (2016), Evaluating a new, rapid zircon and titanite dissolution method for (U-Th)/He thermochronology, in *Geological Society of America Annual Meeting 2016*, Denver, Colorado.
Morrow, D. W., and W. C. Miles (2000), The Beaver River Structure: a cross-strike discontinuity of possible crustal dimensions in the southern Mackenzie Fold Belt, Yukon and Northwest territories, Canada, *Bull. Can. Pet. Geol.*, *48*(1), 19–29.
Nielsen, S. B., O. R. Clausen, and E. Mcgregor (2015), Basin%Ro: A vitrinite reflectance model derived from basin and laboratory data, *Basin Res.*, 1–22, doi:10.1111/bre.12160.
Pickering, J. E., W. Matthews, and B. Guest (2015), In-Situ apatite laser ablation U-Th-Sm/He dating, methods and challenges, in *American Geophysical Union Fall Meeting 2015*, San Francisco, California.
Powell, J., D. Schneider, D. Stockli, and K. Fallas (2016), Zircon (U-Th)/He thermochronology of Neoproterozoic strata from the Mackenzie Mountains, Canada: Implications for the Phanerozoic exhumation and deformation history of the northern Canadian Cordillera,

Tectonics, *35*(3), 663–689, doi:10.1002/2015TC003989.
Powell, J., D. A. Schneider, and D. R. Issler (2017), Application of multi-kinetic apatite fission track and (U-Th)/He thermochronology to source rock thermal history: a case study from the Mackenzie Plain, NWT, Canada, *Basin Res.*, doi:10.1111/bre.12233.
Snowdon, L. R., P. W. Brooks, G. K. Williams, and F. Goodarzi (1987), Correlation of the Canol Formation source rock with oil from Norman Wells, *Org. Geochem.*, *11*(6), 529–548, doi:10.1016/0146-6380(87)90008-8.
Staples, R. D., H. D. Gibson, M. Colpron, and J. J. Ryan (2016), An orogenic wedge model for diachronous deformation, metamorphism, and exhumation in the hinterland of the northern Canadian Cordillera, *Lithosphere*, (1), L472.1–20, doi:10.1130/L472.1.
Sweeney, J. J., and A. K. Burnham (1990), Evaluation of a simple model of vitrinite reflectance based on chemical kinetics, *Am. Assoc. Pet. Geol. Bull.*, *74*(10), 1559–1570.
Thomson, D., C. J. Schröder-Adams, T. Hadlari, G. Dix, and W. J. Davis (2011), Albian to Turonian stratigraphy and palaeoenvironmental history of the northern Western Interior Sea in the Peel Plateau Region, Northwest Territories, Canada, *Palaeogeogr. Palaeoclimatol. Palaeoecol.*, *302*(3-4), 270–300, doi:10.1016/j.palaeo.2011.01.017.
Tian, Y., N. Qiu, B. P. Kohn, C. Zhu, S. Hu, A. J. W. Gleadow, and B. I. a. McInnes (2012), Detrital zircon (U–Th)/He thermochronometry of the Mesozoic Daba Shan Foreland Basin, central China: Evidence for timing of post-orogenic denudation, *Tectonophysics*, *570-571*, 65–77, doi:10.1016/j.tecto.2012.08.010.

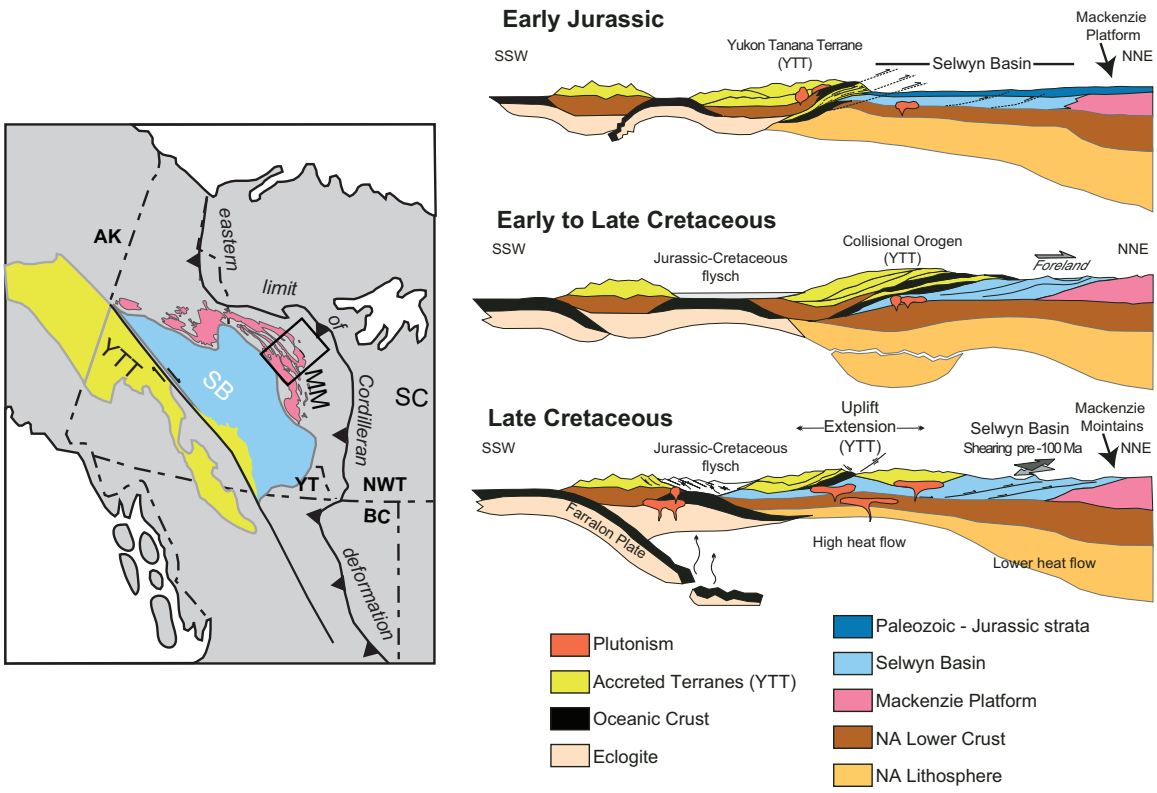

Fig. 1: Schematic cross sections of the Jurassic through Late Cretaceous evolution of the northern Canadian Cordillera (modified after Mair et al., 2006). Inset map: YTT = Yukon-Tanana terrane; SB = Selwyn Basin; MM = Mackenzie Mountains; SC = Slave craton. Black box delineates the location of schematic block diagrams in Figs. 2 and 3.

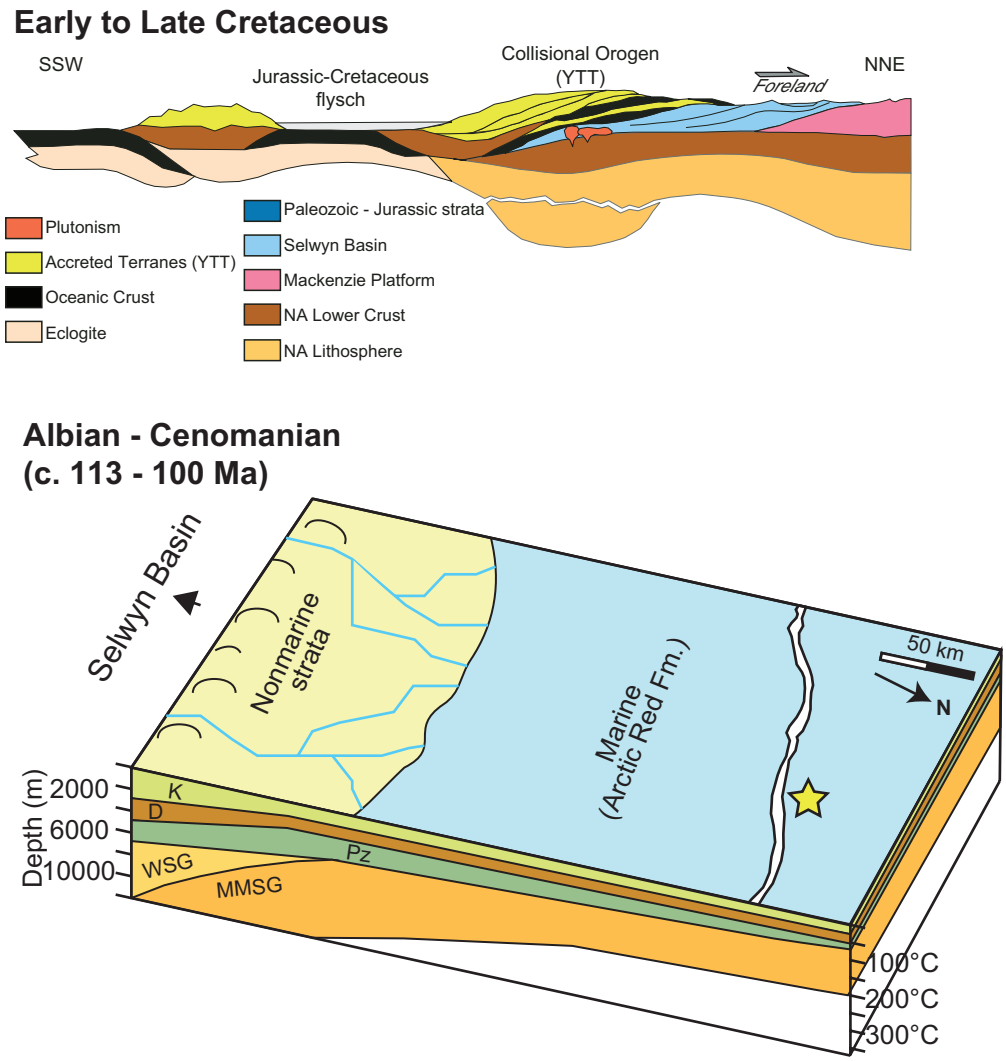

Fig. 2: Schematic block diagram of the Mackenzie Mountains fold-thrust belt from the Albian to Cenomanian. Geology is modified after Fig. 9 of Chapter 2 [*Powell et al.*, 2016]. Star indicates the present day location of Norman Wells, whereas the white polygon references the location of the Mackenzie River.

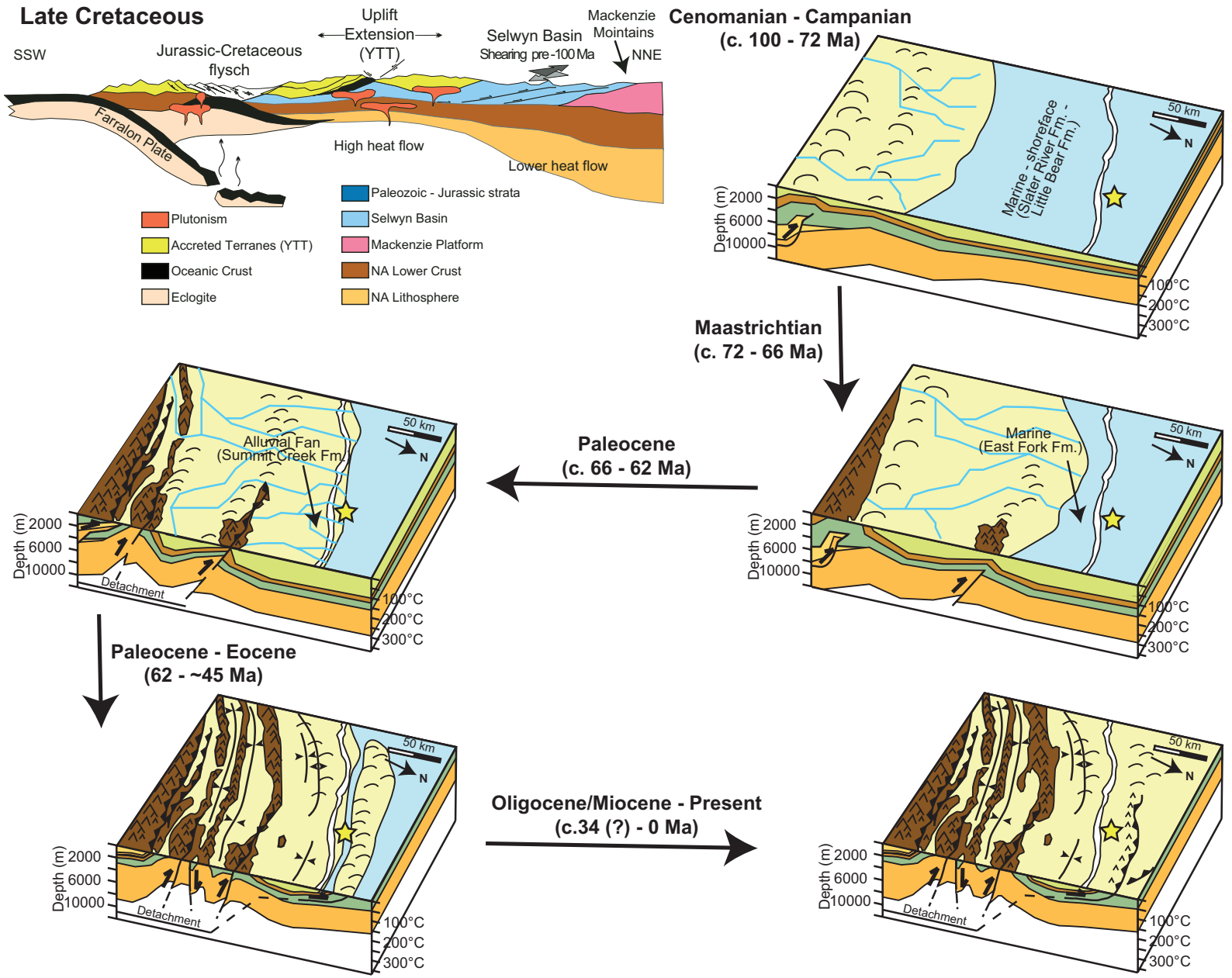
Late Cretaceous
SSW
Jurassic-Cretaceous flysch
Uplift
Extension
(YTT)
Selwyn Basin
Shearing pre-100 Ma
Mackenzie Mointains
NNE
Farralon Plate
High heat flow
Lower heat flow
Plutonism
Accreted Terranes (YTT)
Oceanic Crust
Eclogite
Paleozoic - Jurassic strata
Selwyn Basin
Mackenzie Platform
NA Lower Crust
NA Lithosphere
Cenomanian - Campanian
(c. 100 - 72 Ma)
Marine - shoreface
(Slater River Fm. -
Little Bear Fm.)
50 km
N
Depth (m)
2000
6000
10000
100°C
200°C
300°C
Maastrichtian
(c. 72 - 66 Ma)
Marine
(East Fork Fm.)
Paleocene
(c. 66 - 62 Ma)
Alluvial Fan
(Summit Creek Fm.)
Detachment
Paleocene - Eocene
(62 - ~45 Ma)
Oligocene/Miocene - Present
(c.34 (?) - 0 Ma)

Fig. 3 (previous page): Schematic block diagrams that illustrate the Late Cretaceous propagation of the fold-thrust belt towards the foreland. Geology is modified after Fig. 9 of Chapter 2 [*Powell et al.*, 2016]. Star indicates the present day location of Norman Wells, whereas the white polygon references the location of the Mackenzie River.